Acta Physica Hungarica

VOLUME 63, NUMBERS 1–2, 1988

Akadémiai Kiadó, Budapest

ACTA PHYS. HUNG. APAHAQ 63 (1–2) 1–200 (1988) HU ISSN 0231–4428

ACTA PHYSICA HUNGARICA

A JOURNAL OF THE HUNGARIAN ACADEMY OF SCIENCES

EDITED BY

I. KOVÁCS

Acta Physica publishes original papers on subjects in physics. Papers are accepted in English, French, German and Russian.

Acta Physica is published in two yearly volumes (4 issues each) by

AKADÉMIAI KIADÓ
Publishing House of the Hungarian Academy of Sciences
H-1054 Budapest, Alkotmány u. 21

Subscription information

Orders should be addressed to

KULTURA Foreign Trading Company
1389 Budapest P.O. Box 149

or to its representatives abroad.

Acta Physica Hungarica is abstracted/indexed in Chemical Abstracts, Current Contents–Physical, Chemical and Earth Sciences, Mathematical Reviews, Science Abstracts, Physics Briefs, Risk Abstracts

ACTA PHYSICA HUNGARICA

VOLUME 63

AKADÉMIAI KIADÓ, BUDAPEST

1988

CONTENTS

VOLUME 63

FLUIDS, PLASMAS AND ELECTRIC DISCHARGES

CONDENSED MATTER

OPTICS

Acta Physica Hungarica 63(1–2), pp. 3–5 (1988)

SÁNDOR SZALAY

1909 - 1987

The life and the works of Professor Sándor Szalay (A. Szalay), Member of the Hungarian Academy of Sciences, are characterized by his wide intellectual horizon and broad scientific interests.

His scientific career commenced in the first half of the thirties while working in the institutes of three Nobel prize winners; one after the other he had the opportunity to work with Szent-Györgyi in Szeged, Debye in Leipzig and Rutherford in Cambridge. His first published articles reported on remarkable results on the chemical effects of ultrasound and on some special features of electrolytes. It was Rutherford of the Cavendish Laboratory in Cambridge who influenced him the most. Returning from England to Debrecen in 1936, Szalay became the pioneer of nuclear physics research in Hungary. In his first works dealing with nuclear physics he studied the excitation functions of various nuclear reactions by means of radioactive alpha sources. He carried out his work in a special experimental arrangement of his own invention. Later he demonstrated (in collaboration with Gy. Csikai) the recoil effect by neutrinos in the decay of ^{6}He in a Wilson chamber.

During his life, in addition to nuclear physics, he dealt with a wide spectrum of

issues from nuclear geochronology by mass spectroscopy to medical research using radioactive tracer techniques. The radioactivity in the biosphere was also a subject in which he was interested. The measurement of the radioactivity of precipitation was started in Debrecen in 1952. The usage of the ^{14}C dating method for different purposes in Hungary was initiated by him. During the last period of his life he became very much interested in trace element research, primarily this concerned various types of foods; and for some years before his death he dealt with the primordial atmosphere of the Earth by means of quadrupole mass spectroscopy.

From the outset Professor Szalay devoted himself to instrumental research, too. An ingenious experimental approach mentioned above was of immense help to him in producing his first results in nuclear physics in Hungary. He then initiated and established, in Debrecen, nuclear detection techniques and electronics, as well as concerning himself with the construction of electrostatic accelerators and with the development of a new type of beta- and alpha-spectrometers.

The activities of Professor Szalay were not limited to fundamental scientific research even if the really interdisciplinary topics are also considered. He was very much concerned with practical aspects. Just after the Second World War he instigated the search for uranium in Hungary, recognizing the importance of nuclear power in the future supply of energy. The discovery of uranium on Hungarian territory was carried out later by a large scale geological survey initiated by and based on Szalay's findings. This work of Szalay was, in fact, conducted in collaboration with A. Földvári, professor of geology, utilizing portable equipment constructed by Szalay himself, together with his coworkers. This search for uranium and the study of radioactivity of Hungarian coal led him to the discovery of the mechanism of uranium enrichment in Nature by humic acids which, again, represented an outstanding scientific achievement. He then recognized that not only the uranium but other cations are also strongly adsorbed by humic acids, and this is the reason for some microelement starvation of plants and animals in peat soils. On this basis the microelement fertilization of plants and the microelement nutrition of animals were introduced by him.

Radioactive isotopes were applied by Szalay not only in medical research but also in medical practice. The application of radioactive isotopes (^{131}I) in Hungary was due to him. He prompted several applied works in environmental topics, too. His practical interest is to some extent demonstrated by his six patents.

Professor Szalay was a top-level research worker, but at the same time he was an enthusiastic, devoted, and highly successful teacher of physics. He taught generations of medical students, teachers and physics students during his professorship first at the Faculty of Medicine and later at the Faculty of Sciences in Debrecen. A great deal of his energy was devoted not only to lecturing but also to the demonstration experiments during lectures as well as to the experiments relating to the laboratory practice for the students. Despite these activities he set aside a substantial part of his time to organizational work in the Experimental Physics Department of Debrecen University.

The main result of this successful work was the foundation of the Institute for Nuclear Research of the Hungarian Academy of Sciences (ATOMKI). Here he was able to use his best creative talents as well as amply demonstrating his abilities as a scientific organizer. The institute developed step by step from one with a small staff to the present stage

of having a total of about three-hundred people. Academician Szalay selected the best research workers year by year, this extended to the laboratory assistants, the technicians and the administrators. He designated the main research directions and guided the style of research work in the institute and the whole atmosphere of it by his broad interdisciplinary research horizon and his experimental-instrumental approach. Professor Szalay himself regarded ATOMKI as his greatest work and we feel that he was right in this.

Acta Physica Hungarica mourns Academician Sándor Szalay; the Editorial Board of the journal will sorely miss his presence.

D. Berényi

Acta Physica Hungarica 63(1–2), pp. 7–11 (1988)

A PROPOSED MODEL FOR THE PHOTOLUMINESCENCE OF ZnS : CdS : Ag : Ni : Co PHOSPHORS

Z.S. EL MANDOUH
Electron Microscope and Thin Films Laboratory
National Research Center, Dokki, Cairo, Egypt

(Received in revised form 26 October 1986)

Phosphors with 41% ZnS : 59% CdS : 0.009% Ag : 0.00065% Ni and containing various concentrations of Co dopant are investigated with regard to the fundamental photoluminescence processes involved. The wavelengths of maximum emission intensities in the spectral distributions of excitation and emission remain unaltered with increase in Co concentration. Thus the energy level structures with the silver impurity centres are not affected by the cobalt content.

The temperature dependence of thermoluminescence has been studied over the temperature range of 77 K to 800 K. The thermoluminescence curves show peaks due to chlorine, cadmium, cobalt and nickel impurities. A new trap is identified at 0.065% concentration of cobalt which has an energy of 1.09 eV. An energy band model is proposed to explain this phenomenon. It is suggested that this peak is due to the association of cobalt and silver centres.

Introduction

Impurity-activated ZnS-type phosphors with additional nickel, cobalt or iron impurities as luminescence quenchers have been studied by many investigators. These impurities form trapping states at which electrons and holes may recombine without giving visible emission. It is well known that cobalt in phosphors of ZnS-type causes a decrease of visible luminescence within the visible range [1]. On the other hand Garlick and Dumbleton [2] found the presence of cobalt in the phosphors to be the reason for an infrared emission with a peak near 3 μ. Furthermore, in ZnS and (Zn, Cd)S cobalt creates an electron trap about 0.52 eV below the conduction band, as has been investigated by Hoogenstraaten [3] . Recently, the transfer of energy from luminescence centres to the Co has been studied by means of electrophotoluminescence and electroluminescence [4] . From the experiment it is found that energy is transported by free carriers. Gumlich [5] explained the changes in optical properties by additional radiation and by cooling the crystals by charge transfer processes $Co^{++} \rightleftharpoons Co^{+}$. Elmanharawy [6] detected a glow peak due to Ni which had an energy of 0.78 eV.

The aim of the present work is to study the effect of cobalt on photoluminescence of ZnS : CdS : Ag : Ni : Co.

Experimental

All phosphors, prepared in the presence of chlorine, were in powder form.

The dobule chopper technique [6] was developed for measuring excitation and emission spectra. Measured excitation and emission spectra were both corrected for the variation of photomultiplier response and the angular dispersion of the prism material with wavelength. A small cryostat with a large optical aperture, easy to set up and similar to that set by Garlick [7] was applied. The temperature can be varied from 77 K to 800 K.

Results and discussion

Figure 1 shows the variation of excitation efficiency with wavelength of the exciting radiation of a constant intensity. The curves were recorded at room temperature. Excitation occurs in two bands, fundamental absorption band and a second band of longer wavelength. The curves show some indication of tails extending into longer wavelength regions of the spectra, which attributed to the perturbation of the silver activators centres by nickel and cobalt. The wavelength of maximum excitation efficiency is independent of the cobalt concentration.

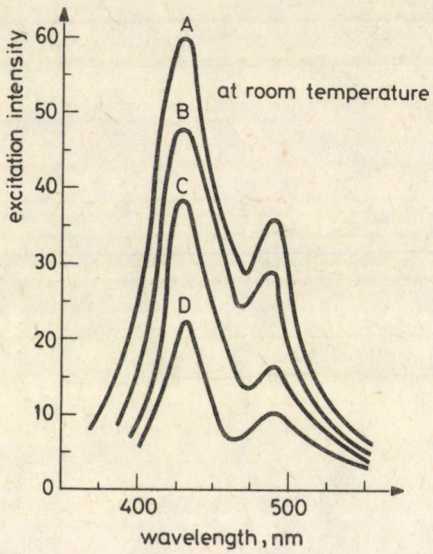

Fig. 1. Excitation spectra for 41% ZnS: 59% Cds: 0.009% Ag: 0.00065% Ni: x% Co phosphors
A) x = 0.00 B) x = 0.00013
C) x = 0.00325 D) x = 0.065

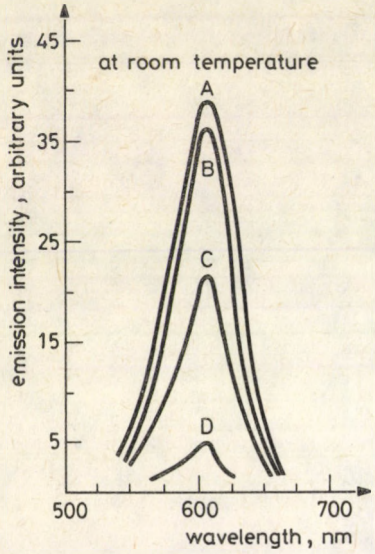

Fig. 2. Emission spectra for 41% ZnS: 59% CdS: 0.009% Ag: 0.00065% Ni: x% Co phosphors
A) x = 0.00 B) x = 0.00013
C) x = 0.00325 D) x = 0.065

The spectrum is the same as ZnS : CdS : Ag and ZnS : CdS : Ag : Ni phosphors. This shows that the energy level structure of the phosphor is not changed by the addition of cobalt. The Figure shows also a decrease in excitation efficiency due to the increase of quenching action with the increase of cobalt concentration.

Emission spectra recorded at room temperature are shown in Fig. 2. The wavelengths of the silver emission band are very similar to those reported before [6] for ZnS : CdS : Ag and ZnS : CdS : Ag : Ni. No new emission due to nickel or cobalt is found in the wavelength range of 400 — 900 nm. It is clear that the increase in cobalt concentration causes the emission intensity to decrease. This gives evidence that the energy level structure with silver centre remains unaltered by the inclusion of coactivators and this agrees well with Schön [8] and was elaborated by Klasens and his coworkers [9—11] .

Introduction of Co in ZnS:Cu produces a peak in the glow curve as mentioned by Krylova [12] which increases in height with increasing amounts of cobalt. The original low tempera-

ture glow peak is reduced which is probably caused by an increasing degree of retrapping of the electrons released from the Cl traps, in the deeper Co traps. This is possible because even after excitation to saturation the Co traps are never completely filled.

Thermoluminescence curves for phosphors with varying cobalt concentration are shown in Fig. 3. Curve (A) for cobalt free phosphors exhibits three thermal glow peaks, which have been clarified as due to trapping states associated with chlorine, cadmium and nickel impurities. The variation of heating rate method suggested by Booth [13] was used to estimate the energy depths of such traps which are 0.26 eV, 0.53 eV and 0.78 eV, respectively. The energy depths associated with chlorine and cadmium are similar to those reported in ZnS : CdS (Ag, Co) phosphors [7] . It is of interest to mention that a thermoluminescence peak due to trapping states caused by nickel dopant has been found to appear only when the cadmium sulphide concentration in the matrix is 59% or more.

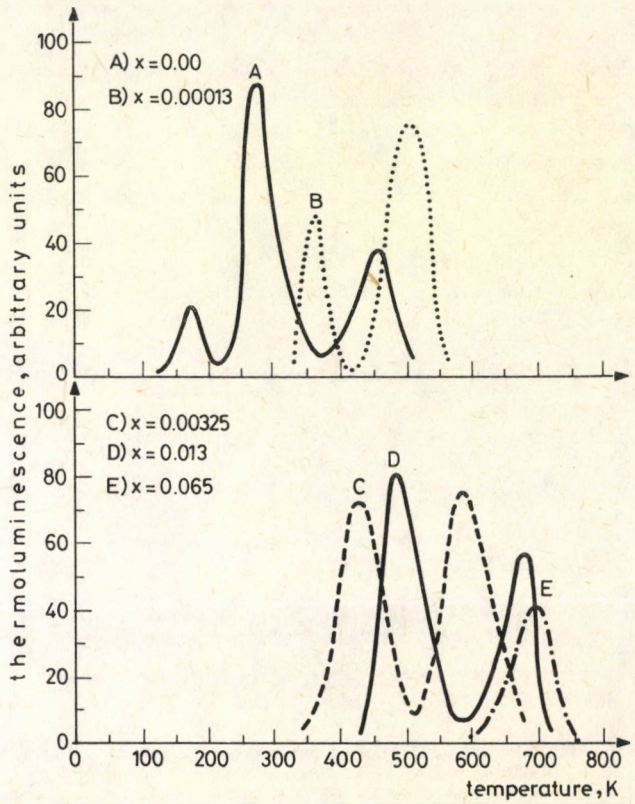

Fig. 3. Thermoluminescence curves for 41% ZnS : 59% CdS : 0.00065% Ni : x% Co phosphors

The absence of this peak from thermoluminescence curves of phosphors of low concentration of CdS is due to the fact that such peak appears at very high temperature (800 K) in case of ZnS(Ag:Ni).

A peak at 310 K appears which is clarified as due to trapping states associated with cobalt which is similar to that observed by Hoogenstraaten [3] . As cobalt concentration increases the peaks due to chlorine and cadmium decrease in height until cobalt concentration of 0.00325 % where they disappear completely (Curve C). This is due to the increased degree of retrapping, into the deeper nickel and cobalt trapping states, of electrons released from shallower traps during the heating process.

A new trap with energy depth of 1.09 eV appears at a temperature higher than 500 K and it shifts to higher temperature as cobalt concentration increases and it decreases in height as shown in curves (D, E). This new peak is attributed to the association of activator (Ag) and coactivator (Co) centres.

During the preparation of these phosphors, the silver impurity ion enters the lattice to form a luminescent centre in accordance with Kroger's theory of charge compensation [14] . Thus, there is a possibility that the emission and trapping phenomena originate in activator — coactivator pairs at neighbouring sites. Since emission spectra of silver, copper, gold and self-activated ZnS phosphors are unchanged when different halogen or trivalent cation coactivator are employed, it has been suggested by Kröger [14] that the activator centre consists of a M^{+1} (S_4^{-2}) activator group, well separated from the activator. However, Prener and Williams [15] have proposed that associated pairs of activators with second-nearest neighbour coactivators constitute the luminescent and trapping centres in ZnS phosphors.

It is observed from our results that the energy level structure with silver centres remains unchanged by the inclusion of the coactivator. This is agrees well with Schon [16] and Klasens [17] .

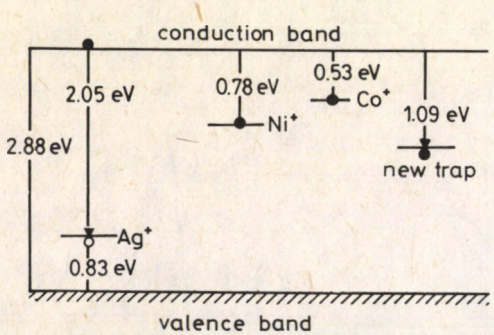

Fig. 4. The proposed energy model

The energy band gap of these phosphors is 2.88 corresponding to a matrix lattice concentration of 41% ZnS : 59% CdS. From emission spectra measurements, the silver level is 2.05 eV below the lower edge of the conduction band. The proposed energy model for such phosphors is shown in Fig. 4. It is very difficult to know the origin of this new peak from thermoluminescence measurements only. Conductivity and electron spin resonance measurements are necessary to elucidate the origin of this new peak.

References

1. N. Arpiarian and D. Curie, C.R. Acad. Sci. Paris, 234, 75, 1952.
2. G.F.J. Garlick and M.J. Dumbleton, Proc. Phys. Soc., B67, 442, 1954.
3. W. Hoogenstraaten, Philips Res. Repts. 13, 515, 1958.
4. I. Broser, H.E. Cumblich and R. Moser, Physik Verhandl., 3, 227, 1963; H.E. Gumlich Meeting.
5. H.E. Gumlich and H.J. Schulz, J. Phys. Chem. Solids, 27, 187, 1966.
6. M.S. El Manharawy, Acta Physica Polonica, A40, 421, 1971.
7. G.F.J. Garlick, Handbuch der Phys., 26, 1, 1958.
8. M. Schön, Z. Physik, 119, 463, 1942.
9. H.A. Klasens, Nature, 158, 306, 1946.
10. H.A. Klasens, W. Ramsden and C.J. Quantie, J. Opt. Soc. Am., 38, 60, 1948.
11. M.E. Wise and H.A. Klasens, J. Opt. Soc. Am., 38, 226, 1948.
12. E.S. Krylova, Dokl. Akad. Nauk. S.S.S.R., 64, 495, 1949.
13. A.H. Booth, Can. J. Chem., 32, 214, 1954.
14. F.A. Kröger, J. Opt. Soc. Am., 39, 670, 1949.
15. F.A. Kröger and J. Dikhoff, Physica, 16, 297, 1950.
16. M. Schön, Z. Naturf., 6, 251, 1951.
17. H. Klasens, J. Electrochem. Soc., 100, 72, 1953.

Acta Physica Hungarica 63(1–2), pp. 13–16 (1988)

A NONLINEAR EXTENSION OF THE LOCAL FORM OF GYARMATI'S GOVERNING PRINCIPLE OF DISSIPATIVE PROCESSES

B. NYÍRI
Institute of Physics, Technical University
1521 Budapest, Hungary

(Received in revised form 26 April 1987)

A proof of the validity of Gyarmati's Principle to non-Onsagerian constitutive equations is given. A generalisation of the Principle, independent of reciprocity relations, is suggested for nonlinear constitutive equations.

Introduction

Recently, Verhás has given "An Extension of the Governing Principle of Dissipative Processes to Nonlinear Constitutive Equations" [1] on the basis of the Onsager Reciprocity Relations (ORR). This Principle was proposed by Gyarmati in the sixties for linear and for certain nonlinear constitutive equations [2, 3]:

$$\mathcal{L} = \sigma - \dot{\Phi} - \dot{\Psi} = \max \quad . \tag{1}$$

Here σ is the entropy production, which is a bilinear function of the J_i fluxes and X_i forces:

$$\sigma = \sum_i J_i X_i \quad . \tag{2}$$

The functions Φ and Ψ are dissipation potentials. The first depends on the J_i, β type and the second on the X_i, α type variables, viz.

$$\Phi = \frac{1}{2} \sum_{i;k} R_{ik} J_i J_k \quad ; \quad \Psi = \frac{1}{2} \sum_{i;k} L_{ik} X_i X_k \quad . \tag{3}$$

The conductivity matrix L_{ik} and its inverse, the resistance matrix R_{ik} are positive definite due to the second law of thermodynamics. They are constant in the strictly linear theory, while in the quasilinear theory they depend on the equilibrium state variables Γ_j [3, 4]. These matrices are symmetric in the absence of magnetic field, due to the ORR [3, 4, 5, 6].

The existence of potentials proved to be very useful, especially in the discussion of problems where local constraints and/or constraint type restrictions are present [7, 8, 9, 10, 11]. The potential character of Ψ and Φ, i.e.

$$J_i = \frac{\partial \Psi}{\partial X_i} \; ; \quad X_i = \frac{\partial \Phi}{\partial J_i} \tag{4}$$

is guaranteed by the ORR. In the presence of magnetic field symmetry relations were obtained in a "four-fold representation" by Muschik and Szer [12]. Thus the generalisation

of the Principle to nonlinear equations seemed to demand the generalisation of the ORR as well. Such a generalisation of the ORR was proposed by Gyarmati and by Li [6, 13], assuming

$$\frac{\partial J_i}{\partial X_k} = \frac{\partial J_k}{\partial X_i} \quad . \tag{5}$$

If these conditions hold, the Ψ potential can be constructed, as proved by Verhás [14]. The extension of the Principle based on the existence of dissipation potentials was worked out by Gyarmati and by Farkas and Noszticzius [3, 15]. Relations (5), however, are not consistent with the equations of chemical kinetics, in the customary approach, viz. if the affinities are regarded the thermodynamical forces in the nonlinear region too, as it is usual in the linear approximation [16].

In the linear and symmetric case there is an equivalent form of (1) that reads

$$\mathcal{L} = -\frac{1}{2} \sum_{i;k} R_{ik} \left(J_i - \sum L_{is} X_s\right)\left(J_k - \sum_r L_{kr} X_r\right) = \max. \tag{6}$$

This Gaussian type local form was also proposed by Gyarmati [2, 9], and it offers other ways of generalisations. Actually, Verhás [1] has shown that if the ORR hold in the linear case, then the L_{ik} coefficients can always be chosen to constitute a symmetric matrix, i.e. when the L_{ik}-s and so the R_{ik}-s depend on the forces X_i, too. Thus (6) remains valid, and it is still equivalent to (1). The crucial difference is that Ψ and Φ cease to be potentials.

Though there is no reason to doubt the ORR that are symmetry relations only in the absence of magnetic field [9, 12, 17], it is shown that the symmetry relations are not necessary to the validity of (6), which is thus more general than (1). A generalisation of Gyarmati's Principle for nonlinear constitutive equations without reciprocity relations is also proposed.

1: Non-Onsagerian constitutive equations

For the sake of convenience, let (6) be written in the form

$$\mathcal{L} = \frac{1}{2} \sum_i \left(J_i - \sum_r L_{ir} X_r\right)\left(X_i - \sum_s R_{is} J_s\right) = \max. \tag{7}$$

It can be done even if the matrices L_{ik} and R_{ik} are not symmetric. Necessary conditions of the maximum are

$$\frac{\partial \mathcal{L}}{\partial X_k} = 0 \quad ; \quad \frac{\partial \mathcal{L}}{\partial J_i} = 0 \, . \tag{8}$$

Thus, regarding the first group of these equations,

$$J_j - \sum_r L_{kr} X_r - \sum_i L_{ik} \left(X_i - \sum_s R_{is} J_s\right) = 0 \tag{9}$$

must hold, that by matrix notation, after rearrangement, reads

$$\left(\underline{\underline{\delta}} + \underline{\underline{L}}^T \underline{\underline{R}}\right) \underline{J} - \left(\underline{\underline{L}} + \underline{\underline{L}}^t\right) \underline{X} = 0 \quad . \tag{10}$$

Using the identity $\underline{\underline{\delta}} = \underline{\underline{L}}\underline{\underline{R}}$, we get

$$(\underline{\underline{L}} + \underline{\underline{L}}^T)(\underline{\underline{R}}\underline{J} - \underline{X}) = 0 \quad , \tag{11}$$

whence it is seen that

$$\underline{X} = \underline{\underline{R}}\,\underline{J} \quad , \tag{12}$$

since $(\underline{\underline{L}} + \underline{\underline{L}}^T)$ is positive definite (due to the second law of thermodynamics). Consequently, the inverse equation

$$\underline{J} = \underline{\underline{L}}\underline{X} \tag{13}$$

holds as well, and it can directly be derived from the second group of equations (8) by the same procedure.

To show that Gyarmati's subsidiary theorem pertains to this case, we show that conditions

$$\frac{\partial \mathcal{L}}{\partial \dot{\Gamma}_j} = 0 \tag{14}$$

are fulfilled at the maximum. Executing the differentiations the conditions

$$\left(\frac{\partial \underline{\underline{L}}}{\partial \dot{\Gamma}_j}\,\underline{X}\right)(\underline{X} - \underline{\underline{R}}\,\underline{J}) + \left(\frac{\partial \underline{\underline{R}}}{\partial \dot{\Gamma}_j}\,\underline{J}\right)(\underline{J} - \underline{\underline{L}}\,\underline{X}) = 0 \tag{15}$$

are obtained, that are automatically satisfied at the maximum with respect to $\underline{X}$ or $\underline{J}$.

Thus the Gaussian type local form of Gyarmati's Principle is valid for non-Onsagerian constitutive equations as well.

2. Extension for nonlinear constitutive equations

In the nonsymmetric case Ψ and Φ cease to be potentials and (6) or (7) cannot be reduced to (1). Though (6) and (7) are equivalent, the latter form will be preferred because of its more accentuated symmetry in the $\underline{X}$-$\underline{J}$ and $\underline{\underline{L}}$-$\underline{\underline{R}}$ pairs. Moreover, the form of (7) suggests that the extremum principle

$$\mathcal{L} = \sum_i [J_i - f_i(X_1, \ldots, X_n)]\,[X_i - g_i(J_1, \ldots, J_n)] = \max \tag{16}$$

be used for nonlinear constitutive equations. Here f_i and g_i are inverse function systems, i.e.

$$f_i(g_1(J_1, \ldots, J_n), \ldots, g_n(J_1, \ldots, J_n)) = J_i \quad . \tag{17}$$

It is easily seen that the conditions

$$\frac{\partial \mathcal{L}}{\partial X_k} = 0 \quad ; \qquad \frac{\partial \mathcal{L}}{\partial J_\ell} = 0 \tag{18}$$

as well, as the conditions

$$\frac{\partial \mathcal{L}}{\partial \dot{\Gamma}_j} = 0 \tag{19}$$

are satisfied by the constitutive equations

$$J_i = f_i (X_1, \ldots, X_n) \quad ,$$

or $\qquad i = 1, \ldots, n \qquad (20)$

$$X_i = g_i (J_1, \ldots, J_n) \quad ,$$

since executing the prescribed differentiations

$$J_i - f_i(\underline{X}) - \sum_k \frac{\partial f_k}{\partial X_i} (X_k - g_k (\underline{J})) = 0 \quad , \qquad (21)$$

$$X_i - g_i(\underline{J}) - \sum_k \frac{\partial g_k}{\partial J_i} (J_k - f_k (\underline{X})) = 0 \qquad (22)$$

and

$$\sum_k \frac{\partial f_k}{\partial \Gamma_j} (X_k - g_k (\underline{J})) + \sum_k \frac{\partial g_k}{\partial \Gamma_j} (J_k - f_k (\underline{X})) = 0 \qquad (23)$$

are obtained respectively.

The next question is whether (18) has any other solution, different from (20), or not.

Conclusions

From the results of Section 1 it is seen that the Gaussian type local form of Gyarmati's Principle (6) is independent of the existence of reciprocity relations of any kind, thus it is based solely on the second law of thermodynamics (in the linear approach). Specially in the Onsagerian case it remains valid in its original form (6) even in the presence of magnetic field. It is also independent of the representation, i.e. of that Onsager or Casimir [17] type reciprocities are valid.

Consequently, the generalisation of the principle to nonlinear cases should not necessarily be based on reciprocity relations. Such a generalisation is given in Section 2, which is not the only possible, but maybe a quite natural one.

Acknowledgement

I would like to express my sincere gratitude to Dr. J. Verhás for his helpful advice.

References

1. J. Verhás, Ann. Physik (Leipz.), 40, 189, 1983.
2. I. Gyarmati, Acta Chim. Hung., 43, 353, 1965.
3. I. Gyarmati, Ann. Physik, 7, 23, 2727, 1969.
4. I. Gyarmati, J. Non-equilib. Thermodyn., 2, 233, 1977.
5. L. Onsager, Phys. Rev., 37, 405, 1931; 37, 2265, 1931.
6. I. Gyarmati, Period. Polytechn., 5, 219, 1961; 5, 321, 1961.
7. J. Verhás, Zhur. Fiz. Khim., 40, 6, 1213, 1966.
8. J. Verhás, Acta Phys. Hung., 55, 275, 1984.
9. I. Gyarmati, Non-Equilibrium Thermodynamics, Springer, Berlin-Heidelberg-New York, 1970.
10. B. Nyíri, Acta Phys. Hung., 60, 245, 1986.
11. D.K. Bhattacharya, Ann. Physik, 39, 325, 1982.
12. W. Muschik and J. Szer, J. Non-Equilib. Thermodyn., 1, 61, 1976.
13. J.H.C. Li, J. Chem. Phys., 29, 4, 747, 1958; 37, 8, 1592, 1962.
14. J. Verhás, Z. Phys. Chem., 249, 119, 1972.
15. H. Farkas, Z. Noszticzius, Ann. Physik, 7, 27, 341, 1971.
16. S. Lengyel, I. Gyarmati, Period. Polytechn., 25, 63, 1981.
17. H.B.G. Casimir, Rev. Mod. Phys., 17, 343, 1945.

Acta Physica Hungarica 63(1–2), pp. 17–19 (1988)

SOFT MODE OF SPIN WAVES IN THIN FERROMAGNETIC FILMS

K. RADOWICZ - SARNOT
Institute of Physics, Pedagogical University of Kielce
Lesna 16, 25–509 Kielce, Poland

(Received 8 May 1987)

The dispersion relation of the spin waves in thin ferromagnetic film near the phase transition point from the homogeneous magnetization state to the domain structure has been obtained. Calculations have been carried out within the pheonomenological theory utilizing the Holstein — Primakoff expansion in the first approximation.

We will consider a ferromagnetic thin film near the phase transition point from the homogeneous magnetization state to the domain structure. The easy magnetization axis is perpendicular to surfaces of the film and parallel to the z axis of the Cartesian co-ordinate system. The dimensions of the film in (x, y) plane are much larger than its thickness L along the z axis. Our considerations concern a case in which external magnetic field is parallel to y axis. For the value $H^e > H^c(L)$ of the homogeneous magnetic field the ground state is the homogeneous magnetization state in the plane of the film, and for $H^e < H^c(L)$ the ground state is a flat parallel domain structure [1, 2, 6]. $H^c(L)$ is the critical value of the external magnetic field responsible for continuous phase transition [1, 2] from the state of the homogeneous magnetization to the domain structure. In our considerations we will assume that the ground state is the state of the homogeneous magnetization, i.e. $\underline{M}_o = (0, M_o, 0)$.

The energy F_a of the sample can be written in the form [1, 2]:

$$F_a = \frac{1}{2}\int_V \left[\alpha(\nabla \underline{M})^2 - \beta M_z^2 - 2H^e M_y - \underline{H}^d \underline{M}\right] dV \quad , \tag{1}$$

where $\underline{H}^e = (0, H^e, 0)$ is the vector of the external magnetic field, β is the anisotropy constant, α is the macroscopic exchange constant, $H^d = \underline{H}^d(\underline{r})$ is the vector of demagnetization field. This vector can be expressed by the magnetization vector $\underline{M}$, $\underline{M} = \underline{M}_o(m_x, 1 - \frac{1}{2}(m_x^2 + m_z^2), m_z)$, using the Maxwell equations in magnetostatic approximation [3]:

$$\operatorname{rot} \underline{H}^d = 0 \quad , \quad \operatorname{div}(\underline{H}^d + 4\pi \underline{M}) = 0 \quad . \tag{2}$$

The magnetization vector $\underline{M}$ should satisfy appropriate boundary conditions. In the case of the strong surface anisotropy, the boundary conditions are in the form [4, 6]:

$$m_z(z = 0) = m_z(z = L) = 0; \quad \left.\frac{\partial m_x}{\partial z}\right|_{z=0} = \left.\frac{\partial m_x}{\partial z}\right|_{z=L} = 0 \quad . \tag{3}$$

Let us take the Holstein — Primakoff transformation [3, 4] in the first approximation:

$$M^{+}(\underline{x}) = (4\mu_0 M_s)a(\underline{x}) \quad ,$$

$$M^{-}(\underline{x}) = (4\mu_0 M_s)a^{+}(\underline{x}) \quad ,$$

$$M_y(\underline{x}) = M_s - 2\mu_0 a^{+}(\underline{x})a(\underline{x}) \quad , \tag{4}$$

$$M^{\pm}(\underline{x}) = M_x(\underline{x}) \pm iM_z(\underline{x}) \quad .$$

The operators $a(\underline{x})$ and $a^{+}(\underline{x})$ satisfy the following commutation relations:

$$\left[a(\underline{x}),\ a^{+}(\underline{x}')\right] = \delta(\underline{x} - \underline{x}') \quad ,$$

$$\left[a(\underline{x}),\ a(\underline{x}')\right] = \left[a^{+}(\underline{x}),\ a^{+}(\underline{x}')\right] = 0 \quad . \tag{5}$$

We will take the Fourier transformation of the operators $a(\underline{x})$ and $a^{+}(\underline{x})$ [4]:

$$a(\underline{x}) = \frac{1}{\sqrt{s}} \sum_k b_k \exp\left(-i\,\underline{\varkappa}\,\underline{\varrho}\right) \quad ,$$

$$a^{+}(\underline{x}) = \frac{1}{\sqrt{s}} \sum_k b_k^{+} \exp\left(i\underline{\varkappa}\,\underline{\varrho}\right) \quad , \tag{6}$$

where $\underline{\varrho} = (x,0,z)$, $\underline{\varkappa} = (k_1,0,k_3)$, and s is the cross-sectional area of the sample in the plane (x,z).

Operators b_k and b_k^{+} satisfy the commutation relations:

$$\left[b_k,\ b_{k'}^{+}\right] = \delta_{kk'} \quad ,$$

$$\left[b_k,\ b_{k'}\right] = \left[b_k^{+},\ b_{k'}^{+}\right] = 0 \quad . \tag{7}$$

Excitation energy ΔF represented by b_k and $b_{k'}^{+}$ in bilinear approximation, has the form:

$$\Delta F = F\{\underline{M}\} - F\{\underline{M}_0\} = \sum_k \left(A_k b_k^{+} b_k + B_k^{+} b_k^{+} b_{-k}^{+} + B_k b_k b_{-k}\right) \quad , \tag{8}$$

where

$$A_k = 2\mu_0 M_s \left\{2\alpha k^2 + 2h - \beta + 2\pi\right\} ,$$

$$B_k = 2\mu_0 M_s \left\{\tfrac{1}{2}\beta - \pi k^{-2}\left(k_x^2 - k_z^2\right) - 2\pi i k^{-2} k_x k_z\right\} \quad , \tag{9}$$

and

$$\underline{h} = \underline{H}^{e}\underline{M}_0^{-1} \quad .$$

The motion equations [3, 4] have the form:

$$i\frac{\partial b_k}{\partial t} = \left[b_k, \Delta F\right] = A_k b_k + 2B_k^{+} b_{-k}^{+} \quad ,$$

$$i\frac{\partial b_{-k}^{+}}{\partial t} = \left[b_{-k}^{+}, \Delta F\right] = A_k b_{-k}^{+} + 2B_k b_k \quad . \tag{10}$$

We assume that operators $b_k(t)$ and $b_{-k}^{+}(t)$ depend on the time as follows:

$$b_k(t) = b_k(e^{i\omega t}) \ ,$$

$$b^+_{-k}(t) = b^+_{-k}(-e^{-i\omega t}) \ . \qquad (11)$$

Inserting (8) to (10) we obtain the set of the homogeneous equations. The condition of the solution of motion equations (10) gives us the following dispersion relation:

$$\omega^2 = 16\mu_0^2 M_s^2 \left[(4\pi + \alpha k^2 + h - \beta)(\alpha k^2 + h) - 4\pi\beta k^{-2} k_x^2\right] \ , \qquad (12)$$

where $k^2 = k_x^2 + k_z^2$; $\mu_0 = \frac{1}{\hbar} g\mu_B$. (13)

From the boundary conditions (3) we obtain:

$$k_z = n\pi L^{-1} \ . \qquad (14)$$

The dispersion relation for the spin waves with the soft mode is well known and on the basis of the Landau — Lifshitz classical motion equation it has been discussed in [1, 2]. It has been shown [1, 2], utilizing relation (14), that dispersion relation (12) describes the soft mode of the spin waves. It corresponds to the continuous phase transition from the state of the homogeneous magnetization to the domain structure with the period:

$$D = \left[\frac{4\alpha(4\pi + h_c)}{\pi^3 h_c}\right]^{1/4} \sqrt{L} \ .$$

The magnitude of the external field h in this case is equal to the critical value h_c [1, 2, 5]:

$$h_c(L) = \beta - \frac{4\pi}{L}\left(\frac{\pi\alpha\beta}{4\pi+\beta}\right)^{1/2} \ . \qquad (15)$$

The calculations presented above can be considered as a first step in future calculations of the thermodynamical properties of the thin ferromagnetic film near the phase transition point from the homogeneous magnetization state to the domain structure.

References

1. V.V. Tarasenko, E. Chenski, I.E. Dickstein, Zh. Eksp. Teor. Fiz., 70, 2178, 1976.
2. A.Z. Patashinski, W. Wasilewski, Acta Phys. Pol., A57, 789, 1980.
3. C. Kittel, Quantum Theory of Solids, John Wiley and Sons, Inc., New York, London, 1963.
4. A.J. Akhiezer, W.G. Baryakhtar, S.W. Peletminski, Spin Waves, North Holland, Amsterdam, 1968.
5. W. Wasilewski, Acta Phys. Pol., A68, 613, 1985.
6. N.M. Solanski, M.S. Erukhimov, The Physical Properties and Application of the Magnetic Films, Nauka, Novosybirsk, 1975.

Acta Physica Hungarica 63(1–2), pp. 21–50 (1988)

EFFECTS OF THE POLARISATION POTENTIALS ON POSITRON — HYDROGEN INELASTIC SCATTERING

M.A. ABDEL-RAOUF
Institute for Theoretical Chemistry, Friedrich-Alexander University
Erlangen-Nürnberg, 8520 Erlangen, West Germany

(Received in revised form 20 June 1987)

The effects of various possibilities of "switching on" the polarisation potentials of e^+ — H inelastic scattering on the coupled-static model are investigated in details. The partial elastic and positronium formation cross-sections of the new models are calculated for seven values of the total angular momentum $\ell (0 \leq \ell \leq 6)$ at seventeen values of the incident energy k_i^2 within the Ore gap ($6.8 \leq k_i^2 \leq 10.2$ eV). The comparison between the present calculations and the elaborate variational results of Humberston [1, 2] and Brown and Humberston [3, 4] shows that the "switching on" of the polarisation potentials leads to overestimated values for the partial and total elastic and positronium formation cross-sections. This conclusion raises, at least to us, some doubts about the consistency of the polarized orbital principle when higher channels than the elastic one are opened. It seems that this principle is completely insufficient for describing the positron — atom inelastic processes.

1. Introduction

Few years ago, Horbatch, Darewych and McEachran [5] have expressed their concern about the reliability of the polarized orbital method (POM) when applied to the elastic scattering of positrons by large atoms. Their main criticism was concentrated on the adiabatic nature of the POM and the computational difficulties associated with the calculation of the polarisation potentials of these processes. In spite of these critical points, however, it was found, (see McEachran et al [6–10]), that the POM is extremely successful in the treatment of the elastic scattering of positrons by noble gases. Furthermore, having in mind the static model of the elastic collisions of positrons with small atoms, it was noticed by different authors (see e.g. Drachman and Temkin [11]) that the POM yields considerable improvements upon the static phase shifts which were always shifted towards the elaborate variational ones. These improvements were clearly attributed to the effect of the polarisation potentials and led to the commonly accepted argument that the contribution of these potentials is always towards the real physical picture of the collision process under investigation. The purpose of the present paper is to test the validity of this argument in inelastic collisions of positrons with small atoms, i.e. to investigate whether the "switching on" of the polarisation potentials to the coupled static models of these processes would improve their elastic and positronium formation cross-sections in comparison with the variational ones. As an example for our investigation, we treat the e^+ — H inelastic scattering, which has been extensively treated by Abdel-Raouf et al [12] using the coupled static approximation, and considered, for years, by Humberston and coworkers, (see e.g. the above mentioned papers), using Kohn's variational method. From the work of the former authors [12] , we know that, although the coupled-static model of the e^+ — H inelastic scattering is associated with enormous computational difficulties, it is still simpler than

its variational treatment, and provides useful (first order) estimation of the corresponding partial and total cross-sections. This fact emphasizes the necessity of establishing another (more accurate but still simple) approach for investigating this type of problems, and explains the increasing interest in the results of the present work.

The "switching on" of the polarisation potentials of the e^+ - H inelastic scattering — (where only elastic and rearrangement channels are opened) — is carried out in the present paper using four different models:

i) by including the polarisation potential of the first channel ($V_{pol}^{(1)}$ to the coupled-static model (or Model 0), i.e. by allowing only for the polarisation of the hydrogen atom;

ii) by including the polarisation potentials of the second channel ($V_{pol}^{(2)}$ to Model 0, i.e. by allowing only for the polarisation of the positronium atom (Model 2);

iii) by including $V_{pol}^{(1)}$ and $V_{pol}^{(2)}$ to Model 0; this case is referred to as Model 3;

iv) by using a generalisation of Stone's polarized orbital method with symmetrized kernels (Model 4).

Section 2 of this paper deals with the formation of these four models. Section 3 is devoted to the discussion of the partial and total cross-sections computed by these models. There we find also a comparison between the new cross-sections and the ones obtained by other authors. The analysis of the kernels and the details of the method of iteration are accumulated in Appendix 1 and Appendix 2, respectively.

2. Theory

Let H and E be the total Hamiltonian and total energy of the collision of positrons with hydrogen atoms in any channel. Therefore, they can be split to the forms

$$H = H_o^{(i)} + H_1^{(i)} + V_{int}^{(i)} , \qquad i=1,2 \tag{1}$$

and

$$E = E_1 + k_1^2 = E_2 + \tfrac{1}{2} k_2^2 \ . \tag{2}$$

The operators in the right-hand-side of Eq. (1) are defined (in the static approximation) as

$$H_o^{(1)} = -\nabla_r^2 - \frac{2}{r} \ , \qquad H_o^{(2)} = -2\nabla \frac{2}{\rho} - \frac{2}{\rho} \ , \tag{3a}$$

$$H_1^{(1)} = -\nabla_x^2 \ , \qquad H_1^{(1)} = -\tfrac{1}{2}\nabla_\sigma^2 \ , \tag{3b}$$

$$V_{int}^{(1)} = \frac{2}{x} - \frac{2}{\rho} \quad \text{and} \quad V_{int}^{(2)} = \frac{2}{x} - \frac{2}{r} \ . \tag{3c}$$

E_1 and E_2, Eq. (2), are the ground-state energies of the hydrogen and positronium atoms, (-1.0 Ryd and -0.5 Ryd, respectively), and k_1^2 and $\frac{1}{2} k_2^2$ are the kinetic energies of the incident positrons and the center-of-mass of the positronium atom relative to the proton. x and r are the position vectors of the positron and the bounded electron with respect to the hydrogen nucleus. ρ and σ are given by $\rho = x - r$ and $2\sigma = x + r$, (see Fig. 1).

Let $|\Psi_1>$ and $|\Psi_2>$ be the total wave functions of channels 1 and 2, respectively, then we can express the full wave function which describes the two channel process as

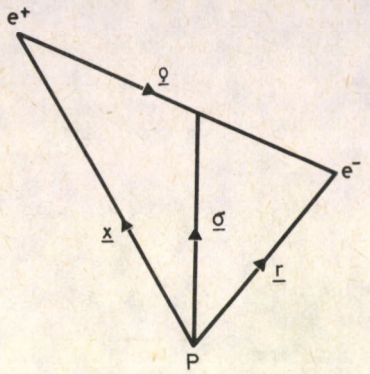

Fig. 1. Coordinates of positron — hydrogen scattering

$$|\Psi> = |\Psi_1> + |\Psi_2> , \tag{4a}$$

where

$$|\Psi_i> = |\Phi_i>|\psi_i> . \tag{4b}$$

If we assume that the hydrogen and positronium atoms are polarized, then $|\Phi_i>$ takes the form

$$|\Phi_i> = |\Phi_{i1}> + \beta_i |\Phi_{i2}>, \qquad i=1,2 \tag{4c}$$

where $|\Phi_{i1}>$ and $|\Phi_{i2}>$ are the ground-state wave function and the polarized orbitals of channel i. They are defined, for i=1,2, by

$$\Phi_{11} = (1/\pi)^{\frac{1}{2}} e^{-r} , \quad \Phi_{12} = (8/43\pi)^{\frac{1}{2}} r(1+r/2)\, e^{-r}(\hat{r}.\hat{x}) , \tag{4d}$$

$$\Phi_{21} = (1/8\pi)^{\frac{1}{2}} e^{-\varrho/2} , \quad \Phi_{22} = (1/172\pi)^{\frac{1}{2}} \varrho(1+\varrho/4)\, e^{-\varrho/2}(\hat{\varrho}.\hat{\sigma}) . \tag{4e}$$

$|\psi_1>$, $|\psi_2>$, Eq. (4b), are the scattering wave functions of the positrons and positronium atom, respectively.

Fors Eqs (4d) and (4e), we notice that, for each channel i, the following relations are true

$$<\Phi_{ij}|\Phi_{ij}> = 1 , \qquad j=1,2 . \tag{4f}$$

We also remark that $|\Phi_{12}>$ and $|\Phi_{22}>$ represent all P-states of the hydrogen and positronium atoms, respectively.

Following Stone [13], the parameters β_i, Eq. (4c), are calculated using the variational principles

$$\delta E_i^{ad} = \delta\{<\Phi_i|H_i^{ad}|\Phi_i>/<\Phi_i|\Phi_i>\}$$

$$= 0 , \qquad i=1,2 \tag{5}$$

where E_i^{ad} and H_i^{ad} are the adiabatic energy and Hamiltonian of the i-th channel. Thus, we have

$$H_i^{ad} = H_o^{(i)} + V_{int}^{(i)} \quad , \qquad i=1,2 \quad . \tag{6}$$

Substitution from Eqs (3a), (3c), (4c), (4d) and (4e) into Eq. (5), we find

$$\beta_1/(1 - \beta_i^2) = V_{1,2}^{(i)} /(E_1^{(i)} - E_2^{(i)} + V_{1,1}^{(i)} - V_{2,2}^{(i)} \quad , \tag{7a}$$

where $E_i^{(i)} = E_i$, $E_2^{(1)} = -21/129$ Ryd, is the binding energy of the polarized hydrogen atom, and $E_2^{(2)} = -21/258$ Ryd, is the binding energy of the polarized positronium atom.

Equation (7a) provides us with two roots for each β_i. The proper ones are those which yield minimum values for E_i^{ad}, i=1,2, where

$$E_i^{ad} = (1 + \beta_i^2)^{-1}(E_1^{(i)} + V_{1,1}^{(i)} + 2\beta_1 V_{1,2}^{(i)} + (E_2^{(i)} + V_{2,2}^{(i)} \beta_i^2) \quad . \tag{7b}$$

The potentials $V_{m,m}^{(i)}$, appearing at Eq. (7a) are determined by

$$V_{m,m'}^{(i)} = \langle \Phi_{im} \left| V_{int}^{(i)} \right| \Phi_{im'} \rangle \quad , \qquad i,m,m'=1,2 \quad . \tag{7c}$$

Substituting from Eqs (3c), (4d) and (4e) into Eq. (7c), we obtain

$$V_{1,1}^{(1)}(x) = 2(1 + \tfrac{1}{x})\, e^{-2x}, \tag{8a}$$

$$V_{1,2}^{(1)}(x) = (\tfrac{8}{43})^{1/2} \left\{(x^2 + 5x + 9 + 9/x)\, e^{-2x} - \frac{9(1-e^{-2x})}{2x^2}\right\} \quad , \tag{8b}$$

$$V_{2,2}^{(1)}(x) = \tfrac{1}{4} \left\{(\tfrac{x^4}{2} + \tfrac{9x^3}{2} + 18x^2 + 45x + \tfrac{325}{4} + \tfrac{427}{4x} + \tfrac{96}{x^2})\, e^{-2x} - \frac{48(1-e^{-2x})}{x^3}\right\}, \tag{8c}$$

$$V_{1,1}^{(2)}(\sigma) = 0 \quad , \tag{9a}$$

$$V_{1,2}^{(2)}(\sigma) = (\tfrac{32}{43})^{1/2} \left\{(\sigma^2 + 5\sigma + 9 + 9/\sigma)\, e^{-2\sigma} - \frac{9(1-e^{-2\sigma})}{2\sigma^2}\right\}, \tag{9b}$$

$$V_{2,2}^{(2)}(\sigma) = 0 \quad . \tag{9c}$$

The polarisation potential of channel i is defined by

$$V_{pol}^{(i)} = \beta_i\, V_{1,2}^{(i)} \quad . \tag{10}$$

The solution of the inelastic problem is obtained in the coupled-static as well as the polarized orbital approximation by demanding that the projections of the vector $(H - E)|\Psi\rangle$ onto the $\langle\Phi_{i1}|$, i = 1,2, are zero. Thus we have

$$\langle \Phi_{i1} \left| H - E \right| \Psi \rangle = 0 \quad , \qquad i=1,2 \quad . \tag{11}$$

Substitution from Eq. (4a) into Eq. (1), leaves us with

$$\langle \Phi_{11} \left| H^{(1)} - E^{(1)} \right| \Psi_1 \rangle = -\langle \Phi_{11} \left| H^{(2)} - E^{(2)} \right| \Psi_2 \rangle \qquad (12a)$$

and

$$\langle \Phi_{21} \left| H^{(2)} - E^{(2)} \right| \Psi_1 \rangle = -\langle \Phi_{21} \left| H^{(1)} - E^{(1)} \right| \Psi_2 \rangle , \qquad (12b)$$

where the superscripts (1), (2) of H and E are introduced in order to distinguish their expansions in the first and second channels, respectively.

Substituting from Eqs (1)-(3c), and Eqs (4a)-(4e) into Eqs (12a,b), we find

$$(\nabla_x^2 + k_1^2) \left| \Psi_1 \right\rangle = U_x^{(1)} \left| \Psi_1 \right\rangle + \langle \Phi_{11} \left| H^{(2)} - E^{(2)} \right| \Phi_2 \, \Psi_2 \rangle , \qquad (13a)$$

$$(\nabla_\sigma^2 + k_2^2) \left| \Psi_2 \right\rangle = U_\sigma^{(2)} \left| \Psi_2 \right\rangle + \langle \Phi_{21} \left| H^{(1)} - E^{(1)} \right| \Phi_1 \, \Psi_2 \rangle , \qquad (13b)$$

where Schrödinger's equations for the hydrogen and positronium atoms are used.

Let us now consider the partial wave expansions of the scattering wave functions $|\Psi_1\rangle$ and $|\Psi_2\rangle$, i.e.

$$\Psi_1(x) = \frac{1}{x} \sum_{\ell=0} (2\ell+1)\, i^\ell \, f_\ell(x)\, Y_\ell^0(\hat{x}) , \qquad (14a)$$

$$\Psi_2(\sigma) = \frac{1}{\sigma} \sum_{\ell=0} (2\ell+1)\, i^\ell \, g_\ell(\sigma)\, Y_\ell^0(\hat{\sigma}) , \qquad (14b)$$

where $f_\ell(x)$ and $g_\ell(\sigma)$ are the (radial) partial wave functions corresponding to the total angular momentum ℓ, of the first and second channels, respectively, $Y_\ell^0(\hat{x})$ and $Y_\ell^0(\hat{\sigma})$ are the related spherical harmonics, and $\hat{x}$ and $\hat{\sigma}$ are the angles between the vectors x and σ and the z axis.

Substitution from Eqs (14a,b) into Eqs (13a,b), we obtain for each value of ℓ, following coupled integro-differential equations:

$$\left(\frac{d^2}{dx^2} - \frac{\ell(\ell+1)}{x^2} + k_1^2\right) f_\ell(x) = U_x^{(1)} f_\ell(x) + \int_0^\infty K_{12}(\sigma,x)\, g_\ell(\sigma)\, d\sigma , \qquad (15a)$$

$$\left(\frac{d^2}{d\sigma^2} - \frac{\ell(\ell+1)}{\sigma^2} + k_2^2\right) g_\ell(\sigma) = U_\sigma^{(2)} g_\ell(\sigma) + \int_0^\infty K_{21}(\sigma,x)\, f_\ell(x)\, dx , \qquad (15b)$$

where the kernels K_{12} and K_{21} are expanded by

$$K_{12}(\sigma,x) = 8\sigma x \iint \{ \Phi_{11}\Phi_{21}\left(-\tfrac{1}{2}\nabla_\sigma^2 - \tfrac{1}{2}k_2^2\right) + \Phi_{11}\Phi_{21}\, V_{int}^{(2)}$$
$$+ \mathcal{E}\left(\left(-\tfrac{1}{2}\nabla_\sigma^2 - 2\,\Delta_\rho^2 - \frac{2}{Q} - E\right)\Phi_{11}\Phi_{22}\right.$$
$$\left. + \Phi_{11}\,\Phi_{22}\, V_{int}^{(2)}\, \beta_2(\sigma)\right\}\, Y_\ell(\hat{x})\, Y_\ell(\hat{\sigma})\, d\hat{x}\, d\hat{\sigma} \qquad (15c)$$

and

$$K_{21}(\sigma,x) = 8.2x\sigma \iint \{ \Phi_{11}\,\Phi_{21}\left(-(\nabla_x^2 + k_1^2)\right) + \Phi_{11}\,\Phi_{21}\, V_{int}^{(1)} + \mathcal{E}\left(\left(-\nabla_x^2 - \nabla\tfrac{2}{r} - \tfrac{2}{r} - E\right)_{21}{}_{12}\right.$$
$$\left. + \Phi_{21}\Phi_{12}\, V_{int}^{(1)}\right)\, \beta_1(x)\} \, Y_\ell^0(\hat{x})\, Y_\ell^0(\hat{\sigma})\, d\hat{x}\, d\hat{\sigma} . \qquad (15d)$$

(The number 8 is due to the transformations $\int dr = 8 \int d\sigma$, $\int d\rho = 8 \int d x'$). The direction of the z axis may now be adjusted such that it is in the direction of x if Eq. (15a) is solved and in the direction of σ if Eq. (15b) is solved. The potentials $U_x^{(1)}$ and $U_\sigma^{(2)}$ appearing in Eqs (13a,b) and (15a,b) are defined by

$$U_x^{(1)} = V_{1,1}^{(1)}(x) + \mathcal{E}_1 V_{pol}^{(1)}(x) \tag{16a}$$

and

$$U_\sigma^{(2)} = \mathcal{E}_2 V_{pol}^{(2)}(\sigma) \quad , \tag{16b}$$

where the polarisation potentials $V_{pol}^{(i)}$, i=1,2, are defined by Eqs (10). The parameters $\mathcal{E}_1$, $\bar{\mathcal{E}}$, $\mathcal{E}_1$ and $\mathcal{E}_2$ appearing in Eqs (15b) – (16b) are introduced for distinguishing the various conditions (Models) under which Eqs (15a,b) are solved. Thus, we distinguish the following cases:

a) $\mathcal{E} = \bar{\mathcal{E}} = \mathcal{E}_1 = \mathcal{E}_2 = 0$. This case is identical with the coupled-static approximation, where $\beta_1 = \beta_2 = 0$, (see Eq. 4c), i.e. where no polarisation effects are taken into account. (In Appendix 1, we show that this case implies that $K_{12}(\sigma,x) = \frac{1}{2} K_{21}(\sigma,x)$, i.e. the kernels are symmetric).

b) $\mathcal{E} = \bar{\mathcal{E}} = \mathcal{E}_2 = 0$ and $\mathcal{E}_1 = 1$. This case represents Model 1 in which the polarisation potential of channel 1 is switched on while the coupled static picture of the system is considered.

c) $\mathcal{E} = \bar{\mathcal{E}} = \mathcal{E}_1 = 0$ and $\mathcal{E}_2 = 1$. This case corresponds to Model 2 in which the polarisation potential of channel 2 is switched on while the coupled static picture of the system is considered.

d) $\mathcal{E} = \bar{\mathcal{E}} = 0$ and $\mathcal{E}_1 = \mathcal{E}_2 = 1$. This is Model 3, or the coupled-static approximation plus the polarisation potentials of both channels.

e) $\mathcal{E}_1 = \mathcal{E}_2 = 1$ and $\mathcal{E}$ and $\bar{\mathcal{E}}$ are defined such that $K_{12}(\sigma,x) = \frac{1}{2} K_{21}(\sigma,x)$. This case identifies Model 4 and is referred to as the Stone polarized orbital method with symmetrized kernels. Obviously, the case $\mathcal{E} = \bar{\mathcal{E}} = \mathcal{E}_1 = \mathcal{E}_2 = 1$ represents the extension of Stone's POM to inelastic scattering.

Let us now rewrite Eqs (15a,b) as follows

$$\left(\frac{d^2}{dx^2} - \frac{\ell(\ell+1)}{x^2} + k_1^2 \right) f_\ell(x) = U_x^{(1)} f_\ell(x) + Q_1(x) \quad , \tag{17a}$$

$$\left(\frac{d^2}{d\sigma^2} - \frac{\ell(\ell+1)}{\sigma^2} + k_2^2 \right) g_\ell(\sigma) = Q_2(\sigma) \quad , \tag{17b}$$

where

$$Q_1(x) = \int_0^\infty K_{12}(\sigma,x)\, g_\ell(\sigma)\, d\sigma \tag{17c}$$

and

$$Q_2(\sigma) = \int_0^\infty K_{21}(\sigma,x)\, f_\ell(x)\, dx \quad . \tag{17d}$$

Equations (17a,b) have the general form

$$(E - H_0)|\xi\rangle = |\zeta\rangle \quad , \tag{18a}$$

where H_0 is an arbitrary part of the total Hamiltonian H which describes, as well as the total energy E and the total wave function $|\xi>$, a given quantum mechanical system. It is well known that the solution of Eq. (18a) is given (formally) by the Lippmann — Schwinger equation

$$|\xi> = |\xi_0> + G_0 |\zeta>, \tag{18b}$$

where G_0 is the Green operator $(E - H_0)^{-1}$.

Comparing Eqs (17a) and (17b) with Eq. (18a) and using the partial wave expansion of the Green operators corresponding to the operators on the left-hand sides of these equations we can prove that

$$f_\ell^{(i)}(x) = \left\{\delta_{i1} + \frac{1}{k_1}\int_0^\infty \tilde{g}_\ell(k_1x')\left\{U_{x'}^{(1)} f_\ell^{(i)}(x') + Q_1^{(i)}(x')\right\} dx'\right\} \tilde{f}_\ell(k_1x)$$
$$- \frac{\tilde{g}_\ell(k_1x)}{k_1}\int_0^\infty \tilde{f}_\ell(k_1x')\left\{U_{x'}^{(1)} f_\ell^{(i)}(x') + Q_1^{(i)}(x')\right\} dx' \ , \tag{19a}$$

and

$$g_\ell^{(i)}(\sigma) = \left\{\delta_{i2} + \frac{1}{k_2}\int_0^\infty \tilde{g}_\ell(k_2\sigma')\, Q_2^{(i)}(\sigma')\, d\sigma'\right\}\tilde{f}_\ell(k_2\sigma)$$
$$- \frac{g_\ell(k_2\sigma)}{k_2}\int_0^\infty \tilde{f}_\ell(k_2\sigma')\, Q_2^{(i)}(\sigma')\, d\sigma' \ . \tag{19b}$$

The delta functions $\delta_{i,j}$, identify two independent solutions for each of $f_\ell(x)$ and $g_\ell(\sigma)$ in the channels i=1,2. The functions $\tilde{f}_\ell(\mu)$ and $\tilde{g}_\ell(\mu)$, (μ=k_1x, $k_2\sigma$), are related to the spherical Bessel functions of the first and second kinds, $j_\ell(\mu)$ and $y_\ell(\mu)$ by the relations $\tilde{f}_\ell(\mu) = \mu j_\ell(\mu)$ and $\tilde{g}_\ell(\mu) = -\mu y_\ell(\mu)$.

Equations (19a,b) can be only solved iteratively and the iterative solutions are obtained by

$$f_\ell^{(i,\nu)}(x) = \left\{\delta_{i1} + \frac{1}{k_1}\int_0^\infty \tilde{g}_\ell(k_1x')\right\} U_{x'}^{(1)} f_\ell^{(i,\nu)}(x') + Q_1^{(i,\nu-1)}(x')\Big\}\, dx'$$
$$\cdot\, \tilde{f}_\ell(k_1x) - \frac{\tilde{g}_\ell(k_1x)}{k_1}\int_0^\infty \tilde{f}_\ell(k_1x')\left\{U_{x'}^{(1)}\, f_\ell^{(i,\nu)}(x') + Q_1^{(i,\nu-1)}(x')\right\} dx', \nu \geq 1 \tag{20a}$$

and

$$g_\ell^{(i,\nu)}(\sigma) = \left\{\delta_{i2} + \frac{1}{k_2}\int_0^\infty \tilde{g}_\ell(k_2\sigma')\, Q_2^{(i,\nu)}(\sigma')\, d\sigma'\right\}\tilde{f}_\ell(k_2\sigma)$$
$$- \frac{\tilde{g}_\ell(k_2\sigma)}{k_2}\int_0^\infty \tilde{f}_\ell(k_2\sigma')\, Q_2^{(i,\nu)}(\sigma')\, d\sigma' \ , \nu \geq 0 \ , \tag{20b}$$

where ν is the order of iteration. The starting values (or zero iterations) of $f_\ell^{(i)}(x)$ are given by

$$f_\ell^{(i,0)}(x) = \left\{\delta_{i1} + \frac{1}{k_1}\int_0^\infty \tilde{g}_\ell(k_1x')\, U_{x'}^{(1)}\, f_\ell^{(i,0)}(x')\, dx'\right\}\tilde{f}_\ell(k_1x)$$
$$- \frac{\tilde{g}_\ell(k_1x)}{k_1}\int_0^\infty \tilde{f}_\ell(k_1x')\, U_{x'}^{(1)} f_\ell^{(i,0)}(x')\, dx' \ . \tag{20c}$$

The last equation defines the solution of the elastic scattering of positrons by hydrogen atoms, (i.e. when the positronium formation channel is closed).

In order to obtain the reactance matrix, R, we rewrite the iterative solutions (20a,b) in the forms

$$f_\ell^{(i,\nu)}(x) = a_1^{(i,\nu)}\, \tilde{f}_\ell(k_1 x) + b_1^{(i,\nu)}\, \tilde{g}_\ell(k_1 x) \quad , \tag{21a}$$

$$g_\ell^{(i,\nu)}(\sigma) = a_2^{(i,\nu)}\, \tilde{f}_\ell(k_2 \sigma) + b_2^{(i,\nu)}\, \tilde{g}_\ell(k_2 \sigma) \quad , \tag{21b}$$

where $a_1^{(i,\nu)}$ is the factor of $\tilde{f}_\ell(k_1 x)$ in Eq. (20a), $b_1^{(i,\nu)}$ is the factor of $\tilde{g}_\ell(k_1 x)$ in the same equation, $a_2^{(i,\nu)}$ is the factor of $\tilde{f}_\ell(k_2 \sigma)$ in Eq. (20b) and $b_2^{(i,\nu)}$ is the factor of $\tilde{g}_\ell(k_2 \sigma)$ in the same equation.

Defining the two matrices

$$a^\nu = \begin{vmatrix} \frac{1}{\sqrt{k_1}}\, a_1^{(1,\nu)} & \frac{1}{\sqrt{k_1}}\, a_1^{(2,\nu)} \\ \sqrt{\frac{2}{k_2}}\, a_2^{(1,\nu)} & \sqrt{\frac{2}{k_2}}\, a_2^{(2,\nu)} \end{vmatrix} \quad , \quad b^\nu = \begin{vmatrix} \frac{1}{\sqrt{k_1}}\, b_1^{(1,\nu)} & \frac{1}{\sqrt{k_1}}\, b_1^{(2,\nu)} \\ \sqrt{\frac{2}{k_2}}\, b_2^{(1,\nu)} & \sqrt{\frac{2}{k_2}}\, b_2^{(2,\nu)} \end{vmatrix} , \tag{22}$$

we can determine the elements of the reactance matrix by using the relations

$$R_{ij}^\nu = \left\{ b^\nu (a^\nu)^{-1} \right\}_{ij} \quad . \tag{23}$$

Thus, we obtain

$$R_{11}^\nu = \left\{ b_1^{(1,\nu)}\, a_2^{(2,\nu)} - b_1^{(2,\nu)}\, a_2^{(1,\nu)} \right\} / \Delta_1^\nu \quad , \tag{23a}$$

$$R_{12}^\nu = \sqrt{\frac{2k_1}{k_2}} \left\{ b_1^{(2,\nu)}\, a_1^{(1,\nu)} - b_1^{(1,\nu)}\, a_1^{(2,\nu)} \right\} / \Delta_1^\nu \quad , \tag{23b}$$

$$R_{21}^\nu = \sqrt{\frac{k_2}{2k_1}} \left\{ b_2^{(1,\nu)}\, a_2^{(2,\nu)} - b_2^{(2,\nu)}\, a_2^{(1,\nu)} \right\} / \Delta_1^\nu \quad , \tag{23c}$$

$$R_{22}^\nu = \left\{ b_2^{(2,\nu)}\, a_1^{(1,\nu)} - b_2^{(1,\nu)}\, a_1^{(2,\nu)} \right\} / \Delta_1^\nu \quad ,$$

where $\Delta_1^\nu = a_1^{(1,\nu)}\, a_2^{(2,\nu)} - a_1^{(2,\nu)}\, a_2^{(1,\nu)}$. (23d)

The iterative transition matrix, T^ν, is related to the reactance matrix R^ν by

$$T^\nu = R^\nu (I - i\, R^\nu)^{-1} \quad , \tag{24}$$

where I is a 2 x 2 unit matrix and $i = \sqrt{-1}$. The iterative partial cross-sections corresponding to the total angular momentum ℓ, i.e. $\sigma_{ij}^{(\ell,\nu)}$'s, are calculated by

$$\sigma_{ij}^{(\ell,\nu)} = \frac{4\pi(2\ell+1)}{k_i^2}\, |T_{ij}^\nu|^2 \quad , \qquad i,j=1,2 \quad , \tag{25}$$

where the analyses of Eq. (24) provide us with

$$\left|T^{\nu}_{11}\right|^2 = \{(R^{\nu}_{11})^2 + (\Delta^{\nu}_2)^2\}/\Delta^{\nu} \quad , \tag{26a}$$

$$\left|T^{\nu}_{12}\right|^2 = (R^{\nu}_{12})^2/\Delta^{\nu} \quad , \tag{26b}$$

$$\left|T^{\nu}_{21}\right|^2 = (R^{\nu}_{21})^2/\Delta^{\nu} \quad , \tag{26c}$$

$$\left|T^{\nu}_{22}\right|^2 = \{(R^{\nu}_{22})^2 + (\Delta^{\nu}_2)^2\}/\Delta^{\nu} \quad , \tag{26d}$$

where

$$\Delta^{\nu}_2 = R^{\nu}_{11} R^{\nu}_{22} - R^{\nu}_{12} R^{\nu}_{21} \tag{26e}$$

and

$$\Delta^{\nu} = (1 - \Delta^{\nu}_2)^2 + (R^{\nu}_{11} + R^{\nu}_{22})^2 \quad . \tag{26f}$$

Finally, the total iterative cross-sections are calculated by

$$\sigma^{\nu}_{ij} = \sum_{\ell=0}^{\infty} \sigma^{(\ell,\nu)}_{ij} \quad , \qquad i,j=1,2, \tag{27}$$

where σ^{ν}_{11} is the total elastic cross-section of the positrons from the hydrogen atom, σ^{ν}_{12} is the total positronium formation cross-section, σ^{ν}_{21} is the total elastic cross-section of the positronium atom from the proton and σ^{ν}_{22} is the total rearrangement cross-section of the second channel.

3. Results and discussion

The computation process has been started by investigating the general features of the four potentials $V^{(1)}_{1,1}$, $V^{(1)}_{1,2}$, $V^{(1)}_{2,2}$ and $V^{(2)}_{1.2}$, Eqs (8a), (8b), (8c) and (9b), respectively. We noticed that $V^{(1)}_{1,1}(x)$ and $V^{(1)}_{2,2}$ fall off exponentially within a range of 2 a.u away from the proton while $V^{(1)}_{1,2}(x)$ and $V^{(2)}_{1,2}(\sigma)$ possess long range tails and a depth at $x=\sigma=1.4$ a.u, (see Figs 2 and 3, respectively). In Figs 4 and 5, we plot the variation of $-x^4 V^{(1)}_{pol}(x)$ and $-\sigma^4 V^{(2)}_{pol}(\sigma)$ with x and σ, respectively. It is clear that the relations $V^{(1)}_{pol}(x) \underset{x\to\infty}{\sim} -\frac{4}{x^2}$ and $V^{(2)}_{pol}(\sigma) \underset{\sigma\to\infty}{\sim} \frac{-36}{\sigma^4}$ are true, which confirms the argument that the polarizability of the positronium atom is eight times the polarizability of the hydrogen atom. (Note that we can test the accuracy of the calculations by investigating the asymptotic behaviours of the quantities $-x^4(E^{ad}_1 + 1)$ and $-\sigma^4(E^{ad}_2 + 1)$, which should be identical with 4.5 and 36, respectively).

Since the Taylor expansions of $V^{(1)}_{pol}(x)$ and $V^{(2)}_{pol}(\sigma)$ vanish around the origin, we conclude that the solution of Eqs (1) and (2) for any of the above mentioned models does not add (apart from the lengthy algebraic analyses connected with the use of the full kernels in Model 4), any particular complications to our original solution of Model 0, (see Eqs 4 and 5 in [12] and the text thereafter). In order to find the iterative solutions of Eqs (15a,b), we followed the procedure summarized in Appendix 2. It was noticed that the Simpson expansion of the integrals over x and σ requires a mesh size h = 3/32 a.u. and 256 mesh points in order to obtain reasonable agreement between R_{12} and R_{21} (to at least two figures). Tables I and II demonstrate the convergence of the reactance matrix elements of Models 1 and 3 with the increase of the integration range (the number of mesh points

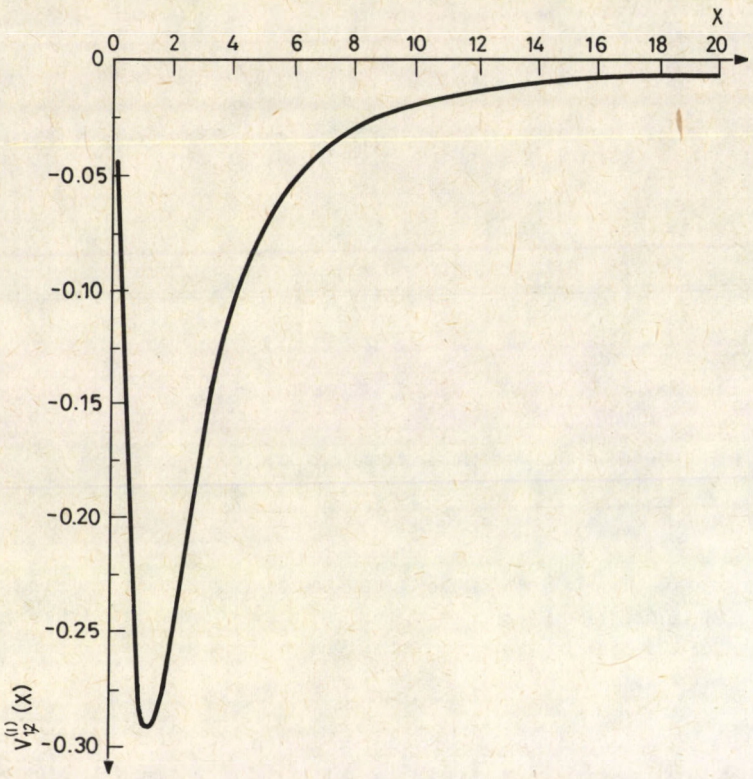

Fig. 2. Variation of $V_{1,2}^{(1)}(x)$ with x

multiplied by the mesh size) up to 24 a.u. away from the proton. From this investigation we conclude the following points:

a) The rate of convergence increases when the momenta k_1 increase.

b) The rate of convergence increases when the total angular momentum ℓ increases.

c) The range 24 a.u. is sufficient for obtaining symmetric reaction matrices at all values of k_1 and ℓ considered.

We have also studied the convergence of R_{ij}^{ν}'s with the number of iterations and found that the stationary variations of these elements are insured after 40 iterations. Therefore, all results presented in the following Tables correspond to the case $\nu = 40$.

Tables III, V, VII contain the partial and total elastic cross-sections of models 1—3 determined for all important values of ℓ at k_1 = 0.71, 0.72, ..., 0.86, 0.866 a.u. There, we find also the cross-sections at k_1 = 0.87 a.u, i.e. when the first excitation channel of the hydrogen atom is opened. Comparing these Tables with Table I in [12], we conclude the following points:

1) The total σ_{11}'s of Model 1 are slightly larger (about 10%) than those of Model 0. However, the inclusion of $V_{pol}^{(1)}(x)$ has shifted the large contributions of the partial cross-

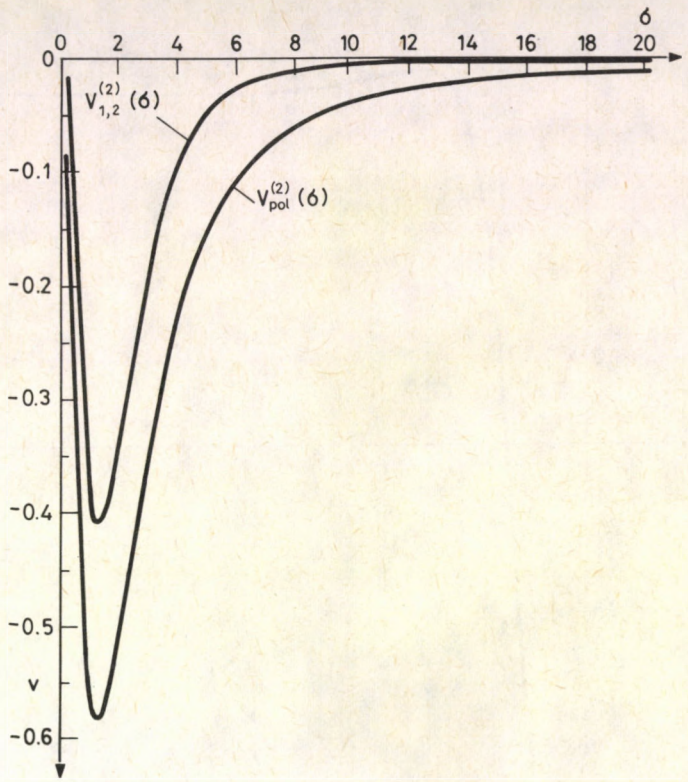

Fig. 3. Variations of $V^{(2)}_{1,2}(\sigma)$ and $V^{(2)}_{pol}(\sigma)$ with σ

sections from the S-wave in Model 0 to the P- and D-wave in Model 1, which is in the correct direction (as it is clear from the comparison presented in Table XI).

2) Model 2 leads to considerable increase in the total cross-sections. The maximum total σ_{11} in this model about 67% larger than in Model 0 and the S-wave contribution is still leading the D-wave contribution.

3) Model 3 produces extremely large cross-sections in which the D-wave plays the role of the S-wave in Model 2 and vice versa. (The use of Model 4 and the extended Stone POM provided us with exploding values for σ_{11} and we have excluded their tabulations).

Tables IV, VI, VIII, IX involve the partial and total cross-sections of the positronium formations in Models 1 — 4 at all previous values of ℓ and k_1. The comparison between these Tables and Tables 2 and 4 in [12] leads to the following conclusions:

1) The total cross-sections of Model 1 are about three times those of Model 0 and the contributions of the D-wave are leading at all $k_1 \geq 0.75$ a.u. The F-wave contributions are larger than those of the S- and P-waves at $k_1 \geq 0.83$ a.u. and the total σ_{12} increases steadily with the increase in k_1.

2) The total σ_{12}'s of Models 2 — 4 are an order of magnitude larger than those of Model 0.

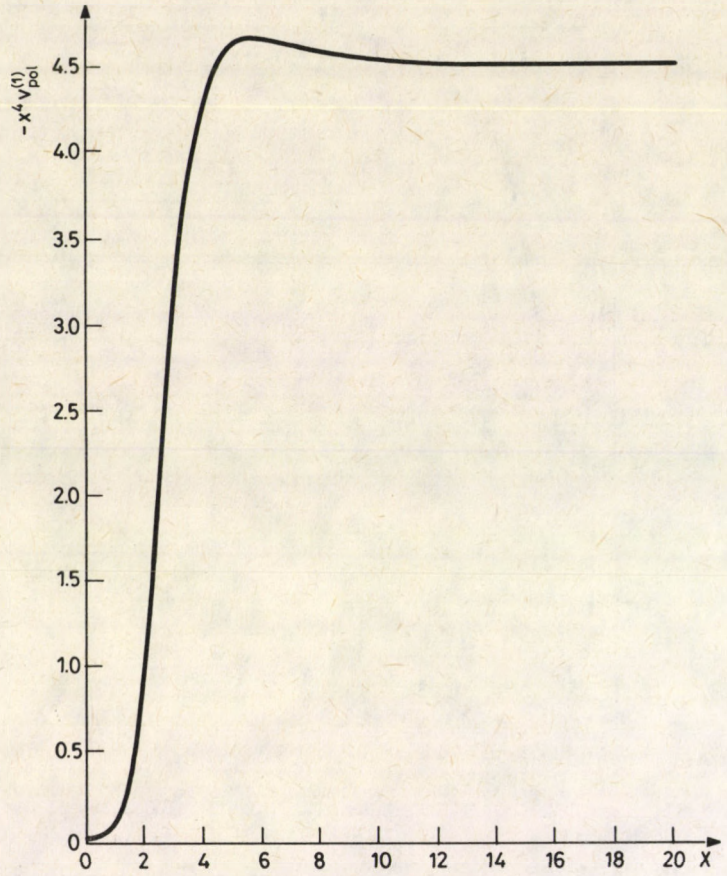

Fig. 4. Asymptotic behaviour of $-x^4 V_{pol}^{(1)}(x)$

3) The switching on of $V_{pol}^{(1)}(x)$ in Models 3 and 4 reduces slightly the total positronium formation cross-sections comparative to Model 2 at all $k_1 \geq 0.72$ a.u.

4) All five models (Model 0 is included), support the importance of calculating the F-, (and sometimes the G-), wave partial cross-sections in order to gain sufficient information about the size of the total σ_{12}.

Table X contains the elements of the P-wave reactance matrix calculated at four values of k_1 for Models 0 — 4 as well as the results of Chan and McEachran [14] and Brown and Humberston [3]. The CM values were obtained using a coupled-static treatment in which 50 short wave correlation functions are added to the total scattering wave functions of both channels. The BH results were determined using Kohn's variational method with 120 (for the S-wave), and 84 (for the P- and D-wave), short range terms in which $e^{-\alpha\rho}$ functions were included. The Table emphasizes the following points:

i) The smallness of the difference between the two off diagonal elements cannot be used as

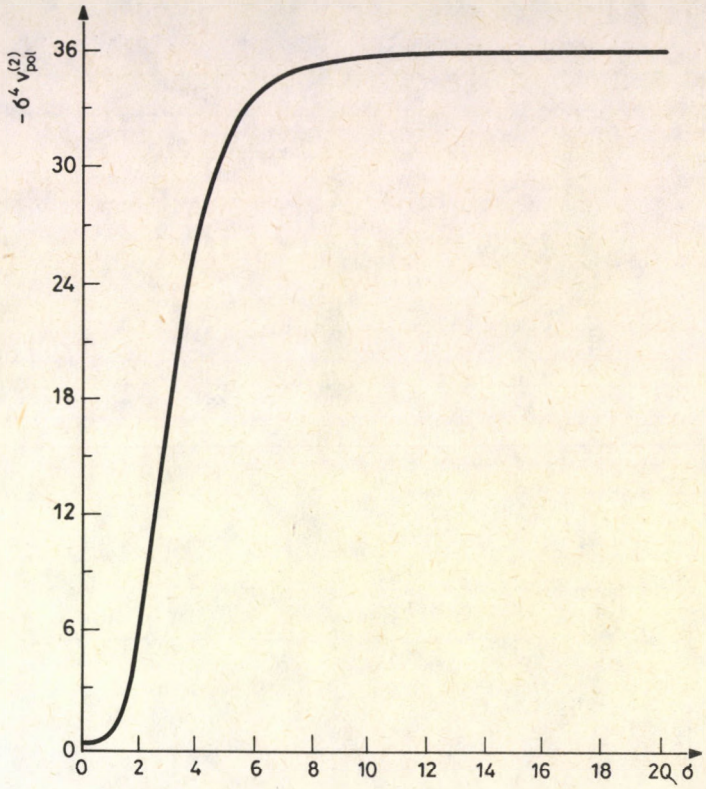

Fig. 5. Asymptotic behaviour of $-\sigma^4 V_{pol}^{(2)}(\sigma)$

an indication to the goodness of the used approximation. (Note that in CM and BH we have $R_{12} = R_{21}$ by construction).

ii) The argument that, the larger the value of R_{11} is, the better is the approximation, is not true unless the employed approximation allows for such a statement. (Remark that R_{11} increases with the order of the Model from Model 0 to Model 4 and that the BH values lie, (for k_1 = 0.71, 0.80 and 0.85), between Model 2 and Model 3).

In Table XI we find a comparison between the S-, P- and D-wave partial cross-sections of Models 0 — 4, the S-wave results of Chan and Fraser [15]. The P-wave results of Chan and McEachran [14] and the S-, P- and D-wave results of Humberston [1,2] and Brown and Humberston [3,4]. (The approximations used by Chan and Fraser and Chan and McEachran are identical.) The Table illustrates that the effect of each polarisation potential varies from one partial wave to the other and from one type of partial cross-sections to the other.

Table XII demonstrates the comparison between the total σ_{11} of different methods at various values of k_1^2. Column 6 contains the sum of the S-, P- and D-wave elastic cross-sections obtained by Brown and Humberston [4], while in column 7, we added the coupled-static results for $\ell \geq 3$ to their total σ_{11}'s. It is clear from the Table that Models 0 and 1 are insufficient for describing the e^+ — H inelastic scattering, while Models 2 and 3 have

Table I

Convergence of the P-wave reactance matrix elements with the increase in the integration range. (Model 1 is used with h = 3/32 and k_1 = 0.8 a.u.)

Range (a.u.)	R_{11}	R_{12}	R_{21}	R_{22}
3	0.0591	0.0144	0.0156	0.0008
6	0.2632	0.4268	0.4271	-0.3939
9	0.1104	0.0320	0.0319	-0.5124
12	0.1118	0.1069	0.1068	-0.5033
15	0.1113	0.1197	0.1196	-0.5111
18	0.1131	0.1155	0.1154	-0.5109
21	0.1129	0.1148	0.1148	-0.5108
24	0.1129	0.1151	0.1150	-0.5108

Table II

Convergence of the P-wave reactance matrix elements with the increase in the integration range. (Model 3 is used with h = 3/32 and k_1 = 0.8 a.u.)

Range (a.u.)	R_{11}	R_{12}	R_{21}	R_{22}
3	0.093	-0.146	-0.138	1.250
6	0.645	0.961	0.965	0.693
9	0.214	0.253	0.255	0.357
12	0.213	0.329	0.332	0.457
15	0.214	0.339	0.342	0.453
18	0.219	0.342	0.345	0.457
21	0.218	0.340	0.343	0.457
24	0.218	0.340	0.343	0.459

shifted the total elastic cross-sections higher than the variational ones. Thus, both $V_{pol}^{(1)}$ and $V_{pol}^{(2)}$ have positive influence upon the total σ_{11}'s. Fig. 6 shows the general behaviours of σ_{11}'s, calculated by different approaches, as a function of the momentum of the incident positrons.

On the other hand, Table XIII contains in addition to the corresponding positronium formation cross-sections obtained by our Models, the ones determined by Drachman et al [16] using the modified Born approximation and those of Khan and Ghosh [17] using the distorted wave approximation. From the Table we conclude that it is very unlikely that the full polarisation of Ps will take place in the second channel and that the distortion due to the presence of the proton may be adequately described by a less attractive potential. (Remember that $V_{pol}^{(1)}(x) \sim -4.5/x^2$, while $V_{pol}^{(2)}(\sigma) \sim -36/\sigma^2$). In Fig. 7, we presented a comparison between the total positronium formation cross-sections obtained by our Models. The Figure illustrates the behaviour of these cross-sections under the variation of the momentum of the incident positrons.

Table III

Partial and total elastic cross-sections of e^+ - H scattering. (Model 1 is used)

k_1 \ ℓ	0	1	2	3	4	5	6	total σ_{11} in a_o^2 a.u.
0.71	0.32769	0.09724	0.85850	0.17645	0.03566	0.00987	0.00370	2.60911
0.72	0.35488	1.16618	0.89209	0.18562	0.03742	0.01027	0.00383	2.65029
0.73	0.38208	1.12504	0.92699	0.19573	0.03929	0.01070	0.00395	2.68378
0.74	0.40911	1.07955	0.95968	0.20679	0.04129	0.01115	0.00409	2.71166
0.75	0.43587	1.03235	0.98821	0.21865	0.04344	0.01163	0.00422	2.73437
0.76	0.46226	0.98479	1.01174	0.23109	0.04575	0.01213	0.00437	2.75213
0.77	0.48823	0.93763	1.03009	0.24385	0.04822	0.01266	0.00452	2.76520
0.78	0.51372	0.89130	1.04340	0.24669	0.05085	0.01322	0.00468	1.77386
0.79	0.53869	0.84608	1.05214	0.26935	0.05364	0.01381	0.00485	2.77856
0.80	0.56308	0.80214	1.05666	0.28163	0.05656	0.01442	0.00503	2.77952
0.81	0.58687	0.75960	1.05740	0.29337	0.05960	0.01507	0.00522	2.77713
0.82	0.61003	0.71854	1.05479	0.30443	0.06272	0.01574	0.00541	2.77166
0.83	0 63253	0.678902	1.04920	01.31471	0.06589	0.01645	0.00561	2.76341
0.84	0.65436	0.64108	1.04100	0.32416	0.06909	0.01719	0.00581	2.75269
0.85	0.67549	0.60473	1.03049	0.33271	0.07229	0.01796	0.00602	2.73969
0.86	0.69592	0.56996	1.01799	0.34034	0.07545	0.01875	0.00624	2.72465
0.866	0.70783	0.54985	1.00965	0.34448	0.07733	0.01924	0.00637	2.71475
0.87	0.71563	0.53675	1.00377	0.34704	0.07856	0.01957	0.00646	2.70778

Table IV

Partial and total positronium formation cross-sections of e^+ - H (Model 1 is used)

k_1 \ ℓ	0	1	2	3	4	5	6	total σ_{12} in a_o^2 a.u.
0.71	0.01271	0.01398	0.00078	0.00001	0.00000	0.00000	0.00000	0.02748
0.72	0.02694	0.10155	0.02797	0.00112	0.000003	0.000000	0.00000	0.15761
0.73	0.03588	0.19352	0.10058	0.00733	0.00029	0.00001	0.00000	0.33761
0.74	0.04290	0.27653	0.21275	0.00130	0.00130	0.00006	0.00000	0.55642
0.75	0.04875	0.34934	0.35339	0.05083	0.00374	0.00023	0.00001	0.80629
0.76	0.05380	0.41291	0.51169	0.09278	0.00838	0.00061	0.00004	1.08021
0.77	0.05825	0.46850	0.67880	0.14899	0.01601	0.00136	0.00011	1.37202
0.78	0.06225	0.51728	0.84813	0.21866	0.02731	0.0262	0.00024	1.67649
0.79	0.06588	0.56019	1.01504	0.30025	0.04282	0.00460	0.00047	1.98925
0.80	0.06919	0.59800	1.17640	0.39183	0.06287	0.00747	0.00082	2.30658
0.81	0.07222	0.63135	1.33017	0.49130	0.08761	0.01143	0.00136	2.62544
0.82	0.07499	0.66082	1.47507	0.59660	0.11698	0.01665	0.00211	2.94322
0.83	0.07751	0.68690	1.61035	0.70582	0.15078	0.02328	0.00314	3.24778
0.84	0.07979	0.71005	1.73564	0.81721	0.18866	0.03142	0.00450	3.56727
0.85	0.08186	0.73067	1.85088	0.92919	0.23022	0.04114	0.00624	3.8702

Table IV (cont.)

k_1 \ ℓ	0	1	2	3	4	5	6	total σ_{12} in a_o^2 a.u.
0.86	0.08371	0.74912	1.95621	1.04041	0.27499	0.05245	0.00843	4.16532
0.866	0.08473	0.75928	2.01477	1.10626	0.30319	0.06000	0.00997	4.33820
0.87	0.08538	0.76571	2.051935	1.14965	0.32249	0.06534	0.01101	4.45152

Table V

Partial and total elastic cross-sections of e^+ - H (Model 2)

k_1 \ ℓ	0	1	2	3	4	5	6	total σ_{11} in a_o^2 a.u.
0.71	1.67066	1.80562	0.37772	0.02659	0.00137	0.00006	0.00000	3.88202
0.72	1.72114	2.00479	0.44958	0.03061	0.00160	0.00008	0.00000	4.20780
0.73	1.74509	1.88734	0.53325	0.03557	0.00187	0.000009	0.00000	4.20321
0.74	1.76347	1.75945	0.61626	0.04160	0.00217	0.00011	0.00001	4.18307
0.75	1.77934	1.65619	0.69013	0.04871	0.00255	0.00012	0.00001	4.17705
0.76	1.79327	1.57039	0.75176	0.05678	0.00300	0.00015	0.00001	4.17536
0.77	1.80560	1.50161	0.79963	0.06570	0.00353	0.00018	0.00001	4.17626
0.78	1.81661	1.44539	0.83505	0.07523	0.00415	0.00021	0.00001	4.17665
0.79	1.82643	1.39623	0.86078	0.08514	0.00486	0.00025	0.00001	4.17370
0.80	1.83508	1.35237	0.87842	0.09521	0.00567	0.00030	0.00002	4.16707
0.81	1.84260	1.31383	0.88888	0.10529	0.00657	0.00035	0.00002	4.15754
0.82	1.84906	1.28018	0.89354	0.11519	0.00756	0.00041	0.00002	4.14596
0.83	1.85454	1.24997	0.89405	0.12474	0.00864	0.00049	0.00003	4.13246
0.84	1.85906	1.22200	0.89147	0.13380	0.00979	0.0057	0.00003	4.11672
0.85	0.86265	1.19601	0.88616	0.14231	0.01101	0.00067	0.00004	4.09885
0.86	1.86536	1.17227	0.87828	0.15025	0.01228	0.00077	0.00004	4.07925
0.866	1.86657	1.15916	0.87252	0.15472	0.01307	0.00084	0.00005	4.06693
0.87	1.86721	1.150845	0.86834	0.15756	0.01360	0.00089	0.00005	4.05850

Table VI

Partial and total positronium formation cross-sections of e^+ - H (Model 2)

k_1 \ ℓ	0	1	2	3	4	5	6	total σ_{12} in a_o^2 a.u.
0.71	0.16712	0.39113	0.00275	0.00001	0.00000	0.00000	0.00000	0.56101
0.72	0.12589	2.57989	0.11270	0.00208	0.00004	0.00000	0.00000	2.82060
0.73	0.11412	3.88425	0.42635	0.01409	0.00041	0.00001	0.00000	4.43933
0.74	0.10737	4.56892	0.92200	0.04517	0.00184	0.00008	0.00000	5.64488
0.75	0.10188	4.99704	1.52270	0.10281	0.00535	0.00028	0.00002	6.73008
0.76	0.09678	5.28218	2.16315	0.19079	0.01217	0.00076	0.00005	7.74588
0.77	0.09204	5.48505	2.79197	0.31005	0.02350	0.00168	0.00013	8.70442

Table VI (cont.)

k_1 \ ℓ	0	1	2	3	4	5	6	total σ_{12} in a_o^2 a.u.
0.78	0.08748	5.64171	3.37291	0.45933	0.04043	0.00328	0.00028	9.60542
0.79	0.08295	5.76223	3.89425	0.63437	0.06388	0.00578	0.00054	10.44400
0.80	0.07845	5.85065	4.35503	0.82934	0.09449	0.00945	0.00095	11.21836
0.82	0.06982	5.96093	5.09113	1.25830	0.17768	0.02126	0.00245	12.58157
0.83	0.06571	5.99202	5.37344	0.48192	0.22983	0.02984	0.00360	13.17636
0.84	0.06170	6.00760	5.60838	1.70439	0.28848	0.04040	0.00526	13.71621
0.85	0.05727	6.00840	5.80116	1.92162	0.35292	0.05304	0.00733	14.20174
0.86	0.05410	5.99681	5.95471	2.13097	0.42221	0.06780	0.00991	14.63651
0.866	0.05194	5.98494	6.02930	2.25192	0.46569	0.07767	0.01174	14.87320
0.87	0.05053	5.97518	6.07228	2.33032	0.49537	0.08466	0.01308	15.02142

Table VII

Partial and total elastic cross-sections of e^3 - H (Model 3)

k_1 \ ℓ	0	1	2	3	4	5	6	total σ_{11} in a_o^2 a.u.
0.71	0.49306	3.44398	0.29514	0.20351	0.03718	0.00997	0.00371	5.48655
0.72	0.54259	3.48078	1.41165	0.21687	0.03916	0.01039	0.00384	5.70528
0.73	0.57286	3.18676	1.53733	0.23218	0.04130	0.01083	0.00397	5.58523
0.74	0.59925	2.91301	1.65047	0.24953	0.04361	0.01131	0.00410	5.47128
0.75	0.62408	2.68320	1.73882	0.26867	0.04614	0.01181	0.00424	5.37696
0.76	0.64765	2.48499	1.79968	0.28911	0.04889	0.01234	0.00439	5.28705
0.77	0.67021	2.31386	1.83331	0.31029	0.05188	0.01290	0.00454	5.04699
0.78	0.69199	2.16160	1.84419	0.33156	0.05510	0.01350	0.00471	5.10265
0.79	0.71305	2.02171	1.83804	0.35226	0.05855	0.01413	0.00488	5.00262
0.80	0.73332	1.89233	1.81832	0.37190	0.06219	0.01479	0.00506	4.89791
0.80	0.75283	1.77302	1.78745	0.39011	0.06599	0.01550	0.00525	4.79015
0.82	0.77160	1.66231	1.74837	0.40658	0.06990	0.01624	0.00545	4.68095
0.83	0.78969	0.55835	1.70389	0.42017	0.07387	0.01701	0.00566	4.56864
0.84	0.80708	1.46012	1.65563	0.43328	0.07787	0.01783	0.00587	4.45768
0.85	0.82378	1.36757	1.60429	0.44339	0.08183	0.01868	0.00609	4.34563
0.86	0.83977	1.28073	1.55047	0.45142	0.08571	0.01956	0.00631	4.23977
0.866	0.84904	1.23124	1.51740	0.45523	0.08798	0.02010	0.00645	4.16744
0.87	0.85509	1.19924	1.49517	0.45736	0.08947	0.02046	0.00654	4.12333

Table VIII

Partial and total positronium formation cross-sections of e^+ - H (Model 3)

k_1 \ ℓ	0	1	2	3	4	5	6	total σ_{12} in a_o^2 a.u.
0.71	0.30530	0.29947	0.00252	0.00001	0.00000	0.00000	0.00000	0.60730
0.72	0.23340	2.01715	0.10313	0.00202	0.00000	0.00000	0.00000	2.35570
0.73	0.21651	3.05464	0.38939	0.01370	0.00040	0.00001	0.00000	3.67465
0.74	0.20875	3.59488	0.84075	0.04386	0.00181	0.00008	0.00000	4.69013
0.75	0.20304	3.92996	1.38671	0.09973	0.00528	0.00028	0.00001	5.62501
0.76	0.19781	4.14961	1.96778	0.18487	0.01202	0.00075	0.00005	6.51289
0.77	0.19303	4.30382	2.53821	0.30010	0.02320	0.00167	0.00012	7.35915
0.78	0.18834	4.42129	3.06211	0.44409	0.03980	0.00326	0.00027	8.15926
0.79	0.18340	4.50940	3.53189	0.61263	0.06301	0.00575	0.00053	8.90661
0.80	0.17823	4.57127	3.94572	0.80003	0.09316	0.00938	0.00095	9.59874
0.81	0.17298	4.61324	4.30226	1.00112	0.13053	0.01442	0.00156	10.23611
0.82	0.16772	4.64079	4.60231	1.21113	0.17499	0.02110	0.00244	10.82048
0.83	0.16241	4.65545	4.85154	1.42480	0.22623	0.02962	0.00365	11.35370
0.84	0.15701	4.65689	5.05708	1.63692	0.28379	0.04009	0.00524	11.83702
0.85	0.15154	4.64579	5.22374	1.84354	0.34698	0.05261	0.00729	12.27119
0.86	0.14608	4.62424	5.35426	2.04218	0.41486	0.06723	0.00987	12.66772
0.866	0.14283	4.60714	5.41643	2.15670	0.45742	0.07701	0.01168	12.85870
0.87	0.14066	4.59414	5.45168	2.23081	0.48645	0.08393	0.01302	13.00069

Table IX

Partial and total positronium formation cross-section of e^+ - H (Model 4)

k_1 \ ℓ	0	1	2	3	4	5	6	total σ_{12} in a_o^2 a.u.
0.71	0.10099	0.00482	0.00255	0.00005	0.00000	0.00000	0.00000	0.10586
0.72	0.09968	0.01689	0.09089	0.00824	0.00007	0.00000	0.00000	0.21577
0.73	0.06439	0.01546	0.30058	0.05084	0.00073	0.00000	0.00000	0.43200
0.74	0.02379	0.00931	0.58526	0.14862	0.00315	0.00002	0.00000	0.77015
0.75	0.00023	0.00325	0.89980	0.30969	0.00878	0.00007	0.00000	1.22182
0.76	0.02861	0.00008	1.22386	0.52918	0.01905	0.00023	0.00001	1.80102
0.77	0.15758	0.00211	1.54825	0.79704	0.03507	0.00072	0.00002	2.54079
0.78	0.42176	0.01164	1.86610	1.10203	0.05765	0.00629	0.00004	3.46551
0.79	0.78236	0.03119	2.17643	1.43063	0.08747	0.00006	0.00007	4.50821
0.80	1.11791	0.06359	2.48260	1.76988	0.12501	0.00017	0.00010	5.55926
0.81	1.32793	0.11195	2.78734	2.11082	0.17039	0.00040	0.00012	6.50895
0.82	1.40352	0.17959	3.09161	2.44751	0.22342	0.00050	0.00009	7.34624
0.83	1.38706	0.27018	3.39654	2.77475	0.28373	0.00048	0.00001	8.11275
0.84	1.32083	0.38779	3.70463	3.08805	0.35072	0.00037	0.00036	8.85275
0.85	1.23172	0.53671	4.01863	3.38515	0.42334	0.00020	0.00838	9.60413
0.86	1.13417	0.72140	4.33993	3.66630	0.50019	0.00004	0.03694	10.39897
0.866	1.07482	0.85128	4.53616	3.82789	0.54771	0.00001	0.03183	10.86970
0.87	1.03551	0.94643	4.66829	3.93281	0.57981	0.00001	0.02819	11.09105

Table X

Comparison between the P-wave reactance matrix of different approximations. (CM refers to Chan and McEachran [14]. BH = Brown and Humberston [3])

k_1	Model	R_{11}	R_{12}	R_{21}	R_{22}
0.71	0	0.0355	0.0166	0.0165	-0.0065
	1	0.1275	0.0138	0.0137	-0.0064
	2	0.1586	0.0740	0.0764	0.1050
	3	0.2211	0.0654	0.0684	0.1067
	4	67.2611	-0.5408	-0.3603	0.0548
	CM	0.165	0.0250	0.0250	0.0092
	BH	0.185	0.0321	0.0321	0.0699
0.75	0	0.0348	0.0910	0.0907	-0.229
	1	0.1244	0.0750	0.0748	-0.2252
	2	0.1977	0.3438	0.3464	0.5553
	3	0.3485	0.3075	0.3112	0.5975
	4	6.4211	-0.0469	-0.0456	-0.2686
	CM	0.171	0.133	0.133	0.0486
	BH	0.174	0.110	0.110	0.171
0.80	0	0.0237	0.1414	0.1412	-0.522
	1	0.1129	0.1151	0.1150	-0.511
	2	0.1655	0.3848	0.3867	0.3992
	3	0.2183	0.3402	0.3432	0.4590
	4	3.2510	0.1490	0.1482	-0.8735
	CM	0.161	0.173	0.173	-0.160
	BH	0.176	0.171	0.171	-0.0611
0.85	0	0.0072	0.1917	0.1916	-0.813
	1	0.0973	0.1539	0.1540	-0.7908
	2	0.1253	0.4080	0.4097	0.2804
	3	0.1823	0.3552	0.3580	0.3548
	4	2.2841	0.5006	0.5011	-1.5924
	CM	0.148	0.210	0.210	-0.361
	BH	0.169	0.211	0.211	-0.289

Table XI

Comparison between the partial cross-sections of e^+ - H inelastic scattering calculated using different approximations. (* = Chan and Fraser [15], CM = Chan and McEachran [14], BH = Brown and Humberston [4])

k_1	Model	Partial σ_{11} (in a_o^2 a.u.)			Partial σ_{12} (in a_o^2 a.u.)		
		S-wave	P-wave	D-Wave	S-Wave	P-wave	D-wave
0.71	0	2.1000	0.1000	0.1481	0.0000	0.0206	0.0009
	1	0.3277	1.1972	0.8585	0.0127	0.0140	0.0008
	2	1.6707	1.8056	0.3777	0.1671	0.3911	0.0028
	3	0.4931	3.4440	1.2951	0.3053	0.2995	0.0025
	4	-	-	-	0.1010	0.0048	0.0026
	CM	0.1053*	1.9894	-	0.0047*	0.0462	-
	BH	0.0817	2.4794	1.0151	0.0129	0.0849	0.0020
0.75	0	2.1095	0.0972	0.2145	0.0001	0.5190	0.3907
	1	0.4359	1.0324	0.2145	0.0488	0.3493	0.3534
	2	1.7793	1.6562	0.6901	0.1019	4.9970	1.5227
	3	0.6241	2.6832	1.7388	0.2030	3.9300	1.3867
	4	-	-	-	0.0002	0.0033	0.8998
	CM	0.1637*	1.8450	-	0.0091*	1.1220	-
	BH	0.1351	2.2754	1.2666	0.0138	1.1471	1.0529
0.80	0	2.1025	0.0758	0.2736	0.0006	0.8963	1.3145
	1	0.5631	0.8021	1.0567	0.0692	0.5980	1.1764
	2	1.8351	1.3524	0.8784	0.0785	5.8507	4.3550
	3	0.7333	1.8923	1.8183	0.1782	4.5713	3.9457
	4	-	-	-	1.1179	0.0636	2.4826
	CM	0.2363*	1.5400	-	0.0097*	1.5871	-
	BH	0.2043	1.9549	0.3294	0.0154	1.5149	2.5520
0.85	0	2.0779	0.0586	0.2981	0.0013	1.1019	2.0877
	1	0.6755	0.6047	1.0305	0.0819	0.7307	1.8509
	2	1.8627	1.1960	0.8862	0.0573	6.0084	5.8012
	3	0.8238	1.3676	1.6043	0.1515	4.6458	5.2237
	4	-	-	-	1.2317	0.5367	4.0186
	CM	0.3039*	1.3074	-	0.0101*	1.8354	-
	BH	0.2671	1.7191	1.2980	0.01823	1.7631	3.3220

Table XII

Comparison between the total elastic cross-sections (in a_0^2 a.u.) calculated using different approximations

k_1^2 (Ryd)	Model 0 [a]	Model 1	Model 2	Model 3	Kohn's Method [b]	Kohn's Method + CS for $\ell \geq 3$
0.5041	2.3678	2.6091	3.8820	5.4866	3.5829	3.6016
0.5625	2.453	0.6344	4.1771	5.3770	3.6771	3.7078
0.6400	2.5071	2.7795	4.1671	4.8979	3.4886	3.5429
0.7225	2.5162	2.7397	4.0989	4.3456	3.2686	3.3492
0.7500	2.5105	2.7078	4.0669	4.1674	-	-

a) Abdel-Raouf et al [12]

b) Brown and Humberston [4]

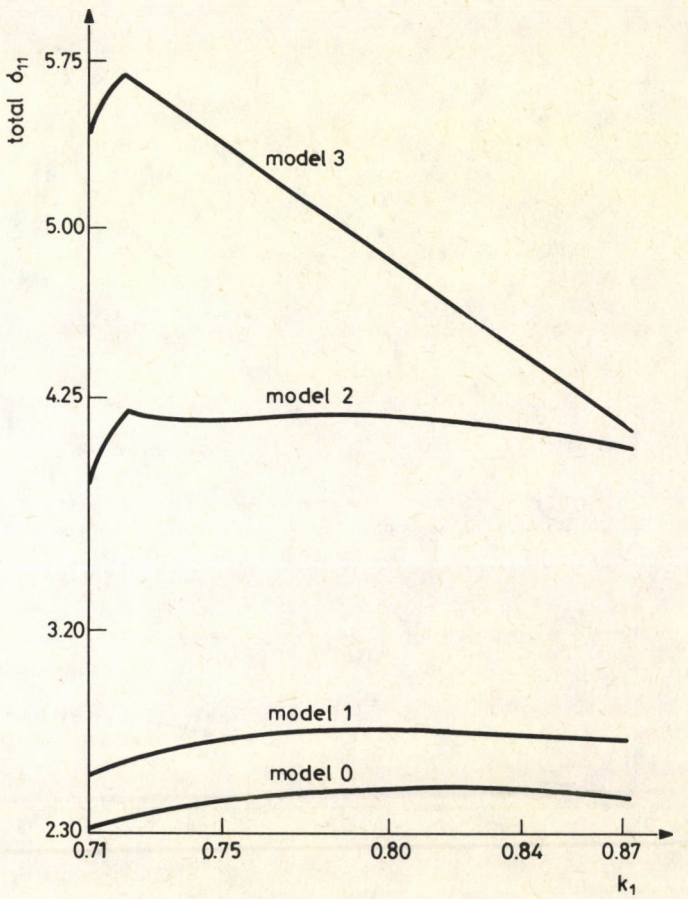

Fig. 6. Comparison between the total elastic cross-sections of Models 0 — 3

Table XIII

Comparison between total positronium formation cross-sections (in a_0^2 a.u.) calculated using different approximations

k_1^2 (Ryd)	Model 0	Model 1	Model 2	Model 3	Model 4	Born Approx. b)	Dist. wave Approx.	Kohn's Method c)	Kohn's + CS for $\ell > 2$ d)
0.5041	0.0214	0.0275	0.5610	0.6073	0.1059	0.0512	0.0722	0.1066	0.10061
0.5625	0.9667	0.8063	6.7301	5.6250	0.2218	1.7129	1.9651	2.200	2.2564
0.6400	2.6909	2.3066	11.2184	9.5987	5.5593	4.3686	4.5765	4.0857	4.5642
0.7225	4.4437	3.8702	14.2017	12.2712	9.6041	7.0714	6.6577	5.2486	6.4997
0.7500	5.0905	4.3382	14.8732	12.8587	10.870	7.8571	7.0144	-	-

a) Abdel-Raouf et al [12]
b) Drachman et al [16]
c) Khan and Ghosh [17]
d) Brown and Humberston [4]

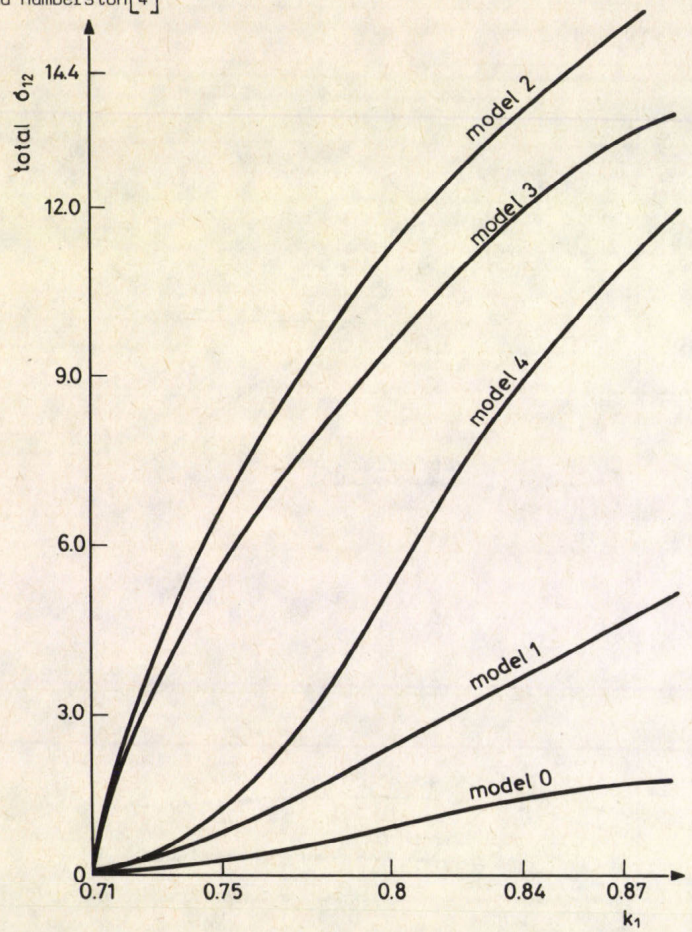

Fig. 7. Comparison between the total positronium formation cross-sections of Models 0 — 4

Finally, it is interesting to refer to our investigation of the extended Stone POM. In this case the kernels K_{12} and $\frac{1}{2} K_{21}$ are far from being symmetric and the off diagonal elements of the reactance matrix are of completely different orders (often of different signs), which raises our doubt about the consistency and applicability of this method to inelastic collisions of positrons with atoms. This has also emphasized the argument that the polarized orbital principle fails in describing any collision process more complicated than the elastic scattering of positrons by small atoms.

Acknowledgment

The author is extremely indebted to Prof. Dr. J. Ladik for his generous support and encouragement. Discussions with Prof. Dr. J. Ladik and the members of the Institute are deeply acknowledged.

References

1. J.W. Humberston, Canad. J. Phys., 60, 591, 1982.
2. J.W. Humberston, J. Phys., B17, 2353, 1984.
3. C.J. Brown and J.W. Humberston, J. Phys., B17, L423, 1984.
4. C.J. Brown and J.W. Humberston, J. Phys., B18, L401, 1985.
5. M. Horbatsch, J.W. Darewych and R.P. McEachran, J. Phys., B16, 4451, 1983.
6. R.P. McEachran, D.L. Morgan, A.G. Ryman and A.D. Stauffer, J. Phys., B10, 663, 1977.
7. R.P. McEachran, D.L. Morgan, A.G. Ryman and A.D. Stauffer, J. Phys., B11, 951, 1978.
8. R.P. McEachran, A.G. Ryman and A.D. Stauffer, J. Phys., B11, 551, 1978.
9. R.P. McEachran, A.G. Ryman and A.D. Stauffer, J. Phys., B12, 1031, 1979.
10. R.P. McEachran, A.D. Stauffer and L.E.M. Cambell, J. Phys., B13, 1281, 1980.
11. R.J. Drachman and A. Temkin, Case Studies in Atomic Collision Physics, Vol. 2, ed. E.W. McDaniel and M.R.C. McDowell, North-Holland, Amsterdam, Chap. 6.
12. M.A. Abdel-Raouf, J.W. Darewych, R.P. McEachran and A.D. Stauffer, Phys. Lett., 100A, 353, 1984.
13. P.M. Stone, Phys. Rev., 141, 137, 1966.
14. Y.F. Chan and R.P. McEachran, J. Phys., B9, 1869, 1976.
15. Y.F. Chan and P.A. Fraser, J. Phys., B6, 2504, 1972.
16. R.J. Drachman, K. Omidvar and J.H. McGuire, Phys. Rev., A14, 100, 1976.
17. P. Khan and A.S. Ghosh, Phys. Rev., A27, 1904, 1983.
18. P.A. Fraser, Proc. Phys. Soc. (London) LXX III, 329, 1961.
19. P.A. Fraser, private communication
20. A. Messiah, Quantum Mechanics I, North-Holland Publishing Comp., Amsterdam, 1970.

Appendix 1

Our main goalin this Appendix is to express the kernels $K_{12}(\sigma,x)$ and $K_{21}(\sigma,x)$, Eqs (15c,d), in closed forms as functions of x and σ. Let us first consider K_{12} and replace the functions Φ_{11}, Φ_{21} and Φ_{22} by their explicit forms using Eqs (4d,e). This provides us with

$$K_{12}(\sigma,x)=(8\sigma x \int\int (1/4\pi\sqrt{2})\, e^{-r} \{- (\nabla^2_\sigma D\, k_2^2) + 2(\tfrac{2}{x} - \tfrac{2}{r})\}\, e^{-\rho/2} +$$

$$+ (\mathcal{E}/\pi\sqrt{43})\{\rho(1+\rho/4)\,(-\nabla^2_\sigma) - 0.5E\rho(1+\rho/4) - (\nabla^2_\rho + /\rho)\rho(1+\rho/4) +$$

$$+ 0.5\rho(1+\rho/4)(2+x-2/r)\}\, e^{-\rho/2}(\hat{\rho}\cdot\hat{\sigma}')\}\, \beta_2(\sigma)\}\, Y^0_\ell(\hat{x})\, Y^0_\ell(\hat{\sigma})\, dx\, d\hat{\sigma}\,. \qquad (1.1)$$

In order to avoid the operation with ∇^2_σ on the functions of σ and $\hat{\sigma}$ in Eq. (1.1), we use Green's theorem which has the net effect that $\zeta(r,\rho)\nabla^2_\sigma\chi(\sigma) = (\nabla^2_\sigma \zeta(r,\rho))\,\chi(\sigma)$, where $\zeta(r,\rho)$ and $\chi(\sigma)$ are arbitrary functions.

In order to express ∇^2_σ in terms of ∇_ρ and ∇_r, we use the relations

$$\underline{r} = 2\underline{\sigma} - \underline{x} \quad \text{and} \quad \underline{\rho} = 2(\underline{\sigma} - \underline{x})$$

and hence

$$\frac{\partial}{\partial \sigma_i} = 2\frac{\partial}{\partial r_i} + 2\frac{\partial}{\partial \rho_i} \quad , \qquad i = 1,2,3 \quad , \tag{1.2}$$

$$\frac{\partial}{\partial x_i} = -\frac{\partial}{\partial r_i} - 2\frac{\partial}{\partial \rho_i} \quad , \qquad i = 1,2,3 \quad .$$

Therefore, the required relation is given by

$$\nabla^2_\sigma = 4\,\nabla^2_r + 4\,\nabla^2_\rho + 8\,\nabla_r \cdot \nabla \quad . \tag{1.3}$$

Consequently, we can prove that

$$\nabla^2_\sigma (e^{-r}\, e^{-\rho/2}) = 4\left\{5/4 - 2/r - 1/\rho + (\hat{r}.\hat{\rho})\right\} e^{-r}\, e^{-\rho/2} \tag{1.4}$$

$$\nabla^2_\sigma (e^{-r}\, e^{-\rho/2})\rho(1+\rho/4)\hat{\rho})$$

$$= 4\,(1-2/r)\, e^{-r}e^{-\rho/2}\rho(1+\rho/4)\hat{\rho} + (\rho^2/4-2\rho-4)\, e^{-r}e^{-\rho/2}\rho +$$

$$+ (6+\rho)\rho\, e^{-r}e^{-\rho/2}(\hat{r}.\hat{\rho})\hat{\rho} - 2(4+\rho)\rho\, e^{-r}e^{-\rho/2}\,\hat{r} \quad , \tag{1.5}$$

where the following relation is used

$$\nabla^2_\rho\, (e^{-\rho/2}\ \rho(1+\rho/4)\hat{\rho}) = (\rho^2/16-\rho/2-1)\, e^{-\rho/2}\hat{\rho} \quad . \tag{1.6}$$

Substitution from Eqs (1.4) – (1.6) into (1.1) leads to a simpler form for $K_{12}(\sigma,x)$ which contains the functions e^{-r}, $e^{-\rho/2}$, $(\hat{r}.\hat{\rho})$, $(\hat{r}.\hat{\sigma})$, $(\hat{\rho}.\hat{\sigma})$ and a polynomial in r and ρ. In order to evaluate the integrals involved in Eq. (1.1), we have to use the transformations in (1.2) for r and ρ. Also we have to use the following definitions

$$\begin{aligned}
(\hat{r}.\hat{\sigma}) &= (2\sigma-\mu x)/(4\mu^2+x^2 - 4\sigma x\mu)^{1/2} \quad , \\
(\hat{r}.\hat{\rho}) &= (2\mu\sigma-x)/\left\{(\sigma^2+x^2 - 2\sigma x\mu)(4\sigma^2+x^2-4\sigma x\mu)\right\}^{1/2} \quad , \\
(\hat{\rho}.\hat{\sigma}) &= (\sigma-\mu x)/(\sigma^2+x^2-2\sigma x\mu)^{1/2} \quad , \\
(\hat{r}.\hat{x}) &= (2x-2\mu\sigma)/(4\sigma^2+x^2-4\sigma x\mu)^{1/2} \quad , \\
(\hat{\rho}.\hat{x}) &= (2\mu\sigma-x)/(\sigma^2+x^2-2\sigma x\mu)^{1/2} \quad , \\
\mu &= (\hat{x}.\hat{\sigma}) \quad .
\end{aligned} \tag{1.7}$$

It is now possible to reduce the integrals in (1.1) into integrals over μ only from $\mu = -1$ to $\mu = +1$. In order to carry out the integrations numerically we use the following expansion for a given function $W(\left|2\underline{\sigma}-\underline{x}\right|, \left|\underline{\sigma}-\underline{x}\right|, \hat{\xi})$, where $\hat{\xi}$ is one (or a combination) of the angles appearing in Eqs (1.7):

$$W(|2\underline{\sigma}-\underline{x}|,\ |\underline{\sigma}-\underline{x}|,\hat{\xi}) = \frac{1}{\sigma x}\sum_{\ell=0}^{\infty}(2\ell+1)\,\tilde{W}(\sigma,x)\,P_\ell(\mu)\ , \tag{1.8}$$

where the function $\tilde{W}(\sigma,x)$ is a pure function of x and σ and is determined by

$$\tilde{W}(\sigma,x) = \frac{\sigma x}{2}\int_{-1}^{+1} P_\ell(\mu)\ W(|2\underline{\sigma}-\underline{x}|,|\underline{\sigma}-\underline{x}|,\hat{\xi})\,d\mu\ . \tag{1.9}$$

The integral at the right-hand side of Eq. (1.9) can be calculated with large accuracy using a Gauss quadrature of order 10. In order to obtain the seeked form of $K_{12}(\sigma,x)$ we introduce a function $G_\ell(x,\sigma,i_1,i_2,m_1,m_2,n_1,n_2,\ldots,n_6)$ such that

$$G_\ell(x,\sigma,i_1,i_2,m_1,m_2,n_1,n_2,n_3,n_4,n_5,n_6) =$$

$$= \frac{\sigma x}{2}\int_{-1}^{+1} P_\ell(\mu)\exp(-|2\underline{\sigma}-\underline{x}|)\exp(-|\underline{\sigma}-\underline{x}|)\,F_{m_1}F_{m_2}$$

$$(\hat{r}.\hat{x})^{n_1}(\hat{\rho}.\hat{\sigma})^{n_2}(\hat{\rho}.\hat{x})^{n_3}(\hat{r}.\hat{\sigma})^{n_4}(\hat{r}.\hat{\sigma})^{n_5}(\hat{x}.\hat{\sigma})^{n_6}\,d\mu\ , \tag{1.10}$$

where

$$F_{m_1} = \begin{cases} 1 & \text{for } m_1 = 1\ , \\ 2/x - 2/|2\underline{\sigma}-\underline{x}| & \text{for } m_1 = 2\ , \\ 2/x - 2/|2\underline{\sigma}-\underline{x}| - E & \text{for } m_1 = 3\ , \end{cases} \tag{1.11}$$

and

$$F_{m_2} = \begin{cases} 1 & \text{for } m_2 = 1\ , \\ 2/x - 2/2\,|\underline{\sigma}-\underline{x}| & \text{for } m_2 = 2\ , \\ 2/x - 2/2\,|\underline{\sigma}-\underline{x}| - E & \text{for } m_2 = 3\ . \end{cases} \tag{1.12}$$

For simplicity of representation of $K_{12}(\sigma,x)$, we denote the function in Eq. (1.10) as $G_\ell^{(j)}$, where j is an integer and refers to a set of values of the numbers $i_1,i_2,m_1,m_2,n_1,n_2,\ldots,n_6$, (see Table A). It is now an easy matter to reduce $K_{12}(\sigma,x)$, Eq. (1.1), to the form

Table A

The values of $i_1,i_2,m_1,m_2,n_1,\ldots,n_6$ in $G_\ell^{(j)}$ at a given j

j	i_1	i_2	m_1	m_2	n_1	n_2	n_3	n_4	n_5	n_6
1	0	0	1	1	0	0	0	0	0	0
2	1	0	1	1	0	0	0	0	0	0
3	0	1	1	1	0	0	0	0	0	0
4	0	0	2	1	0	0	0	0	0	0
5	0	0	1	1	0	1	0	0	0	0
6	0	-1	1	1	0	1	0	0	0	0
7	0	-2	1	1	0	1	0	0	0	0
8	1	-1	1	1	0	1	0	0	0	0

Table A (cont.)

j	i_1	i_2	m_1	m_2	n_1	n_2	n_3	n_4	n_5	n_6
9	1	-2	1	1	0	1	0	0	0	0
10	0	-1	1	1	0	1	0	0	1	0
11	0	-2	1	1	0	1	0	0	1	0
12	0	0	1	1	0	0	0	1	0	0
13	0	-1	1	1	0	0	0	1	0	0
14	0	-1	2	1	0	1	0	0	0	0
15	0	-2	2	1	0	1	0	0	0	0
16	0	0	1	1	0	0	0	0	1	0
17	0	0	1	2	0	0	0	0	0	0
18	0	0	1	1	0	0	0	0	0	0
19	-1	0	1	1	1	0	0	0	0	0
20	-2	0	1	1	1	0	0	0	0	0
21	-1	1	1	1	1	0	0	0	0	0
22	-2	1	1	1	1	0	0	0	0	0
23	-1	0	1	1	1	0	0	0	1	0
24	-2	0	1	1	1	0	0	0	1	0
25	0	0	1	1	0	0	1	0	0	0
26	-1	0	1	1	0	0	1	0	0	0
27	-1	0	1	2	1	0	0	0	0	0
28	-2	0	1	2	1	1	0	0	0	0

$$K_{12}(\sigma,x) = K_{12}^{(1)}(\sigma,x) + K_{12}^{(2)}(\sigma,x) + K_{12}^{(3)}(\sigma,x) \quad , \tag{1.13a}$$

where

$$K_{12}^{(1)}(\sigma,x) = 8\sqrt{2}\left\{G^{(4)} - (3+E)\, G_\ell^{(1)} - 2\, G_\ell^{(16)}\right\}$$

$$+ (2\beta_2\xi/\sqrt{43})\left\{16\, G_\ell^{(5)} - 4\,(1+2E)\, G_\ell^{(6)} - \right.$$

$$- (21+2E)\, G_\ell^{(7)} - 12\, G_\ell^{(10)} - 2\, G_\ell^{(11)} + 32_\ell G^{(12)} +$$

$$\left. + 8\, G_\ell^{(13)} + 8\, G_\ell^{(14)} + G_\ell^{(15)}\right\} \quad , \tag{1.13b}$$

$$K_{12}^{(2)}(\sigma,x) = 32\sqrt{2}\; G_\ell^{(2)} + (16\beta_2\xi/\sqrt{43})\,(4\, G_\ell^{(18)} + G_\ell^{(4)}) \quad , \tag{1.13c}$$

and

$$K_{12}^{(3)}(\sigma,x) = 16\sqrt{2}\, G_\ell^{(3)} \quad . \tag{1.13d}$$

From Table A we deduce that $K_{12}^{(1)}(\sigma,x)$ is a continuous function of x and σ, $K_{12}^{(2)}(\sigma,x)$ is discontinuous at $x = 2\sigma$ and $K_{12}^{(3)}(\sigma,x)$ is discontinuous at $x = \sigma$. Thus, the total kernel $K_{12}(\sigma,x)$, Eq. (1.13a), is singular at $x = \sigma$ and $x = 2\sigma$, and special attention should be paid during the numerical calculation of $Q_1(x)$, (Eq. 17c).

The explicit form of the kernel $K_{21}(\sigma,x)$, Eq. (15d), is given by

$$K_{21}(\sigma,x) = 16\sigma x \int\int \{(1/\pi\sqrt{2})\, e^{-r} \{-(\nabla_x^2+k_1^2)+(2/x-2/\rho) + \\ + \bar{\varepsilon}\, (2/\pi\sqrt{43})\, e^{-\rho/2} \{r(1+r/2)(-\nabla_x^2) - rE(1+r/2) - \\ - (\nabla_r^2+2/r)r(1+r/2) + r(1+r/2)(2/x-2/\rho)\}\, e^{-r(\hat{r}.\hat{x})/\beta_1}\}\, Y_\ell^0(\hat{x})\, Y_\ell^0(\hat{\sigma})\, d\hat{x}\, d\hat{\sigma}\ . \tag{1.14}$$

In order to exclude the operation with ∇_x^2 on the functions of x appearing in Eq. (1.14), we use (similar to Eq. 1.3) the following transformation

$$\nabla_x^2 = \nabla_r^2 + 4\,\nabla_\rho^2 + 4\,\underline{\nabla}_r.\underline{\nabla}_\rho\ . \tag{1.15}$$

Therefore, we have

$$\nabla_x^2\, (e^{-r}e^{-\rho/2}) = \{2 - 2/r - 1/\rho + 2(\hat{r}.\hat{\rho})\, e^{-r}e^{-\rho/2}\ , \tag{1.16}$$

$$\nabla_x^2\, (e^{-r}e^{-\rho/2}\, r(1+r/2)\hat{r}) \\ = 4(1/4 - 1/\rho)r(1 + r/2)\, e^{-r}\, e^{-\rho/2}\, \hat{r} + (r^2/2 - 2r - 2)\, e^{-r}e^{-\rho/2}\, \hat{r} + \\ + r^2\, e^{-r}\, e^{-\rho/2}\, (\hat{r}.\hat{\rho})\, \hat{r} - (2 + r)\, e^{-r}\, e^{-\rho/2}\hat{\rho}\ , \tag{1.17}$$

and

$$\nabla_x^2(e^{-r}\, r(1+r/2)\, \hat{r}) = (r^2/2 - 2r - 2)\, e^{-r}\, \hat{r}\ . \tag{1.18}$$

Substituting from Eqs (1.15) – (1.18) into Eq. (1.14) and integrating over the angles, we obtain

$$K_{21}^{(1)}(\sigma,x) = K_{21}^{(1)}(\sigma,x) + K_{21}^{(2)}\, (\sigma,x) + K_{21}^{(3)}\, (\sigma,x)\ , \tag{1.19a}$$

where $K_1^{(1)}\, (\sigma,x)$ is continuous in x and σ and determined by

$$K_{21}^{(1)}(\sigma,x) = 16\sqrt{2}\{G_\ell^{17)} - (3+E)\, G_\ell^{(1)} - 2\, G_\ell^{(16)}\} + \\ + \bar{\varepsilon}\, (32\beta_1/\sqrt{43})\, \{4\, G_\ell^{(18)} + 2(2 - E)\, G_\ell^{(19)} - (3 + E)\, G_\ell^{(20)} - \\ - 2\, G_\ell^{(24)} + 4\, G_\ell^{(25)} + 2\, G_\ell^{(26)} + G_\ell^{(27)} + 2\, G_\ell^{(28)}\}\ , \tag{1.19b}$$

$K_{21}^{(2)}\, (\sigma,x)$ is discontinuous at $x = 2\sigma$ and has the final form

$$K_{21}^{(2)}\, (\sigma,x) = 32\sqrt{2}\, G_\ell^{(2)}\ , \tag{1.19c}$$

and $K_{21}^{(3)}(\sigma,x)$ is singular at $x = \sigma$ and is calculated by

$$K_{21}^{(3)}\, (\sigma,x) = 64\sqrt{2}\, G_\ell^{(3)} + \bar{\varepsilon}\beta_1\, (128/\sqrt{43})\, (2\, G_\ell^{(21)} + G_\ell^{(22)})\ . \tag{1.19d}$$

From Table A, we can easily prove that

$$G_\ell^{(17)} = G_\ell^{(4)} + G_\ell^{(2)} - G_\ell^{(3)} \quad ,$$

which implies the following relation

$$2\,K_{12}(\sigma,x) = K_{21}(\sigma,x) \qquad \text{at} \quad \mathcal{E} = \bar{\mathcal{E}} = 0 \quad . \tag{1.20}$$

Equation (1.20) indicates that the kernels of Models 0–3 are symmetric.

Appendix 2

This Appendix contains a brief discussion of the iteration procedure used for calculating the elements of the reactance matrix, (see Eqs 20a – 23d). This has been achieved by rewriting Eqs (20a) – (20c) as

$$f_\ell^{(i,\nu)}(x) = \Big\{\delta_{i1} + \frac{1}{k_1}\int_0^X \tilde{g}_\ell(k_1x')\Big\{U_{x'}^{(1)}\, f_\ell^{(i,\nu)}(x') + Q_1^{(i,\nu-1)}(x')\Big\}\,dx'\Big\}\,\tilde{f}_\ell(k_1x) - \frac{\tilde{g}_\ell(k_1x)}{k_1}\int_0^X \tilde{f}_\ell(k_1x')\Big\{U_{x'}^{(1)}\, f_\ell^{(i,\nu)}(x') + Q_1^{(i,\nu-1)}(x')\Big\}, \nu \geq 1 \quad , \tag{2.1}$$

$$g_\ell^{(i,\nu)}(\sigma) = \Big\{\delta_{i2} + \frac{1}{k_2}\int_0^\Sigma \tilde{g}_\ell(k_2\sigma')\,Q_2^{(i,\nu)}(\sigma')\,d\sigma'\Big\}\,\tilde{f}_\ell(k_2\sigma) - \frac{\tilde{g}_\ell(k_2\sigma)}{k_2}\int_0^\Sigma \tilde{f}_\ell(k_2\sigma')\,Q_2^{(i,\nu)}(\sigma')\,d\sigma', \nu \geq 0 \tag{2.2}$$

and

$$f_\ell^{(i,0)}(x) = \Big\{\delta_{i1} + \frac{1}{k_1}\int_0^X \tilde{g}_\ell(k_1x')\,U_{x'}^{(1)}\, f_\ell^{(i,0)}(x')\,dx'\Big\}\,\tilde{f}_\ell(k_1x) - \frac{\tilde{g}_\ell(k_1x)}{k_1}\int_0^X \tilde{f}_\ell(k_1x')\,U_{x'}^{(1)}\, f_\ell^{(i,0)}(x')\,dx' \quad , \tag{2.3}$$

where X and Σ represent the ranges of integrations over x and σ, respectively. (Physically, X (=nh, where n is the number of mesh points and h is the Simpson step, or mesh size), represents the distance at which we assume that the scattered positrons are not affected by the hydrogen atoms, and Σ(=nh) is the distance at which the positronium atom and the proton are totally separated). The functions $Q_1^{(i,\nu-1)}(x')$ and $Q_2^{(i,\nu)}(\sigma')$, in Eq. (2.1) and (2.2), are now defined by

$$Q_1^{(i,\nu-1)}(x') = \int_0^\Sigma K_{12}(\sigma,x')\,g_\ell^{(i,\nu-1)}(\sigma)\,d\sigma \quad , \nu \geq 1 \tag{2.4a}$$

and

$$Q_2^{(i,\nu)}(\sigma') = \int_0^X K_{21}(\sigma',x)\,f_\ell^{(i,\nu)}(x)\,dx \quad , \nu \geq 0 \quad . \tag{2.4b}$$

Thus, the iteration process starts by calculating $f_\ell^{(i,0)}(x)$, i=1,2, using Eq. (2.3) and introducing its values into Eq. (2.4b) in order to find $Q_2^{(i,0)}(\sigma')$ which can be used in the right-hand side of Eq. (2.2) for obtaining $g_\ell^{(i,0)}(\sigma)$. The values of the last quantity can be introduced into Eq. (2.4) in order to calculate $Q_1^{(i,0)}$ which may be employed in Eq. (2.1) for determining $f_\ell^{(i,1)}(x)$. This iteration process can be repeated as many times as we need and the judge of its quality is the stationary variation of the elements of the reactance matrix R_{ij}^{ν}, Eqs (23a) – (23d), when ν increases.

In order to calculate the integrals in Eqs (2.1) – (2.4b) we use Simpson's rule. Thus, we expand $Q_1^{(i,\nu-1)}(x)$ and $Q_2^{(i,\nu)}(\sigma)$ at the point q of the configuration space, as follows

$$Q_1^{(i,\nu-1)}(x_q) = \sum_{p=1}^{n}\Big\{\omega_p^{(1)}K_{12}^{(1)}(\sigma_p,x_q) + \omega_p^{(2)}K_{12}^{(2)}(\sigma_p,x_q) + \omega_p^{(3)}K_{12}^{(3)}(\sigma_p,x_q)\Big\}\; g_\ell^{(i,\nu-1)}(\sigma_p), \nu \geq 1 \quad , \tag{2.5a}$$

$$Q_2^{(i,\nu)}(\sigma_q) = \sum_{p=1}^{n}\Big\{\omega_p^{(1)}K_{21}^{(1)}(\sigma_q,x_p) + \omega_p^{(2)}K_{21}^{(2)}(\sigma_q,x_p) + \omega_p^{(3)}K_{21}^{(3)}(\sigma_q,x_p)\Big\}\; f_\ell^{(i,\nu)}(x_p) \quad , \nu \geq 0 \quad , \tag{2.5b}$$

where $\omega_p^{(1)}$'s are the usual Simpson weights $(\frac{h}{3}, \frac{4h}{3}, \frac{2h}{3}, \ldots, \frac{2h}{3}, \frac{4h}{3}, \frac{h}{3})$ and $\omega_p^{(2)}$'s, $\omega_p^{(3)}$'s are modified weights used for avoiding the singularities at $x=\sigma$ and $x=2\sigma$, respectively, (see e.g. Fraser [8,19] and Chan and Fraser [15]). The variables σ_p and x_p are chosen such that $x_p = \sigma_p = ph$, p=1,2,...,n.

An essential point in the determination of the integrals in Eqs (2.1) – (2.7) is the calculation of the starting values of the functions $f_\ell^{(i,\nu)}(x)$ and $g_\ell^{(i,\nu)}(\sigma)$, i.e. their values at $x_p = h$, $\sigma_p = h$. (Note that $f_\ell^{(i,\nu)}(0) = 0$, $g_\ell^{(i,\nu)}(0) = 0$). In order to find the starting value of $f_\ell^{(i,0)}(x)$ we consider the Taylor expansion of $U_x^{(1)}$, $\tilde{f}_\ell(\mu)$ and $\tilde{g}_\ell(\mu)$ around the origin. From Eqs (8a), (10), (16a), we can prove that

$$U_x^{(1)} \sim \left(\frac{2}{x} - 2 + \frac{4x^2}{3} - \frac{4x^3}{3} + \ldots\right) + \varepsilon_1\beta_1(x)\,(-0.431\,x + 0.345\,x^3 + \ldots) \quad . \tag{2.6}$$

Also, it is known, (see e.q. [20], p.490), that

$$\tilde{f}_\ell(\mu) \simeq \frac{(\mu)^{\ell+1}}{(2\ell+1)!!}\left\{1 - \frac{\mu^2/2}{1!(2\ell-1)} + \frac{(\mu/2)^2}{2!(2\ell+3)(2\ell+5)} + \ldots\right\} \quad , \tag{2.7}$$

and

$$\tilde{g}_\ell(\mu) \simeq \frac{(2\ell+1)!!}{(2\ell+1)\mu^\ell}\left\{1 + \frac{\mu^2/2}{1!(2\ell-1)} + \frac{(\mu^2/2)^2}{2!(2\ell-1)(3\ell-2)} + \ldots\right\} \quad , \tag{2.8}$$

where $\mu = k_1 x$.

Assuming that $f_\ell^{(i,0)}(x)$ behaves close to the origin as

$$f_\ell^{(i,0)} \simeq C_1 x^{\ell+1} + C_2 x^{\ell+2} + C_3 x^{\ell+3} + \ldots \quad , \tag{2.9}$$

therefore, substitution from Eqs (2.6) – (2.9) into Eq. (2.3) yields

$$C_1 = \delta_{i1} \frac{k_1^{\ell+1}}{(2\ell+1)!!} \quad , \tag{2.10a}$$

$$C_2 = C_1/(\ell+1) \tag{2.10b}$$

and

$$C_3 = \frac{C_1}{2\ell+3} \left(\frac{1}{\ell+1} - (1 + k_1^2/2)\right) \quad . \tag{2.10c}$$

Introducing the constants C_1, C_2 and C_3 into Eq. (2.9) and setting $x = h$, we obtain a starting value for $f_\ell^{(i,0)}(x)$. (Note that the first three terms of Eq. (2.9) are enough for obtaining this value especially when h is reasonably small). Remark also that the main contribution to the starting value is due to the static potential involved in $U_x^{(1)}$ and the inclusion of the polarisation potential has almost no effect on this value.

In order to find the starting values of $f_\ell^{(i,\nu)}(x)$ and $g_\ell^{(i,\nu)}(\sigma)$, we have to know the behaviour of $Q_1^{(i,\nu-1)}(x)$ and $Q_2^{(i,\nu)}$ close to the origin. Our investigation of this problem enabled us to express $Q_1^{(i,\nu-1)}(x)$ as

$$Q_1^{(i,\nu-1)}(x) = \bar{C}_1 x^{\ell+1} + \bar{C}_2 x^{\ell+2} + \ldots \quad , \tag{2.11}$$

where $\bar{C}_1$, $\bar{C}_2$, ... are dependent on i and ν. Again, assuming that $f^{(i,\nu)}(x)$ is expanded by

$$f_\ell^{(i,\nu)}(x) = C_1 x^{\ell+1} + C_2 x^{\ell+2} + C_3 x^{\ell+3} + \ldots \quad , \tag{2.12}$$

one can show from Eqs (2.6), (2.7), (2.8), (2.11) and (2.12) that C_1 and C_2 are identical to those given by Eqs (2.10a) and (2.10b), respectively, while C_3 relates to C_1 and $\bar{C}_1$ by

$$C_3 = (C_1/(2\ell+3)) \left\{1/(\ell+1) - (1+k_1^2/2)\right\} + \bar{C}_1/(2\ell+3). \tag{2.13}$$

The constants $\bar{C}_1$ and $\bar{C}_2$ are roughly estimated by the relations

$$\bar{C}_1 \quad Q_1^{(i,\nu-1)}(h)/h^{\ell+1} - \bar{C}_2 h \quad , \tag{2.14a}$$

and

$$\bar{C}_2 \simeq (1/h) \left\{ Q_1^{(i,\nu-1)}(2h)^{\ell+1}/(2h)^{+1} - Q_1^{(i,\ -1)}(h)/h^{\ +1} \right. \quad . \tag{2.14b}$$

Therefore, we can use Eqs (2.10a), (2.10b), (2.13) and (2.14a,b) in order to obtain a starting value for $f_\ell^{(i,\nu)}(x)$ at $x = h$ by employing Eq. (2.12). The preceding procedure can be applied for calculating starting values for $g_\ell^{(i,\nu)}(\sigma)$ at different ℓ's, i's and ν's.

Acta Physica Hungarica 63(1–2), pp. 51–54 (1988)

VIBRATIONAL TRANSITION PROBABILITY DATA FOR THE BAND SYSTEM $A^1\Pi \rightarrow X^1\Sigma^+$ of AsP

N. RAJAMANICKAM
Department of Physics, University of Mysore
Mysore 570 006, India

(Received 15 July 1987)

The Franck–Condon factors (vibrational transition probabilities) and r-centroids have been evaluated by the more reliable numerical integration procedure for the bands of the $A^1\Pi \rightarrow X^1\Sigma^+$ system of the AsP molecule, using a suitable potential. The reported values of Franck–Condon factors by Sinha and Chatterjee are found to be erroneous.

1. Introduction

The theoretical prediction of intensity distribution in the molecular band system requires the knowledge of vibrational transition probabilities which are to a good approximation proportional to the Franck–Condon factors ($q_{v'v''}$). A precise knowledge of Franck-Condon (FC) factors and related quantities are essential to understand and to calculate many important aspects of the molecules, e.g. radiative life-times, vibrational temperatures and kinetics of energy transfer.

While constructing potential energy curves for the evaluation of dissociation energy of AsP molecule [1], some discrepancies were noticed between the curves reported by Sinha and Chatterjee [2]. Therefore, the reliable values of FC factors ($q_{v'v''}$) and r-centroids ($\bar{r}_{v'v''}$) for the bands of the $A^1\Pi \rightarrow X^1\Sigma^+$ system of the AsP molecule have been computed in the present study by the more accurate numerical integration procedure, using the suitable potential. The reported values of FC factors by Sinha and Chatterjee [2] are found to be erroneous.

2. Franck–Condon factors and r-centroids

One of the parameters which controls the intensity distribution in the emmission of molecular bands is the FC factor. The square of the overlap integral is termed as FC factor [3],

$$q_{v'v''} = \left[\int \psi_{v'}\, \psi_{v''} dr\right]^2 , \tag{1}$$

where $\psi_{v'}$ and $\psi_{v''}$ are the vibrational wave functions for the upper and lower states, respectively. The r-centroid is a unique value of internuclear separation which may be associated with a $v' \longrightarrow v''$ band and defined as

$$\bar{r}_{v'v''} = \frac{\int \psi_{v'} r\, \psi_{v''} dr}{\int \psi_{v'}\, \psi_{v''} dr} . \tag{2}$$

Present address: Department of Physics, VHNSN College, Virudhunagar — 626 001, India

For a proper understanding of the intensity distributions in the band systems of the molecules, it is necessary to choose a suitable potential. The Morse [4] potential yields accurate FC factors, especially for vibrational transitions involving low quantum numbers [5]. The potential energy curves for the electronic states of A- and X- of AsP have been constructed using the Morse function [4] and by Rydberg – Klein – Rees (RKR) procedure as modified by Vanderslice et al [6]. In Table I, the computed values of the turning points are given for the molecular vibration in the electronic states A- and X- of AsP. It is found that the Morse function represents the potential energy curves of the two states quite adequately since the RKR curve is nearly similar as the Morse curve.

Table I

Turning points for the molecular vibration in A and X states of AsP

v	G(v) $(m^{-1}) \times 10^2$		Morse				RKR			
	A	X	A		X		A		X	
			r_{max}	r_{min}	r_{max}	r_{min}	r_{max}	r_{min}	r_{max}	r_{min}
					(m)x 10^{-10}					
0	237.23	301.51	2.1597	2.0457	2.0516	1.9505	2.1601	2.0461	2.0518	1.9508
1	708.51	901.57	2.2072	2.0090	2.0929	1.9174	2.2074	2.0092	2.0932	1.9176
2	1175.55	1497.67	2.2420	1.9852	2.1229	1.8957	2.2419	1.9851	2.1231	1.8958
3	1638.35	2089.81	2.2716	1.9666	2.1483	1.8786	2.2713	1.9663	2.1484	1.8787
4	2096.91	-	2.2983	1.9511	..	-	2.2977	1.9505	-	-

The computation of the FC factors are made by Bates's method [7] of numerical integration according to the detailed procedure provided by Tawde and Sreedhara Murthy [8] and Rajamanickam [9]. Morse wave functions were calculated using TDC-316 computer at intervals of 0.005 x 10^{-10} m for the range of r from 1.65 x 10^{-10} m to 2.35 x 10^{-10} m for every observed vibrational level of each state. Once the appropriate wave functions are obtained, the FC factors can be evaluated by integrating the expression (1). In the case of Morse function, Fraser and Jarmain [10] gave a procedure for analytical integration of the overlap integral. The results are generally, however, only indicative of trends [11]. The integration is therefore carried out numerically in the present study. The definition of r-centroid offers a method of computing r-centroids directly. Integrals in the Eqs (1) and (2) for the FC factors ($q_{v'v''}$) and r-centroids ($\bar{r}_{v'v''}$) were computed numerically and the results are entered in Table II. The r-centroids were computed by graphical and quadratic equation methods [12] and listed for comparison. The wavelengths ($\lambda_{v'v''}$) data [13] are also entered. The molecular constants [13] used in the present study are listed in Table III.

3. Results and discussion

Sinha and Chatterjee [2] have reported Morse FC factors by approximate analytical integration method for the band system (A-X) of AsP and r-centroids by the graphical and quadratic equation methods which are not safest [14]. The reported $q_{v'v''}$ and $\bar{r}_{v'v''}$ values by Sinha and Chatterjee are also given in Table II for comparison. They have also used the same molecular constants provided by Harding et al [13].

Table II

Franck–Condon factors ($q_{v'v''}$) and r-centroids ($\bar{r}_{v'v''}$) for the band system (A – X) of AsP

v',v''	$\lambda_{v'v''}$ (m) x 10^{-10}	$q_{v'v''}$		$\bar{r}_{v'v''}$ (m) x 10^{-10}				
		Present study	Sinha and Chatterjee	Numerical integration	Graphical		Quadratic	
				Present study	Present study	Sinha and Chatterjee	Present study	Sinha and Chatterjee
0,0	3090.7	0.166	0.119	2.049	2.049	2.045	2.048	2.041
0,1	3149.1	0.308	0.566	2.081	2.082	2.076	2.079	2.073
0,2	3209.3	0.276	0.196	2.112	2.112	2.106	2.110	2.106
1,0	3046.3	0.281	0.201	2.024	2.025	2.017	2.023	2.016
1,1	3103.0	0.106	0.037	2.056	2.055	2.050	2.055	2.048
1,3	3221.8	0.146	-	2.119	2.118	2.114	2.116	2.112
2,0	3003.6	0.253	0.181	2.000	2.001	1.993	1.998	1.991
2,1	3058.6	0.002	0.003	2.032	2.031	2.024	2.030	2.022
2,2	3115.3	0.153	-	2.063	2.064	2.057	2.062	2.055
3,0	2962.4	0.162	-	1.976	1.977	1.969	1.973	1.967
3,1	3016.2	0.097	-	2.007	2.007	2.002	2.005	1.998
4,1	2975.5	0.166	-	1.983	1.983	1.974	1.980	1.972

Table III

Molecular constants for the band system (A – X) of AsP

Molecular state	A	X
$\omega_e(m^{-1}) \times 10^2$	475.52	604.02
$\omega_e X_e(m^{-1}) \times 10^2$	2.12	1.98
$B_e\ (m^{-1}) \times 10^2$	0.1744	0.1925
$\alpha_e(m^{-1}) \times 10^2$	0.0009	0.0008
$r_e(m) \times 10^{-10}$	2.100	1.999

Harding et al have analyzed 5 most intense bands (2,0), (1,0), (0,0), (0,1), (0,2). As is shown in Table II, the orders of magnitude of the FC factors of these bands suggest that they are more intense. There are, however, large differences in Sinha and Chatterjee values of $q_{v'v''}$ from the present results. In the case of YO band systems also such large differences in $q_{v'v''}$ values have been reported by approximate analytical and accurate numerical integration methods [15 – 18]. The FC factors of (1,3), (2,2), (3,0), (3,1), (4,1) bands indicate that they also have appreciable intensity. Harding et al have observed these intense bands experimentally. But Sinha and Chatterjee have not reported the values of $q_{v'v''}$ for these bands.

Since $r'_e > r''_e$, $\bar{r}_{v'v''}$ increases with wavelength which is expected in a red-degraded band system. The sequence difference for this system is found to be constant and is less than 0.01×10^{-10} m.

In the present study, the $q_{v'v''}$ and $\bar{r}_{v'v''}$ values have been evaluated by the more accurate numerical integration method and therefore can be considered reliable.

Acknowledgements

The author thanks the University Grants Commission, New Delhi, and the University of Mysore for the award of FIP fellowship.

References

1. N. Rajamanickam, U.D. Prahllad and B. Narasimhamurthy, Spectrosc. Lett., 15, 557, 1982.
2. S.P. Sinha and C.L. Chatterjee, Ind. J. Pure and Appl. Phys., 11, 878, 1973.
3. D.R. Bates, Mon. Not. R. Astro. Soc., 112, 614, 1952.
4. P.M. Morse, Phys. Rev., 34, 57, 1929.
5. D.C. Patil, Comparative study of Transition Probabilities of Diatomic Molecules, Ph.D. Thesis, Karnatak University, Dharwar, India, 1978.
6. J.T. Vanderslice, E.A. Mason, W.G. Maisch and E.R. Lippincott, J. Chem. Phys., 33,614, 1960.
7. D.R. Bates, Proc. Roy. Soc., A196, 217, 1949.
8. N.R. Tawde and N.S. Murthy, Physica, 25, 610, 1959.
9. N. Rajamanickam, Acta Phys. Hung. to be published.
10. P.A. Fraser and W.R. Jarmain, Proc. Phys. Soc., A66 1145, 1953.
11. W.R. Jarmain and P.A. Fraser, Proc. Phys. Soc., A66, 1153, 1953.
12. R.W. Nicholls and W.R. Jarmain, Proc. Phys. Soc., A69, 253, 1956.
13. L. Harding, W.E. Jones and K.K. Yee, Can. J. Phys., 48, 2842, 1970.
14. T.C. James, J. Mol. Spectrosc., 20, 77, 1966.
15. F.S. Ortenberg and V.B. Glasko, Soviet Astr., 6, 714, 1963.
16. S.S. Prasad, Proc. Phys. Soc., 79, 1078, 1962.
17. N.R. Tawde and N.S. Murthy, J. Opt. Soc. Amer., 53, 298, 1963.
18. N.S. Murthy and B.N. Murthy, Proc. Phys. Soc., 90, 881, 1967.

Acta Physica Hungarica, 63(1–2), pp. 55–69 (1988)

COULOMB PAIR-CREATION I

P. HRASKÓ, L. FÖLDY and A. TÓTH

Central Research Institute for Physics
1525 Budapest, Hungary

(Received in revised form 4 August 1987)

Electron — positron pair creation in strong Coulomb fields is outlined. It is shown that the singular behaviour of the adiabatic basis can be removed if solutions of the time dependent external field Dirac equation are used as a basis to expand the fermion field operator. This latter "asymptotic basis" makes it possible to introduce Feynman-propagator. Applying the reduction technique, the computation of all of the basic quantities can be reduced to the solution of an integral equation. The positron spectrum for separable potential model with Lorentzian time dependence and for potential jump is analyzed in the pole approximation in the second part of our series.

1. Introduction

External field problems constitute a special class of problems in quantum field theory, which though easily reducible to c-number problem, at the same time exhibits particle creation, one of the most remarkable effects of quantum fields [1 — 6]. Physically the origin of the created particles can be traced to the influence of the external fields on the vacuum state vector whose change is accompanied by release (or, in some cases, by capture) of particles.

A rather unique possibility for the study of the reaction of the vacuum on the variation of the external fields is offered by the collision of two heavy-ions like uranium [7, 8]. To very good accuracy, the motion of the ions can be treated classically with the back reaction of the quantum fields neglected.

Confining ourselves to adiabatic approximation, the process is best described in terms of the energy E_B of the lowest bound state of the electronic Dirac equation in the field of two charges fixed at a distance R.

Obviously, for large separations E_B is less than mc^2, where m is the electron mass, and larger than zero since the ion charge is less than 137e [9]. When R becomes smaller the energy E_B of the lowest bound state, decreasing monotonically, becomes negative and eventually at some critical value R_c of the ionic distance reaches $-mc^2$, the top of the negative energy continuum. For even closer approach ($R < R_c$) the state under consideration ceases to exist as an individual eigenstate of the two-center Dirac Hamiltonian, but its effect manifests itself in the strong perturbation of the negative energy continuum states within a narrow energy interval whose center, which for decreasing R goes lower and lower, can be interpreted as a continuation of E_B. When this state is empty, the energy of the electron — positron field may decrease by means of creating an electron in this state and, simultaneously, emitting an outcoming positron in order to ensure charge conservation. In short, one may expect that the stable electron — positron vacuum at $R < R_c$ has an excess charge e with respect to the stable vacuum at $R > R_c$. We will refer to these vacuum states as charged and

neutral vacuum, respectively [8]. When the state B is originally filled, no positron emission is possible.

Up to now we have considered R as a fixed parameter in the Dirac equation. Actually R depends on time and, as a consequence, in Schrödinger picture the state vector of the system will, in general, depend on time as well. As the ions approach each other in the region $R > R_c$, then, depending on their velocity, the state vector acquires components, describing one or more electron — positron pairs of various energy on the background of the neutral vacuum. This type of pair production which is induced by the motion of the nuclei becomes zero in the adiabatic limit when the motion of the ions is very slow.

However, when the distance between the centers becomes smaller than R_c the situation changes drastically since the adiabaticity of the motion can no longer prohibit pair production, and a new spontaneous pair production process appears. One may expect that in the supercritical period the time dependence of the state vector becomes to a large extent independent of the motion of the centers, and similarly to a radioactive decay, a new state will be approached, corresponding to an outgoing positron on the background of the charged vacuum. Later, when R becomes large again, in conjunction with the distant positron an electron on the background of the neutral vacuum appears also, which is bound to the lowest state, reestablished at $R > R_c$. (We note, that, now and in the following, we do not take care of spin degeneracy.)

The properties of the spontaneous positron production just described depend critically on the single particle states of the two-center Dirac equation at the top of the negative energy continuum. The law of spontaneous positron decay is essentially governed by the kinetics of the rearrangement of the electrons in the Dirac sea among these single-particle continuum states.

At first sight, nothing seems to prohibit this rearrangement process and, therefore, instantaneous positron emission is expected with smooth energy distribution [10]. However, as clarified in the beautiful paper [9], when the Dirac equation is transformed into second order form of a Schrödinger equation, at energies about $-mc^2$ there appears a strong barrier and the necessity of penetration through it presumably makes positron emission exponential in time with Lorentzian energy distribution. Though this conclusion was drawn for a spherically symmetric potential rather than for the two-center Dirac equation it may well survive for a real collision process, too.

We see that heavy ion collisions provide a much more sensitive test of our notion of the quantum field theoretic vacuum than do the problems mentioned earlier. During the last ten years great efforts have been made [12] to observe the solitary positron peak which was predicted to accompany a supercritical heavy ion collision, but so far no part of the positron spectrum could be convincingly identified with the expected peak.

External field problems exhibiting particle creation, are always time dependent[1] and their quantitative treatment requires solution of time dependent quantum mechanical equations. This is obvious for induced pair production but the actual properties of the spontaneous creation may also be influenced by the motion of the ions in the region $R < R_c$.

---

[1] An important exception is particle production in a constant electric field [11] which requires special consideration.

This influence which will be called "the effect of the moving pole" has been completely outside of our previous discussion. Indeed, exponential positron production can be expected only if the nuclei are fixed at some $R < R_c$ [9].

Our review, though mainly pedagogical, pays special attention to the time dependent aspect of the problem. In the first part we outline the general description of Coulomb pair-creation. We call attention to the fact that there are two distinct methods to describe quantized fermion fields which differ from each other in single particle states used to expand the fermion field operator. The adiabatic method, employed by the Frankfurt group [7], has the disadvantage that at $R=R_c$ one of the basis functions (the lowest energy bound state) disappears. We point out that such a singular behaviour can be completely avoided with the aid of a basis whose members satisfy the time dependent Dirac equation.

This latter basis, which we call asymptotic, makes it possible to conveniently introduce Feynman propagator whose importance for the calculation of exclusive probabilities has been recognized in cosmological particle production [13]. Using reduction technique, we express the probabilities for the fundamental processes in terms of a single amplitude and derive an integral equation for this amplitude itself. Our considerations will be based on this integral equation.

In the second part we discuss some model calculations. The difficulties connected with the time dependence can be somewhat reduced by expanding the time dependent potential into a sum of separable potentials [14]. This technique has recently been used in nuclear physics for the description of some aspects of heavy-ion collisions [15]. Here we apply the method in conjunction with the Dirac equation. We found it necessary to introduce a further approximation (we call it pole approximation) which in some cases leads to soluble equations without eliminating the effect of the moving pole.

In spite of the partial results in handling time dependence, our review aims first of all at a self-contained introduction into the field of Coulomb pair-production. We confine ourselves to spherical potentials since so far even realistic attempts usually end up with spherically symmetric approximations [8]. A more complete version of this paper can be found in [16]. Dirac equation with separable potentials is considered in separate publications [17, 18].

2. External field problem as a linear canonical transformation

External field problems are most easily treated in the Heisenberg picture. The dynamical variables which describe a fermion quantum field are the spinor operators $\Psi(\underline{x},t)$, $\Psi^+(\underline{x},t)$ which must obey the equal-time anticommutation relations

$$\{\Psi(\underline{x},t);\ \Psi^+(\underline{x}',t)\} = \delta(\underline{x} - \underline{x}') \qquad \{\Psi(\underline{x},t);\ \Psi(\underline{x}',t)\} = 0 \ . \tag{2.1}$$

In Heisenberg picture $\Psi(\underline{x},t)$ depends on time in a canonical manner

$$\partial_t \Psi(\underline{x},t) = i\ [\mathcal{H}(t),\ \Psi(\underline{x},t)] \ , \tag{2.2}$$

where

$$\mathcal{H}(t) = \int d^3x\ \Psi^+(\underline{x},t)\ H(\underline{x},t)\ \Psi(\underline{x},t) \tag{2.3}$$

and $\mathcal{H}$ is the single-particle Dirac Hamiltonian:

$$H(\underline{x},t) = -\underline{\alpha}(i\frac{\partial}{\partial \underline{x}} + e\,\underline{A}(\underline{x},t) + e\,V(\underline{x},t) + m\gamma^0 \quad . \tag{2.4}$$

The above relations lead to the equation

$$i\,\partial_t\,\Psi(\underline{x},t) = H(\underline{x},t)\,\Psi(\underline{x},t) \quad , \tag{2.5}$$

which can be cast into the form of the Dirac equation

$$\not{D}(A)\,\Psi \equiv \left\{i\gamma^{\mu}(\partial_{\mu} + eA_{\mu}) - m\right\}\Psi = 0 \quad . \tag{2.6}$$

Equations (2.2) and (2.6) which are the basic formulae of the theory can be satisfied by either of the following two Ansatzes:

$$\Psi(\underline{x},t) = \sum_j \left\{b_j(t)\,\eta_j^{(+)}(\underline{x},t) + d_j^{+}(t)\,\eta_j^{(-)}(\underline{x},t)\right\} \quad , \tag{2.7}$$

$$\Psi(\underline{x},t) = \sum_j \left\{b_j\psi_j^{(+)}(\underline{x},t) + d_j^{+}\psi_j^{(-)}(\underline{x},t)\right\}. \tag{2.8}$$

In the first line $b_j(t)$, $d_j^{+}(t)$ are time dependent operators which obey the equal-time anticommutation relations

$$\left\{b_i(t),\, b_j^{+}(t)\right\} = \left\{d_i(t),\, d_j^{+}(t)\right\} = \delta_{ij} \quad , \tag{2.9}$$

$$\left\{b_i(t),\, b_j(t)\right\} = \left\{d_i(t) d_j(t)\right\} = \left\{b_i(t),\, d_j(t)\right\} = \left\{b_i(t),\, d_j^{+}(t)\right\} = 0$$

and the Dirac spinors $\eta_j^{(\pm)}(\underline{x},t)$ are eigenfunctions of $H(\underline{x},t)$:

$$H(\underline{x},t)\,\eta_j^{(\pm)}(\underline{x},t) = E_j^{(\pm)}(t)\,\eta_j^{(\pm)}(\underline{x},t) \quad . \tag{2.10}$$

Here negative energy continuum states are labelled by minus (antiparticle states) all the remaining states by plus sign (particle states). The degree of arbitrariness of this assignment will be discussed in a later section.

The spinors η, being eigenstates of the Hermitean operator H, form a complete and orthonormal basis. It is easy to verify that these relations together with (2.9) are sufficient for the validity of the commutation relations (2.1). In order to satisfy (2.2), Eq. (2.7) can be substituted into (2.5) and using the orthonormality and the completeness of the eigenfunctions, the following equations of motion for the annihilation operators can be obtained.

$$i\frac{d}{dt}\,b_i(t) = E_i^{(+)}(t)\,b_i(t) - i\sum_j \left\{(\eta_i^{(+)}(t), \frac{\partial \eta_j^{(+)}(t)}{\partial t}\,b_j(t)) + \right.$$
$$\left. + (\eta_i^{(+)}(t), \frac{\partial \eta_j^{(-)}(t)}{\partial t}\,d_j^{+}(t))\right\} \quad , \tag{2.11}$$

$$i\frac{d}{dt}d_i^+(t) = E_i^{(-)}(t)\,d_i^+(t) - i\sum_j\Big\{(\eta_i^{(-)}(t), \frac{\partial\eta_j^{(+)}(t)}{\partial t}\,b_j(t)) +$$

$$+ (\eta_i^{(-)}(t), \frac{\partial\eta_j^{(-)}(t)}{\partial t}\,d_j^+(t))\Big\} ,$$

It can be shown that the equations of motion (2.11) are consistent with (2.9). The only remaining step in the characterization of the solution (2.7) is to define the operators b(t) and d(t) at some given moment of time. To this end we first substitute (2.7) into (2.3):

$$\mathcal{H}(t) = \sum_j\Big\{E_j^{(+)}(t)\,b_j^+(t)\,b_j(t) - (E_j^{(-)}(t))\,d_j^+(t)\,d_j(t)\Big\}\sum_j E_j^{(-)}(t) . \qquad (2.12)$$

Since only energy differences are observable the remaining constant, in the limit $t \longrightarrow -\infty$, of the last term of (2.12) can be disregarded. Before the variation of the external field $\underline{A}(\underline{x},t)$ sets in $\eta_i^{(+)}(t)$ and $E_j^{(+)}(t)$ are independent of time and we can write the solution of the operator equations of motion (2.11) in a somewhat lose notation as

$$b_i(t) = b_i(-\infty)\,e^{-iE_i^{(+)}.t} , \quad d_i^+(t) = d_i(-\infty)\,e^{-iE_i^{(-)}.t} , \quad (E_i^{(\pm)} = E_i^{(\pm)}(\pm\infty)) .$$

Then, as $t \longrightarrow -\infty$, H(t) takes on the same particle form as a free field hence $b_j(-\infty)$, $b_j^+(-\infty)$, $d_j(-\infty)$, $d_j^+(-\infty)$ can be interpreted as absorption and emission operators and

$$N_j^{(+)}(-\infty) = b_j^+(-\infty)\,b_j(-\infty) , \qquad N_j^{(-)}(-\infty) = d_j^+(-\infty)\,d_j(-\infty)$$

as fermion and antifermion number operators at $t \longrightarrow -\infty$. Therefore,

$$\mathcal{H}(-\infty) = \sum_j\Big\{E_j^{(+)}\,N_j^{(+)}(-\infty) + (-E_j^{(-)})\,N_j^{(-)}(-\infty)\Big\} .$$

The vacuum is defined by the relations

$$b_j(-\infty)\,|0, \text{in}\rangle = d_j(-\infty)\,|0, \text{in}\rangle = 0$$

and has zero energy.

Throughout the paper we will confine ourselves to the case when the static external fields before and after the process are the same and for $H(+\infty)$ we obtain again the form

$$\mathcal{H}(+\infty) = \sum_j\Big\{E_j^{(+)}\,N_j^{(+)}(+\infty) + (-E_j^{(-)})\,N_j^{(-)}(+\infty)\Big\} ,$$

where

$$N_j^{(+)}(+\infty) = b_j^+(+\infty)\,b_j(+\infty) , \qquad N_j^{(-)}(+\infty) = d_j^+(+\infty)\,d_j(+\infty) .$$

$b_j(+\infty)$, $b_j^+(+\infty)$, $d_j(+\infty)$, $d_j^+(+\infty)$ being the absorption and emission operators for times after the process has been accomplished. At $t \longrightarrow +\infty$ the vacuum state $|0, \text{out}\rangle$ is the solution of the equations

$$b_j(+\infty)\,|0, \text{out}\rangle = d_j(+\infty)\,|0, \text{out}\rangle = 0 . \qquad (2.13)$$

Owing to the "particle form" of $H(-\infty)$ we can identify the vectors $b_j^+(-\infty)\,|0,\ in\rangle$, $d_j^+(-\infty)\,|0,\ in\rangle$ with the single electron and positron states at the beginning of the process. For continuum states when the indices i,j beside spin projection contain the momentum $\underline{k}$ this identification imposes certain constraints on the spinors $\eta_{\underline{k}}^{(\pm)}(\underline{x},t)$ which are the wave functions of the above states:

$$\lim_{t\to-\infty} \langle 0,\ in|\,\Psi(\underline{x},t)\,b_k^+(t)\,|0,\ in\rangle = \eta_{\underline{k}}^{(+)}(\underline{x},-\infty) = \chi_{\underline{k}}^{(+)}(\underline{x}) \quad ,$$

$$\lim_{t\to-\infty} \langle 0,\ in|\,\Psi(\underline{x},t)\,d_k^+(t)\,|0,\ in\rangle = \eta_{\underline{k}}^{(-)}(\underline{x},-\infty) = \chi_{\underline{k}}^{(-)}(\underline{x}) \quad ,$$

where the functions $\chi_{\underline{k}}^{(\pm)}(\underline{x})$ are the solutions of the eigenvalue equations

$$H(\underline{x},-\infty)\,\chi_{\underline{k}}^{(\pm)}(\underline{x}) = H(\underline{x},+\infty)\,\chi_{\underline{k}}^{(\pm)}(\underline{x}) = E_{\underline{k}}^{(\pm)}\,\chi_{\underline{k}}^{(\pm)}(\underline{x}) \quad .$$

In the continuous spectrum the eigenvalue does not specify uniquely the spinors $\eta_{\underline{k}}^{(\pm)}(\underline{x},t)$ – their asymptotic form contains beside the plane wave of momentum $\underline{k}$ either an outgoing or an incoming scattered wave. These solutions will be denoted by $\eta_{\underline{k}}^{(\pm)in}(\underline{x},t)$ and $\eta_{\underline{k}}^{(\pm)out}(\underline{x},t)$, respectively. When a wave packet is formed from the solutions near $\underline{k}_0$ only the in type solutions lead at $t\longrightarrow-\infty$ to a pure incoming packet and for $t\longrightarrow+\infty$ only the out spinors give rise to an outgoing packet. Therefore, only if we employ the in type solutions in (2.7) can $b_j^+(-\infty)\,|0,\ in\rangle$, $d_j^+(-\infty)\,|0,\ in\rangle$ be interpreted justly as electron and positron states at $t\longrightarrow-\infty$ and can $b_j(-\infty)$, $d_j(-\infty)$, $N_j^{(\pm)}$ be denoted consistently as b_j^{in}, d_j^{in}, $N_j^{(\pm)in}$. For bound states $\eta_i^{(\pm)in} = \eta_i^{(\pm)out} = \eta_i^{(\pm)}$ and the index in of the corresponding operators can be omitted also.

Now it is clear that since the wave function at $t\longrightarrow+\infty$ must be an out type spinor $b_j^+(+\infty)\,|0,\ out\rangle$ and $d_j^+(+\infty)\,|0,\ out\rangle$ must <u>not</u> be interpreted as state vectors for final states because e.g.:

$$\langle 0,\ out|\,\Psi(\underline{x},t)\,b_k^+(t)\,|0,\ out\rangle \underset{t\to+\infty}{\sim} \chi_{\underline{k}}^{(+)in}(\underline{x}) \neq \chi_{\underline{k}}^{(+)out}(\underline{x}) \quad .$$

The reason is that once we have fixed the type of the solution of (2.10) at $t\longrightarrow-\infty$ it is not allowed to change this definition at some intermediate instant because this would lead to singularities in the equations of motion (2.11) of the operators b(t) and d(t). Instead, we introduce the S-matrix for the static Hamiltonian $H(x,\pm\infty)$

$$S_{ij}^{(\pm)} = (\chi_i^{(\pm)out},\ \chi_j^{(\pm)in})$$

and define

$$b_i^{out} = \sum_j S_{ij}^{(+)}\ b_j(+\infty) \quad , \qquad d_i^{out} = \sum_j S_{ij}^{(-)}\ d_j(+\infty) \quad . \tag{2.14}$$

Then the wave functions, corresponding to the states $b_j^{+out}\,|0,\ out\rangle$ and $d_j^{+out}\,|0,\ out\rangle$ will be of out type ones as required. Moreover, since S is unitary and conserves energy the out operators satisfy (2.9) and provide a "particle form" for $H(+\infty)$:

$$\mathcal{H}(+\infty) = \sum_j \left\{ E_j^{(+)}\,N_j^{(+)out} + (-E_j^{(-)})\,N_j^{(-)out} \right\} \quad . \tag{2.15}$$

We have accomplished the description of the first approach which will be called "adiabatic" since it is the set of the adiabatic eigenstates $\eta_j^{(\pm)}$ of H(x,t) which serves as a basis in (2.7) for the expansion of $\Psi(\underline{x},t)$.

The second approach based on (2.8) can be given the name "asymptotic" since the basis $\psi_j^{(\pm)}(\underline{x},t)$ will be assumed to satisfy the Dirac equation (2.6), and from the variety of the solutions an orthonormal complete set will be selected with the aid of the asymptotic condition

$$\psi_j^{(\pm)in}(\underline{x},t) \underset{t\to-\infty}{\sim} \chi_j^{(\pm)in}(\underline{x})\, e^{-iE_j^{(\pm)}t} = \chi_j^{(\pm)in}(\underline{x},t) \ . \tag{2.16}$$

Then for $t\to-\infty$ both expansions (2.7) and (2.8) are identical and b_j; d_j^+ in (2.8) may be identified with b_j^{in}; d_j^{+in}

$$\Psi(\underline{x},t) = \sum_j \left\{ b_j^{in} \psi_j^{(+)in}(\underline{x},t) + d_j^{+in}\ \psi_j^{(-)in}(\underline{x},t) \right\} \ . \tag{2.17}$$

We note that in this case the operators b_j^{in} and d_j^{+in} are independent of time. Obviously $\Psi(\underline{x},t)$ also satisfies (2.6). The canonical anticommutation relations are also fulfilled since the functions $\psi_j^{(\pm)in}$ at any instant form a complete orthonormal set. Indeed, for $t\to-\infty$ they do so because of the condition (2.16) but the scalar product of two arbitrary solutions to (2.5) is independent of time.

Consider now the limit $t\to+\infty$. If we substitute (2.17) into (2.3) we obtain a "particle form" only for $t\to-\infty$ since for intermediate and large moments of time the elements of the set $\psi_j^{(\pm)in}(\underline{x},t)$ are not eigenstates of H(x,t). In order to obtain a "particle form" for $H(+\infty)$ too we define another set of solutions by the condition

$$\psi_j^{(\pm)out}(\underline{x},t) \underset{t\to+\infty}{\sim} \chi_j^{(\pm)out}(\underline{x})\, e^{-iE_j^{(\pm)}t} = \chi_j^{(\pm)out}(\underline{x},t) \ . \tag{2.18}$$

Obviously, this set is also orthonormal and complete set at any given t and we can expand either set in terms of the other. In an obvious matrix notation

$$\psi^{(+)in} = \psi^{(+)out} W_1 + \psi^{(-)out} W_3 \ , \qquad \psi^{(+)out} = \psi^{(+)in} W_1^+ + \psi^{(-)in} W_2^+ \ ,$$

$$\psi^{(-)in} = \psi^{(+)out} W_2 + \psi^{(-)out} W_4 \ , \qquad \psi^{(-)out} = \psi^{(+)in} W_3^+ + \psi^{(-)in} W_4^+ \ ,$$

where the time independent matrices W_1 defined as

$$W = \begin{pmatrix} W_1 & W_2 \\ W_3 & W_4 \end{pmatrix} = \begin{pmatrix} (\psi^{(+)out}, \psi^{(+)in}) & (\psi^{(+)out}, \psi^{(-)in}) \\ (\psi^{(-)out}, \psi^{(+)in}) & (\psi^{(-)out}, \psi^{(-)in}) \end{pmatrix}$$

satisfy the relations

$$W_1 W_1^+ + W_2 W_2^+ = 1 \quad , \qquad W_3 W_3^+ + W_4 W_4^+ = 1 \quad ,$$

$$W_1 W_3^+ + W_2 W_4^+ = 0 \quad , \qquad W_1^+ W_2 + W_3^+ W_4 = 0 \quad , \tag{2.19}$$

$$W_1^+ W_1 + W_3^+ W_3 = 1 \quad , \qquad W_2^+ W_2 + W_4^+ W_4 = 1 \quad ,$$

which follow from the orthonormality and completeness of the out and in sets of ψ.

We can now express the in type spinors in (2.17) in terms of the out type ones:

$$\Psi(\underline{x},t) = \sum_j \left\{ b_j^{out} \psi_j^{(+)out}(\underline{x},t) + d_j^{+out} \psi_j^{(-)out}(\underline{x},t) \right\} \quad , \tag{2.20}$$

where we introduced the coefficients

$$b^{out} = W_1 b^{in} + W_2 d^{+in} \quad , \qquad b^{in} = W_1^+ b^{out} + W_3^+ d^{+out} \quad ,$$

$$d^{+out} = W_3 b^{in} + W_4 d^{+in} \quad , \qquad d^{+in} = W_2^+ b^{out} + W_4^+ d^{+out} \quad . \tag{2.21}$$

As the notation implies these new coefficients may be consistently identified with the out operators since when (2.20) is substituted into (2.3) we obtain for $H(+\infty)$ the expression (2.15) and due to (2.18) the wave packets formed from the states $b_k^{+out}|0, out>$ and $d_k^{+out}|0, out>$ behave correctly for large times. Due to (2.19) the anticommutation relations are also preserved so (2.21) can be properly called a linear canonical transformation. Notice that for a potential which is constant for all moments of time

$$W_1 = S^{(+)} \quad , \qquad W_4 = S^{(-)} \quad , \qquad W_2 = W_3 = 0 \quad .$$

As it will turn out later the matrix elements of W normally called Bogoliubov coefficients are of basic importance for the expression of the observable quantities.

Both approaches when applicable are equivalent but the asymptotic approach is of wider scope. In the definition (2.10) of the adiabatic basis it is tacitly assumed that states with a given index vary continuously in time. For the continuum states this requirement seems not to pose special problems because the continuous spectrum is unchanged in time and states with given momentum and polarization can be naturally associated at different moments of time. In the discrete spectrum the identity of the levels is unambiguously conserved only if there is no level crossing. Moreover, for a supercritical system the lowest bound state of H disappears of the spectrum (see Section 5 for details) when the critical point is reached and reappears again when the system crosses the critical point in the backward direction.

At these moments the annihilation operators corresponding to the aforementioned eigenstates, disappear and reappear again and a rather awkward matching procedure is required to ensure continuity at these moments of time [7].

These severe singularities at the moments of critical transitions are the properties of the basis used in the adiabatic approach rather than those of the solution and in this respect they resemble coordinate singularities. They are completely avoided in the

asymptotic approach which from this point of view seems superior. It must be noted, however, that from a computational point of view neither of these schemes seems efficient and in fact we lack a computationally effective approach to particle production in time dependent fields.

The end product of the solution by either adiabatic or asymptotic method is the matrix W, i.e. the Bogoliubov coefficients whose existence, however, does not itself guarantee the possibility to obtain answers to physical questions. One of the most important quantities is $|\langle 0,\text{out}\,|\,0,\text{in}\rangle|^2$ the vacuum persistence probability, i.e. the probability that no pairs are created at all. The necessary and sufficient condition for $|\,0,\text{in}\rangle$ and $|\,0,\text{out}\rangle$ to lie in the same Hilbert space is that the matrices W_2 and W_3 be Hilbert – Schmidt [19]:

$$\sum_{i,j} |(W_2)_{ij}|^2 < \infty \,, \qquad \sum_{i,j} |(W_3)_{ij}|^2 < \infty \,. \tag{2.22}$$

When this condition is not met no vector exists in the Hilbert space which is annihilated by the operators $b^{out}\, d^{out}$ computed according to (2.21) and no immediate physical interpretation can be given to the theory. In particular, the amplitude $\langle 0,\text{out}|\,0,\text{in}\rangle$ becomes a meaningless symbol.

A unitary operator U, connecting in and out operators

$$b^{out} = U b^{in} U^{-1} \,, \qquad d^{out} = U d^{in} U^{-1} \tag{2.23}$$

exists only if (2.22) is satisfied because (2.23) implies the existence of the state $|\,0,\text{out}\rangle = U|0,\text{in}\rangle$. If this is the case, the Bogoliubov transformation is said to be implementable in the Hilbert space by unitary transformation [19 – 21].

3. Expectation values and transition amplitudes

The average number of fermions or antifermions in state j produced from the vacuum is given by the expressions

$$\langle 0,\text{in}|\, N_j^{(+)\text{out}}\,|\,0,\text{in}\rangle = \langle 0,\text{in}|\, b_j^{+\text{out}}\, b_j^{\text{out}}\,|\,0,\text{in}\rangle = \sum_i |(W_2)_{ij}|^2 \,,$$

$$\langle 0,\text{in}|\, N_j^{(-)\text{out}}\,|\,0,\text{in}\rangle = \langle 0,\text{in}|\, d_j^{+\text{out}}\, d_j^{\text{out}}\,|\,0,\text{in}\rangle = \sum_i |(W_3)_{ji}|^2 \,.$$

More complicated expectation values can be calculated in the same manner. Comparing the above expressions with (2.22), we see that the physical meaning of implementability is that the average number of fermions and antifermions created in a single process must be finite.

Transition amplitudes which contain more detailed information about the process can be derived also. The four basic processes and their amplitudes are listed in Table I. As it can be shown using some operator algebra [19]

$$\langle 0,|\,\text{out}|\, b_j^{\text{out}}\, d_k^{\text{out}}\,|\,0,\text{in}\rangle = -A_{jk}\langle 0,\text{out}\,|\,0,\text{in}\rangle \,, \tag{3.1}$$

$$\langle 0,|\,\text{out}|\, d_j^{+\text{in}}\, d_k^{+\text{in}}\,|\,0,\text{in}\rangle = (B^+)_{kj}\langle 0,\text{out}\,|\,0,\text{in}\rangle, \tag{3.2}$$

where

$$A = -W_1^{+-1} W_3 = W_2 W_4^{-1} , \qquad B = -W_1^{-1} W_2 = W_3^{+} W_4^{+-1} .$$

These formulae furnish physical interpretation of the matrices A and B as relative (i.e. divided by $\langle 0,\text{out} \mid 0,\text{in}\rangle$) amplitudes.

Table I

	Initial state	Final state	Amplitude	Relative amplitude
Pair creation	Vacuum	Fermion in state j antifermion in state k	$\langle 0,\text{out}\mid b_j^{\text{out}} d_k^{\text{out}} \mid 0,\text{in}\rangle$	$-A_{jk}$
Annihilation	Fermion in state j antifermion in state k	Vacuum	$\langle 0,\text{out}\mid b_j^{+\text{in}} d_k^{+\text{in}} \mid 0,\text{in}\rangle$	$(B^{+})_{kj}$
Particle scattering	Fermion in state k	Fermion in state j	$\langle 0,\text{out}\mid b_j^{\text{out}} b_k^{+\text{in}} \mid 0,\text{in}\rangle$	$(W_1^{+-1})_{jk}$
Antiparticle scattering	Antifermion in state k	Antifermion in state k	$\langle 0,\text{out}\mid d_j^{\text{out}} d_k^{\text{in}} \mid 0,\text{in}\rangle$	$(W_4^{-1})_{kj}$

A commonly quoted expression for the vacuum persistence probability can be obtained from $|\det W_4|^2$ with the aid of the unitarity relations (2.19) and the definitions of matrices A and B:

$$|\langle 0,\text{out} \mid 0,\text{in}\rangle|^2 = |\det W_4|^2 = \frac{1}{\det(1+A^{+}A)} = \frac{1}{\det(1+B^{+}B)} .$$

There exists a well defined approximation in which we discard pair creation and annihilation. Formally this approximation consists in neglecting the "frequency mixing" matrices W_2 and W_3. Then obviously A=B=0, and $\langle 0,\text{out} \mid 0,\text{in}\rangle$ is equal to a phase factor and through (2.19) we obtain the expressions

$$\langle 0,\text{out}\mid b_j^{\text{out}} b_k^{+\text{in}} \mid 0,\ \text{in}\rangle \cong (W_1)_{jk} ,$$

$$\langle 0,\text{out}\mid d_j^{\text{out}} d_k^{+\text{in}} \mid 0,\ \text{in}\rangle \cong (W_4)^{*}_{jk} ,$$

which indicate that many-particle contributions are neglected. Such a single particle approximation used e.g. in [9] becomes applicable when external fields depend adiabatically on time provided the division of the states into particle and antiparticle states is properly chosen (see Section 5).

4. The Feynman – propagator approach

Canonical transformations which are linear when self-interaction is absent are an ideal tool for the clarification of the physical content of a quantum field theory but they

turn out unsuited to the calculation of transition amplitudes because of the existence of the inverses $(W_1)^{-1}$; $(W_4)^{-1}$ in the corresponding formulae. This problem is successfully handled with the aid of the Feynman-propagator.

The Feynman-propagator is defined by the formula

$$K(x,x') = -i \frac{\langle 0,\text{out}|T\,(\Psi(x)\Psi^{+}(x'))\,|0,\text{in}\rangle}{\langle 0,\text{out}\,|0,\text{in}\rangle} \quad , \tag{4.1}$$

where $x \equiv (\underline{x},t)$ and T means time-ordering. This expression incorporates the inverses $(W_1^{+})^{-1}$ and $(W_4)^{-1}$. Indeed by substituting for Ψ and Ψ^{+} the expressions (2.17) or (2.20), we obtain

$$K(x,x') = -i \sum_{j,k} \Big\{ \theta(t-t')\,(W_1^{+-1})_{jk}\,\psi_j^{(+)\text{out}}(x)\,\psi_k^{+(+)\text{in}}(x') - \\ - \theta(t'-t)(W_4^{-1})_{kj}\,\psi_k^{(-)\text{in}}(x)\,\psi_j^{+(-)\text{out}}(x') \Big\} \quad . \tag{4.2}$$

Now, the usefulness of K hinges on the possibility of whether it can be calculated independently of the Bogoliubov coefficients or not. Since K is one of the Green functions of the single-particle Dirac equation which for potentials confined in space and time obeys well defined boundary conditions, the first possibility is realized. Indeed, it can be easily verified that K statisfies the Green-function equations

$$\not{\partial}_x\, K(x,x') = K(x,x')\overleftarrow{\not{\partial}}_{x'} = \gamma^0\,\delta^{(4)}(x-x') \quad . \tag{4.3}$$

In order to establish the condition which selects (4.2) from the variety of solutions to (4.3) we fix the space coordinates and t' and investigate the behaviour of (4.2) at $t \longrightarrow +\infty$. When $t \longrightarrow +\infty$ only the first term survives and, owing to (2.18), the j-th term of the sum is proportional to $\exp\{-iE_j^{(+)}t\}$. Since particle states are those which lie above the lower continuum we have $E_j^{(+)} > -m$ i.e. as $t \longrightarrow +\infty$ K approaches a function of t whose Fourier transform consists of frequencies above (-m). We will refer to such functions as "positive frequency" functions though among bound states negative values of $E_j^{(+)}$ may occur.

When $t \longrightarrow -\infty$ the terms in K behave as $\exp\{-iE^{(-)}_k t\}$ where $E^{(-)}_k < -m$ i.e. K tends to a "negative frequency" function.

For fixed t, K is again of positive frequency as $t' \longrightarrow +\infty$ and negative frequency as $t' \longrightarrow -\infty$, but this time it is (+m) rather than (-m) which distinguishes between the two cases. Any redefinition of the particle and antiparticle states leads to a corresponding change in the precise meaning of the positive and negative frequency function which, however, can always be established from the context.

We are now led to a rule which permits us to select the Feynman propagator among various Green functions as that solution of the Green function equation which approaches a positive (negative) frequency function when any of its time arguments tends to positive (negative) infinity. Clearly, this principle permits us to calculate K(x,x') independently of the right hand side of (4.2).

A practical way of doing this is to transform (4.3) into integral equations with inhomogeneities which incorporate the above boundary conditions. Retaining only the scalar potential V, the appropriate integral equations are of the form

$$K(x,x') = K_\lambda(x,x') + \int_{-\infty}^{\infty} d^4x''\, K_\lambda(x,x'')\, \Delta V(x'')\, K(x'',x') \quad , \tag{4.4}$$

$$K(x,x') = K_\lambda(x,x') + \int_{-\infty}^{\infty} d^4x''\, K(x,x'')\, \Delta V(x'')\, K_\lambda(x'',x') \quad . \tag{4.5}$$

In writing down these equations we have assumed that V is of the form

$$V(x) = \lambda(t)V(\underline{x}) = (\lambda + \Delta\lambda(t))\, V(\underline{x}) = \lambda V(\underline{x}) + \Delta V(x) \quad ,$$

where $\Delta\lambda(t) \xrightarrow[t\to\pm\infty]{} 0$. $K_\lambda(x,x')$ is the Feynman-propagator solution of the Green-function equation

$$\not{\partial}_{\lambda x}\, K_\lambda(x,x') = (i\gamma^\mu\partial_\mu - m - \gamma^0\lambda\, V(\underline{x}))\, K_\lambda(x,x') = \gamma^0\, \delta^{(4)}(x-x') \tag{4.6}$$

and of its conjugate. Applying $\not{\partial}_{\lambda x}$ to (4.4) and $\overleftarrow{\not{\partial}}^{+}_{\lambda x'}$ to (4.5) and using the relation

$$\not{\partial}_x = \not{\partial}_{\lambda x} - \gamma^0\, \Delta V(x) \tag{4.7}$$

it is easy to show that (4.4) and (4.5) are indeed equivalent to (4.3). If $\Delta V(x) = \Delta\lambda(t)V(\underline{x})$ vanishes sufficiently rapidly as $t\to\pm\infty$ then it follows from (4.4) that the frequency content of $K(x,x')$ as $t,t'\to\pm\infty$ will be the same as that of $K(x,x')$, i.e. the required one.

The only remaining step is to extract from K the inverse matrices $(W_1^{+})^{-1}$, $(W_4)^{-1}$ or, more generally, the amplitudes of the four basic processes discussed in the preceding Section. As it is easily verified with the aid of (4.2) we have

$$A_{j\ell} = -i \int d^3x \int d^3x'\, \psi_j^{+(+)\mathrm{out}}(x)\, K(x,x')\, \psi_\ell^{(-)\mathrm{out}}(x') \quad ,$$

$$B^{+}_{j\ell} = -i \int d^3x \int d^3x'\, \psi_j^{+(-)\mathrm{in}}(x)\, K(x,x')\, \psi_\ell^{(+)\mathrm{in}}(x') \quad ,$$

$$(W_1^{+-1})_{j\ell} = i \int d^3x \int d^3x'\, \psi_j^{+(+)\mathrm{out}}(x)\, K(x,x')\, \psi_\ell^{(+)\mathrm{in}}(x') \quad , \quad (t>t') \quad , \tag{4.8}$$

$$(W_4^{-1})_{j\ell} = -i \int d^3x \int d^3x'\, \psi_j^{+(-)\mathrm{in}}(x)\, K(x,x')\, \psi_\ell^{(-)\mathrm{out}}(x') \quad , \quad (t<t') \quad .$$

Within the domains indicated in the brackets the r.h.s. of these expressions does not depend on t and t'.

The solution ψ of the full time-dependent Dirac equation can be eliminated from (4.8) in favour of the solutions χ of the asymptotic ($t\to\pm\infty$) time-independent Dirac equation by means of a reduction procedure which at the same time eliminates the spurious time dependence too [16], and finally we have

$$A_{j\ell} = -i \int d^4x \int d^4x'\, \chi_j^{+(+)\mathrm{out}}(x)\, M(x,x')\, \chi_\ell^{(-)\mathrm{out}}(x') \quad ,$$

$$B^{+}_{j\ell} = -i \int d^4x \int d^4x'\, \chi_j^{+(-)\mathrm{in}}(x)\, M(x,x')\, \chi_\ell^{(+)\mathrm{in}}(x') \quad ,$$

$$(W_1^{+-1})_{jl} = (\chi_j^{(+)out}, \chi_l^{(-)in}) - i \int d^4x \int d^4x' \, \chi_j^{+(+)out}(x) \, M(x,x') \, \chi_l^{(+)in}(x') \quad ,(4.9)$$

$$(W_4^{-1})_{jl} = (\chi_j^{(-)in}, \chi_l^{(-)out}) + i \int d^4x \int d^4x' \, \chi_j^{+(-)in}(x) \, M(x,x') \, \chi_l^{(-)out}(x') \quad ,$$

where $M(x,x')$ – the analogue of the T matrix in scattering theory – is defined by the equation

$$M(x,x') = \Delta V(x') \, \delta^{(4)}(x-x') + \Delta V(x) \, K(x,x') \, \Delta V(x') \, . \tag{4.10}$$

the inverse of which can be written as

$$K(x,x') = K_\lambda \, (x,x') + \int d^4y \int d^4y' \, K_\lambda \, (x,y) \, M(y,y') \, K_\lambda \, (y'x') . \tag{4.11}$$

Expressions (4.9) contrary to (4.8) contain integration over time variable also. However, the range of these integrations is limited since, owing to the presence of the factors $\Delta V(x)$ in its definition, $M(x,x')$ falls off at large times as rapidly as $\Delta\lambda(t)$. Because of its good behaviour it seems expedient to work solely with $M(x,x')$ instead of $K(x,x')$. Using the definition (4.10), it is easy to transform (4.4,5) into integral equations for M.

$$M(x,x') = \Delta V(x) \, \delta^{(4)}(x-x') + \int d^4x'' \, \Delta V(x) \, K_\lambda \, (x,x'') \, M(x'',x') \quad , \tag{4.12}$$

$$M(x,x') = \Delta V(x) \, \delta^{(4)}(x-x') + \int d^4x'' \, M(x,x'') \, K_\lambda \, (x'',x') \, \Delta V(x') \quad . \tag{4.13}$$

5. Criterion for supercritical transition

Consider that solution $\eta_B(\underline{x},t)$ of the adiabatic equation (2.10) which corresponds to the lowest bound state. Moments t_c of supercritical transition can be defined formally by the relation $\lim_{t \to t_c} E_B(t) = -m$. In a given process one usually encounters two such moments t_{C1} and t_{C2} ($t_{C1} < t_{C2}$). At t_{C1} the system originally subcritical becomes supercritical while at t_{C2} the subcritical situation is restored. Supercritical transitions are characterized by the critical value $\lambda_c = \lambda + \Delta\lambda_c$ of the coupling constant.

However, this definition is a rather formal one which may have no bearing at all on what really happens. The point is that the states η_j serve only as a more or less convenient basis for the expansion of the true state of the system and in terms of the true states no moment of supercritical transition can be defined because true states are not eigenstates of energy. Since we are considering the realistic situation in which the subcritical value of the potential is always restored the very fact of the appearance of the supercritical vacuum in the role of a new vacuum state during the process requires rather special circumstances for being convincingly established.

The most definite signal of a new supercritical vacuum is furnished by the study of the amplitude $< 0,out \mid 0,in >$. Let us assume that the function $\Delta\lambda(t)$ is characterized by an amplitude $\Delta\lambda_m$ and a time parameter T during which $\Delta\lambda(t)$ is approximately equal to $\Delta\lambda_m$. If in the interval T the system is superciritcal ($|\Delta\lambda_m| > |\Delta\lambda_c|$) and the state B has been initially empty then, as explained in the Introduction, a positron is emitted with a

characteristic decay rate $\tau^{-1} = \gamma$. Whenever the positron emission succeeds, the lowest bound state, reappearing in the spectrum at the end of the process, will be filled. When $T \gg \tau$ positron emission will be fully accomplished and the vacuum persistence probability will be approximately equal to zero. If, however, $T \ll \tau$ then in a considerable fraction of the cases positron emission will be absent and the vacuum persistence probability may remain close to unity. We have, therefore,

$$\lim_{T \to +\infty} |\langle 0,\text{out} \mid 0,\text{in}\rangle|^2 \approx \begin{cases} 0 & \text{if } |\Delta\lambda_m| > |\Delta\lambda_c| \\ 1 & \text{if } |\Delta\lambda_m| < |\Delta\lambda_c| \end{cases} . \tag{5.1}$$

In the latter case $|\langle 0,\text{out} \mid 0,\text{in}\rangle|^2$ will remain the closer to unity the slower is the change of the coupling function $\Delta\lambda(t)$ since, when $|\Delta\lambda_m| < |\Delta\lambda_c|$, there is no level crossing and, as a consequence of the adiabatic theorem, the quantum state of the system is maintained if $\left|\frac{\dot{\Delta\lambda}(t)}{\Delta\lambda(t)}\right| \ll 1$. When, on the contrary, $|\Delta\lambda_m| > |\Delta\lambda_c|$ the adiabatic theorem breaks down and the smallness of the ratio $\left|\frac{\dot{\Delta\lambda}(t)}{\Delta\lambda(t)}\right| \ll 1$ no longer prevents the initial state of being transformed into a final state which may even be orthogonal to the original one.

When the lowest bound state is filled at the beginning, i.e. the Heisenberg state is $|\,B,\text{in}\rangle$ rather than $|\,0,\text{in}\rangle$, a supercritical transition, in which the strength of the state B is transferred to the states of the lower continuum, does not create a hole in the vacuum charge density around the center of force and no positron emission can occur. As a result, the nondecay probability $|\langle B,\text{out} \mid B,\text{in}\rangle|^2$ does not tend to zero as $T \longrightarrow +\infty$ even for $|\Delta\lambda_m| > |\Delta\lambda_c|$ but remains close to unity especially when the rate of change of the potential is small.

We may, therefore, replace $|\langle 0,\text{out} \mid 0,\text{in}\rangle|^2$ on the l.h.s. of (5.1) by the ratio $|\langle 0,\text{out} \mid 0,\text{in}\rangle| / |\langle B,\text{out} \mid B,\text{in}\rangle|$. What is gained by this apparent complication is that this new ratio can be computed with the aid of (4.9). To see this we note that our classification of states into particle and antiparticle states is by no means the only possible one. We may, for example, classify the lowest energy bound state B as an antiparticle state without altering the classification of the remaining states. This new description which is as legitimate as the original one will be called the "primed description" and notationally will be distinguished by a prime. The primed description differs from the unprimed one by the replacement of b_B in the expansions (2.7,8) by d_B^+ which is an allowed step since in the original expansion no d_B or d_B^+ occurred. Now, since $b_B = d_B^+$, the Fock vacuum in the primed description is given by[2]

$$|\,0',\text{in}\rangle = b_B^{+\text{in}} \,|\,0,\text{in}\rangle \qquad |\,0',\text{out}\rangle = b_B^{+\text{out}} \,|\,0,\text{out}\rangle$$

since it is these states which in primed description are annihilated by all the absorption operators. In particular

$$d_B'^{\text{in}} \,|\,0',\text{in}\rangle = b_B^{+\text{in}} \,|\,0',\text{in}\rangle = (b_B^{+\text{in}})^2 \,|\,0,\text{in}\rangle = 0 .$$

[2]For simplicity we disregard degeneration due to magnetic quantum number which is equivalent to considering distinct partial waves

But this means that $|B,in\rangle = |0',in\rangle$, $|B,out\rangle = |0',out\rangle$ and

$$|0,in\rangle = b_B^{in}|0',in\rangle = d_B'^{+in}|0',in\rangle \ , \quad |0,out\rangle = b_B^{out}|0',out\rangle = d_B'^{+out}|0',out\rangle .$$

Therefore, using Table I and (4.9),

$$\frac{\langle 0,out\,|0,in\rangle}{\langle B,out\,|B,in\rangle} = \frac{\langle 0',out|\,d_B^{out}\,d_B^{+in}\,|0',in\rangle}{\langle 0',out\,|0',in\rangle} = (W_4'^{-1})_{BB} =$$

$$= 1 + i\int d^4x \int d^4x'\ \chi_B^{+(-)}(x)\ M'(x,x')\ \chi_B^{(-)}(x') \ .$$

In this formula M'(x,x') differs from M(x,x'). Indeed, in the primed description the notion of the positive and negative frequencies is slightly changed with respect to our earlier convention since in the primed description $\chi_B = \chi_B^{(-)}$ while in the unprimed one we had $\chi_B = \chi_B^{(+)}$. As a consequence, the boundary condition for the Feynman propagator K will depend on the kind of description and through (4.12,13) the difference between K and K' influences M.

We have, therefore, our criterion

$$\lim_{T\to+\infty} |(W_4'^{(-)})_{BB}|^2 = \begin{cases} 0 & \text{if } |\Delta\lambda_m| > |\Delta\lambda_c| \ , \\ 1 & \text{if } |\Delta\lambda_m| < |\Delta\lambda_c| \ . \end{cases} \qquad (5.2)$$

We have established the r.h.s. of this equation on the basis of our intuitive notion, described in some detail in the Introduction, of how QED vacuum behaves in strong external time dependent electric fields. Since we have a well defined scheme for the calculation of $(W'_4)^{-1}_{BB}$, it becomes, in principle, possible to judge whether the actual mathematical model confirms our intuitive picture or not.

References

1. S.W.Hawking, Commun. Math. Phys., 43, 199, 1975.
2. J.D. Bekenstein, Phys. Rev., D7, 2333, 1973.
3. B.S. Dewitt, Phys. Rep., 19C, 295, 1975.
4. S.A. Fulling, J. Phys. A, 917, 1975.
5. W.G. Unruh, Phys. Rev., D14, 870, 1976.
6. C.K. Hong and L. Mandel, Phys. Rev., A31, 2409, 1985.
7. J. Reinhardt et al., Phys. Rev., A24, 103, 1981.
8. J. Rafelski et al., Phys. Rep., 38C, 227, 1978.
9. Ya. B. Zeldowich and V.S. Popov, Uspekhi Phys. Nauk, 105, 403, 1971.
10. S.S. Gershtein and Ya. B. Zeldowich, ЖЭТФ, 57, 654, 1971.
11. J. Schwinger, Phys. Rev., 82, 664, 1951.
12. J. Schweppe et al., Phys. Rev. Lett., 51, 2261, 1983.
    M. Clemente et al., Phys. Rev. Lett., 137B, 41, 1984.
    T. Cowan et al., Phys. Rev. Lett., 54, 1761, 1985.
    H. Tsertos et al., Phys. Rev. Lett., 162B, 372, 1985.
13. Ch. Charach and L. Parker, Phys. Rev., D24, 3023, 1981.
14. See e.g. J. Révai, Thesis, Budapest, 1984 (unpublished).
15. J. Révai, Nucl. Phys., A438, 512, 1985.
16. P. Hraskó et al., KFKI-1986-48/A Budapest.
17. L. Földy et al., KFKI-1986-47/A Budapest.
18. A. Tóth et al., KFKI-1986-74/A Budapest.
19. M. Klaus and G. Scharf, Helv. Phys. Acta, 50, 779, 1977.
20. G. Labonte, Can. J. Phys., 53, 1533, 1975.
21. P.A.M. Dirac, Lectures on Quantum Field Theory, New York, 1967.

Acta Physica Hungarica 63(1–2), pp. 71–87 (1988)

COULOMB PAIR CREATION II

P. HRASKÓ, L. FÖLDY and A. TÓTH
Central Research Institute for Physics
1525 Budapest, Hungary

(Received in revised form 4 August 1987)

In a previous paper [1] we investigated the general theoretical background of electron-positron pair creation in strong external electric fields. In this paper we apply the general formalism to calculate the positron spectrum for two types of time dependent separable potential: Lorentzian time dependence and potential jump.

1. A model with separable potential

A nonlocal potential of the form

$$V = \sum_{\ell=1}^{n} \lambda_\ell \, |\beta_\ell\rangle\langle\beta_\ell|$$

is called an n-term separable potential. These types of potentials are often employed, e.g. in scattering theory because their use permits one to replace the integral equation for the scattering amplitude by a system of algebraic equations. Moreover, from the point of view of the amplitudes local potentials can be well approximated by sums of separable potentials. In what follows we do not claim realistic calculations and confine ourselves to a single-term separable potential

$$V(t) = \lambda(t)\, V = \lambda(t)|\beta\rangle\langle\beta| = (\lambda + \Delta\lambda(t))|\beta\rangle\langle\beta| = \lambda V + \Delta V \,, \qquad (1.1)$$

where $|\beta\rangle$ is an appropriately chosen normalized state in the Hilbert-space of the single-particle Dirac – Hamiltonian. In order to incorporate (1.1) into our earlier formulas they have to be rewritten for nonlocal potentials.

We have

$$M(x,x') = \langle \underline{x}|\beta\rangle\langle\beta|M(t,t')|\beta\rangle\langle\beta|\underline{x}'\rangle \,, \qquad (1.2)$$

where

$$\langle\beta|M(t,t')|\beta\rangle = \Delta\lambda(t)\,\delta(t-t') + \Delta\lambda(t)\langle\beta|K(t,t')|\beta\rangle\Delta\lambda(t') = \langle\beta|K(t,t')|\beta\rangle =$$

$$= \int d^3x\, d^3x' \langle\beta|\underline{x}\rangle K(x,x')\langle\underline{x}'|\beta\rangle \,.$$

Utilizing these formulas in (4.10) – (4.11) of [1] we obtain the following integral equations for $\langle\beta|M(t,t')|\beta\rangle$:

$$\langle\beta|M(t,t')|\beta\rangle = \Delta\lambda(t)\,\delta(t-t') + \Delta\lambda(t)\int_{-\infty}^{+\infty} dt''\langle\beta|K_\lambda(t,t'')|\beta\rangle\langle\beta|M(t'',t')|\beta\rangle, \qquad (1.3)$$

$$\langle\beta|\, M(t,t')\,|\beta\rangle = \Delta\lambda(t)\,\delta(t-t') + \int_{-\infty}^{+\infty} dt''\langle\beta|\, M(t,t'')\,|\beta\rangle\langle\beta|K_\lambda\,(t'',t')\,|\beta\rangle\Delta\chi(t') \quad . \tag{1.4}$$

Let us substitute (1.2) into (4.9) of [1] and use (2.16) and (2.18) of [1] for the eigenfunctions χ_λ:

$$\begin{aligned}
A_{j\ell} &= -2\pi i\langle\chi_j^{(+)out}|\beta\rangle\langle\beta|\chi_\ell^{(-)out}\rangle\,\tilde{M}(E_j^{(+)}, E_e^{(-)}) \quad , \\
(B^+)_{j\ell} &= -2\pi i\langle\chi_j^{(-)in}|\beta\rangle\langle\beta|\,\chi_e^{(+)in}\rangle\tilde{M}(E_j^{(-)}, E^{(+)}) \quad , \\
(W_1^{+-1})_{j\ell} &= \langle\chi_j^{(+)out}|\chi^{(+)in}\rangle - 2\pi i\langle\chi_j^{(+)out}|\beta\rangle\langle\beta|\chi_\ell^{(+)in}\rangle\tilde{M}(E_j^{(+)}, E^{(-)}) \quad , \\
(W_4^{-1})_{j\ell} &= \langle\chi_j^{(-)in}|\chi_\ell^{(-)out}\rangle + 2\pi i\langle\chi_j^{(-)in}|\beta\rangle\langle\beta|\chi_\ell^{(-)out}\rangle\tilde{M}(E_j^{(-)}, E^{(-)}) \quad ,
\end{aligned} \tag{1.5}$$

where the Fourier-transform of $\langle\beta|\, M(t,t')\,|\beta\rangle$ is defined as

$$\tilde{M}(E,E') = \frac{1}{2\pi}\int_{-\infty}^{+\infty} dt\,dt'\, e^{iEt}\langle\beta|\, M(t,t')\,|\beta\rangle e^{iE't'}. \tag{1.6}$$

Performing in (1.3), (1.4) Fourier-transformation, we obtain

$$\tilde{M}(E,E') = \Delta\tilde{\lambda}(E-E') + \int_{-\infty}^{+\infty} dE''\Delta\tilde{\lambda}(E-E'')\,\tilde{F}_\lambda\,(E'')\,\tilde{M}\,(E'',E') \quad , \tag{1.7}$$

$$\tilde{M}(E,E') = \Delta\tilde{\lambda}(E-E') + \int_{-\infty}^{+\infty} dE''\,\tilde{M}\,(E,E'')\,\tilde{F}_\lambda\,(E'')\,\Delta\tilde{\lambda}(E''-E') \quad , \tag{1.8}$$

where

$$\Delta\tilde{\lambda}(E) = \frac{1}{2\pi}\int_{-\infty}^{+\infty} dt\,\Delta\lambda\,(t)\,e^{iE^t} \quad ,$$

$$\tilde{F}_\lambda\,(E) = \int_{-\infty}^{+\infty} dt\langle\beta|\, K_\lambda\,(t)|\beta\rangle e^{iEt} \quad , \tag{1.9}$$

since owing to the time-independence of $\lambda|\beta\rangle\langle\beta|$, $K_\lambda\,(t,t') = K_\lambda\,(t-t')$.

We see, that in the case of time dependent potential models with separable potentials are not completely solvable — the scalar integral equations (1.7), (1.8) remain to be solved.

The potential V will be assumed spherically symmetric. Then in any partial wave the Dirac equation can be reduced in a well-known manner [2] to a two-component equation for the two-component spinor $\begin{pmatrix} u \\ v \end{pmatrix}$, in terms of which the solution of the Dirac equation ψ has the form

$$\psi_{j\ell m}(r) = \begin{pmatrix} \frac{u(r)}{r}\;\; (i^\ell\, Y_\ell\chi)_{jm} \\ \frac{v(r)}{r}\;\; (i^{\ell\pm1}\, Y_{\ell\pm1}\chi)_{jm} \end{pmatrix}, \qquad j = \ell \pm 1/2 \tag{1.10}$$

being a Pauli-spinor and

$$(Y_\ell\chi)_{jm} = \sum_{\lambda\mu}\langle\ell\lambda 1/2\mu|\, jm\rangle Y_{\ell\lambda}\chi_\mu \;; \qquad Y_{\ell\lambda} = Y_{\ell\lambda}\left(\frac{r}{r}\right).$$

In working with separable potentials it became customary to employ momentum representation in which (1.10) takes the form

$$\psi_{j\ell m}(p) = \begin{pmatrix} \frac{u(p)}{p}\,(Y_\ell \chi)_{jm} \\ \frac{v(p)}{p}\,(Y_{\ell\pm1}\chi)_{jm} \end{pmatrix} ; \qquad j = \ell \pm 1/2 ,$$

where now $Y_{\ell\mu} = Y_{\ell\mu}\left(\frac{p}{p}\right)$.

The Dirac-equation (2.5 – (2.6) of [1] in a given partial wave and asymptotic indices suppressed yields the two component form

$$\int_0^\infty dp' \langle p| \not{\partial} |p'\rangle \psi(p',t) = 0 , \tag{1.11}$$

where

$$\psi(p) = \begin{pmatrix} u(p) \\ v(p) \end{pmatrix}$$

and

$$\langle p| \not{\partial} |p'\rangle = \langle p| \not{\partial}_0 |p'\rangle - \gamma_0 \langle p| V(t) |p'\rangle ,$$

$$\langle p| \not{\partial}_0 |p'\rangle = \delta(p-p') \begin{pmatrix} i\frac{\partial}{\partial t} - m & p \\ -p & -i\frac{\partial}{\partial t} - m \end{pmatrix} ; \qquad \gamma_0 = \gamma^0 = \begin{pmatrix} 1 & 0 \\ 0 & -1 \end{pmatrix} .$$

The state vector $|\beta\rangle$ in the separable potential (1.1) in the momentum representation has the components g(p), h(p), i.e.

$$\langle p| V(t) |p'\rangle = \lambda(t) \langle p|\beta\rangle\langle\beta| p'\rangle = \lambda(t) \begin{pmatrix} g(p) \\ h(p) \end{pmatrix} \quad (g(p'),\, h(p')) . \tag{1.12}$$

In order to decide whether a given potential produces supercritical transitions or not we must first study the adiabatic states η, i.e. solutions of (1.11) with time independent coupling λ, which belongs to the range of $\lambda(t)$. The eigenvalue equation is

$$\int dp' \langle p| H_\lambda |p'\rangle \chi(p') = E\, \chi(p) , \tag{1.13}$$

where

$$\langle p| H_\lambda |p'\rangle = \begin{pmatrix} m & -p \\ -p & -m \end{pmatrix} \delta(p-p') + \lambda \langle p|\beta\rangle\langle\beta| p'\rangle ; \quad \eta(p,t) = \chi(p)\, e^{iEt} .$$

It can be formally written in the form

$$(H_0 - E)|\chi\rangle = -\lambda |\beta\rangle\langle\beta|\chi\rangle , \tag{1.14}$$

where

$$\langle\beta|\chi\rangle = \int_0^\infty dp\, (gu + hv) = N .$$

Let us first investigate the bound state solutions of (1.14) which will be denoted by $|\chi_B\rangle$ or $|B\rangle$. If N were equal to zero then (1.14) would reduce to the free eigenvalue equation which does not possess normalizable solutions. So, for a bound state we must have $N \neq 0$. If E is any complex number whose imaginary part does not vanish when $|\mathrm{Re}\, E| \geq m$,

then the operator H_0-E has a unique inverse and the eigenvalue equation is

$$1 - \lambda \tilde{F}(E) = 0 \quad , \tag{1.15}$$

where

$$\tilde{F}(E) = \langle\beta| \frac{1}{E - H_0} |\beta\rangle = \langle\beta| \frac{\Lambda_+ + \Lambda_-}{E - H_0} |\beta\rangle =$$

$$= \int_0^\infty dp \left[\frac{\langle\beta|\Lambda_+(p)|\beta\rangle}{E - \sqrt{p^2+m^2}} + \frac{\langle\beta|\Lambda_-(p)|\beta\rangle}{E + \sqrt{p^2+m^2}} \right] \quad . \tag{1.16}$$

Here

$$\Lambda_\pm(p) = \frac{1}{\pm 2\sqrt{p^2+m^2}} \begin{pmatrix} \pm\sqrt{p^2+m^2}+m & -p \\ -p & \pm\sqrt{p^2+m^2}-m \end{pmatrix}$$

are the usual energy-projectors and

$$\langle\beta|\Lambda_\pm(p)|\beta\rangle = (g(p),h(p))\, \Lambda_\pm(p) \begin{pmatrix} g(p) \\ h(p) \end{pmatrix} = (g(p),h(p))\, \Lambda^2_\pm(p) \begin{pmatrix} g(p) \\ h(p) \end{pmatrix}$$

are nonnegative functions. The vanishing of either of these expressions for finite values of p would mean the absence of coupling at these momenta, a nonphysical feature, which we exclude by assuming that $\langle\beta|\Lambda_+(p)|\beta\rangle$ do not vanish at finite values of the argument.

As it can be seen, the energy eigenvalues are real, confined to the interval $-m < E < m$, where $\tilde{F}(E)$ is a real decreasing function, so (1.15) possesses at most a single solution.

The critical coupling constant λ_c is obviously given by the expression

$$1/\lambda_c = \tilde{F}(-m) \quad .$$

Hence, $\tilde{F}(-m)$ must be finite the condition of which is easily seen to be

$$\lim_{p \to 0} \frac{\langle\beta|\Lambda_\pm(p)|\beta\rangle}{p} = 0 \quad .$$

A further natural requirement is that the bound state energy be the lower the larger is $|\lambda|$ which is fulfilled if $\lambda < 0$ and $\tilde{F}(-m) < 0$.

We recall now that the Dirac equation when transformed to a second order form of a Schroedinger-equation possesses at E=-m a barrier which to some extent may be reflected in our model by making the coupling to the negative continuum sufficiently weak. The inequality $\tilde{F}(-m) < 0$ is in conformity with this requirement.

The existence of the barrier manifests itself in the fact that at the critical charge a normalizable bound state still exists. The norm of the state B is

$$\langle B | B \rangle = \lambda^2 N^2 \int_0^\infty dp \left[\frac{\langle\beta|\Lambda_+(p)|\beta\rangle}{(E-\sqrt{p^2+m^2})^2} + \frac{\langle\beta|\Lambda_-(p)|\beta\rangle}{(E+\sqrt{p^2+m^2})^2} \right] \quad , \tag{1.17}$$

which is finite at E= -m provided

$$\lim_{p\to 0} \langle\beta|\Lambda_+(p)|\beta\rangle < \infty \quad , \tag{1.18}$$

$$\lim_{p\to 0} \frac{\langle\beta|\Lambda_-(p)|\beta\rangle}{p^3} = 0 \quad .$$

All these requirements are met, for example, by the form factors

$$g(p) = \frac{1}{C}\,\frac{\mu^{1/2}\,p}{p^2+\mu^2} \quad ; \qquad h(p) = \frac{\alpha}{C}\,\frac{\mu^{3/2}p^2}{(p^2+\mu^2)^2} \quad , \tag{1.19}$$

$$C = \sqrt{\frac{(8+\alpha^2)\pi}{32}} \quad ; \qquad -\frac{2\mu}{m} < \alpha < 0 \quad .$$

For $|E| > m$ Eq. (1.14) has solutions normalized to delta-function, hence the domains $E < -m$, $E > m$ constitute the continuous spectrum of our Hamiltonian. The continuum eigenfunctions are

$$\chi_k^{(+)\,\mathrm{in}}_{\mathrm{out}}(p) = \phi_k^{(+)}(p) + \lambda G_0(p, E\pm i\varepsilon)|\beta\rangle\langle\beta|\chi_k^{(+)\,\mathrm{in}}_{\mathrm{out}}\rangle \quad ,$$

$$\chi_k^{(-)\,\mathrm{in}}_{\mathrm{out}}(p) = \phi_k^{(-)}(p) + \lambda G_0(p, E\pm i\varepsilon)|\beta\rangle\langle\beta|\chi_k^{(-)\,\mathrm{in}}_{\mathrm{out}}\rangle \quad , \tag{1.20}$$

where

$$E = \pm\sqrt{k^2+m^2} \quad , \qquad G_0(p,z) = \frac{\Lambda_+(p)}{z-\sqrt{p^2+m^2}} + \frac{\Lambda_-(p)}{z+\sqrt{p^2+m^2}} \quad ,$$

$$\phi_k^{(+)}(p) = \delta(k-p)\sqrt{\frac{p_0+m}{2p_0}}\begin{pmatrix} 1 \\ -\dfrac{p}{p_0+m}\end{pmatrix} \quad , \qquad \phi_k^{(-)}(p) = \delta(k-p)\sqrt{\frac{p_0+m}{2p_0}}\begin{pmatrix} \dfrac{p}{p_0+m} \\ 1\end{pmatrix} \quad .$$

Let us investigate now the bound state energy E_B as a function of the coupling constant λ. For negative values above λ_c we have E_B in the interval $(-m,m)$. When λ approaches λ_c E_B tends to $-m$. What happens to $E_B(\lambda)$ when λ becomes smaller than λ_c?

As it must be clear from our earlier considerations above equation (1.14) does not possess normalizable states, when $\lambda < \lambda_c$ and the continuum states $\chi_k^{(\pm)}$ are themselves complete. In spite of this there exists a useful extension of the notion of the bound state energy E_B below λ_c by defining it as the solution of the equation

$$1 - \lambda\tilde{F}_-(E) = 0 \quad , \tag{1.21}$$

where $\tilde{F}_-(E)$ is the analytic continuation from below of $\tilde{F}(E)$ through its cut $(-\infty, -m)$ to the Riemann-sheet R_-.

The fact that $\tilde{F}(E)$ is an analytic function of the complex variable E with cuts $(-\infty, -m)$, $(m, +\infty)$ follows from the integral representation (1.16). If in the first integral we replace the integration variable p by $x = \sqrt{p^2+m^2}$, in the second by $x = -\sqrt{p^2+m^2}$ then we obtain

$$\tilde{F}(E) = \int_{-\infty}^{-m} dx\,\frac{f_-(x)}{E-x} + \int_{m}^{+\infty} dx\,\frac{f_+(x)}{E+x} \quad ,$$

where

$$f_{\pm}(x) = \frac{\pm x}{\sqrt{x^2-m^2}} \cdot \langle\beta|\Lambda_{\pm}(p)|\beta\rangle\Big|_{p=\sqrt{x^2-m^2}} > 0$$

If we deform the integration contour into the curve C_- (see Fig. 1) then for values of E between C_- and the real axis

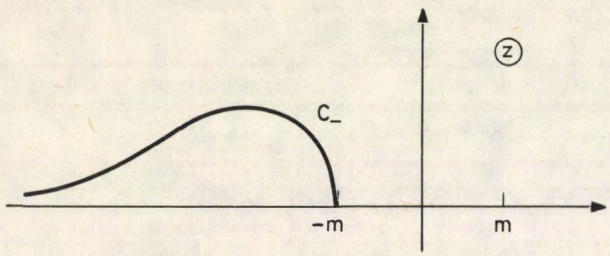

Fig. 1

$$\tilde{F}_-(E) = \int_{C_-} dz \frac{f_-(z)}{E-z} + \int_m^{+\infty} dx \frac{f_+(x)}{E+x} = \tilde{F}(E) + 2\pi i f_-(E)$$

is the required analytic continuation of $\tilde{F}(E)$ (we assumed that $f_-(z)$ is analytic in this domain). As it can be shown (1.21) does have a complex solution E_B even for λ smaller than but close to λ_c. It seems intuitively clear that $E_B'' = \mathrm{Im}E_B$ corresponds to the penetrability of the barrier at $E \cong -m$ in the Dirac equation discussed earlier. The smallness of $f_-(E)$ (see (1.18)) which is the consequence of the normalizability of the eigenstates with $E_B = -m$ leads to $E_B'' << |E_B|$ i.e. to small barrier penetrability. We notice that if $\tilde{F}_+(E)$ is the continuation of $\tilde{F}(E)$ through the cut $(-\infty, -m)$ from above (i.e. into R_+) then $1/\lambda = \tilde{F}_+(E)$ will be satisfied by $E = E_B^*$.

The kernel of the integral equation for $\tilde{M}$ contains the function $\tilde{F}_\lambda(E)$ defined in (1.9) through the Feynman propagator $K_\lambda(t)$. It is easy to verify that in the partial wave under consideration

$$\langle p|K_\lambda(t)|p'\rangle = -i\left[\theta(t)\left(\int_0^\infty dk\, e^{-i\sqrt{k^2+m^2}t}\,\chi_k^{(+)}(p)\,\chi_k^{(+)+}(p') + e^{-iE_Bt}\langle p|B\rangle\langle B|p'\rangle\right) - \theta(-t)\int_0^\infty dk\, e^{i\sqrt{k^2+m^2}t}\chi_k^{(-)}(p)\chi_k^{(-)+}(p')\right], \quad (1.22)$$

where either in or out solutions can be substituted for the χ-s. For $\lambda<\lambda_c$ the term, corresponding to the bound state, is absent. The bound state is handled in (1.22) on equal footing with the particle states, so (1.22) corresponds to the unprimed description. In the primed description we move the bound state term to the antiparticle states. Substituting this equation into (1.9) we obtain

$$\tilde{F}_\lambda(E) = \int_0^\infty dp \left[\frac{\langle\beta|\chi_p^{(+)}\rangle\langle\chi_p^{(+)}|\beta\rangle}{E-\sqrt{p^2+m^2}+i\varepsilon} + \frac{\langle\beta|\chi_p^{(-)}\rangle\langle\chi_p^{(-)}|\beta\rangle}{E+\sqrt{p^2+m^2}-i\varepsilon} + \frac{N^2}{E-E_B+i\varepsilon}\right]. \quad (1.23)$$

$\tilde{F}_\lambda'(E)$ differs from $\tilde{F}_\lambda(E)$ only in the sign of $i\varepsilon$ in the pole term. When $\lambda = 0$ the last term

is absent and we observe that the eigenvalue equation (1.15) can be written as

$$1 - \lambda \tilde{F}_0(E) = 0 \quad . \tag{1.24}$$

Green functions, corresponding to different constant values λ, say λ_1 and λ_2, are connected via integral equations of the type (4.4) – (4.5) of [1] from which the connection between $\tilde{F}_{\lambda_1}(E)$ and $\tilde{F}_{\lambda_2}(E)$ is

$$F_{\lambda_2}(E) = \frac{\tilde{F}_{\lambda_1}(E)}{1 - (\lambda_2 - \lambda_1)\,\tilde{F}_{\lambda_1}(E) - i\varepsilon} \quad . \tag{1.25}$$

The choice of $-i\varepsilon$ is dictated by the pole term in (1.23). For $\lambda_1 = 0$ and $\lambda_2 = \lambda$ this gives

$$\tilde{F}_\lambda(E) = \frac{\tilde{F}_0(E)}{1 - \lambda \tilde{F}_0(E) - i\varepsilon} \quad . \tag{1.26}$$

As a consequence, for values E near E_B

$$\tilde{F}_\lambda(E) \sim \frac{-\tilde{F}_0(E_B)}{\lambda \left(\dfrac{d\tilde{F}_0(E)}{dE} \right)_{E_B} (E - E_B) + i\varepsilon} \quad . \tag{1.27}$$

From this the constant in the pole term is

$$N^2 = -\frac{\tilde{F}_0(E_B)}{\lambda \left(\dfrac{d\tilde{F}_0(E)}{dE} \right)_{E_B}} = -\frac{1}{\lambda^2 \left(\dfrac{d\tilde{F}_0(E)}{dE} \right)_{E_B}} \quad .$$

In the primed description $-i\varepsilon$ is replaced by $+i\varepsilon$.

In the subcritical case the singularity structure of $\tilde{F}_\lambda(E)$ is clearly seen from (1.23) but in the supercritical regime the pole term is absent and the influence of the pole on the R_- Riemann-sheet is hidden in the integral over the lower cut (owing to the particular $i\varepsilon$ prescription, the pole on R_+ does not influence appreciably the behaviour of $\tilde{F}_\lambda(E)$). However, the unphysical pole on R_- manifests itself explicitly in the form of $\tilde{F}_\lambda(E)$ given by (1.26). Indeed, for real values of E below $-m$ $\tilde{F}_0(E) = \tilde{F}_-(E)$ and we have

$$\tilde{F}_\lambda(E) = \frac{\tilde{F}_-(E)}{1 - \lambda \tilde{F}_-(E)} \quad .$$

So far as the imaginary part E_B'' of the solution (1.21) is small, we have for real E-s near E_B

$$F_\lambda(E) = \frac{-\tilde{F}_-(E_B)}{\lambda \left(\dfrac{d\tilde{F}_-(E)}{dE} \right)_{E_B} (E - E_B)} \quad ,$$

which exhibits the pole structure due to the unphysical bound state.

2. Model calculation for Lorentzian time-dependence

There is an essentially unique choice of the function $\Delta\lambda(t)$ for which the integral equation (1.7), (1.8) can be transformed into ordinary differential equations. It is the Lorentzian form

$$\Delta\lambda(t) = \Delta\lambda_m \frac{T^2}{t^2 + T^2} \quad .$$

The Fourier transform of this expression

$$\Delta\tilde{\lambda}(E) = \tfrac{1}{2}\Delta\tilde{\lambda}_m \, T \, e^{-T|E|}$$

satisfies the Green function equation

$$\left(\frac{d^2}{dE^2} - T^2\right)\Delta\tilde{\lambda}(E) = -\Delta\lambda_m T^2 \delta(E) \quad .$$

Applying the operator $\frac{\partial^2}{\partial E^2} - T^2$ to (1.7), $\frac{\partial^2}{\partial E'^2} - T^2$ to (1.8) we obtain the differential equations

$$\left[\frac{\partial^2}{\partial E^2} - T^2\left(1 - \Delta\lambda_m \tilde{F}_\lambda(E)\right)\right] \tilde{M}(E,E') = -\Delta\lambda_m T^2 \delta(E-E'),$$

$$\left[\frac{\partial^2}{\partial E'^2} - T^2\left(1 - \Delta\lambda_m \tilde{F}_\lambda(E')\right)\right] \tilde{M}(E,E') = -\Delta\lambda_m T^2 \delta(E-E') \quad .$$

The necessary boundary conditions can be read off from (4.11) of [1]: $M(E,E')$ must vanish as either of its arguments becomes large in magnitude. This condition conforms with the physical meaning of $\tilde{M}(E,E')$ expressed in (1.5).

Let us put $\nu = \lambda + \Delta\lambda_m$. Then from (1.25) we can write

$$1 - \Delta\lambda_m \tilde{F}_\lambda(E) = \frac{\tilde{F}_\lambda(E)}{\tilde{F}_\nu(E)} \quad . \tag{2.1}$$

Therefore

$$\left(\frac{\partial^2}{\partial E^2} - T^2 \frac{\tilde{F}_\lambda(E)}{\tilde{F}_\nu(E)}\right)\tilde{M}(E,E') = -\Delta\lambda_m T^2 \delta(E-E') \quad ,$$

$$\left(\frac{\partial^2}{\partial E'^2} - T^2 \frac{\tilde{F}_\lambda(E')}{\tilde{F}_\nu(E')}\right)\tilde{M}(E,E') = -\Delta\lambda_m T^2 \delta(E-E') \quad .$$

These equations are satisfied by the Ansatz

$$\tilde{M}(E,E') = \theta(E-E')\,\mathcal{M}_1(E)\mathcal{M}_2(E') + \theta(E'-E)\,\mathcal{M}_1(E')\mathcal{M}_2(E) \tag{2.2}$$

provided $\mathcal{M}_j(E)$ $(j = 1,2)$ obey the equations

$$\left(\frac{d^2}{dE^2} - T^2 \frac{\tilde{F}_\lambda(E)}{\tilde{F}_\nu(E)}\right)\mathcal{M}_j(E) = 0 \tag{2.3}$$

and the boundary conditions

$$\mathcal{M}_1(+\infty) = \mathcal{M}_2(-\infty) = 0 \quad ,$$
$$W_{12} = \mathcal{M}_1' \mathcal{M}_2 - \mathcal{M}_1 \mathcal{M}_2' = -\Delta\lambda_m T^2 \quad . \tag{2.4}$$

We assume now that in (2.3) the ratio $\tilde{F}_\lambda(E)/\tilde{F}_\nu(E)$ can be approximated by the ratio of the pole contributions (2.27) with the relation (2.1) preserved. Due to this last relation the pole approximation incorporates the effect on $\tilde{M}$ of the moving pole as well as the contributions from the virtual processes in which one of the members of the virtual pair is in state B (in case of $\lambda < \lambda_c$ this means a superposition of those continuum states which are strongly disturbed).

We write therefore

$$\tilde{F}_\lambda(E) \to \tilde{F}^p_\lambda(E) = \frac{Z_\lambda R(E)}{E - E_B + i\varepsilon} \quad ; \qquad R(E_B) = 1, \qquad Z_\lambda = N^2$$
$$\tilde{F}_\nu(E) \to \tilde{F}^p_\nu(E) = \frac{Z_\nu R(E)}{E - E_\nu + i\varepsilon} \quad , \tag{2.5}$$

in which R(E) must be chosen so as to satisfy the equation

$$1 - \Delta\lambda_m \tilde{F}^p_\lambda(E) = \frac{\tilde{F}^p_\lambda(E)}{\tilde{F}^p_\nu(E)} \quad .$$

When $|\nu| < |\lambda_c|$ then Z_ν, E_ν are real, when $|\nu| > |\lambda_c|$ both are complex:

$$E_\nu = E'_\nu + iE''_\nu \quad ; \qquad E'_\nu < -m \quad , \qquad E''_\nu > 0 \quad .$$

In what follows the primed description will be primarily employed in which the $i\varepsilon$ term in (2.5) is of negative sign. It will be convenient to treat E as a complex variable. The unprimed (primed) description is obtained by approaching the real axis from above (below).

We have, therefore, in pole approximation

$$\left(\frac{d^2}{dE^2} - T^2 \frac{Z_\lambda}{Z_\nu} \frac{E - E_\nu}{E - E_B} \right) \mathcal{M}_j(E) = 0 \quad . \tag{2.6}$$

The solution, which satisfies the desired boundary conditions is

$$\tilde{M}(E,E') = -2\alpha\, e^{-i\pi a} \frac{\Gamma(a)}{\Gamma(2-a)} \Delta\lambda_m T^2 (E-E_B)\, e^{-\alpha(E-E_B)} \quad .$$
$$. e^{-\alpha(E'-E_B)} (E'-E_B) \quad . \quad \left[\theta(E-E')\, U(a,2,2\alpha(E-E_B)) \right. \quad .$$
$$. \left(e^{i\pi a} \Gamma(2-a)\, M(a,2,2\alpha(E'-E_B)) + U(a,2,2\alpha(E'-E_B)) \right) + \tag{2.7}$$
$$+ \theta(E'-E)\, U(a,2,2\alpha(E'-E_B)) \quad .$$
$$. \left. \left(-e^{i\pi a} \Gamma(2-a)\, M(a,2,2\alpha(E-E_B)) + U(a,2,2\alpha(E-E_B)) \right) \right] \quad .$$

M and U are the two independent confluent hypergeometric functions [3]. a and α are

$$a = 1 + \frac{\alpha}{2}(E_B - E_\nu) \quad ,$$

$$\alpha = T\sqrt{\frac{Z_\lambda}{Z_\nu}} = \frac{TN}{\sqrt{Z_\nu}} = \alpha' + i\alpha'' = |\alpha| e^{i\beta} \quad ; \quad 0 \leqslant \beta \geqslant \pi/2 \quad .$$

The function U(a,b,z) is a many valued function with a cut along the negative real axis. In the primed description the semiaxis arg($\beta - \pi$) which corresponds to negative real values of E must be approached from below, so the cut need not be crossed.

Now we are in a position to verify whether the condition (5.2) of [1] is satisfied or not. The last line of (1.5) gives

$$(W_4'^{-1})_{BB} = 1 + iN^2 \cdot 2\pi \cdot \tilde{M}'(E_B, E_B) \quad .$$

From this we obtain

$$(W_4'^{-1})_{BB} = e^{-2\pi\, ia}$$

and

$$\left|(W_4'^{-1})_{BB}\right| = e^{4\pi \cdot \mathrm{Im}\, a} \quad .$$

Using (2.6), a can be expressed as

$$a = 1 + \frac{1}{2} TN \sqrt{|\Delta\lambda_m|}\sqrt{E_B - E_\nu} \quad .$$

It is always true that $E_\nu < E_B$. If $E_\nu > -m$, no supercritical transition occurs, $\mathrm{Im}\, E_\nu = \mathrm{Im}\, a = 0$ and $|(W_4'^{-1})_{BB}|^2 = 1$. If, on the other hand, $E_\nu < -m$ then $\mathrm{Im}\, E_\nu > 0$ and obviously $\mathrm{Im}\, a < 0$. In particular, if $E_\nu''/(E_B - E_\nu') \ll 1$ then $\mathrm{Im}\, a = -\frac{TN}{2}\sqrt{\frac{|\Delta\lambda_m|}{E_B - E_\nu'}}\, E_\nu'' = -\frac{\gamma_L}{4\pi} T$ and $|(W_4'^{-1})_{BB}|^2 = e^{-\gamma_L T} \to 0$ as $T \to \infty$.

The criterion (5.2) of [1] is, therefore, satisfied. The quantity γ_L can be interpreted as the decay constant of the vacuum. When the unphysical pole E_ν is close to the real axis γ_L is proportional to Im E as expected. However, the proportionality factor is a nontrivial expression which reflects the effect of the moving pole.

If the electron of the pair created is bound then the spectrum of the accompanying positron is determined by the function $\tilde{M}'(E_B, -k_0)$. It is difficult to calculate the large T limit of this quantity – and of the amplitudes $\tilde{M}'(E,E')$ in general – with the aid of (2.7) since this would involve a simultaneous limit in both the argument and the parameter of the functions M and U. However, since T^{-2} plays a role similar to the role of $\hbar^2$ in a Schrödinger equation a quasiclassical treatment is available.

Let us introduce a new variable $x = E_B - E$ and a new function

$$y(x) = \frac{2\pi\, i\, N^2}{e^{-2\pi\, ia} - 1}\, \tilde{M}(E_B, E) \quad ,$$

which satisfies the equation

$$\eta^2\, y''(x) - c\,\frac{x-b}{x}\, = 0 \quad , \qquad (2.8)$$

with the boundary conditions

$$y(-\infty) = 0 \ , \qquad y(0) = 1 \ ,$$

where

$$b = E_\nu - E_B = b' + ib'' \ ; \qquad c = \frac{Z_\lambda}{Z_\nu} \ ; \qquad \eta = \frac{1}{T} \ .$$

Since the imaginary part of E_ν is small we have $b'' \ll |b'|$ and in the domain $|b'| \gg x \gg 0$, x can be neglected as compared to b. We have, therefore,

$$xy'' + \frac{bc}{\eta^2} y = 0 \ .$$

The general solution of this equation can be written as a superposition of Hankel-functions:

$$y(x) = \sqrt{x} \left[A H_1^{(1)} \left(2 \frac{\sqrt{bc}}{\eta} \sqrt{x}\right) + B H_1^{(2)} \left(2 \frac{\sqrt{bc}}{\eta} \sqrt{x}\right) \right] \tag{2.9}$$

the coefficients of which are subject to the constraint

$$y(0) = (B-A) \frac{i}{\pi \sqrt{bc}} = 1 \ . \tag{2.10}$$

In the domain $|x| \gg \eta$ we look for the solution of (2.8) in the form

$$y = e^{\frac{1}{\eta} S} \ ,$$

$$S = S_0 + \eta S_1 + \eta^2 S_2 + \ldots \ .$$

Applying the usual procedure of the quasiclassical calculations we obtain to terms linear in T^{-1}:

$$y(x) \sim K_e \exp\left\{ \frac{1}{\eta} \sqrt{c} \left(\sqrt{x(x-b)} - b \ln\left(\sqrt{x-b} + \sqrt{x} \right) \right) \right\} \left(\frac{x}{x-b} \right)^{1/4} \ . \tag{2.11}$$

The coefficient K can be determined from matching the solutions (2.9) and (2.11) in the domain of overlap $|b'| \gg x \gg \eta$, where they take the form

$$y(x) \sim \sqrt[4]{\frac{x}{bc}} \sqrt{\frac{\eta}{\pi}} \left\{ A e^{-i\frac{3\pi}{4}} e^{i2 \frac{\sqrt{bc}}{\eta} \sqrt{x}} + B e^{i\frac{3\pi}{4}} e^{-i2 \frac{\sqrt{bc}}{\eta} \sqrt{x}} \right\}$$

and

$$y(x) \sim K(-b)^{\left[\frac{1}{2\eta} (-b) \sqrt{c} - \frac{1}{4} \right]} x^{1/4} e^{i2 \frac{\sqrt{bc}}{\eta} \sqrt{x}} \ ,$$

respectively. These expressions together with (2.10) lead to

$$K = e^{-i\frac{\pi}{4}} \sqrt{\frac{\pi}{\eta}} \sqrt[4]{bc} \, (-b)^{\left[\frac{1}{4} - \frac{1}{2\eta} (-b) \sqrt{c} \right]} \ .$$

The asymptotic formula (2.11) with this value of K determines the large T limit of $\tilde{M}'(E_B', -k_0)$.

The positron spectrum was computed numerically and as it can be seen from Fig. 2 and Fig. 3. – which are typical spectra for sub- and supercritical processes – there is not any characteristic line structure which was expected on the basis of our intuitive notion. The reason for this discrepancy needs further clarification.

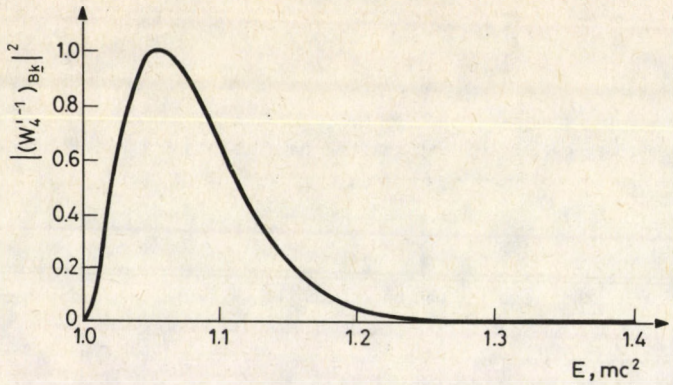

Fig. 2. The subcritical positron spectrum for Lorentzian time dependence, $E_B = -0.9$, $E_\nu = -0.987$, $T = 20$

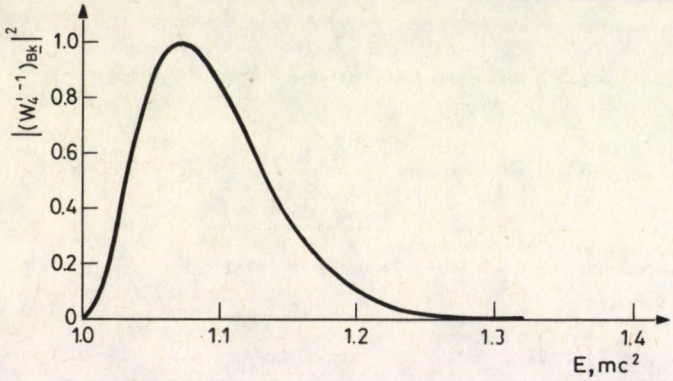

Fig. 3. The supercritical positron spectrum for Lorentzian time dependence, $E_B = -0.9$, $E_\nu = -1.05+0.0018i$, $T = 20$

3. Potential jump in pole approximation

A potential jump of duration T is described by the coupling function

$$\Delta\lambda(t) = \begin{cases} \Delta\lambda_m & \text{if} \quad -T/2 < t < T/2 \ , \\ 0 & \text{otherwise} \ . \end{cases}$$

Then, according to (1.2), $\langle\beta|\, M(t,t')\,|\beta\rangle = 0$ unless both t and t' are within the interval $(-T/2, T/2)$. Therefore, equations (1.3), (1.4) in the primed description take on the form

$$\langle\beta|M'(t,t')|\beta\rangle = \Delta\lambda_m\, \delta(t-t') + \Delta\lambda_m \int_{-T/2}^{+T/2} dt'' \langle\beta|\, K'_\lambda\,(t-t'')|\beta\rangle\langle\beta|M'(t'',t')|\beta\rangle , \qquad (3.1)$$

$$\langle\beta|\, M'(t,t')\,|\beta\rangle = \Delta\lambda_m\, \delta(t-t') + \Delta\lambda_m \int_{-T/2}^{+T/2} dt''\langle\beta|\, M'(t,t'')\,|\beta\rangle\langle\beta|\, K'_\lambda\ (t''-t')\,|\beta\rangle \cdot \qquad (3.2)$$
$$-T/2 < t,t' < T/2$$

The kernel K' given in (1.28) is a highly complicated function which makes the analytic solution of (3.2) hopeless, but the pole approximation applied to the Lorentzian time dependence in the previous section leads again to a soluble problem.

At first sight one might suppose that the pole approximation consists in neglecting all contributions to $\langle\beta|\, K'_\lambda\ (t)\,|\beta\rangle$ except for the pole term $iN^2\theta(-t)e^{-iE_B t}$. In such an approximation, however, equations (3.1), (3.2) would certainly be unable to account for the complexness of E_ν , the unphysical binding energy at $\nu = \lambda + \Delta\lambda_m > \lambda_c$ since the imaginary part of E_ν originates from the coupling to the continuum whose contribution to $\langle\beta|\, K'_\lambda(t)\,|\beta\rangle$ has been completely neglected. In the pole approximation suggested by the example of the preceding section we actually take into account, beside the pole term, an additional contribution also, which is just sufficient to locate E_ν at the right position. From (1.9) and (2.1) we have

$$\Delta\lambda_m \langle\beta|\, K'_\lambda\ (t)\,|\beta\rangle = \frac{1}{2\pi} \int_{-\infty}^{+\infty} dE\ e^{-iEt}\, \Delta\lambda_m\, \tilde{F}'_\lambda\ (E) =$$

$$= \delta(t) - \frac{1}{2\pi} \int_{-\infty}^{+\infty} dE\ e^{-iEt}\ \frac{\tilde{F}'_\lambda\ (E)}{\tilde{F}'_\nu\ (E)} \quad .$$

In pole approximation, according to (2.5)

$$\Delta\lambda_m \langle\beta|\, K'_\lambda\ (t)\,|\beta\rangle^{P} = \delta(t) - \frac{Z_\lambda}{Z_\nu}\ \frac{1}{2\pi} \int_{-\infty}^{+\infty} dE\ e^{iEt}\ \frac{E - E_\nu}{E - E_B - i\varepsilon} =$$

$$= \left(1 - \frac{Z_\lambda}{Z_\nu}\right)\ \delta(t) - i\,\frac{Z_\lambda}{Z_\nu}\ (E_B - E_\nu\ )\ \theta\ (-t)\ e^{-iE_B t} \quad ,$$

which, using (2.6) and the equality $Z_\lambda = N^2$, can be cast into the form

$$\langle\beta|\ K'_\lambda\ (t)\,|\beta\rangle^{P} = \frac{Z_\nu - Z_\lambda}{\Delta\lambda_m\ Z_\nu}\ \delta(t) + iN^2\ \theta\ (-t)\ e^{-iE_B t} \quad .$$

Substituting this kernel into (3.1), (3.2) and multiplying by $e^{iE_B t}$ and $e^{-iE_B t}$, we obtain

$$\frac{Z_\lambda}{Z_\nu}\ e^{iE_B t}\langle\beta|\, M'(t,t')\,|\beta\rangle = \Delta\lambda_m\, e^{iE_B t}\, \delta(t-t') +$$
$$+ \Delta\lambda_m\, iN^2 \int_{t}^{T/2} dt''\ e^{iE_B t''}\langle\beta|\, M'(t'',t')\,|\beta\rangle \quad , \qquad (3.3)$$

$$\frac{Z_\lambda}{Z_\nu}\langle\beta|\, M'(t,t')\,|\beta\rangle\ e^{-iE_B t'} = \Delta\lambda_m\, e^{-iE_B t'}\, \delta(t-t') + \qquad (3.4)$$
$$+ \Delta\lambda_m\, iN^2 \int_{-T/2}^{t'} dt''\langle\beta|\, M'(t'',t')\,|\beta\rangle\ e^{-iE_B t''} \quad , \qquad -T/2 < t,t' < T/2 \quad .$$

In the first equation in which t is a parameter we introduce the notation

$$f(t) = \int_t^{T/2} dt'' \, e^{iE_B t''} \langle \beta | \, M'(t'',t') | \beta \rangle \, .$$

Since

$$e^{iE_B t} \langle \beta | \, M'(t,t') | \beta \rangle = - f'(t) \tag{3.5}$$

equation (3.3) takes on the form

$$\frac{Z_\lambda}{Z_\nu} \, f'(t) + \Delta\lambda_m \, iN^2 \, f(t) = - \Delta\lambda_m \, e^{iE_B t} \, \delta(t-t') \, .$$

The solution of this differential equation, subject to the condition $f(T/2) = 0$ is easily found to be

$$f(t) = \frac{Z_\nu}{Z_\lambda} \, \Delta\lambda_m \, e^{i(E_B + \Delta\lambda_m Z_\nu)t'} \, e^{-i\Delta\lambda_m Z_\nu t} \, \theta(t'-t) \, .$$

Using (3.5), we obtain the solution to (3.3):

$$\langle \beta | \, M'(t,t') | \beta \rangle = \frac{Z_\nu}{Z_\lambda} \, \Delta\lambda_m \, \delta(t-t') + i \, \frac{(Z_\nu \Delta\lambda_m)^2}{Z_\lambda} \, e^{i(E_B + \Delta\lambda_m Z_\nu)(t'-t)} \theta(t'-t) \, ,$$

which satisfies (3.4), too.
Now, from (1.6) we have

$$\tilde{M}'(E,E') = \frac{Z_\nu \Delta\lambda_m}{2\pi \, Z_\lambda} \int_{-T/2}^{+T/2} dt \, e^{i(E-E')t} +$$

$$+ i \, \frac{(Z_\nu \Delta\lambda_m)^2}{2\pi Z_\lambda} \int_{-T/2}^{+T/2} dt dt' \, \theta(t'-t) \, e^{i(E-E_B-\Delta\lambda_m Z_\nu)t} \, e^{i(E'-E_B-\Delta\lambda_m Z_\nu)t'} \, . \tag{3.6}$$

In order to verify criterion (5.2) of [1] we calculate $\tilde{M}'(E_B, E_B)$ with the result

$$\tilde{M}'(E_B,E_B) = \frac{e^{i(E_\nu - E_B)T}}{2\pi \, i \, N^2}$$

from which we obtain

$$(W_4'^{-1})_{BB} = e^{i(E_\nu - E_B)T} \, ,$$

$$\left| (W_4'^{-1})_{BB} \right|^2 = e^{-2 \, \mathrm{Im} \, E_\nu T} = e^{-\gamma_J T} \, .$$

which is again the expected result. A comparison with the Lorentzian time dependence shows that though the criterion (5.2) of [1] is fulfilled in both cases but the decay constants of the vacuum γ_L and γ_J are different.

Performing in (3.6) the integrations, we obtain

$$\tilde{M}'(E,E') = \frac{\Delta\lambda_m Z_\nu}{2\pi Z_\lambda}\, e^{-\frac{i}{2}(E+E')T} \left\{ \frac{\Delta\lambda_m Z_\nu\, e^{iE_\nu T}}{(E-E_\nu)(E'-E_\nu)} + \right.$$

$$\left. + \frac{1}{E-E'} \left[\frac{E-E_B}{E-E_\nu}\, e^{iET} - \frac{E'-E_B}{E'-E_\nu}\, e^{iE'T} \right] \right\} .$$

According to (1.5) the positron spectrum is essentially given by $\tilde{M}'(E_B,E)$ (the other terms are only kinematic factors):

$$\tilde{M}'(E_B,E) = \frac{1}{2\pi i N^2} \frac{E_\nu - E_B}{E_\nu - E} e^{\frac{i}{2}(E_\nu - E_B)T} \left[e^{\frac{i}{2}(E_\nu - E)T} - e^{-\frac{i}{2}(E_\nu - E)T} \right]$$

If we consider subcritical processes then E_ν is real and

$$|\tilde{M}'(E_B,E)|^2 = \frac{1}{\pi^2 N^4} (E_\nu - E_B)^2 \left(\frac{\sin\left(\frac{T(E_\nu - E)}{2}\right)}{E_\nu - E} \right)^2$$

as $E \to \infty$ this function tends to zero as E^{-2} for fixed T. As $T \to \infty$ it is a more and more rapidly oscillating function of E:

$$|\tilde{M}'(E_B,E)|^2 \xrightarrow[T\to\infty]{} \frac{1}{N^4} (E_\nu - E_B)^2 \frac{T}{2} \delta(E_\nu - E) .$$

The positron spectrum has a threshold at E = -m, so in the physically relevant region $E \leqslant -m$, thus E never coincides with E_ν .

In supercritical processes $E_\nu = E'_\nu + iE''_\nu$ is complex and

$$|\tilde{M}'(E_B,E)|^2 = \frac{1}{2\pi^2 N^4} \frac{(E'_\nu - E_B)^2 + E''^2_\nu}{(E'_\nu - E)^2 + E''^2_\nu} e^{-2E''_\nu T} (\mathrm{ch}\, 2E''_\nu T - \cos 2(E'_\nu - E)T) .$$

In the $E \to \infty$ limit it goes to zero as E^{-2} again, and as $T \to \infty$ it has a Lorentzian form

$$|\tilde{M}'(E_B,E)|^2 \xrightarrow[T\to\infty]{} \frac{1}{2\pi^2 N^4} \frac{(E'_\nu - E_B)^2 + E''^2_\nu}{(E'_\nu - E)^2 + E''^2_\nu} .$$

As it can be seen from (3.7) and (3.8) characteristic difference shows up between subcritical (Fig. 4) and supercritical (Fig. 5,6) spectra which is in agreement with our qualitative picture.

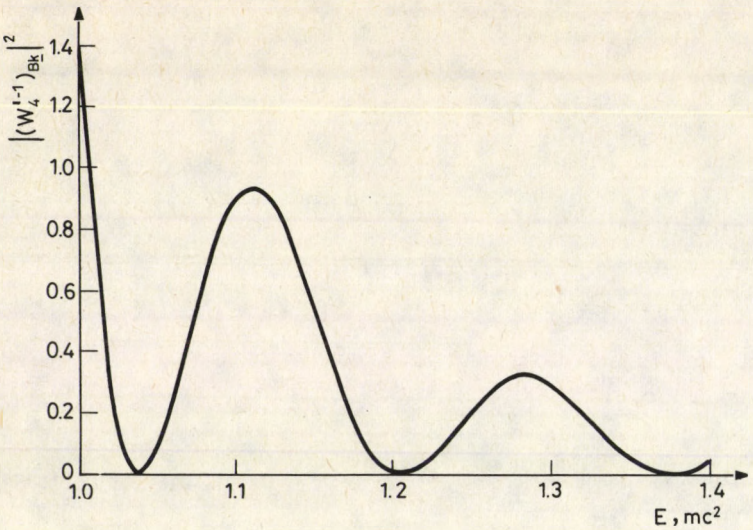

Fig. 4. The subcritical positron spectrum for potential jump, $E_B = -0.9$, $E_\nu = -0.987$, $T = 100$

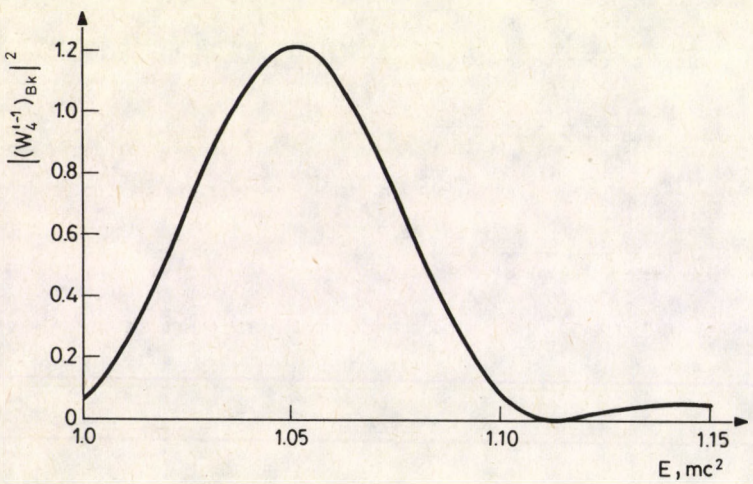

Fig. 5. The supercritical positron spectrum for potential jump, $E_B = -0.9$, $E_\nu = -1.05+0.0018i$, $T = 100$

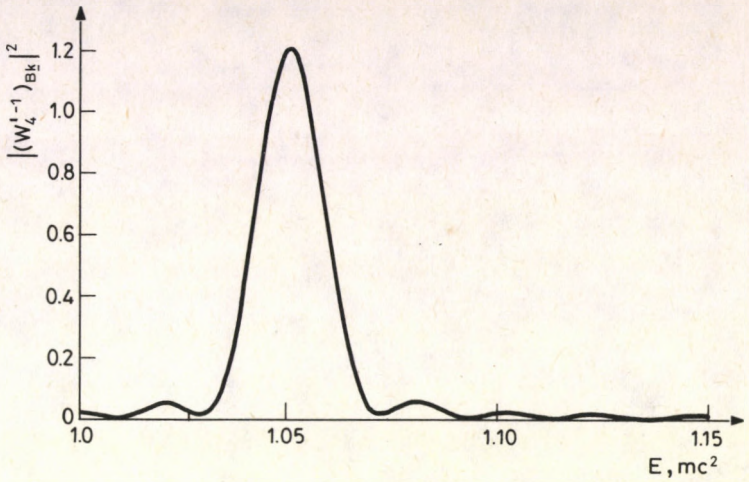

Fig. 6. The supercritical positron spectrum for potential jump, $E_B = -0.9$, $E_\nu = -1.05+0.0018i$, $T = 300$

Acknowledgement

The authors thank A. Frenkel and J. Révai for numerous fruitful discussions.

References

1. P. Hraskó, L. Földy and A. Tóth, Acta Phys. Hung., 63,
2. J.D. Bjorken and S.D. Drell, Relativistic Quantum Mechanics Vol. I., McGraw-Hill, New York, 1964.
3. M. Abramowitz and I.A. Stegun, Handbook of Mathematical Functions, National Bureau of Standards, Washington, D.C., 1964.

Acta Physica Hungarica 63(1–2), pp. 89–96 (1988)

ERNST COORDINATES

Z. PERJÉS
Central Research Institute for Physics
1525 Budapest, Hungary

(Received 4 August 1987)

Ernst coordinates can be introduced in space-times in which the complex Ernst potential exists with functionally independent real and imaginary parts. The real part of the Ernst potential is the norm and the imaginary part is the curl scalar of a Killing vector. As yet only stationary space-times have been investigated by this approach. Some special limiting types must be excluded from the discussion such as the static, the Papapetrou class and Petrov-type N metrics. The Poynting vector of the gravitational field is required to be surface-forming, a mild condition satisfied by most exact solutions of the gravitational equations. As an illustration of the procedure, we discuss axisymmetric vacuum space-times with conformally flat 3-spaces.

1. Introduction

There are at least two reasons why earlier approaches to stationary gravitational fields refrained from the application of Ernst potentials [1] as complex coordinates. Firstly, Ernst coordinates do not exist in well-known simple limiting cases such as the static Weyl problem. Moreover, the Einstein gravitational equations in Ernst coordinates appear at first sight as a frightening calculational barrier. I wish to argue, to the contrary, that in order to tackle the hard core of the stationary problem, it may be advantageous to get rid of a number of limiting classes of fields, and that is precisely what Ernst coordinates offer us. As for the computational obstacles, the new symbolic computing devices can be relied upon to surmount them. And some case studies indicate [2,3] that the field equations eventually "bootstrap" themselves to acceptable simplicity.

In Ernst coordinates, the metric is

$$ds^2 = r(dt + \omega_i dx^i)^2 - r^{-1} D^{-1} \left[\gamma d\mathcal{E}^2 - 2\beta\, d\mathcal{E}\, d\bar{\mathcal{E}} + \alpha d\bar{\mathcal{E}}^2 + \rho^2 d\varphi^2\right] , \tag{1.1}$$

where $x^1 = \mathcal{E}$ is the Ernst coordinate, $x^2 = \bar{\mathcal{E}}$ is a complex conjugate coordinate, $x^3 = \varphi$ and the real variables r and D are defined

$$r = \tfrac{1}{2}(\mathcal{E} + \bar{\mathcal{E}}) , \tag{1.2}$$

$$D = \alpha\gamma - \beta^2 . \tag{1.3}$$

The field variables α and γ are related by complex conjugation,

$$\alpha = \bar{\gamma} \tag{1.4}$$

and the field quantities β and ρ are real. All the field functions are independent of the time coordinate t, and this property is invariant under the coordinate transformations

$$t' = t + F(x^i) \quad ,$$
$$x^{i'} = x^i \quad . \tag{1.5}$$

Although the coordinates x^1 and x^2 have been fixed invariantly, one can still perform the 3-parameter SU(1,1) transformations usually considered [4] to be internal symmetries involving the Ernst potentials.

The condition that the Ernst potentials $\mathcal{E}$ and $\bar{\mathcal{E}}$ can be introduced as coordinates is of course that they exist and are functionally independent. The condition of existence follows from the vacuum field equations. Functional independence is guaranteed by excluding such limiting cases as the Papapetrou-class or the static metrics. Type N fields are characterized by $\alpha = 0$, but they will not be considered here. It is also convenient to require that the Poynting vector of the gravitational field be surface-forming, which is equivalent to saying that the function α is independent of the coordinate x^3. This is a mild condition which follows, for example, from axisymmetry.

Four applications of the Ernst coordinate method have been worked out. We have a theorem that stationary vacuum fields with a conformally flat 3-space are axisymmetric, and a theorem that the most general (non-static, non-Papapetrou and non-null) class of these fields is incompatible with the field equations. We have improved on Simon's characterization of the Kerr metric by relaxing the asymptotic conditions and Kramer has carried out a search for perfect fluid solutions with the Simon property. Most of these results have already appeared elsewhere [2,3,5,6]. As an illustration of the Ernst coordinate method, here we shall describe a somewhat simplified version of the theorem that the most general class of axisymmetric fields with a conformally flat 3-space, i.e., with a vanishing Bach tensor,

$$R_i[k;\ell] - \tfrac{1}{4} g_i\ [k^R,\ell] = 0 \tag{1.6}$$

is incompatible with the field equations.

The utility of the present formalism in finding exact solutions of the gravitational equations has yet to be clarified. Suggestions for further work include space-times for which the invariant α is an analytic function [7]. This class contains the Kerr metric. It has been conjectured by Newman [8] that a larger family of stationary space-times can be proven to be axisymmetric.

2. The field equations

In Ernst coordinates, the metric is constructed from the invariants α and β. Einstein's vacuum equations $R_{\mu\nu} = 0$ in a stationary gravitational field are decomposed with respect to the space-like 3-metric of Killing trajectories

$$g_{ik}dx^i dx^k = D^{-1}(\gamma d\mathcal{E}^2 - 2\beta d\mathcal{E} d\bar{\mathcal{E}} + \alpha d\bar{\mathcal{E}}^2 + \rho^2 d\varphi^2) \quad . \tag{2.1}$$

The Ernst equation becomes a first-order relation and has the role [9] to provide the derivatives of the cylindrical radius ρ algebraically in terms of the invariants α and β:

$$2D\,\frac{\varrho_1}{\varrho} = \alpha\gamma_1 - \gamma\alpha_1 + 2(\beta\gamma_2 - \gamma\beta_2) + \frac{2}{r}(\alpha-\beta)\gamma \quad ,$$
$$2D\,\frac{\varrho_2}{\varrho} = \gamma\alpha_2 - \alpha\gamma_2 + 2(\beta\alpha_1 - \alpha\beta_1) + \frac{2}{r}(\gamma-\beta)\alpha \quad . \tag{2.2}$$

The field quantity ω_i can be obtained by integration of the defining relations of the Ernst potential:

$$\omega_{i,k} - \omega_{k,i} = \epsilon_{ik\ell}\, r^{-2}(\mathrm{Im}\mathcal{E})^{;\ell} \quad , \tag{2.3}$$

where $\epsilon_{ik\ell}$ is the unit skew tensor in 3 dimensions. The 3-vector ω_i is determined by Eq. (2.3) up to an arbitrary gradient term, in accordance with the available coordinate transformations (1.5).

The most difficult part of the procedure consists of solving the spacelike components of the vacuum equations,

$$R^{(3)}_{ik} = 0 \quad (i,k) \neq (1,2) \text{ or } (2,1) \quad ,$$
$$R^{(3)}_{12} = -\frac{1}{4r^2} \quad , \tag{2.4}$$

where $R^{(3)}_{ik}$ are the components of the Ricci tensor of the 3-space with metric (2.1).

3. Axisymmetry and conformally flat 3-spaces

The condition that the Bach tensor vanishes yields the following differential equations [3]:

$$(\beta\partial_1 + \gamma\partial_2)\ln D = \frac{1}{r}(\beta - 2\gamma) + \beta_1 + 2\gamma_2 \quad , \tag{3.1}$$

$$(\alpha\partial_1 + \beta\partial_2)\ln D = \frac{1}{r}(\beta - 2\alpha) + \beta_2 + 2\alpha_1 \quad , \tag{3.2}$$

a pair related by complex conjugation. Axisymmetry means here $\partial_3 = 0$.

Solving (3.1) and (3.2) algebraically for α_2 and γ_1, respectively we have

$$\alpha_2 = \gamma^{-1}\left[-2\beta\alpha_1 + \alpha\gamma_2 + \alpha\beta_1 + \beta\beta_2 + \frac{1}{r}(3\alpha\beta - 2\alpha\gamma - \beta^2)\right] \quad , \tag{3.3}$$

$$\gamma_1 = \alpha^{-1}\left[-2\beta\gamma_2 + \gamma\alpha_1 + \gamma\beta_2 + \beta\beta_1 + \frac{1}{r}(3\gamma\beta - 2\alpha\gamma - \beta^2)\right] \quad , \tag{3.4}$$

(note that $\alpha \neq 0$). We can thus eliminate the derivatives of α and γ and the mixed β derivatives by use of the field equation $R_{33} = 0$ which has the form

$$2D\,\beta_{12} = \gamma(\alpha_1 + \beta_2)\beta_2 + \alpha(\gamma_2 + \beta_1)\beta_1 - \beta(\alpha_1\beta_1 + \gamma_2\beta_2 + 2\beta_1\beta_2) +$$
$$+ \frac{\beta}{r}\left[(\beta-\gamma)\alpha_1 + (\beta-\alpha)\gamma_2\right] + \frac{\beta}{r^2}(\alpha\gamma + \beta^2 - \beta\alpha - \beta\gamma) \quad . \tag{3.5}$$

Taking a combination of $R_{11} = 0$ with other components, we get

$$\alpha D\beta_{11} = \gamma(\alpha\beta_2\gamma_2 - \beta\alpha_1\beta_2) - \beta[\alpha(\beta_1+\gamma_2)\gamma_2 + (\gamma\alpha_1 - 2\beta\gamma_2)\alpha_1] +$$

$$+ (2\alpha\gamma - \beta^2)\alpha_1\beta_1 + \frac{1}{r}[(\gamma-\beta)\alpha(3\beta\gamma_2 - 2\gamma\beta_2) + \gamma\beta(2\alpha\beta_1 - 3\beta\alpha_1) + (\beta^2 - 3\alpha\gamma)\alpha\beta_1 +$$

$$+ (2\alpha\gamma + \beta^2)\beta\alpha_1] + \frac{\alpha}{r^2}[\gamma(5\beta^2 - \alpha\gamma - 2\beta\gamma) - \frac{1}{2}\beta(\alpha\gamma + 3\beta^2)] \quad , \tag{3.6}$$

whence, using also the complex conjugate equation, we will eliminate β_{11} and β_{22}.

Although the derivatives α_1 and γ_2 cannot be removed similarly, it will prove convenient to substitute them by the functions W and $Z = \overline{W}$ according to

$$\alpha_1 = \frac{1}{4\beta}\left[2\beta\beta_2 + 3\alpha\beta_1 + \frac{5}{r}\alpha\beta - \frac{2}{r}\beta^2 + W\right] \quad , \tag{3.7}$$

$$\gamma_2 = \frac{1}{4\beta}\left[2\beta\beta_1 + 3\gamma\beta_2 + \frac{5}{r}\gamma\beta - \frac{2}{r}\beta^2 + Z\right] \quad . \tag{3.8}$$

From $R_{12} = -\frac{1}{4r^2}$ we obtain the real first-order relation

$$F \equiv 9\alpha\gamma(\alpha b_1^2 + \gamma b_2^2 - 2\beta b_1 b_2 - \frac{8}{3}\frac{\beta}{r^2}D) - \alpha Z^2 - \gamma W^2 + 2\beta WZ = 0 \quad , \tag{3.9}$$

where the notation

$$b_1 = \beta_1 - \frac{\beta}{r} \quad , \qquad b_2 = \beta_2 - \frac{\beta}{r} \tag{3.10}$$

has been introduced. The derivatives of the F equation (3.9) and use of the previous results yield

$$24\alpha\gamma\beta D(W_1 - \frac{2}{r}W) = 3\alpha\gamma\{[(9\alpha\gamma - 12\beta^2)W - \alpha\beta Z]b_1 +$$

$$+ [(5\alpha\gamma - 4\beta^2)Z + 3\gamma\beta W]b_2\} + \tag{3.11}$$

$$+ (9\alpha\gamma - 6\beta^2)\gamma W^2 - (14\alpha\gamma - 12\beta^2)\beta WZ + (5\alpha\gamma - 6\beta^2)\alpha Z^2 +$$

$$+ 60\frac{\alpha^2\gamma^2\beta}{r^2}D\frac{2(\alpha Z - \beta W)Z + 3\alpha\gamma(Zb_2 - Wb_1)}{\alpha Z^2 - 2\beta WZ + \gamma W^2} \quad ,$$

$$24\alpha\beta D(Z_1 - \frac{Z}{r}) = (4\alpha\gamma + 6\beta^2)WZ - 3\gamma\beta W^2 - 7\alpha\beta Z^2 +$$

$$+ 3\alpha[3\gamma\beta W + (9\alpha\gamma - 16\beta^2)Z]b_1 + 3[(11\alpha\gamma - 4\beta^2)\beta Z - (5\alpha\gamma - 2\beta^2)\gamma W]b_2 + \tag{3.12}$$

$$+ 60\alpha\gamma\frac{\beta}{r^2}D\frac{2\alpha\beta Z^2 - 2\alpha\gamma WZ - 3\alpha^2\gamma Zb_1 + 3\alpha\gamma(2\beta\gamma Z - \gamma W)b_2}{\alpha Z^2 - 2\beta WZ + \gamma W^2} \quad .$$

Hence we may get rid of all the first derivatives of W and Z. It has been shown [3] that the functions W and Z do not vanish identically.

The integrability condition $Z_{12} = Z_{21}$ provides us another real first-order equation:

$$F_{II} \equiv 6(\alpha Z^2 - 2\beta WZ + \gamma W^2 + \frac{15}{r^2}\alpha\gamma\beta D)\alpha\gamma \mathrm{Re}\{(\beta Z - \gamma W)\alpha b_1\} +$$

$$+(\alpha Z^2 - 2\beta WZ + \gamma W^2)\left[(2\beta^2 - \alpha\gamma)(\alpha Z^2 - 2\beta WZ + \gamma W^2) - \alpha\beta\gamma\frac{D}{r^2}(27\alpha\gamma + 6\beta^2)\right] - 180\alpha^3\gamma^3\beta^2\frac{D^2}{r^4} = 0. \tag{3.13}$$

The $\mathcal{D}_1$ derivative of F_{II} contains a second-order expression. We apply the elimination procedure to this, and subsequently we remove the terms with b_2^2 by adding a suitable multiple of the F equation. We then find that $\mathrm{Im}\{(\beta Z - \gamma W)\alpha\mathcal{D}_1\}F_{II} = 0$ has just the right structure such that we can eliminate terms quadratic in the β derivatives by adding a multiple of the F_{II} equation:

$$(\alpha Z^2 - 2\beta WZ + \gamma W^2 + 15\alpha\gamma\beta\frac{D}{r^2})\left[(\beta\alpha Z^2 - 2\alpha\gamma WZ + \beta\gamma W^2)(3\alpha\gamma b_1 - \gamma W) - 2D(\alpha Z^2 - 2\beta WZ + \gamma W^2)Z - \right.$$

$$\left. - 12(\alpha\gamma + 3\beta^2)\alpha\gamma\beta\frac{D}{r^2}Z\right] + 540\alpha^2\gamma^2\beta^4\frac{D^2}{r^4}Z = 0 \quad . \tag{3.14}$$

We can further simplify this by adding a multiple of F_{II}. The result is strikingly simple:

$$F_{III} = \mathrm{Im}(3\alpha\gamma Z b_2 - \alpha Z^2) = 0 \quad . \tag{3.15}$$

Some information has been lost in the process since in Eq. (3.15) we took the imaginary part. We perform, however, a twin procedure, cancelling first the b_1^2 terms in $\mathcal{D}_1 F_{II}$. The combination $\mathrm{Im}\{(\alpha Z - \beta W)\mathcal{D}_1\}F_{II}$ then yields

$$\mathrm{Im}(\alpha Z b_1) = 0 \quad . \tag{3.16}$$

Equations (3.15) and (3.16) were only independent on the condition that $\gamma W^2 - \alpha Z^2 \neq 0$. Then they had the solution $3\alpha b_1 = W$ and $3\gamma b_2 = Z$, whence substituting in the F equation (3.9),

$$\gamma W^2 - \alpha Z^2 = 0 \quad . \tag{3.17}$$

Computing the $\mathcal{D}_1$ derivative of $\gamma W^2 - \alpha Z^2$ we have [3]

$$\left[(15\alpha\gamma - 3\beta^2)\alpha Z^2 + (9\beta^2 - 21\alpha\gamma)\beta WZ + 90\alpha^2\gamma^2\beta\frac{D}{r^2}\right]\alpha b_1 +$$

$$+ \left[(5\alpha\gamma - 9\beta^2)(\alpha Z^2 - \beta WZ) + 60\alpha^2\gamma^2\beta\frac{D}{r^2}\right]W = 0 \quad . \tag{3.18}$$

We obtain another linear equation in b_1 from the $\mathcal{D}_1$ derivative of the F_{III} equation (3.15), as shown in the Appendix. Introducing the positive functions

$$P^2 = 2(\beta WZ - \alpha Z^2) \tag{3.19}$$

and

$$\Delta = -3\alpha\gamma\beta\frac{D}{r^2} \quad , \tag{3.20}$$

the resulting set of linear first-order equations (3.13), (3.18) and (A.6) can be written

$$3\alpha^2\gamma P^2(P^2+5\Delta)b_1 + \{\alpha\gamma(P^2+5\Delta)(P^2+4\Delta)-2\beta^2P^2(P^2-\Delta)\}\ W = 0\ , \tag{3.21}$$

$$[(-15\alpha\gamma+3\beta^2)P^2 - 12\beta DWZ - 60\alpha\gamma\Delta]\alpha b_1 + \{(-5\alpha\gamma+9\beta^2)P^2 - 40\alpha\gamma\Delta\} = 0, \tag{3.22}$$

$$- [(6\alpha\gamma+3\beta^2)P^2 + 6\beta DWZ]\ P^2\alpha b_1 + \tag{3.23}$$

$$+ \{-(2\alpha\gamma-5\beta^2)P^4 + 2\beta\ DWZP^2 - 2\Delta[(4\alpha\gamma-2\beta^2)P^2 - 8\beta DWZ] + 40\alpha\gamma\Delta^2\}\ W = 0\ .$$

Combining Eqs (3.21) and (3.22) such that the terms with Δb_1 cancel:

$$[-DP^4-4\beta\ DWZP^2]\ 3\alpha b_1 + \{-DP^4 + (8\beta^2-4\alpha\gamma)P^2\Delta + 80\alpha\gamma\Delta^2\}\ W = 0\ . \tag{3.24}$$

Hence we can express βDWZ using the F equation which has the form $3P\alpha b_1 = -W\sqrt{P^2+8\Delta}$. (We see that b_1 must not vanish. From the signs in Eq. (3.24) it follows that the negative square root holds.) We then have

$$\beta DWZ = -\frac{1}{4}DP^2 + \frac{-DP^4+(8\beta^2-4\alpha\gamma)P^2\Delta+80\alpha\gamma\Delta^2}{4P^2(3\alpha b_1/W)}\ . \tag{3.25}$$

A linear combination of Eqs (3.23) and (3.24) has the form

$$3(-\tfrac{3}{2}\alpha\gamma-\tfrac{3}{2}\beta^2)\ P^4\alpha b_1 + \{(-\tfrac{3}{2}\alpha\gamma+\tfrac{9}{2}\beta^2)P^4 + 2\beta DWZ(P^2+8\Delta) - 6\alpha\gamma\Delta P^2\}W=0. \tag{3.26}$$

Eliminating βDWZ by use of (3.25) and the F equation we get

$$3[(-2\alpha\gamma-\beta^2)P^4 + (4\beta^2-2\alpha\gamma)P^2\Delta\ + 40\alpha\gamma\Delta^2]\alpha b_1/W +$$

$$+ (5\beta^2-2\alpha\gamma)P^4 + (4\beta^2-10\alpha\gamma)P^2\Delta\ = 0\ . \tag{3.27}$$

Eq. (3.21) can be brought to a similar form upon multiplying by $3\alpha\ b_1/W^2$:

$$3\ [(\alpha\gamma-2\beta^2)P^4 + (9\alpha\gamma+2\beta^2\ P^2\Delta\ + 20\alpha\gamma\Delta^2]\ \alpha b_1/W +$$

$$+ \alpha\gamma\ (P^2+5\Delta)(P^2+8\Delta) = 0\ . \tag{3.28}$$

Multiplying Eq. (3.21) by (–4), Eq. (3.27) by (–1), Eq. (3.28) by 2 and taking the sum we obtain

$$-3P^3(3\alpha\frac{b_1}{W})+ 13P^2 - 12\Delta = 0\ . \tag{3.29}$$

Since $P^2 > \Delta$ by Eq. (3.21), we have the sum of two positive terms on the left hand side, whence $b_1 = 0$, which is impossible. Thus the class of fields with functionally independent real and imaginary parts of the Ernst potential is empty.

The present treatment of axisymmetric fields with a conformally flat 3-space is somewhat simpler than that given in [3], in that only the special case $\gamma W^2 = \alpha Z^2$ needs consideration because of Eq. (3.16).

Acknowledgments

I thank Dr. M. Huszár for an illuminating discussion. Equation (3.16) has been computed by the R40 machine of CRIP, using a Reduce [10] language program.

Appendix: The $\mathcal{D}_1 F_{III}$ equation

Here we derive a linear equation in the function b_1 which holds as a consequence of

$$S_1 \equiv \mathcal{D}_1 F_{III} = 0 \quad . \tag{A.1}$$

This will exemplify the procedures that lead one up the F series equations.

First we get rid of the derivatives Z_1 and W_1 in S_1 by use of the complex equations (3.11) and (3.12). We then eliminate the terms with an odd explicit power of r and all terms containing b_1^2 by subtracting a multiple of F_{III}:

$$S_2 = S_1 - \frac{1}{16\beta D} F_{III} \left[\frac{4}{r} + 3(19\alpha\gamma - 20\beta^2) b_1\right] \quad . \tag{A.2}$$

Next we remove the second derivatives of β by use of Eqs (3.6) and (3.7). We then replace any first derivative of β overleft by b_i using the notation (3.10). Following this, we remove the terms quadratic in the b_i's by adding a combination of first-order expression:

$$\begin{aligned} S_3 = \mathrm{Num}\, S_2 \; + \\ + \; & Dr^2 F_{III}(\gamma W^2 - 2\beta WZ + \alpha Z^2) \left[(39\alpha\gamma - 12\beta^2)\alpha b_1 + (48\beta^2 - 84\alpha\gamma)\gamma b_1\right] + \\ + \; & 720 D^2 F_{III}(\alpha^3 \gamma^2 \beta b_1 - \alpha^2 \gamma^2 \beta^2 b_2) + \\ + \; & Dr^2 F_I(\gamma W^2 - 2\beta WZ + \alpha Z^2) \left[8\alpha\beta Z + (4\beta^2 - 13\alpha\gamma)W - 120 \frac{D}{r^2} \alpha^2 \gamma^2 \beta W\right] \quad . \end{aligned} \tag{A.3}$$

The expressions S_1, S_2 and S_3 can be evaluated by a symbolic computer program. The result is, dropping an overall factor $4\, D\, r^2$:

$$\begin{aligned} S_3 \equiv -P^2 \; \{ & \left[(33\alpha\gamma - 24\beta^2)\alpha\gamma W^2 + (-27\alpha\gamma + 36\beta^2)\alpha\beta WZ + (6\alpha\gamma - 24\beta^2)\alpha^2 Z^2\right] b_1 + \\ + \; & \left[(12\alpha\gamma - 12\beta^2)\gamma\beta W^2 + (36\beta^2 - 63\alpha\gamma)\alpha\gamma WZ + (51\alpha\gamma - 24\beta^2)\alpha\beta Z^2\right] b_2 + \\ + \; & (8\beta^2 - 11\alpha\gamma)\gamma W^3 + (13\alpha\gamma - 16\beta^2)\beta W^2 Z + (3\alpha\gamma + 12\beta^2)\alpha W Z^2 - 9\alpha^2 \beta Z^3\} + \\ + \; & 24\alpha\gamma\beta \frac{D}{r^2} \left[(3\alpha\gamma - \beta^2)\gamma W^3 + (2\beta^2 - 3\alpha\gamma)\beta W^2 Z + (3\beta^2 - 7\alpha\gamma)\alpha W Z^2 + 3\alpha^2 \beta Z^3\right] + \\ + \; & 180\alpha^2 \gamma^2 \beta \frac{D}{r^2}(\alpha Z - \beta W)(\alpha Z b_1 - \gamma W b_2) + 720\alpha^3 \gamma^3 \beta^2 \frac{D^2}{r^4} W = 0 \quad . \end{aligned} \tag{A.4}$$

Eliminating b_2 by use of Eq. (3.15) and using (3.17) we get

$$-P^2\{[18\alpha^2\gamma^3\beta W^2 - (12\alpha\gamma + 6\beta^2)\alpha^2\gamma^2 WZ]\, b_1 + (2\alpha\gamma - 8\beta^2)\gamma\beta W^3 + (10\beta^2 - 4\alpha\gamma)\alpha\gamma^2 W^2 Z\} +$$

$$+ 6\alpha^2\gamma^2\beta\frac{D}{r^2}[(-8\alpha\gamma + 4\beta^2)\gamma W^2 Z + 4\beta^3 WZ^2] + 360\alpha^4\gamma^4\beta^2\frac{D^2}{r^4}Z = 0 \quad . \tag{A.5}$$

We now multiply by Z, use (3.17) repeatedly to get rid of Z^2, and remove an overall factor $W\gamma^2$:

$$-[(6\alpha\gamma + 3\beta^2)\alpha P^4 + 6\alpha\beta\, DWZP^2]\, b_1 +$$

$$+\{(5\beta^2 - 2\alpha\gamma)P^4 + 2\beta\, DWZP^2 + 6\alpha\gamma\beta\frac{D}{r^2}[(4\alpha\gamma - 2\beta^2)P^2 - 8\beta\, DWZ] + \tag{A.6}$$

$$+ 360\alpha^3\gamma^3\beta^2\frac{D^2}{r^4}\}W = 0 \quad .$$

This complex first-order equation is an algebraic combination of the F, F_{II} and F_{III} equations.

References

1. F.J. Ernst, Phys. Rev., 167, 1175, 1968.
2. Z. Perjés, Gen. Rel. Gravitation, 18, 511, 1986.
3. Z. Perjés, Gen. Rel. Gravitation, 18, 531, 1986.
4. W. Kinnersley, J. Math. Phys., 18, 1529, 1977.
5. Z. Perjés, Improved characterization of the Kerr metric, in: Proceedings of the Third Seminar on Quantum Gravity, Eds M.A. Markov, V.A. Berezin and V.P. Frolov, World Scientific, 1985.
6. D. Kramer, Class. Quantum Grav., 2, L135, 1985.
7. Suggestion by D. Kramer.
8. E.T. Newman, personal communication.
9. Z. Perjés, Stationary vacuum space-times in Ernst Coordinates, in: Proceedings of the Fourth Marcel Grossman Meeting, Ed. R. Ruffini, North-Holland, Amsterdam, 1985.
10. A. Hearn, Reduce User's Manual, Utah, 1979.

Acta Physica Hungarica 63(1–2), pp. 97–107 (1988)

ВЗАИМОДЕЙСТВИЕ ДВИЖУЩИХСЯ ДИСЛОКАЦИЙ И ТОЧЕЧНЫХ ДЕФЕКТОВ В ЩЕЛОЧНО-ГАЛОИДНЫХ КРИСТАЛЛАХ

Й. ШАРКЕЗИ
Физический институт Будапештского политехнического университета
1525 Будапешт, Венгрия

(Поступила в редакцию 3 сентября 1987 г.)

Исследовано влияние количества, типа и состояния двухвалентной примеси на критическое скалывающее напряжение кристаллов NaCl. С целью оценки состояния примеси проведены исследования проводимости, диэлектрических потерь и эффекта Степанова. Изучено влияние на механические и электрические характеристики кристаллов: температуры закалки, времени выдержки при повышенных температурах и предыстории кристалла.

Введение

Исследования последних лет показали, что в реальных кристаллах всегда имеется большое количество разнообразных препятствий, тормозящих движение дислокаций и тем самым оказывающих существенное влияние на процесс пластической деформации. В этой связи большое значение приобретает выделение домнирующих взаимодействий дислокаций с препятствиями, играющих главную роль в различных условиях протекания процесса пластического течения. По имеющемуся опыту в щелочно-галоидных кристаллах взаимодействием дислокаций друг с другом можно пренебречь по сравнению с взаимодействием дислокаций и точечных дефектов. Таким образом пластические свойства определяются последним взаимодействием [1]. Известно, что двухвалентные катионные примеси, внедренные в щелочно-галоидные кристаллы, вызывают значительное упрочнение. Упрочнение зависит от типа и количества примеси, а также от расположения примеси в кристалле. В кристаллической решетке двухвалентные примеси могут существовать в следующих видах: в виде одинарного примесного иона, комплекса из одинарного примесного иона и вакансии (ПВ-комплекса), агрегатов с многообразной структурой и ориентацией, образующихся из ПВ-комплексов, а также в виде преципитатов, образующих вторую фазу. Каждое из перечисленных препятствий, тормозящих дислокацию, наверное вступает во взаимодействие разного типа с движущейся дислокацией [2-5]. Особым вопросом ставится взаимодействие дислокаций со свободными вакансиями, возникающими вследствие наличия примесей или степень тормозящего действия, вызываемого этим взаимодействием.

Наши исследования основаны на той экспериментальной возможности, что путем термической обработки и применяя определенное количество примеси, наличие точечного дефекта данной структуры в образце можно сделать преобладающим. Таким образом новые дислокации, образующиеся в процессе пластической деформации, при своем движении встречаются с хорошо определенными препятствиями. Это дает возможность сравнительно четко отделить взаимодействия различного типа и ис-

следовать их. Таким путем можно создать однозначную связь между макроскопическими механическими характеристиками и соответствующими микропроцессами.

Однако все это справедливо только в случае кристаллов определенного качества. Обыкновенные чистые для анализа кристаллы содержат самые различные примеси, в том числе и гидроксильные ионы (OH^-), которые могут вступать в реакцию с добавленной примесью и изменить ее влияние на критическое скалывающее напряжение (на КСН). Таким образом оценка взаимодействия точечного дефекта и дислокации станет не однозначной. В связи с этим нашим исследованиям придает особую актуальность то условие, что мы располагали такими специально выращенными кристаллами NaCl без гидроксильных ионов, которые кроме добавленной примеси (Mg, Mn, Ca, Sr, Pb, Ba) других примесей практически не содержали [6].

Основной частью наших экспериментальных и теоретических исследований являются исследования, связанные с самыми простыми, но в то же время, очень важными точечными дефектами. Таким образом, подробно исследовали взаимодействие дислокаций и вакансий или дислокаций и ПВ-комплексов. Проблемы более сложных точечных дефектов, состоящих из ПВ-комплексов (димеров, тримеров) и проблемы тормозящего действия их на дислокации мы только коснулись, с той целью, чтобы в более широких рамках заниматься ролью простых точечных дефектов в упрочнении кристаллов.

Экспериментальные результаты

Чтобы объективно судить о всех изменениях состояния примесей в кристалле, параллельно были проведены исследования электрической проводимости кристаллов, диэлектрических потерь, электростатического потенциала, возникающего на поверхности при деформации.

Электропроводность исследовалась электрометрическим методом в интервале температур 20-700°С [7]. Диэлектрические потери измерялись по схеме, сходной с мостом Шеринга при разных температурах, в зависимости от частоты [8]. На кривых $tg\delta - \omega$ наблюдался максимум, по которому определялись эти потери. Величина заряда, возникающего на поверхности кристалла при его деформации, позволяла судить о возможном заряде на дислокациях. Эти измерения проводились при комнатной температуре по методике [9] при деформации кристалла сосредоточенной нагрузкой. Все электрические измерения, а также закалка кристаллов осуществлялись в вакууме в инертной атмосфере. Механические испытания кристаллов проводились на машине "Инстрон" на сжатие вдоль направления <100>.

Термообработка кристаллов может быть очень разнообразной. Мы выбрали две возможности создания примесного состояния при комнатной температуре. Первый способ: примесь в кристалле находится в термическом равновесии. Второй способ: примесь находится в растворенном состоянии, что при комнатной температуре является термически нестабильным состоянием. Однако в течение времени измерений это состояние можно считать стабильным. Эти два состояния можно создать выбором подходящей скорости закалки образцов. Это иллюстрируется на первом рисунке. Формы кривой для каждой использованной примеси согласуются друг с другом. Получению термически стабильного состояния для каждого образца соответство-

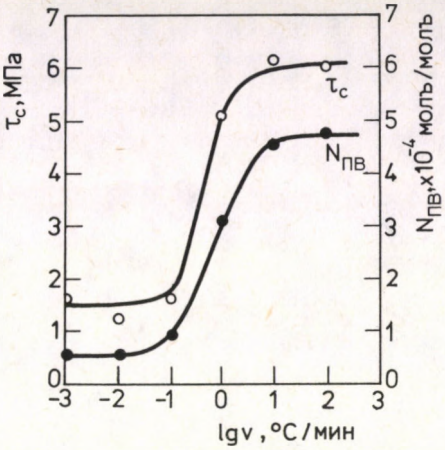

Рис.1. Зависимость критического скалывающего напряжения примесных кристаллов NaCl от скорости закалки

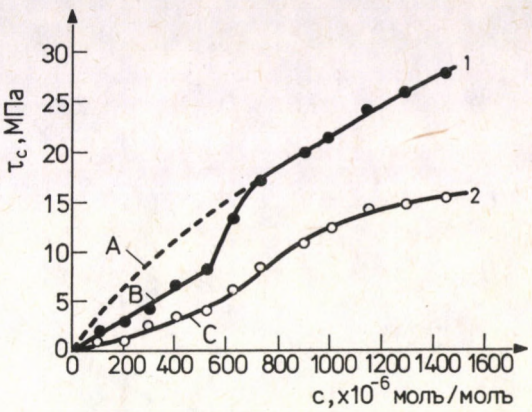

Рис.2. Зависимость КСН кристаллов NaCl:Ca от концентрации примеси. Кривая 1 соответствует быстрой закалке (100°С/мин), кривая 2 - медленной закалке (0,1°С/мин). Температура отжига 600°С, продолжительность отжига 5 часов. (Смысл букв A,B,C связан с рисунком 4.)

вала скорость в одну десятую градуса в минуту. А при создании скорости охлаждения в сто градусов в минуту, примесь полностью растворяется. Это состояние примеси нестабильно при комнатной температуре.

На втором рисунке приведены концентрационные зависимости измеренных при комнатной температуре КСН, для двумя различными способами термически обработанных кристаллов. В этом случае в качестве примеси служит кальций. Быстрой закалке соответствует верхняя кривая: при малых концентрациях КСН линейно зависит от концентрации. При больших концентрациях однако, получаем сложную зависимость. Медленной закалке соответствует нижняя кривая: линейная зависимость не наблюдается. Здесь надо подчеркнуть тот факт, что такого типа кривые получены нами только при термической обработке кристаллов в условии вакуума. На третьем рисунке видна разница в зависимостях КСН от концентрации примеси (при малых концентрациях примесей) в случаях термической закалки образцов в воздухе и в вакууме. Для образцов, термически обработанных в вакууме, получили линейную зависимость для каждой примеси, хотя и с отличающейся кривизной.

Для образцов, закаленных в воздухе, получаем корневую зависимость, при этом пропадает зависимость от типа примеси. Объяснение этого опыта без сомнения связано с обнаруженными на поверхностях термически обработанных в воздухе образцов тонких слоев окислов металлов [10].

Если вернуться к кривым на втором рисунке, то встает вопрос: предположение каких точечных дефектов необходимо для теоретического толкования отдельных участков кривых, а также какова природа взаимодействия соответствующего точечного дефекта и дислокации.

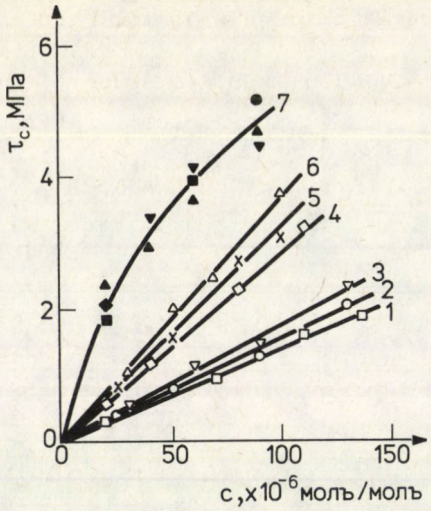

Рис.3. Зависимость полного КСН от типа и концентрации примеси и от способа термообработки. Результаты, полученные при термообработке в вакууме, показывают прямые: 1 - Mg, 2 - Mn, 3 - Ca, 4 - Ba, 5 - Pb, 6 - Sr. Кривая 7 получена на основании измерений после термообработки на воздухе

С целью идентифицирования данных точечных дефектов мы измеряли электропроводность и тангенса угла диэлектрических потерь кристаллов. Согласно результатам измерений, на линейных участках зависимости (рис.2), примесь решающим образом представлена в форме отдельных ПВ-комплексов и кроме этого маленькая доля примеси представлена в виде одинарного примесного иона (вследствие этого в кристалле есть свободная катионная вакансия). Следующий вопрос: какие точечные дефекты соответствуют нелинейному участку верхней кривой, или нижней кривой (рис.2). Зная из литературы функцию, описывающую нелинейный участок верхней кривой [11], которая получена в рамках феноменологической теории в предположении наличия двойных ПВ-комплексов (димеров), мы вычислили величину КСН, отвечающую случаю малых концентраций примеси, и это изображено на втором рисунке прерывистой линией. Затем мы взяли уже закаленные образцы с определенной малой примесью и сделали повторную закалку. Эти новые закалки сделали таким образом, что кристаллы отжигали при разных температурах и в течение разных промежутков времени, а потом, после быстрого охлаждения при комнатной температуре измерили КСН кристаллов и их диэлектрические потери.

На четвертом рисунке видно, как меняется КСН в зависимости от времени отжига при температуре закалки 80^{o}C. Соответствующая величина максимума этой кривой падает на полученный посредством вычисления участок верхней кривой на втором рисунке (рис.2). В случае большого времени отжига величина полученного КСН падает на нижнюю кривую на втором рисунке. Причину упрочнения и раз-

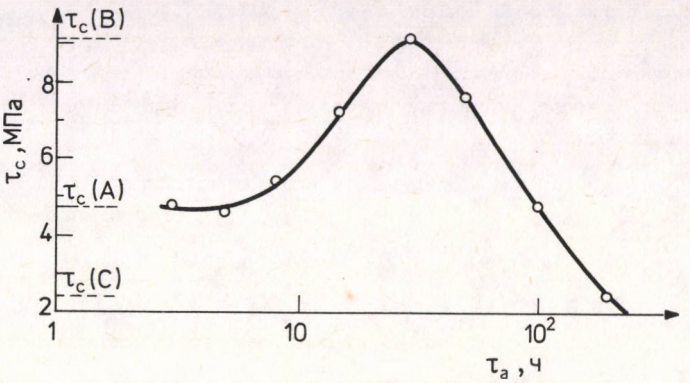

Рис.4. Зависимость КСН кристаллов NaCl:$3\cdot10^{-4}$ моль/моль Са, подвергнутых предварительной закалке, от продолжительности отжига. Отжиг проводился при температуре 80°С. КСН измерялся после быстрого охлаждения при комнатной температуре

упрочнения образцов, демонстрированных на четвертом рисунке, а также ответ на наш первый вопрос - с какими точечными дефектами связан участок верхней кривой на втором рисунке, отвечающий большим концентрациям примесей, можно найти на основе измерения диэлектрических потерь. Эти измерения были проведены на образцах, подобных тем, которые применялись в процессе измерения КСН. На пятом ри-

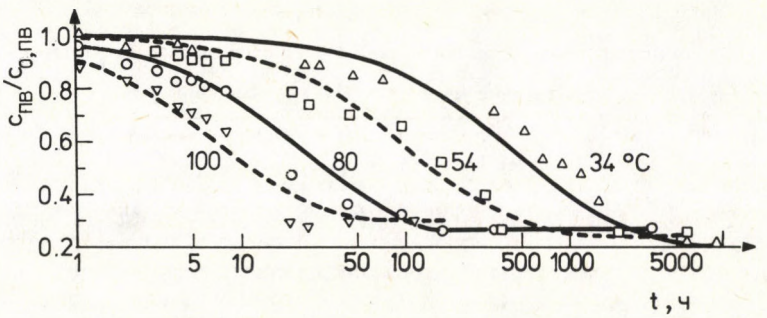

Рис.5. Зависимость относительного числа (количества) ПВ-комплексов в кристаллах NaCl:$3\cdot10^{-4}$ моль/моль Са от продолжительности отжига. Исходные образцы были получены путем быстрого охлаждения с температуры 600°С

сунке изображено изменение во времени диэлектрических потерь или относительного числа ПВ-комплексов в случае различных температур отжига. До того момента времени, пока КСН, измеренное на подобных образцах, не достигает своего макси-

мума, кривая соответствует кинетике второго порядка, т.е. единичные ПВ-комплексы превращаются в двойные ПВ-комплексы, т.е. димеры [12].

Следующий участок кривой формально соответствует кинетике третьего порядка, т.е. с двойным ПВ-комплексом сочетается еще один ПВ-комплекс, и получается тример, и таким образом нижняя кривая на втором рисунке связана с тримерами и большими агрегатами.

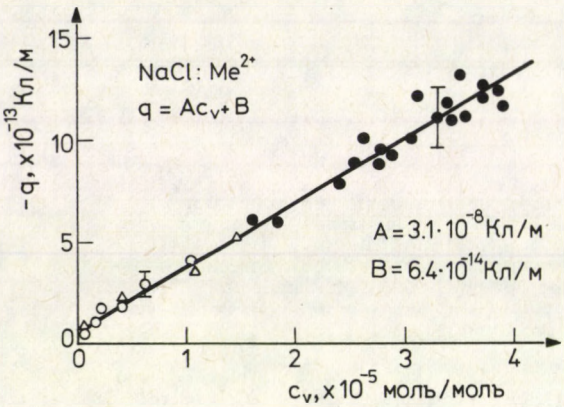

Рис.6. Зависимость заряда (q), перенесенного дислокациями, от концентрации свободных катионных вакансий (C_v) в кристалле NaCl.
Δ - кристаллы, содержащие различное количество примеси ($2 \cdot 10^{-7}$ - 10^{-3} моль/моль) Ca;
o - кристаллы, содержащие двухвалентные катионные примеси различного типа (слева направо: Ba, Pb, Sr, Mg, Mn, Ca) в примерно одинаковом количестве (10^{-5} моль/моль); • - кристаллы, содержащие примесь Ca с концентрацией ~ 10^{-3} моль/моль, подвергнутые термообработке в различных условиях

Кроме вышеуказанных следует выяснить экспериментальным путем еще один вопрос: какая связь имеется между концентрацией катионных вакансий (C_v) в кристаллах NaCl:Me^{2+} и зарядом дислокации (q). Зная эту связь, можно оценить силу, тормозящую дислокацию от катионных вакансий. Поэтому были проведены и такие измерения, которые позволяют непосредственное изучение зависимости между зарядом дислокации и концентрацией вакансий. Для этого на каждом образце измерялся заряд и ионная проводимость, пропорциональная концентрации катионных вакансий. Зависимость заряда дислокаций (q) от концентрации катионных вакансий (C_v) при комнатной температуре приведена на рис. 6. Экспериментальные результаты хорошо описываются линейной зависимостью ($q = A \cdot C_v + B$), причем независимо от того, каким образом изменяется C_v.

Обсуждение результатов и выводы

Теперь, так как экспериментальным путем определенным участкам верхней и нижней кривой на рис. 2 можем сопоставить определенные точечные дефекты (положение похоже в случае других примесей), обратим наше внимание на теоретическое описание взаимодействия идентифицированного точечного дефекта и дислокации. В литературе в рассматриваемой области описание взаимодействия дислокации с точечными дефектами имеет феноменологический характер. Мы, напротив, ставили цель при вычислении эффектов взаимодействия, учитывать точечные дефекты на атомном уровне. Такого рода вычисления основываются на результатах эксперимента, изображенных на рис. 7. Здесь представлены величины КСН, соответствующие прямым рис. 3 в случае одинаковых концентраций примеси, как функции ионных радиусов примеси. Следовало бы ожидать монотонное возрастание. Появление максимума свидетельствует о том, что кроме величины радиуса иона примеси, находящегося в ПВ-комплексе, во взаимодействии ПВ-комплекса с дислокацией играет роль также и другой атомный параметр.

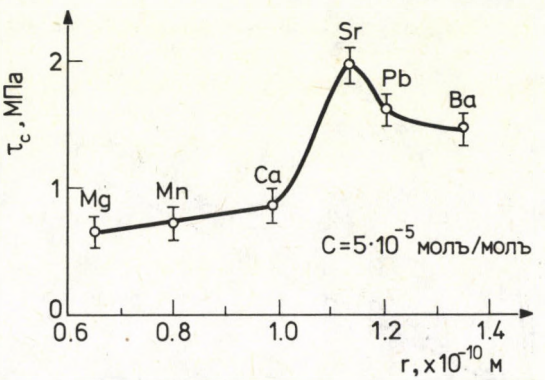

Рис.7. Зависимость полной величины КСН, связанной ПВ - комплексами, от радиуса примесного иона

Кривая, подобная этой, но с меньшими значениями функции, описывает зависимость эффективного напряжения, которое мы измеряли методом релаксации напряжения, от ионного радиуса. Это важно потому, что КСН является суммой внутреннего и эффективного напряжений, в то же время только эффективное напряжение можно непосредственно связывать со взаимодействием диполя с дислокацией.

Все это справедливо, если величина тормозящей силы от взаимодействия свободных катионных вакансий и дислокации пренебрежимо мала. Выяснение этого вопроса возможно путем теоретического толкования линейной зависимости (рис.6) между концентрацией катионных вакансий (C_v) и зарядом дислокаций (q). Для описания заряда, перенесенного дислокациями, в литературе сделан ряд попыток. Однако большинство этих описаний рассматривает заряд, образующийся вокруг неподвижной дислокации при равновесии. Эти теории в условиях пластической де-

формации несправедливы. Для вычисления заряда, перенесенного движущимися дислокациями, имеется в распоряжении только несколько сильно упрощенных квалитативных моделей, в которых введен ряд неизвестных параметров. Мы приближались к данному вопросу, исходя из результатов измерения своих и советских исследователей [13], и разработали диффузионную модель переноса заряда. Сущность этой модели состоит в том, что вакансии, взаимодействующие с механическим и электрическим полями дислокации, следуют за дислокацией вынужденным диффузионным движением. Решение проблемы дает диффузионное уравнение Котрелла с движущимся потенциальным полем. Аналитическое решение уравнения для имеющегося в нашем случае сложного поля неизвестно, поэтому было применено числовое решение; по сути дела - это описание диффузии с атомными скачками, где поле дислокации влияет на частоту скачков, и в данной точке кристалла изменение концентрации вакансий определяется числом вакансий, вскакивающих в эту точку, или выскакивающих оттуда.

В соответствии с изложенными ранее экспериментальными результатами (рис.6) заряд (q) при комнатной температуре пропорционален концентрации катионных вакансий кристалла. Эта зависимость исследовалась с помощью диффузионной модели. Результаты, полученные при разных скоростях дислокации, приведены на рис. 8.

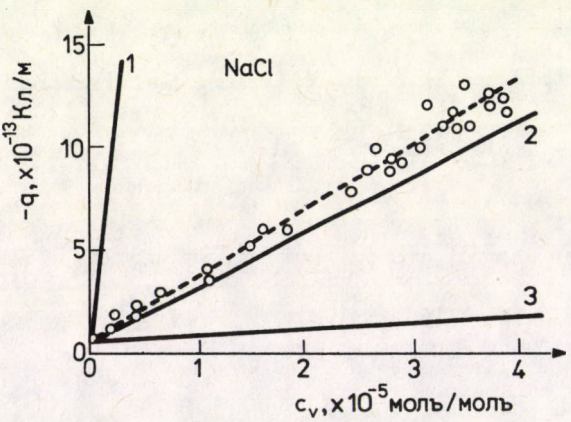

Рис.8. Зависимость заряда дислокации (q) от концентрации катионных вакансий (C_v) в кристалле при разных скоростях дислокации в кристалле NaCl. Кривые изображают результаты расчетов, а кружки - результаты измерений (см. рис. 6). Использованные при расчете величины скорости: $1 - 10^{-6}$, $2 - 10^{-5}$, $3 - 10^{-4}$ м/сек

Сплошные линии получены из расчета, кружки соответствуют результатам (рис. 6) наших измерений. Как видно, расчетные результаты совпадают с линейной зависимостью, полученной экспериментально.

Диффузионная модель дает возможность и для вычисления действующей на движущуюся дислокацию тормозящей силы, возникающей вследствие перенесенного заряда [14]. С помощью модели была вычислена зависимость тормозящей силы от скорости дислокации при трех разных температурах. Результаты показывают, что

тормозящая сила, возникающая вследствие переноса заряда, зависит от скорости дислокации, и максимальная величина напряжения увеличивается с увеличением температуры (рис. 9).

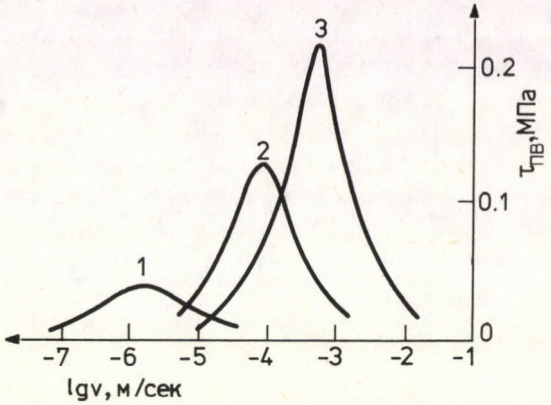

Рис.9. Зависимость тормозящего движение дислокации напряжения (τ_B), возникающего вследствие переноса вакансий, от скорости дислокации (ν) при разных температурах (1 - 293, 2 - 373, 3 - 423 К)

Максимальная величина тормозящего напряжения в зависимости от температуры может составлять меньше 10% величины КСН. Этот результат подтверждает наше исходное предположение, по которому при тормозящем дислокацию действии ПВ-комплексов тормозящим действием вакансий можно пренебречь.

Далее мы хотим рассказать о результатах расчета, связанного с взаимодействием диполя с дислокацией и о схеме теоретического вычисления эффективного напряжения, измеренного при комнатной температуре, и интерпретируемого так называемым эффектом Снока. Этот эффект состоит в том, что способные вращаться ПВ-комплексы под влиянием поля напряжения дислокаций стараются принимать энергетически выгодную ориентацию. Так формирующееся "облако" ПВ-комплексов задерживает дислокации, двигающиеся под действием внешнего напряжения. Во время теоретического анализа мы, оставаясь в рамках теории континуума - взаимодействия дислокаций и точечных дефектов, усовершенствовали прежние вычисления в трех аспектах. Во-первых, с помощью простой атомной модели и вычисления сдвига ионов, находящихся непосредственно вблизи ПВ-комплекса, мы оценили характерный для ПВ-комплекса деформационный тензор. С помощью этого тензора и тензора напряжения дислокации получили выражение для энергии взаимодействия. Таким введением деформационного тензора удалось удалить из описания взаимодействия принятый в литературе стыковочный параметр, так называемую тетрагональность, которая позволяет ощущать деформирующее решетку влияние ПВ-комплекса. Во-вторых: при вычислении эффективного напряжения, в отличие от принятого в литературе способа, мы рассматриваем разной ориентировки ПВ-комплексов, находящиеся на разных расстояниях от плоскости скольжения, как разные тормозные

центры и их совместное влияние учитывали теоретически обоснованным методом. В-третьих: симуляционным методом вычислили величину эффективного напряжения, обусловленного наличием вращающихся диполей. Исходной точкой в вычислениях служило выражение для энергии взаимодействия. Таким образом, если дислокация передвигается в плоскости скольжения с постоянной скоростью, то симуляционным методом можно вычислить величину энергии, диссипируемой окружающими дислокацию вращающимися ПВ-комплексами при их переходах между различными состояниями. Доказали, что диссипирующаяся энергия совпадает с величиной работы, необходимой для передвижения дислокаций [15]. Согласно результатам наших расчетов, эффективное напряжение, которое получается из-за эффекта Снока, является соразмерным числу ПВ-комплексов, и соответствует результатам наших экспериментов. Далее, вычисленная величина эффективного напряжения зависит через деформационный тензор от параметров ионов примеси, иначе говоря, от радиуса и поляризуемости примесных ионов.

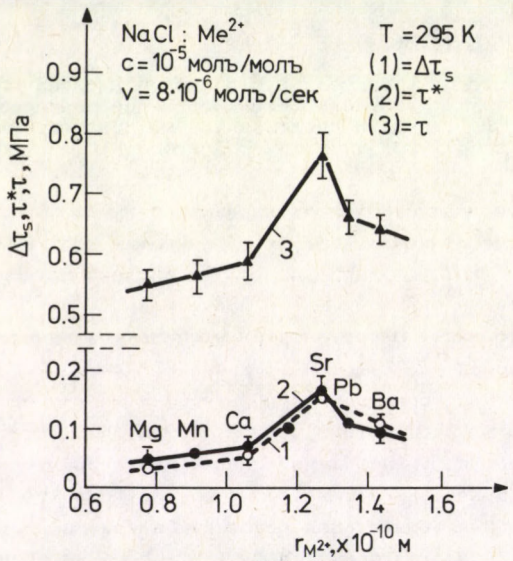

Рис.10. Зависимость дополнительной величины КСН - части Снока, вызванной ПВ-комплексами, от радиуса примесного иона (кривые 1 и 2). Кривая 1 соответствует расчетным величинам, а кривая 2 - измеренным величинам. Кривая 3 изображает полный КСН

На рис. 10 можно видеть, как меняется измеренная (первая кривая) и посчитанная (вторая кривая) величина эффективного напряжения, как функция от радиуса примесного иона. Получено хорошее совпадение, что подтверждает, с одной стороны, правильность метода вычисления, с другой стороны - то предположение, что эффективное напряжение получается от вращающихся ПВ-комплексов и составляет аддитивную часть полного критического скалывающего напряжения. Аномаль-

ное влияние примеси (Sr) объясняется тем, что сдвиг ионов окружающей среды ПВ-комплекса и деформационный тензор, зависит не только от размера ионов примеси, но еще и от их поляризуемости. Третья кривая рис. 10 соответствует полному КСН. Эта кривая похожа на кривую эффективного напряжения, т.е. измерения предела текучести могут дать качественную информацию о роли ПВ-комплексов.

В заключение об исследовании влияния на КСН агрегатов, состоящих из более чем одного ПВ-комплекса, мы хотим заметить следующее: в случае димеров и тримеров необходимо экспериментальным и теоретическим путем выяснить, каким образом связаны друг с другом входящие в эти агрегаты ПВ-комплексы. Только на этой основе можно попытаться провести на атомном уровне вычисление деформационных тензоров этих агрегатов и в конечном счетче, получить выражение для энергии взаимодействия.

Литература

1. А.А. Воробьев, Механические и тепловые свойства щелочно-галоидных кристаллов, Изд. "Высшая школа", 1988.
2. W. Frank, Phys. Stat. Sol. 29, 767, 1968.
3. П. Пратт, Сб. "Вакансия и точечные дефекты", Металлургиздат, Москва, 1969, стр. 123.
4. А.Х. Котрелл, "Дислокация и пластические течения в кристаллах", Л.-М. 1958.
5. A.A. Urusuvskaya, E.V. Darinskaya, R. Voszka, I. Ianszky: Cryst. Res. and Techn. 16, 597, 1981.
6. R. Voszka, Fizikai Szemle, XX, 6, 1, 1970.
7. Й. Шаркези, А.А. Предводителев, Кристаллография 24, т.3, 622, 1979.
8. J. Sárközi, A. Tóth, L. Szabó, Periodica Polytechnica 21, 293, 1977.
9. A. Tóth and J. Sárközi, Phys. Stat. Sol. (a) 30, K193, 1975.
10. K. Orbán, J. Sárközi, Acta Phys. Hung. 58, 267, 1985.
11. J. Sárközi, E. Hartmann, Acta Phys. Hung. 58, 259, 1985.
12. G. Berg, M. Dubiel, J. Sárközi, Cs. Kuti, Acta Phys. Hung. 51, 319, 1981.
13. В.И. Алшиц, М.В. Галусташвили, И.М. Паперно, Кристаллография, 20, 1113, 1975.
14. A. Tóth, T. Keszthelyi, P. Kálmán, J. Sárközi, Phys. Stat. Sol. (b) 122, 501, 1984.
15. A. Tóth, T. Keszthelyi, P. Kálmán, J. Sárközi, Mat. Sci. and Engineering 64, 1984, 223.

Acta Physica Hungarica 63(1–2), pp. 109–113 (1988)

QUANTITATIVE DETERMINATION OF THE QUARTZ CONTENT OF RESPIRABLE DUST BY INFRARED SPECTROPHOTOMETRY*

J. HLAVAY[1], L. ANTAL[1], I. VASSÁNYI[2] and J. KÁRPÁTI[3]

[1]Institute for Analytical Chemistry, University of Chemical Engineering
8201 Veszprém, P.O.Box 158, Hungary

[2]Department of Mineralogy, University of Chemical Engineering
8201 Veszprém, P.O.Box 158, Hungary

[3]State Institute of Occupational Health, Budapest, Hungary

(Received 15 September 1987)

Infrared spectrophotometric method was developed for the determination of crystalline silica in respirable dust samples from a wide range of industrial environments. Samples were collected with personal sampler on a Microsorban filter. The filter was dissolved in benzene and the suspension was separated by centrifuge. The mineral phase content of the dust was determined by X-ray powder diffraction. The particle size of the standards and samples as well as the mineral interference effects were controlled. Different calibration curves using a mixture of crystalline quartz and interference mineral were prepared. The particle size was measured in the pellets. The absorbance of the 800 cm^{-1} band (Si–O–Si symmetrical stretching vibration) was calculated and proved to be proportional to the concentration of quartz.

Introduction

Exposure to silica dust can occur in a wide range of industrial environments, including mining, construction, agriculture and manufacturing. Quartz is the most abundant polymorphic form of silica, occurring naturally in certain types of rocks, in sand, and in most types of soil. Crystobalite and, more rarely, tridymite are formed when quartz or amorphous silica is heated.

Silicosis, the lung disease caused by inhalation of fine particles of crystalline dust, has long been recognised as a health hazard in many work places. The occupational exposure limits in England for respirable dust containing the different types of crystalline silica range from 5 to approximately 0.1 mg/m^3 for quartz-containing dusts, and from 2.5 to approximately 0.05 mg/m^3 for dusts containing crystobalite or tridymite [1]. The practical limit for any particular respirable dust depends on its crystalline silica content.

Many analytical techniques have been developed for the quantitative determination of the quartz in dust. These include gravimetry, spectrophotometry, differential thermal analysis [2], X-ray powder diffraction [3–7] and infrared spectrophotometry [2, 4, 5, 8–10]. Of these, X-ray powder diffractometry and IR spectrophotometry are the principal techniques currently employed; each is capable of identifying free crystalline silica in the presence of silicates [11, 12]. Using IR spectrophotometry, quartz may be analysed by direct filter [13–14], pressed pellet [15, 16], or attenuated total reflectance (ATR) [17] methods. In the

*Presented at the 3rd Hungarian Conference on Molecular Spectroscopy, Debrecen, Hungary, 24–28 August 1987

direct filter and ATR techniques the membrane filter on which the sample dust is deposited is placed directly into the infrared beam or in an ATR unit without further sample preparation. In the pellet method, the sample is recovered from the membrane filter by incineration or dissolution of the filter and the dust is mixed with embedding material and pressed to pellets.

In our work, the pellet method was used for determination of the quartz content of respirable dust originated from different work places.

Experimental

Respirable dust was sampled by personal sampler (PERSOMETER) on a Microsorban membrane filter. The flow rate of the air was about 1.5 dm^3/min. Amount of samples ranged between 1–10 mg. Recovery of the dust from membrane filter was carried out by dissolving the membrane in benzene and centrifuging the suspension.

Standard samples for IR investigation were ground in a laboratory ball-mill (Narva, Brand-Erbisdorf, GDR). Samples were homogenized in spectroscopic grade potassium-bromide and pressed to pellets. Infrared spectra were recorded by a SPECORD 75 IR-spectrophotometer (Carl Zeiss, Jena, GDR). X-ray powder diffractograms were obtained by a M-1051 Philips diffractometer. Particle size distribution in the pellet was measured by a VIDIMAT Image Analyser (Research Institute for Ferrous Metallurgy, Budapest, Hungary).

Results and discussion

During the collection of the respirable dust samples, 1–5 g of sedimented dust was sampled from the immediate work places of the workers. Furthermore, in some cases, 50–100 mg of dust was collected by a high-volume sampler (type: SPG 210) on membrane filter. The higher amounts of samples were needed for the qualitative mineralogical analysis carried out by X-ray powder diffraction.

The precision and the accuracy of the infrared spectrophotometric analysis depend on the effects of the particle size and matrix interferences [8]. Theoretical studies have shown that materials of equivalent chemical composition, but different particle size, have significantly different infrared spectra [18–21]. They indicate that the absorbances of particles smaller than the incident wavelengths increase with decreasing particle size. In order to avoid the reflection and light scattering of the incident beam, the particle size of the samples has to be smaller than 2.5 μm [22]. This limit is usually fulfilled in case of the respirable dust but during the preparation of the calibration curve, the standard samples should be ground. The particle size distribution of each sample collected and standards were determined in the pellet by VIDIMAT Image Analyser [22].

For determination of the quartz content of dust samples, the absorbance of the 800 cm^{-1} band was calculated. This band is originated from the symmetrical stretching vibration of Si–O–Si groups. The base-line method was used for the calculation of the absorbance.

The presence of any minerals in the dust sample that possesses absorption band close to 800 cm^{-1} may produce erroneous results. Therefore, after the qualitative phase analyses carried out by X-ray powder diffraction, the interference mineral was added to the standard quartz used for preparation of the calibration curve. In this case, the interference effects are taken into account in the calculation of the equation of calibration curves.

Consequently, for reliable quantitative analysis, pellet preparation, particle size equivalence and interference effects have to be standardized and controlled.

Determination of quartz content in coal mine dust

Qualitative phase analyses of the sedimented coal mine dust was carried out by X-ray powder diffraction. Along with the quartz, kaolinite, illite, calcite, dolomite, sulfates and plagioclase were identified. From these minerals, the vibration bands of Si–O–Si groups present in the kaolinite and illite have to be considered. Therefore, 0.5 mg of kaolinite was weighed to each pellet and 0.0125–0.5 mg of crystalline quartz were added in eleven pellets for preparation of the calibration curve. The quartz and the kaolinite were homogenized by potassium-bromide in an agate morter for 3 min. Pellets were pressed in a 20 mm diameter die set. All steps of pellet preparation were carefully controlled to allow comparison of the spectra. After pellet preparation, a 6 x 20 mm area of the pellet was selected by masking the other parts of the disc. Both infrared spectra and particle size distribution measurements were taken on the free area and in the whole cross section of the pellets.

The equation of the calibration curve is:

$$A = 2.4 \times 10^{-2} + 4.2 \times 10^{-1}\ C\ ,$$

where A = absorbances at 800 cm^{-1} and C = mass of quartz in the pellets (mg). The standard error of regression, S_{reg}, is $\pm 2.6 \times 10^{-3}$, while the standard deviation of the slope, S_a is $\pm 3 \times 10^{-3}$ and that of the intercept, S_b is $\pm 5.5 \times 10^{-3}$. The regression coefficient, r, is 0.999.

The average particle diameter of the standards in the pellet was d_{ave} = 2.2 µm.

The quartz content found in sedimented and respirable coal mine dust sampled from different places of the mine and different workers is shown in Table I and II, respectively.

Table I

Quartz content of some sedimented coal mine dusts*

Sample	Amount of quartz [%]	d_{ave} [µm]
1	10.7 ± 0.7	2.5
2	9.4 ± 0.7	2.6
3	14.6 ± 1.7	2.5
4	13.0 ± 0.7	2.5
5	14.9 ± 0.7	2.5
6	11.3 ± 0.7	2.7

*2 mg sample was weighed into the pellets

Only 0.46–0.65 mg of respirable samples were recovered from the filters and weighed into the pellets. Therefore, a confidence limit of ±2.3–3.3% was obtained in case of the respirable dusts while that of ±0.7% at the sedimented samples.

Determination of quartz content in foundry atmosphere dust

Some respirable dust samples were collected from different foundries. About 0.5–2.0 mg samples could be separated from the filters. According to the qualitative X-ray powder dif-

Table II

Quartz content of some respirable coal mine dusts

Sample	Sample mass in pellet [mg]	Amount of quartz [%]	d_{ave} [μm]
1	0.65	9.7 ± 2.3	2.5
2	0.53	18.4 ± 2.8	2.3
3	0.46	8.8 ± 3.3	2.1
4	0.58	14.5 ± 2.6	2.4
5	0.55	16.7 ± 2.7	2.4

fraction analysis, calcite, magnetite, albite, hematite, α-Fe, phosphates, chlorite and muscovite were found in different amounts. Since muscovite and chlorite were in the dust as trace clay minerals, they did not interfere with the determination of the quartz. Calcite was identified as main component and the 880 cm^{-1} band of carbonate ion would be a possible interference. Therefore, 0.5 mg calcite was weighed to the standard crystalline quartz for the preparation of the calibration line.

The equation of the calibration curve is:

$$A = 2.9\times10^{-3} + 4.1\times10^{-1}\ C\ ,$$

$$S_{reg} = \pm5.6\times10^{-3},\ S_a = \pm2.7\times10^{-3},\ S_b = \pm7.3\times10^{-3},\ r = 0.999\ .$$

The average particle diameter of the standards in the pellet was d_{ave} = 2.6 μm.

The quartz content found in the respirable foundry dusts is shown in Table III.

Table III

Quartz content of foundry dusts

Sample	Sample mass in pellet [mg]	Amount of quartz [%]	d_{ave} [μm]
1	2.07	8.6 ± 1.4	2.87
2	1.00	6.5 ± 2.9	2.87
3	1.23	5.0 ± 2.4	2.86
4	0.52	6.1 ± 5.7	2.89
5	1.30	3.3 ± 2.3	2.97
6	0.50	8.2 ± 6.0	2.74
7	1.91	18.3 ± 1.5	2.05
8	2.12	10.1 ± 1.3	2.71

The confidence limit (c.l.) of the determination depends on the amount of sample weighed into the pellet. If only 0.5 mg dust is available, even ±6% of c.l. can be obtained.

References

1. Health and Safety Executive, Occupational Exposure Limits 1984, Guidance Note EH 40/84, HM Stationery Office, London, 1984.
2. R.D. Foster and R.F. Walker, Analyst, 109, 1117, 1984.
3. R.L. Gordon and G.W. Harris, Nature (London), 175, 1135, 1955.
4. K.J. Pickard, R.F. Walker and N.G. West, Ann. Occup. Hyg., 29, 149, 1985.
5. A. Mangia, Anal. Chem., 47, 927, 1975.
6. C.J. Toussaint and F. Bo, Intern. J. Environ. Anal. Chem., 21, 1, 1985.
7. C.M. Nenadic and J.V. Crable, Am. Ind. Hyg. Assoc. J., 32, 529, 1971.
8. D. Toffolo and J.N. Lockington, Am. Ind. Hyg. Assoc. J., 42, 579, 1981.
9. W.M. Tuddenhan and R.J.P. Lyon, Anal. Chem., 32, 1630, 1960.
10. L. Antal, J. Hlavay and J. Kárpáti, Periodica Polytechnica, 30, 209, 1986.
11. P.L. Anderson, Am. Ind. Hyg. Assoc. J., 36, 767, 1975.
12. R.L. Henry, J. Opt. Soc. Am., 38, 777, 1948.
13. A.H. Gillieson and D.M. Farrel, Can. Spectrosc., 61, 21, 1971.
14. J. Dodgson and W. Whittaker, Ann. Occup. Hyg., 16, 389, 1973.
15. P.A. Estep, J.J. Kovach and C. Karr, Anal. Chem., 40, 358, 1968.
16. D.J. Larsen, L.J. von Doenhoff and J.V. Crable, Am. Ind. Hyg. Assoc. J., 33, 367, 1972.
17. R. Broxterman, Anal. Tech. Occup. Chem., 120, 67, 1980.
18. R.N. Jones, J. Am. Chem. Soc., 74, 2681, 1952.
19. D. Duyckaerts, Spectrochim. Acta, 7, 25, 1955.
20. J.W. Otvos, H. Stone,and W.R. Harp, Spectrochim. Acta, 9, 148, 1957.
21. G. Duyckaerts, Analyst, 84, 201, 1959.
22. J. Hlavay and J. Inczédy, Spectrochim. Acta, 41A, 783, 1985.

Acta Physica Hungarica 63(1–2), pp. 115–118 (1988)

INVESTIGATION OF THE INTERACTION OF SILICON-ORGANIC COMPOUNDS AND $Ca(OH)_2$*

T. GÁBOR[1], B.N. VINOGRADOV[2], V.P. KNYAZEVA[2], K. PÁLOSSY-BECKER[1], M.N. VALIEVA[2], O.D. GRATSEVA[2], J. NAGY[1] and V.I. SIDOROV[2]

[1]Institute for Inorganic Chemistry, Budapest Technical University
1521 Budapest, Hungary

[2]Insitute for General Chemistry, Moscow Builders' Technical University
129337 Moscow, USSR

(Received 15 September 1987)

The new phases produced in the interaction of chloro-silane distillation residues and $Ca(OH)_2$ are different in the case of alkyl and aryl silane derivatives. X-ray phase analysis results about the composition of the new phases are strongly supported by the IR spectra, too.

Introduction

One of the ways to improve the corrosion resistance of cement-based building materials is to decrease the $Ca(OH)_2$ content of the starting materials. In this case the microstructure of cement stone will change. As an inexpensive hydrophobizing agent the by-product of chloro-silane manufacturing can be applied, namely the distillation residue, which contains chloro-silanes, alkyl-chloro-disiloxanes, bis-silyl-alkylates and $C_6 - C_9$ hydrocarbons. The active chlorine content of the mixture was 48%, which was reduced to 6–7% by hydrolysis or alkoxylation (i.e. treatment with i-propyl alcohol).

The modelling of the optimal hydrophobization circumstances of these cement mixtures was carried out with $Ca(OH)_2$. A $Ca(OH)_2 - H_2O$ suspension with a mass ratio of 2 : 1 was treated with hydrophobizing agents, then after 24 hours the phase composition of the powdered samples was studied based on X-ray phase diagrams and IR spectra.

For the treatment of samples as hydrophobizing agent the residue of the distillation of methyl- (MK), methyl-vinyl- (MVK) and phenyl- (FK) chloro-silane production as well as W-290 (Wacker Chemie, West-Germany) were used. The last product is a polysiloxane oligomer with long alkyl chain and it was used as a solution in an organic solvent.

From the IR spectrum of the model compound $Ca(OH)_2$ (Fig. 1) it can be seen that it was transformed into the carbonate on contacting with air (bands at 1450, 875, 420 cm^{-1}).

The X-ray diffractograms of the $Ca(OH)_2$ sample hydrophobized using MK and MVK (Fig. 2) do not prove the incorporation of Si-O group into the sample. However, the wide band appearing in the IR spectrum refers to the presence of Si-O-Si or Si-O-C bonds. After extraction of samples with hexane the intensity of the wide band characteristic of the stretching vibration of siloxanes decreases and the wide band splits into several peaks (in the range of 1130–1010 cm^{-1}), which means non-reacting low molecular weight siloxanes can be removed

*Presented at the 3rd Hungarian Conference on Molecular Spectroscopy, Debrecen, Hungary, 24–28 August 1987

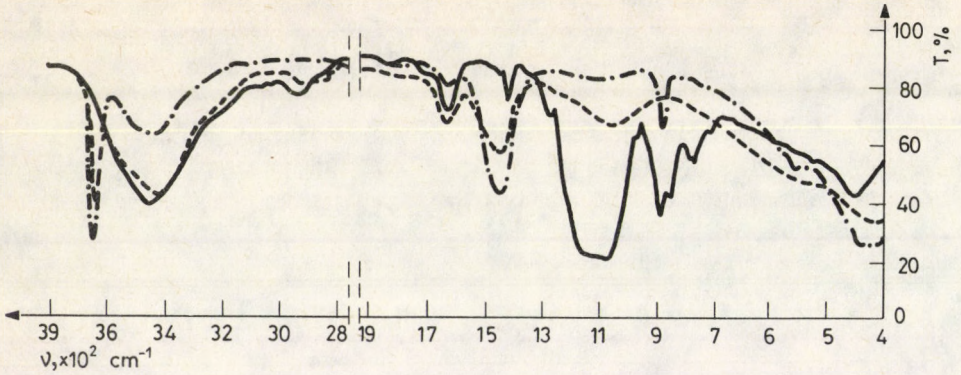

Fig. 1. IR spectra: 1, MVK (——); 2, $Ca(OH)_2$ (–.–.–); 3, Hydrophobized $Ca(OH)_2$ (----)

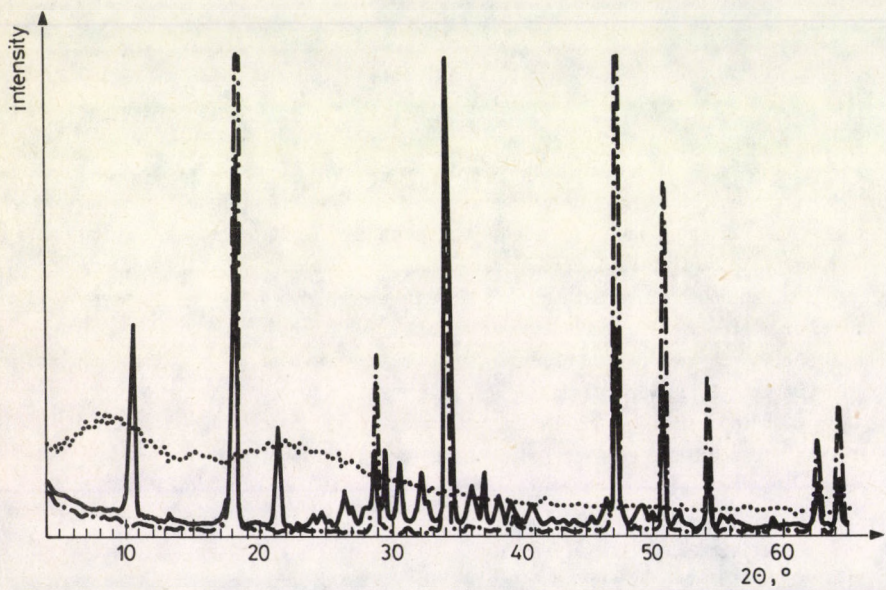

Fig. 2. X-ray diffractograms: 1, MVK (----); 2, $Ca(OH)_2$ (–.–.–); 3, Hydrophobized $Ca(OH)_2$ (——)

from the sample. The bands at 3600–3100 and 1700–1600 cm^{-1} belong to the bound water. The amount of this bound water does not decrease on drying at 180 ^{o}C to constant weight.

In the IR spectrum of MVK the stretching frequency of the Si-H bond can be observed at 2258 cm^{-1}. This band cannot be found in the spectrum of the hydrophobized product because the Si-H bond is hydrolysed in alkaline medium.

On the basis of X-ray diffractograms it has been found that $Ca(OH)_2$ reacts with the residue of distillation only in the presence of water. In the X-ray diffractogram of MK there is a wide band in the range of 2Θ 8–12^{o} (d/n = 0.73–1.25 nm; 0.81–0.821 nm) and a

diffuse band can be observed between 2θ 19–28°. The X-ray diffractograms of MVK, of $Ca(OH)_2$ and of the product of interaction can be seen in Fig. 2. The more combined hydrocarbon group bonded to silicon reduces the regularity of the hydrolysed particles. The calcite bands in the X-ray diffractogram prove the particular transformation of $Ca(OH)_2$ into $CaCO_3$.

In the course of the reaction the amount of $Ca(OH)_2$ decreases. This process is indicated by the IR spectra, but even better by X-ray diffractograms by a decrease in the intensity of the $Ca(OH)_2$ bands (in this respect first of all the d/n = 0.3097–0.3112; 0.1793–0.1798 and 0.1684–0.1687 nm bands are characteristic). The d/n values of the new crystalline phase occurring on hydrophobization are summarized in Table I.

Table I

Relative peak intensities of $Ca(OH)_2$ hydrophobized with MVK or MK

N°	d/n, nm	Relative intensity	N°	d/n, nm	Relative intensity	N°	d/n, nm	Relative intensity
1	0.8328	10	8	0.2926	4	15	0.1952	3
2	0.6605	1	9	0.2771	3	16a	0.1876	1
3	0.4161	5	10	0.2426	3	16b	0.1857	1
4	0.3688	1	11	0.2362	1	17	0.1845	1
5	0.3597	1	12	0.2218	2	18	0.1757	1
6	0.3376	2	13	0.2058	1	19	0.1651	1
7	0.3301	1	14	0.1997	1	20	0.1526	0.5

16a. only for MVK; 16b. only for MK

The data of the X-ray diffractograms of the new phase do not agree with those found in the literature [1–4]. The intense bands observed at d/n = 0.8328 and 0.4161 nm characterise the natural calcium-alumina-silicates ($CaO.Al_2O_3.7SiO_2.1,7H_2O$ and $CaO.Al_2O_3.4SiO_2.6H_2O$), alkali- and alkaline earth metal silicates, as well as calcium-chloro-hydrosulphato-aluminate ($3CaO.Al_2O_3.CaSO_4$, $CaCl_2.12H_2O$). At the same time the band at d/n = 0.832 nm can be found in the X-ray diffractogram of $Ca(CH_3COO)Cl.5H_2O$. The starting components do not contain any alumina and alkali metal, thus organic acids with short chain are formed in the presence of HCl arising from the reaction of the distillation residue and due to the large specific surface area. Hence, the crystalline phase may contain calcium-alkylate-chloride, too. In the differential IR spectrum of the new phase weak bands can be observed at 645, 615 and 465 cm^{-1} (the deformation frequencies of carboxylate ion), but the stretching frequency of carboxylate ion cannot be identified unambiguously.

On the basis of IR spectra it can be stated that during the hydrophobization with FK siloxane chains are built into the product (in the range of the stretching frequencies of Si-O-Si group two peaks occur). In the X-ray diffractograms there are bands characteristic of the new phase, which have not yet been identified, at d/n = 0.8349; 0.5315; 0.2757; 0.2371; 0.1878 and 0.1637 nm.

Hydrophobization made with W-290 (not containing chlorine) yields a product containing a high amount of polysiloxanes with long carbon chain. This material contains the

minimum quantity of OH groups (only one sharp band can be observed at 3635 cm^{-1} in the IR spectrum and only weak bands at d/n = 0.2453 and 0.1637 in the X-ray diffractograms). In this case the siloxane oligomer chain is bonded at the surface and in the pores of material, so it prevents water uptake.

Experimental

The X-ray diffractograms were taken by an X-ray diffractometer type JDX–IOPA applying a copper anticathode and nickel filter in the range of 4–65°. The rotation speed of the goniometer was 0.04 °/ms.

The IR spectra were taken by an IR spectrometer model UR–20 in KBr pellets.

References

1. V.I. Micheev, Rentgenometritseskij Opredelitel Mineralov, Gosbeoltechizdat, Moscow, 1957.
2. Powder Diffraction File JCPDS, USA, 1963.
3. V.S. Gorshkov, V.V. Timashev and V.G. Savetev, Metodi Fiziko-himicheskovo Analisa Viazhushcih Veshceshtv, Vishaja Shkola, Moscow, 1981.
4. L.I. Mirkin, Rentgenostrukturnij Analis, Nauka, Moscow, 1976.

Acta Physica Hungarica 63(1–2), pp. 119–135 (1988)

IDENTIFICATION OF CONCRETE ADDITIVES BY PATTERN RECOGNITION USING IR SPECTRA*

K. ERŐSS–KISS[1], GY. SZAKÁLAS[1], G. VERESS[1] and D. VALTINYI[2]
[1]Institute for General and Analytical Chemistry, Technical University of Budapest
1521 Budapest, Hungary
[2]EMI Chemical Department
1502 Budapest, Hungary

(Received 15 September 1987)

A procedure was developed for the identification of concrete additives on the basis of their infrared transmission properties, using the new supervised classification method PRIMA (Pattern Recognition by Independent Multicategory Analysis).

The training process of identification was carried out using the IR spectral data of known additives. These data were the comparative spectral band intensities of the additives at 15 selected positions, where the absorption of the single additives showed sharp differences.

With the process elaborated identification can be carried out with 100% reliability, and this helps the prediction of expectable concrete-technological properties.

The paper reports on the development of an efficient, well-reproducible, quick and cheap method, suitable for the identification of concrete additives, and thus, for the prediction of their expectable concrete-technological effect. The study of these effects (setting time, consistency, hardening and shrinkage modification, etc.) requires lengthy and expensive measurements, so that demand arose for the introduction of a simpler analytical process, still giving reliable results.

The fundamental principle of our method is the identification of concrete additives on the basis of the characteristic properties of their IR spectra, using a pattern recognition supervised classification method. Identification is carried out in two levels: concrete additives are first grouped into composite classes on the basis of certain IR spectral properties, and then identification is performed within one single composite class under consideration of further spectral properties.

To characterize the IR spectra not only the location of the absorption bands is used for identification, but also the percentage distribution of the intensity of a few selected bands. Thus, the number of data obtained from the IR spectrum considerably increases, which increases also the reliability of our method, identification varying between 98.7 and 100%.

The steps for the development of the method were the following:

– 27 additives were identified [1–5] with the aid of their functional groups, revealed by their IR spectra bands, and then with the assistance of IR spectrum maps.

– From the IR spectra of the additives identified, 15 properties (intensity distribution of the bands of their characteristic groups) were defined, on the basis of which the additives were separated into 10 classes.

---

*Presented at the 3rd Hungarian Conference on Molecular Spectroscopy, Debrecen, Hungary, 24–28 August 1987

– Using the data above a learning program was written, with the help of which we got to know the centre of gravity points. The inhomogeneity of the known classes were calculated and these data were then used for the classification of unknown additives by the method "PRIMA" [8].

The same procedure was also carried out separately for each class, with the marking out of new properties within the classes, on the basis of which identification within the class became also possible.

Preliminaries

The chemical composition of additives, identification of their components, their mode of action, description and survey of methods suitable for their chemical and instrumental analysis were discussed already in earlier works [1–3]. Our present paper deals with the updating of our procedure developed earlier, in so far as the supervised classification method PRIMA (Pattern Recognition by Independent Multicategory Analysis) is used for the evaluation of our IR spectral data [6–8].

Supervised classification by the method PRIMA

Pattern recognition methods form one of the groups of modern mathematical processes solving the problems of classification and grouping. Pattern recognition methods can be subdivided into two groups according to their functions (supervised and non-supervised classification). In the case of pattern recognition in the narrower sense, in the so-called supervised classification or training with a teacher program, material of knowledge is available, that is, the classes of certain objects are known. Using this learning pattern, the location of the classes in the space of essential properties is determined by the alters, defined by the known object points of the known classes. Using our knowledge, during recognition the objects of an unknown class can also be arranged in the respective class of the essential property alter.

Each supervised classification consists of two steps, training and recognition (Fig.1).

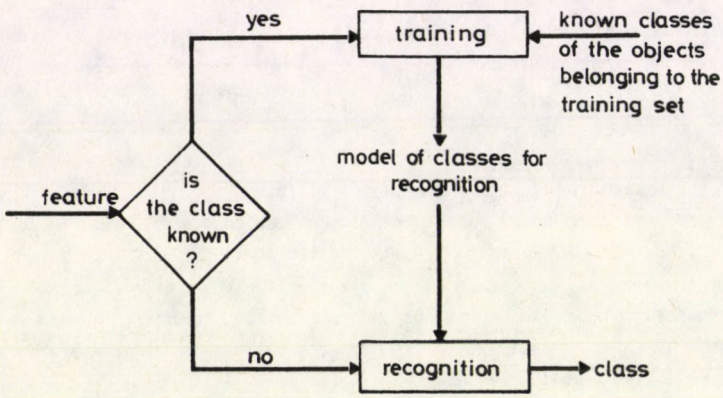

Fig. 1. Steps of supervised classification

IDENTIFICATION OF CONCRETE ADDITIVES

Differences among supervised controlled classification methods are based on the mathematical models describing the location and separation of the points of objects belonging to the different classes.

The supervised classification method PRIMA

The supervised classification method PRIMA is based on the concept of class distance. The essential of the method is that a separate distance concept, the concept of class distance is assigned to each class on the basis of centre of gravity and inhomogeneity, and classification is carried out on the basis of these distances.

In training the classes are characterized by two parameters, the centre of gravity and inhomogeneity. The average of a given property j in a class k can be calculated simply by the formula

$$\bar{x}_j^k = \frac{\sum_{i=1}^{I_k} x_{ij}^k}{I_k} \quad , \qquad j = 1,\ldots, J, \text{ and } k = 1, \ldots, K,$$

where x_{ij}^k is the jth property of the ith object in class k,

$\bar{x}_j^k$ is the average of property j in class k, and

I_k is the number of objects belonging to class k in the training set.

The centre of gravity of the given class k is the vector formed from the property averages

$$\underline{\bar{x}}^k = \begin{pmatrix} \bar{x}_1^k \\ \cdot \\ \cdot \\ \cdot \\ \bar{x}_j^k \end{pmatrix} , \qquad K = 1,\ldots, K,$$

where $\underline{\bar{x}}^k$ is the centre of gravity for class k.

The spread of the classes in pattern space can be characterized by the inhomogeneity of a property j in class k, s_j^k, is the dispersion of the property

$$s_j^k = \left(\frac{\sum_{i=1}^{I_k} \left(x_{ij}^k - \bar{x}_j^k \right)^2}{I^k - 1} \right)^{1/2} , \qquad \begin{matrix} j = 1,\ldots,I \text{ and} \\ k = 1,\ldots,K. \end{matrix}$$

The inhomogeneity vector of a given class $\underline{S}^k$, is a vector formed from the property inhomogeneities

$$\underline{S}^k = \begin{pmatrix} s_1^k \\ \cdot \\ \cdot \\ \cdot \\ s_j^k \end{pmatrix} , \qquad k = 1,\ldots, K .$$

Many different distance notions can be defined between the points of pattern space. Here, the Euclidean distance is used as a class distance; other distance definitions, however, could also be used. Before a definition of the class distance is given, the concept of a property component of the class distance must be introduced. The jth property component of the class distance with respect to the kth class is

$$d_j^k\left(x_{ij}, \bar{x}_j^k\right) = \frac{1}{s_j^k}\left(x_{ij} - \bar{x}_j^k\right), \qquad \begin{array}{l} i = 1,\ldots,I, \\ j = 1,\ldots,J, \\ k = 1,\ldots,K. \end{array}$$

On the basis of property components, the basic idea of this method, the class distance, can be defined as

$$d^k\left(\bar{x}_i, \bar{x}^k\right) = \left(\frac{1}{J}\sum_{j=1}^{J}\left[d_j^k\left(x_{ij}, \bar{x}_j^k\right)\right]^2\right)^{1/2}, \qquad \begin{array}{l} i = 1,\ldots I, \\ k = 1,\ldots K, \end{array}$$

where $\bar{x}_i$ is the property vector of the ith object, and

$\frac{1}{J}$ is the norm factor.

Classification with the method PRIMA (Fig. 2)

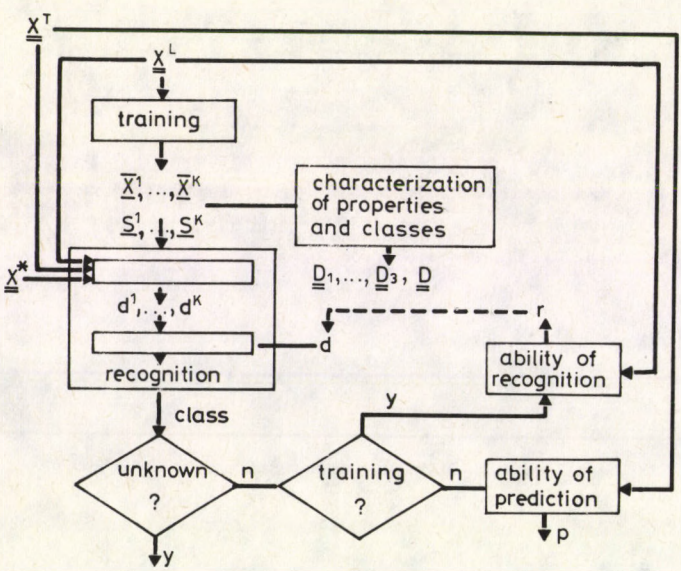

Fig. 2. Algorithm of the PRIMA method

Training with the PRIMA method means the determination of class centres of gravity $\bar{x}_1^k \ldots \bar{x}^k$ and class inhomogeneity vectors $s^1 \ldots s^k$ from the training data matrix X^L. Recognition consists of two steps. First, the class distances of the object X^* (recognition

data matrix) to be recognized, i.e., $d^1(\underline{X}^*,\overline{\underline{X}}^1)$,..., $d^k(\underline{X}^*,\overline{\underline{X}}^k)$ are evaluated. In the second step, the class or classes to which the unknown object belongs must be chosen. There are several possible ways of evaluating the class membership. Classification can be done by assigning the object to the class for which the class distance is minimal, i.e., $\min_k \left\{d^1,\ldots d^k\right\}$. A more practical solution is achieved if the class membership is determined by the condition $d^k(\underline{X}^*,\overline{\underline{X}}^k) \leq d$ which means that object $\underline{X}^*$ belongs to the kth class if the above condition is satisfied, where d is a suitably selected limit value, the so-called class distance threshold.

Classification can be evaluated by the characterization of the distances between the classes and of the classes, with the training set and with the test set.

For solving our problem, the composition of IR spectroscopy and of the supervised classification method PRIMA, the possibility of their joint application had to be created (Fig. 3). By the marking out of specific band locations a feature selection was carried out, that is the feature space was defined.

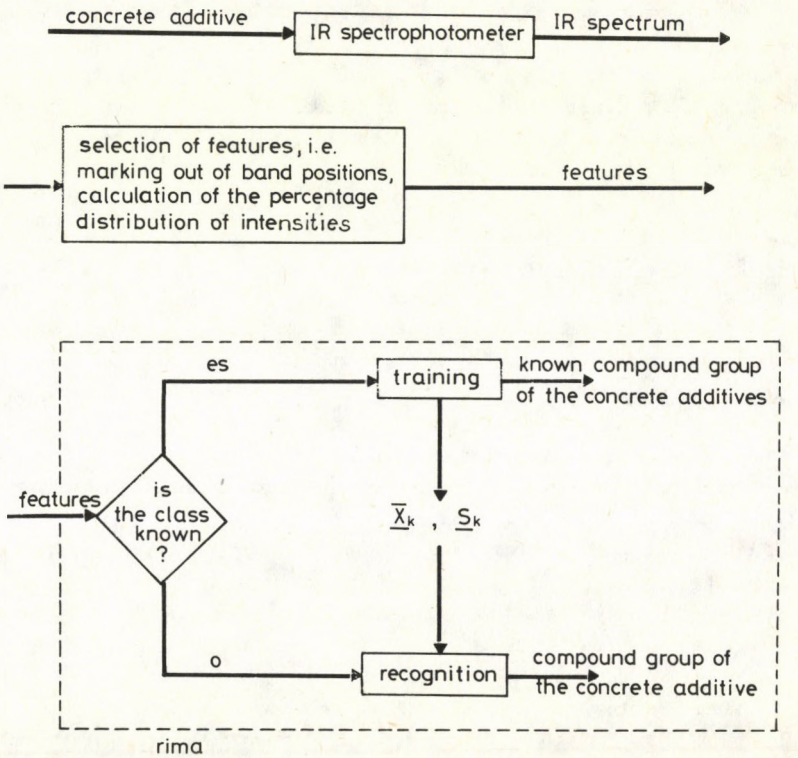

Fig. 3. Application of pattern recognition for the classification of concrete additives

The more important characteristics of concrete additives

Additives are mostly multicomponent systems of undefined composition, influencing the setting and hardening processes of concrete, and the properties of the concrete mix, and hardened concrete. These additives are mainly prepared from industrial wastes and by-pro-

ducts (sulfite liquor, protein hydrolysates, waste liquors of the pharmaceutical industry, etc). Their components are partly high-molecular natural substances, partly salts of long-chain fatty acids,and furthermore sodium carbonate and calcium formate. The composition of synthetic preparations is fixed, however, the composition of their majority is not given in the market. Their qualification requires time and work consuming, expensive concrete-technological investigations; therefore, their replacement by a simpler method would be justified. By the application of the method expensive additives can be replaced by cheaper ones, prepared from by-products and wastes not utilized at present.

Additives are mixed in a concentration of 0.3 to 3% to concrete. Their main types are as follows: plasticizers (Plastificator, P); set-retarders (Fliessmittel, F); set-accelerators (Schnellhärter, S); air-pore formers (Luftporenmittel, L) and sealers (T).

Experimental

Additives in aqueous solution (active substance 10 – 40%) were obtained by evaporation in vacuum at 60 ^{o}C. Their spectra were taken in potassium bromide pellets with a Zeiss Specord 75 IR spectrophotometer.

Solid samples were homogenized with potassium bromide in a vibration mill, then tabletted and their IR spectra recorded.

From the IR spectra taken the characteristic properties of concrete additives were established, which were used in the pattern recognition calculations. For computational work a professional personal computer PROPER 16/A was used.

Experimental results and their evaluation

Classification of concrete additives

Eight kinds of plasticizers, 9 kinds of set-retarders, 3 kinds of set-accelerators, 5 kinds of air-pore formers and 2kinds of sealers were identified on the basis of their IR spectra and of spectral maps. The spectra of the single additives, the interpretation of the absorption bands – using Sohár – Holly – Varsányi's symbol system – are shown in Figs 4 – 13, while the chemical structures of the active substances are displayed in Figs 14 – 15. Table I contains the chemical composition of additives, belonging to the classes established on the basis of spectral bands and of the percentage distribution of the intensities of some selected bands (see later). Though we succeeded in identifying according to the aforegoing on the basis of the IR spectra of the active substances of the 27 additives studied, difficulties arose in distinguishing between some of the additives on the basis of the spectral bands of their scarcely differing active substances.

To facilitate identification, we selected from the spectra intervals or positions, where the absorption of the single additives sharply differs.

After base line correction, absorbance values were determined at these positions, then the distribution of intensity values was calculated as percentage of total absorbance for the marked out bands of the single additives. Selected spectral intervals and positions are shown in Fig. 16 and Table II.

The results of five parallel measurements of each additive were used for the calculations.

In this way, the training set needed for the application of the method PRIMA was prepared.

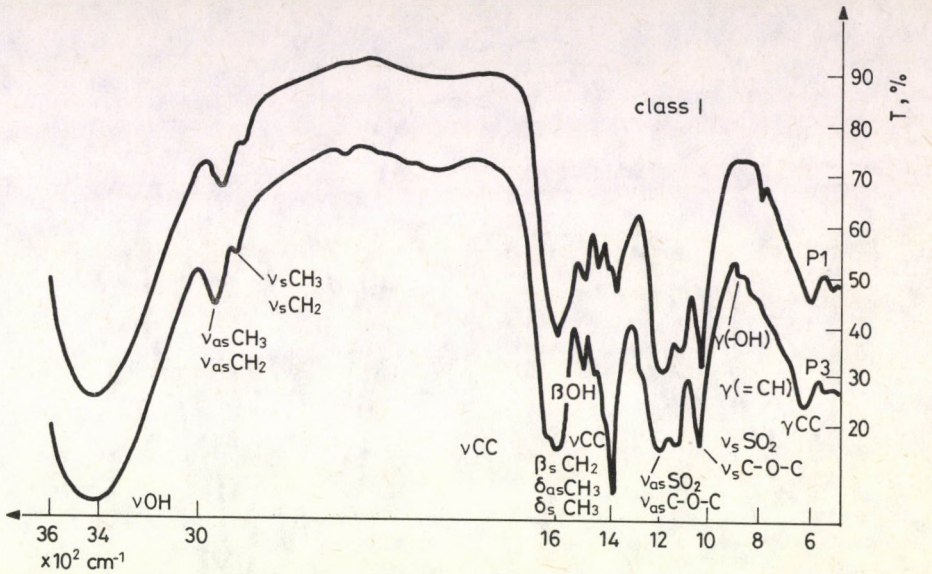

Fig. 4. IR spectra of additives belonging to class I and their interpretation

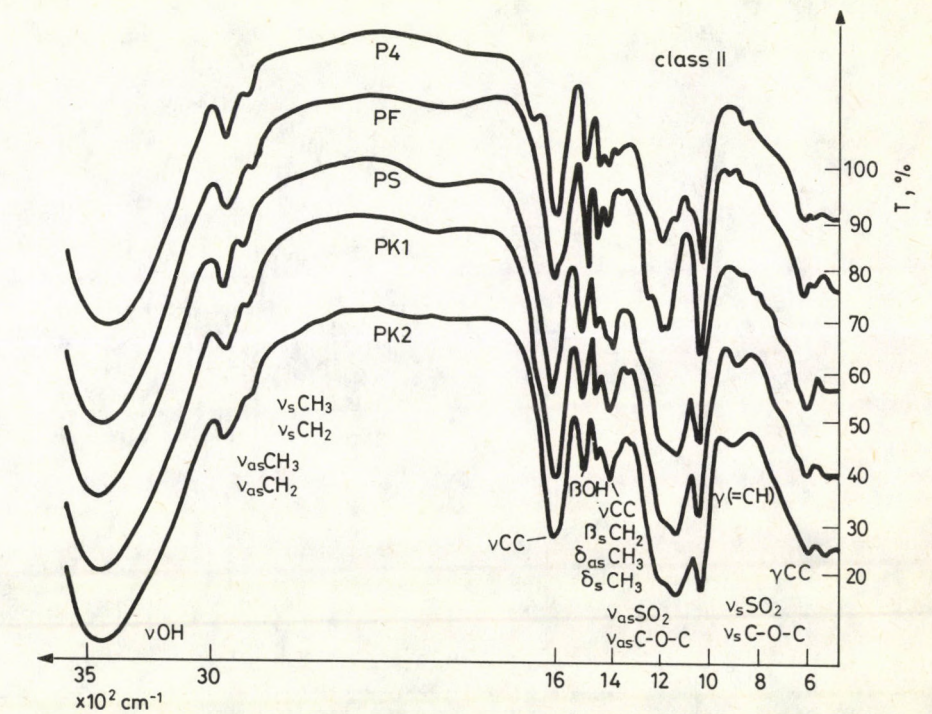

Fig. 5. IR spectra of additives belonging in class II and their interpretation

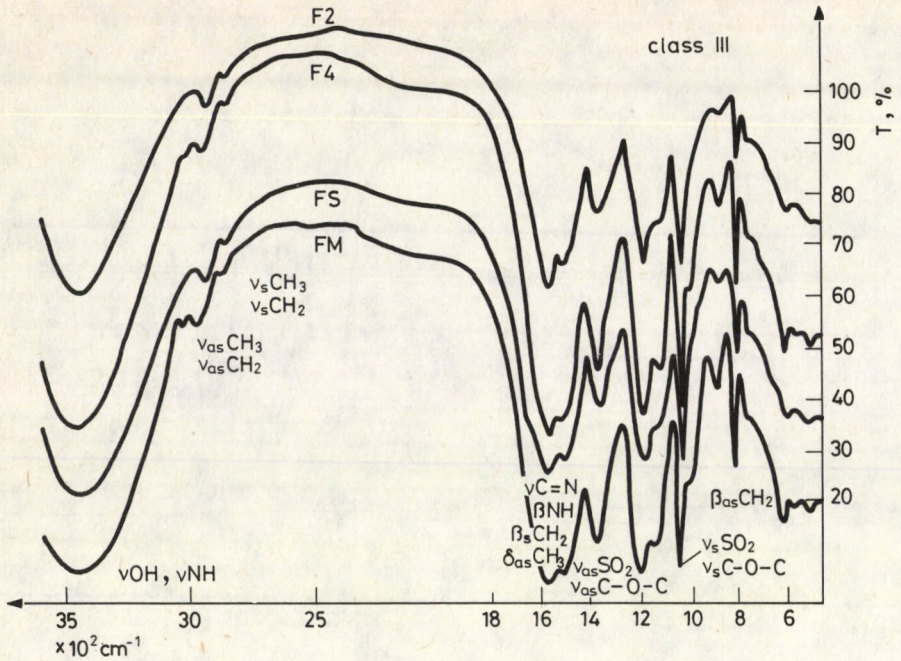

Fig. 6. IR spectra of additives belonging to class III and their interpretation

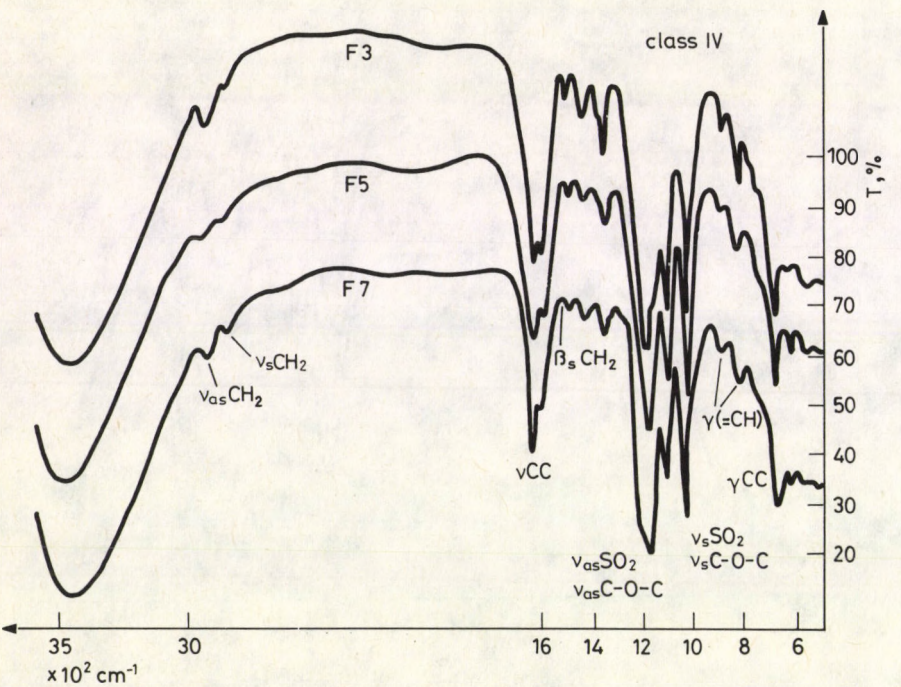

Fig. 7. IR spectra of additives belonging to class IV and their interpretation

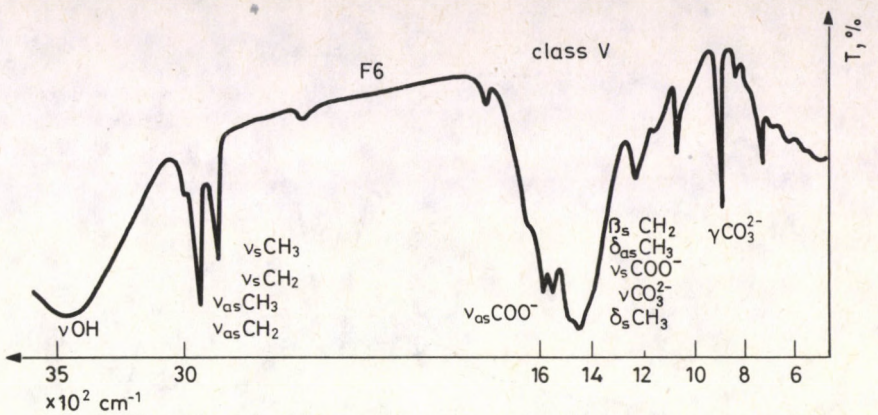

Fig. 8. IR spectra of additives belonging in class V and their interpretation

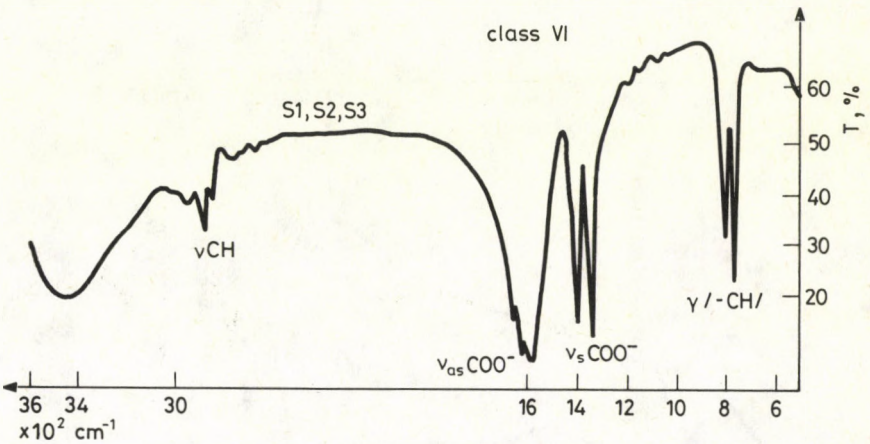

Fig. 9. IR spectra of additives belonging in class VI and their interpretation

With this method the reliability of classification for the training set is 100%. This confirms that the definition of the classes and of the features was correct. Distances between the classes, statistical data, further results of the identification of unknown samples are not given here, standard deviations of intensity values generally vary from 0.1 to 6%.

The classification program thus "trained" was used in the further work for the classification of unkown additives. The preparation of the samples, the recording and evaluation of the spectra were carried out in the same way as in the case of the learning samples.

With the aid of the program, the reliability of the classification of unknown additives was 98.7 to 100%, which proves the very high efficiency of the method.

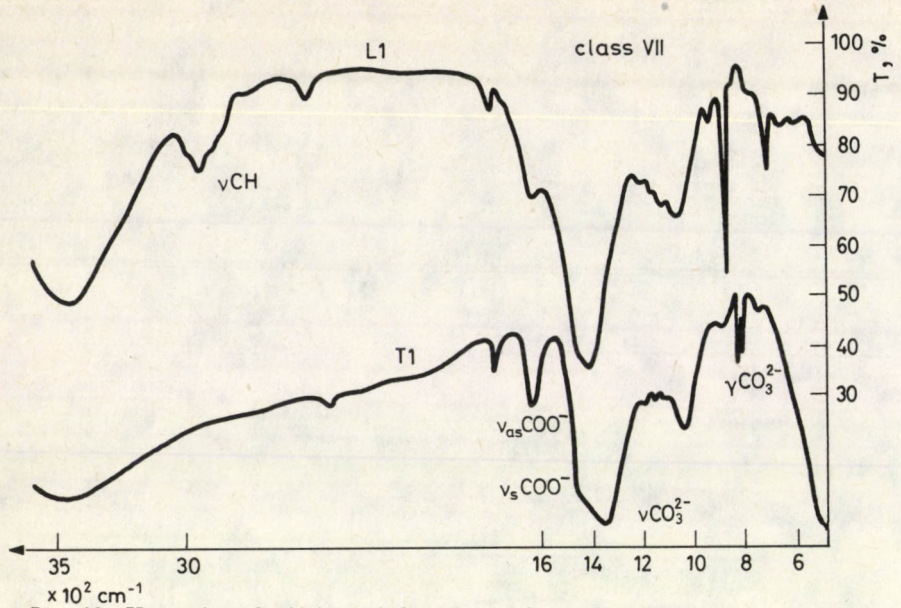

Fig. 10. IR spectra of additives belonging in class VII and their interpretation

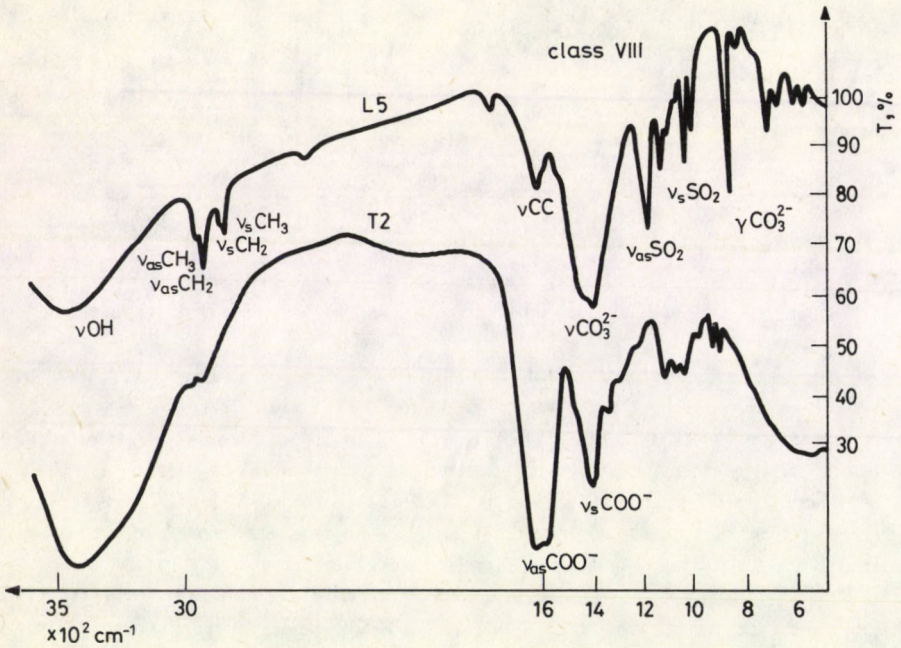

Fig. 11. IR spectra of additives belonging in class VIII and their interpretation

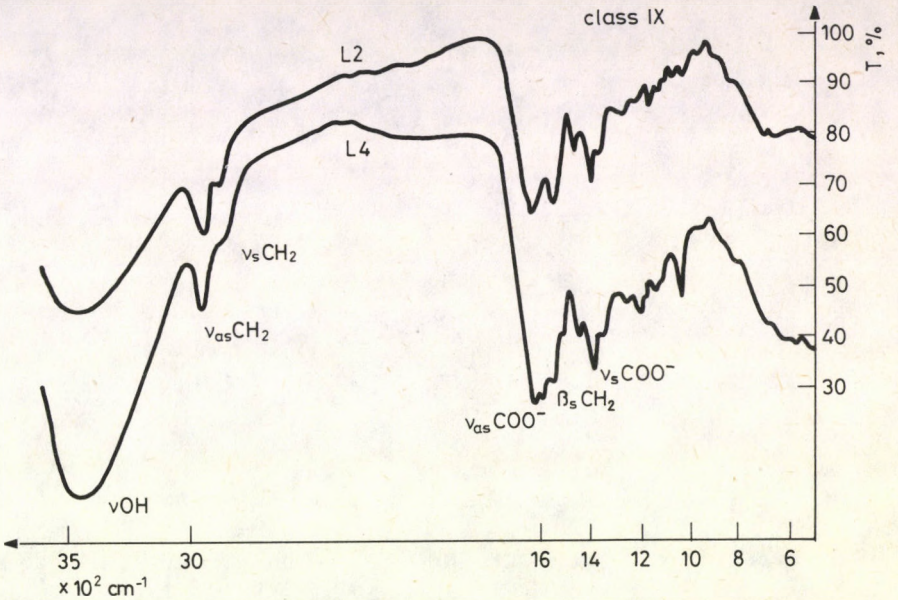

Fig. 12. IR spectra of additives belonging in class IX and their interpretation

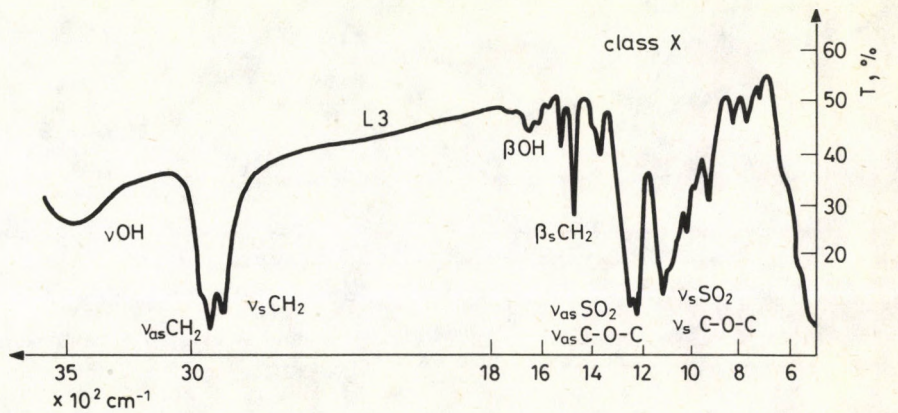

Fig. 13. IR spectra of additives belonging in class X and their interpretation

Identification of concrete additives within the classes

The measures of the effect of concrete additives of identical type (belonging to the same class) differ from one another; therefore, for the exact prediction of their expectable concrete-technological effect identification within the class is also important. Here differences are already so small that the spectroscopist can recognize them only with difficul-

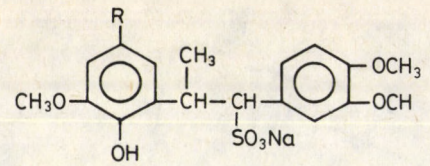

I.

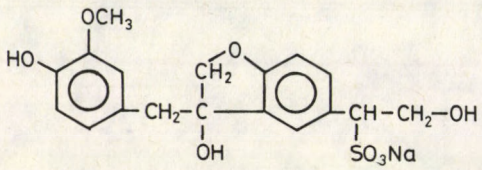

II.

Fig. 14. Presumed chemical structures of sodium lignosulfonate

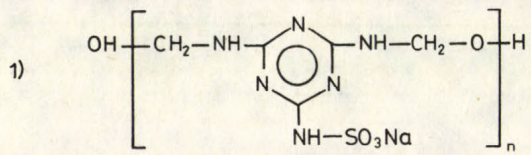

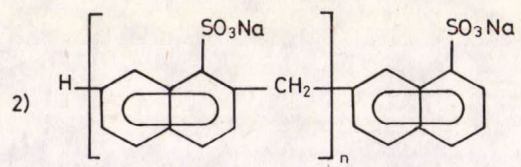

Fig. 15. Chemical structures of the active substances of set-retarder
1 sodium-/melamine-formaldehyde/sulfonate
2 sodium-/naphthalene-formaldehyde/sulfonate

ty, so that for identification within the class by the PRIMA method it became necessary to mark out further new properties in seven out of the ten classes. These properties were the absorbance values of selected absorption bands with respect to one another, and intensity distributions discussed earlier, summarized in Table III.

From the aforesaid data, unknown concrete additives were identified by the PRIMA method with 100% reliability also within the classes. By the identification process within the classes, this work has been accomplished. Its importance consists in distinguishing additives with chemically identical active substance, but of different effect (L1, T1, L5,

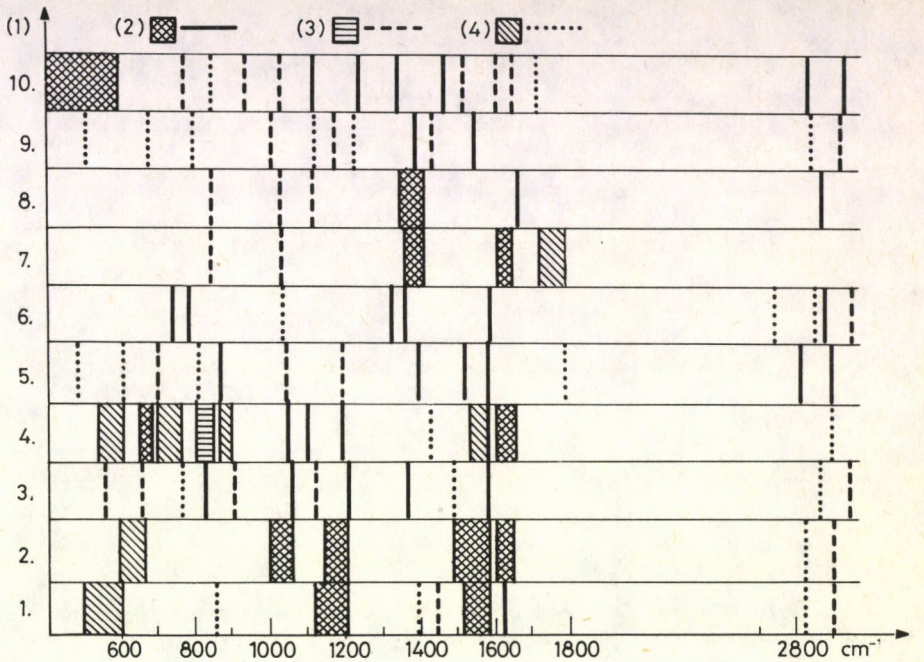

Fig. 16. Spectral intervals and positions selected for the classification of additives
1 -class; 2 -strong; 3 -medium; 4 -weak band

T2), and in the identification of additives of identical type and effect, but differing with respect to the measure of action.

Table I

Summary of the results of infrared spectroscopic analysis, classification of the additives

Marking of sample	Chemical composition	Class series number
P1 P3	sodium lignosulfonate mixture	I
P2 P4 PS PF PK1 PK2	sodium lignosulfonate mixture	II
F1 F2 F4 FS FM	sodium-(melamine-formaldehyde) sulfonate	III

Table I (cont.)

Marking of sample	Chemical composition	Class series number
F3, F5, F7	sodium-(naphthalene-formaldehyde) sulfonate	IV
F6	sodium stearate + sodium carbonate	V
S1, S2, S3	calcium formate	VI
L1, T1	sodium carbonate + salt of fatty acids	VII
L5, T2	sodium carbonate + lignosulfonate	VIII
L2, L4	colophenic acid salt	IX
L3	sodium (lauryl-ethyleneglycol ether) sulfate	X

Table II

Characteristic absorption intervals and positions selected for the application of the PRIMA method

Absorption interval position	Characterization
From 2900 to 2950 cm^{-1}	Agents L1 and T1 do not absorb, as their main mass consists of sodium carbonate. The members of the single classes absorb differently, because the lengths of their aliphatic carbon chains are different
From 2870 to 2850 cm^{-1}	The same as above is valid
From 1650 to 1600 cm^{-1}	The colophenic acid salts (L2, L4) do not exhibit absorption
From 1550 to 1500 cm^{-1}	The S samples, the L2, T1, the L5, T2 additives do not absorb, while in the case of the other additives bands of various intensities are displayed
From 1500 to 1450 cm^{-1}	The IR spectra of samples forming classes IV, V, VI, VII VIII show no sharp absorption bands
From 1420 to 1400 cm^{-1}	Plasticizers and set-retarders of sodium(melamine-formaldehyde) sulfonate type give an absorption minimum, while additives marked with L1, T1, L5, T2, L2, L4 exhibit absorption bands of high intensity. This can be attributed to the high carbonate content and to the $\nu_s CO_2^-$ stretching vibration of fatty acid salts
At 1350 cm^{-1}	At this position plasticizers and set-retarders can be well distinguished from the other additives
At 1250 cm^{-1}	The air-pore former L3 separates sharply, because the other additives do not exhibit absorption at this position

Table II (cont.)

Absorption interval position	Characterization
At 1200 cm^{-1}	Set-accelerators and the additives marked with L1, T1, L5, T2 can be separated, as they do not absorb at this position
At 1120 cm^{-1}	Additives F6, S1, S2, S3, L1, T1 can be separated from the other additives, because they have no considerable absorption
At 1050 cm^{-1}	Additives of sulphonate type separate sharply because of their characteristic band
From 900 to 920 cm^{-1}	Plasticizers and set-accelerators can be separated, because they exhibit no absorption
From 850 to 800 cm^{-1}	Sodium(melamine-formaldehyde) sulfonates give a sharp absorption maximum, that can be assigned to the in-plane skeletal bending vibration of the triazine ring of the melamine part
At 720 cm^{-1}	The set-retarder F6 sharply separates from the other classes, the β_{as} CH_2 vibration appearing in this position is characteristic of the long aliphatic part of the additive
From 650 to 600 cm^{-1}	Additives containing naphthalene ring can be well distinguished on the basis of the out-of-plane bending vibration band of the ring

Table III

Properties selected for identification within the class

Class 1 (P1, P3)

Percentage distribution of the intensities of bands appearing in the regions 1550–1500 cm^{-1}, 1500–1450 cm^{-1}, 1420–1400 cm^{-1}, 1350 cm^{-1}, 1200 cm^{-1}, 850–800 cm^{-1}, and the ratios

$$\frac{A_{1550\text{-}1500\,cm^{-1}}}{A_{1500\text{-}1420\,cm^{-1}}} \quad \text{and} \quad \frac{A_{1420\text{-}1400\,cm^{-1}}}{A_{1350\,cm^{-1}}}$$

Class 2 (P2, P4, PF, PS, PK1, PK2)

Percentage distribution of the intensities of bands appearing in the wavenumber intervals 1730 cm^{-1}, 900–920 cm^{-1}, 850–800 cm^{-1}, and the ratios

$$\frac{A_{1280\,cm^{-1}}}{A_{1200\,cm^{-1}}}, \quad \frac{A_{650\,cm^{-1}}}{A_{520\,cm^{-1}}}, \quad \frac{A_{1500\text{-}1500\,cm^{-1}}}{A_{1420\text{-}1400\,cm^{-1}}},$$

$$\frac{A_{1500\text{-}1450\,cm^{-1}}}{A_{1420\text{-}1400\,cm^{-1}}}, \quad \frac{A_{1500\text{-}1450\,cm^{-1}}}{A_{1500\text{-}1450\,cm^{-1}}}$$

Table III (cont.)

Class 3 (F1, F2, F4, FM, FS)

Percentage distribution of the intensity of bands appearing in the wavenumber regions 1120 cm^{-1}, 980 cm^{-1} (inflection), 900–920 cm^{-1}, 850–800 cm^{-1}, 650–600 cm^{-1}, 500 cm^{-1} and the ratio $\frac{A_{1500-1500\ cm^{-1}}}{A_{1500-1450^{cm^{-1}}}}$

Class 4 (F3, F5, F7)

Percentage distribution of intensities calculated at wavenumbers 1650–1600 cm^{-1}, 1600 cm^{-1}, 750 cm^{-1}, 650–600 cm^{-1}, 550 cm^{-1}, and the ratios

$$\frac{A_{1650\text{-}1600^{cm^{-1}}}}{A_{1600^{cm^{-1}}}} \quad , \qquad \frac{A_{1350^{cm^{-1}}}}{A_{1380^{cm^{-1}}}} \quad .$$

Class 7 (L1, T1)

Percentage distribution of the intensities of bands appearing in the wavenumber regions 2900–2950 cm^{-1}, 2870–2850 cm^{-1}, 1500–1500 cm^{-1}, 900–920 cm^{-1}, 650–600 cm^{-1}, and the ratio

$$\frac{A_{1550\text{-}1500^{cm^{-1}}}}{A_{1500\text{-}1450^{cm^{-1}}}} \quad .$$

Class 8 (L5, T2)

Percentage distribution of the intensities of bands appearing at wavelength regions 2900–2950 cm^{-1}, 2870–2850 cm^{-1}, 1650–1600 cm^{-1}, 1500–1450 cm^{-1}, 1500–1450 cm^{-1}, 1200 cm^{-1}, 900–920 cm^{-1}, and the ratio

$$\frac{A_{1120^{cm^{-1}}}}{A_{1050^{cm^{-1}}}} \quad .$$

Class 9 (L2, L4)

The ratios

$$\frac{A_{1650\text{-}1600^{cm^{-1}}}}{A_{1550\text{-}1500^{cm^{-1}}}} \quad , \qquad \frac{A_{1250^{cm^{-1}}}}{A_{1200^{cm^{-1}}}} \quad , \qquad \frac{A_{1200^{cm^{-1}}}}{A_{1120^{cm^{-1}}}} \quad , \qquad \frac{A_{1050^{cm^{-1}}}}{A_{900\text{-}920^{cm^{-1}}}} \quad .$$

References

1. K. Kiss-Erőss, G. Meszlényi, D. Valtinyi and T. Meisel, Proceedings of the 28th Congress of Hungarian Spectral Analysis, Eger, June 25–28, 1985, pp. 293–300.
2. K. Erőss-Kiss, G. Meszlényi, D. Valtinyi and T. Meisel, Periodica Polytechnica, 30, 185, 1986.

3. T. Gál, L. Leisztner, Gy. Pokol, K. Kiss-Erőss, Magy. Kém. Folyóirat, 92, 406, 1986.
4. Gy. Szakálas, Thesis, Institute for General and Analytical Chemistry, Technical University of Budapest, Budapest, 1986.
5. G. Meszlényi, Dissertation for the Degree of Dr. Eng., Technical University of Budapest, Budapest, 1987.
6. K. Varmuza, Pattern Recognition in Chemistry, Springer Verlag, Berlin, etc. 1980.
7. I. Isaszegi-Vass, Magy. Kémikusok Lapja, 35, 188, 1980.
8. I. Juricskay, G. Veress, Anal. Chim. Acta 171, 61, 1985.

Acta Physica Hungarica 63(1–2), pp. 137–140 (1988)

INFRARED SPECTROSCOPIC INVESTIGATION OF PROPYLENE OXIDE – ETHYLENE OXIDE POLYMERS*

G. MESZLÉNYI[1], M. SIPOS[2], É. JUHÁSZ[1], M. ERŐSS-LELKES[1] and GY. POSZMIK[1]
[1]Research and Development Company for the Organic Chemical Industry
1428 Budapest, POB 41, Hungary
[2]National Institute for Hospital and Medical Engineering
1525 Budapest, POB 32, Hungary

(Received 15 September 1987)

The surfactant properties of the title polymers depend on the total and relative number of the propylene oxide (PO) and ethylene oxide (EO) groups.

These numbers were determined by IR spectroscopy on the basis of the symmetrical bending vibration of the methyl group and the wagging vibration of the methylene group applying the Beer – Lambert law.

Some interesting absorption characteristics of the polymers have been revealed.

Introduction

Propylene oxide – ethylene oxide copolymers (PO/EO copolymers) have, similarly to other surfactants, two main parts; a hydrophobic moiety (here the polypropyleneglycol chain) and the hydrophilic part (here the polyethyleneglycol) (Fig. 1).

$$HO(CH_2\text{-}CH_2\text{-}O)_x(CH_2\text{-}\underset{\displaystyle CH_3}{\underset{|}{CH}}\text{-}O)_n(CH_2\text{-}CH_2\text{-}O)_y\,H$$

$x+y$ = numbers of the EO groups
n = numbers of the PO groups

Fig. 1. General formula of PO/EO copolymers

The absolute and relative quantity of PO and EO groups determine the applicabilities of the members of this group of surfactants. Details are given in Ref. [1].

Formerly conventional analytical methods have been used for the determination of the PO and EO units in PO/EO copolymers [2], [3]. Kotzschmar applied oxidation and subsequent gravimetric and titrimetric determination [3]. His method is accurate but time-consuming and laborious.

Among the instrumental analytical methods pyrolysis gas chromatography was used earlier for solving the task [4].

Recently infrared spectroscopy has been introduced for this purpose. Spanish researchers determined the EO content of p-nonylphenol-polyethylene-glycol ether by estimating the intensity changes of certain bands in the IR spectrum [5].

---

*Presented at the 3rd Hungarian Conference on Molecular Spectroscopy, Debrecen, Hungary, 24–28 August 1987

In our work IR spectroscopy proved to be suitable for determining the PO/EO ratio and, with the knowledge of the molecular mass of a given substance, the absolute number of PO or EO units can be calculated.

Experimental

A PERKIN–ELMER 783 IR spectrophotometer, employing 1.0 mm calcium fluoride sealed liquid cells, and spectroscopic grade tetrachloromethane as solvent were used. For our examinations eight samples of PO/EO copolymers whose chemical compositions were known, were available (see Table I). The concentrations of the prepared solutions were 10 mg/cm^3. The accuracy of the weighing was 0.1 mg. The spectra were recorded between 1600 – 1300 cm^{-1} with compensation of the solvent. The absorbances were calculated by the base-line method.

Table I

Summary of the measured results

$\frac{PO}{EO}$	$\frac{A_{1375}}{A_{1350}}$	PO	EO	M	$A^{1\%}_{1cm}(1375)$	$A^{1\%}_{1cm}(1350)$	$\varepsilon(1375)$	$\varepsilon(1350)$
0.19	0.70	16.4	86.4	4700	1.70	2.44	800	1160
0.32	1.01	35.3	108.7	6600	2.35	2.32	1550	1585
0.76	1.86	16.4	21.6	1900	3.79	2.06	720	388
1.14	2.05	20.7	18.2	2000	4.22	2.04	844	412
1.77	2.53	20.7	11.7	1714	4.93	1.95	845	334
3.04	3.05	20.7	6.8	1500	5.70	1.87	855	281
6.83	3.53	69.0	10.1	4444	6.22	1.78	2862	791
6.86	3.62	30.2	4.4	1944	6.44	1.76	1209	342

Observation of the two IR spectra shown in Fig. 2 reveals why the absorptions of the bands at 1375 cm^{-1} and 1350 cm^{-1} were selected. The two peaks result from the symmetrical bending vibration of the methyl group (1375 cm^{-1}: $\delta_s CH_3$) and the wagging vibration of methylene group (1350 cm^{-1}: $\gamma_s CH_2$).

The δ_s and γ_s denotations correspond to the symbol system introduced by Sohár, Holly and Varsányi [6]. The intensity and the absorptional position of the γ_s CH_2 vibrational band (1350 cm^{-1}) can be explained by the –I effect of the neighbouring oxygen atoms.

Table I presents the PO/EO and A_{1375}/A_{1350} ratios and the determined absorptivities as well as molar absorptivities at 1375 and 1350 cm^{-1}.

Results and discussion

Plotting the determined A_{1375}/A_{1350} against the PO/EO ratios a saturation curve is obtained (Fig. 3).

The shape of the curve can be explained by γ_s CH_2 band that characterizes both the polypropyleneglycol (PPG) and the polyethyleneglycol (PEG) units. The saturation value probably indicates the A_{1375}/A_{1350} rate for pure PPG, which is 3.9 – 4.0 based on our measurements.

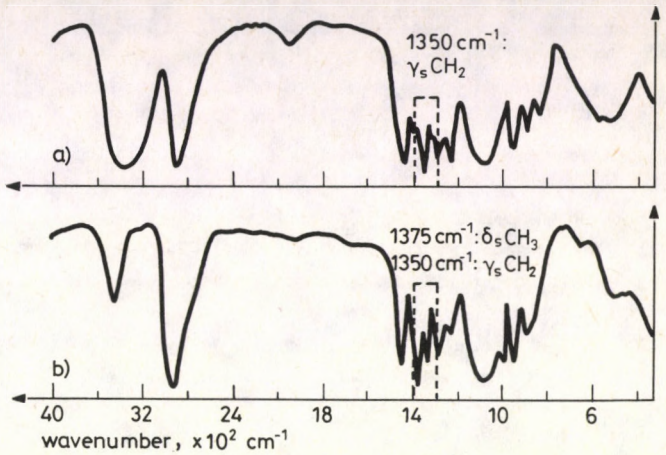

Fig. 2. The spectra of a polyethyleneglycol (a) and a PO/EO copolymer (b)

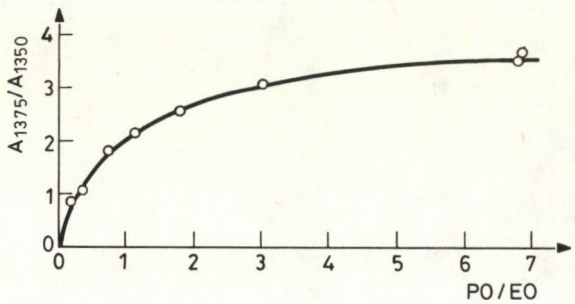

Fig. 3. Plot of A_{1375}/A_{1350} vs PO/EO

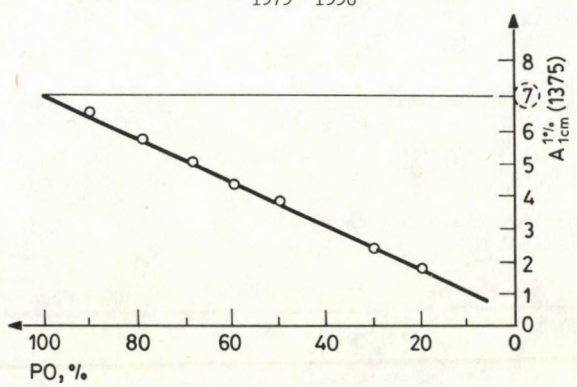

Fig. 4. Plot of $A^{1\%}_{1cm}$ (1375) vs PO(%)

The absorptivity at 1375 cm^{-1} for pure PPG can be calculated by means of the Beer – Lambert law. Fig. 4 depicts $A^{1\%}_{1cm}(1375)$ against the PO content in per cent.

As shown in Fig. 4 the absorptivity at 1375 cm^{-1} is a linear function of the PO content. Extrapolating the function to 100% PPG content we can estimate the value of $A^{1\%}_{1cm}(1375)$ in pure PPG. This value is 7.0.

For the determination of the absolute number of PO and EO units the knowledge of the molecular masses is necessary.

Determination of the molecular masses by measuring the OH stretching vibration at 3490 cm^{-1} is not possible owing to inherent association; at 3490 cm^{-1} the fundamental law is not valid. That is why we worked out a conventional analytical method based on the hydroxyl number determination to solve this problem.

The described relationships are well utilizable in practice. Our spectroscopic method is simple, requires no tedious sample manipulation; it is a useful tool in the analysis of tensides.

References

1. É. Juhász and M. Erős-Lelkes, Felületaktív anyagok zsebkönyve, Műszaki Könyvkiadó, Budapest, 1979. (Manual of Surfactants, in Hungarian)
2. H. König, Neuere Methoden zur Analyse von Tensiden, Springer-Verlag, Berlin, 1971.
3. A. Kotzschmar, Z. Anal. Chem., 183, 30, 1961.
4. E.W. Neumann and H.G. Nadeau, J. Anal. Chem., 35, 1454, 1963.
5. M. De la Gurdia, J.L. Carrion and J. Medina, Analyst, 109, 457, 1984.
6. P. Sohár, S. Holly and Gy. Varsányi, Kémiai Közlemények, 31, 197, 1969. (in Hungarian)

Acta Physica Hungarica 63(1–2), pp. 141–142 (1988)

A COMPUTER DATA ACQUISITION AND PROCESSING SYSTEM FOR RAMAN SPECTROSCOPY*

J. VARGA, G. JALSOVSZKY and S. HOLLY
Central Research Institute for Chemistry
Hungarian Academy of Sciences
Budapest, Hungary

(Received 15 September 1987)

A Varian Cary-82 laser Raman spectrometer was connected to a Nicolet 7199 FT-IR system. The Raman data acquisition system is based on a Commodore-128 microcomputer system. The software consists of two parts.The first one controls the data acquisition, the second one is a spectral data processing program. The new system has opened a series of new possibilities in vibrational spectroscopic research.

The increasing popularity and widening possibilities of the digital processing of spectral data have created a demand of connecting existing spectrometers with analogue data recording to computers. This was the aim of connecting our Varian Cary-82 laser Raman spectrometer to the Nicolet 1180 computer of a Nicolet 7199 FT-IR system [1]. The resulting system has all the benefits of the computer data acquisition and processing of Raman spectra [2], with the only disadvantage that for the time of Raman data acquisition, which may be as long as several hours, the 1180 computer is fully in use, and thus it cannot be used during this time for the control or processing of FT-IR measurements. Therefore, our new system has been developed in order to save time on the 1180 computer.

The new Raman data acquisition system is based on a Commodore-128, an 8-bit microcomputer. As peripherals, a Commodore 1571 floppy disk drive, a Commodore 1901 colour graphic display and an MPS 803 matrix printer are connected.

The microcomputer communicates with the Nicolet 1180 via a serial RS 232 C channel. The main peripherals of the latter computer are a Diablo 44 B hard disk drive and a Zeta digital plotter.

The spectrometer is connected to the microcomputer through two electronic units. The first one is a shaft encoder attached to the wavenumber drive of the Cary-82 spectrometer. Here, a disk with black and white sectors is fastened to a shaft which drives the mechanical wavenumber display wheels of the spectrometer, which gives, by means of opto-electric transducers, square pulses of a frequency proportional to the scan speed of the spectrometer. The second electronic unit is a counter interface. This counts, using a 24-bit synchronous counter, the amplified and shaped pulses arriving from the detector of the spectrometer (a photoelectron multiplier). The counter is controlled and the data are latched by the microcomputer through an INTEL 8255 A Programmable Parallel Peripheral Interface Processor.

The software of the microcomputer was written mostly in BASIC, but some functions

---

*Presented at the 3rd Hungarian Conference on Molecular Spectroscopy, Debrecen, Hungary, 24–28 August 1987

which were too slow or hard to perform in BASIC, were solved by means of ASSEMBLER routines written specially for this purpose.

According to basic functions, the software has been divided into two programs. The first one controls primarily data acquisition, which means mainly the control of the interface unit. Since the CPU time of the data input is relatively short (the input of 3 bytes at intervals of 0.2 to 10s), the peripheral interface processor requests an interrupt from the microcomputer when it is ready to send data. Then the CPU interrupts the execution of the running program and jumps to an interrupt service routine. The data are read by this routine. In the time between the interrupts the computer deals with display functions. In this manner, the progress of measurement can be seen continuously on the colour graphic display (in an arbitrary intensity and wavenumber scale, which may be changed interactively according to the intensity data of the spectrum).

Data acquisition stops automatically at a preset end frequency, it may be terminated, however, manually at any point. Thereafter, the spectrum and the main parameters of the measurement may be stored in a disk file with a name of up to 12 characters.

When developing the second program, for spectral data processing, it was taken into account that the Commodore microcomputer is able to communicate with the Nicolet 1180 computer through a serial RS 232 C channel, and that the software of the 1180 includes fast and user-friendly data processing routines. For this reason, and due to the relatively low speed of the Commodore, only the most important operations of data processing have been programmed on the Commodore microcomputer. These operations include, of course, the display of spectra and the determination of the frequency and intensity data of Raman bands by means of a graphic cursor. An important function of the program is spectrum accumulation, which can be used to improve the signal to noise ratio of the spectra by averaging, when other means for this (e.g. higher laser excitation energy) are not available.

The program also enables base line correction to be performed. This can be used to suppress fluorescence background which often hinders the evaluation of Raman spectra.

There are further data processing options provided by the software of Nicolet 1180:

By means of subtracting two spectra, it is possible to investigate the spectra of solutions in regions where the solvent has Raman band(s). This is equivalent to measurements on a "double beam" Raman spectrometer.

Curve analysis programs make it possible to determine the individual peak maxima and intensities of the components of overlapping band systems.

On the Zeta digital plotter connected to the Nicolet 1180 computer, high quality, optionally smoothed hard copies of the spectrum can be prepared, and any part of the spectrum can be expanded along either axes. It is possible to plot the infrared and Raman spectra of a compound in the same diagram, which is an aid in the assignment of vibrational bands to the normal modes of the molecule.

We feel that our computer controlled Raman data acquisition and processing system has opened new possibilities in theoretical and applied vibrational spectroscopic research.

References

1. G. Jalsovszky, S. Holly and G. Keresztury, J. Mol. Struct., 115, 275, 1984.
2. J.R. Downey Jr. and G.J. Janz, in Advances in Infrared and Raman Spectroscopy (R.J.H. Clark and R.E. Hester, ed.), Vol. 1, 1–34, Heyden and Son, London – New York – Rheine, 1975.

Acta Physica Hungarica 63(1–2), pp. 143–149 (1988)

A NEW TREATEMENT OF THE RING-PUCKERING MOTIONS BY PERIODIC FUNCTIONS IN THE HAMILTONIAN*

L. SZTRAKA
Department of Physical Chemistry, Technical University
1521 Budapest, Hungary

(Received 15 September 1987)

A method is outlined for treating the nonperiodic large amplitude molecular motions by a Hamiltonian which contains only periodic functions. The examples investigated for testing the theory are two pseudo-four-membered ring molecules, cyclopentene (CP) and 2,5-dihydrofuran (DHF) which are doing ring-puckering motions. Our calculations give better results for these two molecules than Malloy's ones [1].

Introduction

The general form of the zero order, one dimensional Hamiltonian of a large amplitude motion is:

$$\hat{H} = -\frac{d}{d\tau}\mu_{(\tau)}\frac{d}{d\tau} + V_{(\tau)} \quad , \tag{1}$$

where τ is the coordinate, $\mu_{(\tau)}$ is the inverse reduced mass or inertial moment and $V_{(\tau)}$ is the potential function. Eq. (1) does not contain the effects of the pure rotation, the vibrations and the Coriolis couplings, i.e. J and K equal zero and all vibrations are in the ground state [2].

In the case of nonperiodic motions both $\mu_{(\tau)}$ and $V_{(\tau)}$ have been given in the form of a finite Taylor series. In some cases it is useful to complete this type of potential function [3] by a Gauss hump of form [4]:

$$a \exp(-c\,\tau^2) \quad . \tag{2}$$

The elements of the energy matrix have been set up in harmonic oscillator representation. These elements are functions of $\mu_{(\tau)}$ and $V_{(\tau)}$ and are described by different and complicated formulae.

In the present paper a new method is suggested for describing the ring-puckering motions in which periodic functions are used for $\mu_{(\tau)}$ and $V_{(\tau)}$ instead of the nonperiodic ones. The finite Fourier series approach very well both $\mu_{(\tau)}$ and $V_{(\tau)}$ in an appropriate $\pm\tau_{max}$ region, where $\tau_{max}<\pi$. The Fourier coefficients of $\mu_{(\tau)}$ depend on the geometry and the atomic masses. The ones of $V_{(\tau)}$ depend only on the constants in the original expression of the expanded potential. Consequently, the expressions of the elements in the energy

*Presented at the 3rd Hungarian Conference on Molecular Spectroscopy, Debrecen, Hungary, 24–28 August 1987

matrix became independent of the form of the chosen potential. This is the main advantage of our method.

We have obtained good experience about this method in the case of the inversion of methylamine [5].

The Hill matrix of ring-puckering

The present paper considers only symmetric problems when $\mu_{(\tau)} = \mu_{(-\tau)}$ and $V_{(\tau)} = V_{(-\tau)}$. Fourier series of the form

$$\mu_{(\tau)} = \sum_{m=0}^{M} \mu_m \cos m\tau \tag{3}$$

and

$$V_{(\tau)} = V_0 + \frac{1}{2} \sum_{l=1}^{L} V_l (1 - \cos l\tau) \tag{4}$$

have been applied in which both μ_m and V_l depend on the constants in the expanded potential. Thus, the energy matrix for the computation of the eigensystem of the Hamiltonian in Eq. (1) can be set up in the representation of the cos and sine functions. This is the so-called Hill matrix. In this representation the energy matrix is separated into two blocks corresponding to the even and the odd energy levels. The elements of the two blocks are [6,7] :

$$H^e_{n,0} = -\frac{1}{2\sqrt{2}} \sum_l V_l \, \delta_{n,l} \, , \tag{5}$$

$$H^e_{n,n'} = \left\{ \frac{1}{2} \mu_0 n^2 + V_0 + \frac{1}{2} \sum_l V_l \right\} \delta_{n,n'} + \frac{1}{4} nn' \sum_m \mu_m (\delta_{|n'-n|,m} - \delta_{n'+n,m}) - \frac{1}{4} \sum_l V_l \, (\delta_{n'-n|,l} + \delta_{n'+n,l}) \, , \tag{6}$$

$$H^0_{n,n'} = \frac{1}{2} \mu_0 n^2 + V_0 + \frac{1}{2} \sum_l V_l \} \delta_{n,n'} + \frac{1}{4} nn' \sum_m \mu_m (\delta_{|n'-n|,m} + \delta_{n'+n,m}) - \frac{1}{4} \sum_l V_l \, (\delta_{|n'-n|,l} - \delta_{n'+n,l}) \, . \tag{7}$$

Application of the method for the ring-puckering of the molecules CP and DHF

For testing the above theory the ring-puckering of some pseudo-four-membered ring molecules was chosen. The molecules investigated are cyclopentene (CP) and 2,5-dihydrofuran (DHF). The following expression can be developed for the inverse reduced inertial moment:

$$\mu_{(\tau)} = \{ I_{\tau\tau} \, (1 - I^2_{y\tau} / I_{yy} I_{\tau\tau}) \}^{-1} \, , \tag{8}$$

where

$$I_{yy} = \sum_i m_i \, (x_i^2 + z_i^2) \, , \tag{9}$$

$$I_{y\tau} = - \sum_i m_i \left\{ x_i \frac{\partial z}{\partial \tau} i - z_i \frac{\partial x}{\partial \tau} i \right\} \tag{10}$$

and

$$I_{\tau\tau} = \sum_i m_i \left\{ \left(\frac{\partial x}{\partial \tau} i\right)^2 + \left(\frac{\partial y}{\partial \tau} i\right)^2 + \left(\frac{\partial z}{\partial \tau} i\right)^2 \right\} . \tag{11}$$

A similar relation as Eq. (8) was derived for the inverse reduced mass by Ueda and Shimanouchi [8] in another way. The formulae (8) – (11) are given in an (x,y,z) coordinate system with an origin fixed to the mass centre of the molecule.

The coordinates of the atoms in CP are collected in Table I. They are given in another molecule fixed system (ξ, η, ζ). The coordinates x_i, y_i and z_i of the i-th atom can be obtained as ($\xi_i - \xi_0$), etc., where the zero index denotes the coordinates of the mass centre.

Table I

Atomic coordinates of cyclopentene in the (ξ, η, ζ) axis system[a]

$$\xi_0 = \{m_C A\sin\tau + 2m_H [A + r_{16}\cos(\delta/2)\sin\tau - 4m_H r_{28}\cos(\delta/2)\sin\vartheta\}/M$$

$$\eta_0 = 0$$

$$\zeta_0 = \{m_C A\cos\tau - 2m_H C + 2m_H [A + r_{16}\cos(\delta/2)\cos\tau + 4m_H r_{28}\cos(\delta/2)\cos\vartheta\sin\varphi - 2m_H [C + r_{310}\sin(\gamma/2)]\}/M$$

$$\xi_1 = A\sin\tau$$

$$\eta_1 = 0$$

$$\zeta_1 = A\cos\tau$$

$$\xi_2 = 0$$

$$\eta_2 = B$$

$$\zeta_2 = 0$$

$$\xi_3 = 0$$

$$\eta_3 = r_{34}/2$$

$$\zeta_3 = -C$$

$$\xi_4 = 0$$

$$\eta_4 = -r_{34}/2$$

$$\zeta_4 = -C$$

$$\xi_5 = 0$$

$$\eta_5 = -B$$

$$\zeta_5 = 0$$

$$\xi_6 = A\sin\tau + r_{16}[\cos(\delta/2)\sin\tau + \sin(\delta/2)\cos\tau]$$

$$\eta_6 = 0$$

$$\zeta_6 = A\cos\tau + r_{16}[\cos(\delta/2)\cos\tau - \sin(\delta/2)\sin\tau]$$

$$\xi_7 = A\sin\tau + r_{16}[\cos(\delta/2)\sin\tau - \sin(\delta/2)\cos\tau]$$

$$\eta_7 = 0$$

$$\zeta_7 = A\cos\tau + r_{16}[\cos(\delta/2)\cos\tau + \sin(\delta/2)\sin\tau]$$

$$\xi_8 = r_{28}[-\cos(\delta/2)\sin\vartheta + \sin(\delta/2)\cos\varkappa]$$

Table I (cont.)

$$\eta_8 = B + r_{28}\,[\cos(\delta/2)\cos\vartheta\cos\varphi + \sin(\delta/2)\sin\chi\sin\varphi]$$

$$\zeta_8 = r_{28}\,[\cos(\delta/2)\cos\vartheta\sin\varphi - \sin(\delta/2)\sin\chi\cos\varphi]$$

$$\xi_9 = r_{28}\,[-\cos(\delta/2)\sin\vartheta - \sin(\delta/2)\cos\chi]$$

$$\eta_9 = B + r_{28}\,[\cos(\delta/2)\cos\vartheta\cos\varphi - \sin(\delta/2)\sin\chi\sin\varphi]$$

$$\zeta_9 = r_{28}\,[\cos(\delta/2)\cos\vartheta\sin\varphi + \sin(\delta/2)\sin\chi\cos\varphi]$$

$$\xi_{10} = 0$$

$$\eta_{10} = r_{34}/2 + r_{310}\cos(\gamma/2)$$

$$\zeta_{10} = -C - r_{310}\sin(\gamma/2)$$

$$\xi_{11} = 0$$

$$\eta_{11} = -r_{34}/2 - r_{310}\cos(\gamma/2)$$

$$\zeta_{11} = -C - r_{310}\sin(\gamma/2)$$

$$\xi_{12} = r_{28}\,[-\cos(\delta/2)\sin\vartheta + \sin(\delta/2)\cos\chi]$$

$$\eta_{12} = -B - r_{28}\,[\cos(\delta/2)\cos\vartheta\cos\varphi + \sin(\delta/2)\sin\chi\sin\varphi]$$

$$\zeta_{12} = r_{28}\,[\cos(\delta/2)\cos\vartheta\sin\varphi - \sin(\delta/2)\sin\chi\cos\varphi]$$

$$\xi_{13} = r_{28}\,[-\cos(\delta/2)\sin\vartheta - \sin(\delta/2)\cos\chi]$$

$$\eta_{13} = -B - r_{28}\,[\cos(\delta/2)\cos\vartheta\cos\varphi - \sin(\delta/2)\sin\chi\sin\varphi]$$

$$\zeta_{13} = r_{28}\,\cos(\delta/2)\cos\vartheta\sin\varphi + \sin(\delta/2)\sin\chi\cos\varphi]$$

---

[a] $A = r_{12}\cos(\alpha/2)$; $B = r_{12}\sin(\alpha/2)$; $C = \{r_{23}^2 - (B - r_{34}/2)^2\}^{1/2}$;

$$M = \sum_i m_i$$

The numbering of the atoms in CP and the fixing of the (ξ, η, ζ) system to the molecule is shown in Fig. 1. The methylene hydrogens 6, 8 and 12 are above the plane 512 in all cases. The hydrogens 10 and 11 lie on the bisector of the corresponding angle (γ). The axes η and ζ lie in the planes 513 and 2345.

The expressions for the atomic coordinates were derived using the assumptions of the rigid reference configuration [9] and the bisector model [1]. According to the rigid reference configuration all the bond lengths and angles except τ and β remain constant during the ring-puckering. The bisector model assumes, however, that at all values of angle τ the bisectors of the methylene angle 829 (δ) and the angle 123 (β) lie on a common axis marked by dashed line in Fig. 1. The situation is similar in the case of angles 12523 and 451. The motion of these two methylene groups can be characterized by the angles ϑ, φ and χ. ϑ is the inclination of the common axis relative to the plane 2345, φ is the angle between the axis η and the projection of the common axis to the plane 2345, χ is the measure of the torsion of these methylene planes around the common axes.

ϑ, φ and χ are given by:

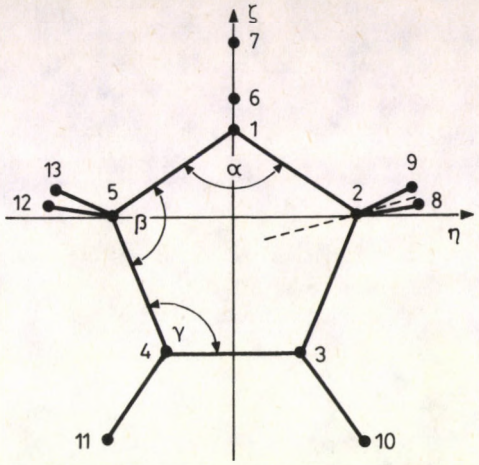

Fig. 1. Numbering of atoms in cyclopentene. Definition of the molecule fixed axis system (ξ, η, ζ). $\tau = 20^{\circ}$

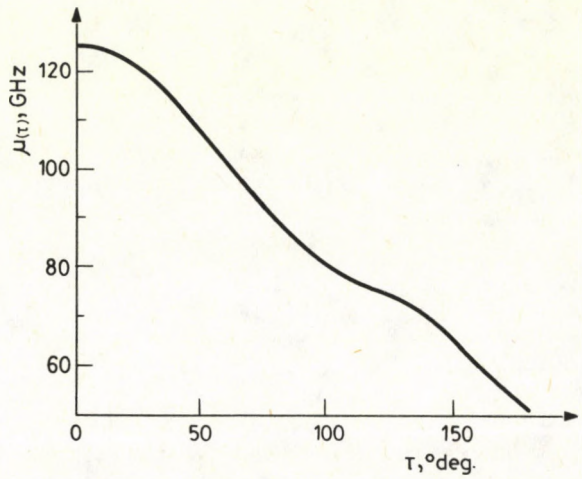

Fig. 2. τ dependence of calculated $\mu_{(\tau)}$ of cyclopentene

$$\vartheta = \arcsin \left\{\cos(\alpha/2) \sin\tau /2 \cos(\beta/2)\right\} , \quad (12)$$

$$\varphi = \arccos \left\{\left[1 + \cos^2(\beta/2) \cos^2\vartheta - \sin^2(\beta/2) + \cos^2(\alpha/2) \sin^2\tau /4\right] / (2\cos(\beta/2) \cos\vartheta) - \arctan \left\{\cos(\alpha/2) \cos\tau /\sin(\alpha/2)\right\}\right. , \quad (13)$$

$$\chi = \arccos \left\{\left[\sin^2(\beta/2) - \cos^2(\alpha/2) \sin^2\tau /4\right]^{1/2}/\sin(\beta/2)\right\} . \quad (14)$$

The structural data of the molecules investigated have been taken from [1]. As it can be seen in Fig. 2 the calculated $\mu_{(\tau)}$ of CP depends strongly on τ. $V_{(\tau)}$ was approximated by a three term polynomial with exponents 2, 4 and 6. This form was completed by a Gauss hump in the case of CP. Both $\mu_{(\tau)}$ and $V_{(\tau)}$ were expanded in finite Fourier series between 160° and -160°. The numbers of the terms in the series were chosen 14 and 25, respectively.

Results

A computer program which contains the diagonalization of the energy matrices and a nonlinear least-squares subroutine has been developed for fitting the potential constants to the far infrared transitions published in [1]. The program has been run on an IBM AT computer using double precision arithmetic. The size of the used blocks was 40 x 40 for both molecules. The results for molecules CP and DHF are collected in Tables II and III, respectively.

Table II

Observed far infrared transitions and deviations of calculated values from experimental ones (in cm^{-1}) for CP

Δv	ΔE	Δ_1 [a]	Δ_2
1 ← 0	0.91	0.10	−0.02
2 ← 1	127.11	0.84	0.26
3 ← 2	25.20	1.30	0.69
4 ← 3	83.06	1.43	-0.09
5 ← 4	76.61	0.21	-0.11
6 ← 5	92.03	0.24	-0.14
7 ← 6	99.81	-0.45	-0.30
8 ← 7	107.46	-0.83	-0.31
9 ← 8	113.27	-2.15	-1.16
10 ← 9	119.38	-2.52	-1.07
11 ← 10	126.10	-1.78	0.15
12 ← 11	132.60	-0.83	1.58
3 ← 0	152.56	1.61	0.27
5 ← 2	184.60	2.70	0.21
	S	30.30	5.85

[a] from [1]

Column Δ_1 contains the deviations obtained by Malloy [1], column Δ_2 contains the ones of our fit. It can be seen that the sums of the squares of the deviations S are smaller in our fit. The calculation for CP resulted a barrier height of 232 cm^{-1} (4.55 $kJ.mol^{-1}$) which is exactly identical with Malloy's [1]. For τ_0 a value of $\pm 26.2^o$ has been obtained. No barrier was found in the case of DHF, its structure is planar [8,1]. The fitted potential functions are for CP and DHF, respectively:

$$V_{(\tau)} = (-12.117 \pm 0.046)\tau^2 + (0.460 \pm 0.023).10^{-3}\,\tau^4 - (0.140 \pm 0.060).10^{-7}\,\tau^6 + \\ + (38.04 \pm 0.520)\,\exp(-(0.206 \pm 0.115).10^{-2}\,\tau^2) \quad ,$$

$$V_{(\tau)} = (0.4430 \pm 0.0070)\,\tau^2 + (0.2813 \pm 0.0025).10^{-3}\,\tau^4 - (0.7513 \pm 0.1077).10^{-8}\,\tau^6 \quad ,$$

where τ is in degree and $V_{(\tau)}$ is in cm^{-1}.

The results show clearly that our method gives a fit better than Malloy's.

Table III

Observed far infrared transitions and deviations of calculated values from experimental ones (in cm^{-1}) for DHF

Δv	ΔE	Δ_1[a]	Δ_2
1 ← 0	99.9	-2.8	-1.8
2 ← 1	116.2	0.8	0.6
3 ← 2	126.8	1.3	0.9
4 ← 3	135.2	1.8	0.9
5 ← 4	142.1	1.4	0.6
6 ← 5	148.1	0.9	0.3
7 ← 6	153.6	0.6	0.1
8 ← 7	158.5	0.1	-0.1
9 ← 8	163.2	-0.3	-0.1
10 ← 9	167.5	-0.7	-0.2
11 ← 10	171.3	-1.3	-0.5
12 ← 11	175.3	-1.5	-0.3
	S	20.8	6.0

[a] from [1]

References

1. T.B. Malloy Jr., J. Mol. Spectr., 44, 504, 1972.
2. J.T. Hougen, P.R. Bunker and J.W.C. Johns, J. Mol. Spectr., 34, 236, 1970.
3. L.R. Somorjai, D.F. Hornig., J. Chem. Phys., 36, 1980, 1962.
4. J.D. Swalen, J.A. Ibers., J. Chem. Phys., 36, 1914, 1962.
5. L. Sztraka, Acta Chim. Hung., 124, 865, 1987.
6. J.D. Lewis, T.B. Malloy, Jr., T.H. Chao, J. Laane, J. Mol. Structure, 12, 427, 1972.
7. J.D. Lewis, J. Laane, J. Mol. Spectr., 53, 417, 1974.
8. T. Ueda, T. Shimanouchi, J. Chem. Phys., 47, 4042, 1967.
9. P.R. Bunker, Molecular Symmetry and Spectroscopy, Academic Press, London, 1979.

Acta Physica Hungarica 63(1–2), pp. 151–154 (1988)

VIBRATIONAL SPECTROSCOPIC CALCULATIONS ON DIFLUORO-PHOSPHINE-BORANE AND ITS ISOTOPE-SUBSTITUTED DERIVATIVES ($F_2XP \cdot BX_3$, X=H,D; B=^{11}B,^{10}B)*

A. SEBESTYÉN
Department of General and Inorganic Chemistry, Veszprém University of Chemical Engineering
8201 Veszprém, Hungary

(Received 15 September 1987)

The mean amplitudes of vibration for five isotope-substituted difluoro-phosphine-boranes $F_2XP \cdot BX_3$ (X=H,D; B=^{11}B,^{10}B), have been calculated on the basis of structural and spectroscopic data from the literature. Potential barriers to internal rotation have also been determined from torsional frequencies, from calculated mean-square amplitudes of vibration and from mean torsional angle differences. Results obtained for various phosphine-boranes are compared.

Introduction

Difluoro-phosphine, HPF_2, is a compound with interesting unusual chemical properties, particularly with respect to its ability to act as a strong Lewis base in contrast with the related compounds, PH_3 and PF_3, which are both extremely weak donors. While the complex of difluoro-phosphine with borane, BH_3 is undissociated at room temperature and stable when protected from the atmosphere, the similar complexes of the latter are almost completely dissociated and thermally unstable under the same conditions [1].

The differences in stability of these complexes were primarily interpreted by structural deviations [4] based on microwave experiments [2,3,4], but the satisfactory explanation is still being searched. The highly different apparent P–B bond strengths in the $F_2HP \cdot BH_3$ and $F_3P \cdot BH_3$ complexes could hardly be rationalised with almost the same P–B bond distances. The additional vibrational spectroscopic experiments and the normal coordinate analysis [5] have supported the interpretation above, but have left the question still open.

Probably the reason of the unusual behaviour of $F_2HP \cdot BH_3$ complex has to be found in several types of fine interactions besides the classic dative bond inside the molecule. The parallel and perpendicular mean amplitudes of vibrations and the potential barrier to internal rotation as fine structural parameters, determined from vibrational spectroscopic calculations, provide additional informations which may contribute to understanding the factors involved. In the present work, continuing the earlier vibrational spectroscpic calculations on donor–acceptor molecules [6,7], the results for the titled compounds are reported with particular respect to the fine structural parameters depending on and characterizing the internal rotation about the P–B bond.

---

*Presented at the 3rd Hungarian Conference on Molecular Spectroscopy, Debrecen, Hungary, 24–28 August 1987

Methods and results

First, normal coordinate analysis was performed on the basis of Pasinski and co-worker's microwave structural data [4] and Taylor and coworker's whole vibrational spectra of five isotopic species [5]. The force field refinement on a total of 90 isotopic fundamentals, after a correction in Taylors' redundancy conditions, was made by the least squares method, using an algorithm of the generalized matrix inversion [8]. The symmetrized force constants are shown in Table I.

Table I

Symmetrized force constants [a] for $F_2XP \cdot BX_3$ (X=H,D; B=^{11}B,^{10}B) molecules

Index	Inital force [5]	Final constants (disp.)	Description	Index	Inital force [5]	Final constants (disp.)
A'						
1,1	3.503	3.488(10)	F(P-H)	2,3	0.040	0.059(30)
2,2	2.932	2.981(75)	F(B-H')	2,5	-0.585	0.437(95)
3,3	3.191	3.210(55)	F(B-H)	3,4	0.251	-0.158(123)
4,4	0.385	0.378(14)	F(HBH)	4,6	0.013	-0.012(21)
5,5	0.644	0.575(34)	F(PBH')	5,6	0.121	0.049(20)
6,6	0.742	0.599(170)	$F(PF_2H)$	5,9	0.131	0.168(38)
7,7	5.887	5.423(196)	F(P-F)	6,7	0.479	-0.265(163)
8,8	0.299	0.238(14)	F(PBH)	6,10	0.182	0.086(94)
9,9	2.566	3.131(142)	F(P-B)	8,11	0.233	0.246(13)
10,10	1.431	1.646(330)	F(FPF)	9,11	-0.019	-0.143(169)
11,11	0.505	0.641(73)	F(BPF)	10,11	-0.241	-0.241
A''						
12,12	3.061	3.090(41)	F(B-H)	12,13	-0.079	-0.048(71)
13,13	0.326	0.296(11)	F(HBH)	13,14	-0.073	-0.116(13)
14,14	0.571	0.571	F(HPF)	13,16	0.137	0.092(44)
15,15	5.443	5.326(52)	F(P-F)	14,15	0.341	0.369(76)
16,16	0.470	0.443(13)	F(PBH)	14,17	0.106	0.071(23)
17,17	0.452	0.500(26)	F(BPF)	16,18	-0.069	-0.104(14)
18,18	0.253	0.266(10)	F(FPBH')			

[a] in N/cm, N/100, Ncm units

The eigenvector matrices, L, obtained during the refinement were then used to compute the mean amplitudes of vibration according to Cyvin [9] at 0 and 298 K and at the temperature of microwave experiment. Results at room temperature are collected in Table II.

The potential barriers to internal rotation calculated in various ways are collected in Table III which also lists the parameters belonging to the free donor (PH_3, PHF_2, PF_3) and free acceptor (B_2H_6) molecules, as well as the related complexes ($H_3P \cdot BH_3$, $F_3P \cdot BH_3$) for the comparison.

Discussion

Inspection of Table III shows the changes in the measured and calculated structural parameters caused by the formation of donor–acceptor bonds. Additionally, it can be seen how the differences in the relative donor strength of various donors are shown in the collected fine structural data.

Table II

Mean amplitudes of vibration[a] for $F_2XP\ BX_3$ (X=H,D; B=^{11}B, ^{10}B) molecules

Atom pairs	R	<l> $HF_2P.BH_3$	$DF_2P.BH_3$	$HF_2P.BD_3$	$DF_2P.BD_3$
P-H/D	140.9	8.39	7.07	8.39	7.06
B-H/D	122.6	8.70	8.68	7.44	7.44
B-H'/D'	120.0	8.74	8.73	7.47	7.47
P-F	155.2	3.98	4.04	3.98	4.04
P-B	183.2	5.75	5.76	5.67	5.71
F...F	237.8	6.80	6.78	6.82	6.79
F...H/D	224.8	11.61	9.88	11.59	9.97
F...B	290.0	9.45	9.38	9.82	9.87
B...H/D	281.6	14.30	12.95	14.56	13.46
P...H/D	237.3	13.73	13.93	12.05	12.08
P...H'/D'	250.9	12.99	13.02	10.77	10.83
H/D...H'/D'	205.6	13.93	13.93	11.82	11.82
H/D...H/D	204.1	14.24	14.27	12.02	12.01
$(F...H/D)_g$	307.4	20.31	20.33	18.35	18.52
$(F...H'/D')_a$	322.2	19.29	19.15	17.82	17.85
$(F...H/D)_t$	378.2	13.31	13.44	11.92	11.96
$(H/D...H/D)_g$	298.8	22.95	21.86	21.91	21.00
$(H/D...H/D)_a$	376.8	15.78	14.93	14.41	13.53

[a] in pm unit, T=298 K, amplitudes for ^{11}B and ^{10}B derivatives are the same in 0.01 pm, a-anti, t-trans, g-gauche

Table III

Comparison of measured and calculated fine structural parameters[a]

Parameters	PH_3	$H_3P.BH_3$	PHF_2[b]	$HF_2P.BH_3$[b]	PF_3	$PF_3.BH_3$	B_2H_6[c]
R(P-X)	142.1	139.9	158.2	155.2	157.0	153.6	
f(P-X)	3.45	3.39		5.38	4.40	5.42	
<l(P-X)>	8.69	8.44		3.98	4.10	4.07	
<(XPX)	93.5	101.3	99.0	100.0	97.8	99.8	
f(XPX)	0.36	(0.46)		(1.12)	0.60	(1.09)	
<l(X...X)>	15.68	14.62		6.80	7.10	6.92	
R(B-H)		121.2		122.6,120.0		120.7	119.7
f(B-H)		3.05		3.15, 2.98		3.19	2.72
<l(B-H)>		8.84		8.70, 8.74		8.69	7.34
<(HBH)		114.6		112.7,115.9		115.1	121.3
f(HBH)		0.42		(0.48)		0.35	
<l(H...H)>		14.21		13.93,14.24		14.18	14.82
R(P-B)		193.7		183.2		183.6	
f(P-B)		1.95		3.13		2.55	
<l(P-B)>		5.99		5.75		5.49	

V_0 [kJ/mol] in $V(\varphi) = (V_0/2)\ (1-\cos 3\varphi)$

PITZER [6,7]	10.4	17.8-19.5	13.9
KARLE,mod. [6,7]	9.8	-	12.9
KARLE,beta [7]	-	14.5-20.9	-
VILKOV [11]	9.8	16.9-18.8	-
MW [4]	10.3	15.0-18.8	13.6

[a] units as in Table I and II, [b] X=F, [c] data for terminal B-H, ( ) combinations

The structural changes for the donor molecules are not so visible as those for the acceptors during complexation as the hybride state of the central atom in the former remains unchanged. Movement of the lone pair towards the acceptor molecule, however, decreases the space demanded by the bonding electron pairs of ligands in the donor molecules. This appeared in shortening of R(P-X) bond distances and in a slight opening of <XPX valence angles in complexes as compared to the values in the free donors. The increase of the f(P-X) valence force constants and decrease of the <l(P-X)> mean amplitudes are in a good correlation with the bond strengthening above. Similarly, the increase in the valence angles around the P atom is followed by the appropriate changes in the values of f(XPX) and <l(X...X)> parameters.

Effect of complexation on parameters of the free acceptor molecule is more definite, considering the increase of the R(B-H) bond length and the decrease of the <HBH valence angles as compared to the values in the hypothetic free BH_3 acceptor. Increase of the <l(H...H)> parallel mean amplitudes are also good indicators of the $sp^2 \rightarrow sp^3$ rehybridisation of the B atom. This pattern of the structural changes fits perfectly into the V.S.E.P.R. theory.

Parameters of the P-B bond are undoubtedly the most interesting data of the boronphosphorous addition complexes. Preceeding experiences have already stressed that the accepted correlation between the bond length and the stability should be applied only cautiously for addition compounds [10]. The f(P-B) force constants and the potential barriers to internal rotation, V_0, obtained in various ways [4,6,7,11], seem to prove the experimental observation, that the stability towards the dissociation decreases in the order of $HF_2P.BH_3$ $F_3P \cdot BH_3 > H_3P \cdot BH_3$. The origin of this phenomenon, however, needs further quantum chemical considerations.

References

1. R.W. Rudolph and R.W. Parry, J. Am. Chem. Soc., 89, 1621, 1967.
2. J.R. Durig, Y.S. Li, L.A. Carreira and J.D. Odom, J. Am. Chem. Soc., 95, 2491, 1973.
3. R.L. Kuczkowski and D.R. Lide, J. Chem. Phys., 46, 357, 1967.
4. J. Pasinski and R.L. Kuczkowski, J. Chem. Phys., 54, 1903, 1971.
5. R.C. Taylor and V.D. Dunning, J. Mol. Struct., 95, 23, 1982.
6. A. Sebestyén, L. Megyeri and B. Vizi, J. Mol. Struct., THEOCHEM, 89, 259, 1982.
7. A. Sebestyén, Per. Polytechn. Chem. Eng., 30, 205, 1986.
8. B. Gellai, J. Mol. Struct., 42, 181, 1977.
9. S.J. Cyvin, Molecular Vibration and Mean Square Amplitudes, Elsevier, Oslo 1968.
10. M. Hargittai and I. Hargittai, A kémia újabb eredményei, 23, Akadémiai Kiadó, Budapest, 1974.
11. L.V. Vilkov, N.A. Penionzhkevich, J. Brunvoll and I. Hargittai, J. Mol. Struct., 43, 109, 1978.

Acta Physica Hungarica 63(1–2), pp. 155–159 (1988)

MATHEMATICAL MODELLING OF DIFFUSE LIGHT SCATTERING. THE ROLE OF INFINITE LAYER THICKNESS IN THE INTERPRETATION OF REMISSION RELATIONS*

GY. MAJOR
Institute of Physics, Section of Physics for Chemical Engineering, Technical University
1521 Budapest, Hungary

(Received 15 September 1987)

Mathematical modelling of the dependence of remittance vs absorption coefficient for assumed pathlength distributions shows the basic relations for diffuse scattering systems. The limiting value of infinite layer thickness is a very important parameter characterizing scattering property.

In previous publications studying the theoretical problems of diffuse light scattering we have reported on results of mathematical modelling which gives simulated density functions of pathlength distribution (later referred to as density function) for remitted and transmitted light [1,2]. Modelling showed [3] that permitting non-discrete step length and making steps over the whole space creates a significant difference from the starting points of theories describing diffuse remission – the so-called continuum [4,5] and discontinuum [6,7,8] theories – because both of them practically summarize pathlengths of one-dimensional discrete step length.

Extension of modelling

For better understanding the mathematical basis of the phenomenon it was necessary to model the dependence of remission or transmission on the absorption coefficient (or concentration) for different arbitrarily chosen density functions of pathlength distribution. Mathematical modelling in this case means the calculations of dependence on the absorption coefficient – according to Eq. (1) – for different density functions f(u) of characteristic shape set up from straight lines and the representation of ϱ, the negative logarithm of remission R vs Z the parameter of the product of absorption coefficient and concentration (Fig. 1).

$$R_Z = \int_0^\infty f(u)\, e^{-Zu}\, du \quad . \tag{1}$$

The distributions are set up within the range 0 – 150 unit pathlength and the total intensity – the number of photons – equals 1000 (Table I, column 1). Parameter Z varied from 0 to 0.5 with steps of 0.01.

The distribution A where the pathlength for the whole light beam equals 20 units (practically the case of scattering free sample) has been set up as a marginal case. Distribution B is the other marginal case – the uniform distribution where the intensity for all

*Presented at the 3rd Hungarian Conference on Molecular Spectroscopy, Debrecen, Hungary, 24–28 August 1987

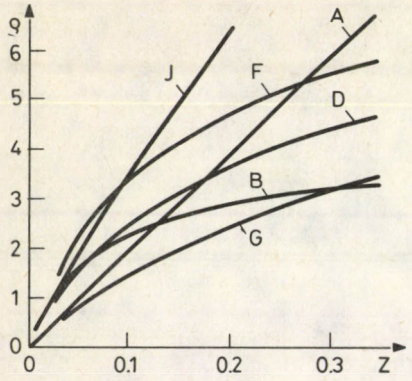

Fig. 1. Dependence of remittance on absorptivity for different assumed density functions. Q = -log (R), Z = parameter of absorptivity

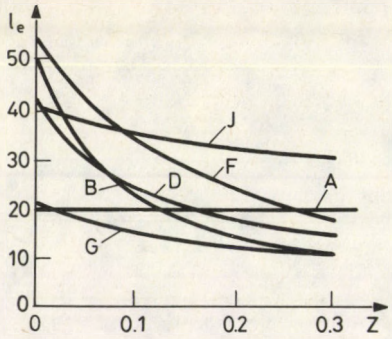

Fig. 2. Dependence of equivalent pathlength l_e on absorptivity Z for assumed density functions

Table I

Assumed model distributions, and their characteristics

1	2	3	4	5	6
distribution	S_0	$S_{0.5}$	l_e^0	$l_e^{0.5}$	Δl_e
A	0.2000	0.2000	20.00	20.00	0.0
B	0.4579	0.0156	45.79	7.36	38.43
C	0.3453	0.0404	34.53	9.73	24.80
D	0.3804	0.0412	38.04	11.10	26.94
E	0.4488	0.0412	44.88	12.49	32.39
F	0.5150	0.0412	51.50	13.30	38.20
G	0.1974	0.0403	19.74	8.37	11.37
H	0.5531	0.0412	55.31	12.72	42.59
I	0.2974	0.1403	29.74	18.37	11.37
J	0.3974	0.2403	39.74	28.37	11.37

pathlengths is the same. To the remittance data calculated from pathlength distributions a so-called equivalent pathlength l_e^Z can be fitted, which corresponds to cell thickness for the same absorption coefficient and concentration in solution giving an absorbance equal to ϱ_Z [1,2]. The value l_e^Z is equal to the distance between the centre-of-weight for the function under integral Eq. (1) to the origo (Table I, columns 4,5). Fig. 2 shows that these equivalent pathlengths depend on the absorption coefficient in a different degree for the different distributions. Several authors say [9] that the average pathlength for remission of an infinite thick layer R_∞ corresponds to about a double length of the thickness of the infinite layer. The data of Fig. 2 modify this premise first of all in that this pathlength decreases with increasing the absorption coefficient Z.

From the data of Fig. 1 and Table I important conclusions can be drawn. On logarithmic scale only the distribution A results in a linear dependence. The other distributions do not result in linear dependence and the curvatures of plots differ significantly even from each other. The increase of steepness S_0 (Table I, column 2) shows that the proportion of light covering a longer path inside the sample increases (E,F,H). A significant part of curves are in this range steeper than graph A. On increase of Z the steepness gradually decreases. Most curves become less steep than graph A. This shows that for a low value of Z remission measurement is more sensitive than solution measurement.

G,I,J represent the pathlength distributions of transmitted light for different layer thicknesses. The steepness S_0b for distributions I,J is higher as they have an equivalent pathlength longer than G, which explains the greater sensitivity of transmission measurement for diffuse samples.

The steepness at high absorption $S_{0.5}$ (Table I, column 3) characterizes the proportion of light covering shorter pathlengths in the distribution. The higher the steepness, the lower the proportion of shorter pathlengths (G). The difference of equivalent pathlengths Δl_e (Table I, column 6) characterizes the flatness of the density function (G,B,H) or the shift of the centre-of-weight of the density function (C – F). Among similar curves the less flat, less extended, more peaked distributions approximate better the limiting value $\Delta l_e = 0$ corresponding to the scattering free sample.

Modelling gives the possibility to investigate the effect of extending the density function, which represents the increase of particle size. Distributions G, D, H. show the extension of the density function to 50, 100, 150 units of maximal pathlength, respectively. The data of calculations show that the extension of distribution moves away the curve in direct proportion (practically similarly to concentration) as a multiplier factor.

As neither the shape of density function nor the measure of its extension can be determined directly, this makes it difficult to evaluate the data. The shape of the density function depends first of all on the shape of particles composing the sample, the extension for the same particle shape depends presumably on the particle size. Therefore, we continued the investigations modelling the dependence of remittance and transmittance vs Z for different layer thicknesses L for samples of different particle size F according to the method described previously [1,2]. Fig. 3 shows the dependence of R and T vs layer thickness L for several particle sizes. Remittance approaches a limiting value and reaches it for samples with larger particle sizes at considerably higher layer thickness. Comparing this limiting value of layer thickness L_∞ and the steepness S_0 with particle size F we get a linear dependence which shows the nearly constant value of quotient S_0/L_∞ (Table II).

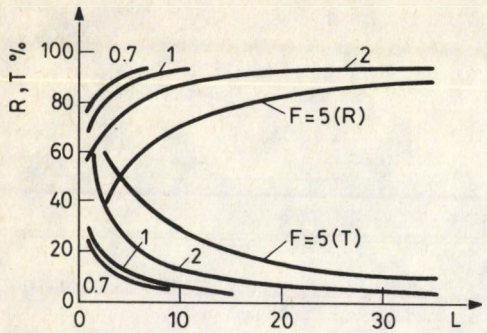

Fig. 3. Modelled dependence of remittance R and transmittance T on layer thickness L (L – arbitrary units)

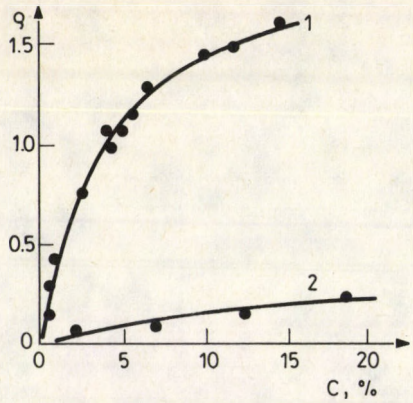

Fig. 4. Measured dependence of remittance of infinite layer ϱ_∞ on concentration C% for K_2CrO_4

1 – diluent KBr
2 – diluent Al_2O_3

Table II

Modelled dependence on particle size

F	S_0	l_∞	T%	S_0/L_∞
10	4.695	93	7.82	0.0505
7	3.666	70	7.00	0.0524
4	2.734	60	5.00	0.0456
2	1.744	24	4.74	0.0727
1	0.945	13	4.54	0.0727
0.7	0.818	11	4.84	0.0744
0.5	0.623	7	5.18	0.0890
0.4	0.530	6	4.75	0.0883
0.2	0.340	4	4.30	0.0850

Measured data

Results obtained by modelling cannot be directly compared with measured data because they are based on assumed functions and values. But several measured data completely support the data of modelling in their character. We measured the dependence of remission for K_2CrO_4 powder diluted with KBr and Al_2O_3 powders, using the uncoloured diluent as reference. On Fig. 4 ϱ_∞ is plotted vs concentration measured at 400 nm. The steepness of the two curves differs essentially and it corresponds to modelled data. The hiding power of the KBr is small, which means that the infinite layer thickness L_∞ is large and the steepness is great. For the Al_2O_3 the hiding power is greater, the infinite layer thickness is small and the steepness is much lower. These data show that the substance with the same absorptivity and concentration (K_2CrO_4) results in different values of remittance in two different colourless diluents.

Conclusions

The measured data concerning the optical spectroscopical behaviour of diffuse scattering systems show that the supporting material or diluent has an other role than the solvent's in measuring solutions – nonscattering systems. The pathlength of light in the sample or rather the pathlength distribution is determined by the size and shape of particles. This is why the supporting material having a relatively small absorption coefficient, can nevertheless result in a considerably large deviation in measured remittance.

The data of modelling show that the value of infinite layer thickness is a very important parameter for diffuse scattering systems. But its determination is difficult, first of all because of the character of dependence R – L. On the other hand, suitable tools are not available for measuring remittance at different exact layer thicknesses. Further investigations into modelling and the realisation of a measuring method for infinite layer thickness may give more interesting and practical results.

References

1. Gy. Major, Dissertation, Leningrad, 1968.
2. Gy. Major, Acta Phys. Hung., 48, 3, 1980.
3. Gy. Major, Per. Polytechn. Chem. Eng., 30, 125, 1986.
4. P. Kubelka, F. Munk, Z. Techn. Phys., 12, 593, 1931.
5. M. Gurevitsch, Phys. Zschr., 31, 753, 1930.
6. Z. Bodó, Acta Phys. Hung., 1, 135, 1951.
7. Z. Bodó, Acta Phys. Hung., 2, 5, 1952.
8. N.T. Melamed, Appl, Phys., 34, 560, 1963.
9. I. Rácz, L. Láng, Magy. Graf., 8, 366, 1964.

Acta Physica Hungarica 63(1–2), pp. 161–164 (1988)

SYSTEMATIC INVESTIGATION OF THE NEAR ULTRAVIOLET SPECTRA OF CHLOROTHIOPHENES*

L. NYULÁSZI and T. VESZPRÉMI
Department of Inorganic Chemistry, Technical University of Budapest
1526 Budapest, Hungary

(Received 15 September 1987)

The near ultraviolet (UV) spectra of all chlorothiophenes have been investigated in vapour phase and n-hexane solution. The Rydberg bands are shown to obliterate in condensed phase spectra and have an almost constant term value throughout the series of the investigated compounds. In order to assign the valence transitions CNDO/S calculations were carried out. The order of the transitions has been shown to be $\pi^*_4 \leftarrow \pi_3$, $\pi^*_4 \leftarrow \pi_2$ and $R_s \leftarrow \pi_3$ in each compound.

Introduction

In our previous works [1] the near UV spectra of thiophene and some of its substituted derivatives have been investigated. The result of our works was the identification of three electronic transitions as $\pi^*_4 \leftarrow \pi_3$, $\pi^*_4 \leftarrow \pi_2$, and $R_s \leftarrow \pi_3$ (Rydberg transition to an s type terminating orbital). The aim of the present work is to investigate all the chlorothiophenes in order to assign their spectra and to draw some conclusions about the electronic structure of these molecules.

Experimental

The investigated compounds were synthetised by known methods [2,3] and their purity was checked by gas chromatography. The spectra have been recorded using a Specord UV VIS spectrophotometer. For the assignment modified CNDO/S quantum-chemical calculations [4] have been carried out. Geometrical data were taken from the literature [5], the applied parameters were described earlier [4].

Results and discussion

The vapour and condensed phase spectra of the investigated compounds are shown in Fig. 1. In the 46–50000 cm^{-1} region a weak band-system is observable in the vapour spectrum of each compound. The effect of the condensed phase is to obliterate these structures as can be seen in Fig. 1. This behaviour is characteristic for Rydberg transitions [6].

Term values calculated from the adiabatic ionization energies [7] are listed in Table I. The observed term values are in good agreement with those calculated by Robin's method [6] for Rydberg orbitals of s type. The term values are roughly constant throughout the whole series as it is expected. Judging from the term value a transition to an s type terminating orbital is favourable. This transition is forbidden for molecules of C_{2v} symmetry ($A_2 \leftarrow A_1$), only a vibronic coupling can make it allowed. This might be the reason for the observed low intensity of the appropriate bands.

*Presented at the 3rd Hungarian Conference on Molecular Spectroscopy, Debrecen, Hungary, 24–28 August 1987

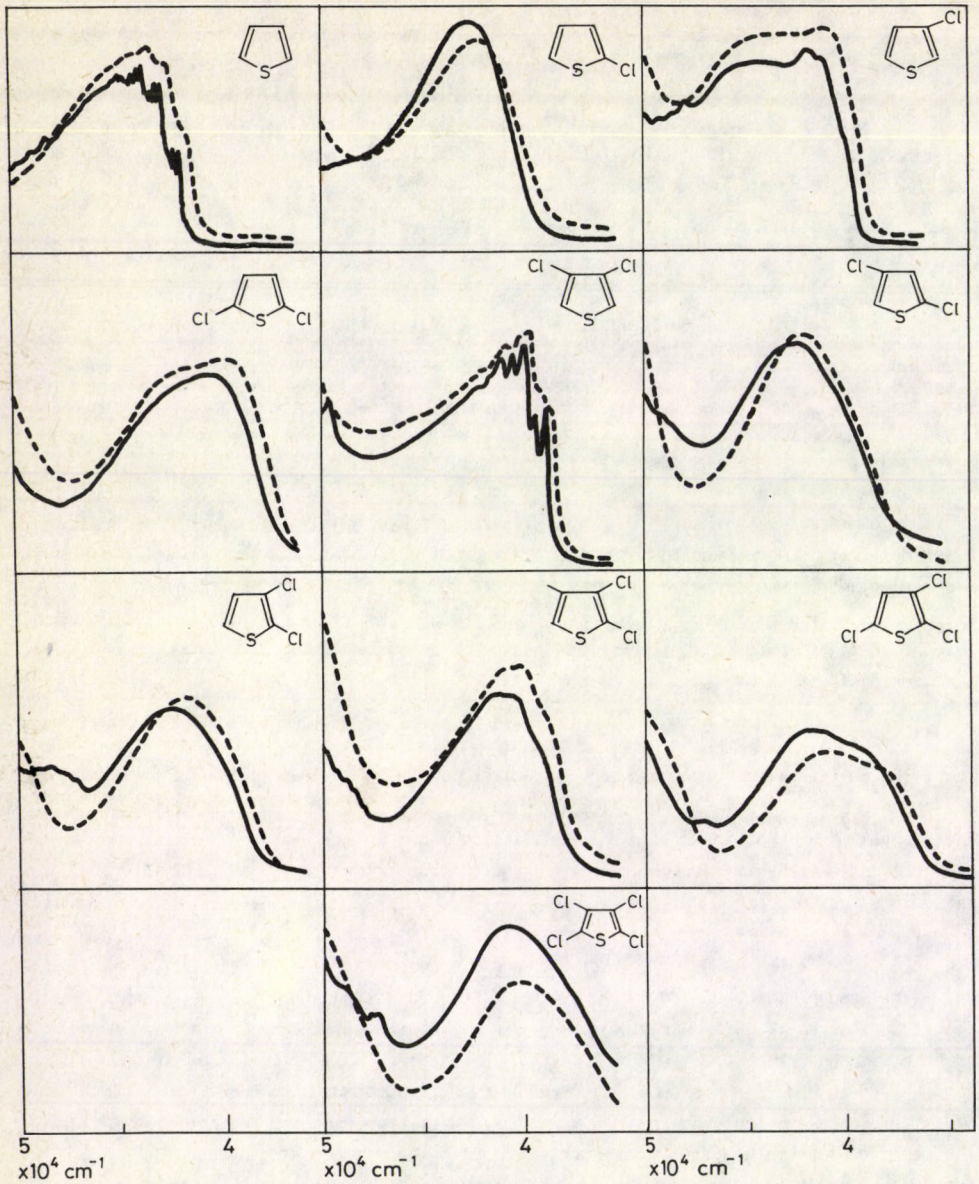

Fig. 1. Near UV spectra of chlorothiophenes in vapour phase (——) and in n-hexane solution (----)

Below 45 000 cm^{-1} an asymmetric band is observed for most of the compounds. However in the case of 3-chloro-, 2,5-dichloro- and 2,3,5-trichlorothiophenes two bands can be clearly distinguished. The bands generally do not show vibronic fine structures with the exception of 3-chloro-, 2,5 dichloro-, 3,4-dichloro- and 2,3,4-trichlorothiophenes. The bands are seen

Table I

Ionization energies, transition energies and term values of chlorothiophenes

Compound	Adiabatic IE	Adiabatic transition energy	Term value	Term value Calc.*
Thiophene	71500	48300	23200	24200
2-Cl-thiophene	70800	46700	24100	24400
3-Cl-thiophene	71900	47900	24000	24400
2,5-Cl-thiophene	69400	46500	22900	24500
3,4-Cl-thiophene	73000	49400	23600	24500
2,4-Cl-thiophene	71300	47400	23900	24500
2,3-Cl-thiophene	70700	47000	23700	24500
2,3,5-Cl-thiophene	70200	46400	23800	24500
2,3,4-Cl-thiophene	71700	47200	24500	24500
2,3,4,5-Cl-thiophene	71000	47000	24000	24600

*Term values are calculated by Robin's method [6]

Table II

Calculated and observed band maxima and oscillator strengths for chlorothiophenes*

Compounds	$\pi_4^* \leftarrow \pi_3$	$\pi_4^* \leftarrow \pi_2$	$\pi_4^* \leftarrow n$	$\pi_5^* \leftarrow \pi_3$
Thiophene	43500 (0.18) 39700 (0.20)	44200 (0.04)	55800 (0.01)	56600 (0.60)
2-Cl	42700 (0.19) 39000 (0.24)	44100 (0.04)	55100 (0.06)	56000 (0.60)
3-Cl	41800 (0.11) 38500 (0.17)	45000 (0.10) 43000 (0.10)	52000 (0.00)	54800 (0.67)
2,5-Cl	40400 (0.25) 38500 (0.25)	42000 (0.24) 44000 (0.03)	54300 (0.00)	56000 (0.70)
3,4-Cl	40100 (0.10) 39500 (0.18)	41500 (0.08)	50500 (0.00)	54000 (0.80)
2,4-Cl	42000 (0.14) 42700 (0.31)	44600 (0.09)	59300 (0.00)	56000 (0.90)
2,3-Cl	42000 (0.13) 42700 (0.36)	44300 (0.05)	59000 (0.00)	55600 (0.88)
2,3,5-Cl	39600 (0.13) 37400 (0.21)	41800 (0.14) 41000 (0.04)	51100 (0.00)	53700 (0.72)
2,3,4-Cl	41400 (0.13) 42300 (0.32)	43200 (0.08)	58100 (0.00)	55100 (0.98)
2,3,4,5-Cl	40600 (0.21) 36900 (0.21)	41000 (0.06)	50200 (0.00)	52400 (0.32)

*The first rows represent the observed transition energies, the second rows the calculated ones. Oscillator strengths are in parentheses. Oscillator strengths were calculated by the formula used in Ref. [4]

in the solution spectra too having about 500–1000 cm^{-1} red shift compared to the vapour phase spectra. This behaviour confirms an assignment to a valence shell transition. In order to interpret these bands CNDO/S calculations were carried out. The results of the calculations together with the vertical transition energies are compiled in Table II.

According to the calculations the lowest energy transition is the $\pi^*_4 \leftarrow \pi_3$ (the notation refers to the thiophene molecular orbitals) in each compound. The next transition at about 2–5000 cm^{-1} higher is a mixture of the $\pi^*_4 \leftarrow \pi_2$ and the $\pi^*_5 \leftarrow \pi_3$ transitions with a stronger $\pi^*_4 \leftarrow \pi_2$ character. The order of the two transitions are the same in each compound regardless of whether they are observed in the spectra or not. The two above mentioned transitions are well separated from the $\pi^* \leftarrow n$ and $\pi^*_5 \leftarrow \pi_3$ transitions by about 10000 cm^{-1}.

References

1. L. Nyulászi, T. Veszprémi, Chem. Scripta, 26, 629, 1986.
2. E. Campaigne, W.H. LeSuer, J. Am. Chem. Soc., 70, 415, 1948.
3. S. Coude, C. Corral, R. Madronero, A.S. Alvarez-Insua, Synthesis, 412, 1976.
4. T. Veszprémi, Chem. Phys. Lett., 88, 325, 1982.
5. Interatomic Distances, L.E. Sutton (Ed.), The Chemical Society, Burlington House, W.1, London, 1958.
6. M.B. Robin, Higher Excited States of Polyatomic Molecules, Vol. I., Academic Press, New York, 1974.
7. T. Veszprémi, L. Nyulászi, J. El. Spectr. in press,

Acta Physica Hungarica 63(1–2), pp. 165–170 (1988)

ASSAY OF THE ACTIVE INGREDIENT CONTENT OF SOME INSECTICIDES, FUNGICIDES BY DERIVATIVE SPECTROSCOPIC METHOD*

GY. MILCH and É. SZABÓ
CHINOIN Pharmaceutical and Chemical Works Ltd.,
1325 Budapest, Hungary

(Received 15 September 1987)

The active ingredient content of some plant protecting agents has been determined by second derivative UV absorption spectrophotometric method, eliminating the background effect caused by the dissolved carriers, excipients. The method has a better performance than the conventional base-line correction method.

Introduction

Difference spectrophotometry [1,2], orthogonal polynomials [3,4,5] and the base-line correction method [6] are often used to eliminate the background effect caused by the dissolved excipients. These methods are sufficient in some cases, but the thorough selection of the optimal parameters of the mentioned methods [1,2,3,4,5,6] is lengthy and tedious.

In the last decade a series of derivative spectrophotometric methods have been published, these aimed at different analytical problems. Some of them eliminated the background effect by scanning second derivative spectra [7,8,9,10]. Our earlier experiences obtained in the analysis of pharmaceutical substances [11,12] supported these observations.

In our opinion a close relation ought to be between the assay of the active substance content of a pharmaceutical dosage form in the presence of its excipients and that of a formulated plant protecting agent in the presence of its carriers. Therefore we have tried to apply the derivative spectrophotometric method also for the assay of the active ingredient content of some pesticide formulations.

It is well known that a derivative of a linear function is constant, its second derivative is zero, so when zeroth order spectra have a linear background, the evaluation of the active component content can be performed based on second derivative spectra.

The ordinate value in a derivative spectrum at any wavelength depends on the slope of zeroth order spectrum at the given wavelength. This technique discriminates therefore in favour of narrow spectral bands against those with broad bandwidths.

If the Beer – Lambert law is obeyed by the analyte at wavelength λ in the zeroth order spectrum, the derivative amplitude in the nth order spectrum will be linearly related to the analyte concentration

$$D_n = \frac{d^n A}{d\lambda^n} = \frac{d^n \varepsilon}{d\lambda^n} \cdot c \cdot d$$

*Presented at the 3rd Hungarian Conference on Molecular Spectroscopy, Debrecen, Hungary, 24–28 August 1987

at wavelength λ, where D = nth derivative amplitude absorbance units nm^{-n}, A = absorbance, ε = molar absorptivity 1 mol^{-1} . cm^{-1}, c = molar concentration and d = cell path length cm [13].

Experimental

Instrument

The spectra were scanned on a Perkin-Elmer Lambda 5 recording spectrophotometer.

Substances

The following active ingredients and their formulations have been tested: Carbendazim, chemical name: benzimidazolyl methyl carbamate. Its formulations: Kolfugo, containing 25.0% of carbendazim in a suspension. Kolfugo extra, containing 20.0% of carbendazim in a suspension. Epidor, containing in suspension form 12.5% of carbendazim and 36.5% of mancozeb. (dithane). Carbofuran chemical name: 2,3-dihydro-2,2-dimethyl-benzofurane-7-yl methyl carbamate. Its formulation: Chinufur 40 FW, containing 40% of carbofuran in suspension form.

The used test solutions were as follows: 3 – 8 $\mu g/cm^3$ of carbendazim in N hydrochloric acid 15 – 25 $\mu g/cm^3$ of carbofuran in methanol or in ethanol.

The evaluation of the second derivative spectra was based on peak to trough measurements. From these values calibration graphs were plotted for each compound as a function of concentration. These were found to be linear passing through the origin, their r values being 0.9990 – 0.9998.

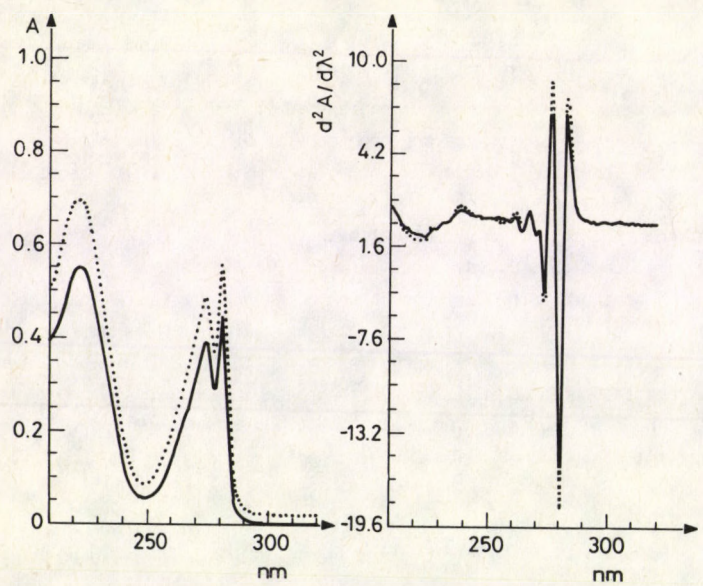

Fig. 1. Zeroth order and second derivative UV spectra of ——— Carbendazim reference substance and of ..... Kolfugo extra in 0.2 N hydrochloric acid
Concentration: 5.0 $\mu g/cm^3$

Results and discussion

As our first examples are related on the assay of active components of benzimidazole structure, a brief survey on their UV spectroscopic properties is given.

It is well known that the ultraviolet absorption spectra of heterocyclic compounds containing nitrogen instead of the metin group are similar to those of the corresponding aromatic compounds, thus also the spectrum of benzimidazole may be retracted to those of naphthalene and of indole.

The absorption of naphthalene is essentially a shifted benzene spectrum. A strong band without fine-structure at about 220 nm, a band of medium intensity with more or less vibrational structure and with a maximum at about 276 nm, and at last a weak band at about 315 nm. According to Clar's nomenclature, the band of the short wavelength is called β-band, the one at 276 nm is the p/para/-band, and at last the low intensity band about 315 nm is the α-band. These bands may be detected in the spectrum of indole, too, at 219, 273 – 278 and at 288 nm. Compared to these, there is no much difference in the spectra of the azaindoles, thus in that of benzimidazole, however, in the latter, the band at the long wavelength is absent [15,16,17,18,19,20].

The spectrum of benzimidazole resembles that of a substituted benzene. The band of shorter wavelength has been related to excitations, whose site is the amidine ring and the bands of longer wavelength have been related to excitations involving the benzene ring. Some transitions may arise from excitations, which include both rings and in those cases it may be expected, that they would produce bands of greater intensity at longer wavelengths [14,15].

The ultraviolet spectrum of the parent compound,benzimidazole, exhibits in the pH range 0 – 5 rather few changes. It exhibits two well defined maxima at 267 and at 274 nm, as well as inflections at about 240 and 262 nm. The twin bands at 267 and 274 nm are very important. They can be assigned as $\pi \rightarrow \pi^*$ transitions and may be found in all benzimidazole derivatives, sometimes melted into a single band. This band may be found in the spectra of benzofuran, benzothiophene, benzoxazole and benzthiazole, too.

In neutral and alkaline media the spectra show a bathochromic shift. The inflexion at 240 nm turns into a maximum at 245 nm, the maximum at 267 nm is shifted to 272 nm and the other of 274 nm to 278 nm, but the intensity of the bands does not change markedly. Neither absorption, nor fluorescence bands depend markedly on the nature of the solvent [17].

Position is an important factor in determining basicity, particularly in the case of substituents, which act predominantly through an inductive effect. Since the effect of a substituent on the basicity of benzimidazol is stronger, the closer this group is to the nitrogen atom, groups in the position 2 are more effective in modifying the basic nature of the imidazole ring than similar groups in the position 5, or 6. Specially high is the effect of substitution with a methyl group at position 2, which can be assigned to the combination of an inductive and a hyperconjugative effect [14,15,16,17,18,19,20,21].

Carbendazim is a systemic fungicide. As a benzimidazol derivative [22], it has a characteristic UV absorption spectrum, which is suitable also for quantitative measurements. When determining the active ingredient content of some simple formulated preparations, the UV spectrum usually serves as a suitable method, but Epidor is a more complicated system [23].

The determination of dithane content will not be treated here, but some of its proper-

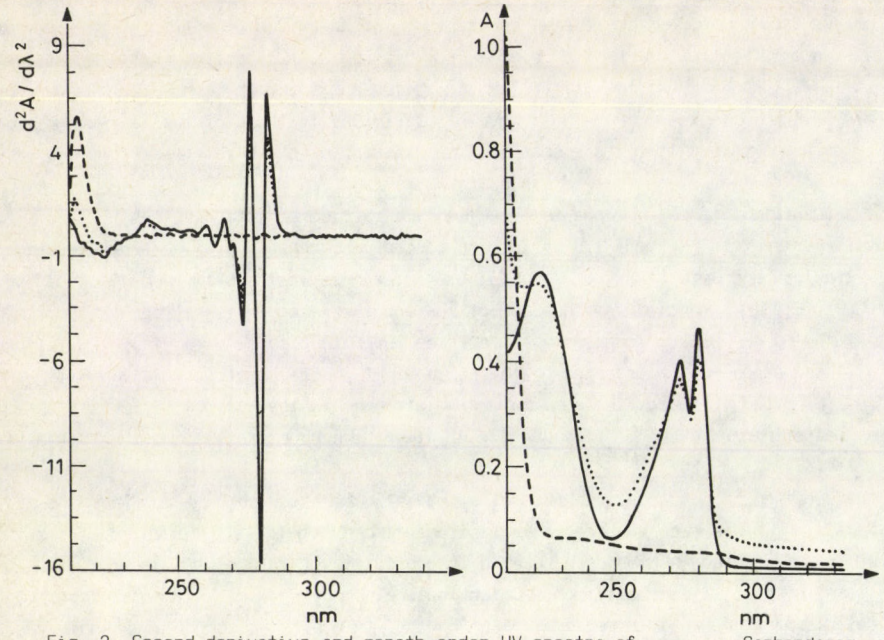

Fig. 2. Second derivative and zeroth order UV spectra of ——— Carbendazim reference substance, of ..... Epidor and of ---- Mancozeb in 0.2 N hydrochloric acid; Concentration: 5.0 µg/cm

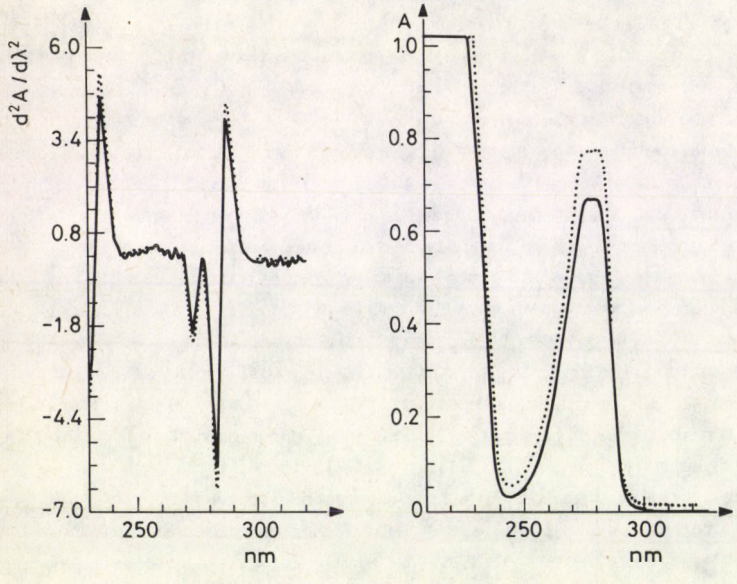

Fig. 3. Second derivative and zeroth order UV spectra of ——— Carbofuran reference substance and of ..... Chinufur 40 FW in methanol; Concentration: 20.0 µg/cm^3

Table I

Results of the assay of the active ingredient content of plant protecting agents

Name of preparation	Labelled amount of active ingredient, per cent	Found amount of active ingredient content by base-line correction method			by second derivative spectrosc. method		
		n	Mean	RSD	n	Mean	RSD
Kolfugo	25.0 w/w (of carbendazim)						
Model experiment		7	24.9	1.8	7	25.0	1.2
Batch(production)		7	24.7	2.2	7	24.9	1.5
Kolfugo "extra"	20.0 w/w (of carbendazim)						
Model experiment		7	20.1	1.9	7	19.9	1.3
Batch(production)		7	19.7	2.2	7	19.8	1.5
Epidor	12.5 w/w (of carbendazim)						
Model experiment		7	12.2	3.0	7	12.4	1.5
Batch(production)		7	12.1	3.3	7	12.3	1.7
Chinufur 40 FW	40.0 w/w (of carbofuran)						
Model experiment		7	39.7	1.7	7	40.0	1.1
Batch(production)		7	39.4	2.0	7	39.7	1.4

ties must be dealt with, as on the effect of the strongly acidic medium necessary for the assay of carbendazim, a degradation process of dithane takes place and its resulting background absorption inhibits the simple determination of the carbendazim content. The use of base-line correction method is less suitable in this case, as the degradation of mancozeb is a relatively quick process, though it does not proceed completely. The derivatization of the spectrum proved to be a much better way of solving this analytical problem. The background absorption caused by dithane, which forms a slightly raising line when approaching the low wavelength UV region, can be excellently eliminated by second derivative spectrophotometry.

Carbofuran is a systemic insecticide [24]. The UV absorption spectrum of carbofuran exhibits a broad absorption band at the maximum at about 280 nm, which can be similarly assigned, as the appropriate band in benzimidazoles. The carriers, excipients of the Chinufur 40 FW suspension distort the spectrum in methanolic solution in a greater or smaller extent. This background absorption could be eliminated also by the base-line correction method, but the use of second derivative spectrophotometry proved to be also in this case more successful. The advantages of second derivative spectrophotometry were verified with model experiments. A suspension has been prepared by weighing in the active substance with analytical accuracy. The active ingredient content of the model suspension has been determined by both the base-line correction and by second derivative spectrophotometric methods in ethanolic, or methanolic solution. The results obtained by the derivative spectrophotometric method have a better reproducibility and their relative standard deviation is less than those obtained by the base-line correction method.

References

1. Th.D. Doyle and F.R. Fazzari, J. Pharm. Sci., 63, 1921, 1974.
2. A.G. Davidson, J. Pharm. Pharmac., 30, 410, 1978.
3. A.L. Glenn, I.U. Agwu, J. Pharm. Pharmac., 19, 765, 1967.
4. L. Coclers, R. Bontemps, J. Pharm. Belg., 40, 295, 1985.
5. A.M. Wahbi, A. Ebel, J. Pharm. Pharmac., 26, 317, 1974.
6. R.A. Morton, A.L. Stubbs, Analyst, 70, 348, 1946.
7. J. Traveset, V. Such, R. Gonzalo, E. Gelpi, J. Pharm. Sci., 69, 629, 1980.
8. A.G. Davidson, S.M. Hassan, J. Pharm. Sci., 73, 413, 1984.
9. Th.C. O'Haver, Anal. Proc., 19, 22, 1982.
10. A.F. Fell, Anal. Proc., 18, 291, 1981.
11. G. Milch, É. Szabó, Coll. Spectr. Int. XXIV, 1985., Garmisch-Partenkirchen, Book of Abstracts. Vol. 1. MO D 146.
12. G. Milch, É. Szabó, Acta Chim. Hung. in press.
13. A.F. Fell, J.G. Allan, Anal. Proc., 18, 291, 1981.
14. D.J. Rabiger, M. Jouillé, J. Org. Chem., 29, 476, 1964.
15. R.D. Rabiger, M. Jouillé, J. Chem. Soc. (London) 915, 1964.
16. R.D. Gordon, R.F. Yang, Can. J. Chem., 48, 1722, 1970.
17. M. Krishnamurthy, P. Phaniraj, S.K. Dogra, J. Chem. Soc. Perkin Trans. II. 1917, 1986.
18. K. Hofmann, Imidazole and its derivatives. Part 1. – Interscience Publishers, Inc. New York, 1953. p. 253.
19. G. Leandri, A. Mangini et al., Gazzetta Chim. Ital., 85, 769, 1955.
20. E.A. Steck, F.C. Nachod et al., J. Am. Chem. Soc., 70, 3406, 1948.
21. P.N. Preston, Chem. Rev., 74, 279, 1974.
22. H. Martin, Ch.R. Worthing (eds), Pesticide Manual, 5th Ed. British Crop Protection Council, 1977. p. 78.
23. Ibidem, p. 328–329.
24. Ibidem, p. 80.

Acta Physica Hungarica 63(1–2), pp. 171–176 (1988)

EFFECT OF SCATTERED PHOTONS ON THE INTENSITIES OF X-RAY CHARACTERISTIC LINES*

L. MÉRAY and E. HÁZI
University of Chemical Engineering, Institute of Radiochemistry and Physics
8201 Veszprém, Hungary

(Received 15 September 1987)

Enhancement effect of scattered photons on line intensities in isotope-radiation induced X-ray emission analysis was studied. Enhancement factors were determined by measurements performed with thin Ca, Cd, Co, Sr and Cs coatings on the surface of graphite and plastic matrices of varying thickness. The results were compared to data obtained by Monte Carlo simulation. A modified version of the simulation yielded to enhancement factors for elements distributed homogeneously in light matrices.

Introduction

The enhancement caused by characteristic X-rays and leading to one side of inter-element effect is well known and taken into consideration in different methods of XRF quantitative analysis [1]. The fact that scattered photons of the primary radiation take also part in the induction of characteristic radiation has been recognized and efforts to describe this effect have been made [2], nevertheless the method introduced ignores inelastic scatterings and multiplex elastic scattering and so it is not suitable for being applied to samples consisting of light elements. Our aim was to obtain reliable data concerning the effect outlined above. This aim can be achieved by direct measurements only in the case of samples containing the elements examined and a matrix behind this layer, free of the elements in question. For homogeneous sample distribution theoretical methods can be used.

Theoretical

When some material is irradiated by X-rays, three kinds of event may happen:

1. ionization on an inner shell, (photoeffect), leading to X-rays (fluorescence) or Auger electrons;

2. inelastic (Compton) scattering, causing changes both in energy and in direction of the photon scattered;

3. elastic (Rayleigh) scattering, affecting only the direction of the photon.

Due to those three possibilities the intensity of the primary X-rays, I_o, decreases to I when passing a layer of thickness d:

$$I = I_o \cdot e^{-\Sigma \mu_i \rho_i d} , \qquad (1)$$

where ρ_i is the density (gcm^{-3}) of the i-th element in the sample and μ_i is the mass absorption coefficient. The latter quantity can be expressed as the sum of three terms

*Presented at the 3rd Hungarian Conference on Molecular Spectroscopy, Debrecen, Hungary, 24–28 August 1987

corresponding to the three events listed above, respectively:

$$\mu_I = \mu_{IP} + \mu_{IC} + \mu_{IR} \quad . \tag{2}$$

The probability of having an X-type scattering – provided that the photon was scattered (where X can be either P, C or R, that is photoeffect, Compton or Rayleigh scattering):

$$P_X = \frac{\sum_i \mu_{iX} \varrho_i}{\sum_i \mu_i \varrho_i} \quad . \tag{3}$$

The energy does not change in Rayleigh scattering and decreases in Compton scattering:

$$E_{Compton} = \frac{E^2 (1 - \cos\theta)}{E(1 - \cos\theta) + mc^2} \quad , \tag{4}$$

where E is primary energy, m is the electron mass, c is light velocity and θ is the scattering angle.

The scattered photon can go in any direction, the probability density of the directions can be nevertheless determined. For Compton scattering on a single electron the differential cross section, $\frac{d\sigma}{d\Omega}$, is given by the Klein – Nishina equation [3]. The probability density is affected by the other electrons as well; this fact can be taken into account with the so-called atomic scattering factors, S(X,Z), where $X = \sin(\theta/\lambda)$, θ is the angle of scattering and Z is the atomic number [4].

For Rayleigh scattering the Thomson equation has to be used [3]. The effect of other electrons is expressed by the atomic form factors, F(X,Z). The other atoms can also take part in the elastic scattering but this interference can be ignored if the material is amorphous.

The differential cross sections of the Rayleigh and Compton scatterings are given by Eqs (5) and (6), respectively:

$$\frac{d\sigma}{d\Omega} = \frac{r_e^2}{2} (1 + \cos^2\theta) \left[F(X,Z)\right]^2 \quad , \tag{5}$$

$$\frac{d\sigma}{d\Omega} = \frac{r_e^2}{2} \left[1 + k(1 - \cos\theta)\right]^{-2} \left[1 + \cos^2\theta + \frac{k^2(1 - \cos\theta)}{1+k(1 - \cos\theta)}\right] \quad , \tag{6}$$

where r_e is the classical electron radius, θ is the scattering angle and k is the photon energy in units of electron restmass energy.

Equations (3), (4), (5) and (6) were used in a Monte Carlo simulation of the processes taking place in the sample when irradiated with monoenergetic primary X-rays [5]. In Fig. 1 a typical simulated spectrum is shown as example; the primary energy was supposed to be 47 keV and the sample simulated consisted of a Sr layer of 0.8 mg/cm^2, formed on the surface of a carbon pellet of 4 mm thickness. The simulation provided not only a spectrum but information concerning the number of different events and therefore it was suitable for determining the enhancement caused by scattered photons.

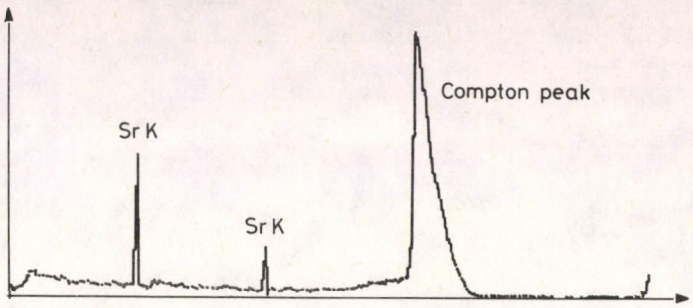

Fig. 1. Simulated Sr spectrum

Experimental

To have well-defined, thin layers of the model elements (Ca, Cd, Co, Sr and Cs) FIXION thin ion-exchanger sheets – commonly applied in thin layer chromatography – were used. The surface concentration of those elements varied in the range of 0.8–800 g/cm^2. These sheets were put onto the sample holder above the detector, with the coated size facing the detector window. To study the effect of scattered photons graphite and perspex plates were piled on the sheet, forming a matrix of variable thickness.

The measuring system consisted of the following units:

– ORTEC Ge(Li) detector (for Cs spectra) on ATOMKI Si(Li) detector for the other elements;

– Fb-210 source for Cs and Ca excitation, Cd-109 source for the other elements;

– Canberra spectroscopic amplifier linked to the Si(Li) detector and ORTEC pulse shaper and amplifier with the Ge(Li) detector;

– ICA 70 (KFKI) multichannel analyzer.

The spectra collected were processed with an R-35 computer.

Results and discussion

Due to multiplex inelastic scatterings in the sample the spectra obtained consist of a rather low characteristic peak piled up on the "tail" of a very high Compton-peak, therefore special care had to be paid when calculating peak areas. For this purpose an iteration method [6,7] was applied. The statistic spread of peak areas was not negligible, especially not for low concentrations.

In Table I the peak areas (counts/time) are given for different thickness of graphite matrices, obtained with the greatest surface concentrations.

The spectra corresponding to lower concentrations were used only to check the simulations [5]. Spectra simulated were accepted only if deviations from spectra measured under the conditions assumed in simulation were within the margin of statistical spread, otherwise the model used was refined.

In Figs 2–3 the simulated enhancement $\Delta I/I$ is plotted against thickness for different primary energies where I is the intensity of the characteristic line without excitations by scattered photons and ΔI is the intensity increment due to the fact that scattered

Table I

Peak areas obtained with different matrices

Graphite thickness mm	Ca Counts/1000s	Co Counts/1000s	Sr Counts/1000s	Cd Counts/3600s	Cs Counts/3600s
0	1.93 ± 0.05	14.35 ± 0.20	62.12 ± 0.45	26.2 ± 0.7	38.1 ± 0.3
2	1.90 ± 0.07	15.07 ± 0.25	65.30 ± 0.61	27.2 ± 1.0	39.1 ± 0.5
4	2.24 ± 0.11	15.74 ± 0.21	66.53 ± 0.51	28.7 ± 0.6	40.0 ± 0.9
12	2.12 ± 0.09	16.89 ± 0.31	70.49 ± 0.68	32.2 ± 1.9	42.2 ± 1.2

photons may also induce characteristic radiation.

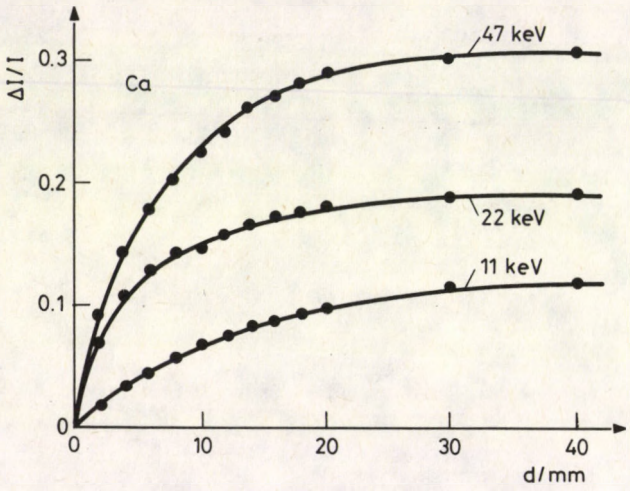

Fig. 2. Enhancement of Ca line, plotted against sample thickness for surface coating

From the results introduced in Figs 2–3 the following conclusions can be drawn:

1. The enhancement caused by scattering can be neglected only if the sample is thin (< 1 mm) or the primary energy just exceeds the K absorption edge.

2. The thicker is the matrix the greater enhancement occurs above a certain thickness – that is roughly equal to $(1/\mu\varrho)$ the enhancement is independent of thickness.

3. In the range in which usually the primary energy is the enhancement increases if the energy is raised. In higher energy ranges this relationship is not generally valid.

With a little modification the Monte Carlo method was made suitable for simulating spectra of homogeneous samples. The results of such simulations are shown in Figs 4–5.

As can be seen the enhancement in question can be considerable, in some cases about 30%. It is especially important to know its value when samples of great volume are analyzed with any kind of standardless methods. Since such methods are more and more widely used, the subject introduced is slowly slipping from theory toward the field of practical analysis.

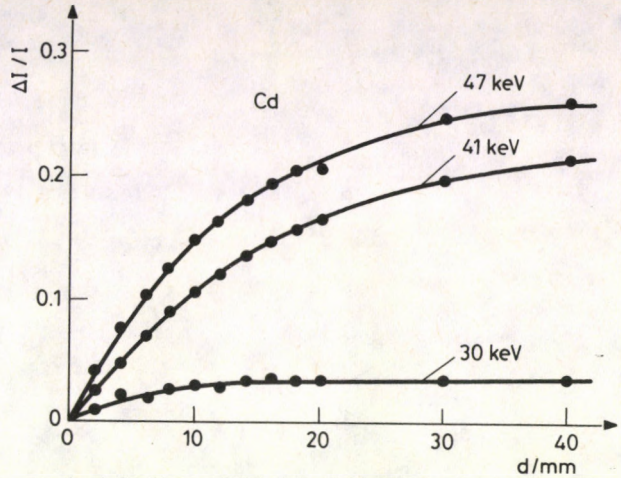

Fig. 3. Enhancement of Cd line, plotted against sample thickness for surface coating

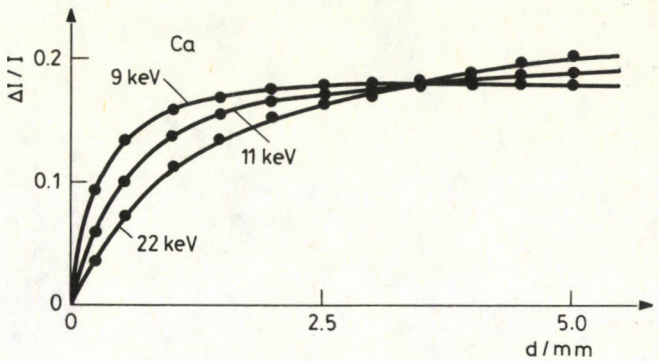

Fig. 4. Enhancement of Ca line, plotted against sample thickness for surface coating

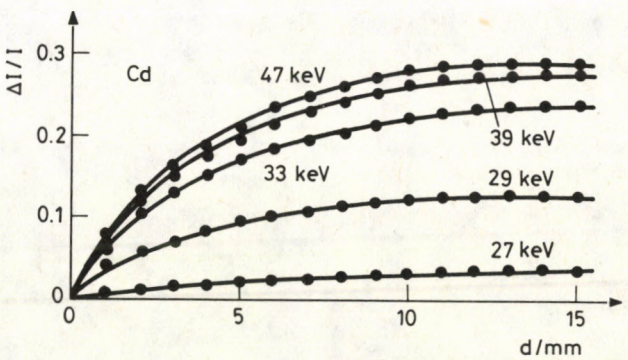

Fig. 5. Enhancement of Cd line, plotted against sample thickness for surface coating

References

1. L.S. Birks, X-Ray Spectrochemical Analysis, Wiley-Interscience, New York, 1969.
2. H.D. Heith, T.C. Loomis, Corrections for scattering in X-Ray Fluorescence Experiments, Y-Ray Spectrom., 7, 225, 1978.
3. O. Klein, Y. Nishina, Z. Phys:, 52, 853, 1929.
4. J.H. Hubbel, J. Phys. Chem. Ref. Data, 4, 3, 1975.
5. L. Méray, Zs. Révay, Proceedings of the conference "XXVIII. MSZEV", p. 233, 1985.
6. L. Méray, Proceedings of the conference "XXIX. MSZEV", p. 245, 1986.
7. L. Méray, E. Házi, Decomposition of Gamma or Energy-dispersive X-Ray Spectra Using Iteration, J. of Radioanal and Nucl. Chem. – Letters, 198 (in press), 1987.

Acta Physica Hungarica 63(1–2), pp. 177–185 (1988)

COMPUTER SIMULATION OF PINNING IN TYPE-II SUPERCONDUCTORS AND THE THEORY OF COLLECTIVE PINNING*

E.H. BRANDT
Max Planck Institute for Metal Research, Institute for Physics,
Stuttgart, FRG

(Received 20 October 1987)

The problem of pinning of flux-lines by random inhomogeneities is discussed. The theory of collective pinning, which was established recently by Larkin and Ovchinnikov and has proven successful in weak-pinning amorphous alloys, is discussed in some detail. Then computer simulation of pinning is described and the results are discussed. They confirm collective pinning theory for weak two-dimensional pinning and modify it at strong pinning where the flux-line lattice becomes amorphous.The threshold-behaviour predicted by the "dilute limit theories" proves to be an artifact which is due to the non-existence of this limit in sufficiently large specimens.

1. Introduction

The statistical summation of the pinning forces exerted by material inhomogeneities on the flux-line lattice (FLL) in type-II superconductors is still a challenging problem. Since the first idea of flux pinning [1], the first summation theories [2, 3], the excellent review [4], up to the appearance of the collective pinning (CP) theory [5] it has been clear that the calculation of the maximum loss-free current density j_c in a type-II superconductor is a complicated problem. Even if the nature of the pins were known and even if the elementary interaction of each pin with the FLL could be estimated reliably from a microscopic theory, one would still have to solve the summation problem. For real superconductors this often appears impossible since the pins are either too strong, too large, or too correlated for simple summation theories to apply. Most theories fail in particular when the pins generate plastic deformation of the FLL. This in general leads to a dependence of j_c on the "history" of the specimen, i.e. on the previously applied current or magnetic field.

In spite of numerous works quoted in [6], the summation remained essentially unsolved even for the idealized case of weak identical pins at random positions acting on a FLL which is only elastically deformed (i.e. topologically ideal). This situation changed when the CP idea came up.The CP concept was applied independently, with similar results, to FLs [5] and to charge-density waves in quasi-one-dimensional metals (e.g. $NbSe_3$) [7]. Its two-dimensional (2D) version was tested successfully on very weak pinning amorphous layers of Nb_3Ge [8] and by computer simulations [6]. Recently, the CP concept has been applied to pinning of a crystal dislocation line (the problem of solution hardening) [9].

In our opinion, experiments in the past often seemed to confirm summation theories which were not well founded (or even wrong). In this sense, the reason why we believe in the concept of collective pinning is not so much its agreement with experiments but its con-

*Presented at CRYOSEM '86, IIIrd International Seminar on Low-Temperature Physics, Visegrád, Hungary, 26–31 May 1986

ceptual clarity and transparency. In cases where experiments do not fit the 3D version of CP theory we ascribe this to the presence of screw dislocations in the FLL which can move easily along the FLs (screw dislocations are at a right angle to the FLs and feel no Peierls potential since the FLs have no structure). As a consequence the FLs now can adjust easily to the pins and j_c becomes larger than predicted from mere elastic deformation of the FLL.

The presence of screw dislocations in the FLL in our opinion has been demonstrated clearly in a very recent experiment by Kes and Wördenweber [10]. In amorphous films of thickness d=5 - 18 μm an abrupt jump of j_c by more than a factor of ten was observed when the induction B was increased to a value $B_{co} \approx 0.7\ B_{c2}$ (B_{c2}= upper critical field of the superconductor). This fascinating finding demonstrates a sharp transition from 2D to 3D pinning (called "dimensional cross-over"). Moreover, the sharpness of this jump, its reversibility (with slight hysteresis), and a subsequent further steep increase of j_c by another factor of ten immediately above B_{co}, unambiguously proves that the FLL has switched from the ordered state of nearly stiff, straight, parallel FLs (the case of 2D pinning) to a disordered "spaghetti state" with strong plastic deformation. This state may formally be described by the presence of screw dislocations, dislocation loops, or kinks. Such defects are generated at the film surface where the FL tilt and shear is largest, and then move rapidly into the bulk until a high defect density is reached. Apparently a threshold value of the elastic distortion has to be reached (a kind of flow stress) before the FLL switches to the spaghetti state. There remain fascinating questions: for the theorist, to explain this transition quantitatively, and for the experimenter, to check whether a similar transition occurs again at low inductions where the stiffness of the FLL decreases again (the ratio of pinning strength and FLL stiffness is large at high and low inductions and has a minimum in between).

2. The theory of collective pinning

For transparency we will split the concept of CP into three basic ideas. This will facilitate generalizations since it makes clear which of the three ideas has to be modified.

1st idea. Inside a coherently moving (almost rigid) "correlation volume" V_c containing $n_p V_c$ pins (n_p = volume density of pins) the elementary pinning forces $\underline{f}_i$ are statistically independent when the pin positions are uncorrelated. Here and in the following $\underline{f}_i$ means the force which the i-th pin exerts on the FLL at this moment. The statistical fluctuation of the total force on this volume is interpreted as the maximum pinning force on V_c. The maximum volume pinning force $j_c B$ is then obtained by dividing the root mean square of the fluctuating force by the volume V_c:

$$j_c B = (n_p V_c \langle \underline{f}_i^2 \rangle_{pins})^{1/2} / V_c = (W/V_c)^{1/2} ,$$

where

$$W = n_p \langle \underline{f}_i^2 \rangle_{pins} = n_p f_p^2 .$$

2nd idea. The correlation volume, or its diameter $2R_c$ and length along the FLs $2L_c$, is estimated from the autocorrelation function $g(\underline{r})$ of the FL displacement field $\underline{u}(\underline{r})$ caused by the pins. V_c is defined as the region inside which $|\underline{u}(\underline{r})|$ is smaller than the range r_p of the pinning forces,

$$g(\underline{r}) = \langle |\underline{u}(\underline{r}) - \underline{u}(0)|^2 \rangle_{\text{ensemble}} \leqslant r_p^2 \quad .$$

It is a peculiarity of this theory that the force range r_p enters: In CP theory the pin ensemble is characterized only by its strength W and range r_p. The physical meaning of r_p is that of a correlation length of the force field. Very recent results [11] show that in almost all cases one has $r_p \approx 0.195$ a (a = FL-spacing) except for point pins (pins with radius $\ll$ the coherence length ξ) at low inductions, where $r_p \approx \xi \approx$ core radius of the FLs. The correlation lengths R_c and L_c depend on the dimensionality of the problem. The shape and size of the correlated volume V_c is an ellipsoid $(4\pi/3)R_c^2 L_c$ (3D), circle πR_c^2 (or cylinder $\pi R_c^2 d$, 2D case, realized in thin films or flat specimens when pinning is sufficiently weak so that the FLs are not curved), or the length $2L_c$ (1D case, pinning of isolated FLs or dislocation lines in crystals) [9].

3rd idea. In the weak-pinning limit W and $g(\underline{r})$ may be calculated from the uncorrelated forces $\underline{f}_i$ which would act if the FLL were rigid. This means: the correlation between the FL and pin positions, which is caused by the elastic response of the FLL to the pins and without which there were no average pinning force at all, is disregarded at this step for consistency. It is here where the weak pinning assumption is required. The $g(\underline{r})$ resulting in this weak-pinning limit is proportional to W. Note that this limit even applies to an already plastically deformed FLL if only the pins are weak enough to introduce no irreversible motion of dislocations.

3. Predictions of collective pinning theory

From its basic assumptions alone, without explicit evaluation, the CP theory predicts that:

a) The critical current j_c depends only on the combination $W = n_p \langle f_i^2 \rangle$, on the range r_p, and on the elastic constants of the FLL.

b) The mean square f_p^2 of the actual pinning forces $\underline{f}_i$ enters, not the maximum force a pin can exert. Most previous summations express j_c as a function of f_{max} and n_p. In general one has $f_p < f_{max}$ except when all (strong) pins are activated.

c) j_c is the same for attractive and repulsive pins as long as these are weak. Strong attractive pins are, however, more effective since strong repulsive pins (with the sign of the pinning potential reversed) are partly avoided by the pins.

d) The threshold predicted by the "dilute-limit theories" [2, 3] does not exist, even for $n_p \to 0$, if only the number of pins is sufficiently large for the averaging to apply. In specimens containing only a few pins a threshold may appear (see the computer simulations below).

e) The CP theory only estimates the prefactor of $j_c B$ as becomes clear from the 1st idea and from the definition of V_c. This prefactor may be determined from computer simulations (see below). A further slight arbitrariness, which we had assumed in [6], namely, that the prefactor slightly depends on the shape of the pinning potential, was removed very recently by introducing a definition of r_p which applies to any pinning potential [11]. In particular, j_c may now be calculated for superconductors containing pins of various types and sizes.

The explicit results of CP theory for various dimensionalities are:

$$\text{3D:} \qquad R_c = r_p^2\, 8\pi\sqrt{c_{44}c_{66}^3}\,/W, \quad L_c = \sqrt{c_{44}/c_{66}}\,R_c \ ,$$

$$j_cB = (\sqrt{3/2}\,/32\pi^2)\, W^2/r_p^3\, c_{44}c_{66}^2 \ ,$$

$$\text{2D:} \qquad R_c = r_p c_{66}\sqrt{8\pi d\,/W \ln(R_{cut}/R_c)} \ ,$$

$$j_cB = \sqrt{\ln(R_{cut}/R_c)\,/8\pi}\,W/r_p d c_{66} \ ,$$

$$\text{1D:} \qquad L_c = 2\, r_p\, c_{44}^{3/4}\, \alpha^{1/4}\, (Wn)^{1/2} \ ,$$

$$j_cB = (Wn)^{2/3}\, 1^{1/9} \,/\, 2^{8/9}\, r_p^{4/9}\, c_{44}^{1/3} \ ,$$

where $n = B/\varphi_0$ is the FL density, R_{cut} a cut-off radius ($\approx$the half width of the specimen), c_{44} is the tilt modulus and c_{66} the shear modulus of the FLL. The Labusch parameter α in the one-dimensional case has to be determined selfconsistently writing $\alpha = j_cB/l$ where l is a length of the order of $a/2\pi$. Expressions for the cross-over 2D $\rightarrow$ 3D in films of thickness d are given in [12].

The exponents of n_p, f_p, and of the effective elastic constant c follow from general scaling arguments [13]. In cases where only the combination $W = n_p f_p^2$ enters one has for D = 1, 2, and 3:

$$j_cB \sim (n_p f_p^2)^{2/(4-D)}\, c^{-D/(4-D)} \ .$$

The applicability of this formula is discussed critically in [9].

4. Computer simulation of flux-line pinning

The observation of 2D FL pinning [8] encouraged us to perform computer simulations of 2D pinning [6]. 3D simulations require considerably more numerical effort but are within the range of modern computers and will be performed in the near future. The general 3D interaction between FL elements [14, 6] leads to the total energy of an arbitrary arrangement of curved or straight FLs:

$$U_{FLL}^{(3)} = \frac{1}{2}\sum_i \sum_j \frac{\varphi_0^2/\mu_0}{2\pi\lambda'^2}\left(\int d\underline{r}_i \int d\underline{r}_j \frac{e^{-r_{ij}/\lambda'}}{r_{ij}} - \int\left|d\underline{r}_i\right| \int\left|d\underline{r}_j\right| \frac{e^{-r_{ij}/\xi'}}{r_{ij}}\right) \ ,$$

where

$$\lambda' = \lambda/\sqrt{1-b} \qquad \text{and} \qquad \xi' = \xi/\sqrt{2-2b}$$

are effective penetration depth (λ) and coherence length ($\xi = \lambda/\kappa$) $b = B/B_{c2}$, and $r_{ij} = |\underline{r}_i - \underline{r}_j|$. The integrals are over the FLs. From this energy expression the elastic and plastic properties of the FLL may be obtained in principle. In the 2D case, i.e. for straight parallel FLs of unit length, one obtains from it the energy of an arbitrarily deformed FLL:

$$U_{FLL}^{(2)} = \sum_i \sum_{j>i} \frac{\varphi_0^2/\mu_0}{2\pi\lambda'^2} \left[K_0(r_{ij}/\lambda') - K_0(r_{ij}/\xi')\right] .$$

Note that in $U_{FLL}^{(3)}$ the self energy of the FLs is contained (the terms i=j depending on the curvature of the FL) but in $U_{FLL}^{(2)}$ it is omitted since it does not depend on the arrangement of the FLs. From $U_{FLL}^{(2)}$ the shear and compressional modulus of the (ideal or plastically deformed) FLL may be obtained and also the energy and distortion field of the edge dislocation. Note that the range λ' of the FL-FL interaction may be much larger than the FL spacing a; in this case the elastic properties of the FLL are non-local. This means that the tilt and compressional modulus depends on the wavelength of periodic distortions if this is smaller than $2\pi\lambda'$. The shear modulus for most purposes may be treated as local; c_{66} depends on the direction of shear waves only if their wavelength gets close to 4a. For this reason non-locality is not important for 2D pinning, but becomes crucial for 3D pinning in superconductors with large Ginzburg — Landau parameter κ. The 3D CP result presented in Section 3 is derived from local elasticity theory. Its non-local extension is given in [12].

For our simulation of flux pinning we use simplified potentials between FLs and between FLs and pins:

$$V_v(r) = A_v \exp(-r^2/R_v^2) ,$$

$$V_p(r) = A_p \exp(-r^2/R_p^2) .$$

From $V_v(r)$ the shear modulus follows ($\underline{R}_i$ = vectors of triangular FLL, $R_i = |\underline{R}_i|$):

$$c_{66} = (n/16) \sum_i \left[R_i^2 V_v''(R_i) + 3R_i V_v'(R_i)\right] .$$

We generate N_v FLs (ideal or amorphous lattice) and N_p randomly positioned pins in a nearly cubic area with periodic boundary conditions. The energy of this system is then

$$U = \sum_i \sum_{j>i} V_v(|\underline{r}_i - \underline{r}_j|) \sum_i \sum_j V_p(|\underline{r}_i - \underline{r}_j^p|) ,$$

where the sums are over all FL ($\underline{r}_i$) and pin positions ($\underline{r}_i^p$). Our simulation thus contains 5 parameters: The vortex and pin numbers N_v and N_p (proportional to the densities n and n_p), the range R_v of the FL-FL interaction (or the shear modulus c_{66}) and of the FL-pin interaction, R_p, and the amplitude A_p of the pinning potential. We put $A_v = 1$ (this fixes the energy scale).

The main variables of our simulation are a constant force F on all FLs (which is compensated by the total pinning force) and the mean x-coordinate of the FLs $X = \langle x_i \rangle$. We may perform dynamic or static pinning simulations. For dynamic simulations we apply a viscose force on the FLs (proportional to their velocity). Then we increase the force F gradually from zero and let the FLs move such that at each moment all forces on a FL are compensated by the viscose force. In this way we get curves X(F) or, physically more sensible, dX(F)/dt which resemble the measured current ($\sim$F) - voltage ($\sim$velocity dX/dt) curves. One of these curves is presented in Fig. 1. Note that the FL-motion starts only

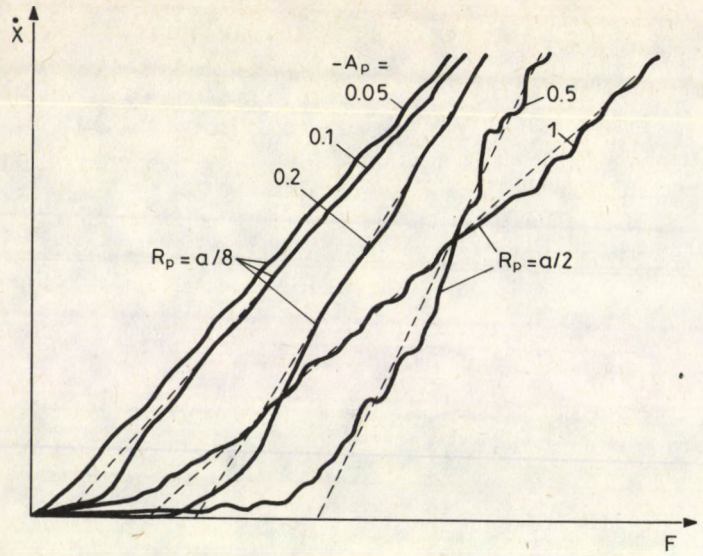

Fig. 1. Typical curves velocity X versus force F (corresponding to voltage versus current) in arbitrary units. N_v = 340 flux lines, N_p = 210 pins, R_v = 0.6a, R_p = a/8 and a/2, A_p = -0.05,-0.1,-0.2,-0.5, and -1

when the force F exceeds a critical value F_{stat}, the static pinning force, and then increases with dX/dt approximately proportional to $F - F_{dyn}$ where $F_{dyn} \approx F_{stat}$ is the dynamic pinning force. We have generated a large quantity of such curves (for various values of N_v, N_p, R_v, R_p, and A_p, and for ideal triangular and amorphous FLL) which are not yet published.

We present here the static simulations in more detail. As the first step we relax the FL positions, with the pin potentials switched on, by minimizing the energy U. In the resulting state the FLs are completely force free (all forces on each FL compensate). As a next step we apply an external force F and minimize the Gibbs potential

$$G\{\underline{r}_i\} = U - N_v F X \quad .$$

Then we increase F by a constant increment and repeat this procedure. In this way we obtain a curve X(F). However, when F reaches a critical value the FLL "runs away". Therefore, in order to get stable, fluctuating force-displacement curves F(X) we prescribe in each iteration step the mean FL displacement X and, by some feed-back mechanism, obtain the value of F which keeps the FLL at this position. At each moment the FL positions are fully relaxed. The resulting F(X) first increases linearly (slope α) and gradually goes towards a saturation value which may be interpreted as the static volume pinning force. Since our system is finite (we used up to N_v = 2000 FLs and N_p = 1000 pins) the real F(X) (Fig. 2) deviates from the idealized one by statistical fluctuations. A good value for the volume pinning force is then the average of F(X) over X, $\bar{F} = \langle F(X) \rangle$. For comparison with CP theory we

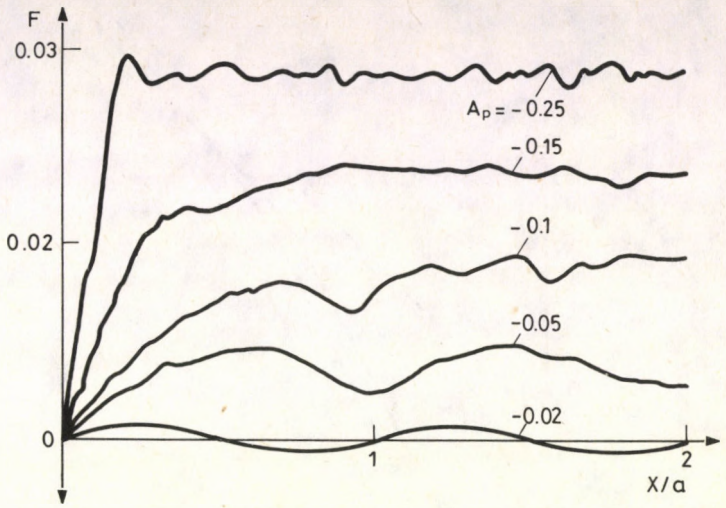

Fig. 2. Force-displacement curves of an initially periodic FLL pinned by randomly positioned attractive point pins of strength $-A_p$ and range a/4 (schematic)

also calculated the mean square W(X) of the actual pinning forces (times N_p/N_v) and average this over X getting $\bar{W} = W(X)$. From the ratio $\bar{F}/\bar{W}$ we get the prefactor of $j_c B$. This ratio was found to be constant in the limit of weak pinning. It yields a prefactor which is smaller than that in Section 3 (2D) by only a factor 0.45. This nice agreement proves the good estimate of the prefactor in 2D CP theory. (Originally, Larkin and Ovchinnikov [5] assumed $V_c \approx R_c^2 d$ rather than our improved value $V_c \approx \pi R_c^2 d$.)

Fig. 3 shows some curves $\bar{F}(A_p)$ and $\bar{W}(A_p)$ where A_p is proportional to the elementary pinning force since R_p=const. Note that for small A_p one has $W \sim A_p^2$ in agreement with the assumption in the third idea of Section 2. When the pinning strength increases, $\bar{W}$ increases more (less) than $\sim A_p^2$ for attractive (repulsive) pins, respectively. But even then in many cases, and even when we started with an amorphous FLL, we obtained $\bar{F} \sim \bar{W}$. The 2D CP result is thus more general than originally assumed if only the correct value of $W=n_p \langle f_i^2 \rangle$ (now with the actual pinning forces, with the FLL distortion considered) is taken. For weak pinning we also confirmed the relationships $\bar{F} \sim 1/c_{66}$ and $\bar{F} \sim 1/R_p$.

5. Some results of the simulation and outlook

We summarize the main results of our 2D simulation of flux-line pinning in type-II superconductors:

1. The collective-pinning formula of Larkin and Ovchinnikov, $j_c \sim n_p \langle f_i^2 \rangle / r_p c_{66}$, turns out to be valid not only for weak pinning but also in some cases for strong pinning (when the pins are repulsive or dense) and even for plastically deformed (or amorphous) FLL. The prefactor of j_c is obtained.

2. For amorphous FLL the prefactor of j_c is larger than that for the ideal (only elastically deformed FLL) by a factor 1.3 to 3. This finding explains the "history effect" and the hysteresis in $j_c(b)$. For example, if the ideal FLL is moved against sufficiently

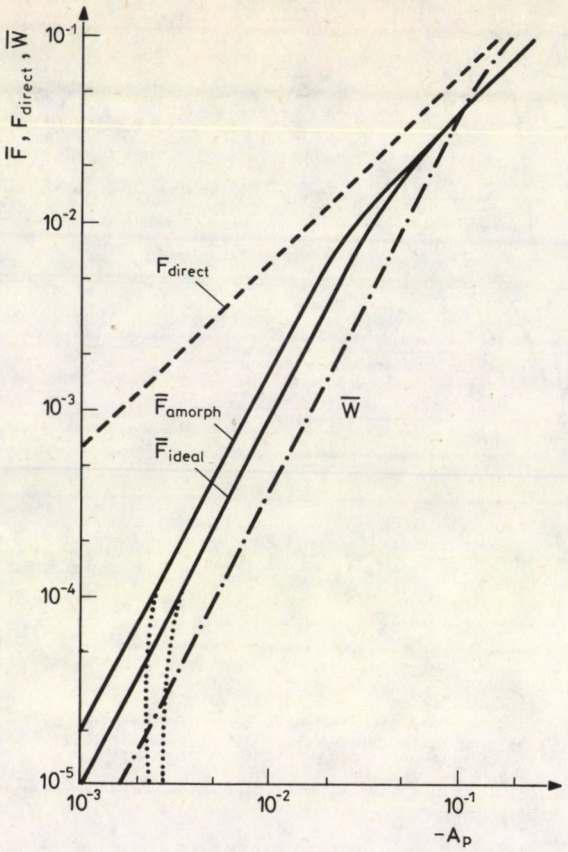

Fig. 3. The averages $\bar{F} \sim j_c$ (solid lines) and $\bar{W} \sim n_p < f_i^2 >$ (dash-dotted line) (see text) versus the pin strength $-A_p$ for attractive, randomly positioned, dense point pins ($N_p = 2N_v \approx 10^5$, $R_v = 0.6a$, $R_p = 0.25a$). $\bar{F}_{amorph}$ and $\bar{F}_{ideal}$ are for initially periodic and for amorphous flux-line lattices, respectively, extrapolated to very large systems. The dotted lines indicate the artificial threshold caused by the finiteness of our system.

$$F_{direct} = n_p f_p$$

strong pins the FLL becomes more and more deformed plastically resulting in a larger $j_c(b)$ which persists until superconductivity is destroyed, say, by rising the field or temperature. Thus j_c depends on the "history" of the specimen.

3. $j_c(A_p)$ exhibits a jump when plastic deformation sets in. As mentioned in Section 1 this jump is even more pronounced in 3D pinning. Such a jump may be interpreted as a "threshold effect". However, the original threshold, obtained in "dilute-limit" theories, is an artifact which is not observed in our simulations. In fact, we do observe a threshold; this is, however, due to the finite periodicity area we use: When the maximum relative displacement caused by the pins in the FLL within this area is smaller than the force range r_p,

then the total volume pinning force exactly vanishes. This artificial threshold value for A_p decreases with increasing periodicity area.

4. For strong pinning a modified direct summation applies:

$$j_c B \gtrsim n_p \langle f_i^2 \rangle^{1/2} = n_p f_p \ .$$

This value is in general much smaller than the original direct summation result $j_c B = n_p f_{max}$. Note that this modified direct summation formula requires the knowledge of the actual pinning forces; these depend on the deformation of the FLL and are thus not easily calculated. Therefore, for strong pinning one should look for a new summation theory or modify the CP ideas by introducing some effective correlation volume, perhaps saturating when R_c reaches the FL spacing a.

5. Many more interesting features of pinning may be investigated by this simulation: Trapping of vortices by pins (this, too, leads to a threshold effect). Extended pins, pin-walls (e.g. grain boundary pinning), and flowing of the FLL around extended pins. In all these cases it is interesting to look at the shape of the force-displacement curve F(X). The initial slope may then be much larger than $F/(a/2\pi)$, i.e. F(X) is strongly curved near X=0. In some cases F(X) goes to its saturation only very slowly, over several a. As shown in [6], even pinning by one single pin is not a trivial problem since the displacements of the FLL may become large so that non-linear elasticity comes in and computation becomes necessary.

6. A further topic on which future computer simulations should concentrate is the three-dimensional plastic properties of the FLL, in particular the critical flow stress [15, 16] at which the abrupt transition to the disordered "spaghetti state" observed in [10] sets in. An even more challenging task would be to conceive models for nucleation and proliferation of dislocations in the FLL [17]. Such models should account for the pronounced elastic non-locality and non-linearity which (besides its topological peculiarity) is characteristic for the FLL. Both analytical and numerical calculations should be based on the general interaction potential between the FL elements presented in Section 4. This pair potential accounts for both the non-local and non-linear effects: It yields the correct non-local elastic moduli of the FLL and applies also to merging or cutting FLs and to FL loops.

References

1. P.W. Anderson, Phys. Rev. Lett., 9, 309, 1962.
2. K. Yamafuji and F. Irie, Phys. Lett., A25, 387, 1967.
3. R. Labusch, Cryst. Lattice Defects, 1, 1, 1969.
4. A.M. Campbell and J.E. Evetts, Adv. Phys., 21, 199, 1972.
5. A. I. Larkin and Yu. N. Ovchinnikov, J. Low Temp. Phys., 34, 409, 1979.
6. E.H. Brandt, J. Low Temp. Phys., 53, 41 and 71; Phys. Rev. Lett., 50, 1599, 1983.
7. P.A. Lee and T.M. Rice, Phys. Rev., B19, 3970, 1979.
8. P.H. Kes and C.C. Tsuei, Phys. Rev. Lett., 47, 1930, 1981; Phys. Rev., B28, 5126, 1983.
9. E.H. Brandt, Phys. Rev. Lett., 56, 1381, 1986.
10. R. Wördenweber and P.H. Kes, Phys. Rev. B., 34, 494, 1986.
11. E.H. Brandt, Phys. Rev. Lett., 57, 1347, 1986.
12. E.H. Brandt, J. Low Temp. Phys., 64, 375, 1986.
13. H.R. Hilzinger, Phil. Mag., 36, 225, 1977.
14. E.H. Brandt, J. Low Temp. Phys., 26, 709, 735; 28, 263, 291, 1977.
15. A. Seeger, Handbuch der Physik (Springer, Berlin, 1955, 1958), Vol. VII, 1, 1955, Vol. II, 2, 1958.
16. R. Schmucker, Phil. Mag., 35, 430, 1977.
17. S.J. Mullock and J.E. Evetts, J. Appl. Phys., 57, 2588, 1985.

Acta Physica Hungarica 63(1–2), pp. 187–193 (1988)

ANALOGIES BETWEEN GRANULAR SUPERCONDUCTORS AND SPIN-GLASSES*

J. ROSENBLATT

Laboratoire de Physique des Solides
U.A. N° 040786, INSA, BP 14A, F 35043 RENNES-CEDEX

(Received 20 October 1987)

Scaling in the transition to coherence of randomly coupled granular superconductors is described by critical exponents unexpectedly close to those reported for the spin-glass transition. We discuss a model of non-homogeneous transitions, localised in the regions of highest coupling energy in the sample. Thermal exponents are expressed in terms of percolation exponents; the numerical values thus obtained are in good agreement with the experimental ones.

1. Introduction

The transition to phase coherence [1] in granular superconductors may depend strongly on grain size when the latter is of the order of a few nanometres [2 – 5]. In particular, charge fluctuations across the junctions may be deleterious for coherence [3,5]. In order to reduce the problem to its very essentials, we have simply pressed together large (tens of micrometers) oxidized grains in an epoxy matrix. In this way we obtain three-dimensional (3D) arrays of about 10^8 superconducting junctions. The grains are bulk superconductors, so the amplitude fluctuations of the order parameter are negligible. The behaviour of the whole system is rather governed by phase fluctuations in the weakly coupled grains. Furthermore the large size of the grains results in large capacities and therefore very small charge fluctuations.

It is easily shown then [6] that the tunnelling Hamiltonian of the grains is

$$H = -\sum_{<rr'>} J_{rr'} S_r^+ S_{r'}^- - 2\mu_0 \sum_i S_{zi} \quad . \tag{1.1}$$

Here the $J_{rr'}$ are Josephson coupling energies of junctions of normal resistance $R_{rr'}$ between first neighbours located at points indicated by primed and unprimed subscripts:

$$J_{rr'} = \frac{R_0}{R_{rr'}} \Delta(T) \tanh \Delta(T)/2k_BT \quad , \tag{1.2}$$

where $R_0 = \pi\hbar/4e^2 = 3250\ \Omega$. The quantity μ_0 is the pair chemical potential, $S_r^\pm = S_{xr} \pm S_{yr}$ are pair destruction and creation operators in grain r, while S_{zi} is a pair number operator: $S_{zi} = \pm 1/2$ indicates the absence or presence of a Cooper pair in grain i. They satisfy spin commutation relations:

$$[S_{zj}, S_k^+] = \pm S_j^+ \delta_{kj} \quad , \qquad [S_j^+, S_k^-] = 2S_{zj} \delta_{kj} \quad . \tag{1.3}$$

---

*Presented at CRYOSEM'86, IIIrd International Seminar on Low-Temperature Physics, Visegrád, Hungary, 26–31 May 1986

Acta Physica Hungarica 63, 1988
Akadémiai Kiadó, Budapest

Equations (1.1) and (1.3) characterize equally well a ferromagnet with neighbouring spins coupled only through their x- and y- components, i.e., the X – Y model. In analogy with the ferromagnetic phase transition, the zero-resistance (and phase coherent) state is reached below a critical temperature $T_c < T_{cg}$ where T_{cg} is the superconducting critical temperature of individual grains. As T_c is approached from above or from below, the susceptibility, the order parameter and the specific heat display non analytic behaviour, i.e. they follow power laws in $t = |T - T_c|$ with non integral critical exponents $-\gamma$, β and $-\alpha$, respectively. The spin – spin correlation function $< S_0^+ S_r^- > - < S^+ >< S^- > = D(r/\xi)/r^{d-2+\eta}$, where η is still another exponent and d the dimensionality of space. At $T \neq T_c$ the correlation length $\xi(T) \sim t^{-\nu}$ describes the decay of the correlation function with distance through the function $D(r/\xi)$.

The critical exponents must satisfy the scaling relations:

$$d\nu = 2 - \alpha = 2\beta + \gamma \quad ; \qquad \tilde{\gamma} = \gamma/\nu = 2 - \eta \quad , \tag{1.4}$$

which show that two exponents suffice to obtain all the others. In our case we rather had to test if the exponents obtained experimentally were indeed those of a second order phase transition, which led us to measure four of them. We show in Section 2 that the values obtained are unexpectedly different from those calculated for the X – Y model but similar to those reported for spin-glasses. We discuss a possible model for this behaviour in Section 3. Concluding remarks are made in Section 4.

2. Spin-glass and random network exponents

We shall not dwell here on the specific physical phenomena connected with the critical exponents of the arrays [7,8]. We simply recall that (i) the Josephson penetration depth of a 3D array [8]

$$\lambda_J \sim t^{-\beta} \quad , \qquad T < T_c \quad ; \tag{2.1}$$

(ii) the critical current density [7,8]

$$j_c \sim t^{2\beta+\nu} \quad , \qquad T < T_c \quad ; \tag{2.2}$$

(iii) the excess conductivity of a Josephson junction between the granular sample and a bulk metal, at $T > T_c$ [9], as well as that of the granular sample itself [10].

$$\Delta\sigma = \sigma - \sigma_N \sim t^{-\gamma} \quad , \qquad T > T_c \quad ; \tag{2.3}$$

(iv) the voltage – supercurrent characteristic at $T = T_c$ [10]

$$V \sim I_S^a \quad , \qquad a = \frac{d+1}{d-1+\eta} = \frac{4}{2+\eta} \quad , \tag{2.4}$$

provide the basis for the determination of four exponents from electromagnetic measurements. By using "alloys" of Nb and Ta grains of different sizes we could recently follow the transition of only a fraction of the sample [11] and obtain a rather precise and direct measurement of η.

The experimental results can be summarized as follows: $\beta = 0.7 \pm 0.1$, $2\beta + \nu = 2.5 \pm 0.3$, $\gamma = 2.8 \pm 0.3$, $\eta = 0.027 \pm 0.015$. The first two give $\nu = 1.1 \pm 0.3$ ($T < T_c$, cf. (i) and (ii)) while from (iii) and (iv) and (1.4) $\nu = \gamma/(2-\eta) = 1.4 \pm 0.2$ ($T \geq T_c$). The scaling relations (1.4) are satisfied within the experimental error. We are then justified in imposing that ν should verify hyperscaling through $2\beta + \nu + \gamma = (d+1)\nu = 5.3 \pm 0.5$ to get $\nu = 1.3 \pm 0.1$ from (ii) and (iii) above. The remaining exponents are obtained similarly; they are shown in Table I. On the other hand, several authors have reported a scaling behaviour of spin-glass transitions [12]; the corresponding exponents, also shown in Table I, are strikingly close to ours.

Table I

Random granular superconductor (RGS), spin-glass (SG) and model calculated critical exponents

	β	γ	ν	η	δ
X–Y model[a]	0.346 ± 0.001	1.316 ± 0.001	0.6693 ± 0.001	0.0335 ± 0.0025	4.805[b] ± 0.015
RGS	0.68 ± 0.05	2.6 ± 0.2	1.3 ± 0.1	0.027 ± 0.01	4.84 ± 0.1[b]
Fractal model	0.69 ± 0.02	2.62 ± 0.1	1.33 ± 0.05	$0.0335 \pm 0.0.0025$	4.805 ± 0.015
Cu Mn 4.6%[c]	1.1 ± 0.2	3.4 ± 0.4	1.8 ± 0.2		4.2 ± 0.1
Cu Mn 1%[c]	0.75 ± 0.1	3.25	1.6 ± 0.1		5.7 ± 0.5
Al Gd 37%[c]	0.6 ± 0.1	2.7 ± 0.1	1.3 ± 0.1		5.7 ± 0.2
Mn-alumina[c]	1.4 ± 0.1	3.1 ± 0.1	2 ± 0.2		

[a] Le Guillou and Zinn-Justin, Ref. [22]
[b] Calculated from $\delta = (d+2-\eta)/(d-2+\eta)$
[c] SG results quoted by Tholence, Ref. [12]

This apparent universality is surprising in view of a number of features of spin glasses not shared by arrays. The interactions are believed to be long-range in the former, while manifestly they exist only between first neighbours in the latter. An important property of spin glasses is frustration [13], absent from granular superconductors under zero field [14,15]. On the other hand, the most conspicuous common feature to the two systems is randomness in the coupling energies. However, as discussed in the next Section, one would not expect, on the basis of the Harris criterion [16], that disorder should affect the pure system exponents of the X – Y model, also shown in Table I. A possible way out of thsi paradox is discussed in the next Section.

3. Localized phase transitions

3.1 Relevance of disorder

Consider the exact result of statistical mechanics

$$\langle \Delta E^2 \rangle = k_B T^2 C_V \quad , \tag{3.1}$$

relating the energy fluctuation in a volume V to the heat capacity of this volume. If we take $V = \xi^d$, recalling Eq. (1.1),

$$\sum_{\substack{<rr'> \\ <nn'>}} J_{rr'}\, J_{nn'} \langle \Delta(S_r^+ S_{r'}^-) \Delta(S_n^+ S_{n'}^-) \rangle \sim \xi^{d+\tilde{\alpha}} = \xi^{2/\nu} \quad , \tag{3.2}$$

where $\tilde{\alpha} = \alpha/\nu$ and the last equation follows from the scaling relations (1.4). Hereafter a summation over first neighbours of summed indices will be simply indicated by a primed sum sign. The singularity in the specific heat results from the scaling properties of the correlation function between pairs of spins, which gives, in the above notation:

$$\sum_r{}' \langle \Delta(S^+ S^-)_0 \Delta(S^+ S^-)_r \rangle \sim \xi^{\tilde{\alpha}} \quad . \tag{3.3}$$

Now, let us define:

$$\Delta J_{rr'} = J_{rr'} - \bar{J} \quad , \tag{3.4}$$

$$\sum_r{}' \overline{\Delta J_0 \, \Delta J_r} \sim \xi^{d-a} \quad , \tag{3.5}$$

where the upper bar indicates a spatial average in a region of linear size ξ. The exponent a is a measure of the degree of correlation in the J's [17]. If they are independent random variables,

$$\overline{\Delta J_{00'} \, \Delta J_{rr'}} = \overline{\Delta J^2} \, \delta_{0r} \, \delta_{0'r'} \tag{3.6}$$

and a = d. For a homogeneous system a = 0, indicating that the sum in Eq. (3.5) increases as the number of points in the lattice.

Let us assume that intermediate values of a are also possible and study their relation with critical exponents. Consider the energy fluctuation $\langle \Delta E_0^2 \rangle$ of the ordered system having all couplings equal to $\bar{J}$ and specific heat exponent α_0. Then for disorder to be irrelevant, that is for the system described by (3.4) and (3.5) to have the same critical exponents as the homogeneous system,

$$\langle \Delta E^2 \rangle - \langle \Delta E_0^2 \rangle \sum_{rn'}{}' \overline{\Delta J_r \, \Delta J_n} \langle \Delta(S^+ S^-)_r \Delta(S^+ S^-)_n \rangle \sim \xi^{d-a+\tilde{\alpha}_0} \to 0 \tag{3.7}$$

as $T \to T_c$, that is

$$a \geq d + \tilde{\alpha}_0 = 2/\nu_0 \quad . \tag{3.8}$$

When a = d, as in (3.6), Eq. (3.8) becomes $\alpha_0 \leq 0$, the well-known Harris criterion [16]. In the general case it is equivalent to extending the latter to "correlated" disorder [17].

What happens when $a < 2/\nu_0$? If there is still a transition, it should have a different correlation length exponent $\nu(a)$, say. Suppose we replace a fraction s of the J's by new values (or a rearrangement of the old ones) $J^s_{rr'}$, such that $\overline{\Delta^s J_{rr'}} = \overline{J^s_{rr'} - J_{rr'}} = 0$. At the same time the $\Delta^s J$'s are chosen to have $\sum_r \overline{\Delta^s J_0 \, \Delta^s J_r} \sim L^{d-a_s}$ in large regions L^d. At least a fraction of the system keeps the original exponent a. Finally assume that the exponent $\nu(a)$ is not affected by all these operations. The difference between new and old energy fluctuations is

$$<\sum_s \Delta^s E^2> - <\Delta E^2> \sim \sum_s C_s \xi^{2/\nu - a_s} \quad , \tag{3.9}$$

where C_s are constants. This should not increase $(a_s \geq 2/\nu)$ when $T \rightarrow T_c$, if it is to be consistent with the assumption $\nu = \nu$ (a). Furthermore, as $\xi \rightarrow \infty$ only the terms with the smallest a_s survive in Eq. (3.9), i.e. [17]:

$$\nu(a) = 2/a \quad , \qquad a = \min\{a_s \geq 2/\nu\ (a)\} \quad . \tag{3.10}$$

Indeed, if the first Eq. (3.10) were not true, the presence of an $a_s < a$ would have induced a change in the exponents, contrary to our assumption. Conversely the exponent ν is determined by that fraction of the system which displays the slowest rate of decrease of the bond-bond correlation function.

3.2 Fractal segregation from random couplings

Intermediate values of a, between 0 and d, can in principle show up in fractal [18] objects. For example, the infinite percolation cluster near the threshold has a fractal dimensionality [19]

$$D = d - \tilde{\beta}_p \quad , \tag{3.11}$$

where $\tilde{\beta}_p = \beta_p / \nu_p$ is a quotient between percolation critical exponents. If the system is restricted to this D-dimensional cluster with independent random couplings as in Eq. (3.6), $a = D < d$.

Now, let Q be an extensive quantity with density $q \sim t^{-\varphi}$, singular for an infinite system in d dimensions. However, if the singularity in q is due to non analyticities restricted to D-dimensional clusters embedded in d-dimensional space, finite size scaling implies, for a finite volume L^d,

$$Q_L = L^d q \sim L^{d+\tilde{\varphi}} \sim L^{D + \tilde{\varphi} + \tilde{\beta}_p} \tag{3.12}$$

which gives the density in D-dimensional clusters and defines a cluster exponent [20]:

$$Q_L / L^D \sim t^{-\varphi_c} \quad , \qquad \varphi_c = \varphi + \nu \tilde{\beta}_p \quad . \tag{3.13}$$

It is worth pointing out that cluster exponents, defined as in (3.13) satisfy scaling in D dimensions:

$$D = (2/\nu) - \tilde{\alpha}_c = 2\tilde{\beta}_c + \tilde{\gamma}_c = 2\tilde{\beta}_c + 2 - \eta_c \quad , \tag{3.14}$$

that is, they are the critical exponents of a phase transition in D dimensions. In particular, $\nu = \nu\ (D) > \nu\ (d)$ [21].

When the steps leading to (3.7) and (3.8) are retraced for a fractal, one finds

$$<\Delta E^2> - <\Delta E_0^2> \sim \xi^{D-a+\tilde{\alpha}_{c0}} = \xi^{d-a+\tilde{\alpha}_0} \quad , \tag{3.15}$$

where the last expression results from (3.11) and (3.13). We obtain

$$a \geq D + \tilde{\alpha}_{c0} = 2/\nu_0 \quad (D) \tag{3.16}$$

as a condition for stability of the pure (though fractal) system exponents against disorder. For independent random couplings in fractal space a = D and the condition becomes $\tilde{\alpha}_{c0} = \tilde{\alpha}_0 + \tilde{\beta}_p \leq 0$; in other words, a d-dimensional system may be thought to be insensitive to disorder because $\nu_0 > 2/d$ ($\alpha_0 < 0$) but actually be the site of an underlying fractal transition in a "correlated" region with $2/a = \nu > 2/D > \nu_0(D) > \nu_0(d) > 2/d$.

We believe this to be the case of our random X – Y samples. For ordered systems the value of $\nu_0(d = 3)$ has been calculated [22] and measured [23]; from $\alpha_0 = 2 - d\nu_0$ the corresponding α_0-values are -0.0079 ± 0.003 and -0.025 ± 0.003, respectively. Since both are negative within the announced confidence limits, we should conclude, in the light of Harris's criterion that disorder has nothing to do with the observed exponents. We argue, however, that $\tilde{\beta}_p \simeq 0.5$ [19] and therefore $\tilde{\alpha}_0 + \tilde{\beta}_p > 0$, i.e. disorder is relevant in fractal percolation clusters. The question is how to define a meaningful percolation parameter p. We remark that the regions of the sample with the highest coupling energies will be the most effective in defining the critical properties. This justifies taking as a possible percolation parameter the probability $p(J^*) = \text{Prob}\ (J_{rr'} > J^*)$. The clusters thus defined have an average bond energy $\bar{J}^* > J^*$. If the distribution of J-values is large enough, they interact with their surroundings through bonds of the order of $\bar{J} \ll \bar{J}^*$. Defining the differences $\Delta^* J_{rr'} = J_{rr'} - J^*$, the double sum

$$\sum_{rn} \overline{\Delta^* J_r \ \Delta^* J_n} \sim \sum_s s^2 p_s \sim \xi_p^{2d-3\tilde{\beta}_p} \tag{3.17}$$

simply goes as the number of pairs of elements in percolation clusters of all sizes. This is $s(s-1) \simeq s^2$ in a cluster of s elements, while p_s above is the probability of belonging to such a cluster. The last expression in Eq. (3.17) results from the scaling properties of percolation clusters [19]. A comparison with Eq. (3.5) suggests immediately

$$a = 3\tilde{\beta}_p \ , \qquad \xi(T) \sim \xi_p \sim (p_c - p)^{-\nu_p} \ . \tag{3.18}$$

Percolation and thermal correlation lengths increase simultaneously as T_c is approached, which allows (3.10) to be satisfied. From (3.18) and (3.10) $\nu = 2\nu_p/3\beta_p = 1.33 \pm 0.05$ using numerical values for percolation exponents quoted by Essam [19]. The agreement with the experimental result is extremely good, as can be seen from Table I. Now, if the scaling relations (1.4) are to be satisfied, the ratios $\tilde{\beta} = \beta/\nu$, $\tilde{\gamma} = 2 - \eta$ should not be affected by disorder. Consequently, the exponent $\eta = 0.033 \pm 0.003$ calculated for an ordered system [22] should apply also to random arrays. This (cf. Table I) is actually the case.

We must emphasize that the condition $J > J^*$, although physically plausible for a ferromagnet is by no means the only possible one. In a different system the definition of p may result from other criteria, but would give the same exponents if Eq. (3.18) applies. For example, the obvious extension of the present ideas to spin glasses, where ferromagnetic and antiferromagnetic interactions coexist, is to define a percolation parameter $p = \text{Prob}\ (|J| > J^*)$.

4. Discussion

Table I shows that the agreement between calculated and experimental values is not so good for spin glasses as it is for random networks. Since the primed summation in Eq. (3.5) included only first neighbours, one is tempted to imagine that correlations due to longer range interactions are at work in actual spin glasses. In any case, it is worth pointing out that the percolation description given here would become incompatible with an exponent a in Eq. (3.5) that could imply a rate of decrease of the correlation function between the Δ J's, slower than that of the pair connectedness [19]. This gives a lower bound, $2\tilde{\beta}_p$, for a and an upper bound ν_p/β_p, for ν. The maximum 3D value of $\nu \simeq 2$ is not in contradiction with the results shown in Table I for spin glasses. This upper bound coincides with the minimum (mean field) value of $\nu = \frac{1}{2}$ for d = 6, which is thus the upper critical dimensionality; then D = 4, while the condition $D\nu - 2 \geq 0$ (cf. Eq. (3.16)) corresponds to the irrelevance of disorder in percolation clusters. This is another, more theoretical, test of the consistency of the present description.

References

1. P. Pellan, G. Dousselin, H. Cortes and J. Rosenblatt, Sol. St. Comm., 11, 427, 1972.
2. B. Abeles, P. Sheng, M.I. Coutts and Y. Arie, Adv. Phys., 23, 407, 1975.
3. E. Simanek, Sol. St. Comm., 31, 419, 0979.
4. G. Deutscher, Y. Imry and L.C. Gunther, Phys. Rev., B 10, 4598, 1974.
5. B.G. Orr, H.M. Jaeger, A.M. Goldman and C.G. Kuper, Phys. Rev. Lett., 56, 378, 1986.
6. J. Rosenblatt, A. Raboutou and P. Pellan, Proc. of LT 14, ed. by M. Krusius and M. Vuorio, North Holland, Amsterdam, 1975, Vol. 2, p. 361.
7. J. Rosenblatt in Percolation, Localization and Superconductivity, ed. by A.M. Goldman and S.A. Wolf, NATO A.S.I. Series, Plenum Press N.Y., 1984, 9. 431.
8. A. Raboutou, J. Rosenblatt and P. Peyral, Phys. Rev. Lett., 45, 1035, 1980.
9. J. Rosenblatt, P. Peyral and A. Raboutou, Phys. Lett., 98A, 463, 1983.
10. C. Lebeau, J. Rosenblatt, A. Raboutou and P. Peyral, Europhys. Lett., 1, 313, 1986.
11. P. Peyral, A. Raboutou, C. Lebeau and J. Rosenblatt, to be published in J. Phys. C.
12. J.L. Tholence, Proceedings of LT 17, Physica 126B, 157, 1984.
13. G. Toulouse, Commun. Phys., 2, 155, 1977.
14. W.Y. Shih, C. Ebner and D. Stroud, Phys. Rev., B 30, 134, 1984; C. Ebner and D. Stroud, Phys. Rev., B29, 5053, 1983.
15. J. Sajeev and T.C. Lubensky, Phys. Rev. Lett., 55, 1014, 1985.
16. A. Brooks Harris, J. Phys. C7, 1671, 1974.
17. A. Weinrib and B.I. Halperin, Phys. Rev., B 27, 413, 1983.
18. B.B. Mandelbrot, "The Fractal Geometry of Nature", Freeman, San Francisco, 1982.
19. D. Stauffer, Phys. Rep., 54, 1, 1979; J.W. Essam, Rep. Prog. Phys., 43, 53, 1980.
20. J. Rosenblatt, Phys. Rev., B28, 5316, 1983.
21. M. Susuki, Phys. Lett., A38, 23, 1972, Prog. Theor. Phys., 69, 65, 1983.
22. J.C. Le Guillou and J. Zinn-Justin, Phys. Rev. Lett., 39, 95, 1977.
23. K.H. Mueller, F. Pobell and G. Ahlers, Phys. Rev. Lett., 34, 513, 1975.

Acta Physica Hungarica 63(1–2), pp. 195–200 (1988)

SHORT COMMUNICATION

TOTAL ELASTIC AND DIFFUSION CROSS-SECTIONS OF e^+ - H SCATTERING USING STONE'S POLARIZED ORBITAL METHOD

M. A. ABDEL-RAOUF
Institute for Theoretical Chemistry, Friedrich-Alexander University Erlangen-Nürnberg, 8520 Erlangen, West Germany

(Received 13 July 1987)

This letter is concerning with the calculation of the total elastic and diffusion cross-sections of the scattering of positrons by hydrogen atoms using Stone's polarized orbital method. For this purpose, we can easily derive the method from the preceeding paper [1] by setting the second term at the right-hand-side of Eq. (15a) equal to zero. Thus, we deal with the following differential equation

$$\left(\frac{d^2}{dx^2} - \frac{\ell(\ell+1)}{x^2} + k_1^2\right) f_\ell(x) = U_x^{(1)} f_\ell(x) \quad , \tag{1}$$

where

$$U_x^{(1)} = V_{1,1}^{(1)}(x) + V_{pol}^{(1)}(x) \quad , \tag{2}$$

and $V_{1,1}^{(1)}(x)$ and $V_{pol}^{(1)}(x)$ can be determined using Eqs (7a) – (10) of [1].

Following Eq. (20a) [1], the iterative solution of Eq. (1) is given by

$$f_\ell^\nu(x) = \left\{1.0 + \frac{1}{k_1}\int_0^x \tilde{g}_\ell(k_1x')\, U_{x'}^{(1)}\, f_\ell^{\nu-1}(x')\, dx'\right\} \tilde{f}_\ell(k_1x) -$$

$$- \frac{\tilde{g}_\ell(k_1x)}{k_1}\int_0^x \tilde{f}_\ell(k_1x')\, U_{x'}^{(1)}\, f_\ell^{\nu-1}(x')\, dx' \quad , \quad \nu \geq 1 \tag{3}$$

and

$$f_\ell^0(x) = \tilde{f}_\ell(k_1x) \quad . \tag{4}$$

The position vector x and the functions $\tilde{f}_\ell(k_1x)$, $\tilde{g}_\ell(k_1x)$, as well as the momentum k_1 are defined as in [1]. The only difference is that k_1 varies between zero and 0.7, i.e. below the rearrangement channel. Therefore, the iterative solution of Eq. (1) can be written as

$$f_\ell^\nu(x) = a_\ell^\nu \tilde{f}_\ell(k_1x) + b_\ell^\nu \tilde{g}_\ell(k_1x) \quad , \tag{5}$$

which provides us with the ℓ-wave scattering phase shifts, η_ℓ^ν, through the relation

$$\tan(\eta_\ell^\nu) = b_\ell^\nu / a_\ell^\nu \quad . \tag{6}$$

The total elastic and diffusion cross-sections, σ_{el}^ν and σ_{diff}^ν, respectively, are defined by

$$\sigma_{el}^{\nu} = \frac{4\pi}{k_1^2} \sum_{\ell} (\ell+1) \sin^2(\eta_\ell^{\nu}) \quad , \tag{7a}$$

$$\sigma_{diff}^{\nu} = \frac{4\pi}{k_1^2} \sum_{\ell} (\ell+1) \sin^2(\eta_\ell^{\nu} - \eta_{\ell+1}^{\nu}) \quad . \tag{7b}$$

The calculation of $f_\ell^{\nu}(x)$, a_ℓ^{ν} , b_ℓ^{ν} is carried out using the iteration procedure described in [1] Appendix 2. Table I demonstrates the convergence of the S- and P-wave phase shifts with the increase in the integration range (X). The results are obtained after two interations. From the Table we notice that the phase shifts become stationary with respect to the variation of n when the integration range is equal to 32 a.u. away from the proton. Table II contains all partial wave phase shifts computed with this integration range for a large number of values of k_1 in the range $0 \leq k_1 \leq 0.7$ a.u. It is obvious that the phase shifts corresponding to $\ell \geq 2$ increase steadily with k_1 while the S- and P-wave phase shifts reach their maximum values at $k_1 = 0.16$ and 0.54, respectively. Fig. 1 contains a comparison between the behaviours of the S-, P- and D-wave phase shifts with the increase of k_1. Table III involves the S-, P-, D-, and G-wave phase shifts calculated by Winick and Reinhardt [2] using the moment T-matrix method in which an elaborate L^2-trial wave function was employed. The number of terms of this wave function was varying between 76, for the F-wave, and 105, for the S-wave, terms of Hylleraas' functions. Comparing Tables II and III, we conclude the following points:

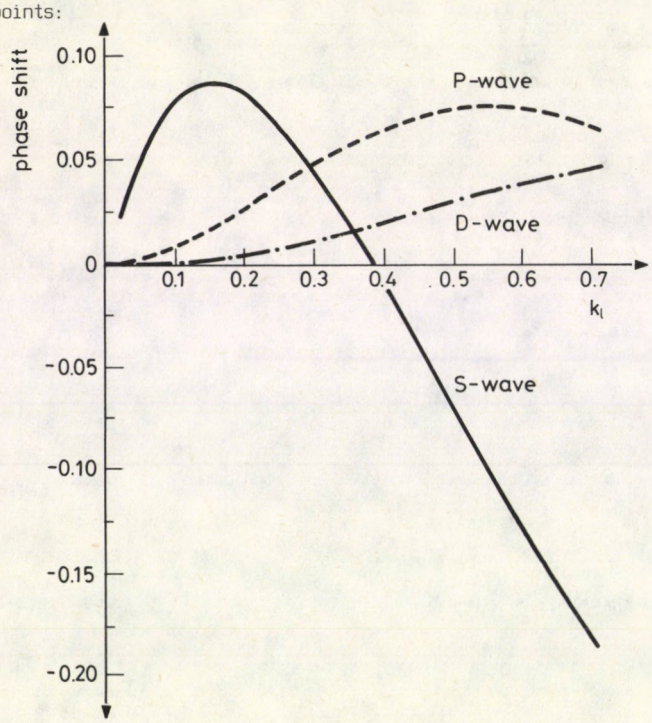

Fig. 1

Table I

Convergence of η_0 and η_1, at k = 0.2 a.u, with the increase of the range of integration

n	Integration range in a.u.	η_0	η_1
128	8	0.0805699	0.0271153
160	10	0.0806635	0.0271573
240	15	0.0806817	0.0271898
320	20	0.0806826	0.0271925
480	30	0.0806823	0.0271923
512	32	0.0806822	0.0271922
800	50	0.0806822	0.0271922

Table II

Phase shifts of e^+-H elastic scattering as functions of the momentum of the incident positrons. (Stone's method is used)

k_1(a.u.)	η_0	η_1	η_2	η_3	η_4	η_5	η_6
0.00	-1.29244*						
0.02	0.02383	0.00037	0.00005	0.00002	0.00001	0.00000	0.00000
0.04	0.04349	0.00143	0.00022	0.00007	0.00003	0.00002	0.00001
0.06	0.05904	0.00313	0.00049	0.00016	0.00007	0.00004	0.00002
0.08	0.07077	0.00540	0.00086	0.00029	0.00013	0.00007	0.00004
0.10	0.07901	0.00817	0.00135	0.00045	0.00020	0.00011	0.00007
0.12	0.08415	0.01139	0.00195	0.00065	0.00029	0.00016	0.00010
0.14	0.08655	0.01497	0.00265	0.00088	0.00040	0.00022	0.00013
0.16	0.08657	0.01884	0.00346	0.00115	0.00052	0.00028	0.00017
0.18	0.08451	0.02294	0.00438	0.00146	0.00066	0.00036	0.00021
0.20	0.08068	0.02719	0.00541	0.00180	0.00082	0.00044	0.00026
0.22	0.07533	0.03153	0.00653	0.00218	0.00099	0.00053	0.00032
0.24	0.06868	0.03590	0.00776	0.00260	0.00118	0.00063	0.00038
0.26	0.06092	0.04021	0.00908	0.00306	0.00138	0.00074	0.00045
0.28	0.05226	0.04443	0.01049	0.00355	0.00161	0.00086	0.00052
0.30	0.04282	0.04851	0.01199	0.00408	0.00184	0.00099	0.00059
0.32	0.03274	0.05239	0.01357	0.00464	0.00210	0.00113	0.00068
0.34	0.02215	0.05603	0.01521	0.00525	0.00237	0.00127	0.00076
0.36	0.01115	0.05940	0.01692	0.00589	0.00266	0.00143	0.00086
0.38	-0.00018	0.06247	0.01868	0.00656	0.00297	0.00159	0.00095
0.40	-0.01175	0.06523	0.02049	0.00727	0.00329	0.00177	0.00106
0.42	-0.02350	0.06764	0.02233	0.00802	0.00363	0.00194	0.00117
0.44	-0.03535	0.06970	0.02419	0.00880	0.00399	0.00214	0.00128
0.46	-0.04727	0.07140	0.02607	0.00961	0.00437	0.00233	0.00140
0.48	-0.05921	0.07273	0.02795	0.01045	0.00476	0.00255	0.00152
0.50	-0.07112	0.07371	0.02982	0.01132	0.00517	0.00277	0.00166
0.52	-0.08297	0.07433	0.03168	0.01222	0.00560	0.00300	0.00179
0.54	-0.09473	0.07460	0.03350	0.01315	0.00604	0.00323	0.00193
0.56	-0.10637	0.07452	0.03529	0.01410	0.00650	0.00348	0.00208
0.58	-0.11787	0.07412	0.03703	0.01507	0.00698	0.00374	0.00223
0.60	-0.12921	0.07340	0.03872	0.01606	0.00747	0.00400	0.00239

Table II (cont.)

k_1(a.u.)	η_0	η_1	η_2	η_3	η_4	η_5	η_6
0.62	-0.14037	0.07238	0.04034	0.01706	0.00798	0.00428	0.00255
0.64	-0.15134	0.07108	0.04188	0.01807	0.00850	0.00456	0.00272
0.66	-0.16210	0.06951	0.04334	0.01910	0.00904	0.00486	0.00290
0.68	-0.17265	0.06768	0.04473	0.02013	0.00959	0.00516	0.00308
0.70	-0.18297	0.06562	0.04601	0.02116	0.01016	0.00547	0.00327

*Scattering length

Table III

Winick – Reinhardt's phase shifts of e^+-H elastic scattering as functions of the momentum of the incident positrons. (T-matrix method is used)

k_1(a.u.)	η_0	η_1	η_2	η_3	η_4
0.1	0.147	0.0073	0.00044	0.00000	0.00000
0.2	0.178	0.0321	0.0050	0.00000	0.00000
0.3	0.160	0.064	0.0124	0.0036	0.00000
0.4	0.120	0.098	0.0235	0.0069	0.00289
0.5	0.062	0.130	0.0386	0.117	0.00466
0.6	0.0015	0.155	0.0587	0.0185	0.00733
0.7	-0.053	0.171	0.0858	0.0291	0.0111

η_0 is determined by employing 105 Hylleraas' functions
η_1 is determined by employing 87 Hylleraas' functions
η_2 is determined by employing 100 Hylleraas' functions
η_3 is determined by employing 76 Hylleraas' functions
η_4 is determined by employing 87 Hylleraas' functions

Table IV

Total elastic and diffusion cross-sections of e^+-H scattering determined by Stone's method (a_0^2 units are used)

k_1(a.u.)	σ_{el}	σ_{dif}	k_1(a.u.)	σ_{el}	σ_{dif}
0.00	20.9908	0.0	0.26	1.6841	0.4627
0.02	17.8558	17.3030	0.28	1.4940	0.4051
0.04	14.8946	13.9078	0.30	1.3637	0.4064
0.06	12.2615	10.9512	0.32	1.2797	0.4503
0.08	9.9967	8.4605	0.34	1.2310	0.5235
0.10	8.0938	6.4150	0.36	1.2088	0.6157
0.12	6.5240	4.7722	0.38	1.2061	0.7186
0.14	5.2488	3.4810	0.40	1.2172	0.8259
0.16	4.2277	1.4890	0.42	1.2378	0.9328
0.18	3.4211	1.7469	0.44	1.2645	1.0358
0.20	2.7932	1.2099	0.46	1.2947	1.1326
0.22	2.3121	0.8387	0.48	1.3264	1.2215
0.24	1.9502	0.5992	0.50	1.3583	0.3016
			0.52	1.3894	1.3723

Table IV (cont.)

k_1(a.u.)	σ_{el}	σ_{dif}
0.54	1.4188	0.4337
0.56	1.4461	1.4858
0.58	1.4711	1.5292
0.60	1.4935	1.5642
0.62	1.5133	1.5914
0.64	1.5305	1.6116
0.66	1.5452	1.6252
0.68	1.5575	1.6331
0.70	1.5674	1.6357

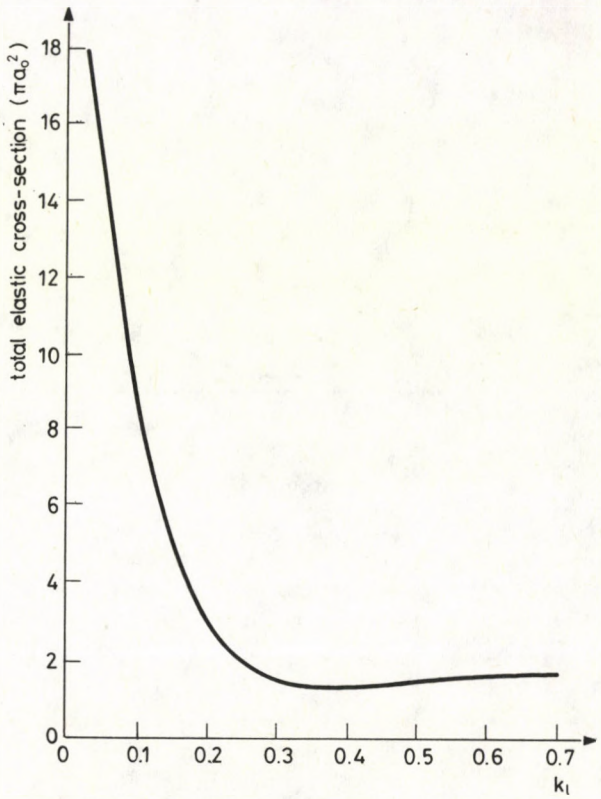

Fig. 2

a) The F- and G-wave phase shifts of both Tables are in good agreement with each other, which emphasizes that polarisations are the only important effects in the higher partial wave collisions.

b) The D-wave phases of both Tables agree with each other at $k_1 \leq 0.4$ and diverge steadily at large values of k_1.

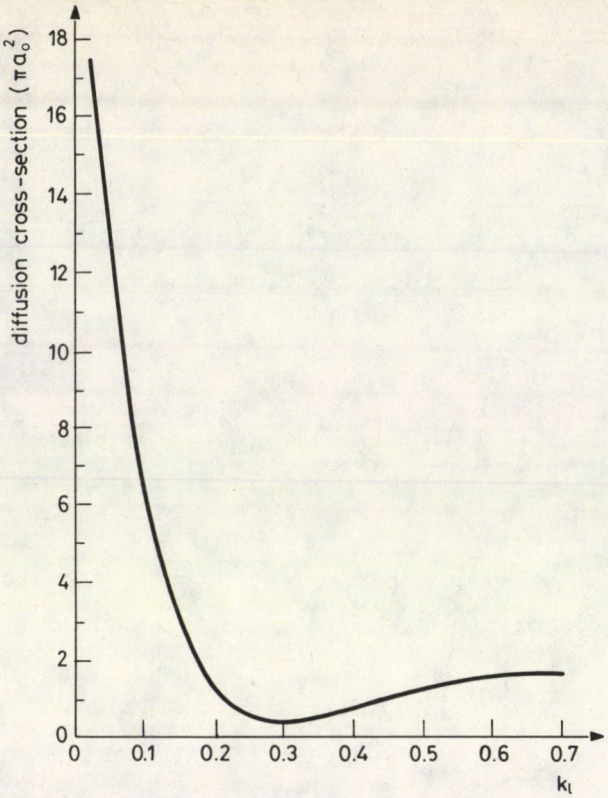

Fig. 3

c) Disagreements are noticed among the S- and P-wave phase shifts of both Tables, where the correlation terms play a considerable role and a large number of Hylleraas' functions is required in order to achieve convergence in the moment T-matrix method.

Table IV involves the quantities of our interest, i.e. the total elastic and diffusion cross-sections determined by virtue of Eqs (7a) and (7b), respectively. Figs 2 and 3 illustrate the general behaviours of both cross-sections with the variation of k_1. Both Table IV and Fig. 2 show that σ_{el} calculated by Stone's polarized orbital method has the same behaviour as the one determined by Winick and Reinhard [2], (see Fig. 11 in their paper), i.e. it falls off very rapidly in the region $0 \leq k_1 \leq 0.38$ and increases very slowly at higher values of k_1.

Acknowledgment

I would like to express my deep gratitude to Prof. Dr. J. Ladik for his generous help and for fruitful discussions.

References

1. M.A. Abdel-Raouf, Acta Phys. Hung., 63,
2. J.R. Winick and W.P. Reinhardt, Phys. Rev., A18, 910, 1978.

NOTES TO CONTRIBUTORS

I. PAPERS will be considered for publication in Acta Physica Hungarica only if they have not previously been published or submitted for publication elsewhere. They may be written in English, French, German or Russian.

Papers should be submitted to

Prof. I. Kovács, Editor
Department of Atomic Physics, Technical University
1521 Budapest, Budafoki út 8, Hungary

Papers may be either articles with abstracts or short communications. Both should be as concise as possible, articles in general not exceeding 25 typed pages, short communications 8 typed pages.

II. MANUSCRIPTS

1. Papers should be submitted in three copies.
2. The text of papers must be of high stylistic standard, requiring minor corrections only.
3. Manuscripts should be typed in double spacing on good quality paper, with generous margins.
4. The name of the author(s) and of the institutes where the work was carried out should appear on the first page of the manuscript.
5. Particular care should be taken with mathematical expressions. The following should be clearly distinguished, e.g. by underlining in different colours: special founts (italics, script, bold type, Greek, Gothic, etc.); capital and small letters; subscripts and superscripts, e.g. x^2, x_3; small *l* and l; zero and capital O; in expressions written by hand: *e* and *l*, *n* and *u*, *v* and v, etc.

A List of Symbols on a separate sheet should be attached to each paper.

6. References should be numbered serially and listed at the end of the paper in the following form: J. Ise and W. D. Fretter, Phys. Rev., *76*, 933, 1949.

For books, please give the initials and family name of the author(s), title, name of publisher, place and year of publication, e.g.: J. C. Slater, Quantum Theory of Atomic Structures, I. McGraw-Hill Book Company, Inc., New York, 1960.

References should be given in the text in the following forms: Heisenberg [5] or [5].

7. Captions to illustrations should be listed on a separate sheet, not inserted in the text.
8. In papers submitted to Acta Physica all measures should be expressed in SI units.

III. ILLUSTRATIONS AND TABLES

1. Each paper should be accompanied by three sets of illustrations, one of which must be ready for the blockmaker. The other sets attached to the copies of the manuscript may be rough drawings in pencil or photocopies.
2. Illustrations must not be inserted in the text.
3. All illustrations should be identified in blue pencil by the author's name, abbreviated title of the paper and figure number.
4. Tables should be typed on separate pages and have captions describing their content. Clear wording of column heads is advisable. Tables should be numbered in Roman numerals (I, II, III, etc.).

IV. RETURN OF MATERIAL

Owing to high postage costs, the Editorial Office cannot undertake to return *all* material not accepted for any reason for publication. Of papers to be revised (for not being in conformity with the above Notes or other reasons) only *one* copy will be returned. Material rejected for lack of space or on account of the Referees' opinion will not be returned to authors outside Europe.

Periodicals of the Hungarian Academy of Sciences are obtainable at the following addresses:

AUSTRALIA
C.B.D. LIBRARY AND SUBSCRIPTION SERVICE
Box 4886, G.P.O., *Sydney N.S.W. 2001*
COSMOS BOOKSHOP, 145 Ackland Street
St. Kilda (Melbourne), Victoria 3182

AUSTRIA
GLOBUS, Höchstädtplatz 3, *1206 Wien XX*

BELGIUM
OFFICE INTERNATIONAL DES PERIODIQUES
Avenue Louise, 485, *1050 Bruxelles*
E. STORY-SCIENTIA P.V.B.A.
P. van Duyseplein 8, *9000 Gent*

BULGARIA
HEMUS, Bulvar Ruszki 6, *Sofia*

CANADA
PANNONIA BOOKS, P.O. Box 1017
Postal Station "B", *Toronto, Ont. M5T 2T8*

CHINA
CNPICOR, Periodical Department, P.O. Box 50
Peking

CZECHOSLOVAKIA
MAD'ARSKA KULTURA, Národni třida 22
115 66 Praha
PNS DOVOZ TISKU, Vinohradská 46, *Praha 2*
PNS DOVOZ TLAČE, *Bratislava 2*

DENMARK
EJNAR MUNKSGAARD, 35, Nørre Søgade
1370 Copenhagen K

FEDERAL REPUBLIC OF GERMANY
KUNST UND WISSEN ERICH BIEBER
Postfach 46, *7000 Stuttgart 1*

FINLAND
AKATEEMINEN KIRJAKAUPPA, P.O. Box 128
00101 Helsinki 10

FRANCE
DAWSON-FRANCE S.A., B.P. 40, *91121 Palaiseau*
OFFICE INTERNATIONAL DE DOCUMENTATION ET LIBRAIRIE, 48 rue Gay-Lussac
75240 Paris, Cedex 05

GERMAN DEMOCRATIC REPUBLIC
HAUS DER UNGARISCHEN KULTUR
Karl Liebknecht-Straße 9, *DDR-102 Berlin*

GREAT BRITAIN
BLACKWELL'S PERIODICALS DIVISION
Hythe Bridge Street, *Oxford OX1 2ET*
BUMPUS, HALDANE AND MAXWELL LTD.
Cowper Works, *Olney, Bucks MK46 4BN*
COLLET'S HOLDINGS LTD., Denington Estate,
Wellingborough, Northants NN8 2QT
WM DAWSON AND SONS LTD., Cannon House
Folkstone, Kent CT19 5EE
H. K. LEWIS AND CO., 136 Gower Street
London WC1E 6BS

GREECE
KOSTARAKIS BROTHERS INTERNATIONAL BOOKSELLERS, 2 Hippokratous Street, *Athens-143*

HOLLAND
FAXON EUROPE, P.O. Box 167
1000 AD Amsterdam
MARTINUS NIJHOFF B. V.
Lange Voorhout 9–11, *Den Haag*
SWETS SUBSCRIPTION SERVICE
P.O. Box 830, 2160 Sz Lisse

INDIA
ALLIED PUBLISHING PVT. LTD.
750 Mount Road, *Madras 600002*
CENTRAL NEWS AGENCY PVT. LTD.
Connaught Circus, *New Delhi 110001*
INTERNATIONAL BOOK HOUSE PVT. LTD.
Madame Cama Road, *Bombay 400039*

ITALY
D. E. A., Via Lima 28, *00198 Roma*
INTERSCIENTIA, Via Mazzé 28, *10149 Torino*
LIBRERIA COMMISSIONARIA SANSONI
Via Lamarmora 45, *50121 Firenze*
SANTO VANASIA, Via M. Macchi 58
20124 Milano

JAPAN
KINOKUNIYA COMPANY LTD.
Journal Department, P.O. Box 55
Chitose, *Tokyo 156*
MARUZEN COMPANY LTD., Book Department
P.O. Box 5050 Tokyo International, *Tokyo 100-31*
NAUKA LTD., Import Department
2-30-19 Minami Ikebukuro, Toshima-ku, *Tokyo 171*

KOREA
CHULPANMUL, *Phenjan*

NORWAY
TANUM-TIDSKRIFT-SENTRALEN A.S.
Karl Johansgata 43, *1000 Oslo*

POLAND
WĘGIERSKI INSTYTUT KULTURY
Marszalkowska 80, *00-517 Warszawa*
CKP I W, ul. Towarowa 28, *00-958 Warszawa*

ROUMANIA
D. E. P., *Bucuresti*
ILEXIM, Calea Grivitei 64–66, *Bucuresti*

SOVIET UNION
SOYUZPECHAT — IMPORT, *Moscow*
and the post offices in each town
MEZHDUNARODNAYA KNIGA, *Moscow G-200*

SPAIN
DIAZ DE SANTOS Lagasca 95, *Madrid 6*

SWEDEN
ESSELTE TIDSKRIFTSCENTRALEN
Box 62, *101 20 Stockholm*

SWITZERLAND
KARGER LIBRI AG, Petersgraben 31, *4011 Basel*

USA
EBSCO SUBSCRIPTION SERVICES
P.O. Box 1943, *Birmingham, Alabama 35201*
F. W. FAXON COMPANY, INC.
15 Southwest Park, *Westwood Mass. 02090*
MAJOR SCIENTIFIC SUBSCRIPTIONS
1851 Diplomat, P.O. Box 819074,
Pallas, Tx. 75381-9074
READ-MORE PUBLICATIONS, INC.
140 Cedar Street, *New York, N. Y. 10006*

YUGOSLAVIA
JUGOSLOVENSKA KNJIGA, Terazije 27, *Beograd*
FORUM, Vojvode Mišića 1, *21000 Novi Sad*

Index: 26.022

Acta Physica Hungarica

VOLUME 63 · NUMBERS 3–4, 1988

Akadémiai Kiadó, Budapest

ACTA PHYS. HUNG. APAHAQ 63 (3–4) 201–383 (1988) HU ISSN 0231–4428

ACTA PHYSICA HUNGARICA

A JOURNAL OF THE HUNGARIAN ACADEMY OF SCIENCES

EDITED BY
I. KOVÁCS

Acta Physica publishes original papers on subjects in physics. Papers are accepted in English, French, German and Russian.

Acta Physica is published in two yearly volumes (4 issues each) by

AKADÉMIAI KIADÓ
Publishing House of the Hungarian Academy of Sciences
H-1054 Budapest, Alkotmány u. 21

Subscription information

Orders should be addressed to

KULTURA Foreign Trading Company
1389 Budapest P.O. Box 149

or to its representatives abroad.

Acta Physica Hungarica is abstracted/indexed in Chemical Abstracts, Current Contents–Physical, Chemical and Earth Sciences, Mathematical Reviews, Science Abstracts, Physics Briefs, Risk Abstracts

CONTENTS

CONDENSED MATTER

OPTICS

Acta Physica Hungarica, 63 (3—4), pp. 201—212 (1988)

OPTICAL TRANSMISSION ANISOTROPY OF AMORPHOUS METAL FILMS

D. KORN

Faculty for Physics of the University
D-7750 Konstanz, F.R.G.

(Received in revised form 28 May 1985)

Amorphous and disordered metal and alloy films are produced by a vapour beam impinging obliquely on a quartz glass substrate at 90 K. After evaporation the transmission is measured for perpendicular incidence of light within the wavelength range 400 nm to 900 nm. The films have an anisotropy of the transmission of linearly polarized light. The transmission has its lowest value when the electric vector in the plane of the film is oriented perpendicular to the vapour beam. The anisotropy is found for e.g. CuSn, BiPb and Cu, Ag, Au and Bi. The transmission anisotropy decreases with the transition to the crystalline state or with the reduction of disorder.

1. Introduction

Measurements of the optical properties of metals often yield anomalies. Mayer and coworkers [1] observed a structure within the high frequency conductivity of bulk Na. The structure depends upon the surface being Na-vacuum, Na-glass or Na-sapphire (short review [2]). The difference between the experimental situations is given by the surface tension and the adhesion to the substrate. Hunderi [3] reports the optical conductivity of quench condensed Ag films. The optical properties of quench condensed films show a strong deviation from annealed crystalline films and bulk material. Hunderi explains the difference with the influence of grain boundaries. Hutchinson and Hansen [4] measured the reflectance and transmittance of Au films. The optical properties of the Au films depend on the plane of the polarization of the light. The authors explain this effect with surface scattering. But there remains some anisotropy in the optical properties which they ascribe to an anisotropy of the crystal structure. All the experimental situations as surfaces interfaces, grain boundaries and anisotropy of the crystal structure have in common the anisotropy of the wave functions of the atoms which build up the mentioned situations.

The optical properties of amorphous metals show a more simple dependence on the light wavelength than the optical properties of crystalline metals. Especially the parallel band interband transitions are non-existent [5, 6]. Regarding long wavelength the model of free electrons is valid. That has been shown very carefully by Hunderi and Ryberg [5] for amorphous Ga. The free electron model is also a

good approximation for the electron density which has been measured by Häussler and Baumann for a series of amorphous alloys (review [7]). Further on the nearly free electron model is used for the calculation of the electrical resistivity of amorphous metals (Froböse and Jäckle [8]). The electrical resistivity of amorphous metals has negative and positive temperature coefficients. The temperature coefficients can be correlated with the *P*- and *D*-states of the atoms from which the amorphous metals are built up [9]. For example amorphous Cu and Au have a very high electrical resistivity. Therefore the atoms of amorphous Cu and Au are at least partially in the *D*-state. Concerning amorphous Sn, Mössbauer measurements by Bolz and Pobell [10] yield a s^2p^2 configuration which is in accordance with the *P*-ground state of Sn atoms.

2. Experimental details

a) Light path

A light source (Xenon high pressure) and a monochromator supply light with wavelength λ between 400 and 900 nm. By an appropriate optical setup (Fig. 1) a parallel light ray with a diameter of 3 mm is produced. The light ray is chopped and ends up in a photomultiplier. The signal of the photomultiplier is measured by a Lock-In amplifier referring to the frequency and the phase of the chopper. The lenses and the windows of the cryostat are made of glass. The quartz glass substrate has the dimensions 18 mm × 12 mm and the thickness 1 mm.

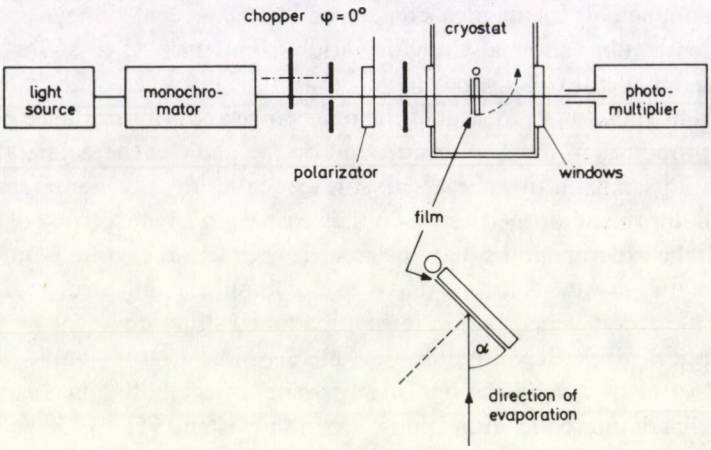

Fig. 1. Sketch of the arrangement for the measurement of the optical transmission of obliquely evaporated metal films

b) Measurements

The optical transmission of polarized light with perpendicular incidence on a metal film is measured. The light is linearly polarized by a Glan–Thompson polarizator before passing through the film. The normal on the film and the vapour beam define a plane (also plane of drawing of Fig. 1). If the electric vector of the light lies in this plane, the polarization angle is noted as $\varphi = 0°$. If $\varphi = 90°$, the electrical vector (always in the plane of the film) stands perpendicular to the vapour beam.

The substrate can be rotated about an axis for evaporation, and measurement of the incident light intensity (this axis is perpendicular to the plane of drawing: Fig. 1). α is the angle between the film plane and the vapour beam direction x during evaporation. After evaporation the film is rotated out of the light ray and the incident intensity I_0 is determined. The incident light intensity is measured for every value of φ and λ. Then the intensity I is measured with the light passing through the film and the substrate. The transmission of the sandwich film–substrate is defined as $\tau = \frac{I}{I_0}$. Before evaporating the film the transmission of the quartz glass substrate is determined as $\tau = 93\%$ in the mentioned range for λ. Then the transmission τ is measured mainly for $\varphi = 0°$ and $\varphi = 90°$. If not otherwise stated the error is $\frac{\Delta\tau}{\tau} = \pm 3\%$.

c) Details concerning the films

The film is condensed on the cold substrate in situ in an ultrahigh vacuum cryostat. The cryostat [11] and the production of the films [12] is already described. The vacuum during evaporation amounts to 10^{-8} mbar. Evacuation occurs by a titanium sublimation and a turbomolecular pumping system. During evaporation and measurement the substrate is held at $T_K = 90$ K. Then the film can be warmed up to 300 K and measured again at $T_m = 90$ K. The film has the geometry 14 mm × 10 mm × 20 nm. The thickness of about 20 nm can be determined interferometrically. The light passes through the film in the centre. The direction of the vapour beam is $\alpha = 45°$ if not otherwise stated.

3. Results

All transmission measurements refer to the sandwich metal film–glass substrate.

a) Vapour beam perpendicular to the substrate ($\alpha = 90°$)

For the first check measurement the vapour beam is oriented perpendicular to the plane of the substrate. Fig. 2a shows for the example of an amorphous CuSn film that the transmission is independent of the angle of polarization (φ). That is the normal behaviour of a light ray with perpendicular incidence on a metal film. Later on (Section 3b) films will be discussed which are obliquely evaporated. By oblique condensation the metal film has a slight wedge angle of $\leq 2 \cdot 10^{-7}$ rad.To consider the wedge angle as a possible cause of a transmission anisotropy a second check measurement is made. By inserting a half plane into the vapour beam, films with wedges are artificially produced. The wedge angles are larger or equal to that one mentioned. Fig. 2b shows as an example an amorphous CuSn film condensed by perpendicular impinge of the vapour beam on the substrate. As may be seen the transmission does not depend on the angle φ of light polarization. The measurement with the wedge (film) is done to rule out *experimentally* that a thickness gradient of an amorphous metal film causes dichroism.

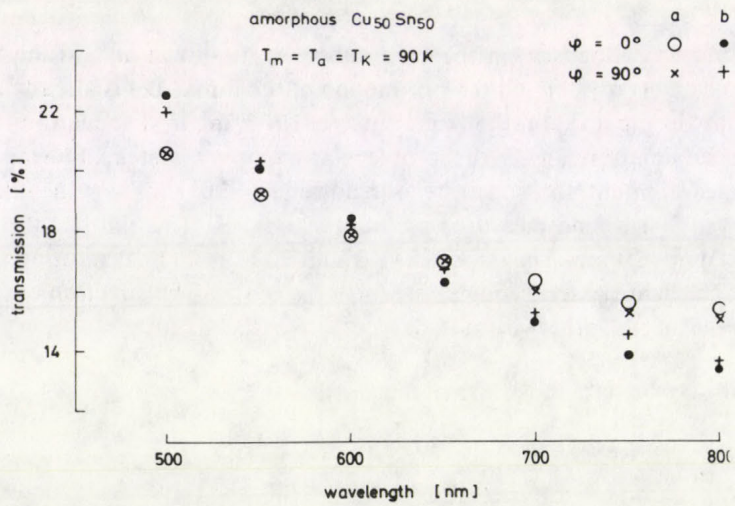

Fig. 2. Optical transmission of amorphous CuSn films evaporated perpendicular ($\alpha = 90°$): a) without wedge, b) with wedge angle $2 \cdot 10^{-6}$ rad. φ marks the plane of polarization

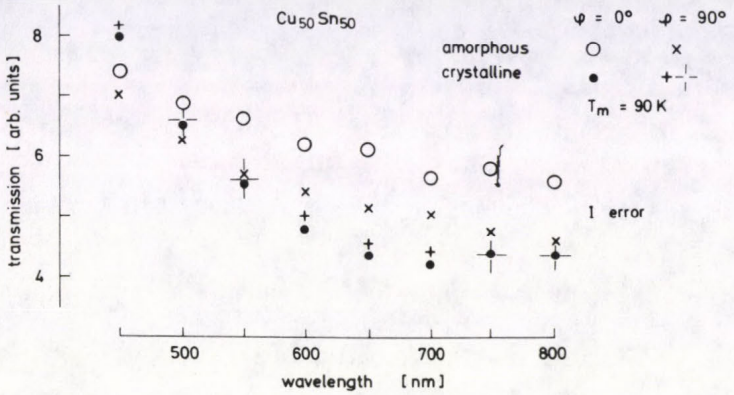

Fig. 3. Optical transmission of a $Cu_{50}Sn_{50}$ film in the amorphous ($T_a = 90$ K) and crystalline ($T_a = 300$ K) phase. Film obliquely ($\alpha = 45°$) evaporated. φ marks the direction of the electric vector of the light

b) Vapour beam oblique to the substrate

The angle between the vapour beam and the plane of the substrate is held at $\alpha = 45°$. $Cu_{50}Sn_{50}$ films, thus grown, have an optical transmission for which Fig. 3 shows a representative example. The transmission depends on the angle φ of the linearly polarized light. The transmission is larger for $\varphi = 0°$ than for $\varphi = 90°$. Thus there exists a transmission anisotropy for obliquely ($\alpha = 45°$) evaporated metal films. This is valid for the amorphous film. Annealing to $T_a = 300$ K brings the CuSn film into the crystalline phase [13], [14]. Within experimental error the optical transmission of the crystalline film has no difference between $\varphi = 0°$ and $\varphi = 90°$ (Fig. 3). The transmission anisotropy has vanished for the film in the crystalline phase.

The transmission of the amorphous film varies with the plane of the polarized light. For perpendicular incidence the electric vector lies in the plane of the substrate and the electric vector is given by the angle φ. $\varphi = 90°$ means that the electric vector stands perpendicular to the vapour beam. Fig. 4 shows how the transmission τ varies with the angle φ of the linearly polarized light. Within experimental error $\tau(\varphi)$ of Fig. 4 obeys the relation

$$\tau = \tau_n + \tau_a \cos^2 \varphi.$$

The transmission anisotropy is axial and not unidirectional. The magnitude $\tau(\varphi = 0°) - \tau(\varphi = 90°) = \tau_a$ of the anisotropy depends upon the alloy. In Fig. 5 is plotted the transmission of amorphous $Cu_{21}Sn_{79}$ and amorphous $Cu_{80}Sn_{20}$. Regarding additionally Fig. 3 yields as result that the alloy with the highest Cu concentration has the largest anisotropy. Amorphous Sn with 21% Cu shows no anisotropy (Fig. 5). No anisotropy is found for amorphous InAg (Fig. 6). Fig. 7 gives a further

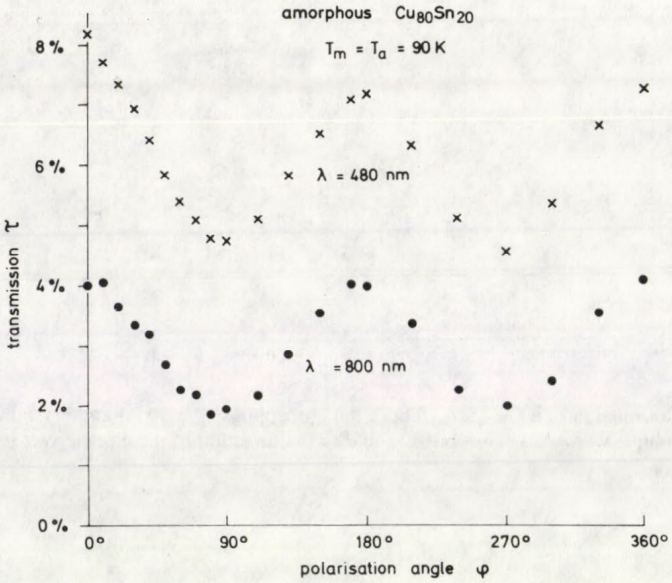

Fig. 4. Transmission τ as a function of the angle φ of the plane polarized light (wavelength λ). Sample: Amorphous $Cu_{80}Sn_{20}$ film condensed obliquely ($\alpha = 45°$) on a glass substrate at 90 K and measured at $T_m = 90$ K

example for an alloy system with transmission anisotropy. The transmission of amorphous BiPb is lower for $\varphi = 90°$ than for $\varphi = 0°$ as in the case of CuSn.

Table I summarizes the existence of a transmission anisotropy of amorphous alloy films. The observation of a transmission anisotropy τ_a larger than the experimental error of τ is quoted with "yes". Additionally the transmission anisotropy appears in disordered films. For example Bi, quench condensed on a substrate at 90 K, grows microcrystalline and disordered. The disordered films can be described as a sum of crystalline and amorphous material [15]. The disorder sits in grain boundaries, in all types of lattice defects and in structure independent [16] imperfections. Quench condensed Bi films have an anisotropy similar as amorphous BiPb. Pure microcrystalline and disordered Cu, Ag and Au films have the anisotropy but not with the same sign for τ_a in the whole range of the light wavelength. Disordered Sn and In have no transmission anisotropy. When the anisotropy exists the films annealed at 300 K always have a lower anisotropy than the amorphous or disordered films condensed at 90 K. The only exception is Te, but Te is no metal. The following results are concluded:

1. Quench condensed films evaporated with an angle of $\alpha = 45°$ between vapour beam and substrate can have a transmission anisotropy for perpendicular incidence of light.
2. The transmission anisotropy for polarized light does not exist for $\alpha = 90°$ even if the film is a wedge.

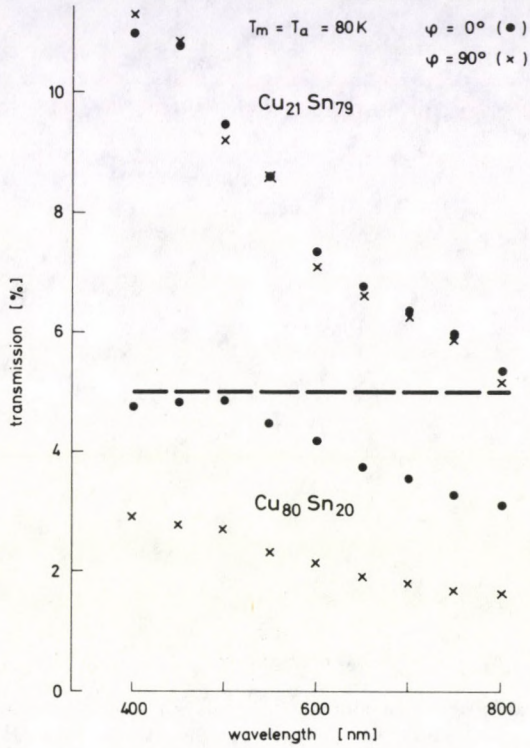

Fig. 5. Transmission of amorphous CuSn with different concentration. φ marks the plane of the polarized light. T_a = annealing temperature

3. The transmission anisotropy grows monotonically with decreasing α between $\alpha = 90°$ and $\alpha = 30°$. (Measured but not shown here. The transmission anisotropy exists also at angles lower than $\alpha = 30°$).
4. Besides oblique incidence of the vapour beam, the disorder of the film is a necessary condition for the transmission anisotropy.
5. For amorphous films the optical transmission has its lowest value when the electric vector (here always in the plane of the substrate) is perpendicular to the vapour beam.
6. The transmission anisotropy τ_a is roughly independent of the thickness of the film (measured but not shown here). Tolansky interferometer and optical properties are used to measure the thickness of the films. The thickness of the films of the same material was calculated from the optical transmission. The thickness varies between 20 nm and 34 nm. The error of τ_a of this preliminary measurements amounts to $\frac{\Delta\tau_a}{\tau_a} = 25\%$.
7. The magnitude $\tau_a = \tau(\varphi = 0°) - \tau(\varphi = 90°)$ of the transmission anisotropy depends on the material.

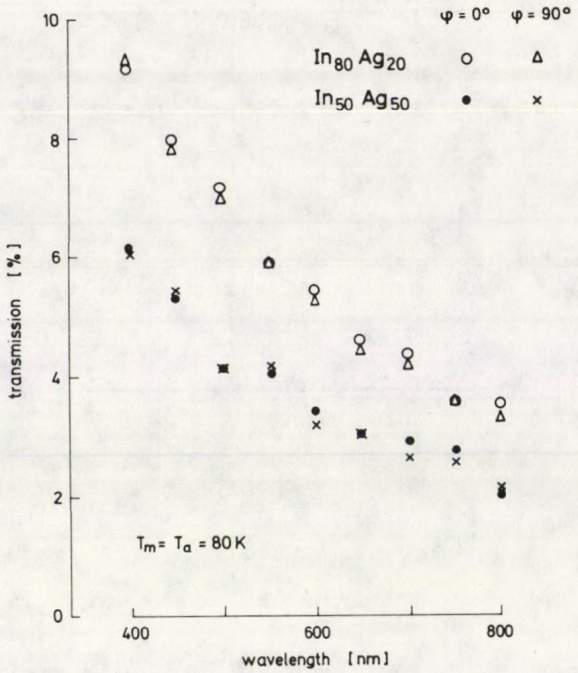

Fig. 6. Optical transmission of amorphous InAg alloys as a function of wavelength

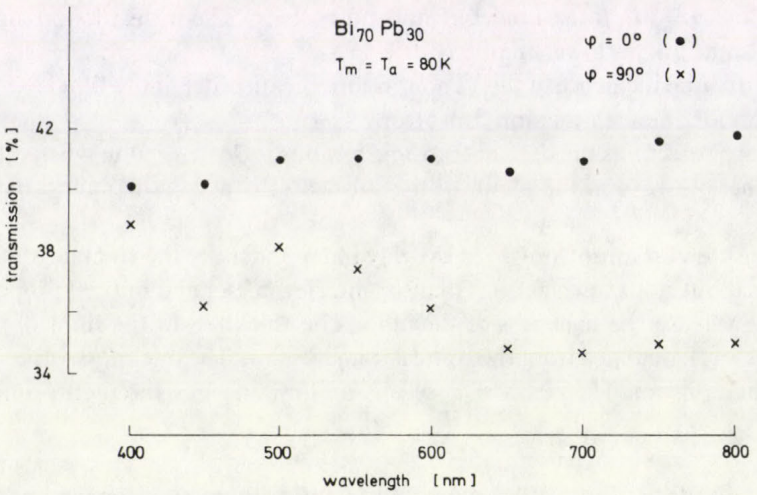

Fig. 7. Transmission of a $Bi_{70}Pb_{30}$ film measured at T_m and annealed at T_a. Polarisation angle φ

4. Discussion

The optical transmission of linearly polarized light has an anisotropy which is given by the angle α between the vapour source direction and the film plane. The anisotropy rises with decreasing α. That means the projection of the vapour beam on the plane of the film may be essential. Optical anisotropy of obliquely evaporated films is known for crystalline films [17, 18]. In crystalline films the direction of the grain boundaries lies often near the vapour beam direction. Grain boundaries are disordered parts of the crystal. Therefore the anisotropy is connected with a special sort of disorder. Amorphous metals have a disordered structure but no grain boundaries which may define a direction. A possible cause of the anisotropy of amorphous metals is an anisotropy in the disorder of the chemical bond introduced by the vapour direction. In the following two possible causes for the development of the anisotropy are discussed. These two causes may not be the only ones.

One possible mechanism is the influence of the direction of the arriving atoms on the orientation of the wave functions of the atoms. The atoms form the temporary surface during growth of the film. The wave functions of the atoms themselves, or hybrids, or the chemical bond (combined wave functions of different atoms) may have a preferred direction caused by the oblique impinge. Amorphous alloys can have the anisotropy, for example *Cu*Sn and *Bi*Pb (Table I). The atoms of these amorphous alloys are in the excited state. The thermal energy of the evaporated elements (e.g. 2000 K) or the kinetic energy of the atoms does not bring enough atoms in the lowest excited state. The excited states are caused by the condensation (binding) energy of one atom to the solid surface. The condensation energy has a value which is higher than the kinetic energy by a factor 10 and about half of the atoms are in the excited state. It is a general feature of the solid state that atoms may be in excited states. Let us regard e.g. solid silicon. The Si-tetrahedrons are built up by an sp^3 electronic configuration. That is an excited state. The ground state s^2p^2 of the silicon atoms in the gas is lower by 48 399 cm^{-1}. Although the energy difference is so high, the atoms are in excited states in the solid. In metal physics the atoms of crystalline intermetallic compounds are at least in excited states. Amorphous alloys are higher in energy (metastable state) than crystalline alloys and the latent heat at the transition amorphous–crystalline has been measured [15]. Hence the atoms forming an alloy with transmission anisotropy are at least partially excited. Mixing of excited states to the ground states results in hybrids. Hybrids are oriented bonds and are anisotropic. On the other hand the excited states themselves can cause anisotropy. The excited atomic states possess an electric quadrupole moment Q_J. That is valid for e.g. Cu and Au with the atomic state $^2D_5$ and for Bi ($^2D_3$). Amorphous Cu, Au and Bi show the transmission anisotropy. Indium ($^2P_{\frac{1}{2}}$) and Sn ($^3P_0$) have no Q_J and for amorphous In and Sn the anisotropy is not observed (Fig. 6 and Table I).

Let us consider the case of the electric quadrupole moment Q_J. J is the total angular momentum of the electrons of the atom. The beam of the atoms defines the

Table I

Transmission anisotropy τ_a of obliquely evaporated metal films. Temperature of condensation and measurement $T_K = T_m = 90$ K

Amorphous alloy		$\tau_a = \tau(0°) - \tau(90°)$
$Cu_{80}Sn_{20}$		positive
$Cu_{50}Sn_{50}$		positive
$Cu_{21}Sn_{79}$		0
$In_{50}Ag_{50}$		0
$In_{80}Ag_{20}$		0
$Bi_{70}Pb_{30}$		positive
Sn_xAu_{1-x}	$25\% \leq x \leq 80\%$	yes
$Si_{18}Au_{82}$		yes
$Si_{20}Cu_{80}$		yes
$Sn_{20}Ag_{80}$		yes
$Ga_{20}Au_{80}$		yes
Disordered metal films		
Ga (amorphous)		yes
Bi		positive
Cu_xFe_{1-x}	$0 \leq x \leq 100\%$	yes
Ag		yes
Au		yes
In		0
Sn		0
Te		positive

x-axis. By the impact the atom must deliver its momentum to the surface in the x-direction. This is possible if the atoms stick to the microscopically rough surface at places with the surface mainly perpendicular to x. Electrical forces favour an extension of the electron charge of the atomic quadrupole perpendicular to x. During growth of the film the electrical quadrupoles orient in the electric field gradient of the quadrupoles at the film surface. If the x-axis is oblique to the plane of the substrate, a component of the anisotropic electron charge extension of the atom exists with respect to the plane of the substrate. From that follows a transmission anisotropy for the electric vector of the electromagnetic wave in the plane of the substrate. The transmission has its lowest value when the electric vector lies in the plane of the substrate perpendicular to x (that is $\varphi = 90°$) since in that direction the component of the charge extension is largest. This explanation agrees with the results.

The results of the optical measurements are in accordance with magnetic investigations of obliquely evaporated films. The magnetic anisotropy energy depends upon the direction of the vapour beam relative to the plane of the substrate [19]. Especially the easy axis of pure Ni is parallel to the vapour beam direction [16]. For

Fe the easy axis lies perpendicular to the vapour beam direction. The causes are microscopic strains associated with imperfections in the film or with the imperfection itself [16]. This observation agrees with the results of the optical measurements (Section 3b). The responsible imperfections do not correlate with the crystal structure [16]. Such structure independent imperfections (disorder: Section 3b) can be regarded as local amorphous regions and an explanation as in the case of amorphous metals can be applied. The 3*d* atoms with unfilled *d*-shells do not have spherical symmetry. The largest charge extension lies perpendicular to the vapour beam direction x. The electric quadrupole moment Q_J of Fe ($^5D_4$) is prolate and hence the total angular momentum J is oriented perpendicular to the x-axis. The easy axis for the spin is caused by spin orbit interaction. For Fe, Co and Ni the spin is parallel to J. Therefore the easy axis is perpendicular to the x-axis as observed for Fe. The Ni atom has in the ground state ($^3F_4$) an oblate quadrupole moment. J lies perpendicular to the largest electron charge extension. Since the largest charge extension is perpendicular to the x-axis, J and S are parallel to the x-axis. The easy axis is parallel to the vapour beam direction as observed for Ni.

A second possible explanation lies in the assumption that an amorphous film consists of grains as known from crystalline films. This is really a hypothesis since no grain boundaries are observed e.g. for amorphous SnCu and SnAu. The diameter of a hypothetical grain calculated from the line width of diffraction measurements would be 2 nm (20 Å [13]). But the amorphous metal films differ essentially from microcrystalline material with comparable grain size. Amorphous metal films have properties similar to liquid metals. That is true e.g. for the structure [13], electron density [7] and the electrical resistivity [9]. Especially the absence of mechanical stress [20] is contrary to crystalline films with grain boundaries. Just the first layer shows mechanical stress. So only the initial formation of islands may perhaps introduce a certain anisotropy. Grains exist in crystalline films. In this case an explanation for the anisotropy of the optical transmission is found by E. F. Pócza [21]. He measured the dichroism of crystalline Al layers. The crystallographic axes are oriented at random and the grains extend perpendicular with respect to the vapour beam. The prolate grains are regarded as parallel splits and in this way Pócza explained the anisotropy of the optical transmission of metal films.

Conclusion

In amorphous metals the wave functions of the electrons of the atoms are not fixed to certain crystal directions. They can be oriented with respect to the direction of impinging atoms. Assuming the wave functions and the electron charge to have its largest extension perpendicular to the atom beam direction, the anisotropy of the optical transmission of obliquely evaporated films can be explained. Additionally the magnetic anisotropy of obliquely evaporated ferromagnetic films can be understood in the same manner.

Acknowledgement

Support by the Deutsche Forschungsgemeinschaft is gratefully acknowledged.

References

1. H. Mayer and M. H. ElNaby, Z. Phys., *174*, 289, 1963.
2. A. J. Sievers, Phys. Rev. Lett., *45*, 386, 1980.
3. O. Hunderi, Thin Sol. Films, *57*, 15, 1979.
4. F. E. Hutchinson and W. N. Hansen, Phys. Rev., *B20*, 4076, 1979.
5. O. Hunderi and R. Ryberg, J. Phys., *F4*, 2084, 1974.
6. D. Korn and H. Pfeifle, J. Phys., *F9*, 1175, 1979.
7. P. Haussler, Z. Phys., *B53*, 15, 1983.
8. K. Froböse and J. Jackle, J. Phys., *F7*, 2331, 1977.
9. D. Korn, H. Pfeifle and G. Zibold, Z. Phys., *270*, 195, 1974.
10. J. Bolz and F. Pobell, Z. Phys., *B20*, 95, 1975.
11. D. Korn, H. Pfeifle and G. Zibold, J. Phys., *F9*, 1709, 1979.
12. E. Blasberg, D. Korn and H. Pfeifle, J. Phys., *F9*, 1821, 1979.
13. W. Buckel, Z. Phys., *138*, 136, 1954.
14. D. Korn, W. Mürer and G. Zibold, J. Physique, *35C4*, 257, 1974.
15. W. Mönch, Z. Phys., *164*, 229, 1961.
16. E. W. Pugh, Matisoo, D. E. Speliotis and E. L. Boyd, J. Appl. Phys., *31*, 293, 1960.
17. L. Reimer, Optik, *14*, 83, 1957.
18. R. T. Kivaisi, Thin Sol. Films, *97*, 153, 1982.
19. T. G. Knorr and R. W. Hoffman, Phys. Rev., *113*, 1034, 1959.
20. H. J. Bauer and W. Buckel, Z. Physik, *220*, 293, 1969.
21. E. F. Pócza, Acta Phys. Hung., *15*, 89, 1962.

Acta Physica Hungarica, 63 (3—4), pp. 213—218 (1988)

WIDE-APERTURE HYBRID TEA CO_2 LASERS*

C. A. EMSHARY

University of Basrah, College of Education
Department of Physics, Basrah, Iraq

(Received 3 July 1985)

The single mode performance of a wide aperture CW–TEA CO_2 hybrid laser is reported, single longitudinal mode (SLM) is obtained from a wide aperture laser. The SLM from small aperture laser is given also for comparison.

Introduction

The need in certain fields of research (e.g. optical pumping and nonlinear optics) for spectrally-pure radiation has led to the development of a number of methods inducing single longitudinal mode (SLM) operation of TEA CO_2 Lasers [1]. The ultimate usefulness of any such technique is strongly dependent on its scalability to large aperture multijoule output systems. Among the most promising and versatile methods, injection locking and hybrid systems are emerging as genuinely useful practical tools, by virtue of their operational efficiencies, stability robustness [2, 3, 4]. The scalability of both techniques has been demonstrated for large aperture systems operated with unstable geometries [2, 5, 6]. Selection of the TEM_{00} mode is automatic for such systems but the arrangement as a whole may be totally unsatisfactory for some applications due to the annular form of output beam profile [7]. While high quality (TEM_{00}) beams are often mandatory for some purposes, the increased energy-extraction capability occurring in large spot-size multitransverse mode emission of wide aperture stable resonator configurations can be equally beneficial for other applications, where spatial mode quality plays a less crucial role. Experiments for achieving SLM operation in locking and hybrid systems are generally based on the selection of TEM_{00} mode by insertion of an intracavity iris (see e.g. [8–9]) reflecting the commonly held assumption that reliable SLM operation is to a certain extent dependent on the elimination of all but the fundamental transverse mode of the laser. In this paper following a recent publication [10], we report on the operation of a hybrid wide aperture TEA CO_2 laser and describe the quality of performance that was obtained.

* The experimental work was carried out at the Physics Department, Heriot-Watt University, Edinburgh, Scotland, U.K.

Theory

Studies of the dynamics of the laser intensity built up in TEA CO_2 lasers can be found elsewhere [11].

The introduction of a CW CO_2 laser section inside the optical resonator affects the dynamics of the TEA CO_2 laser pulse. If the gain in the CW laser is too small to overcome the resonator losses, the situation will be modified to that illustrated by the dashed curves in Fig. 1. The points to be noted are that the build up in the resonator will begin earlier as the threshold gain G_t is reached earlier and the rate of rise of the laser intensity will be higher resulting in a laser pulse which occurs earlier. In the case where the CW laser gain is above the threshold value there will be a laser field inside the resonator prior to the excitation of the TEA section. This situation is illustrated by the dotted curve in Fig. 1. Since the initial signal in the TEA resonator is of the order of watts rather than where spontaneous emission is the only source of signal, the build up time for the TEA laser will be greatly reduced. It should be reduced to an extent that the signal intensity will reach a large value and as a result the stimulated emission transitions will be sufficiently strong to prevent any further increase in gain. In such a case the giant laser pulse will be eliminated while the resultant single mode pulse, having a relatively slow rise time, will never reach a very high value and will be of long duration. Due to the operation at atmospheric pressure, the laser transitions are greatly broadened by collisions. The bandwidth of a typical TEA CO_2 laser transition is of the order of 4 GHZ/atm, when such medium is placed in a 3 m long optical resonator which has resonant frequencies

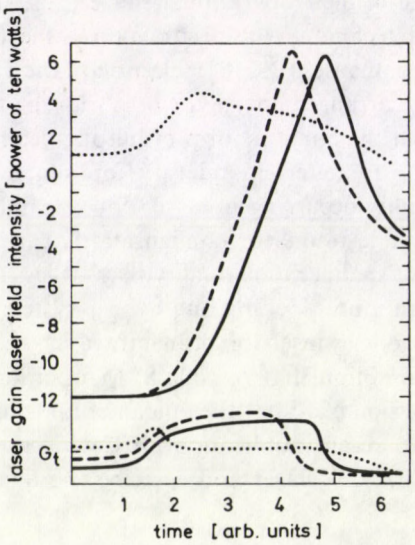

Fig. 1. Laser field intensity and net round trip gain buildup as a function of time in case of a normal TEA CO_2 laser without a CW CO_2 laser inside the cavity (solid curves), with a CW laser under the lasing threshold (dashed curves), and with a CW laser above the lasing threshold (dotted curves)

spaced 50 MHz, the laser tends to oscillate on many different frequencies simultaneously corresponding to the different resonance frequencies of the resonator. Fig. 2 illustrates the situation by indicating on the frequency axis all the resonance frequencies of the resonator and the broadened gain profile of the TEA laser. The narrow gain profile of the CW low-pressure CO_2 laser superimposed at the center of this gain profile. In the absence of this CW laser, it can be seen that there are over 20 resonator frequencies for which the gain coefficient differs by less than 5%. Thus, in the absence of the CW laser, the TEA laser field will build up approximately equally for all these frequencies, and the presence of a large number of oscillations at different frequencies will give rise to a modulation of the total laser output. With a CW laser giving an additional peak in the gain spectrum of the amplifying medium in the resonator, it can be readily seen from the difference between the solid and the dashed curve of Fig. 1 that the only resonator mode whose frequency lies within the narrow bandwidth of the CW oscillator will give rise to a very rapidly increasing field. This field will not only have the strength as to make the other modes insignificant but will actually prevent them from ever becoming important by depopulating the upper laser level of the transition before these other modes can reach a significant intensity. It is therefore not necessary to operate the CW laser above threshold value to eliminate the spontaneous mode-locking and in this way it is possible to generate giant pulses.

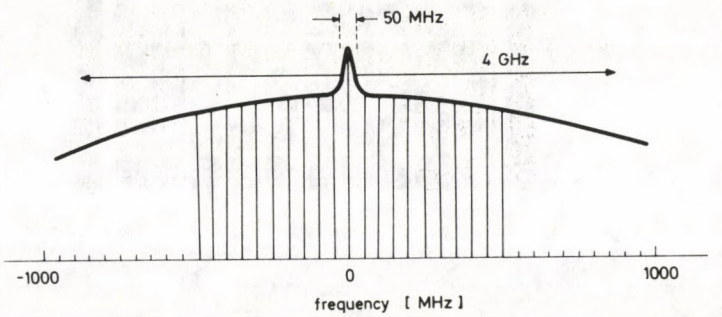

Fig. 2. Gain profile of the TEA CO_2 laser medium as a function of frequency, with some resonator frequencies (solid lines) for which the gain coefficient differs by less than 5%. At the centre of the gain profile is superimposed the narrow gain profile of the CW low pressure CO_2 laser

Results and discussion

The apparatus used for this study consisted of a discharge chamber ($122 \times 22 \times \times 20$ cm perspex box) with one cathode ($100 \times 15 \times 1$ cm) made of solid aluminium profiled to prevent field concentration and anode ($108 \times 8 \times 1$ cm) made of the same material. Ten tungsten wires (100 cm long) embedded in capillary tubes (0.7 cm diameter) were used as the trigger electrodes [12].

The electrodes were 4 cm apart. The CW section comprised a water cooled glass chamber supplied with two Brewster windows (total length 66 cm and inner diameter 2.0 cm). The cavity length of the hybrid laser was 3 m. The resonator comprised a plane grating and a 36% reflecting curved, 10 m, A/R coated Ge output-coupler of a diameter of 20 mm.

The CW CO_2 section was well below threshold as a result of low reflectivity optics.

As a control, the laser was stopped down to 8 mm diameter (using an aperture) for TEM_{00} operation and the spatial and temporal distribution of the SLM as well as the multimode output were viewed by means of a 100 μm pin hole, a joule meter and a photon-drag detector, respectively. The signals from the photon-drag detector were monitored on a Tektronix 7104 1GHZ bandwidth. Figure 3a clearly shows the temporally smooth form of the output along with Gaussian spatial distribution (Fig. 3b) associated with single axial and single transverse mode emission. The corresponding results for operation with the aperture opened to the full 20 mm are shown in Fig. 4. Fig. 4b reveals a strong multitransverse mode structure, Fig. 4a shows no 50 MHZ beating of multiaxial mode interaction in the main spike. The digitised form of the wide aperture SLM output is shown in Fig. 5.

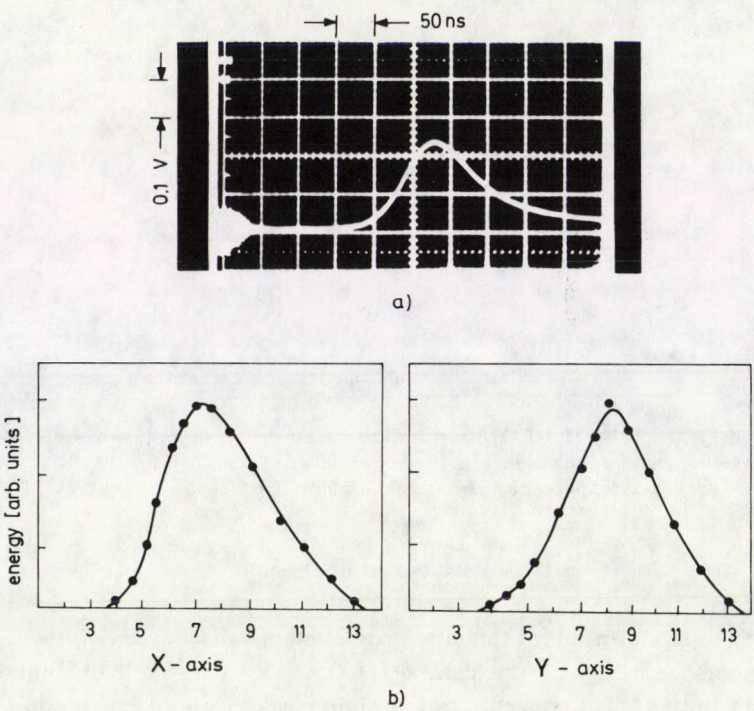

Fig. 3. a) Typical TEM_{00} SLM pulse. Horizontal axis: 50 ns div^{-1}, vertical axis: 0.1 V div^{-1}; b) Transverse horizontal (a) and vertical (b) beam profiles of TEM_{00} emission

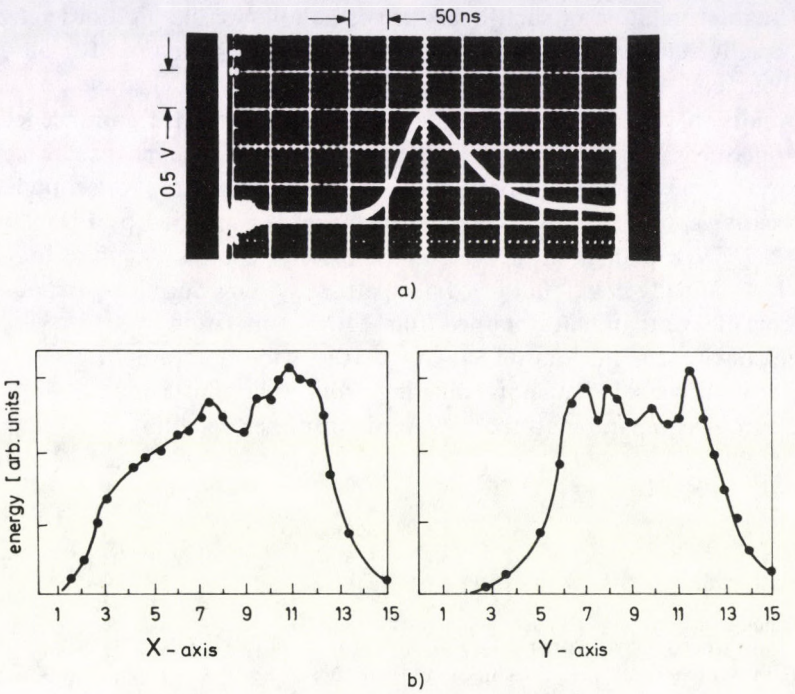

Fig. 4. a) Typical multitransverse mode SLM pulse. Horizontal axis: 50 ns div^{-1}, vertical axis: 0.5 V div^{-1}; b) Transverse horizontal (a) and vertical (b) beam profiles of wide-aperture emission

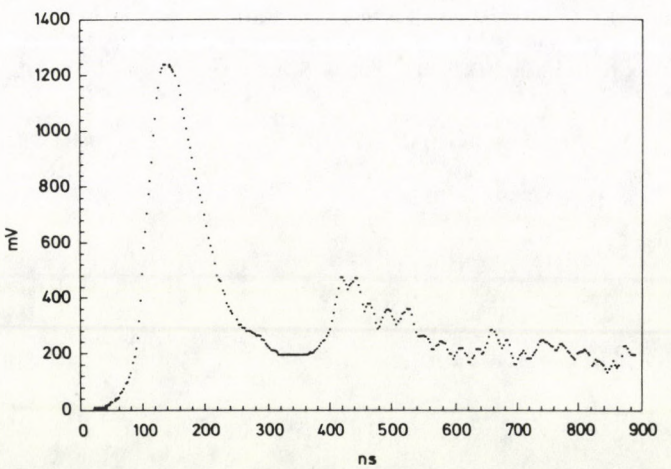

Fig. 5. Digitised form of wide-aperture SLM pulse. Horizontal axis: 100 ns div^{-1}, vertical axis: 200 mV

The interpretation of such behaviour is as follows: the high order transverse modes usually suffer great diffraction losses as a result of the use of small diameter output couplers. As a result, the fundamental mode, TEM_{00}, grows at a faster rate which results in gain saturation by the main spike. The extra gain needed by the higher transverse mode will be available when the main spike disappears, i.e. during the recovery time; resulting in oscillation on two or more transverse modes giving rise to beating in the tail only. This interpretation is confirmed by Fig. 5, 10 MHZ and 50 MHZ oscillations both exist which belong to transverse and longitudinal modes. It was finally noted that for wide aperture systems output power was greater by a factor of five than that obtained from TEM_{00} operation.

In conclusion, the reproducibility of the wide aperture SLM output was impressive, with only 5% shots differing from that illustrated in Fig. 5. This performance is comparable to that obtained with laser operating at TEM_{00}.

References

1. S. L. Chin, Opt. and Laser Technol., *12*, 85, 1980.
2. C. A. Emshary, W. J. Firth, R. G. Harrison, A. K. Kar, J. G. H. Mathew, S. D. Smith, D. M. Tratt and E. M. Wright, Quantum Electronics and Electro-Optics, Ed., P. L. Knight, John Wiley and Sons Ltd. New York, 1983.
3. G. McClelland, S. D. Smith, R. G. Harrison and D. Tratt, Int. J. IR and mm Waves, *2*, 571, 1981.
4. A. Girard, Opt. Commun., *11*, 346, 1974.
5. L. C. Johnson, D. K. Mansfield and G. Taylor, Int. J. IR and mm Waves, *2*, 231, 1981.
6. T. Stamatakis, D. A. Reynolds, I. J. Spalding and A. C. Walker, Quantum Electronics and Electro-Optics, Ed. P. L. Knight, John Wiley and Sons Ltd. New York, 1983.
7. C. A. Emshary, Ph. D. Thesis, Heriot-Watt University, (unpublished, 1983).
8. J. R. Izatt, C. J. Budhiraja and P. Mathieu, IEEE J. Quant. Electron., QE-*13*, 396, 1977.
9. N. R. Heckenberg, Ipp IV/83 (July, 1975).
10. D. M. Tratt, A. K. Kar, J. G. H. Mathew and R. G. Harrison, Appl. Opt., *22*, 208, 1983.
11. J. Gilbert, J. L. Lachambre, F. Rheault and R. Fortin, Can. J. Phys., *50*, 2523, 1972.
12. E. Dumanchin, R. Bhatnager, P. E. Dyer and G. Salvetti, Opt. Commun., *26*, 228, 1978.

Acta Physica Hungarica, 63 (3—4), pp. 219—228 (1988)

A MODEL OF CHARGE

L. PARRAGH

*8400 Ajka, Hungary**

(Received in revised form 5 November 1985)

In this work a new, fundamentally non-linear term supplements Maxwell's and Einstein's Lagrangians. This term contains the acceleration of the charge. The field equations obtained from the variation principles are examined qualitatively only. The model gives a classical explanation of spin.

1. Introduction

The classical electron models (Thomson, Lorentz, Abraham, Poincaré, ..., Dirac), the Quantum Mechanics and the Quantum Field Theory have not, as yet, solved the problems of the inner structures of the elementary particles. In view of this, it was thought reasonable to look for new ways in this field.

The new approach followed here is somewhat unusual: In the scope of General Relativity the acceleration of the charge is taken into the Lagrangian. The most important purpose is to explain the spin of a charged particle with the help of some non-linearities in the Lagrangians. The field equations obtained with the simple tools of Classical Field Theory will be highly complex and hardly interpretable, but perhaps some quantum properties of the charge can be explained classically, too. It is important to mention that this model also contains Maxwell's Electromagnetic Field.

The Lagrangian Functions will be detailed first, then the field equations will be listed; following these the interactions written by the vector potential will be examined and the problem of the gauge-invariancy will be touched on; finally some macroscopic quantities of the charge will be calculated.

2. The action principle

The starting point is the action:

$$S = \int\int\int\int (L_g + L_e + L_{eq} + L_q) \sqrt{-g}\, d\Omega. \tag{1}$$

* Address: H-8400, Ajka, Hungary, Rákóczi út 41.

Here L_g is the Lagrangian of Einstein's Gravitational Field. In this work the basic vectors build up the metric tensor:

$$g_{\alpha\beta} = g_{\Lambda\Delta} e^{\Lambda}{}_{\alpha} e^{\Delta}{}_{\beta}. \tag{2}$$

Here $g_{\Lambda\Delta}$ is the constant Minkowski's Tensor, $e^{\Lambda}{}_{\alpha}$ are the basic vectors. Thus, the following expression is obtained for L_g

$$L_g = \frac{c^4}{16\pi\gamma} g_{\Lambda\Delta}(e^{\Lambda\delta}{}_{;\delta} e^{\Delta\rho}{}_{;\rho} - e^{\Lambda\delta}{}_{;\rho} e^{\Delta\rho}{}_{;\delta}). \tag{3}$$

This expression is invariant scalar and does not contain the second order derivatives.

The use of the basic vectors is advantageous when the macroscopic momentum is calculated, and when there are some spinors in the curved space-time. In the latter case the energy-momentum tensor cannot be calculated without the basic vectors.

L_e is the well-known Maxwell's Electromagnetic Lagrangian:

$$L_e = -\frac{1}{4\mu_0} F_{\alpha\beta} F^{\alpha\beta}. \tag{4}$$

Here

$$F_{\alpha\beta} = \mu_0(A_{\beta;\alpha} - A_{\alpha;\beta}) \tag{5}$$

and A_α is the vector potential.

L_{eq} is the interacting Lagrangian between the current density and the potential field. In this work it is taken in the following form:

$$L_{eq} = \alpha(-I_\delta I^\delta)^d I^\rho A_\rho . \tag{6}$$

Here α is a constant, and d is a power index. I^α is a vector field, which generally is not equal to the current density except for $d=0$. The power factor makes it possible to describe, for instance, the case of the identically constant proper charge density.

The Lagrangian of the charge has the form:

$$L_q = -\beta(-I_\delta I^\delta)^b a^f . \tag{7}$$

Here β is a constant, b and f are power indices, and

$$a = \sqrt{a_\rho a^\rho}, \tag{8}$$

$$a_\rho = u^\rho{}_{;\delta} u^\delta, \tag{9}$$

$$u^\rho = I^\rho / \sqrt{-I_\delta I^\delta}. \tag{10}$$

In equation (10), u^α is the unit velocity vector of the current density, so a^α is its acceleration vector. As the velocity vector is created algebraically and does not contain any derivatives, the acceleration contains the first order derivatives only. For this reason the variation problems can easily be solved.

With regard to Lagrangians (3), (4), (6) and (7), it seems that there are three variables, viz. A_α, I^α, $e^\Lambda{}_\alpha$.

3. The field equations

The resultant Lagrangian is:

$$L = L(e^\Lambda{}_\alpha, \partial e^\Lambda{}_\alpha/\partial x^\beta, A_\alpha, \partial A_\alpha/\partial x^\beta, e^\Lambda{}_\alpha, \partial e^\Lambda{}_\alpha/\partial x^\beta), \tag{11}$$

so three sorts of field equations can be derived from the variational principles.

First, let the action be varied with respect to the vector potential. The well-known Maxwell's Equations have the following form:

$$F^{\alpha\delta}{}_{;\delta} = \alpha(-I_\delta I^\delta)^d I^\alpha = \mu_0 J^\alpha. \tag{12}$$

Here J^α is the current density vector. This equation defines the current density vector.

Varying action (1) with respect to vector I^α gives the equation:

$$\begin{aligned}
&\alpha(-I_\delta I^\delta)^d A_\alpha - 2\alpha d(-I_\delta I^\delta)^{d-1} A_\rho u^\rho I_\alpha = \\
&= -2\beta(b-f)(-I_\delta I^\delta)^{b-\frac{1}{2}} a^f u_\alpha + \\
&+ \beta f(-I_\delta I^\delta)^{b-\frac{1}{2}} a^{f-2} a_\rho u^\rho{}_{;\alpha} - \\
&- \frac{\beta f}{\sqrt{-I_\rho I^\rho}} [(-I_\delta I^\delta)^b a^{f-2} a_\alpha u^\xi]_{;\xi}.
\end{aligned} \tag{13}$$

If d is not equal to $-1/2$, and I^α is not equal to zero, and I^α is not light-like, the vector potential can be calculated explicitly from Eq. (13) and we get:

$$\begin{aligned}
A_\alpha = &\frac{\beta}{\alpha}\left(\frac{-2b}{1+2d} + 2f\right)(-I_\delta I^\delta)^{b-d-\frac{1}{2}} a^f u_\alpha + \\
&+ \frac{\beta}{\alpha} f(-I_\delta I^\delta)^{b-d-\frac{1}{2}} a^{f-2} a^\rho u_{\rho;\alpha} - \\
&- \frac{\beta}{\alpha} f[(-I_\delta I^\delta)^{b-d-\frac{1}{2}} a^{f-2} a_\alpha]_{;\rho} u^\rho.
\end{aligned} \tag{14}$$

If d is equal to $-1/2$, the absolute value of the current density (the proper charge density) will be constant. In this case there is no explicit expression for the vector potential. However, the following equation will be valid:

$$A_\alpha + A_\rho u^\rho u_\alpha = -2\frac{\beta}{\alpha}(b-f)(-I_\delta I^\delta)^b a^f u_\alpha +$$

$$+\frac{\beta}{\alpha} f(-I_\delta I^\delta)^b a^{f-2} a_\rho u^\rho{}_{;\alpha} - \frac{\beta}{\alpha} f[(-I_\delta I^\delta)^b a^{f-2} a_\alpha u^\rho]_{;\rho}. \tag{15}$$

Multiplying Eq. (15) by u^α gives:

$$2\frac{\beta}{\alpha} b(-I_\delta I^\delta)^b a^f = 0. \tag{16}$$

There are two valid possibilities for Eq. (16):

i) $b=0$. In this case we get for the vector potential:

$$A_\alpha + A_\rho u^\rho u_\alpha = 2\frac{\beta}{\alpha} f a^f u_\alpha +$$

$$+\frac{\beta}{\alpha} f a^{f-2} a_\rho u^\rho{}_{;\alpha} - \frac{\beta}{\alpha} f(a^{f-2} a_\alpha u^\rho)_{;\rho}. \tag{17}$$

ii) $a^f = 0$. The $A_\alpha + A_\rho u^\rho u_\alpha$ vector can be finite and non zero if a^α is light-like, and f is equal to 2. We get for the vector potential:

$$A_\alpha + A_\rho u^\rho u_\alpha = 2\frac{\beta}{\alpha}(-I_\delta I^\delta)^b a_\rho u^\rho{}_{;\alpha} - 2\frac{\beta}{\alpha}[(-I_\delta I^\delta)^b a_\alpha u^\rho]_{;\rho}. \tag{18a}$$

The limit of the vector $A_\alpha + A_\rho u^\rho u_\alpha$ can be finite and non zero if a^α is not light-like, and f is equal to 1. In this case the vector potential is:

$$A_\alpha + A_\rho u^\rho u_\alpha = \frac{1}{2}\frac{\beta}{\alpha}(-I_\delta I^\delta)^b \frac{a_\rho}{\sqrt{a_\varphi a^\varphi}} u^\rho{}_{;\alpha} -$$

$$-\frac{1}{2}\frac{\beta}{\alpha}\left[(-I_\delta I^\delta)^b \frac{a_\alpha}{\sqrt{a_\varphi a^\varphi}} u^\rho\right]_{;\rho}. \tag{18b}$$

In the direction of vector u^α Eq. (18a) and (18b) are identities.

If a^α is light-like, and f is greater than 2, or if a^α is not light-like, and f is greater than 1, we get:

$$A_\alpha + A_\rho u^\rho u_\alpha = 0. \tag{19}$$

(The $I_\delta I^\delta = 0$ case should not be taken into consideration because in this case the Lagrangian L_{eq} would be infinite.)

It is important to mention that Eq. (15), (16), (17), (18a), (18b) and (19) must not be taken into account if d is not equal to $-1/2$.

Finally let the action be varied with respect to the basic vectors. The third group of field equations consists of Einstein's Gravitational Equations:

$$\frac{c^4}{8\pi\gamma}\left(R_{\alpha\beta}-\frac{1}{2}g_{\alpha\beta}R\right)=$$

$$=-\frac{1}{4\mu_0}F_{\delta\gamma}F^{\delta\gamma}g_{\alpha\beta}+\frac{1}{\mu_0}F_{\alpha\delta}F_{\beta}{}^{\delta}+K_{\alpha\beta}. \tag{20}$$

If d is not equal to $-1/2$, we shall get for the tensor:

$$K_{\alpha\beta}=\beta\left(\frac{2b}{1+2d}-1\right)(-I_\delta I^\delta)^b a^f g_{\alpha\beta}-$$

$$-\beta\left(2f-\frac{2b}{1+2d}\right)(-I_\delta I^\delta)^b a^f u_\alpha u_\beta-\beta f(-I_\delta I^\delta)^b a^{f-2}a_\alpha a_\beta+$$

$$+\beta f[(-I_\delta I^\delta)^b a^{f-2}(a_\alpha u_\beta u^\rho+a_\beta u_\alpha u^\rho-\mu_\alpha u_\beta a^\rho)]_{;\rho}. \tag{21}$$

If d is equal to $-1/2$, the $K_{\alpha\beta}$ tensor will have the form:

$$K_{\alpha\beta}=\alpha u^\delta A_\delta(g_{\alpha\beta}+u_\alpha u_\beta)-\beta(-I_\delta I^\delta)^b a^f g_{\alpha\beta}-$$

$$-2\beta(b-f)(-I_\delta I^\delta)^b a^f u_\alpha u_\beta-\beta f(-I_\delta I^\delta)^b a^{f-2}a_\alpha a_\beta+$$

$$+\beta f[(-I_\delta I^\delta)^b a^{f-2}(a_\alpha u_\beta u^\rho+a_\beta u_\alpha u^\rho-a^\rho u_\alpha u_\beta)]_{;\rho}. \tag{22}$$

4. Some remarks on the field equations

In view of the difficulty of surveying the field equations and because of their complexity, I could calculate approaching solutions in the Euclidean Field only. However, many useful conclusion can be reached without any solutions, too.

It is very important that the field equations should be interpreted where the current density is equal to zero. There are at least three possibilities for the field equations and the vector potential to be interpretable in this case:

i) Let vector I^α be light-like where the current density is equal to zero. The conditions of the existence of the vector potential not to be identically equal to zero, and not to be infinite are:

$$b-d-f-1=0, \tag{23}$$

$$d>0, \tag{24}$$

$$b>0. \tag{25}$$

For the vector potential we get:

$$\lim_{I_\delta I^\delta \to 0} A_\alpha = \frac{\beta}{\alpha}\left(2f - \frac{2b}{1+2d}\right)\left(I^\delta{}_{;\rho} I^\rho I_{\delta;\gamma} I^\gamma\right)^{\frac{f}{2}} I_\alpha . \tag{26}$$

This is a light-like vector.

ii) The second possibility is the following: Let vector I^α be equal to a product of an s scalar and a u^α unit vector:

$$I^\alpha = s u^\alpha . \tag{27}$$

If s is equal to zero, there is no current density (if d is not equal to $-1/2$). The vector potential and the field equations can exist if the following conditions are realized:

$$b - d - \frac{1}{2} = 0, \tag{28}$$

$$b > 0, \tag{29}$$

$$d > 0. \tag{30}$$

The vector potential is:

$$\lim_{s\to 0} A_\alpha(s, u^\rho) = \frac{\beta}{\alpha}\left(2f - \frac{2b}{1+2d}\right) a^f u_\alpha +$$

$$+ \frac{\beta}{\alpha} f a^{f-2} a^\delta u_{\delta;\alpha} - \frac{\beta}{\alpha} f (a^{f-2} a_\alpha)_{;\delta} u^\delta . \tag{31}$$

In this case, vector u^α assigns the possible orbit of the charge and determines the vector potential, but the vector potential does not contain the scalar explicitly. This case resembles one of de Broglie's [1] ideas.

iii) There are many cases when Eq. (13) is an identity. Firstly, let the direction of vector I^α be not light-like. If

$$d > 0, \tag{32}$$

and

$$b - 1/2 > 0, \tag{33}$$

and

$$\lim I^\alpha = 0, \tag{34}$$

then both sides of Eq. (13) are identically equal to zero.

Secondly, let vector I^α be light-like. If

$$d - 1 > 0, \tag{35}$$

and

$$b - f - 1 > 0, \tag{36}$$

then both sides of Eq. (13) are identically equal to zero, too.

In these cases we get Maxwell's Electro Vacuum.

Of course further potentials can be derived from Eq. (13) but these are identically equal to zero when the current density is equal to zero. These potentials do not describe any interactions among the remote current densities.

With regard to the gauge-invariancy it is remarkable that action (1) is gauge-invariant, but that Eq. (13) generally breaks this invariancy. If d is equal to $-1/2$, there will be a restricted gauge-invariancy. The transformation rules are:

$$A'_\alpha = A_\alpha + \partial\lambda/\partial x^\alpha, \tag{37}$$

$$I'_\alpha = tI_\alpha. \tag{38}$$

The conditions of transformation (37), (38) is the following if the acceleration is light-like:

$$\frac{\partial\lambda}{\partial x^\alpha} + \frac{\partial\lambda}{\partial x^\delta} u^\delta u_\alpha = \frac{1}{2}\frac{\beta}{\alpha}(t^{2b}-1)(-I_\delta I^\delta)^b a_\rho u^\rho{}_{;\alpha} -$$

$$-2\frac{\beta}{\alpha}(t^{2b}-1)[(-I_\delta I^\delta)^b a_\alpha u^\rho]_{;\rho} + 4\frac{\beta}{\alpha} b t^{2b-1}(-I_\delta I^\delta)^b a_\alpha t_{;\rho} u^\rho . \tag{39a}$$

If the acceleration is not light-like, we get for the conditions of transformation (37, 38).

$$\frac{\partial\lambda}{\partial x^\alpha} + \frac{\partial\lambda}{\partial x^\delta} u^\delta u_\alpha = \frac{1}{2}\frac{\beta}{\alpha}(t^{2b}-1)(-I_\delta I^\delta)^b \frac{a_\rho u^\rho{}_{;\alpha}}{\sqrt{a_\varphi a^\varphi}} -$$

$$-\frac{1}{2}\frac{\beta}{\alpha}(t^{2b}-1)\left[(-I_\delta I^\delta)^b \frac{a_\alpha u^\rho}{\sqrt{a_\varphi a^\varphi}}\right]_{;\rho} -$$

$$-\frac{\beta}{\alpha} b t^{2b-1} t_{;\rho}(-I_\delta I^\delta)^b \frac{a_\alpha u^\rho}{\sqrt{a_\varphi a^\varphi}}. \tag{39b}$$

Here λ and t are scalar functions. If either Eq. (39a) or (39b) is valid, the transformation (λ, t) can be used. If Eq. (39a) or (39b) is not valid, then transformation (λ, t) should not be used. In the direction of the u^α vector, Eq. (39a) and (39b) are identities. For this reason there is no explicit expression for $\partial\lambda/\partial x^\alpha$. Equations (39a) and (39b) are very strong constraints. Because of the non-linearities these transformations do not create any group, unless $1-t$ is infinitesimal. If $1-t$ is infinitesimal, and (λ_1, t_1) and (λ_2, t_2) are possible transformations, then $(\lambda_1+\lambda_2, t_1 \cdot t_2)$ will be possible transformations, too.

5. The macroscopic quantities

The macroscopic momentum can be defined as follows: Let the transformation $x'^{\alpha}=x^{\alpha}+\varepsilon^{\alpha}$ be applied to action (1). (The ε^{α} quantities are infinitesimal.) The continuity-type quantities are the components of the momentum. After this calculation we get:

$$P_{\alpha}=\frac{c^4}{8\pi\gamma}\iiint_F\sqrt{-g}\,(e_{\Lambda}{}^{\delta}{}_{;\delta}e^{\Lambda\bar{\gamma}}\delta_{\alpha}{}^{0}-e_{\Lambda}{}^{\delta}{}_{;\delta}e^{\Lambda 0}\delta_{\alpha}{}^{\bar{\gamma}}-$$

$$-e^{\Lambda\bar{\gamma}}e_{\Lambda}{}^{0}{}_{;\alpha})dF_{\bar{\gamma}}+\iiint_F\sqrt{-g}\,F^{0\bar{\gamma}}A_{\alpha}dF_{\bar{\gamma}}+$$

$$+\beta f\iiint_F\sqrt{-g}(-I_{\delta}I^{\delta})^{b}a^{f-2}(a^{\bar{\gamma}}u^{0}-a^{0}u^{\bar{\gamma}})u_{\alpha}dF_{\bar{\gamma}}. \tag{40}$$

Here $F_{\bar{\gamma}}$ is the two-dimensional surface of the three-dimensional space, and $\bar{\gamma}=1, 2, 3$. The zero indices denote the time-components of the quantities.

The third part is the momentum of the current density. This is equal to zero if there is no current density at the surface.

The second part is the momentum of the potential field. If the distance between the surface and the current density is sufficiently large, this part can generally be neglected.

The first part is the momentum of the gravitational field. This is simple enough because of the basic vectors that are used. This part represents the momenta of the current density and the potential field far from the current.

With the help of the fourth part of action (1) the angular momentum of the charge moving in a narrow world-tube can be calculated. In this case the current density can be written in the form:

$$\mu_0 J^{\alpha}=\alpha(-I_{\delta}I^{\delta})^{d}I^{\alpha}\cong c\frac{\Delta K}{\sqrt{-g}d\Omega}ds^{\alpha}. \tag{41}$$

Here ΔK is the charge, ds^{α} is the element of the orbit of the charge. The third and the fourth parts of action (1) will have the following forms:

$$S_{eq}+S_{q}=c\Delta K\int_{\sigma}\left(A_{\alpha}\frac{ds^{\alpha}}{d\sigma}-\frac{\beta}{\alpha}\frac{\sqrt{-ds^{\delta}ds_{\delta}}}{d\sigma}a^{f}\right)d\sigma \tag{42}$$

if

$$b-d-1/2=0.$$

Here σ is the parameter of the orbit of the charge. After some circuitous calculations the law of motion of the charge moving in the given potential field A_α and in the given gravitational field $e^{A\alpha}$ is obtained by varying action (42) with respect to σ:

$$c\Delta K\left\{\frac{1}{\mu_0}F_{\alpha\delta}u^\delta+\frac{\beta}{\alpha}(2f-1)(a^f u_\alpha)_{;\delta}u^\delta-\right.$$

$$\left.-\frac{\beta}{\alpha}f[(a^{f-2}a_\alpha)_{;\delta}u^\delta]_{;\gamma}u^\gamma-\frac{\beta}{\alpha}fa^{f-2}a^\rho u^\delta u^\gamma R_{\rho\delta\alpha\gamma}\right\}=0. \tag{43}$$

It is important to mention that this equation can have a stable (not self-accelerating) solution in the stationary state. The factor of the curvature tensor is the angular momentum of the charge [2] in Eq. (43), thus the spin is:

$$S_{\alpha\beta}=\frac{\beta}{\alpha}fc\Delta Ka^{f-2}\frac{1}{2}(a_\alpha u_\beta-a_\beta u_\alpha). \tag{44}$$

In reality the electromagnetic field and the gravitational field of the charge and the interaction have angular momenta, too. With the help of the field equation it is possible to calculate these angular momenta, and for the resultant spin we get:

$$\Sigma S_{\alpha\beta}=\left(3-2b-\frac{f}{2}\right)S_{\alpha\beta}. \tag{45}$$

If f is equal to 1, the absolute value of the spin will be constant. The greatest success of this model is that the proportion of the spin/charge can be explained classically, e.g. in the case of electrons. If, in Lagrangian (6), $\alpha=ce\mu_0 B$ and in Lagrangian (7) $f=1, \beta=c\hbar B/\left(3-2b-\frac{f}{2}\right)$ (B is an arbitrary constant), this model gives the classical description of electrons. This model gives the classical descriptions of several elementary particles in this case, too. That is, in action (1) there are two undefined signs. One of them is at the $\sqrt{-I_\rho I^\rho}$ factor corresponding to the two signs of the electrical charge. This does not influence the energy-momentum tensor or the spin. The other undefined sign is at the $\sqrt{a_\rho a^\rho}$ factor in Lagrangian (7). This does not influence the charge or the spin but it does influence the energy-momentum tensor. This picture corresponds to the e^+, e^-, μ^+, μ^- particles in quality.

The field equations of the particles of constant spin can be divided into many groupings of four if $d=1/2+n$, and $b=1+n$. Here n is an arbitrary integer number. Perhaps one of these cases describes the elementary particles.

6. Conclusions

In this work a conceptually very simple quantity, the acceleration of the charge, complements Maxwell's and Einstein's Lagrangians. This complementation leads to highly complicated and fundamentally non-linear field equations, and their interpretation is problematic. Many surprising consequences result from this complementation:

— In the scope of this model at least three sorts of interaction written by the vector potential can be interpreted. One of them is the Maxwell's Electromagnetic Interaction.

— The model can classically explain the spin.

— We can infer e^+, e^-, μ^+, μ^- elementary particles from this model in quality. Conclusions can be drawn for further groupings of four elementary particles.

Perhaps it would be useful to examine a model such as this more accurately.

The stationary solution of this model is able to give the classical interpretation of the accelerating and still not radiating states of the charges. After all this model is an example of how the geometry of motion can be used in Theoretical Physics.

Acknowledgement

I should like to thank Dr. B. Lukács for his extremely useful help.

References

1. Louis de Broglie, Certitudes et Incertitudes de la Science, Ed. Albin Michel, Paris, 1966.
2. J. L. Anderson, The Principles of Relativity Physics, W. B. Saunders Company, Philadelphia, 1967.

Acta Physica Hungarica, 63 (3—4), pp. 229—232 (1988)

THERMOLUMINESCENCE GLOW CURVES AND EMISSION SPECTRA OF THERMALLY PRE-TREATED PURE AND BARIUM DOPED SODIUM CHLORIDE

O. H. MAHAJAN[+], R. V. JOSHI, S. P. KATHURIA* and T. R. JOSHI

Applied Physics Department, Faculty of Technology and Engineering
M. S. University of Baroda, Baroda-1 India

(Received in revised form 10 November 1985)

The thermal glow curves and emission characteristics of annealed and air-quenched pure NaCl and NaCl: Ba(10^{-2} m.f.) specimens have been examined after the standard gamma exposure of 2.4×10^2 Gy at room temperature. The comparison of thermal glow curves and TL-emission spectra of these specimens reveals the important role of Ba^{2+} ions in the thermoluminescence behaviour of NaCl: Ba. The Tl-emissions at 495 and 435 nm are presumed to be associated with the observed glow peaks at 90 and 220 °C, respectively.

Introduction

Thermoluminescence (TL) is the emission of visible radiation from the pre-irradiated phosphor during warm-up. The knowledge of the TL centres requires information regarding the nature of the emission centres and the trapping sites. The TL-emission results from the recombination of the trapped electrons with the holes and vice-versa. It is normally believed that the TL emission occurs as a result of the electron–hole recombination at the impurity centre [1–3]. It has been possible to identify the emission centres by examining the TL-emission of the phosphor. The present measurements were undertaken to investigate the nature of the emitters. It is concluded that the emission occurring at the 220 °C peak arises due to electron–hole recombination at Ba^{2+} ion sites.

Experimental

The host material used in the present work was analar grade sodium chloride (99.90% pure) obtained from British Drug House Laboratory, Bombay. Powder specimens of pure and Ba-doped (10^{-2} m.f.) NaCl were prepared from the aqueous solution by the method of recrystallization. The powder specimens so obtained have been subjected to thermal treatment, namely annealing at 750 °C in open air for two

* Low level counting Laboratory, B.A.R.C., Hospital, Bombay-400 094, India
[+] Presently at Physics Department, M. J. College, JALGAON–425002, India

hours followed by rapid cooling (quenching rate 450 °C/min). Such specimens are designated as NaCl(T) and NaCl : Ba(T). All the specimens were exposed to standard saturated gamma dose, 4.2×10^2 Gy at room temperature. 20 mg of the powder was spread uniformly on Kanthal plate and TL-emission spectra were recorded for the thermally pre-treated NaCl and NaCl : Ba specimens (at 85, 120, 160, 200 and 230 °C) by using a 0.25 metre Jarrel Ash Ebert Monochromator. The TL glow curves of the above specimens were also recorded in the 30–400 °C temperature region. The heating rate for the present work was 200 °C/min. The TL measurements are carried out with the reader system described by Nambi [4] and Kathuria [5].

Results and discussion

The thermal glow curves of pretreated NaCl : Ba specimens were recorded along with those of undoped NaCl (Fig. 1A). The TL-emission spectra of these specimens at different temperatures were also examined and the same are presented in Fig. 1B. The experimental data reveals the following notable features:

(i) The NaCl(T) specimens display measurable TL output at 90 and 240 °C (Fig. 1A). The corresponding TL-emission around 230 °C is broad and weak with diffused maxima at 425 and 475 nm (Fig. 1(5B)).

(ii) The thermal glow curve of NaCl : Ba(T) specimen exhibits dominant glow peak at 220 °C with subsidiary peaks at 90 and 140 °C.

(iii) The emission spectra for NaCl : Ba(T) clearly demonstrate that at lower temperature (85 °C) the 495 nm band is prominent. With the rise in temperature there is a radical change in the emission spectrum which involves suppression of the 495 nm band and an emergence of pronounced emission at 435 nm. This characteristic is observed around 200 °C. If the temperature is raised beyond 200 °C the overall emission is suppressed.

On the basis of the present state of understanding of TL mechanism in divalent doped alkali halides [6–11], it is inferred that barium impurity–cation vacancy dipoles are the important components of the TL-centres responsible for the observed TL-emission in NaCl : Ba. In the present experiments only the emission spectra of NaCl(T) specimens displayed measurable output when recorded at 230 °C. This emission is presumed to be due to impurity unavoidably present in the base material. It is believed that such an impurity which remained in the precipitated state in the normally annealed and cooled base material got redissolved when the specimen was annealed and quenched from 750 °C.

In the present experiments the NaCl : Ba specimens were prepared from aqueous solution by the method of recrystallization. In such specimens one may not expect uniform distribution of barium impurity in the host lattice and at higher concentration the quenching of emission may result in leading to low TL output. On the other hand, quenching of NaCl : Ba specimens from elevated temperature would favour dissolution as well as uniform distribution of Ba^{2+} impurity in the host lattice. This would give

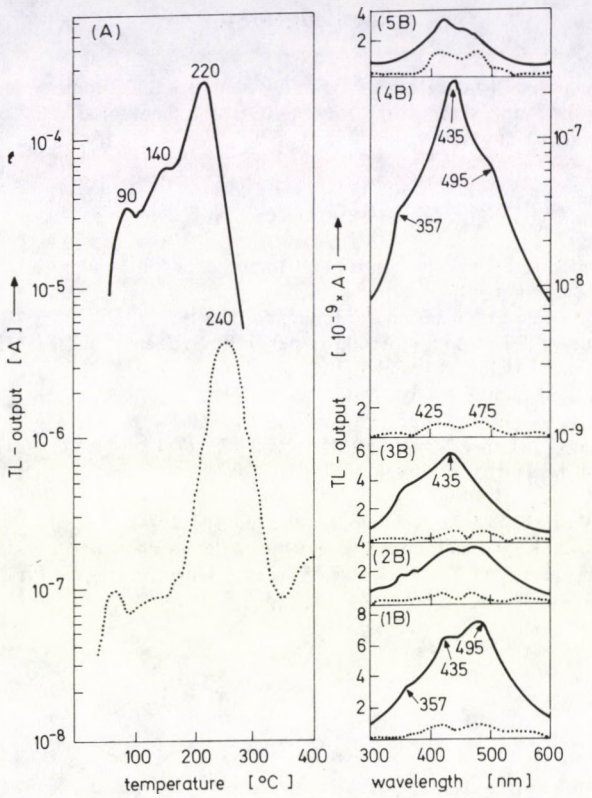

Fig. 1. (A): TL-glow curves and (B): TL-emission spectra at 85 °C (1B), 120 °C (2B), 160 °C (3B), 200 °C (4B) and 230 °C (5B), gamma-dose 2.4×10^2 Gy
——— curves for NaCl: Ba (T)
– – – – curves for NaCl: (T)

rise to a large concentration of impurity–vacancy dipoles in the NaCl: Ba(T) specimens and the consequential enhancement in the observed TL-emission. Changes in the relative intensities of the three emission bands with temperature indicate that the TL-centres associated with the 495 nm emission band are susceptible to thermal bleaching at temperatures lower than those for 357 and 435 nm emission. It is therefore concluded that the 495 nm emission relates to shallower traps and the remaining two emissions are associated with comparatively deeper traps.

The comparison of TL-glow curves and emission spectra of NaCl: Ba(T) (10^{-2} m.f.) reveals that the substantial TL-emission output at 435 nm corresponds to the glow peak at 220 °C whereas the glow peak at 90 °C can be correlated with the 495 nm emission band. The remaining emission band around 357 nm may be associated with the glow peak at 140 °C. Since the TL-emissions observed in the present experiments can be identified with characteristic Ba-emissions [12–13], it is believed that the Ba impurity plays an important role as an emitter in the TL of NaCl: Ba(T).

Acknowledgement

The authors are grateful to the Health Physics Division, B.A.R.C., Bombay, for the experimental facility provided during the course of this work. One of us (OHM) is thankful to M.S. University of Baroda for the award of a Research Fellowship.

References

1. P. D. Townsend and J. Kelly, Colour Centres and Imperfections in Insulators and Semiconductors, Chatto and Windus, London, 1973.
2. S. B. S. Sastry and K. Balasubramanyam, J. Lumin., *15*, 267, 1977.
3. F. J. Lopez, F. Jaque, A. J. Fort and F. Agullo-Lopez, J. Phys. Chem. Solids, *38*, 1101, 1977.
4. K. S. V. Nambi, Science To-day, December, p. 12, 1981.
5. S. P. Kathuria and C. M. Sunta, J. Phys. D *12*, 1537, 1979.
6. R. M. Grant and J. R. Cameron, J. Appl. Phys., *37*, 3791, 1968.
7. F. Agullo-Lopez and F. J. Lopez, Cryst. Latt. Defect., *9*, 131, 1981.
8. J. H. Jackson and A. M. Harris, J. Phys. C., *3*, 1967, 1970.
9. J. S. Dryden and B. Shuter, J. Phys. *D 6*, 123, 1973.
10. R. V. Joshi and N. L. Kekan, Z. für Kristallographie, *139*, 153, 1974.
11. R. V. Joshi, T. R. Joshi, K. P. Dhake and S. P. Kathuria, Health Physics, *44*, 29, 1983.
12. A. N. Zaidel, Prof'evs and S. M. Raiskii, 'Table of Spectral Lines', Pergamon Press, Oxford, 1961.
13. K. Kojima, J. Phys. Soc. Japan, *19*, 868, 1964.

Acta Physica Hungarica, 63 (3—4), pp. 233—242 (1988)

ON THE VALIDITY OF THE DISCONTINUOUS STOPPING TECHNIQUE IN DOPPLER SHIFT ATTENUATION MEASUREMENTS

M. M. ABDEL HADY*, Á. Z. KISS, E. KOLTAY and B. NYAKÓ

Institute of Nuclear Research of the Hungarian Academy of Sciences
4001 Debrecen, Hungary

(Received 10 November 1985)

Monte Carlo calculations have been performed to investigate some quantitative features of the slowing process underlying nuclear lifetime determination in Doppler Shift Attenutation Method (DSAM). Kregar et al's numerical method developed for a simplified description of the process was found to be applicable in strongly limited intervals of recoil velocity and lifetime only.

Introduction

In recent years the Doppler energy shift of gamma radiation from excited nuclei recoiled in nuclear reactions has become widely used in many nuclear laboratories as a tool for the determination of the lifetimes of nuclear excited states. One of the techniques referred to as Doppler Shift Attenuation Method (DSAM) is appropriate for lifetime determination in the time interval 10^{-15}–10^{-12} s. In DSAM the decay of the excited level is observed on the time base given by the slowing down of the recoil in the target layer and in the target backing. The slowing process itself consists of a series of elastic and inelastic collisions between the recoil and stopper atoms, which result in a step-by-step loss of the initial velocity. The energy shifts observed in the spectrum of emitted gamma rays are determined by the ratio of the lifetimes to slowing time for the system composed of recoil and slowing atoms.

In practical evaluation work, $F(\tau)=\langle v\rangle/v_0$ curves are deduced from the slowing theory for the actual reaction, where $\langle v\rangle$ and v_0 denote average and initial recoil velocities, respectively. Lifetime τ is then determined from a comparison with the experimental F value, defined as the ratio of the average energy shift to the maximum one.

For a complete evaluation of the measurements the details of the slowing process should be known and taken into consideration. The reliability of the measured lifetimes — still questionable in many respects (see e.g. [1]) — depends on the accuracy

* Permanent address: Ain Shams University, Cairo, Arab Republic of Egypt

of the theoretical description and on practical approximations used in the treatment of the slowing process.

The theoretical study of the slowing of a recoil nucleus penetrating through a stopper medium was pioneered in the works of Lindhard, Scharff and Schiøtt (LSS-theory) [2, 3]. Their results are of vital importance in the evaluation of DSAM measurements. These works serve as the best theoretical frame for the calculation of energy loss rates due both to elastic and inelastic collisions of the recoils on atoms (nuclear stopping) and shell electrons (electronic stopping). The basic characteristics of the slowing process are related to the potential function adopted for the description of Coulomb interaction between recoil and stopping atoms; Thomas–Fermi potential is normally used in calculating the scattering function. On the other hand, the energy loss due to inelastic collisions with the electron shell of the stopper atoms can be treated in different energy ranges using different models (e.g. [3]).

The most widely used practical formalism in DSAM was developed by Blaugrund [4] from Lindhard's stopping theory.

Due to the statistical nature of the parallel processes of electronic and atomic stopping, the Monte Carlo treatment [5] is a realistic procedure for the generation of the spectrum of Doppler shifted gamma quanta, which reflects the kinematic conditions of the recoil at the instant of its deexcitation. The physical parameters of statistical determination are:

— the depth of the target layer in which nuclear reaction occurs;
— the initial value and direction of the recoil velocity related through the kinematic equations of the nuclear reaction;
— the mean free path between successive events as the function of energy;
— the scattering direction of the recoil in a scattering event;
— the decay time of the excited level by gamma emission determined in the form of the exponential law of decay;
— the direction of the gamma quantum as it enters the gamma detector.

The energy shift of a single gamma quantum is finally determined by the actual values of the above parameters which are selected for the recoil considered in a random way. The Monte Carlo treatment performs a simulation of the history of the recoil by selecting the parameter values randomly both for initial conditions and for all the successive scattering events, for a high number of recoils.

The Monte Carlo technique is the most promising way in DSAM-based research. On the one hand, it is well applicable in routine evaluation work, while on the other, it represents a good tool for checking other less time consuming evaluation methods.

Recently, Latta [6] presented a comparison of Blaugrund and Monte Carlo centroid-shift calculations. He came to the conclusion that the standard Blaugrund analysis at low initial recoil energy and large $F(\tau)$ values results as a rule in lifetime estimates at least 20% too low.

Low initial recoil energy values occur in the case of (p, γ) reactions, where DSAM is widely used for the determination of short lifetimes. For this case Kregar et al [7, 8] proposed a discontinuous stopping model for an approximative description of the slowing process of the recoil nucleus.

Kregar et al's method is based on the argument that the average free path of the recoil in the target and/or backing layer exceeds in many cases the distance travelled by the excited nucleus before de-excitation through gamma emission. Therefore, under the condition of low velocity and short lifetime the neglection of all possible scattering events except for the first three of four ones represents a good approximation of the real case. Their numerical method is equivalent to the truncation of the whole chain of atom–atom scattering at a low number of scattering events. They came to the conclusion that for an excited nucleus with a lifetime less than 10^{-13} s the conditions for the truncation method are fulfilled, if the recoil velocity is less than $\beta_0 = 0.2\%$.

Kregar was engaged in discussion with Latta and Scanlon [9, 10] on the validity of the discontinuous stopping method in DSAM [11]. Latta et al concluded that the available information was not sufficient to justify the method. The results of Caraca and Correa [12] from Monte Carlo calculation did not support the few-step slowing in the case of ^{28}Si recoil penetrating in aluminium with an initial velocity of $\beta_0 = 0.14\%$, nevertheless they considered the method as a valuable and illuminating contribution to the DSA discussion.

Taken the fact into consideration that the mean free path depends on the atomic structure and density of the slowing medium, it is plausible that a more detailed investigation is needed on the condition of applicability of the discontinuous stopping method.

With a proper modification of the Monte Carlo code of Currie [5] we obtained a direct tool for the systematic investigation of the effect of the truncation by stopping the calculation after a prescribed number of scattering events for each recoil. Calculations were performed with the aim of contributing to the question of the validity interval of Kregar et al's method.

Computational details

Part of the investigation was performed through calculations of $F(\tau)$ curves for recoil nucleus ^{14}N entering a tantalum layer with several initial velocities in the range of $0.052\% \leq \beta_0 \leq 0.414\%$, corresponding to the proton energy interval in $^{13}C(p,\gamma)^{14}N$ reaction 0.03 MeV $\leq E_p \leq$ 1.95 MeV. Another set of calculations was performed for the case of recoil nucleus ^{28}Si slowing down in aluminium at initial velocities $\beta_0 = 0.14\%$ and 0.2% which correspond to proton energies in the $^{27}Al(p,\gamma)^{28}Si$ reaction $E_p = 0.767$ and 1.800 MeV, respectively.

The Monte Carlo calculations were performed both in truncated mode with the number of scattering events for each recoil limited to a selected number n and in the original mode, where Monte Carlo chains are stopped only when the initial recoil energy E_i decreases to the final value $E_f = 0.97^{512} E_i$.

Results and discussion

Some of the results are shown in Figs 1 and 2 where calculated $F(\tau)$ curves are plotted for ^{14}N recoils entering Ta stopper with $\beta_0 = 0.0522\%$ and 0.35% initial velocities, respectively. Here full curves correspond to the full chains of scattering events while dashed lines represent the different versions of truncated calculations. In these figures the qualitative features of Kregar et al's statement are confirmed. The truncation model seems to be valid for very short lifetimes and low ion velocities, but the method breaks down with increasing values of these parameters.

The same tendency appears in Fig. 3 for the case of ^{28}Si slowing in aluminium. The remarkable difference with respect to the case of ^{14}N is a closer approximation of the untruncated $F(\tau)$ curve by truncated ones at a certain n value, which calls one's attention to the influence of the mass ratio M_1/M_2 on the validity of the approximation. (Here M_1 and M_2 refer to the mass of the recoil and stopping nuclei, respectively).

As for the quantitative results, the limits of applicability seem to be overestimated in paper [7], as it turns out from the calculated data presented in the Figures.

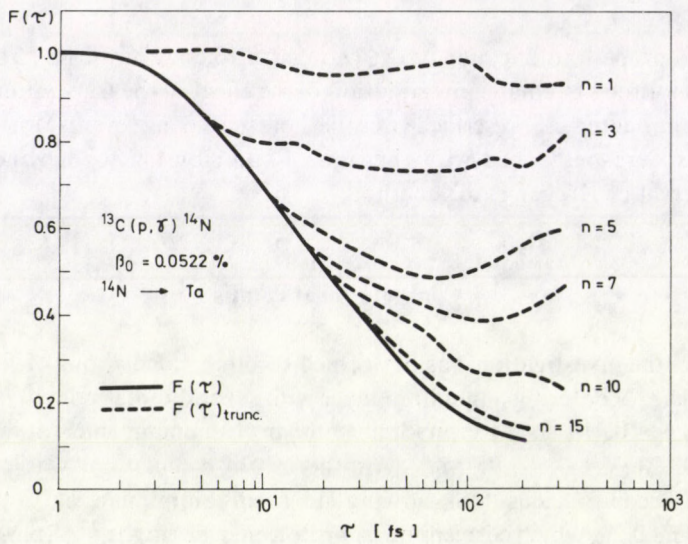

Fig. 1. Computed $F(\tau)$ functions for the $^{13}C(p, \gamma)^{14}N$ reaction at $E_p = 31$ keV bombarding energy as obtained using $n = 1$–15 and infinite events of scattering (dashed and full lines, respectively)

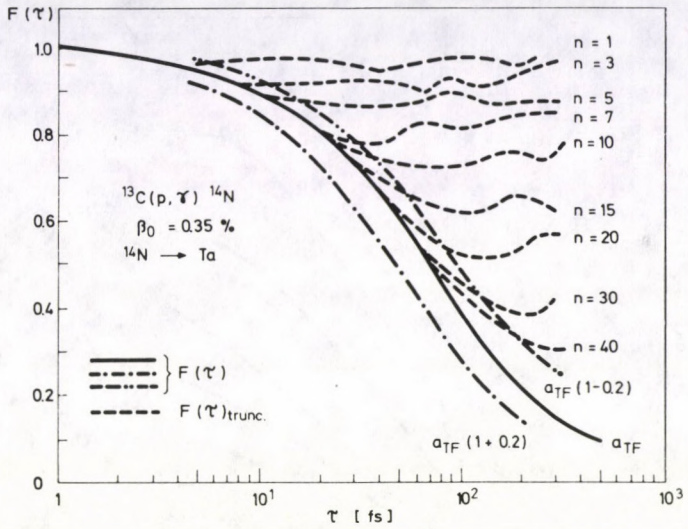

Fig. 2. Same as in Fig. 1, at $E_p = 1.15$ MeV. Dashed–dotted lines were calculated for infinite events, with modified a_{TF} parameters

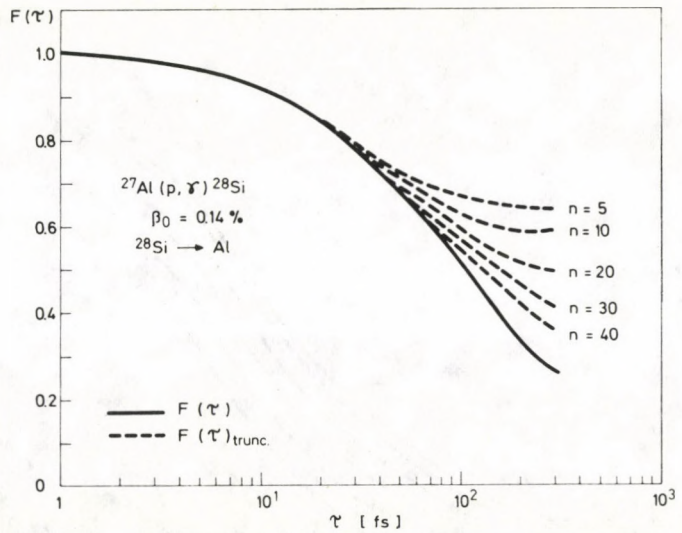

Fig. 3. Same as in Fig. 1, for $^{27}Al(p, \gamma)^{28}Si$, at $E_p = 0.767$ MeV

The minimum number of scattering events to be taken into consideration can be well estimated for the case of the selected recoil and stopping medium from Figs 4 and 5, where the differences appearing between $F(\tau)$ curves for truncated and non-truncated calculations are presented for the case of ^{14}N in tantalum. The difference measuring the validity of the approximation decreases with increasing

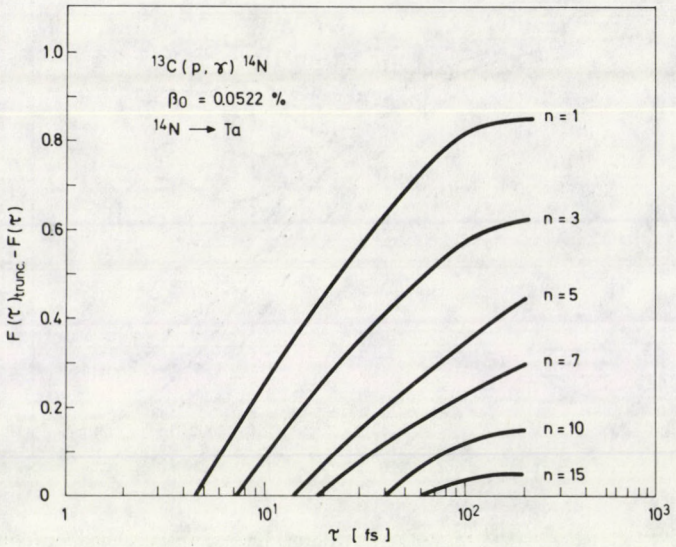

Fig. 4. The difference of truncated and non-truncated $F(\tau)$ values as the function of lifetime τ in the case of ^{14}N recoils in tantalum, at $\beta_0 = 0.052\%$

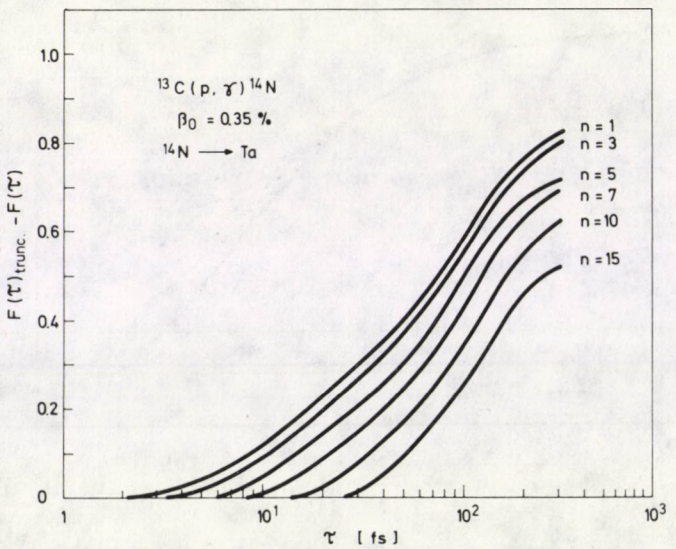

Fig. 5. Same as in Fig. 4 for $\beta_0 = 0.35\%$

number of scattering events in the truncated case. To sum up the results, Fig. 6 gives, as the function of lifetimes, the number of scattering events, at which the truncation will result in an error

$$\Delta = F(\tau)_{\text{trunc}} - F(\tau) \leq 0.005.$$

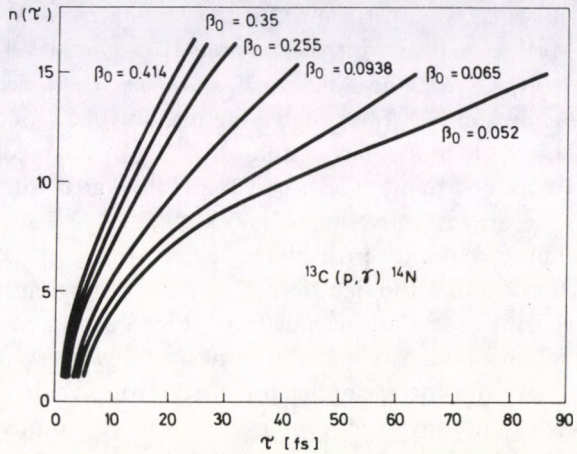

Fig. 6. Number of scattering events, as the function of life-time, at which a truncation would result in an error less than 0.5%. Data are given for different β_0 values in the reaction $^{13}C(p, \gamma)^{14}N$

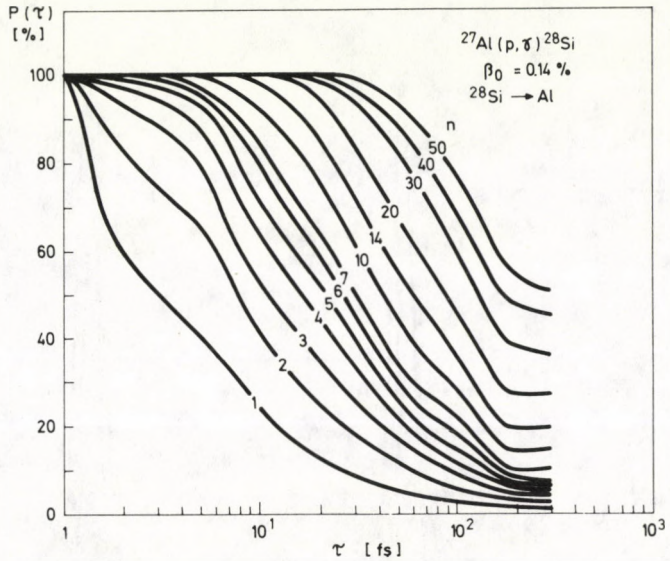

Fig. 7. Number of ^{28}Si recoils de-excited before the n-th collision during slowing in aluminium. Initial recoil velocity $\beta_0 = 0.14\%$, lifetime $\tau = 60$ fs

The parameter of the curves is the initial velocity. The curves can be considered as limits for the applicability of the discontinuous stopping technique.

For another way of checking the actual conditions, the Monte Carlo code was modified to calculate the relative number of excited recoils de-excited before the n-th collision event. Results for ^{28}Si recoils slowing in aluminium are presented in Fig. 7, where $P(\tau)$ is the number of decay events before the n-th collision, as the function of

lifetime τ. The calculations were performed for the 4.62→1.78 MeV transition in ^{28}Si on the $E_p = 0.767$ MeV resonance (which corresponds to an initial velocity $\beta_0 = 0.14\%$). A lifetime value $\tau = 60$ fs for the 4.62 MeV state has been derived from DSA measurements. As shown in Fig. 7, for such a lifetime only 4.6% of the excited nuclei will emit a γ-ray before the first collision and only 23% of the recoils will suffer less than 4 collisions before de-excitation. These values fully agree with those of Caraca and Correa who gave the respective numbers 5 and 20%.

The nature of systematic error made by a strong truncation is clearly demonstrated by the theoretical γ-line shapes derived from truncated (finite n) and non-truncated ($n = \infty$) Monte Carlo calculations. Fig. 8 shows results obtained for ^{14}N recoils in tantalum backing. The build-up of the "slow peak" at lower energies proceeds continuously with increasing length of scattering chains, the effect of the lifetime on the speed of the convergence can be seen from the comparison of the cases with $\tau = 80$ and 160 fs.

As pointed out by Kregar [13] the number of collisions experienced by the recoil nucleus during lifetime depends critically upon the choice of the average free

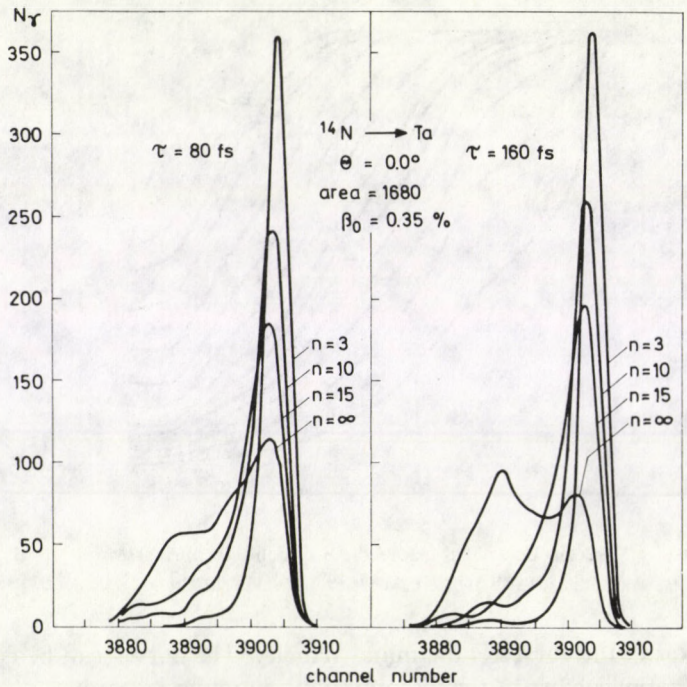

Fig. 8. Calculated gamma line shapes for the decay of ^{14}N with the emission of 3891 keV gamma quanta, at $\beta_0 = 0.35\%$ corresponding to the proton energy $E_p = 1.15$ MeV (tantalum backing)

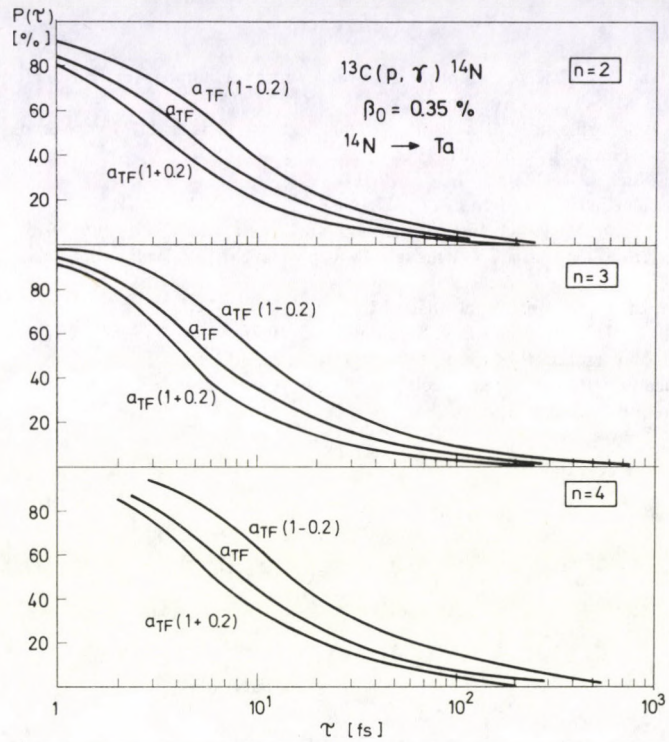

Fig. 9. Number of ^{14}N recoils de-excited before the n-th collision during slowing in tantalum. Initial recoil velocity $\beta = 0.35\%$, lifetime 160 fs. The effect of modified a_{TF} parameters is indicated by the parallel curves

path, or alternatively upon the scattering radius a appearing in Thomas–Fermi potential. The influence of the variation of a by $\pm 20\%$ upon the $F(\tau)$ curve is indicated in Fig. 2 with dashed–dotted line. The same effect on $P(\tau)$ is shown in Fig. 9. It is obvious that the validity interval for the truncation method will be more or less modified by the actual value of the parameter. Making the good interatomic potential still remains an open question. The comparison of accurately measured gamma line shapes with calculated ones might well reveal the information upon the true interatomic potential.

Acknowledgement

The authors are indebted to M. Kregar for valuable comments.

References

1. M. M. Abdel Hady, Á. Z. Kiss, E. Koltay, B. Nyakó and M. Hautala, Acta Phys. Hung., *58*, 11, 1985.
2. J. Lindhard and M. Scharff, Phys. Rev., *124*, 128, 1961.
3. J. Lindhard, M. Scharff and H. E. Schiøtt, K. Dan, Vidensk. Selsk. Mat. Fys. Medd., *33*, 14, 1963.
4. A. E. Blaugrund, Nucl. Phys., *88*, 501, 1966.
5. W. M. Currie, Nucl. Instr. Meth., *73*, 173, 1969.
6. B. M. Latta, Nucl. Instr. and Meth., *211*, 447, 1983.
7. M. Kregar, P. Kump, M. Pavsic and M. Vakselj, Nucl. Instr. Meth., *109*, 109, 1973.
8. M. Kregar, P. Kump, M. Pavsic, V. Ramsak, P. Rupnik and M. Vakselj, Nucl. Instr. Meth., *127*, 243, 1975.
9. B. M. Latta and P. J. Scanlon, Nucl. Instr. Meth., *114*, 179, 1974.
10. B. M. Latta, B. C. Robertson and P. J. Scanlon, Nucl. Instr. Meth., *133*, 583, 1976.
11. M. Kregar, M. Vakselj and P. Rupnik, Nucl. Instr. Meth., *133*, 585, 1976.
12. J. M. G. Caraca and P. M. Correa, Nucl. Instr. Meth., *155*, 331, 1978.
13. M. Kregar, private communication, 1984.

Acta Physica Hungarica, 63 (3—4), pp. 243—247 (1988)

THE ROLE OF ELECTRONEGATIVITIES IN THE CALCULATION OF DIATOMIC MOLECULAR PARAMETERS*

[Halides of group III elements]

A. VARADA RAJULU**, R. VISWANATH

Spectroscopic Laboratories, S. K. University
Anantapur-515 003, India

and

S. SZŐKE

Central Research Institute for Chemistry
Budapest, Hungary

(Received in revised form 10 December 1985)

The force constants for diatomic molecules and isolated bonds may be expressed by using equalized electronegativities, bond strengths and interatomic distances. Some halides of group III elements have been studied and the proportionality constant d, as well as the Lennard-Jones parameters ab and b determined for the potential energy functions used by Szőke in calculating the anharmonicity $\omega_e x_e$ and the rotational-vibrational coupling constant α_e. The variations of molecular parameters with atomic number Z have been studied.

1. Introduction

The concept of electronegativity introduced by Pauling [1] is useful in understanding the nature of chemical bonds. The theory was modified by Iczkowski and Margrave [2] and Mulliken [3] and used by Szőke [4–7]. Pasternak [8] explained deviations of Pauling's formula from experiments on the basis of the simple bond charge model of Parr and Borkman [9]. Mohammad [10] stated that the bond energy of a molecule can be represented by the sum of the electronegativities of the constituent atoms forming the bond and their product partially represents the charge density. The concept of equalized electronegativity was introduced by Sanderson [11] and later extended to orbital electronegativities. The authors have used electronegativities together with spectroscopic constants and have adopted the relations of Szőke [4–7] for the evaluation of d, ab, b, $\omega_e x_e$ and α_e for some halides of group III elements.

* Work carried under Indo-Hungarian Cultural Exchange Programme
** To whom correspondence should be addressed

2. The estimation of d

Szőke's relation [4–7]

$$k_e = d\varepsilon D_e^{1/2} r_e^{-1} \tag{1}$$

was used, where k_e is the force constant, r_e the internuclear distance, D_e the dissociation energy and the mean electronegativity is

$$\varepsilon = (e_i e_j)^{1/2}, \tag{2}$$

where e_i and e_j are atoms in the molecules and

$$k_e = 5.8883 \times \omega_e^2 \mu 10^{-5} \text{ N/m}. \tag{3}$$

The electronegativities from Pauling [1], the molecular parameters from Huber and Herzberg are used in the evaluation of d from Eq. [1]. Parameters used can be found in Table I.

The proportionality constant d may be assumed to be approximately constant considering the uncertainties in D_e and approximate estimates of electronegativities used in this calculation. The individual values of d do not deviate appreciably (the standard deviation being 0.132) from the mean value of 0.951, thus establishing the validity of Eq. (1) which is based on the above approximation.

Table I

Molecule	k_e [N/m]	r_e [nm]	D_e [KJ/mol]	$=(e_i e_j)^{1/2}$	d
BF	807	0.1263	754	2.828	1.313
AlF	423	0.1654	665	2.449	1.107
GaF	340	0.1774	577	2.523	0.994
InF	275	0.1985	507	2.608	0.931
TlF	233	0.2084	441	2.449	0.946
Bcl	347	0.1716	531	2.449	1.056
AlCl	208	0.2130	494	2.121	0.939
GaCl	182	0.2017	474	2.191	0.770
InCl	159	0.2401	428	2.258	0.817
TlCl	142	0.2485	369	2.121	0.865
AlBr	169	0.2295	425	2.049	0.917
TlBr	126	0.2618	330	2.049	0.887
AlI	131	0.2537	364	1.936	0.900
GaI	123	0.2575	335	2.000	0.868
			Standard deviation		0.132

3. Variation of molecular parameters with atomic number Z

In a class of similar type of molecules such as oxides, halides, hydrides, etc., the molecular parameters vary in a periodic fashion as functions of atomic number Z [13]. This is clearly evident in Fig. 1, which shows the plots of internuclear distance r_e (dotted line) and the force constant k_e (solid line) of the molecules under study in their ground states as functions of Z. It is observed that r_e exhibits a minimum within each period while k_e exhibits exactly an opposite trend for a particular value of Z in line with theoretical expectations.

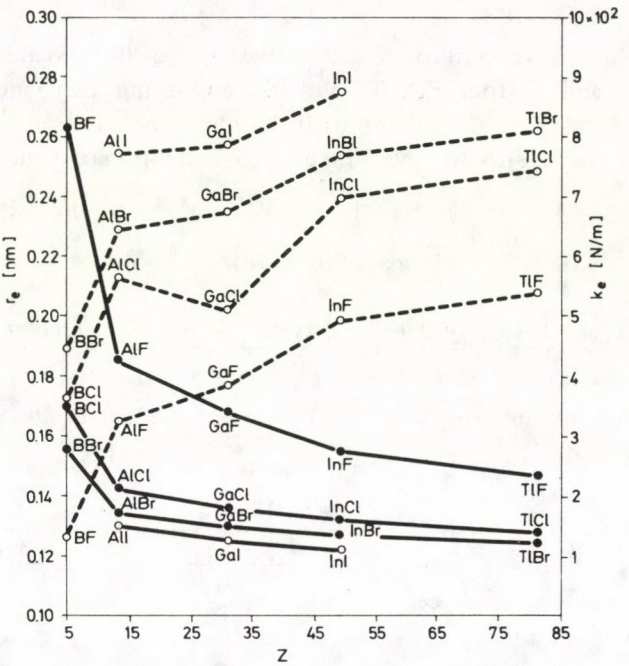

Fig. 1. Dependence of the force constants and internuclear distances on the atomic number Z

4. Validity of Lennard-Jones parameters and the evaluation of $\omega_e x_e$ and α_e

To construct an empirical potential energy function with more than three parameters, it is advisable to use physico-chemical parameters in addition to the spectroscopic constants. Such a function proposed by Szőke is presented in Eq. (4)

$$U = D_e[1 - \exp - \gamma(r - r_e)^2/r], \tag{4}$$

where

$$\gamma = d(e_i e_j / D_e)^{1/2} \tag{5}$$

and U is the potential energy.

In general, the potential energy functions do not describe the lower and higher energy levels with the same accuracy. Hence the original Lippincott energy function is modified by the addition of Lennard-Jones [14] supplementary term to take care of the Van der Waals forces and is given by Eq. (6)

$$U = D_e[1 - \exp - \gamma(r - r_e)^2/r]\,[1 + af(r)], \tag{6}$$

where $f(r)$ is a function of the internuclear distance, such that $f(r) \to 0$ as $r \to \infty$ and $f(r) \to \infty$ as $r \to 0$.

The authors have verified the correctness of Eq. (6) by calculating first the parameters ab and b from Eqs (8) and (9), and using their mean values, the anharmonicity and rotational–vibrational coupling constants are then evaluated employing Eqs (7) and (8) as done by Dunham [15] and Lippincott and Schroeder [16].

$$\omega_e x_e = 1.5 B_e[0.25 + \gamma r_e/2 + ab(\gamma r_e)^{1/2} + (a^2 b^2/1.6 - ab^{2/2})2r_e], \tag{7}$$

$$\alpha_e \omega_e / 6B_e^2 = ab(\gamma r_e) \tag{8}$$

and

$$b = \frac{5/4(-1 - \alpha_e \omega_e / 6B_e^2)^2 - 2\omega_e x_e / 3B_e - 1 + \gamma r_e/2 - 3/2ab(\gamma r_e)^{1/2}}{ab\gamma r_e}. \tag{9}$$

These values are presented in Table II. The average values of ab and b are 15.353 and 8.623, respectively.

Table II

Molecule	ab	b	$\omega_e x_e$ [m^{-1}] Cal.	Expt.	Difference [%]	α_e [m^{-1}] Cal.	Expt.	Difference [%]
BF	15.588	8.431	1138	1184	−3.88	1.950	1.980	−1.51
AlF	16.553	9.184	423	427	−11.32	0.462	0.498	−7.24
GaF	16.882	10.307	288	320	−10.00	0.260	0.286	−9.05
InF	16.555	9.572	235	264	−10.98	0.173	0.188	−7.81
TlF	15.844	8.253	212	230	−7.82	0.146	0.150	−3.10
BCl	13.919	6.996	566	511	+10.76	0.713	0.646	+10.29
AlCl	15.723	9.996	200	195	+2.56	0.157	0.161	−2.35
GaCl	17.207	10.615	106	120	−11.66	0.071	0.079	−10.77
InCl	15.731	8.940	98	101	−2.97	0.051	0.052	−2.40
TlCl	14.628	8.347	88	82	+7.32	0.042	0.039	+4.95
AlBr	14.811	8.922	140	128	+9.38	0.089	0.086	+3.66
TlBr	14.012	7.700	44	39	+12.82	0.014	0.013	+9.57
AlI	13.956	7.313	122	100	+12.00	0.061	0.056	+10.01
GaI	13.431	6.144	56	50	+12.00	0.022	0.019	+14.31
		Average values			8.21%			8.56%

The average deviations between the estimated and experimental values of $\omega_e x_e$ and α_e are 8.21% and 8.56%, respectively, justifying the use of Lennard-Jones parameters for the evaluation of $\omega_e x_e$ and α_e on the concept of mean electronegativity.

Acknowledgements

One of the authors (A.V.R.) expresses his sincere thanks to both the Hungarian Ministry of Education and the University Grants Commission of India for making it possible to carry out this work in Budapest.

References

1. L. Pauling, The Nature of the Chemical Bond, Cornell University Press, Ithaka, New York, 1960.
2. P. P. Iczkowski and J. L. Margrave, J. Am. Chem. Soc., *83*, 3547, 1961.
3. R. A. Mulliken, J. Intern. Quant. Chem., *1*, 1, 1967.
4. S. Szőke, Acta Chim. Acad. Sci. Hung., *57*, 129, 1968.
5. S. Szőke, Acta Chim. Acad. Sci. Hung., *51*, 183, 1967.
6. S. Szőke, Acta Chim. Acad. Sci. Hung., *58*, 399, 1968.
7. S. Szőke, Acta Chim. Acad. Sci. Hung., *68*, 345, 1971.
8. A. Pasternak, Chem. Phys., *26*, 101, 1977.
9. R. G. Parr and R. F. Borkman, J. Chem. Phys., *49*, 1055, 1968.
10. S. Noor Mohammad, Ind. J. Pure. Appl. Phys., *17*, 403, 1979.
11. R. T. Sanderson, Science, *114*, 670, 1951.
12. K. P. Huber and G. Herzberg, Constants of Diatomic Molecules, Van Nostrand Reinholds Co., New York, 1979.
13. G. Herzberg, Molecular Spectra and Molecular structure, Vol. I, Van Nostrand Co., New York, 1967.
14. J. E. Lennard-Jones, Proc. Roy. Soc. London, *A106*, 463, 1924.
15. J. L. Dunham, Phys. Rev., *41*, 421, 1932.
16. E. R. Lippincott and J. Schroeder, J. Chem. Phys., *23*, 1131, 1955.

Acta Physica Hungarica, 63 (3—4), pp. 249—255 (1988)

INTENSITY DISTRIBUTION IN THE ROTATIONAL STRUCTURE OF $^1\Delta$–$^3\Sigma$ AND $^1\Pi$–$^3\Sigma$ TRANSITIONS IN DIATOMIC MOLECULES

T. K. BALASUBRAMANIAN and V. P. BELLARY

Spectroscopy Division, Bhabha Atomic Research Centre
Trombay, Bombay-400 085 India

(Received in revised form 8 January 1986)

Rigorous analytic formulae are derived for the rotational intensity factors of the lines of all the branches resulting from the spin-forbidden electronic transitions $^1\Delta$–$^3\Sigma$ and $^1\Pi$–$^3\Sigma$ in diatomic molecules. The present derivation incorporates a full-fledged intermediate coupling treatment of the $^3\Sigma$ state which includes the effects of centrifugal distortion on spin uncoupling. These formulae when applied to the transition $a^1\Delta_g$–$X^3\Sigma_g^-$ in diatomic sulphur predict an intensity pattern that markedly differs from the predictions of previous formulae based on case (b) treatment of $^3\Sigma$.

1. Introduction

Beginning with the work of Hönl and London [1] analytic formulae describing the rotational intensity distribution in the band spectra of diatomic molecules arising from a number of multiplet electronic transitions have been derived over the years, many of them by Kovács. Extensive tabulations of these may be found in his book [2]. Barring those transitions involving singlet, doublet and most triplet states, these formulae are based on limiting schemes of coupling of the angular momenta in the molecule. In particular, the derivation of line strength expressions for transitions involving Σ states of multiplicity three and above has always assumed Hund's case (b) scheme of coupling for the multiplet Σ state. However, it is known that when the splitting parameter λ of the multiplet Σ state is large, significant departure from case (b) can occur, especially for low J transitions. On the other hand, $^3\Sigma$ and $^4\Sigma$ states are amenable for a rigorous analytic treatment holding for intermediate (between Hund's cases (a) and (b)) coupling. It is, therefore, to be expected that the rotational line strengths for transitions involving these states may be made equally rigorous. The works of Tatum and Watson [3] and of others [4–7] represent generalizations, on these lines, of the line strength formulae for some triplet and quartet transitions. In the present work, we derive rigorous expressions for the rotational line strengths for the two spin-forbidden transitions $^1\Delta$–$^3\Sigma$ (int) and $^1\Pi$–$^3\Sigma$ (int). The former is known in the molecules O_2 and NF and is also expected in other isovalent molecules SO, S_2, etc.

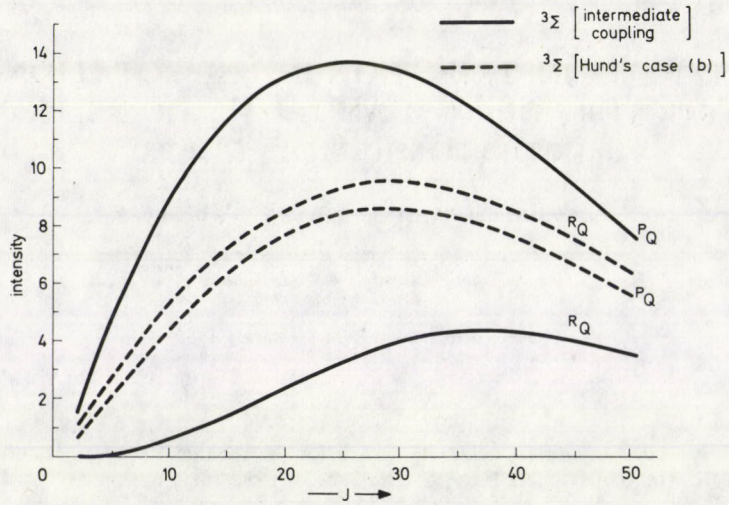

Fig. 1. Theoretical intensity distribution in the ^PQ and ^RQ branches of a $^1\Delta_g \leftarrow X^3\Sigma_g^-$ ($v=0$) (hypothetical) transition in $^{32}S_2$. ($kT/hc = 525\ \text{cm}^{-1}$)

2. Theory

2.1 Rotational eigenfunctions

Any line strength calculation hinges on a knowledge of the rotational eigenfunctions of the participating electronic states. For degenerate singlet states, these functions may be written as

$$|F(J); p\rangle = 2^{-1/2}[|^1\Lambda_\Lambda; JM\rangle + p|^1\Lambda_{-\Lambda}; JM\rangle] \tag{1}$$

with $p = \pm 1$, where $\Lambda = 1$ for Π state and 2 for Δ state. The rotational eigenfunctions of the $^3\Sigma$ state are obtained by diagonalizing the spin-rotation Hamiltonian

$$H = B\mathbf{R}^2 + \gamma \mathbf{R}.\mathbf{S}. + (2\lambda/3)(3S_z^2 - \mathbf{S}^2) - D\mathbf{R}^4 + [(\lambda_D/3)(3S_z^2 - \mathbf{S}^2), \mathbf{R}^2]_+ \tag{2}$$

with $\mathbf{R} = \mathbf{J} - \mathbf{S}$, (see, for example [3]). The last two terms in (2) allow for centrifugal distortion effects and are important only in very accurate calculations. Centrifugal corrections for γ and higher order ($\mathbf{R}^4$, etc.) centrifugal terms relating to λ have been omitted in (2). The diagonalization is conveniently effected employing symmetrized Hund's case (a) basis functions given by

$$2^{-1/2}[|^3\Sigma_{-1}; JM\rangle \pm |^3\Sigma_1; JM\rangle] \equiv |^3\Sigma_1; JM; \pm\rangle$$

and

$$|^3\Sigma_0; JM\rangle.$$

Elegant expressions of general validity for the various matrix elements of the terms occurring in (2) have been derived by Kovács [2, 8]. Accordingly we obtain

	$\lvert^3\Sigma_1; JM; +\rangle$	$\lvert^3\Sigma_0; JM\rangle$	$\lvert^3\Sigma_1; JM; -\rangle$
$\langle^3\Sigma_1; JM; +\rvert$	H_{11}	H_{12}	0
$\langle^3\Sigma_0; JM\rvert$	H_{21}	H_{22}	0
$\langle^3\Sigma_1; JM; -\rvert$	0	0	H_{33}

where

$$\begin{aligned} H_{11} &= Bx - Dx(x+4) - \gamma + (2/3)(\lambda + \lambda_D x), \\ H_{22} &= B(x+2) - D[(x+2)^2 + 4x] - 2\gamma - (4/3)[\lambda + \lambda_D(x+2)], \\ H_{33} &= Bx - Dx^2 - \gamma + (2/3)(\lambda + \lambda_D x), \\ H_{12} &= -2x^{1/2}[B - \gamma/2 - \lambda_D/3 - 2D(x+1)], \end{aligned} \tag{3}$$

with $x = J(J+1)$.

In this evaluation the phase convention of Hougen [9] has been followed. The roots of the secular equation $|H - EI| = 0$ lead to the three rotational term series $F_1(J)$, $F_2(J)$ and $F_3(J)$ of the $^3\Sigma$ state. We shall not write them down explicitly. The corresponding eigenfunctions are readily obtained and are given by

$$\begin{aligned} |F_1(J)\rangle &= s_J|^3\Sigma_1; JM; +\rangle + c_J|^3\Sigma_0; JM\rangle, \\ |F_2(J)\rangle &= |^3\Sigma_1; JM; -\rangle, \\ |F_3(J)\rangle &= c_J|^3\Sigma_1; JM; +\rangle - s_J|^3\Sigma_0; JM\rangle, \end{aligned} \tag{4}$$

where

$$\begin{aligned} c_J &= [\{2f(J) + (H_{11} - H_{22})\}/4f(J)]^{1/2}, \\ s_J &= [\{2f(J) - (H_{11} - H_{22})\}/4f(J)]^{1/2}, \\ 2f(J) &= F_3(J) - F_1(J) \end{aligned} \tag{5}$$

and

$$H_{11} - H_{22} = 2[\lambda - B + \gamma/2 + 2D + 4\lambda_D/3 + (2D + \lambda_D)x].$$

2.2 Line strength calculation for $^1\Delta$–$^3\Sigma$ transition

A lucid exposition of the details of general line strength calculation may be found in the works of Kovács [2] and of Hougen [9]. Essentially, the calculation involves evaluating

$$S(J', J'') = \sum_{M'M''} |\langle F'(J'); p|\mu_R|F_i''(J'')\rangle|^2. \tag{6}$$

(Note that the rotational eigenfunctions $|F(J)\rangle$ have an M labelling which is not explicit in our notation). In (6) μ_R is Rth component of the dipole moment operator in a space fixed frame X, Y, Z. Because the rotational eigenfunctions are expressed in case (a) basis, it is necessary to express μ_R in (6) in terms of the molecule fixed (x, y, z) components μ_r through the direction cosines. We shall exploit the isotropy of space to specialize relation (6) for the Z component μ_Z which gives the particularly simple M selection rule $\Delta M = 0$. Accordingly we have

$$\mu_Z = (\mu_x - i\mu_y)(\alpha_{Zx} + i\alpha_{Zy})/2 + (\mu_x + i\mu_y)(\alpha_{Zx} - i\alpha_{Zy})/2 + \mu_z\alpha_{Zz}. \tag{7}$$

We recall that the intensity of the spin-forbidden transition $^1\Delta - ^3\Sigma$ results from spin orbit mixing, for instance, of the $^3\Sigma$ with $^1\Pi$ states. The $^1\Delta$ state rotational eigenfunctions have $|\Omega| = 2$ whereas $^3\Sigma$ eigenfunctions are mixtures of substates with $|\Omega| = 1$ and 0. Evidently, for this electronic transition there will be just one non-vanishing transition moment $\mu_\perp$ corresponding to the orbitally allowed sub-transitions

$$\Omega' = \pm 2(^1\Delta_2) \rightarrow \Omega'' = \pm 1(^3\Sigma_1).$$

Explicitly,

$$\begin{aligned} \mu_\perp &= \langle \Omega' = 2 | \mu_x + i\mu_y | \Omega'' = 1 \rangle \\ &= \pm \langle \Omega' = -2 | \mu_x - i\mu_y | \Omega'' = -1 \rangle \end{aligned} \tag{8}$$

Table I

Transition amplitudes for $^1\Delta_{\pm 2} - ^3\Sigma_{\pm 1}$ subtransition

Branch	Amplitude
P	$\pm[(J-2)(J-1)/2J]^{1/2}$
Q	$[(J+2)(J-1)(2J+1)/2J(J+1)]^{1/2}$
R	$\mp[(J+2)(J+3)/2(J+1)]^{1/2}$

Table II

Line strength expressions for the nine rotational branches of $^1\Delta - ^3\Sigma$ (int) transition

$^OP(J)$	$c_J^2(J-1)(J-2)/2J$
$^PQ(J)$	$c_J^2(J-1)(J+2)(2J+1)/2J(J+1)$
$^QR(J)$	$c^2(J+2)(J+3)/2(J+1)$
$P(J)$	$(J-1)(J-2)/2J$
$Q(J)$	$(J-1)(J+2)(2J+1)/2J(J+1)$
$R(J)$	$(J+2)(J+3)/2(J+1)$
$^QP(J)$	$s_J^2(J-1)(J-2)/2J$
$^RQ(J)$	$s_J^2(J-1)(J+2)(2J+1)/2J(J+1)$
$^SR(J)$	$s_J^2(J+2)(J+3)/2(J+1)$

governs the overall intensity of this transition. The effective transition amplitudes for the P, Q and R branches of the above sub-transition have been evaluated according to Hougen [9] and are given in Table I. Using these amplitudes, and the relevant rotational eigenfunctions (relations (1) and (4) of Section 2.1), line strengths for the nine rotational branches that can arise are readily obtained and are given in Table II.

2.3 Line strength calculation for $^1\Pi$–$^3\Sigma$ transition

The occurrence of this spin-forbidden transition may be visualized by assuming that the $^3\Sigma$ state is mixed with $^1\Pi$ and $^1\Sigma$ states through spin–orbit interaction. The line strengths calculations follow similar lines but now we need two independent transition moments $\mu_{||}$ and $\mu_\perp$ given by

$$\begin{aligned}\mu_{||} &= \langle {}^1\Pi_{\pm 1}|\mu_z|{}^3\Sigma_{\pm 1}\rangle,\\ \mu_\perp &= \langle {}^1\Pi_1|\mu_x + i\mu_y|{}^3\Sigma_0\rangle \\ &= \pm\langle {}^1\Pi_{-1}|\mu_x - i\mu_y|{}^3\Sigma_0\rangle.\end{aligned} \tag{9}$$

As before we need the effective transition amplitudes of the P, Q and R branches for the two sub-transitions $^1\Pi_{\pm 1}$–$^3\Sigma_{\pm 1}$ and $^1\Pi_{\pm 1}$–$^3\Sigma_0$. These are given in Table III. Using these the line strengths for the nine rotational branches have been worked out and are given in Table IV. Experimentally only the ratio $\mu_{||}/\mu_\perp$ is determinable. To demonstrate the reality of this ratio, we apply the operation σ_v (reflection in a plane passing through the molecular axis z) followed by ϑ, the operation of time reversal, to the ratio of the matrix elements. Whiting and Nicholls [10] have shown that for a system with even number of electrons

$$\begin{aligned}&\vartheta(\sigma_v\langle \Lambda' S'\Sigma'|\mu_e^{\pm,0}|\Lambda'' S''\Sigma''\rangle)\\ &= \pm(-1)^{S'+S''}\langle \Lambda' S'\Sigma'|\mu_e^{\pm,0}|\Lambda'' S''\Sigma''\rangle.\end{aligned} \tag{10}$$

Therefore,

$$\begin{aligned}&\vartheta[\sigma_v(\mu_{||}/\mu_\perp)] = (\mu_{||}/\mu_\perp)^*\\ &= \vartheta\{\sigma_v\langle {}^1\Pi_1|\mu_e^0|{}^3\Sigma_1\rangle\}/\vartheta\{\sigma_v\langle {}^1\Pi_1|\mu_e^+|{}^3\Sigma_0\rangle\}\\ &= \langle {}^1\Pi_1|\mu_e^0|{}^3\Sigma_1\rangle/\langle {}^1\Pi_1|\mu_e^+|{}^3\Sigma_0\rangle\\ &= \mu_{||}/\mu_\perp.\end{aligned}$$

In the above relations $\mu_e^{\pm,0}$ stand for the molecule fixed spherical components of the electric dipole moment operator. One can show that an identical relation holds for the magnetic dipole operator as well. Therefore, the formulae given in Table II and IV hold for both electric and magnetic dipole transitions. This is not surprising since both electric dipole and magnetic dipole operators transform alike under rotations.

Table III

Transition amplitudes for the subtransitions of $^1\Pi - ^3\Sigma$

Branch	Subtransitions	
	$^1\Pi_{\pm 1} - ^3\Sigma_{\pm 1}(\mu_\parallel)$	$^1\Pi_{\pm 1} - ^3\Sigma_0(\mu_\perp)$
P	$\{(J+1)(J-1)/J\}^{1/2}$	$\pm\{(J-1)/2\}^{1/2}$
Q	$\pm\{(2J+1)/J(J+1)\}^{1/2}$	$\{(2J+1)/2\}^{1/2}$
R	$\{J(J+2)/(J+1)\}^{1/2}$	$\mp\{(J+2)/2\}^{1/2}$

Table IV

Line strength expressions for the nine rotational branches of $^1\Pi - ^3\Sigma$ (int)

$^OP(J)$	$(J-1)[\mu_\parallel c_J\{(J+1)/J\}^{1/2} - \mu_\perp s_J]^2$
$^PQ(J)$	$(2J+1)[\mu_\parallel c_J\{1/J(J+1)\}^{1/2} - \mu_\perp s_J]^2$
$^QR(J)$	$(J+2)[\mu_\parallel c_J\{J/(J+1)\}^{1/2} + \mu_\perp s_J]^2$
$P(J)$	$\mu_\parallel^2(J-1)(J+1)/J$
$Q(J)$	$\mu_\parallel^2(2J+1)/J(J+1)$
$R(J)$	$\mu_\parallel^2 J(J+2)/(J+1)$
$^QP(J)$	$(J-1)[\mu_\parallel s_J\{(J+1)/J\}^{1/2} + \mu_\perp c_J]^2$
$^RQ(J)$	$(2J+1)[\mu_\parallel s_J\{1/J(J+1)\}^{1/2} + \mu_\perp c_J]^2$
$^SR(J)$	$(J+2)[\mu_\parallel s_J\{J/(J+1)\}^{1/2} - \mu_\perp c_J]^2$

The fact that the magnetic dipole operator is an axial vector unlike the electric dipole which is polar, merely alters the Λ component of the terms of $^1\Delta$ or $^1\Pi$ involved in the transition.

3. Discussion

The formulae in Tables II and IV are based on a rigorous intermediate coupling treatment of $^3\Sigma$ state, which includes centrifugal distortion effects. When we set $\lambda = \lambda_D = 0$, these formulae reduce to the ones derived by Kovács [2] based on case (b) assumption of $^3\Sigma$. In order to illustrate the effect of intermediate coupling in $^3\Sigma$ on the intensities, we applied the present formulae (Table II) to the (hypothetical) magnetic dipole transition $a\,^1\Delta_g \leftarrow X^3\Sigma_g^-$ in the S_2 molecule. This example has been chosen because the splitting parameter λ_0 of this state is 11.88 cm^{-1} and its $B_0 = 0.29468$ cm^{-1} which would definitely warrant an intermediate coupling treatment. In Fig. 1, the intensities of the ^PQ and ^RQ branches calculated on the basis of intermediate coupling (formulae of Table II) are compared with those based on case (b) assumption (Kovács [2] or formulae of Table II with $\lambda = \lambda_D = 0$). The significant mismatch between the curves of each pair clearly demonstrates the need for incorporating intermediate coupling. An interesting point revealed by the curves for

the ^RQ branch is that while the formulae based on pure case (b) assumption predict substantial intensity for this branch even at low J values, the formulae based on intermediate coupling give almost zero intensity in this range of J. This situation arises for the following reason. The ^RQ branch involves the $F_1(J)$ component of $^3\Sigma$ as the lower level. At small J values relations (4) and (5) of Section 2.1 show that $|F_1(J)\rangle \sim |^3\Sigma_0; JM\rangle$. The transition $^1\Delta$–$^3\Sigma_0$ is orbitally forbidden which accounts for the vanishing intensity of this branch at low J values. At larger J values the eigenfunction $|F_1(J)\rangle$, owing to spin uncoupling, acquires a progressively increasing admixture of $|^3\Sigma_1; JM; +\rangle$. Since the transition $^1\Delta$–$^3\Sigma_1$ is orbitally allowed an intensity increase results with increasing J. Fig. 1 shows that at large J values the curves for intermediate coupling tend to their case (b) limits asymptotically, as expected. It will be worthwhile to observe this transition and compare the experimental intensities with the results of the present theory.

Acknowledgement

The authors wish to thank Dr. S. L. N. G. Krishnamachari for his keen interest in the work and for critically reading the manuscript.

References

1. H. Hönl and F. London, Z. Physik, *33*, 803, 1925.
2. I. Kovács, Rotational Structure in the Spectra of Diatomic Molecules, Akadémiai Kiadó, Budapest and Adam Hilger, Ltd., London, 1969.
3. J. B. Tatum and J. K. G. Watson, Can. J. Phys., *49*, 2693, 1971.
4. A. Schadee, Astron. Astrophys., *41*, 203, 1975.
5. N. A. Narasimham, K. V. S. R. Apparao and T. K. Balasubramanian, J. Mol. Spectr., *59*, 244, 1976.
6. T. K. Balasubramanian and N. A. Narasimham, Indian J. Pure & Appl. Phys., *17*, 682, 1979.
7. T. K. Balasubramanian and V. P. Bellary, Pramana (Indian Acad. Sciences), *24*, 503, 1985.
8. I. Kovács, Acta Phys. Hung., *48*, 323, 1980.
9. J. T. Hougen, NBS Monograph No. 115, U.S. Government Printing Office, Washington D.C., 1970.
10. E. E. Whiting and R. W. Nicholls, Astrophys. J. Suppl. Ser. *27*, 1, 1974.

Acta Physica Hungarica, 63 (3—4), pp. 257—269 (1988)

LOCAL ORDERING IN THE DISORDERED PHASES I AND II OF NH_4Cl AND NH_4Br

F. EL-KABBANY and S. EL-DESSOUKI

Physics Department, Faculty of Science, Cairo University
Giza, Egypt

(Received in revised form 9 January 1986)

A complete infrared study of NH_4Cl and NH_4Br has been carried out and new results are reported for the two disordered phases I and II. The study includes measurements and interpretations of the IR spectral bands, band width, intensities and frequencies of the internal modes as functions of temperatures. Special attention is paid to the doubly degenerate symmetric deformation mode ν_2 and to the triply degenerate asymmetric deformation mode ν_4. For both of the two ammonium halides, the disordering inherent in these two phases generates spectral anomalies. The results reveal the presence of local ordering accompanying the disordering. The energy required for orientation of NH_4^+ ion is calculated to be 0.52 eV (for NH_4Cl) and 0.48 eV (for NH_4Br).

Introduction

Ammonium chloride and ammonium bromide salts are well known to undergo a number of structural modifications at atmospheric pressure, at a certain well defined transition temperature. X-ray [1], neutron [2] and electron diffraction studies [3] have established the variations of crystallographic structures and transformation temperatures. The different known phases are referred to as phases I, II, III and IV in order of the decreasing temperature (Table I). Phases I and II are disordered phases while phases III and IV are ordered phases.

Several models [4, 5] have been proposed to explain the behaviour of the vibrational modes of the ammonium ion through phase transitions. Neutron inelastic scattering [6, 7] and near infrared investigations have provided experimental tests for these theoretical studies. The IR results were restricted to either the fundamental internal motions of the NH_4^+ ion or combinations involving the external modes. Experimental studies of specific heat [8], expansion coefficient [9], piezoelectric effect [10] and the elastic [11, 12] and the dielectric properties [13] have been reported in attempts to understand the origin of these transitions. However, all of these various properties are dependent on many modes of vibrations in the Brillouin zone and cannot yield direct information about the detailed nature of the phase transitions [14]. But it is thought that the most powerful and direct method is the study of the

Table I

Ammonium halide	Phase I (disordered) $O_h^5(Fm3m)$	Phase II (disordered) $O_h^1(Pm3m)$	Phase III (ordered) $D_{4h}^7(P4/nmm)$	Phase IV (ordered) $T_d^1(Pm3m)$
NH_4Cl	I $\xrightarrow{185\,°C}$	II $\xrightarrow{-30\,°C}$		IV
NH_4Br	I $\xrightarrow{138\,°C}$	II $\xrightarrow{-38\,°C}$	III $\xrightarrow{-190\,°C}$	IV

dynamical properties by determining the frequencies and the life times of every phonon mode in the Brillouin zone.

The connection between the phonon spectra, the extent and nature of the disorder prevailing in a crystal is a matter to which spectroscopists have more recently turned their attention and which is likely to play an increasingly important role, since detailed studies of frequencies and life times of phonon modes should give valuable information about the lattice dynamics and hence the mechanism of transition.

In the present work, all pertain to the disordered phases to provide a clear indication of the normal behaviour of NH_4Cl and NH_4Br free from the effect of ordering. It seems that new IR investigation of the disordered phases of these two compounds can provide more interesting information about their nature of transformation. It is our objective to report and compare the type of behaviour of the disordered transitions of these two salts predicted by IR spectroscopic analysis. To do so, we have an approach which incorporates the physical concepts of the phase transition phenomena.

Experimental

The apparatus used and experimental techniques employed were essentially identical with those described previously [15]. The IR spectra have been recorded using Beckman G.R. 7224 Spectrometer. The materials used were ultra pure NH_4Cl and NH_4Br obtained by the British Drug House (B.D.H), Laboratory Chemical Division, England. The NH_4Br samples employed were necessarily somewhat thicker than those of the corresponding chloride salt because the absorption coefficients are somewhat less for the heavier halide salts. The spectrum measurements were recorded in the region 400–4000 cm^{-1} on a graphical paper with a scanning time of 30 min.

Results

In the present work, we have recorded the IR spectra of NH_4Cl and NH_4Br in a temperature range covering both of phases I and II. Herzberg's notations [16] are used here for the internal fundamental normal vibrations of the NH_4^+ ions. Thus,

ν_1 denotes the totally symmetric stretch, ν_2 the doubly degenerate symmetric deformation, ν_3 and ν_4 the triply degenerate asymmetric stretch and deformation, respectively, ν_5 the lattice mode and ν_6 the torsional oscillation mode. The splitting of the degeneracies gives the additional components which are indicated by primes. The presently observed IR spectrum of the two phases of NH_4Cl and NH_4Br did not exhibit any bands which could be attributed to any mode other than those due to NH_4^+ ions.

1) Infrared spectrum of NH_4Cl

Figure 1 shows the IR absorption band spectra of phase I of NH_4Cl at three different temperatures, 210, 200 and 190 °C, and the spectra of phase II of NH_4Cl at three different temperatures, 150, 160 and 170 °C. The frequencies of the bands and their assignments (for the two phases) are collected in Table II.

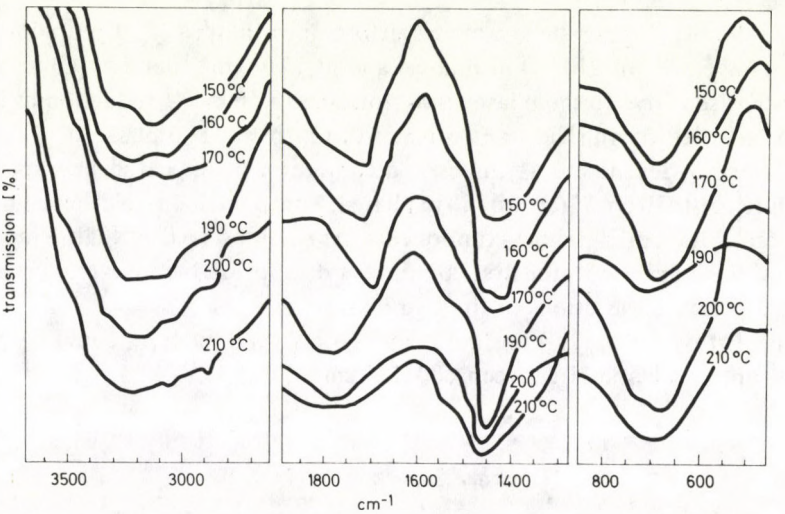

Fig. 1. IR spectra of phases I and II of NH_4Cl in the region 400–4000 cm^{-1}

The triply degenerate asymmetric stretching ν_3 appeared as a broad band at 3210 cm^{-1} and as a shoulder at $\sim$3320 cm^{-1} (ν_3') in phase I (at 190, 200 and 210 °C). In phase II (at 150, 160 and 170 °C) the shoulder ν_3' is shifted by $\sim$40 cm^{-1} while ν_3 is not sensitive to alteration of temperature.

The totally symmetric stretching mode ν_1 appeared in the two phases as weak shoulders between 3050 and 3070 cm^{-1}.

The combination mode ($\nu_2 + \nu_4$) is not clearly observed in the spectrum so that an accurate evaluation of this band could not be performed.

Table II

Phase II			Phase I		
150 °C	160 °C	170 °C	190 °C	200 °C	210 °C
3220 ν_3	3220 ν_3	3210 ν_3	3220 ν_3	3210 ν_3	3200 ν_3
3360 ν'_3	3360 ν'_3	3350 ν'_3	3320 ν'_3	3320 ν'_3	3300 ν'_3
3070 ν_3	3090 ν_1	3070 ν_1	3050 ν_1	3050 ν_1	3070 ν_1
$-(\nu_2+\nu_4)$	$-(\nu_2+\nu_4)$	$-(\nu_2+\nu_4)$	$-(\nu_2+\nu_4)$	$-(\nu_2+\nu_4)$	$-(\nu_2+\nu_4)$
2920 ($2\nu_4$)	2950 ($2\nu_4$)	$-(2\nu_4)$	2850 ($2\nu_4$)	2870 ($2\nu_4$)	2890 ($2\nu_4$)
1720 ν_2	1720 ν_2	1710 ν_2	1775 ν_2	1775 ν_2	1760 ν_2
$-\nu'_4$	$-\nu'_4$	$-\nu'_4$	-1500 ν'_4	-1510 ν'_4	-1520 ν'_4
1430 ν_4	1445 ν_4	1440 ν_4	1450 ν_4	1480 ν_4	1470 ν_4
1380 ν''_4	1420 ν''_4	1360 ν''_4	$-\nu''_4$	1370 ν''_4	1380 ν''_4
700 ($2\nu_6$)	700 ($2\nu_6$)	700 ($2\nu_6$)	680 ($2\nu_6$)	690 ($2\nu_6$)	680 ($2\nu_6$)

The first overtone ($2\nu_4$) appeared as a clear shoulder at 2890 cm^{-1} (at 210 °C) and at 2850 cm^{-1} (at 190 °C) in phase I. But in phase II, this overtone shifted up and appeared at 2950 cm^{-1}.

The doubly degenerate symmetric deformation mode (ν_2) appeared as a clear band at 1760 cm^{-1} (at 210 °C) in phase I and at 1710 cm^{-1} (at 170 °C) in phase II. This mode is sensitive to the phase transition since a 50 cm^{-1} reduction in its value could be recorded during the transformation from phase I to phase II.

The triply degenerate asymmetric deformation ν_4 appeared here as a broad band centred at 1470 cm^{-1} (at 210 °C) in phase I. This band has two other components at 1520 and 1380 cm^{-1}. These components are still observed at high temperatures of phase I. But in phase II, the first component disappeared. However, ν_4 is sensitive to any temperature variations in the two phases.

The first overtone ($2\nu_6$) of the torsional oscillation mode ν_6 could be observed in the two phases I and II between 680–700 cm^{-1}.

2) *Infrared spectrum of* NH_4Br

Figure 2 shows the IR spectra of phase I of NH_4Br at three different temperatures 160, 150 and 140 °C, and also shows the spectra of phase II at three different temperatures 130, 120 and 110 °C. The frequencies of the bands and their assignments (for the two phases) are collected in Table III.

In general, the NH_4Br IR spectrum is very similar to that of NH_4Cl. The only significant frequency differences occur for the bands ν_2, ν_3 and ν_4 appearing in NH_4Br. These characteristic differences can be summarized as follows:

i) The mode ν_2 appeared in NH_4Br at 1580–1665 cm^{-1}. This band occurs at frequency 50–180 cm^{-1} lower than the corresponding bands in NH_4Cl.

ii) The mode ν_3 appeared in NH_4Br at 3120–3180 cm^{-1}. This band occurs at 40–90 cm^{-1} lower than the corresponding bands in NH_4Cl.

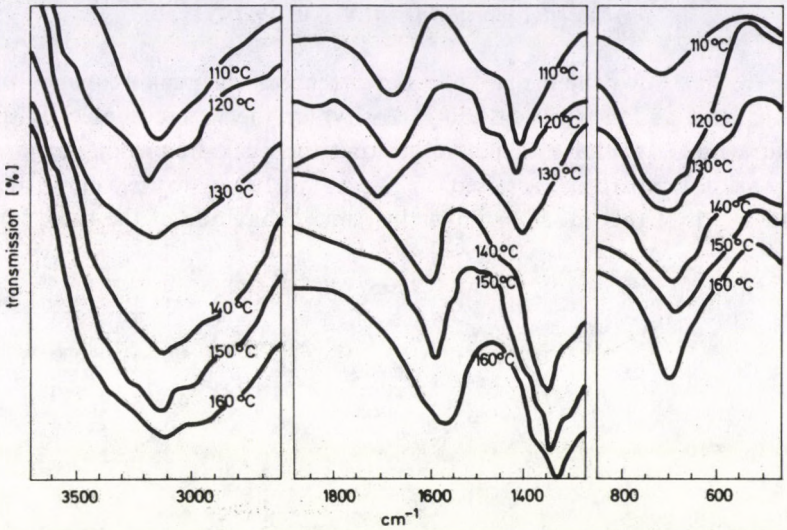

Fig. 2. IR spectra of Phases I and II of NH_4Br in the region 400–4000 cm^{-1}

Table III

Phase II			Phase I		
110 °C	120 °C	130 °C	140 °C	150 °C	160 °C
3160 ν_3	3180 ν_3	3160 ν_3	3120 ν_3	3140 ν_3	3130 ν_3
3250 ν_3'	3290 ν_3'	3270 ν_3'	3230 ν_3'	3240 ν_3'	3230 ν_3'
$-\nu_1$	$-\nu_1$	$-\nu_1$	$-\nu_1$	$-\nu_1$	$-\nu_1$
3030 $(\nu_2+\nu_4)$	3025 $(\nu_2+\nu_4)$	3020 $(\nu_2+\nu_4)$	3020 $(\nu_2+\nu_4)$	3025 $(\nu_2+\nu_4)$	3030 $(\nu_2+\nu_4)$
2790 $(2\nu_4)$	2800 $(2\nu_4)$	2810 $(2\nu_4)$	2815 $(2\nu_4)$	2800 $(2\nu_4)$	2810 $(2\nu_4)$
1665 ν_2	1655 ν_2	1660 ν_2	1620 ν_2	1605 ν_2	1580 ν_2
1440 ν_4'	1440 ν_4'	1430 ν_4'	1400 ν_4'	1375 ν_4'	1360 ν_4'
1400 ν_4	1410 ν_4	1395 ν_4	1350 ν_4	1340 ν_4	1330 ν_4
1370 ν_4''	1380 ν_4''	1380 ν_4''	1330 ν_4''	1320 ν_4''	1300 ν_4''
700 $(2\nu_6)$	720 $(2\nu_6)$	715 $(2\nu_6)$	700 $(2\nu_6)$	690 $(2\nu_6)$	710 $(2\nu_6)$

iii) The mode ν_4 appeared in NH_4Br at 1330–1410 cm^{-1}. This band occurs at 30–140 cm^{-1} lower than the corresponding bands in NH_4Cl.

iv) The most striking difference between the spectra of NH_4Br and NH_4Cl is the disappearance of ν_1 in the spectrum of NH_4Br. Also, the combination mode $(\nu_2+\nu_4)$ could not be detected in NH_4Cl in spite of its appearance in NH_4Br.

3) *Internal vibrations in* NH_4Cl *and* NH_4Br

Figure 3(a) shows the temperature dependence of the peak frequency and band width (measured as full-width at half intensity) for the ν_2 mode of NH_4Cl. In the temperature range of phase II, it is clear that the peak frequency shifts to lower frequency as the temperature is raised (1720 cm^{-1} at 150 °C to 1695 cm^{-1} at 180 °C). The band width of this mode exhibits the same behaviour of the peak frequency.

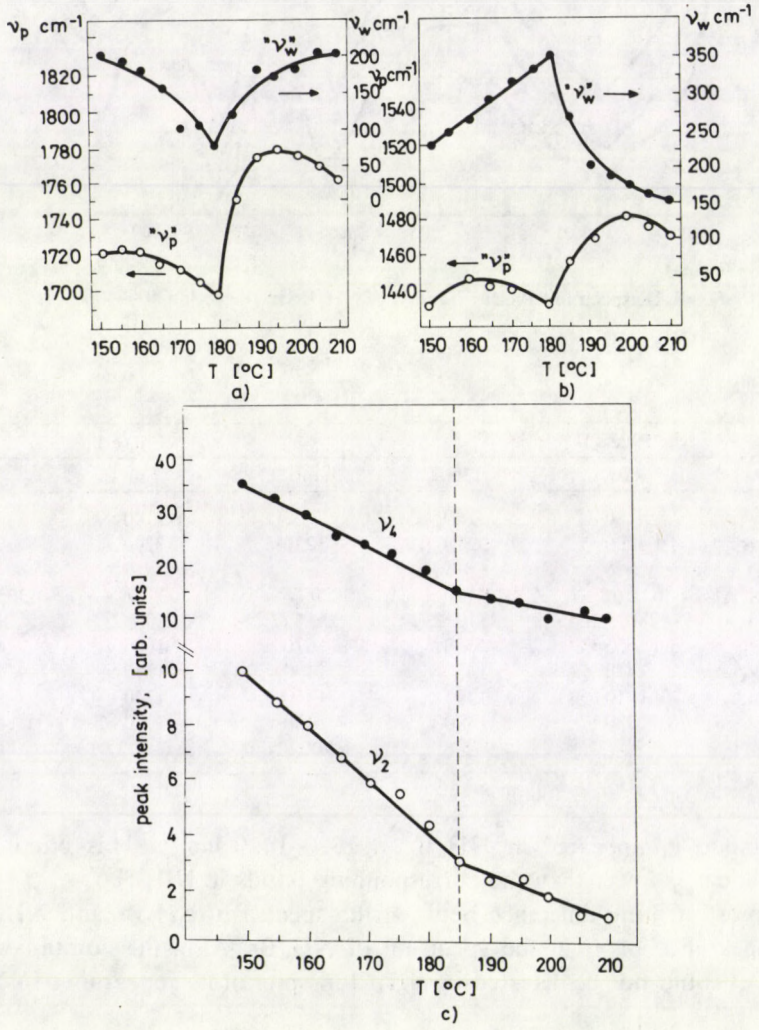

Fig. 3(a). Temperature dependence of the peak frequency ν_p and band width ν_w for ν_2 mode during phase transition II–I of NH_4Cl

Fig. 3(b). Temperature dependence of the peak frequency ν_p and band width ν_w for ν_4 mode during phase transition II–I of NH_4Cl

Fig. 3(c). Variation of peak intensity with temperature for the two modes ν_2 and ν_4 of NH_4Cl

However, in phase I ($T > 185$ °C) the peak frequency shifts to higher values and the band width increased, too.

In Fig. 3(b), the temperature dependence of peak frequency of ν_4 mode of NH_4Cl shows approximately the same behaviour of ν_2 with temperature. But the band width of ν_4 mode increases with temperature in phase II and decreases in phase I.

The peak intensities as functions of temperature for these two modes ν_2 and ν_4 of NH_4Cl are shown in Fig. 3(c). A linear temperature dependence is cleared for

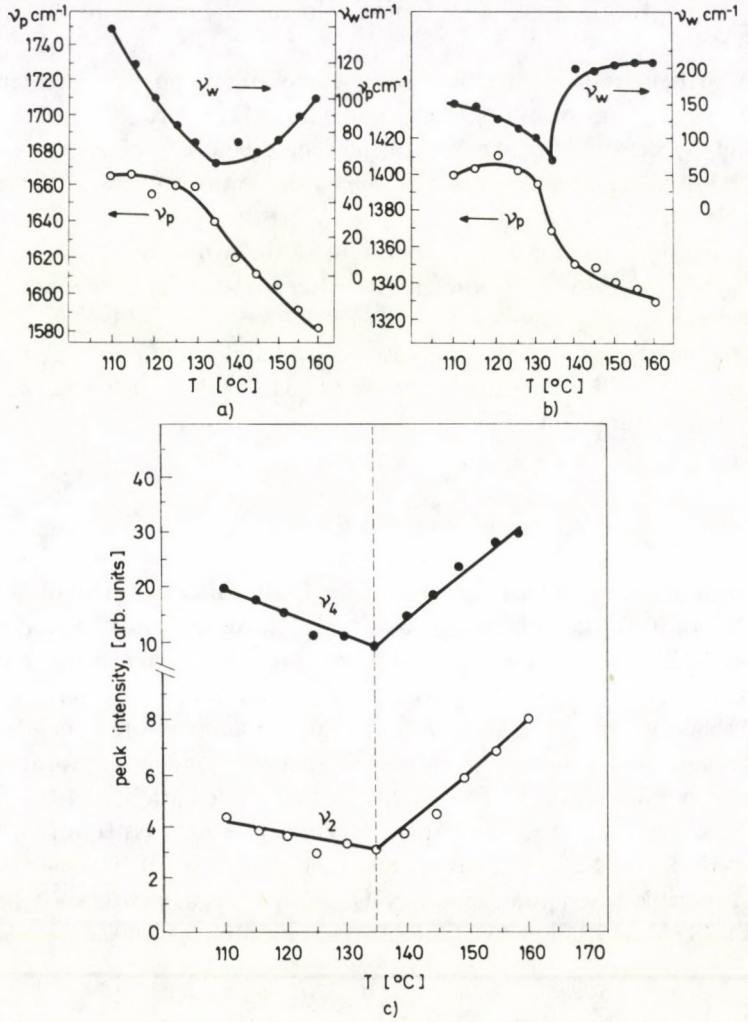

Fig. 4(a). Temperature dependence of the peak frequency ν_p and band width ν_w for ν_2 mode during phase transition II–I of NH_4Br

Fig. 4(b). Temperature dependence of the peak frequency ν_p and band width ν_w for ν_4 mode during phase transition II–I of NH_4Br

Fig. 4(c). Variation of peak intensity with temperature for the two modes ν_2 and ν_4 of NH_4Br

both of intensities of ν_2 and ν_4. There is an observed intensity decay during the elevation of temperature of these two modes ν_2 and ν_4. However, the rate of decrement is lower in phase I rather than in phase II.

Figure 4(a) shows the temperature dependence of the peak frequency and spectral band width for ν_2 mode of NH_4Br. It is clear that the behaviour of NH_4Br is somewhat different from that of NH_4Cl since the peak frequency decreases with the increase of temperature in both of the two phases. The peak frequency of ν_2 mode is reduced by ~ 85 cm^{-1} during the elevation of temperature by 50 °C. The band width (Fig. 4(a)) of ν_2 indicates a minimum value of 62 cm^{-1} in the region of phase transition.

The peak frequency variation with temperature and also the temperature dependence of the band width of the ν_4 mode for NH_4Br are shown in Fig. 4(b). A reduction of ~ 75 cm^{-1} of the peak frequency could be observed over a temperature region 40 °C. Also, the band width indicates a minimum value (~ 70 cm^{-1}) at the transition region.

The intensity variation with temperature for the two modes ν_2 and ν_4 of NH_4Br is shown in Fig. 4(c). This variation denotes a linear character of the intensities of ν_2 and ν_4 modes in both of phases I and II of NH_4Br.

One can easily see that the peak frequency, band width and peak intensity for the two internal modes ν_2 and ν_4 (for NH_4Cl and NH_4Br) showed anomalous character during the phase transition II–I.

4) Rotational energy

The rotational energy barriers separating the two orientations of the ammonium ion were determined for both NH_4Cl and NH_4Br according to the relaxation time equation [15, 17]. The rotational energy barrier "U" at certain absolute temperature depends on the relaxation time "τ". Also, the relaxation time is inversely proportional to the half band width of the absorption band. The temperature dependence of the relaxation time in the region of the doubly degenerate symmetric deformation mode ν_2 is shown in Figs 5 and 6. The results of these calculations indicated that the rotational energy values are 1.38 eV (phase I) and 0.86 eV (phase II) for NH_4Cl while those for NH_4Br are 1.29 eV (phase I) and 0.81 eV (phase II). The energy required for certain possible orientation of the NH_4^+ ion in NH_4Cl is 0.52 eV while that in NH_4Br is 0.48 eV which assumes that such orientations take place.

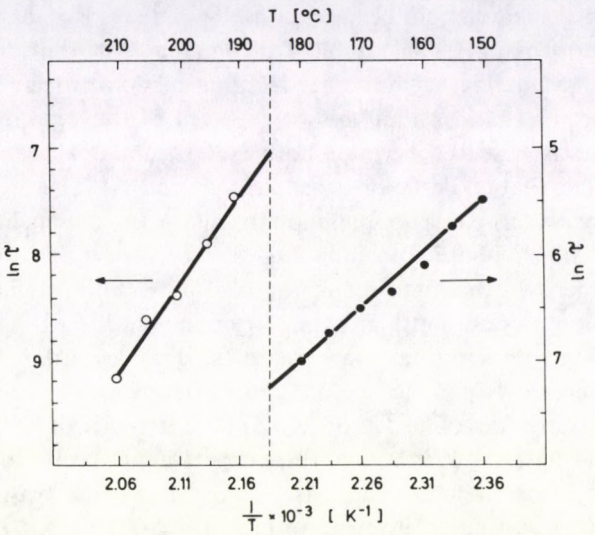

Fig. 5. Temperature dependence of the relaxation time in the region of phase transition II–I of NH_4Cl

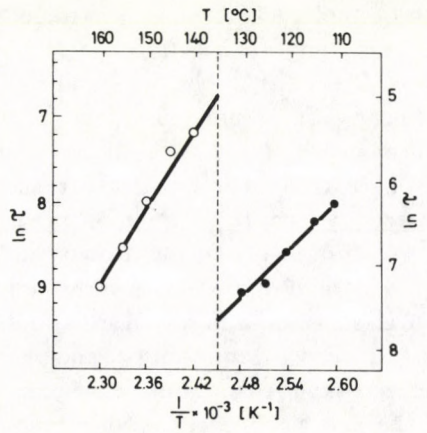

Fig. 6. Temperature dependence of the relaxation time in the region of phase transition II–I of NH_4Br

Discussion

It is well known that in the case of highly symmetrical ions in crystals it should be possible to obtain considerable informations about symmetry and structure of the crystals from the vibrational spectrum.

According to the present IR analysis, the disordering inherent in phase I and II of NH_4Cl and NH_4Br generates spectral anomalies. Within the crystal dimension

corresponding to the wavelength of the exciting light, there is a loss of translational symmetry and consequently, the sampling of phonons with only very small wave vectors, $K=0$ is not mandatory upon the IR transmission process. Thus, the usual sharp and symmetrical bands should not be expected. However, a reasonably strong broad spectrum was observed here for both NH_4Cl and NH_4Br. There are three main distinct bands that could be observed ($2\nu_6$, ν_4 and ν_3). The broadening feature of the spectrum is due to phonon–phonon interactions which occur at high temperatures at which phase transition takes place. Also, the existence of some subsidiary shoulders on the high frequency band is possibly originating from two phonon summation processes at high symmetry points in the Brillouin zone, or is a result of a coupling with a normally inactive infrared mode with the main oscillator.

Special attention is paid to the differences between the numbers, intensities and different characteristics of the IR modes of phases I and II of NH_4Cl and NH_4Br. For both salts no unusual splittings of the internal modes could be observed. But the present spectroscopic analysis suggests that the similarities between NH_4Cl and NH_4Br are much closer than previously supposed [4, 5].

We have presented measurements of peak frequency, peak intensity and band width of the two internal modes ν_2 and ν_4 in NH_4Cl and NH_4Br spectra as functions of temperature.

The transformation from phase II to phase I in these two ammonium halides was monitored by the variations in these spectral parameters with temperature. The temperature of transition is 185 °C for the chloride and 135 °C for bromide. These values are in good agreement with the previously reported [8, 13]. This transition may arise from mechanical instability of the lattice in which an external mode elsewhere in the Brillouin zone assumes an imaginary frequency [18].

The doubly degenerate symmetric deformation mode ν_2 corresponds to an atomic motion in which the hydrogen atoms vibrate perpendicular to the N–H bonds. The triply degenerate asymmetric deformation ν_4 corresponds to an internal NH_4^+ motion in which the nitrogen atom vibrates with respect to the four hydrogen atoms as a whole. The present results showed that both ν_2 and ν_4 internal modes are very sensitive probes which reflects slight changes in site symmetry and local crystalline processes that occur as the crystal undergoes transformation from one phase to another.

The peak intensity of the two modes ν_2 and ν_4 decreases as the transition point is approached (Figs 3 and 4). This is due to the slight variation of the disordering state accompanying the transition or in other words the difference in the degree of disordering in the two phases of the two ammonium halides. Also, the decay of peak frequency is attributed to fluctuations of the order parameter in the vicinity of the phase transition. However, these results support the previous conclusions that the ν_2 and ν_4 internal modes are very sensitive probes for phase transition.

In general, the two modes ν_2 and ν_4 exhibited peculiar line shape and intensity variations as the transition II–I approached. These peculiar spectral features are

associated with the presence of residual short range order in the disordered phase II. But during the process of phase transition, a rapid replacement of this short range order by long range order takes place. This replacement causes the intensity variations and the accompanied anomalies. The spectrum of a disordered phase is no longer rigorously controlled by selection rules, but at the same time it must be remembered that local order can persist in a disordered phase, i.e. occurrence of local order. This local ordering changes with temperature. The appearance of two definite shoulders for the mode ν_4 in the IR spectra (Figs 1 and 2) arises from the fact that the symmetry of the crystal field about any NH_4^+ ion is no longer strictly complete. In more detail, as the transition temperature is approached in the high temperature phase transition II–I, the longer range ordering of NH_4^+ ions begins to occur, which slightly displaces the halide ion (Cl^- or Br^-) and in turn gives rise to the major NH_4^+ ion perturbation by modifying the tetrahedral crystal field. Thus, the lifting of the degeneracy for the triply degenerate vibrations is expected and is observed to manifest itself in the shoulder which develops specially on the high frequency side of ν_4. Also, it is expected that the near neighbour structures are predominantly those of the most stable crystalline forms although over any extended crystal volume there is still complete randomness.

The microscopic interaction is the main element responsible for the phase transition. This interaction depends on the relative spacing of the particles. Also, the transition temperature depends on these spacings. The frequencies of the majority of the vibrational modes of ammonium halides increase as the interatomic distance decreases. However, the magnitude of frequency shift depends upon the particular mode and are measure of the anharmonicities of the mode.

The nature of disordering of the two phases I and II of the present two ammonium halides can be distinguished as:

a) Positional disordering, which arises either when atoms or ions occupy appropriate sublattice positions or when more positions are available for the atoms than are necessary.

b) Orientational disordering, which takes place in situations where the ions occupying the lattice sites contain more than one atom. The orientational disorder here implied small energy difference since it takes place by thermal agitation. In general, the energy required for disordering is a progressively decreasing function of the disorder itself. Previous disordering events help the next disordering event to occur. Ultimately, the energy required for disordering decreases to zero at the end of transition. However, in phase I the disordering is effectively still greater than in phase II.

According to X-ray and neutron diffraction studies [19] phase I (of NH_4Cl and NH_4Br) is a disordered face-centred cubic structure similar to NaCl and possesses O_h^5 (Fm3m) space group symmetry with four molecules per unit cell. The ammonium ions are not freely rotating but undergo restricted rotations hindered by a potential barrier corresponding to orientations in which one, two or three hydrogen atoms

make close approach to the chloride or bromide ions. Phase II has a structure of the CsCl type (space group O_h^1). In phases I and II, the ammonium ions are randomly distributed between two possible energetically equivalent orientations giving rise to long range orientational disorder of the ammonium ions [19, 20]. Two unit cells of the crystal are shown in Fig. 7. Whithin any one cell, the nitrogen atoms sit at the body centres of the chlorine simple cubic lattice and the N–H bonds point at the chlorine ions along the $\langle 111 \rangle$ axes of the lattice. The two possible orientations of the tetrahedral NH_4^+ ions are shown in Fig. 7, where they are labelled "a" and "b". In the high temperature state, the probability of an ion being in orientation "a" is equal to the probability of it being in "b". The two orientations of the NH_4^+ ions can be associated with the two states of the Ising spin [21].

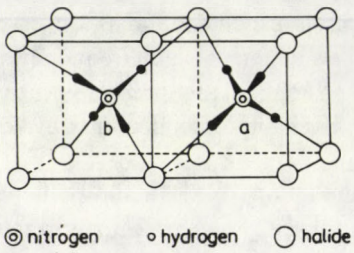

Fig. 7. Two possible orientations for NH_4^+ ions in the disordered state

Under these assumptions, the optical phonons belong to the F_{1u} type for both phases (I and II) so that they are infrared active but Raman inactive at wave vectors $K=0$ [22].

Fraser and Kennedy [23, 24] have studied the NaCl(I)→CsCl(II) transition in NH_4Br in some detail and found that the $\langle 111 \rangle$ direction had rotated by 14–25°. The energy of a particular NH_4^+ ion with respect to neighbouring cations depends on the degree of orientational order so that the potential energy of ion as it rotates must also be a function of the degree of order. However, an NH_4^+ ion in the two ammonium halides can change its orientation directly from any one equilibrium position to any other, or in other words, it is not restricted to a single-step reorientation about symmetry axis. The reorientation rate of the cations in phase I is considerably faster than in phase II.

The spectra of the disordered crystals of the two ammonium halides show less detail of the structure than those of the ordered form, since whereas the environment of a molecule or ion at a particular site in the unit cell in the ordered crystal should be uniform, variability in this environment from a molecule to molecule is to be expected in the disordered crystal.

It can be noticed that the frequency of the torsional oscillations of the NH_4^+ ions (ν_6) appeared as its binary overtone ($2\nu_6$) in the IR spectra at 700 cm^{-1}. Also,

when the NH_4^+ ions become orientationally disordered, the triply degenerate bending vibration ν_4 appears at 1440 cm^{-1} which is a consequence of disappearance of the translational symmetry.

It is clear that our present experimental results on band intensities, frequencies and band width of the two modes ν_2 and ν_4 together with those presented previously can provide significant information on the nature of disordering phenomenon and local ordering in the two phases I and II of NH_4Cl and NH_4Br compounds. However, further experimental and theoretical work is needed on the various physical properties of these two disordered phases. A full understanding of the mechanism of transition and hence the associated changes in their properties, which are determined by the crystal lattice vibrations, will be obtained only when the lattice dispersion curve can be predicted throughout the Brillouin zone. However, the present measurements of the $K=0$ optic mode frequencies can be used in conjunction with other data to provide important result for lattice dynamics.

References

1. J. Poyhonen, K. Mansika and K. Heiskanen, Ann. Acad. Sci. Fennicae Ser. A vi, *168*, 3, 1964.
2. H. A. Levy and S. W. Peterson, J. Am. Chem. Soc., *75*, 1536, 1953.
3. V. N. Kolomiichuk, Krystallografiya, *10*, 565, 1965; or Sov. Phys. Crystallogr., *10*, 475, 1966.
4. H. S. Gutowsky, G. E. Pake and R. Bersohn, J. Chem. Phys., *22*, 643, 1954.
5. Y. Ebisuzaki, Chem. Phys. Letters, *19*, 503, 1973.
6. H. Palevsky, J. Phys. Soc. Japan., 17, suppl. B *11*, 367, 1962.
7. G. Venkataraman, K. Usha Deniz, P. K. Lyengar, A. P. Roy and P. R. Vijayaraghavaus, J. Phys. Chem. Solids, *27*, 1103, 1966.
8. M. Sorai, H. Suga and S. Seki, Bull. Chem. Soc. Japan, *38*, 1125, 1965.
9. G. Fredericks, Phys. Rev. B *4*, 911, 1970.
10. A. Hettich, Z. Physik. Chem., A *168*, 353, 1934.
11. C. W. Garland and C. F. Yarnell, J. Chem. Phys., *44*, 1112, 1966.
12. C. W. Garland and R. Renard, J. Chem. Phys., *44*, 1130, 1966.
13. K. Kamiyoshi, Sci. Res. Inst. Tohoku Univ., A *8*, 252, 1956.
14. Y. Badr, F. El-Kabbany, G. Said and O. W. Saleh, Phys. Status Solidi (a), *60*, 297, 1980.
15. F. El-Kabbany, Y. Badr and M. Tosson, Phys. Status Solidi, (a) *63*, 699, 1981.
16. G. Herzberg, Infrared and Raman Spectra of Polyatomic Molecules, Van Nostrand Co., Princeton, New York, 1966.
17. Y. C. Frenbel,Kinetic Theory of Liquids, Izd. Akad. Nauk (SSSR), Moscow, 1959.
18. J. R. Hardy and A. M. Karo, Lattice Dynamics, R. F. Wallis, Ed., Pergamon Press Ltd., Oxford, 1963.
19. H. A. Levy and S. W. Peterson, J. Am. Chem. Soc., *76*, 1356, 1954.
20. J. K. A. Ketelaar, Nature, London, *134*, 250, 1934.
21. P. Charles, S. Horst, S. Paul and F. George, Phys. Rev., B *4*, 907, 1971.
22. R. B. Wright and C. H. Wang, J. Phys. Chem. Solids, *34*, 787, 1973.
23. W. L. Fraser and S. W. Kenedy, Acta Cryst., B *28*, 3101, 1972; or A *30*, 13, 1974.
24. S. W. Kenedy, J. Mat. Sci., *9*, 1043, 1974.

Acta Physica Hungarica, 63 (3—4). pp. 271—290 (1988)

INSTABILITY AND NON-LINEARITY

I. KIRSCHNER

Department for Low Temperature Physics
Roland Eötvös University, 1088 Budapest, Hungary

(Received 29 January 1986)

In this paper the most important features of instabilities are summarized and the most effective methods used to investigate them are analysed. These problems may arise, in addition to physics, in natural, technical, economic and social sciences and the methods developed in different parts of physics facilitate their description. We try to demonstrate that the problem of thermodynamic stability, instable states, quick changes, transitions accompanying singularity, catastrophes and chaotic behaviour are closely related phenomena occurring in real, non-linear nature, which can be ultimately included in the same group and which we investigate by different research methods because we do not have a universally valid non-linear theory.

Introduction

The problems of instabilities have recently become an intensively investigated sphere of physics. On the other hand, the stability conditions of macroscopic objects are most generally regulated by thermodynamic stability criteria. This is an ambiguous statement equally referring to terrestrial or cosmic scales, inorganic materials, or biological objects, the natural and artificial environment, technical, economic and social spheres.

The investigation of closed or open systems and the analysis of spontaneous or generated processes provides another possibility for classification. In principle, of course, all of them can be characterized by thermodynamic stability theories of general validity, the final build-up of which is a long-lasting process. Ceasing stability criteria lead to change in the stability state of the investigated system [1, 2, 3] and is accompanied by singularities in characterizing functions, changes in state, in certain cases intensive increase in disorder, or the dominance of random, non-linear nature, that is the chaos.

During the evolution in nature the opposite of these processes becomes predominant when either due to external effects or self-regulation disorder systems transform to a highly regular state and a form of existence more valuable from the point of view of the investigation is created. Such a process is e.g. the development of living material, or of social patterns.

In this attitude the thermodynamics of states and processes, the investigation of stability problems, the theory of singularities and catastrophes, and the investigation of synergetics and chaotic features form an unambiguous logical chain, the elements of which are able to specify with their own apparatus parts of phenomena actually becoming predominant, which, however, cannot be separated from each other. In this respect the problem may be considered in such a way that the most general theory of states and processes, i.e. thermodynamics, may be extended so that due to the mentioned, associated principles of physics very rapid, random and very instable phenomena also become suitable for consideration.

The general frame for the investigations is provided by the theory of thermodynamics which has not been completely developed yet [4, 5] being able even today to characterize certain instable and rapidly changing phenomena and this range is supplemented by such sections of physics as e.g. the theory of stability–instability, the theory of catastrophes, the theory of singularity, synergetics or the theory of chaotic phenomena.

There are frequent cases in nature where the state of a system becomes unstable to such an extent that consequently a totally new state is formed. This kind of phenomena may occur in every sphere of nature such as the fields covered by physics, chemistry, biology, geology and technical sciences. It is interesting that processes of a similar kind may develop in economics and social sciences, too.

Strong instabilities developing in certain fields and the associated rapid transformations have the common feature that external and internal reasons work together to establish them. Of course, there may be cases when the instability is due either to external or internal reasons only.

Some illustrative examples demonstrate it well that strong instabilities and consequent radical and rapid transitions really take place in almost all fields of investigations. Such as e.g. earthquakes or tidal waves in geology, collapses in astronomy, accidents in traffic, break of structural elements in technical equipment, birth and death in biology, boom or crisis in economy, revolution or counterrevolution in society, phase transformations or chaos in physics, the effect of toxic matters or acute diseases in the living organism, reactions or the formation of new compounds by mixing different materials in chemistry, etc. This means that instabilities, rapid changes, singularities, catastrophes and chaotic phenomena equally occur in the natural, technical and social environment (including economy).

We have three basic methods for studying the mentioned phenomena: 1. thermodynamics, 2. the theory of singularity or catastrophes, and 3. the investigation of the phenomena of chaos, or synergetic methods. Of course other methods may also be successful.

Scope of thermodynamics

The theory of thermodynamics used today may be essentially considered as a method of second approach because quantities representing actual dynamism, the general thermodynamic forces are produced with the help of the second term of entropy series. In these calculations we start from the fact that there is an entropy function S including all the possible thermodynamic information

$$S = F(x_1, x_2, \ldots, x_n). \tag{1}$$

in which extensive parameters x_i play the role of the independent variables, the number of which agrees with that of the possible interactions [6, 7, 8].

Here, the change in time is included in time dependence of the extensive quantities

$$x_i = f_i(t), \qquad i = 1, 2, \ldots, n \tag{2}$$

and this stimulates the entropy change in time, too.

Using specific quantities (or densities) the non-equilibrium specific entropy s (or the entropy density ρ_s) may be sequenced in the vicinity of the equilibrium value s_0(or ρ_{s0}) according to the non-equilibrium extensive deviations (α-parameters) [9, 10, 11]:

$$s = s_0 + \sum_{i=1}^{n} \left(\frac{\partial s}{\partial \alpha_i}\right)_0 \alpha_i + \frac{1}{2} \sum_{i,k=1}^{n} \left(\frac{\partial^2 s}{\partial \alpha_i \partial \alpha_k}\right)_0 \alpha_i \alpha_k + \ldots, \tag{3}$$

where

$$\left(\frac{\partial^2 s}{\partial \alpha_i \partial \alpha_k}\right)_0 = -g_{ik} \tag{4}$$

and

$$\left(\frac{\partial s}{\partial \alpha_i}\right)_0 = -\left(\frac{y_i}{T}\right)_0. \tag{5}$$

In these formulae $\mathbf{g} = \mathbf{g}[g_{ik}]$ is the so-called entropy matrix being of nth order, quadratic, symmetric and positive-definite, $-y_i/T$ is the ith entropic intensive parameter, in which T is the temperature and y_i is the conventional intensive quantity originating from the energy [8].

The entropy change of a system being in non-equilibrium must be positive-definite, that is with the following quantities

$$\Delta s = s - s_0 = -\sum_i \frac{y_i}{T_0} \alpha_i - \frac{1}{2} \sum_{i,k} g_{ik} \alpha_i \alpha_k < 0. \tag{6}$$

Deriving it according to α_i the expression for the occurring X_ith general thermodynamic force is obtained:

$$X_i = \frac{y_i}{T_0} - \frac{y_i}{T} = -\sum_k g_{ik} \alpha_k, \qquad i = 1, 2, \ldots, n, \tag{7}$$

which is the difference between the equilibrium and non-equilibrium value of the intensive parameters in case of a single system, the difference between the intensive quantities in two-system interactions and the gradient of intensive variables in continuous case [8, 9, 10, 11].

The irreversibility of thermodynamic processes is expressed by the fact that during equalization

$$X_i \to 0 \qquad \text{and} \qquad \alpha_i \to 0. \tag{8}$$

Irreversible thermodynamics in its present form is essentially a linear theory. Attempts have already been made to elaborate a nonlinear theory, but the results are still preliminary. Such results have been obtained e.g. by Gyarmati [11] and Li [13], completed later [14, 15], but as far as we know experimental evidence [16] is still missing.

This is well reflected in the second component of the theory, the description of thermodynamic currents or fluxes. Here the basis is the work of Onsager, which means the generalisation of the classical dynamic equations [17, 18].

Accordingly, in the development of any thermodynamic flux (or current) $j_i = \dot{\alpha}_i$ all existing thermodynamic forces participate, that is

$$j_i = \dot{\alpha}_i = \sum_{k=1}^{n} L_{ik} X_k, \qquad i = 1, 2, \ldots, n, \tag{9}$$

where the conductivity matrix $\mathbf{L} = \mathbf{L}[L_{ik}]$ is also of n-th order, quadratic, symmetric and positive-definite. These are the general conductivity equations of the thermodynamic theory which are linear that is the matrix elements L_{ik} may depend on the place and time, but they are independent of y_i and Δy_i or ∇y_i [8, 9, 19, 20].

Having written the equations (7) and (9) in matrix form and combining them after suitable time derivation we obtain the so-called thermodynamic equations of motion, containing the decay in time that is the real dynamics, which give the temporal change of general forces and α-parameters expressed by themselves

$$\dot{X} = -\mathbf{gL}X \tag{10}$$

and

$$\dot{\alpha} = -\mathbf{Lg}\alpha. \tag{11}$$

These differential equations contain the actual dynamism of the spontaneous processes. Their formal solution

$$X(t) = X_{\text{initial}} e^{-\mathbf{gL}t} \tag{12}$$

and

$$\alpha(t) = \alpha_{\text{initial}} e^{-\mathbf{Lg}t}, \tag{13}$$

where matrices **gL** and **Lg** are not diagonal and not symmetric, but they are positive definite, which may express the physical fact that initially produced thermodynamic forces and non-equilibrium deviations decay in time and the state moves towards equilibrium.

Due to the cross-effects, $X = X(t)$ and $\alpha = \alpha(t)$ are not necessarily definitely monotonous-decreasing functions of time but only produce the ultimate decay of non-equilibrium disturbances. It should be noticed, however, that in case of real systems and actual processes, current (or flux) density j_i generally contains convective member j_{cv} in addition to the conductive member j_{cd}, meaning that

$$j_i = j_{cd} + j_{cv} = \sum_k L_{ik} X_k + \rho_i \mathbf{v}_i, \tag{9'}$$

where ρ_i is the density of the i-th extensive quantity and $\mathbf{v}_i$ is its velocity of flow [21].

Thermodynamic processes are generally initiated by the condition that the system examined is in connection with another system which exerts influence on it and at the same time internal changes (e.g. chemical reactions) occur in it. Denoting the external generation by $G = G(t)$ and the internal source by $Q = Q(t)$, the general thermodynamic equation of motion for such changes of state including external generation and internal source, [22] are

$$\dot{X}(t) = -\mathbf{gL}X(t) + \mathbf{g}G(t) - \mathbf{g}Q(t), \tag{14}$$

$$\dot{\alpha}(t) = -\mathbf{Lg}\alpha(t) - G(t) + Q(t), \tag{15}$$

which characterize the dynamism of the generated processes.

Formal solutions of these differential equations contain the change of thermodynamic forces and non-equilibrium deviations in time. Their general forms are

$$X(t) = \left[\int_0^t (\mathbf{g}G(t) - \mathbf{g}Q(t)) e^{\mathbf{gL}t} dt + X_{\text{initial}} \right] e^{-\mathbf{g}Lt}, \tag{16}$$

$$\alpha(t) = \left[\int_0^t (-G(t) + Q(t)) e^{\mathbf{Lg}t} dt + \alpha_{\text{initial}} \right] e^{-Lgt}, \tag{17}$$

which means of course that $X(t)$ and $\alpha(t)$ are the vectors of all possible forces and deviations, respectively.

With the supposition of $G(t) = G_0 = \text{const}$ and $Q(t) = Q_0 = \text{const}$, these solutions may be clearly separated into two parts

$$X(t) = (-\mathbf{L}^{-1}G_0 + \mathbf{L}^{-1}Q_0 + X_{\text{initial}}) e^{-\mathbf{gL}t} + \mathbf{L}^{-1}G_0 - \mathbf{L}^{-1}Q_0, \tag{18}$$

$$\alpha(t) = (\mathbf{g}^{-1}\mathbf{L}^{-1}G_0 - \mathbf{g}^{-1}\mathbf{L}^{-1}Q_0 + \alpha_{\text{initial}}) e^{-\mathbf{Lg}t} - \mathbf{g}^{-1}L^{-1}G_0 + \mathbf{g}^{-1}\mathbf{L}^{-1}Q_0, \tag{19}$$

from which the first one includes in both cases members depending on time, and the second one includes members independent in time. After a sufficiently long time has elapsed just these latter ones create the basic non-equilibrium level, resulting by external generation

$$X(t = \infty) = \mathbf{L}^{-1}G_0 - \mathbf{L}^{-1}Q_0, \tag{20}$$

$$\alpha(t = \infty) = -\mathbf{g}^{-1}\mathbf{L}^{-1}G_0 + \mathbf{g}^{-1}\mathbf{L}^{-1}Q_0. \tag{21}$$

The build-up of the differential equations referring to $\ddot{X}(t)$ and $\ddot{\alpha}(t)$ and their solutions provide a possibility for describing the rapid changes of state thermodynamically.

We have examined the second-order derivates according to time of dynamic quantities participating in the characterization of the generated processes, that is the general thermodynamic forces X_i and the non-equilibrium deviations α_i. In this way we have obtained such "equations of motion" which are suitable for describing phenomena quickly changing in time that is for describing rapid processes.

Differential equations obtained in this way specify the second derivates in time of the general thermodynamic forces and non-equilibrium parameters. The equations—in addition to the above mentioned quantities—include the effect of the external generation and the internal source. These differential equations will be

$$\ddot{X}(t) = -\mathbf{gL}\dot{X}(t) + \mathbf{g}\dot{G}(t) - \mathbf{g}\dot{Q}(t), \tag{22}$$

$$\ddot{\alpha}(t) = -\mathbf{Lg}\dot{\alpha}(t) - \dot{G}(t) + \dot{Q}(t), \tag{23}$$

whose solutions give the velocity of time-change of the general thermodynamic forces and the non-equilibrium deviations

$$\dot{X}(t) = \left[\int_0^t (\mathbf{g}\dot{G}(t) - \mathbf{g}\dot{Q}(t)) e^{\mathbf{gL}t} dt + \dot{X}_{\text{initial}} \right] e^{-\mathbf{gL}t}, \tag{24}$$

$$\dot{\alpha}(t) = \left[\int_0^t -\dot{G}(t) + \dot{Q}(t) e^{\mathbf{Lg}t} dt + \dot{\alpha}_{\text{initial}} \right] e^{-\mathbf{Lg}t}. \tag{25}$$

If $G(t) = G_0 = \text{const}$ and $Q(t) = Q_0 = \text{const}$, then the general solutions (24) and (25) go over into the form of

$$\dot{X}(t) = \dot{X}_{\text{initial}} e^{-\mathbf{gL}t} \tag{26}$$

and

$$\dot{\alpha}(t) = \dot{\alpha}_{\text{initial}} e^{-\mathbf{Lg}t}, \tag{27}$$

which give analytic expressions—finally disappearing in time—for the changing velocity of the forces and equalization currents.

Starting from the fact that **g** and **L** are independent of time, and supposing a functional relation of this type for $G(t)$ and $Q(t)$

$$G(t) = G_0 e^{-\mathbf{Lg}t} \quad \text{and} \quad Q(t) = Q_0 e^{-\mathbf{Lg}t} \tag{28}$$

the differential equations

$$\ddot{X}(t) = -\mathbf{gL}\dot{X}(t) - \mathbf{gLg}\, G(t) + \mathbf{gLg}\, Q(t) \tag{29}$$

and

$$\ddot{\alpha}(t) = -\mathbf{Lg}\dot{\alpha}(t) + \mathbf{Lg}\, G(t) - \mathbf{Lg}\, Q(t) \tag{30}$$

and obtained for describing the rapid change in time.

The general solutions of these differential equations are:

$$\dot{X}(t)=\left[\int_0^t(-\mathbf{gL}g\,G(t)+\mathbf{gLg}\,Q(t))e^{\mathbf{gL}t}dt+\dot{X}_{\text{initial}}\right]e^{-\mathbf{gL}t}, \tag{31}$$

$$\dot{\alpha}(t)=\left[\int_0^t(\mathbf{Lg}\,G(t)-\mathbf{Lg}\,Q(t))e^{\mathbf{Lg}t}dt+\dot{\alpha}_{\text{initial}}\right]e^{-\mathbf{Lg}t}, \tag{32}$$

which include the phenomena of rapid, macroscopic changes.

It is clear from these considerations that the sphere of irreversible thermodynamics may be extended even to the description of rapid changes of state on the condition that we must know the parameters which may be substituted into the theory and which in this way provide concrete information on the processes and phenomena.

Stability and instability

The theory of thermodynamics starts from the features of the entropy

$$S=S(x_1, x_2, \ldots, x_n), \qquad x_1=E, \tag{33}$$

of the internal energy

$$E=E(x_1, x_2, \ldots, x_n), \qquad x_1=S, \tag{33'}$$

as the fundamental functions for the stability investigation.

The necessary condition for an equilibrium state of a system is that the relation

$$dS=0, \tag{34}$$

or

$$dE=0 \tag{34'}$$

should be satisfied which is at the same time the necessary condition of extremum, namely $S=S_{\max}$ for entropy and $E=E_{\min}$ for energy. The sufficient condition together with the above one is that

$$d^2S<0, \tag{35}$$

or

$$d^2E>0, \tag{35'}$$

which, however, mean the condition of state stability, too [23]. Should these conditions fail to be fulfilled (of course just in alternate sense) the macroscopic state looses its stability and becomes instable. On the other hand, thermodynamic stability or instability are essentially caused by the entropy matrix **g** and the conductivity matrix **L**.

Entirely generalising their features, the change of state at place **r** and in time t is described by a continuity type equation [24]

$$-\frac{k}{f}\frac{\partial f}{\partial t}+k\,\mathrm{div}_{\rho}\left(\frac{1}{f}\nabla_{\rho}\mathbf{a}f\right)=-\frac{k}{f^2}\left(\nabla_{\rho}f,\nabla_{\rho}\mathbf{a}f\right), \tag{36}$$

where k is a constant, f is the probability density meant for the state-space stressed by $\{\rho_1, \rho_2, \ldots, \rho_n\}$ extensive densities and normalized to unity

$$\int f(\rho, t)d^n\rho=1 \tag{37}$$

and **a** is the dispersion tensor. Macroscopic entropy density in the place **r** and time t is given by the expectable value $\langle\rho_s\rangle$

$$\rho_s(r, t)=-k\int f\ln f\,d^n\rho, \tag{38}$$

and its mixed second derivates by $\langle\rho_i\rangle$ and $\langle\rho_k\rangle$ provide the elements for the matrix **g**

$$\frac{\partial^2\langle\rho_s\rangle}{\partial\langle\rho_i\rangle\partial\langle\rho_k\rangle}=-g_{ik}=-g_{ki}. \tag{39}$$

Consequently, the positive definite nature of **g** is the result of Eq. (38). The value of the integral is maximum when $f=f(\rho)$ is constant, or when it is the smoothest. Because of sub-conditions only this latter one can be realized.

It is clear from (36) that the conduction matrix L_{ik} corresponds to the dispersion tensor a_{ik}, and therefore it is positive definite. The semidefinite character

$$a_{ii}=\leftrightarrow L_{ii}=0 \tag{40}$$

represents a case where the distribution according to ρ is point-like and the state is deterministic. (Just one state may exist with a single probability, which is practically never realized). In case of very sharp, but not point-like distribution a_{ii} and thus L_{ii} have very small values.

The elements with mixed indices $a_{ik}\leftrightarrow L_{ik}$ measure the dependence of ρ_i and ρ_k on probability for the case $i\neq k$. Therefore, if ρ_i and ρ_k are independent probability variables, then

$$a_{ik}=0\leftrightarrow L_{ik}=0, \qquad i\neq k, \tag{40'}$$

thus **L** is diagonal and cross-effects do not occur.

Concerning the behaviour of the matrices **g** and **L** the following general rules may be formulated [24]:

1. The elements of the matrix **L** cannot behave so irregularly that would cause lability in itself (and at the same time a strongly instable state, catastrophe-like change or perhaps phase transition). This is shown clearly by experimental results and the deeper reason for it is that the dispersion tensor can never be indefinite. The value $g_{ii}=0$ occurring in certain cases demands—in order to maintain stability—that

$L_{ii} \to \infty$ in the proper order. This case corresponds to indefinite large ($a_{ii} = \infty$) dispersion.

2. In certain cases however when $L_{ii} = \infty$, this by itself and alone may ultimately cause only neutral equilibrium.
3. On this basis it is justified that we causally relate instabilities to the matrix **g** pointing out that transitions are generally characterized by the rapid change of the matrix **L**, which results in physically very important phenomena.
4. The possible singularity of the matrices **gL** or **Lg** prevent the decay of the matrix functions $X_t = e^{-\mathbf{gL}t} X_{\text{initial}}$, and $\alpha_t = e^{-\mathbf{Lg}t} \alpha_{\text{initial}}$, that is it means the violation of equalization endeavour. It occurs in the case of rapid transformations.
5. Such abrupt, catastrophe-like transformations generally take place due to the disturbance of the static, stable equilibrium states and the new states satisfy the stability criteria of the static equilibrium.

Summing up the above we may say that the joint and abrupt change of the corresponding elements of the matrices g and L is necessary for the unstable states to arise.

The stability of states may be examined—in a general way—by the help of a variational principle. Now we set a variation principle, where the independent variables of the Lagrange function $\mathscr{L}$ are the space coordinates r_1, r_2, r_3, the time t, the intensive parameters $y_1, y_2, \ldots, y_n$ and their gradients $\nabla y_1, \nabla y_2, \ldots, \nabla y_n$ [22, 25]:

$$\int_t \int_V \mathscr{L}(r_1, r_2, r_3, t;\ y_1, y_2, \ldots, y_n;\ \nabla y_1, \nabla y_2, \ldots, \nabla y_n) dr_1 dr_2 dr_3 dt = \text{extremum}. \quad (41)$$

Denoting $\dfrac{\partial y_i}{\partial r_k} = y_i^{(r_k)}$, $k = 1, 2, 3$ the Euler–Lagrange equations will be

$$\frac{\partial}{\partial r_1} \frac{\partial \mathscr{L}}{\partial y_i^{(r_1)}} + \frac{\partial}{\partial r_2} \frac{\partial \mathscr{L}}{\partial y_i^{(r_2)}} + \frac{\partial}{\partial r_3} \frac{\partial \mathscr{L}}{\partial y_i^{(r_3)}} - \frac{\partial \mathscr{L}}{\partial y_i} = 0, \quad (42)$$

$$i = 1, 2, \ldots, n$$

which applied for the corresponding thermodynamic Lagrange function gives the equation of the entropy balance. Expressing this with the α-parameter of entropy (α_s) in stationary case it would have the form of

$$\operatorname{div} \dot{\alpha}_s = \sum_{i=1}^{n} (\nabla y_i, \dot{\alpha}_i) + \sum_{i=1}^{n} y_i q_i \quad (43)$$

in which, in addition to the spontaneous entropy-production, members originated from the source densities of extensive quantities q_i also appear.

Performing the calculations for the determination of the necessary and sufficient condition of extremum, leads to the relation

$$\int \mathscr{L}(\ldots) d^3r\, dt = \text{minimum}, \quad (44)$$

which is just the condition of stability. It means that when it is fulfilled the state is stable, when not, it is unstable.

One of the direct physical results of the investigations is that during processes entropy is produced at each place of the physical system and at each instant of time, namely by

$$|\int \mathscr{L}_{dt}|_{\text{instac}} > |\int \mathscr{L}_{dt}|_{\text{stac}}, \tag{45}$$

that is

$$\int\left(\frac{\partial \rho_s}{\partial t} + \operatorname{div} \dot{\alpha}_s + \sum_i y_i q_i\right) dV dt > \int\left(\operatorname{div} \dot{\alpha}_s + \sum_i y_i q_i\right) dV dt, \tag{46}$$

and in this way

$$\int_V \frac{\partial \rho_s}{\partial t} dV dt \geqq 0, \tag{47}$$

where the sign of equality just corresponds to the stationary state. Therefore instationary entropy production (or that occurring with rapid change) is always larger than that belonging to the stationary state [22, 24].

Attempts have been made in thermodynamics, too, in order to deduce the fundamental equations of thermodynamics from a general variation principle, similarly to mechanics and electrodynamics. For this purpose the following functions are needed:

1. the spontaneous entropy production

$$\sigma(\alpha_i, X_i) = \sum_i \dot{\alpha}_i X_i, \tag{48}$$

2. the dissipation potential depending on the forces

$$\Psi(X_i, X_k) = \frac{1}{2} \sum_{i,k} L_{ik} X_i X_k, \tag{49}$$

3. and the dissipation potential depending on the fluxes

$$\Phi(\dot{\alpha}_i, \dot{\alpha}_k) = \frac{1}{2} \sum_{i,k} R_{ik} \dot{\alpha}_i \dot{\alpha}_k, \tag{50}$$

where $\mathbf{R} = \mathbf{R}[R_{ik}]$ is the so called resistivity matrix. By the help of these the "principle of least dissipation of energy" [26, 27] of Onsager may be obtained in flux representation by a variation according to $\dot{\alpha}_i$ with constant X_i:

$$(\sigma - \Phi)_X = \text{maximum}, \tag{51}$$

or in force representation by a variation according to X_i with constant values of $\dot{\alpha}_i$[8]

$$(\sigma - \Psi)_{\dot{\alpha}} = \text{maximum}. \tag{51'}$$

It should be noticed that the original Onsager's flux representation of the principle has proven to be very special and its applications are rather restricted, at least in case of continua.

In thermodynamics two different variational principles have been widely applied, namely the principles elaborated by Prigogine and Gyarmati.

Prigogine's "principle of minimum entropy production" may be summarized as follows [28, 29, 30]. When a system, characterized with a number n of independent forces $X_1, X_2, \ldots, X_n$, is kept in the state of fixed $X_1, X_2, \ldots, X_k$ $(k<n)$ and minimum entropy production then fluxes $\dot{\alpha}_i = I_i$ belonging to the indices $i=k+1, k+2, \ldots, n$, disappear. This means that the fluxes which—as conjugate variables—correspond to the non-fixed $X_{k+1}, X_{k+2}, \ldots, X_n$ forces will be zero. This state is called stationary of k-th order. (We remark that entropy production means here only spontaneous production, independent of the possible sources of extensive quantities characterizing the individual interactions).

Entropy production belonging to this state may be easily calculated. The necessary minimum condition for the indices $i=k+1, k+2, \ldots, n$ will be

$$\frac{\partial \sigma}{\partial X_i} = \frac{\partial}{\partial X_i} \sum_{i,j=1}^{n} L_{ij} X_i X_j = 2 \sum_{j=1}^{n} L_{ij} X_j = 2\dot{\alpha}_i = 0. \tag{52}$$

Consequently, when we have non-zero values among the fixed X_i belonging to indices $i=1, 2, \ldots, k$ this index is $\dot{\alpha}_i \neq 0$, for $i=1, 2, \ldots, k$. In this way the minimum entropy production has the form of

$$\sigma = \sum_{i=1}^{k} \sum_{j=1}^{n} L_{ij} X_i X_j = \sum_{i=1}^{k} \dot{\alpha}_i X_i = \sigma_{\min}. \tag{53}$$

A general variational principle of non-equilibrium thermodynamics is the "governing principle of the dissipative processes" of Gyarmati expressed by the relation [31]

$$\delta \int_V (\sigma - (\Psi + \Phi)) dV = 0 \tag{54}$$

and written in a more detailed form in the following expression

$$\delta \int_V \left[\sum_i \dot{\alpha}_i \nabla y_i - \frac{1}{2} \sum_{i,k} L_{ik} \nabla y_i \nabla y_k - \frac{1}{2} \sum_{i,k} R_{ik} \dot{\alpha}_i \dot{\alpha}_k \right] dV = 0. \tag{54'}$$

This principle is suitable for deducing thermodynamic transports and gives some possibility for certain quasi-linear and non-linear description [32, 33, 34].

The wide range of analysed examples shows that the variational principles are as fruitful in thermodynamics as in the other fields of physics [35–43].

Singularity and catastrophe

Phenomena of nature, society (e.g. economy) and technology are generally non-linear. Linear apparatus used to describe them can actually follow the real phenomena just up to the level of modelling. However, the "model" is almost perfect in many areas, it describes a wide range of phenomena and their elements important for us with great accuracy.

There are phenomena, however, for which the non-linear nature is obvious and for which it can be easily stated that a linear approach cannot provide a reliable picture and acceptable results of the relevant effects. Such typically non-linear phenomena are e.g. turbulence, fluctuations, the critical dynamic effects occurring during phase transitions, singularity, catastrophes and the disordered conditions of chaotic features. The investigation of these phenomena clearly leads us out of the world of linear principles. Catastrophes are abrupt, in certain cases unexpected events, causing a drastic change or crisis in the system concerned [44, 45, 46].

The different principles of singularity may play an important role in working out the catastrophe principles, as its introductory elements. This is made possible by the fact that any of the characteristic functions show singularity when the catastrophe takes place.

One of these singularity theories is that of Lifshitz [47], who elaborated the principle for characterizing abrupt and radical change developing due to the change of external circumstances in metals. The theory concerns concretely the topologic change of the Fermi surface in metals and the behaviour of the function of electronic state density due to external pressure, but it may certainly be applied to other similar problems, as well.

The essence of the Lifshitz electronic transition may be summarized in the following way: when the critical energy value ε_c for which the change of the Fermi surface topology characteristic for the given metal takes place is near to the Fermi energy ε_F, then in case of a very small change in ε_F the topology change may occur actually, and the electronic state density function $\nu(\varepsilon)$ has a singularity near the Fermi surface $\varepsilon_F \approx \varepsilon_c$. In this case $\nu(\varepsilon)$ may be produced as the sum of a smooth function $\nu_0(\varepsilon)$ and of a non-monotonous additive part $\delta\nu(\varepsilon)$:

$$\nu(\varepsilon) = \nu_0(\varepsilon) + \delta\nu(\varepsilon). \tag{55}$$

Consequently, closed–open, or open–closed Fermi surface change, the appearance or disappearance of electron groups may take place, which strongly influences the physical characteristics of the metal.

We applied this principle in the research of superconductors using the fact that as a result of the mentioned behaviour of state density a non-analytic contribution appears in the characteristic thermodynamic potential function:

$$\delta\Omega = \begin{cases} 0 & \text{if } z < 0, \\ k\beta z^{3/2} & \text{if } z > 0, \end{cases} \tag{56}$$

where k is a constant, $\beta \sim N/\mu^{3/2} > 0$, $z = \mu - \varepsilon_c$, in which N is the number of the conductive electrons and μ is the electronic chemical potential.

Applying this method for the present case, on the one hand, we succeeded in determining the order of the specific superconducting phase transition developing due to increasing the concentration of the alloying material [48], and, on the other hand, we obtained valuable information on the effects of paramagnetic and diamagnetic contaminations in superconductors [49, 50]. It is evident that this theory may be applied to other kinds of rapid and radical transformations, catastrophe phenomena, too [51].

Another approach of the catastrophe theory is to draw conclusions from certain mathematical features as regards the nature of the catastrophe phenomena. Things which are changing rapidly and irregularly have resisted the correct mathematical analysis for a longtime, because it is very difficult to describe them. The method deduced from topology handles these phenomena as "elementary catastrophes" and attempts to interpret them on the basis of common features.

There are two different methods of developing the catastrophe theory:

1. a mathematical interpretation with the corresponding mathematical formalism,
2. the application of the mathematical principles (or the mathematical analyses) of the physical problem.

Catastrophe theory—as a mathematical discipline—in its own usual form actually is a classification theorem of degenerated singularity, extensively using the theories of extension and singularity [52]. The other form even provides possibility for the examination of different applications, because it may use theoretical descriptions of the solutions of linear partial differential equations and propagation phenomena. Here the analysis of interesting physical, biological, chemical, geological and even economic and sociological problems may be considered.

The problem of "shock-waves" is very important in applied mathematics, physics and engineering sciences, as it occurs in several physical phenomena. This effect develops when a physical phenomenon (or physical system) rapidly changes from one state to another. Due to the discontinuous nature of matter this is a very complicated problem with sophisticated mathematical statements.

Thom's classification, grouping singularities into certain classes of functions, has greatly contributed to the understanding of discontinuities occurring in natural processes. The meaning of this classification is that it makes possible the definition of equilibrium states subjected to a few constraints and describes how these equilibrium states change with the change of the constraints [53].

Several phenomena are governed by certain kinds of potential functions. These have in the stable equilibrium state minimum (or maximum) extrema. We can change the governing potential function in an experiment—changing the control parameters—so that all of the local minima (maxima) are covered. This means that we produce all the equilibrium states that the system can have. In this way the stable

equilibrium states of the system may change discontinuously when the control parameters change continuously. These discontinuous changes of state may be called "catastrophes".

According to these considerations we may interpret different types of elementary catastrophes [54].

It is a rather general procedure that the appearance (or existence) of certain phenomena may be interpreted by minimizing (or maximizing) a potential function. It was due to Lagrange, who supposed that Newton-type motions may be characterised with the minimum of the action integral

$$\int_{t_1}^{t_2} (\mathbf{r}, t)dt = \text{minimum}, \tag{57}$$

where $\mathscr{L}$ is the difference of the kinetic and potential energy, $\mathbf{r}$ is the place variable and t the time variable. This way of description is equivalent to the Euler–Lagrange equations.

Next we show some demonstrative examples for the extreme values:

1. If a chain of length l, fixed at its two ends, is affected only by the gravitation space, then the Euler–Lagrange equations for the shape of the curve give the formula:

$$y = \frac{1}{a}\cosh(ax), \tag{58}$$

where

$$a = \frac{y''}{\sqrt{1+(y')^2}},$$

which is the well-known equation of the "chain curve".

2. When light passes from one medium to another there are several possibilities for the path of light. Light chooses the shortest of time intervals according to the principle of

$$\int n(s)ds = \text{minimum}, \tag{59}$$

where n is the refractive index and s is the path of light.

3. If a ring placed into soapy water is slowly removed, we get a surface with minimum area, which—depending on the shape of the ring—may be either a two-dimensional form or a bubble. At the same time the surface stress must be maximum.

4. In architecture the basic principle is to minimize the expenses, and maximize the useful area and esthetic quality.

5. In thermodynamics the maximum or the minimum value of the characterizing potential functions describes the distinguished states.

In the following some examples are shown for discontinuity and singularity:

1. The density of boiling water is abruptly discontinuous from 1 to 0 during boiling. The characteristic function has a singularity. This is a type of stable discontinuity.

2. Water waves break when they arrive at the shore. The waves are symmetric before breaking and cresty after breaking.

3. In wind channels with a narrow neck the velocity increases at the narrow part and may reach even the velocity of sound. If local pressure is considered as the function of velocity, a sharp peak appears at this point and the pressure diagram becomes discontinuous.

In describing phenomena the method of topology comes to the foreground. Elementary catastrophes may be considered as certain singularities in the continuous projection of four- or less-dimensioned spaces. This is important because it appears in space-time in a structurally stable way.

The catastrophe (or bifurcation) is the system of points in the parameter space where the location of the minima (or maxima) of potential functions changes abruptly (discontinuity) when the parameters change. In this way the central question of the catastrophe theory is the investigation of the change of topology, the results of which are directly used in its own apparatus [55]. Considered from this aspect, Thom's theory distinguishes between seven different types of catastrophes, according to the change of topology in the case of four or fewer dimensions (Table I).

Table I

Different types of elementary catastrophes

Name	Germ	Universal	Codimension
1. Fold	x^3	x^3+ux	1
2. Cusp (Riemann–Hugoniot)	x^4	x^4+ux^2+vx	2
3. Swallow tail	x^5	$x^5+ux^3+vx^2+wx$	3
4. Butterfly	x^6	$x^6+ux^4+vx^3+wx^2+zx$	4
5. Hyperbolic umbilic	x^3+y^3	$x^3+y^3+wxy+ux+vy$	3
6. Elliptic umbilic	x^3+3xy^2	$x^3+3xy^2+w(x^2+y^2)+ux+vy$	3
7. Parabolic umbilic	x^2y+y^4	$x^2y+y^4+wx^2+zy^2+ux+vy$	4

Two fundamental regulating principles play a role in the description of these phenomena:

1. The so-called Maxwell convention (using the concept of "attractor" which is the range of the phase space to which the trajectory characterizing the changing system moves on after a while, i.e. in time). It means that when two or more stable attractors are in concurrence at any point of the parameter space, the system will select the state of the absolute minimum potential. Catastrophic conflict develops when there is more than one absolute minimum for the function [56, 57, 58].

2. The so-called rule of delay stating that once a stable attractor has been selected, then it must be continuously and systematically selected until it disappears at any degenerated critical point. At this moment the minimum will produce a rapid

change. Geometrical place of the parameter is such that the potential function will possess degenerated critical points [59, 60, 61].

Two examples for the extension of singularity are given as follows:

1. Universal extension of the singularity type

$$V=\frac{1}{3}x^3 \tag{60}$$

is

$$V(x,u)=\frac{1}{3}x^3+cx^4+ux, \qquad c\sim 0. \tag{60'}$$

Here the compatibility member cx^4 does not influence the minimum at the critical point when only close neighbourhood is taken into consideration. However, it is able to produce one minimum point rather far from the start.

2. Similarly, universal extension of the singularity type

$$G=\frac{1}{4}x^4 \tag{61}$$

is the potential

$$G(x,u,v)=\frac{1}{4}x^4+u\frac{x}{2}+vx \tag{61'}$$

which characterizes the well-known cusp catastrophe. These ideas come partially from thermodynamical investigations performed for the specification of catastrophe-like jumps occurring in boiling liquids, and, on the other hand, from geometrical and mechanical investigations.

Synergetics and chaos

In the everyday concept the picture of disorder is associated with the idea of the chaos. In a general image disordered or totally unarranged things are referred to as "chaotic". However, is there any unambiguous criterion of the chaos in physics? The chaos may be described by two characteristics: by random nature, on the one hand, and by non-linearity, on the other. Accordingly, chaotic state is the evolution of random phenomena in non-linear systems [62, 63, 64].

The phenomenon may be illustrated by giving either a characteristic time, or a characteristic length.

The former one means that—during the time of measurement—the system undergoes several changes of state with nonexpert direction. In this representation rapid and disordered changes of state result in the chaotic character.

The essence of the latter one is that there is a great number of different states existing within a distance characterizing the system at a given time. In this concept

the different states existing at the same time may be considered as the cause of the chaos.

Studying non-linear behaviour has started in two closely related ways: the theories of synergetics and of chaos [65, 66]. These two research trends are strongly connected to each other, they deal in most cases with similar or identical phenomena and arrive at the same result. They can perhaps be distinguished by their different attitudes.

In synergetics research started by gathering non-linear phenomena from different chapters of physics and other natural sciences, trying to find their common features. Synergetics' own major task is considered to be to investigate highly organized structures and self-organization.

Beside the fact that the non-linear basis is common, the theory of the phenomena of chaos may be perhaps separated from synergetics by the consideration that its major research field is development in the reverse direction, the disorder originating from the random character and the evolution of the chaotic states.

Considering the problem from a methodological aspect the random nature of phenomena occurring in non-linear systems is outlined better in the theory of the chaos whereas the operation with probability distribution functions receives more attention in synergetics. Of course the common features are of basic and decisive importance and the differences have a rather conceptual meaning [57, 68, 69].

Up-to-date computer techniques are widely used for these investigations.

Some years ago when the theory of similarity was studied intensively, attempts were made to describe the real reason for physical similarity by different methods, e.g. similarity criteria. This idea appeared to be slightly mysterious until the theorem—according to which phenomena described by the same type of differential equations may be considered similar—gained unambiguous approval.

In the course of investigating the chaos this uncertain element has appeared again and this is why it is necessary to mention the relevant fundamental recognition. Accordingly, each system, given phenomena of which are described by nonlinear differential equations, may take chaotic features.

The reason for chaos, as a mode of behaviour may be found in the non-linear features of the investigated system, and in the mathematical apparatus actually describing them, which means that solutions of the characteristic differential equations reflect the chaotic features occurring in the different cases [70, 71, 72, 73].

Under certain circumstances the non-linear systems show completely irregular chaotic behaviour. This has the main feature of being extremely sensitive to the initial conditions in the sense that at the given moment two trajectories, being near to each other, move away with exponential velocity. However, due to the fact that motion is generally limited to a finite range, trajectories mixing in a very complicated way are formed which show random features for real measurements of finite accuracy. This phenomenon is interesting because it appears typically for each non-linear system,

if the system has more than one degree of freedom and it occurs both for conservative and dissipative systems.

As an example, let us examine a simple mechanical system, the one-dimensional, dampened, anharmonic oscillator with unit frequency generation, the so called Duffing oscillator. The equation of motion for this system will be

$$\ddot{r}+\lambda\dot{r}+r^3=A\sin(2\pi t). \tag{62}$$

Introducing the new $x_1=r$, $x_2=\dot{r}$, $x_3=2\pi t$ coordinates it is obvious that in case of sufficiently high dampening (large λ) the system has a stable limit cycle, which may be described by a closed curve on the phase plane (x_1, x_2). In phase space stressed by coordinates (x_1, x_2, x_3) the motion may be characterized with an equivalent field of velocity $dx/dt=f(x)$ and in this space the trajectories intersect neither each other, nor themselves.

Reducing the measure of dampening, under a certain value $\lambda=\lambda_1$ the limit cycle of unit periodic time becomes unstable and a stable limit cycle with a period twice the former one appears. Further reducing the value of λ, doubling of the periodic times occurs again for $\lambda_1, \lambda_2, \lambda_3, \ldots$, dampening. According to numerical experiments, this period doubling is continued infinitely and the series $\lambda_1, \lambda_2, \lambda_3, \ldots$ has a congestion point λ_0. If dampening is reduced to below λ_0, the periodicity of the system's asymptotic motion ceases and the motion in the phase space becomes irregular (chaotic). However, this chaotic motion does not fill the entire phase space, but—totally independently of the initial conditions—it moves on to a partial set of it, which is the so-called strange attractor. The most characteristic feature of this is the very high sensitivity for the initial conditions, which means that a very slight change in them causes significant deviation of the trajectories from the original ones, within a very short time period, resulting in that it becomes totally impossible to predict the motion according to the initial values. The appearance of this strange attractor in non-linear systems is a typical phenomenon, and due to the effect of further changing of the control parameter the structure of the attractor becomes more and more complicated, which means that the dimension number of the strange attractor is ever increasing.

It would take much time even to enumerate chaotic system. To mention just a few examples, chaotic systems include non-linear electrical networks (due to dissipation on resistances these are generally non-conservative), certain chemical reactions (e.g. reactions of Belousov–Zhabotinski, certain enzyme reactions), hydrodynamical turbulence phenomena, the Benard problem, certain nervous diseases, economic and control technical phenomena, etc. [74, 75].

For example we demonstrated in earlier papers that the interaction between magnetic vortices and pinning forces in type II superconductors has some specific features [76, 77] and may also result in a chaotic behaviour [78].

The development of the chaotic state may take place in different ways, e.g. by period-doubling bifurcation series, but the special attractor may also develop after a

few (generally two or three) bifurcations. In this case during the change of the control parameter, first a limit cycle appears and then the system gets into the state of biperiodic motion, the characteristic frequencies of which cannot be compared. The Fourier spectrum of the system first shows some discrete peaks, corresponding to the incomparable frequencies, and at the appearance of the strange attractor the spectrum becomes continuous [79, 80].

We also have to mention the so-called intermittent transition to the chaotic phase, when chaotic intervals appear at a certain value of the changing control parameter in the periodic phase and these become dense and fill the periodic phase completely.

References

1. H. J. Kreuzer, Non-Equilibrium Thermodynamics and its Statistical Foundation, Clarendon Press, Oxford, 1980.
2. M. W. Zemansky, Heat and Thermodynamics, McGraw-Hill Book Comp., New York, Toronto, London, 1957.
3. E. C. Zeeman, Scientific American, *234*, 65, 1976.
4. H. Whitney, Ann. Math., *66*, 545, 1957.
5. D. A. Frank-Kamenyeckij: Diffusion and Heat Transfer, Nauka, Moscow, 1968 (in Russian).
6. I. Kirschner, Acta Phys. Hung., *10*, 351, 1959.
7. I. Gyarmati, Acta Chim. Hung., *30*, 147, 1962.
8. I. Kirschner, Energy and Nuclear Engineering, *32*, 97, 1979 (in Hungarian).
9. I. Gyarmati, Non-Equilibrium Thermodynamics, Springer Verlag, Berlin, 1970.
10. S. R. de Groot and P. Mazur, Non-Equilibrium Thermodynamics, North-Holland Publ. Comp., Amsterdam, 1969.
11. P. T. Landsberg, Thermodynamics and Statistical Mechanics, Oxford University Press, Oxford, 1979.
12. I. Gyarmati, Period. Polytechn., *5*, 233, 1961; Ann. Phys., *7*, 353, 1969.
13. J. M. C. Li, Journ. Chem. Phys., *33*, 2, 616, 1962.
14. J. Verhás, Z. Phys. Chem., (Leipzig), *24*, 119, 1972.
15. D. G. B. Edelen, Z. Phys. Chem. (Neue Folge), *88*, 37, 1974.
16. S. Lengyel and I. Gyarmati, Period. Polytechn., *25*, 63, 1981.
17. L. Onsager, Phys. Rev., *37*, 405, 1931.
18. L. Onsager, Phys. Rev., *38*, 2265, 1931.
19. I. Fényes, Thermostatics and Thermodynamics, Műszaki Könyvkiadó, Budapest, 1968 (in Hungarian).
20. E. A. Guggenheim, Thermodynamics, North-Holland Publ. Comp., Amsterdam, 1957.
21. I. Kirschner, Energy and Nuclear Engineering, *37*, 193, 1984 (in Hungarian).
22. I. Kirschner, Acta Phys. Hung., *30*, 61, 1971.
23. P. Glansdorff and I. Prigogine, Thermodynamic Theory of Structure, Stability and Fluctuations, J. Wiley, Interscience, London, New York, Sidney, Toronto, 1972.
24. I. Kirschner, Acta Phys. Hung., *29*, 319, 1970.
25. I. Kirschner and R. Tőrös, Journ. Non-Equilib. Thermodyn., *9*, 165, 1984.
26. L. Onsager and S. Machlup, Phys. Rev., *91*, 1505, 1953.
27. L. Onsager and S. Machlup, Phys. Rev., *91*, 1512, 1953.
28. I. Prigogine, Etude thermodynamique des processes irréversibles, Dunod, Paris, Liége, 1947.
29. S. R. de Groot, Thermodynamics of Irreversible Processes, North-Holland Publ. Comp., Amsterdam, 1951.
30. I. Prigogine and P. Glansdorff, Physica, *20*, 773, 1954.
31. I. Gyarmati, Ann. d. Phys., *23*, 353, 1969.

32. H. Farkas, Int. J. Engng. Sci., *13*, 1035, 1975.
33. J. Sándor, Electrochim. Acta, *17*, 673, 1972.
34. Gy. Vincze, Ann. Phys., *27*, 225, 1971; *30*, 55, 1973.
35. L. S. Polak (ed.), Variational Principles of Mechanics Fiz. Mat. Izdat., Moscow, 1959 (in Russian).
36. F. Schlögl, Z. Physik, *244*, 199, 1971.
37. B. D. Coleman, Arch. Rat. Mech. Anal., *36*, 1, 1970.
38. R. M. Clever and F. H. Busse, Journ. Fluid Mech., *65*, 625, 1974.
39. R. J. Knops and E. W. Wilkes, Theory of Elastic Stability, in Handbuch der Physik, Vol. 3: Mechanics of Solids III., ed. C. Truesdell.
40. P. Singh, Int. J. Heat and Mass Transfer, *19*, 581, 1976.
41. P. Singh, J. Non-Equilibrium Thermodyn., *1*, 105, 1976.
42. P. Singh and D. K. Bhattacharya, Acta Mechanica, *30*, 137, 1978.
43. D. K. Bhattacharya, Wärme und Stoffübertragung, *17*, 27, 1982.
44. R. Thom, Stabilité structurelle et morphogénése, W. A. Benjamin Inc., Reading, Massachusetts, 1972.
45. T. Bröcker, Differentiable Germs and Catastrophes, Cambridge Univ. Press, Cambridge, 1975.
46. Yung Chen Lu, Singularity Theory and an Introduction to Catastrophe Theory, Springer Verlag, New York, Heidelberg, Berlin, 1976.
47. I. M. Lifshitz, Zh. Exp. i Teor. Fiz., *38*, 1569, 1960.
48. I. Kirschner and K. Sajó, Journ. Low Temp. Phys., *39*, 235, 1980.
49. I. Kirschner, A. Stark and M. Falkó, Acta Phys. Hung., *29*, 243, 1970.
50. I. Kirschner and A. Stark, Acta Phys. Hung., *30*, 33, 1971.
51. I. Stewart, Rep. Progr. Phys., *45*, 185, 1982.
52. E. C. Zeeman, Breaking of Waves (Symposium on Differential Equations and Dynamical Systems) Lecture Notes in Math. No. 206, Springer Verlag, Berlin 1968.
53. R. Thom, Local Properties of Differentiable Mappings in Differential Analysis, Oxford University Press, Oxford, London, 1964, p. 191.
54. I. Stewart, The Seven Elementary Catastrophes, The New Scientist, 1975, p. 474.
55. A. A. Andronov, L. S. Pontryagin, Dokl. Akad. Nauk SSSR, *14*, 247, 1937.
56. G. Wasserman, Stability of Unfoldings, Lecture Notes in Math. No. 393, Springer Verlag, Berlin, 1974.
57. T. Poston and A. E. R. Woodcock, A Geometrical Study of the Elementary Catastrophes, Lecture Notes in Math. No. 373, Springer Verlag, Berlin, 1974.
58. I. Stewart, Rep. Progr. Phys., *45*, 185, 1982.
59. T. Poston and I. Stewart, Catastrophe Theory and its Applications, Pitman Publ. Co., London, 1975.
60. D. G. Schäffer and M. Golubitsky, Comm. Mat. Phys., *69*, 209, 1979.
61. R. Gilmore, Chatastrophe Theory for Scientists and Engineers, J. Wiley, Interscience, New York, 1981.
62. G. Joos and D. D. Joseph, Elementary Stability and Bifurcation Theory, Springer Verlag, Berlin, Heidelberg, New York, 1980.
63. P. Szépfalusy and T. Tél (ed.), Chaos, Akadémiai Kiadó, Budapest, 1982 (in Hungarian).
64. H. Haken, Synergetics, Springer Verlag, Berlin, Heidelberg, 1978.
65. M. J. Feigenbaum, Los Alamos Sci., *1*, 4, 1980.
66. H. Haken, Synergetik, Springer Verlag, Berlin, Heidelberg, New York, 1983.
67. Y. Ueda, Journ. Stat. Phys., *20*, 181, 1979.
68. M. Hénon, Quart. Appl. Math., *27*, 291, 1969.
69. J. P. Gollab, E. J. Romerand J. E. Socolar, Journ. Stat. Phys., *23*, 321, 1980.
70. M. J. Feigenbaum, Commun. Math. Phys., *77*, 65, 1980.
71. A. N. Kolmogorov, Dokl. Akad. Nauk, *98*, 527, 1954.
72. T. Tél, L. Liszkay, Fiz. Szemle, *34*, 404, 1984 (in Hungarian).
73. Z. Kaufmann, Fiz. Szemle, *33*, 361, 1983 (in Hungarian).
74. M. Rosenblatt and C. Van-Atta (ed.), Statistical Models of Turbulence, Springer Verlag, Berlin, Heidelberg, New York, 1972.
75. K. Yto, Journ. Geophys. Res., *85*, 1399, 1980.
76. I. Kirschner and K. Martinás, Journ. Low Temp. Phys., *14*, 427, 1974.
77. I. Kirschner and K. Martinás, Journ. Low Temp. Phys., *47*, 105, 1982.
78. I. Kirschner and K. Martinás, Proc. 17th Intern. Conf. Low Temp. Phys., p. 591., Karlsruhe, 1984.
79. J. D. Farmer, Physica, *D4*, 336, 1982.
80. O. E. Rössler, Z. Naturforsch., *31A*, 259, 1976.

Acta Physica Hungarica, 63 (3—4), pp. 291—294 (1988)

PHONON DISPERSION OF SILVER

K. K. CHOPRA and H. NAIT-LAZIZ

Département de Physique, INES en Electrotechnique
Université de Tizi-Ouzou, Tizi-Ouzou, Algeria

(Received in revised form 20 February 1986)

Recent studies based on microscopic theories have supported the existence of three-body forces in solids. A phenomenological model incorporating three-body forces is proposed and applied to calculate the phonon dispersion curves of silver which are found to be in very good agreement with experimental results.

1. Introduction

Recent studies [1–3] of lattice dynamics of metals based on pseudopotential theories have met with only a limited success in the case of noble metals. The chief complexity in these metals arises from the presence of *d*-shell electrons which are neither tightly bound to be considered as core electrons, nor so free as to be regarded as conduction electrons. Nevertheless, the pseudopotential studies have yielded some important informations regarding the nature of interactions in metals. Using pseudopotential theory Brovman et al [4–6] and Pethick [7] have shown that three-body interactions play an important role in metals and are essential to obtain the required equality of static and dynamic elastic constants. In the present paper we have adopted a phenomenological approach [8] to incorporate the effect of three-body forces on the lattice vibrations of a noble metal. The resulting model has been applied to calculate the phonon dispersion curves of silver in the principal symmetry directions. Extremely good agreement with the experimentally measured values is obtained.

2. Theory

We consider the energy of a metal as made up of three parts:

(i) E_c, due to core–core interactions,

(ii) E_d, due to *d*-shell–*d*-shell interactions, and

(iii) E_v, the volume energy which represents the combined effects of the interactions among (a) core-conduction electrons and (b) *d*-shell–conduction electrons.

Pseudopotential studies of Pick et al [9] and Resolt et al [10] have shown that interactions among cores are essentially central. We have also, therefore, supposed core–core interactions for E_c to be purely central. These have been calculated in the usual manner [11] extended to second neighbours. The presence of d-shell electrons is well known to be responsible for the breakup of the sphericity of the charge distribution resulting in non-central interactions [12, 13] among clouds of d-shell charges. We have considered these non-central interactions to be of three-body character which can be phenomenologically described by the Clark–Gazis–Wallis type angular forces [14]. We have used these forces as given by Yuen et al [15] for a FCC metal.

The volume energy E_v is connected to many-body interactions. We follow the idea of Sarkar et al [16] who have developed this energy in terms of the volume strain Δ around the equilibrium volume. The term of interest in the expression is $1/2K_eV_0\Delta^2$, where K_e is the bulk modulus of the electron gas and V_0 the equilibrium volume. Interpreting Δ as a local strain one can express it in terms of the coordinates of the ions of the region. The region considered for the purpose is confined to the twelve nearest neighbours. As the term in Δ is quadratic, the sum over the twelve nearest neighbours compresses the many-body interactions into an effective three-body interaction.

The total dynamical matrix elements are found to be:

$$D_{ii}=[2\alpha_1+16(\gamma'_1+\gamma'_2)]\,[2-C_i(C_j+C_k)]+4\alpha_2S_i^2-$$
$$-8\gamma'_1(2S_i^2-S_j^2-S_k^2)+K'S_i^2(C_j+C_k)^2,$$
$$D_{ij}=[2\alpha_1-16\gamma'_1+K'(C_j+C_k)\,(C_k+C_i)]S_iS_j,$$

where

$$\gamma'=\gamma/a^2;\quad K'=K_ea/4;\quad S_i=\sin(\pi ak_i);\quad C_i=\cos(\pi ak_i);$$

a is the lattice constant, k the phonon wave vector and the subscripts i, j, k, denote the Cartesian directions.

3. Results and discussion

The matrix elements given above contain five parameters — α_1, α_2 for the central forces, γ_1, γ_2 for the three-body angular forces and K_e for the volume forces. These are determined from three elastic constants and two zone boundary frequencies. The input data and the calculated parameters are given in Table I. The calculated phonon dispersion curves are shown in Fig. 1 along with the experimental points of Kamitakahara et al [17].

As is evident from the dispersion curves, a very good agreement is obtained with the experimental values for all directions. The maximum discrepancies are within

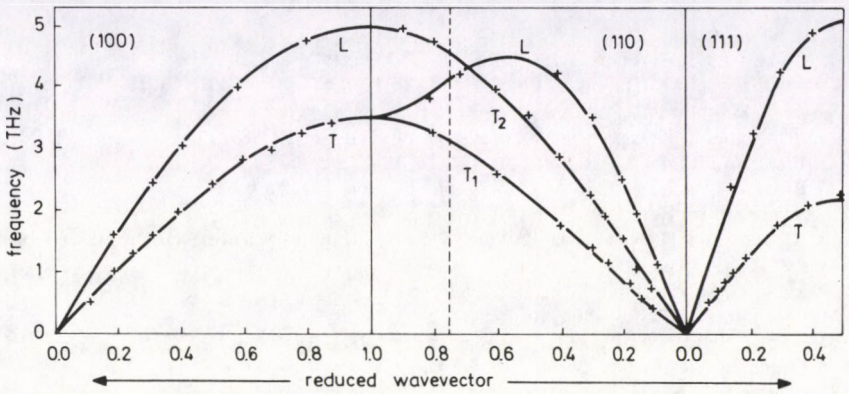

Fig. 1. Dispersion curves of silver in the three principal symmetry directions. Phonon frequencies in THz are shown as function of reduced wavevector: $ak/2\pi$ for (100) direction, $ak/2\pi\sqrt{2}$ for (110) and $ak/2\pi\sqrt{3}$ for (111) direction. Also shown are the experimental points of Kamitakahara et al, Ref. [17]

Table I

Input data and calculated parameters

Input data			Model parameters [N/m]	
Elastic constants:	C_{11}:	12.399	α_1:	28.124
[10^{10} Newton/m^2]	C_{12}:	9.367	α_2:	−1.336
Ref. [18]	C_{44}:	4.612	γ_1/a^2:	0.364
			γ_2/a^2:	−1.161
			$K_e a$:	6.699
Lattice constant:	'a':	4.08		
[10^{-10} m]				
Atomic mass:	'M':	107.868		
[amu]				
Zone boundary frequencies:	ν_L(100):	4.96		
[THz]. Ref. [17]	ν_L(1/2 1/2 1/2):	5.08		

3%. Our model employs physically realistic interactions supported by microscopic studies based on pseudopotentials. The close agreement obtained justifies the importance of various interactions considered. In particular, the many-body volume energy seems to be effectively well described by the resulting three-body interactions.

Acknowledgements

The authors express gratitude to their Colleagues Messrs S. Bouarab, M. Benakki and H. Sadat for many useful discussions and to Mr. S. Guermah, Director of the Institut National d'Enseignement Supérieur en Electrotechnique de Tizi-Ouzou, for the facilities provided.

References

1. B. A. Oli and A. O. E. Animalu, Phys. Rev., B-*13*, 2398, 1976.
2. J. C. Upadhaya and L. Dagens, J. Phys., F-*8*, L-21, 1978.
3. J. Singh, N. Singh and S. Prakash, Phys. Rev., B-*18*, 2954, 1978.
4. E. G. Brovman, Yu Kagan and A. Kholas, Sov. Phys. JETP, *30*, 883, 1970.
5. E. G. Brovman and Yu Kagan, ibid., *30*, 721, 1970.
6. E. G. Brovman, Yu Kagan and A. Kholas, ibid., *34*, 394, 1972.
7. C. J. Pethick, Phys. Rev., B-*2*, 1789, 1970.
8. K. K. Chopra and H. Nait-Laziz, 2nd Int. Sem. on 'Material Sciences', Université de Constantine, May 1985.
9. R. Pick and G. Sarma, Phys. Rev., *135*, 1363, 1964.
10. J. M. Resolt and R. Taylor, Phys. Rev., B-*11*, 2717, 1975.
11. J. de Launay, Solid State Physics, 2, Academic Press, N.Y. 1956.
12. H. S. Leigh, Proc. Phys. Soc. London, A-*71*, 33, 1958.
13. M. Simizu and H. Niu, J. Phys. Soc. Japan, *27*, 577, 1962.
14. B. C. Clark, D. C. Gazis and R. F. Wallis, Phys. Rev., *134*, A1486, 1964.
15. P. S. Yuen and Y. P. Varshini, ibid., *164*, 895, 1967.
16. S. K. Sarkar, S. K. Das, D. Roy and S. Sengupta, Phys. Stat. Sol. (b), *83*, 615, 1977.
17. W. A. Kamitakahara and B. N. Brockhouse, Phys. Lett., A-*2*, 639, 1969.
18. J. R. Neighbours and G. A. Alers, Phys. Rev., *111*, 707, 1958.

Acta Physica Hungarica, 63 (3—4), pp. 295—302 (1988)

THE EMISSION BAND SPECTRUM OF NiCl IN THE REGION $\lambda\lambda$ 340.0–560.0 nm

C. V. REDDY*, A. L. NARAYANA and P. T. RAO**

Department of Physics, Andhra University
Waltair, India

(Received 27 February 1986)

The emission spectrum of NiCl has been reinvestigated in a H.F. discharge from a 500 W oscillator using high dispersion. This study has led to a revision of the vibrational analysis of several doublet systems of bands recently reported in thermal emission using low dispersion. The bands of NiCl in the region $\lambda\lambda$ 340.0–560.0 nm have been analysed as belonging to several doublet systems of bands degraded to red, some of which have a common lower $A^2\Pi_i$ state and others with a common ground state $X^2\Sigma$, analogous to $A^2\Pi_i$ and $X^2\Sigma$ states of NiF recently established from a detailed rotational analysis of two doublet systems in the visible region. The vibrational analysis of some of the systems have also been confirmed from a study of both chloride and nickel isotope effects observed in $\Delta v = \pm 1$ sequences.

1. Introduction

The emission spectrum of NiCl has been investigated by Mesnage [1, 2], More [3], Krishnamurty [4], Reddy and Rao [5], Rao, Reddy and Rao [6], Rao and Rao [7], Darji and Shah [8] and Shah, Darji and Shah [9] in various electrical sources of excitation. The spectrum was known to consist of several brief systems of bands in the visible region $\lambda\lambda$ 340.0–560.0 nm. Recently Gopal and Joshi [10, 11, 12, 13] reported for the first time the occurrence of the spectrum of NiCl in thermal emission in the visible region $\lambda\lambda$ 399.0–555.5 nm. They reported the vibrational analyses of several doublet systems of bands corresponding to transitions from the ground $X^2\Delta$ state to various excited states designated as A, B, C, D, E, F, G, H, I, J, K and L in order of increasing energy. The ground doublet state is suggested as $a^2\Delta$ state by analogy with NiH. Similar doublet systems of bands corresponding to transitions from the ground $^2\Delta$ state to various stable excited states in the spectra of NiF and NiBr have also been recently reported in a series of papers by Gopal and Joshi [14, 15, 16, 17].

* Department of Physics, T. R. R. Govt. College, Kandukur, Prakasam Dt. India
** To whom all correspondence should be addressed.

According to a detailed rotational analysis of two doublet systems of bands of NiF by Pinchemel et al [18] and Pinchemel [19], the ground state of NiF has been established as $X^2\Sigma$ state and higher excited states as $A^2\Pi_i$, $B^2\Pi_{3/2}$ and $C^2\Delta$ in order of increasing energy.

In the region $\lambda\lambda$ 344.0–395.0 nm, Darji and Shah [8] reported the vibrational analysis of α, β, γ, δ, A_0 and A_1 systems.

However, the vibrational analyses of all the doublet systems of NiCl reported by Gopal and Joshi have been based on spectrograms taken under the low dispersion of a Hilger E-492 large quartz spectrograph.

A reinvestigation of the various systems of NiCl in the visible region $\lambda\lambda$ 340.0–560.0 nm has therefore been undertaken using the first and second order dispersion of a PGS-2 spectrograph of Carl Zeiss. This study has led to a revision of the vibrational analysis of some of the systems reported by Darji and Shah in the region $\lambda\lambda$ 344.0–395.0 nm and Gopal and Joshi in the region $\lambda\lambda$ 399.0–555.5 nm and to a new interpretation of the spectrum of NiCl in this region as described in this paper.

2. Experimental

The spectrum of NiCl has been excited in a radio frequency (30–40 MHz) discharge from a 500 W oscillator, using an anhydrous specpure sample of $NiCl_2$. The bands in the above region have been photographed in the first and second order dispersion 0.7 nm/mm and 0.35 nm/mm of a PGS-2 spectrograph of Carl Zeiss. Exposures of about 10 minutes to two hours duration on ORWO-WU 3 and Ilford R-20 photographic plates have been found sufficient to obtain good spectrograms of NiCl. Measurements of band heads have been made using iron arc spectral lines as standards for comparison.

3. Results and analysis

According to the vibrational analysis proposed by Gopal and Joshi, the common lower state with a doublet separation of about 9.614×10^{-21} J for all the observed doublet systems has been suggested as $^2\Delta$ state. The doublet interval between X_1 and X_2 has been derived from the vibrational analyses of C–X, D–X, I–X, J–X and L–X systems. Taking the example of the L–X system, they deduced the interval between X_1 and X_2 from the vibrational analysis of L_1–X_1 and L_1–X_2 systems. The vibrational frequency of the X_1 state has been determined as 8.482×10^{-21} J while that of the X_2 state could not be determined as only the $\Delta v = 0$ sequence is obtained. They reported the vibrational analysis of another system designated as L_2–X_2, from which the vibrational frequency of the X_2 state is determined as 8.621×10^{-21} J. The separation between L_1 and L_2 is thus equal to 4.032×10^{-21} J. We may thus assume

Hund's case (a) as a good approximation for both X and L states. As the bands in each of these systems have been observed to be double headed (R and Q), it has been assumed by Gopal and Joshi that the transition involved in the L–X system is either $^2\Pi$–$^2\Delta$ or $^2\Phi$–$^2\Delta$. For such transitions, only two component systems can occur according to the selection rule $\Delta\Sigma = 0$. Thus there is no possibility for the occurrence of three sub-systems L_1–X_1, L_1–X_2 and L_2–X_2. It has been shown below that L_1–X_1 and L_1–X_2 systems arise from a doublet–doublet transition of the type $^2\Sigma$–$^2\Pi$ with nearly equal vibrational frequencies for X_1 and X_2 and the L_2–X_2 system arises from one component of another doublet system with a lower state vibrational frequency of 8.641×10^{-21} J. Similar remarks will apply for each of the systems C–X, D–X, I–X and J–X in which three subsystems have been reported by Gopal and Joshi.

According to our analysis based on high dispersion spectrograms of NiCl in the region $\lambda\lambda$ 340.0–560.0 nm the spectrum of NiCl, can be classified as belonging to several doublet systems of bands degraded to red, some of which have a common lower state $^2\Pi_i$ with merely equal vibrational frequencies of 8.466×10^{-21} J and 8.446×10^{-21} J and others with a common lower state $^2\Sigma$ with a vibrational frequency of 8.641×10^{-21} J. By analogy with the $A^2\Pi_i$ and $X^2\Sigma$ states of NiF, deduced by Pinchemel et al [18] and Pinchemel [19] from a detailed study of the rotational analysis of two systems, it has been suggested that the ground state of NiCl is $X^2\Sigma$ while the first excited state is $A^2\Pi_i$. In three prominent doublet systems of NiCl designated as H'–A, I'–A and L' –A shown in Fig. 1, the corresponding bands of the strong $\Delta v = 0$ sequences are separated by an interval of 9.634×10^{-21} J which is regarded as the doublet interval of the $A^2\Pi$ state. Each of these systems has been suggested to belong to a transition $^2\Sigma$–$^2\Pi$. Two of these systems H'–A and L_1–A have been earlier obtained by More and attributed to $^2\Sigma$–$^2\Pi$ transitions with a common lower state $^2\Pi$ with a doublet separation of 9.634×10^{-21} J. As the C–X and D–X systems of NiCl reported by Gopal and Joshi are fragmentary, they are not considered in the present work.

All systems having either $A^2\Pi_{3/2}$ or $A^2\Pi_{1/2}$ as lower state have been designated as B', C', D', E', F', G', J', K', M', N' and O' in the order of increasing energy relative to $A^2\Pi_{3/2}$. Of these, B'–A_1, K'–A_1, M'–A_2 and O'–A_1 systems are observed to be single headed and interpreted as R heads. Each of these systems is characterised by a strong $\Delta v = 0$ sequence and a weak $\Delta v = +1$ or -1 sequence. In few cases both weak $\Delta v = \pm 1$ sequences have observed and analysed. The transition involved in each of these systems is suggested as one component of a $^2\Pi$–$^2\Pi$ transition.

The C'–A_2, D'–A_2, E'–A_1, F'–A_1, G'–A_2, J'–A_2 and N'–A_2 systems consist of double headed bands interpreted as R and Q heads. Bands corresponding to a strong $\Delta v = 0$ sequence and a weak $\Delta v = \pm 1$ sequence are observed and analysed. The transition involved in each of these systems is suggested as one component of a $^2\Delta$–$^2\Pi$.

All the systems with a common lower $X^2\Sigma$ ground state are designated as B, C, D, E, F, G, H, I, J, K, L and M. Of these, the B, C, D, G, L and M systems with a common lower $^2\Sigma$ state are observed to be single headed and interpreted as R

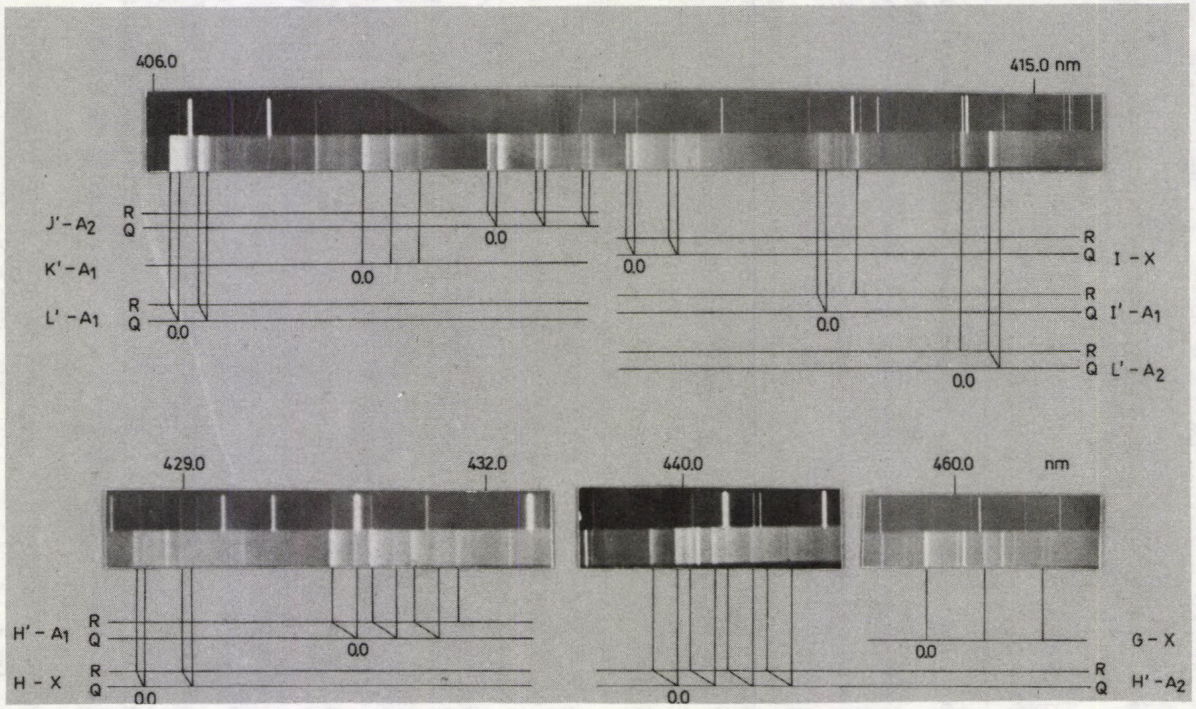

Fig. 1. Grating spectrograms of NiCl (second order) $\Delta v = 0$ sequences

Table I

Band head data of Ni^{58} Cl^{35} molecule in the region $\lambda\lambda$ 340.0–560.0 nm

Wavelength [nm]	Int.	Classification v',v''	Wavelength [nm]	Int.	Classification v',v''
B–$\bar{X}$ system			L–X system		
541.65	3	0.0	366.42*	7	0.0
542.31	3	1.1	366.61	6	1.1
554.61	5	0.1	372.31	5	0.1
C–X system			M–X system		
526.80	1	1.0	349.08	6	0.0
538.48	4	0.0	349.30	4	1.1
551.28	3	0.1	354.39	4	0.1
D–X system			B'–A_1 system		
523.73	2	1.0	351.29	4	0.0
535.24	5	0.0	352.05	4	1.1
547.86	3	0.1	C'–A_2 system		
E–X system			490.80	3	1.0 R
486.81	6	0.0 R	490.99	2	1.0 Q
487.04	5	0.0 Q	500.66	6	0.0 R
487.36	7	1.1 R	500.33	4	0.0 Q
497.25	4	0.1 R	511.50	3	0.1 R
F–X system			511.67	3	0.1 Q
470.55	5	0.0 R	D'–A_2 system		
470.74	5	0.0 Q	484.14	2	1.0 Q
470.90	6	1.1 R	493.13	3	0.0 R
471.06	4	1.1 Q	493.32	4	0.0 Q
G–X system			503.77	3	0.1 Q
451.35	5	1.0	E'–A_1 system		
459.70	9	0.0	473.21	2	1.0 R
469.02	3	0.1	482.37	6	0.0 R
H–X system			482.91*	5	1.1 R
428.45	7	0.0 R	483.08	4	1.1 Q
428.54	5	0.0 R	F'–A_1 system		
428.94	5	1.1 R	454.14	4	1.0 Q
429.02	4	1.1 Q	462.25	8	0.0 R
436.49	3	0.1 R	462.56	9	0.0 Q
I–X system			471.77	4	0.1 Q
404.13	2	1.0 R	G'–A_2 system		
404.23	2	1.0 R	448.06	3	1.0 R
410.85	7	0.0 R	456.29	7	0.0 R
410.93	8	0.0 Q	456.40	6	0.0 Q
418.31	2	0.1 R	465.25	3	0.1 R
J–X system			H'–A_2 system		
366.80*	7	1.0 R	439.66	6	0.0 R
372.19	8	0.0 R	439.92	8	0.0 Q
372.24	3	0.0 Q	440.05	7	1.1 R
378.24	3	0.1 R	440.31	9	1.1 Q
K–X system			447.97	2	0.1 R
367.62	6	0.0 R	H'–A_1 system		
367.67	4	0.0 Q	423.21	3	1.0 R
367.89	2	1.1 R	430.49	9	0.0 R
373.52	2	0.1 R	430.73	7	0.0 Q
373.61	2	0.1 Q	438.46	4	0.1 R

* Superposed by atomic line

Table I (cont.)

Wavelength [nm]	Int.	Classification v',v''	Wavelength [nm]	Int.	Classification v',v''
$I'-A_2$ system			$L'-A_2$ system		
421.25	4	0.0 R	407.48	2	1.0 R
421.30	3	0.0 Q	414.31	5	0.0 R
421.60	5	1.1 R	421.67	4	0.1 R
421.67	4	1.1 Q	$L'-A_1$ system		
$I'-A_1$ system			399.65	2	1.0 Q
412.85	4	0.0 R	406.14	10	0.0 R
412.92	4	0.0 Q	406.24	9	0.0 Q
413.22	5	1.1 R	413.24	4	0.1 R
413.29	3	1.1 Q	$M'-A_2$ system		
420.17	3	0.1 R	378.76	1	1.0
$J'-A_2$ system			384.63	8	0.0
402.94	2	1.0 R	390.99	3	0.1
403.00	2	1.0 Q	$N'-A_2$ system		
409.42	8	0.0 R	376.21	1	1.0 Q
409.53	9	0.0 Q	381.81	6	0.0 R
416.61	2	0.1 R	381.87	7	0.0 Q
416.72	3	0.1 Q	388.16	2	0.1 Q
$K'-A_1$ system			$O'-A_1$ system		
401.50	4	1.0	362.91	2	1.0
408.13	8	0.0	368.39	4	0.0
415.29	2	0.1	368.59	4	1.1

Table II

Vibrational constants for various electronic states of $Ni^{58}Cl^{35}$ molecule

State	(a)			State	(b)		
	v_e $\times 10^{-19}$J	ω_e $\times 10^{-21}$J	$\omega_e x_e$ $\times 10^{-23}$J		v_e $\times 10^{-19}$J	ω_e $\times 10^{-21}$J	$\omega_e x_e$ $\times 10^{-23}$J
M*	5.6889	...	...	O'*	5.3907	...	...
L	5.4211	8.3828	4.5688	N'	5.2032	7.8803	2.5824
K*	5.4012	...	...	M'	5.1649	8.0789	3.1783
J'	5.3393	7.9299	4.1716	L'	4.8915	8.1087	3.0790
I	4.8362	8.1127	3.6749	K'	4.8687	8.1206	3.8736
H	4.6378	8.0889	4.0722	J'	4.8519	7.8852	2.8406
G	4.3228	8.0739	3.4167	I'*	4.8102	...	...
F*	4.2187	...	...	H'	4.6153	8.0233	4.5688
E	4.0818	8.1544	2.4831	G'	4.3541	8.0769	4.0722
D	3.7124	8.2299	3.9729	F'	4.2954	8.0481	4.3702
C	3.6900	8.2339	3.4763	E'	4.1189	8.0729	5.3634
B	3.6685	8.2061	3.6749	D'	4.0294	7.7055	4.8668
$X(2\Sigma)$	0	8.6411	3.3769	C'	3.9674	8.0094	2.8804
				B'*	3.7379	...	...
				$A_2{}^2\Pi_{1/2}$	...	8.4469	4.0722
				$A^2\Pi_{3/2}$	..	8.4663	3.7743

* As only the strong $\Delta v=0$ sequences are observed the assignment of these systems to F–X, K–X, M–X, B'–A_1, I'–A and O'–A_1 transitions is tentative.

heads. Each of these systems, which consist of a strong $\Delta v=0$ sequence and a weak $\Delta v=+1$ or -1 sequence is attributed to a $^2\Sigma$–$^2\Sigma$ transition.

The E, F, H, I, J and K systems consist of double headed bands interpreted as R and Q heads. Bands corresponding to a strong $\Delta v=0$ sequence and a weak $\Delta v=+1$ or -1 sequences are observed and analysed. Each of these systems is assumed to arise from one component of a $^2\Pi-^2\Sigma$ transition. In addition to the bands of NiCl attributed to the above transitions, there are other fragmentary systems of NiCl in the region $\lambda\lambda$ 340.0–560.0 nm, some of which have been reported by earlier workers.

In order to save space the data and classification of a few prominent band heads of $Ni^{58}Cl^{35}$ molecule in the region $\lambda\lambda$ 340.0–560.0 nm are presented in Table I. Grating spectrograms of the $\Delta v=0$ sequences of some prominent systems G–X, H'–A_2, H'–A_1, H–X, I'–A_1, I–X, J'–A_2, K'–A_1, L'–A_2 and L'–A_1 of NiCl are shown in Fig. 1. The vibrational constants given in Table II refer to the most abundant molecule $Ni^{58}Cl^{35}$. Table II(a) gives the vibrational constants of all states whose heights are known relative to the ground $X^2\Sigma$ state, while Table II(b) gives vibrational constants of all states whose heights are known relative to the $A^2\Pi_{3/2}$ state. However, the separation between $X^2\Sigma$ and $A^2\Pi_{3/2}$ states is not known from the analysis.

4. Isotope effect

Bands corresponding to the molecular species $Ni^{58}Cl^{35}$ and $Ni^{60}Cl^{35}$ have been observed in either $\Delta v=+1$ or -1 sequences of systems C'–A_2, F'–A_1, G–X, G'–A_2, H'–A_1, K'–A_1, L'–A_1, J–X and N'–A_2 with a separation of about 0.049×10^{-21} J in satisfactory agreement with the values calculated for these molecules. Similarly, bands corresponding to the molecules $Ni^{58}Cl^{35}$ and $Ni^{58}Cl^{37}$ have been observed in either $\Delta v=+1$ or -1 sequences of systems C'–A_2, D–X, F'–A, G–X, H–X, G'–A_2, H'–A_1, K'–A_1, L'–A_1, J–X and N'–A_2 with a separation of about 0.139×10^{-21} J in satisfactory agreement with the values calculated for these molecules.

5. Discussion of results

Thus we have in NiCl a set of states whose relative heights are known with respect to $A^2\Pi_{3/2}$ and another set of levels whose heights are known with respect to $X^2\Sigma$. It is of interest to note that Pinchemel et al [18] and Pinchemel [19] have shown that there are two doublet systems of bands of NiF molecule attributed to transitions $C^2\Delta$–$A^2\Pi_i$ and $B^2\Pi_{3/2}-X^2\Sigma^+$ respectively from a detailed study of the rotational analysis using very high dispersion. But the heights of the $A^2\Pi_{1/2}$ and $A^2\Pi_{3/2}$ levels above the $X^2\Sigma^+$ state are not known in NiF also. By analogy with NiF, it may be assumed that the ground state of NiCl molecule is the $X^2\Sigma$ state and the $A^2\Pi_{3/2}$ state, the first excited state of NiCl.

Taking into account the $3d^9\ 4s$ valence electrons of the Ni and the $3p^5$ valence electrons of the Cl atom, we may represent the ground $X^2\Sigma$ and the $A^2\Pi_i$ states of NiCl by the following two configurations using atomic and molecular orbitals.

$$1 \ldots (3d\delta)^4_{Ni}\,(3d\pi)^4_{Ni}\,(3d\sigma)_{Ni}$$
$$(4s\sigma_{Ni}+3p\sigma_{Cl})^2\,(3p\pi)^4_{Cl}-X^2\Sigma;$$
$$2 \ldots (3d\delta)^4_{Ni}\,(3d\pi)^3_{Ni}\,(3d\sigma)^2_{Ni}$$
$$(4s\sigma_{Ni}+3p\sigma_{Cl})^2\,(3p\pi)^4_{Cl}-A^2\Pi_i.$$

In these configurations the $3d\sigma$ orbital lies lower in energy than the $3d\pi$ which again lies lower than the $3d\sigma$ as assumed by Pinchemel [19] in the case of NiF. The stability of $X^2\Sigma$ and $A^2\Pi$ states of NiCl can be attributed to the presence of two electrons in the $(4s\sigma_{Ni}+3p\sigma_{Cl})$ bonding orbital in each case.

Acknowledgement

One of the authors (C.V.R) is thankful to the U.G.C. New Delhi, for the award of a Teacher Fellowship.

References

1. P. C. Mesnage, C. R. Acad. Sci., *200*, 2072, 1935.
2. P. C. Mesnage, Ann. D. Phys., *12*, 5, 1939.
3. K. R. More, Phys. Rev., *54*, 122, 1938.
4. V. G. Krishnamurty, Indian J. Phys., *26*, 207, 1952.
5. S. P. Reddy and P. T. Rao, Proc. Phys. Soc., *75*, 275, 1960.
6. S. V. K. Rao, S. P. Reddy and P. T. Rao, Z. Phys., *166*, 261, 1962.
7. N. V. K. Rao and P. T. Rao, Curr. Sci., *38*, 489, 1969.
8. A. B. Darji and N. R. Shah, Indian J. Pure and Appl. Phys., *18*, 802, 1980.
9. P. M. Shah, A. B. Darji and N. R. Shah, Indian J. Pure and Appl. Phys., *21*, 617, 1983.
10. R. Gopal, Curr. Sci., *50*, 854, 1981.
11. R. Gopal and M. M. Joshi, Indian J. Phys., *55B*, 368, 1981.
12. R. Gopal and M. M. Joshi, Indian J. Pure and Appl. Phys., *20*, 280, 1982.
13. R. Gopal and M. M. Joshi, Indian J. Pure and Appl. Phys., *21*, 595, 1983.
14. R. Gopal and M. M. Joshi, Indian J. Phys., *55B*, 507, 1981.
15. R. Gopal and M. M. Joshi, Curr. Sci., *50*, 530, 1981.
16. R. Gopal and M. M. Joshi, Pramana, *15*, 349, 1980.
17. R. Gopal and M. M. Joshi, Indian J. Pure and Appl. Phys., *20*, 763, 1982.
18. B. Pinchemel, Y. Lefebvre and J. Schamps, J. Mol. Spectrosc., *77*, 29, 1979.
19. Bernard Pinchemel, J. Phys. B., *14*, 2569, 1981.

Acta Physica Hungarica, 63 (3—4), pp. 303—310 (1988)

ELEVEN DIMENSIONAL COSMOLOGY AND DYNAMICAL SCALE SYMMETRY BREAKING

C. WOLF

Department of Physics, North Adams State College, North Adams, Mass. (01247) U.S.A.
Institut für Theoretische Physik, 7400 Tübingen, West Germany

(Received in revised form 8 April 1986)

The unjustified assumption that the universe possesses a fixed gravitational constant prior to compactification is remedied by assuming an 11 dimensional scale invariant Lagrangian with a possible scale breaking potential whose minimum generates the 4 dimensional gravitational constant. The cosmological evolution equations are followed and a model is studied wherein the scalar field evolves to the minimum of the potential with the subsequent generation of G_4, while the 7 dimensional space compactifies and the 4 dimensional space inflates.

1. Introduction

The emergence of the 4 dimensional world from a splitting of the primal 11 dimensions into 4 observable and 7 unobservable dimensions has been the subject of many papers [1, 2]. The precise nature of the splitting process is not entirely understood and the assumption that a Casimir-like effect produced the compactification process is subject to the same scrutiny that any quantum gravitational calculation is subject to. Appelquist and Chodos [3] have calculated the influence of quantum fluctuations in a 5 dimensional Kaluza–Klein theory by computing the one-loop contributions to the effective potential. They find an infinite attractive potential after the divergent term is subtracted with the subsequent collapse of the 5th dimension. Rohrlich [4] repeated the calculation and obtained exactly the same result. Later investigations showed that the sign of the Casimir energy depended on the topology of the background manifold which leaves the compactification process somewhat arbitrary [5]. The above calculation is subject to questions of cut-off and background topologies along with the validity of the one loop approximation and it was hoped that super-symmetry would remedy these problems. Unfortunately, there is no super-symmetric Casimir effect [6]. Of course the intense interest in the 11 dimensional case was motivated by Wittens proof that the 7 sphere is the minimum compactified space that can generate the low energy $SU_3 \times SU_{2L} \times U_1$ particle theory on $M4$ [7]. The hope is that particle phenomenology is represented by small fluctuations away from a ground state solution of the 11 dimensional Einstein theory. But what is the ground state, is it stable and how did the universe evolve toward it.

The present approach to 11 dimensional cosmology is to assume a metric of the form

$$g_{AB}=\begin{pmatrix} -1 & & \\ & R_3^2\,\tilde{g}_{ij}(x^i) & \\ & & R_7^2\,\tilde{g}_{m,n}(y^m) \end{pmatrix} \tag{1.1}$$

$A, B=0, 1, 2, \ldots, 10$; $i, j=1, 2, 3$; $m, n=4, 5, 6, \ldots, 10$; $R_3=$three dimensional scale factor; $R_7=$seven dimensional scale factor, where $\tilde{g}_{ij}(x^i)$, $\tilde{g}_{mn}(y^m)$ are the maximally symmetric metric of the d and D dimensional subspaces. Here x^i represent coordinates in the three dimensional subspace and y^m represent coordinates in the seven dimensional subspace, $x^0=t$. The form

$$T_{AB}=\begin{pmatrix} \varepsilon(t) & & \\ & Pg_{ij} & \\ & & P'g_{mn} \end{pmatrix}, \tag{1.2}$$

for the energy momentum tensor is used in the eleven dimensional Einstein equation. Here $\varepsilon=$energy density, P,P' are pressure in three dimensional and seven dimensional space, respectively. We have for the Einstein equations

$$R_{AB}-\frac{1}{2}Rg_{AB}=-\frac{8\pi G_{11}}{c^4}T_{AB}, \tag{1.3}$$

and the evolution of the scale factors is studied for given spatial curvatures K, K'. One of the weaknesses of the above approach is that nobody knows whether in fact there is a gravitational constant at such early stages of the universe. A. Zee [8] has suggested that gravity may be "cooked away" at early times meaning that the symmetry breaking mechanism that is operative in generating G_4 at conventional energies is not present since the scale invariance at high energies and early times is preserved. Only when the scalar field responsible for generating G_4 sinks into a potential well is the gravitational constant generated and the scale symmetry broken. We adopt the philosophy of Zee at early times in eleven dimensions and demonstrate how the theory will lead to compactification of the seven dimensional subspace, inflation of the M_4 space and the generation of G_4 (four dimensional gravitational constant).

Scale invariant 11 dimensional gravity and compactification

Consider the following scale invariant Lagrangian in 11 dimensions,

$$\mathscr{L}=\left(\varphi^2 R+\frac{\partial_A\varphi\partial_B\varphi g^{AB}}{2}+V(\varphi)+\mathscr{L}_M\right)\sqrt{-g}, \tag{2.1}$$

where $R=$scalar curvature, $\mathscr{L}_M=$Lagrangian of matter, $\varphi=$scalar field. For conformal invariance

$$g_{AB}\to\Lambda^2 g_{AB},$$

$$\varphi\to\frac{1}{\Lambda^{\frac{9}{2}}}\varphi.$$

Here Λ is the conformal rescaling factor and the above transformation is constructed to preserve scale invariance in 11 dimensions [9].

For

$$\mathscr{L}_M=0, \qquad V(\varphi)=C\varphi^{\frac{22}{9}}$$

to preserve scale invariance.

For

$$\varphi\to\infty, \qquad V(\varphi)=C\varphi^{\frac{22}{9}};$$

$$\varphi\to\varphi_0,\ V(\varphi)=C(\varphi^{\frac{11}{9}}-C_1)^2,$$

where the C_1 term dynamically breaks the scale invariance, for $\varphi\to\varphi_0=C_1^{\frac{9}{11}}$. In other words the scale symmetry is preserved for high scalar field values. Varying equation (2.1) with respect to g_{AB} yields

$$\varphi^2\left(R_{AB}-\frac{1}{2}Rg_{AB}\right)=-\frac{1}{\sqrt{-g}}\frac{\partial\mathscr{L}}{\partial g^{AB}}+g_{AB}\Box\varphi^2-\nabla_A\nabla_B\varphi^2,$$

where

$$\mathscr{L}=\frac{1}{2}\partial_A\varphi\partial_B\varphi g^{AB}+V(\varphi),\ \Box\varphi^2=\frac{1}{\sqrt{-g}}\frac{\partial}{\partial x^A}(\varphi^2_{,B}g^{AB}\sqrt{-g}), \tag{2.2}$$

$\nabla\mu=$covariant derivative.

Varying Eq. (2.1) with respect to φ yields

$$-\Box\varphi+2\varphi R+\frac{\partial V}{\partial\varphi}=0. \tag{2.3}$$

The program now is to study Eq. (2.2) and Eq. (2.3) for the metric

$$g_{AB}=\begin{pmatrix} -1 & & \\ & R_3^2\,\tilde{g}_{ij} & \\ & & R_7^2\,\tilde{g}_{mn} \end{pmatrix}. \tag{2.4}$$

The Ricci components for the metric are [10],

$$R_{00}=\frac{3\ddot{R}_3}{R_3}+\frac{7\ddot{R}_7}{R_7}, \tag{2.5}$$

$$R_{ij}=-g_{ij}\left(\frac{2K}{R_3^2}+\frac{d}{dt}\left(\frac{\dot{R}_3}{R_3}\right)+\left(\frac{3\dot{R}_3}{R_3}+\frac{7\dot{R}_7}{R_7}\right)\frac{\dot{R}_3}{R_3}\right), \tag{2.6}$$

$$R_{mn}=-g_{mn}\left(\frac{6K'}{R_7^2}+\frac{d}{dt}\left(\frac{\dot{R}_7}{R_7}\right)+\left(\frac{3\dot{R}_3}{R_3}+\frac{7\dot{R}_7}{R_7}\right)\frac{\dot{R}_7}{R_7}\right). \tag{2.7}$$

Here a dot refers to time differentiation. Also $d=3$, $D=7$, K, $K'=$spatial curvatures of d and D subspaces, $i,j=1,2,3$; $m,n=4,5,6,7,8,9,10$. To compute R we use Eq. (2.4) with Eq. (2.5), Eq. (2.6) and Eq. (2.7)

$$\begin{aligned} R=R_{AB}g^{AB}=R_{00}(-1)-g_{ij}g^{ij}&\left(\frac{2K}{R_3^2}+\frac{d}{dt}\left(\frac{\dot{R}_3}{R_3}\right)+\left(\frac{3\dot{R}_3}{R_3}+\frac{7\dot{R}_7}{R_7}\right)\frac{\dot{R}_3}{R_3}\right)\\ &-g_{mn}g^{mn}\left(\frac{6K'}{R_7^2}+\frac{d}{dt}\left(\frac{\dot{R}_7}{R_7}\right)+\left(\frac{3\dot{R}_3}{R_3}+\frac{7\dot{R}_7}{R_7}\right)\frac{\dot{R}_7}{R_7}\right), \end{aligned} \tag{2.8}$$

$$\begin{aligned} R=-\frac{3\ddot{R}_3}{R_3}-\frac{7\ddot{R}_7}{R_7}-3&\left(\frac{2K}{R_3^2}+\frac{d}{dt}\left(\frac{\dot{R}_3}{R_3}\right)+\left(\frac{3\dot{R}_3}{R_3}+\frac{7\dot{R}_7}{R_7}\right)\frac{\dot{R}_3}{R_3}\right)-\\ &-7\left(\frac{6K'}{R_7^2}+\frac{d}{dt}\left(\frac{\dot{R}_7}{R_7}\right)+\left(\frac{3\dot{R}_3}{R_3}+\frac{7\dot{R}_7}{R_7}\right)\frac{\dot{R}_7}{R_7}\right). \end{aligned}$$

Also

$$\frac{1}{\sqrt{-g}}\frac{\partial\mathscr{L}}{\partial g^{AB}}=\frac{1}{2}\,\partial_A\varphi\partial_B\varphi-\frac{g_{AB}}{4}(\partial_C\varphi\,\partial^C\varphi)-\frac{V(\varphi)}{2}g_{AB}. \tag{2.9}$$

In Eq. (2.2) the only term in $\nabla_A\nabla_B\varphi^2$ that survives is

$$\nabla_0\nabla_0\varphi^2=\frac{\partial^2}{\partial t^2}(\varphi^2)=(\ddot{\varphi}^2). \tag{2.10}$$

Now the field equations read

$$\varphi^2(R_{00}-\frac{1}{2}Rg_{00})=-\frac{1}{2}(\dot{\varphi})^2+\frac{g_{00}}{4}((-\dot{\varphi})^2)+g_{00}\Box\varphi^2+\frac{g_{00}C}{2}(\varphi^{\frac{11}{9}}-C_1)^2-(\ddot{\varphi}^2), \tag{2.11}$$

where

$$\varphi = \varphi(t) \tag{2.12}$$

$$\begin{aligned}
&\varphi^2 \left\{ -g_{ij}\left(\frac{2K}{R_3^2} + \frac{d}{dt}\left(\frac{\dot R_3}{R_3}\right) + \left(\frac{3\dot R_3}{R_3} + \frac{7\dot R_7}{R_7}\right)\frac{\dot R_3}{R_3}\right)\right. \\
&\quad - \frac{1}{2} g_{ij}\left(-\frac{3\ddot R_3}{R_3} - \frac{7\ddot R_7}{R_7} - 3\left(\frac{2K}{R_3^2} + \frac{d}{dt}\left(\frac{\dot R_3}{R_3}\right) + \left(\frac{3\dot R_3}{R_3} + \frac{7\dot R_7}{R_7}\right)\frac{\dot R_3}{R_3}\right)\right. \\
&\quad\quad \left.\left. -7\left(\frac{6K'}{R_7^2} + \frac{d}{dt}\left(\frac{\dot R_7}{R_7}\right) + \left(\frac{3\dot R_3}{R_3} + \frac{7\dot R_7}{R_7}\right)\frac{\dot R_7}{R_7}\right)\right)\right\} \\
&= \frac{-g_{ij}}{4}(\dot\varphi)^2 + \frac{g_{ij}}{2} C(\varphi^{\frac{11}{9}} - C_1)^2 + g_{ij}\left(-(\ddot\varphi^2) - \frac{3\dot R_3}{R_3}(\dot\varphi^2) - \frac{7\dot R_7}{R_7}(\dot\varphi^2)\right),
\end{aligned} \tag{2.13}$$

$$\begin{aligned}
&\varphi^2 \left\{ -g_{mn}\left(\frac{6K'}{R_7^2} + \frac{d}{dt}\left(\frac{\dot R_7}{R_7}\right) + \left(\frac{3\dot R_3}{R_3} + \frac{7\dot R_7}{R_7}\right)\frac{\dot R_7}{R_7}\right)\right. \\
&\quad - \frac{g_{mn}}{2}\left(-\frac{3\ddot R_3}{R_3} - \frac{7\ddot R_7}{R_7} - 3\left(\frac{2K}{R_3^2} + \frac{d}{dt}\left(\frac{\dot R_3}{R_3}\right) + \left(\frac{3\dot R_3}{R_3} + \frac{7\dot R_7}{R_7}\right)\frac{\dot R_3}{R_3}\right)\right. \\
&\quad\quad \left.\left. -7\left(\frac{6K'}{R_7^2} + \frac{d}{dt}\left(\frac{\dot R_7}{R_7}\right) + \left(\frac{3\dot R_3}{R_3} + \frac{7\dot R_7}{R_7}\right)\frac{\dot R_7}{R_7}\right)\right)\right\} \\
&= -\frac{g_{mn}}{4}(\dot\varphi)^2 + \frac{g_{mn}}{2} C(\varphi^{\frac{11}{9}} - C_1)^2 \\
&\quad + g_{mn}\left(-(\ddot\varphi^2) - \frac{3\dot R_3}{R_3}(\dot\varphi^2) - \frac{7\dot R_7}{R_7}(\dot\varphi^2)\right).
\end{aligned} \tag{2.14}$$

Upon setting $g_{00} = -1$ in Eq. (2.11) and cancelling g_{ij}, g_{mn} from Eq. (2.13) and Eq. (2.14) we have

$$\begin{aligned}
&\varphi^2 \left\{ \left(\frac{3\ddot R_3}{R_3} + \frac{7\ddot R_7}{R_7}\right) - \frac{1}{2}\left(\frac{3\ddot R_3}{R_3} + \frac{7\ddot R_7}{R_7} + 3\left(\frac{2K}{R_3^2} + \frac{d}{dt}\left(\frac{\dot R_3}{R_3}\right) + \left(\frac{3\dot R_3}{R_3} + \frac{7\dot R_7}{R_7}\right)\frac{\dot R_3}{R_3}\right)\right.\right. \\
&\quad \left.\left. +7\left(\frac{6K'}{R_7^2} + \frac{d}{dt}\left(\frac{\dot R_7}{R_7}\right) + \left(\frac{3\dot R_3}{R_3} + \frac{7\dot R_7}{R_7}\right)\frac{\dot R_7}{R_7}\right)\right)\right\} \\
&= -\frac{1}{4}(\dot\varphi)^2 + \left((\ddot\varphi^2) + \frac{3\dot R_3}{R_3}(\dot\varphi^2) + \frac{7\dot R_7}{R_7}(\dot\varphi^2)\right) - \frac{C}{2}(\varphi^{\frac{11}{9}} - C_1)^2 - (\ddot\varphi^2),
\end{aligned} \tag{2.15}$$

$$\begin{aligned}
&\varphi^2 \left\{ -\left(\frac{2K}{R_3^2} + \frac{d}{dt}\left(\frac{\dot R_3}{R_3}\right) + \left(\frac{3\dot R_3}{R_3} + \frac{7\dot R_7}{R_7}\right)\frac{\dot R_3}{R_3}\right)\right. \\
&\quad - \frac{1}{2}\left(-\frac{3\ddot R_3}{R_3} - \frac{7\ddot R_7}{R_7} - 3\left(\frac{\partial K}{R_3^2} + \frac{d}{dt}\left(\frac{\dot R_3}{R_3}\right) + \left(\frac{3\dot R_3}{R_3} + \frac{7\dot R_7}{R_7}\right)\frac{\dot R_3}{R_3}\right)\right.
\end{aligned}$$

$$-7\left(\frac{6K'}{R_7^2}+\frac{d}{dt}\left(\frac{\dot R_7}{R_7}\right)+\left(\frac{3\dot R_3}{R_3}+\frac{7\dot R_7}{R_7}\right)\frac{\dot R_7}{R_7}\right)\Bigg\} \tag{2.16}$$

$$=-\frac{1}{4}(\dot\varphi)^2+\frac{C}{2}(\varphi^{\frac{11}{9}}-C_1)^2+\left(-(\ddot\varphi^2)-\frac{3\dot R_3}{R_3}(\varphi^2)-\frac{7\dot R_7}{R_7}(\dot\varphi^2)\right),$$

$$\varphi^2\Bigg\{-\left(\frac{6K'}{R_7^2}+\frac{d}{dt}\left(\frac{\dot R_7}{R_7}\right)+\left(\frac{3\dot R_3}{R_3}+\frac{7\dot R_7}{R_7}\right)\frac{\dot R_7}{R_7}\right)$$

$$-\frac{1}{2}\left(-\frac{3\ddot R_3}{R_3}-\frac{7\ddot R_7}{R_7}-3\left(\frac{2K}{R_3^2}+\frac{d}{dt}\left(\frac{\dot R_3}{R_3}\right)+\left(\frac{3\dot R_3}{R_3}+\frac{7\dot R_7}{R_7}\right)\frac{\dot R_3}{R_3}\right)\right. \tag{2.17}$$

$$\left.-7\left(\frac{6K'}{R_7^2}+\frac{d}{dt}\left(\frac{\dot R_7}{R_7}\right)+\left(\frac{3\dot R_3}{R_3}+\frac{7\dot R_7}{R_7}\right)\frac{\dot R_7}{R_7}\right)\right)\Bigg\}$$

$$=-\frac{1}{4}(\dot\varphi)^2+\frac{C}{2}(\varphi^{\frac{11}{9}}-C_1)^2+\left(-(\ddot\varphi^2)-\frac{3\dot R_3}{R_3}(\dot\varphi^2)-\frac{7\dot R_7}{R_7}(\dot\varphi^2)\right).$$

The above equations are extremely complicated but we can draw some qualitative conclusions on the behaviors of R_3, R_7, $\varphi(t)$. Equating the left hand side of Eq. (2.16) and Eq. (2.17) we obtain

$$\frac{d}{dt}\left(\frac{\dot R_7}{R_7}\right)=-\frac{6K'}{R_7^2}+\frac{2K}{R_3^2}+\frac{d}{dt}\left(\frac{\dot R_3}{R_3}\right)+\left(\frac{3\dot R_3}{R_3}+\frac{7\dot R_7}{R_7}\right)\frac{\dot R_3}{R_3}$$

$$-\left(\frac{3\dot R_3}{R_3}+\frac{7\dot R_7}{R_7}\right)\left(\frac{\dot R_7}{R_7}\right). \tag{2.18}$$

For small R_7 the term $-\frac{6K'}{R_7^2}$ dominates Eq. (2.18) with the result that if $K'>0$, $\frac{\dot R_7}{R_7}<0$. If we further assume that $K=0$ we find by solving Eq. (2.16) and Eq. (2.17) for $\dot R_3\dot R_7$

$$\frac{4\dot R_3}{R_3}\frac{\dot R_7}{R_7}=\frac{6K'}{R_7^2}+\frac{d}{dt}\left(\frac{\dot R_7}{R_7}\right)-2\left(\frac{\dot R_3}{R_3}\right)^2+7\left(\frac{\dot R_7}{R_7}\right)^2-\frac{\ddot R_3}{R_3}. \tag{2.19}$$

If in Eq. (2.19) the term $-2\left(\frac{\dot R_3}{R_3}\right)^2-\frac{\ddot R_3}{R_3}$ dominates for large time the left hand side is negative since $\frac{d}{dt}\left(\frac{\dot R_7}{R_7}\right)+\frac{6K'}{R_7^2}\approx 0$, and this implies $\dot R_3>0$ if $\dot R_7<0$. We also observe that away from the minimum of $V(\varphi)$ before the symmetry is broken we have from Eq. (2.3) if we neglect the $R\varphi$ term which is assumed small compared to $\frac{\partial V}{\partial\varphi}$

$$\frac{1}{\sqrt{-g}}\frac{d}{dt}(\sqrt{-g}\dot\varphi)=-\frac{\partial V}{\partial\varphi}. \tag{2.20}$$

Note that Eq. (2.20) yields $\sqrt{-g}\dot{\varphi} = -\int \frac{\partial V}{\partial \varphi}\sqrt{-g}\, dt < 0$ after setting the integration constant equal to zero since the scalar yield settles to a constant value for large times to generate the gravitational constant. Notice, however, we have neglected the effect of curvature on the evolution of φ.

In summary, if $K' > 0$, $K = 0$, then the equations predict $\frac{\dot{R}_7}{R_7} < 0$, $\frac{\dot{R}_3}{R_3} > 0$, $\dot{\varphi} < 0$ as in Fig. 1.

Let us notice that point P represents the point of symmetry breaking where $\varphi_0^2 = \frac{C^4}{16\pi G_{11}} = \frac{C^4}{16\pi G_4 V_7}$; $V_7 =$(volume of compactified seven space), $G_4 =$(four dimensional gravitational constant).

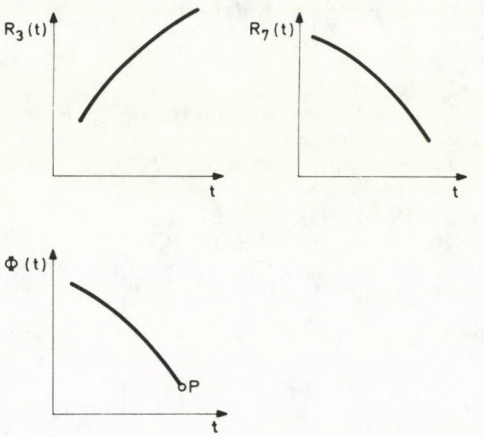

Fig. 1. Variation of $R_3(t)$, $R_7(t)$, $\Phi(t)$ with t

2. Conclusions

The assumption that $\varphi = \varphi(t)$ is justified on the basis that a spatially inhomogeneous φ would have a higher energy. The crude estimate suggesting inflation in M_4, compactification in S_7 and $\varphi \to \varphi_0$; would have to be substantiated by a more rigorous solution to Eqs (3), (15), (16) and (17). If the potential had many minimum it might be possible for gravity to pass through a series of changes wherein the gravitational constant kept increasing toward its present value. Such a series of freezings might leave its trace in relic particle symmetries; only the relevant scale would exceed the Planck scale in each case giving rise to interactions that we have never seen or ever will see. The general features of the discussion above present a consistent classical

picture of dynamical scale breaking of a conformally invariant 11 dimensional gravitational system and a more complete numerical analysis will be the subject of future work.

Acknowledgements

I would like to thank Stephen Adler for originally suggesting the simplicity of the scale breaking mechanism. I would also like to thank David Park for a discussion on the subject and the Physics Department at Williams College for the use of their facilities along with D. Grosser and the Institut for Theoretische Physik at the University of Tübingen for their kind hospitality. Lastly, I thank Manfred Gnirb for helping me prepare the manuscript.

References

1. T. Kaluza, Sitz. Preuss. Akad. Wiss. Phys. Math. Klasse, 966, 1921.
2. D. Sahdev, Phys. Lett., *137B*, 155, 1984.
3. T. Appelquist and A. Chodos, Phys. Rev., D. *28*, 772, 1983.
4. D. Rohrlich, Phys. Rev., D. *29*, 330, 1984.
5. T. Appelquist, A. Chodos and E. Meyers, Phys. Lett., *127B*, 51, 1983.
6. M. Dresden and J. Zanelli, Physica, in press.
7. E. Witten, Nucl. Phys., *B186*, 412, 1981.
8. A. Zee, 1981 Erice lecture, ed. A. Aichichi, Plenum, N.Y.
9. S. Fubini, Il Nuovo Cimento, *34A*, 521, 1976.
10. P. G. O. Freund, Nucl. Phys., *B209*, 146, 1982.

Acta Physica Hungarica, 63 (3—4), pp. 311—319 (1988)

ON GAUSS–MARKOV ARBITRARY KINETIC LEVEL STOCHASTIC DYNAMICS OF PLASMAS I.

K. LELKES

Institute for Physics, Technical University of Budapest
1521 Budapest, Hungary

(Received 8 April 1986)

The paper presents the nonequilibrium statistical (kinetical) treatment of Gauss–Markov "external" and selfconsistent "intrinsic" fluctuations in the "embedded" plasma systems based on the separation and decoupling of the statistical and stochastical time-scales. This description yields both arbitrary kinetic level decomposition of the statistical distributions and Gauss–Markov momentum equations with coherent structure.

Introduction

The statistical fluctuations in classical plasma systems always reflect a lack of information about the exact state of the system. A large plasma system is described in terms of a few macrovariables (mechanical, electrodynamic and thermodynamic variables [1]) obtained by different "coarse-graining" procedures in phase space [2], and the loss of knowledge about the microscopic (kinetic) plasma degrees of freedom gives rise to "intrinsic" fluctuations of the plasma microvariables. Furthermore, a large number of "intrinsic" (collective turbulent) fluctuations are excited through the presence of instabilities in the plasma system. Finally, the external forces in the plasma statistical equations of motion, which describe the electromagnetic coupling of the plasma system to the outside, have also to be considered as fluctuating quantities, because they are produced by other macroscopic systems or outer plasma instabilities. They excite "external" (collective turbulent) fluctuations in the plasma system under consideration. The distinction between "intrinsic" and "external" fluctuations will of course depend on where the boundary is drawn between "plasma system" and "outside" [3].

The paper studies the arbitrary kinetic level stochastic dynamics of a plasma system embedded in Gauss–Markov "external" electromagnetic fields. These "external" electromagnetic fields impose "external" (collective turbulent) fluctuations on the plasma system exciting Gauss–Markov "intrinsic" selfconsistent fluctuations in it.

The Gauss–Markov treatment

Neglecting the radiation processes $\tau_{RAD} \gg \tau_{PL}$, the plasma system is supposed to obey a classical, nonrelativistic, subcritical $\Lambda_{PLN} = 4n_0 \lambda_D^3/3 \gg 1$ dynamics having Coulomb particle interaction potential $\Phi = e/|\mathbf{r}|$, and coupling $\pi_{co} = \Phi_c/m \cdot V_c^2 \leq O(1)$, density $\Pi_D = r_c^3/n_0^{-1} \in R^+ \setminus \{0\}$, and correlation $O(\Lambda_{PLN}^{-1})\Pi_{DC} = \Pi_{co}\Pi_D \leq O(1)$ parameters of given orders [8]. The plasma system is considered so large $N = N_1 + N_2 + \ldots N_{\mathcal{N}} \gg 1$, $V \gg 1$ that the behaviour of its particles is not affected by the presence of boundaries. Here N_i, $i = 1, \ldots, \mathcal{N}$ mean the numbers of identical plasma particles. The "outside" is supposed to be much larger than the plasma system under consideration $V_{\text{out.}} > > > > V$. The stochastic states and properties of the "outside" are completely given by the probability space $(\Omega, \mathcal{F}, \mu_{P_r})$ and stochastic process $\tilde{\omega}_\tau$: $T \to L^0(\Omega, \mathcal{F}; M)$ with state space M [4]. The $\tau \in T$ represents the time-scale of the "outside" $(T \subset (-\infty, +\infty))$, and the state space M is usually a separable Hilbert space. For fixed $\tau \in T$ the $\tilde{\omega}_\tau(\omega)$ is a random variable, and for fixed $\omega \in \Omega$ the $\tilde{\omega}_\tau(\omega)$ is a sample state path of the "outside". The one dimensional distribution of $\tilde{\omega}_\tau(\omega)$ is given by the induced measure $F_\tau(x) = \mu_{P_r} o \tilde{\omega}_\tau^{-1}(x)$ for all time $\tau \in T$ and $x \in M$. A sufficient condition for the existence of mean value is $\tilde{\omega}_\tau(\omega) \in L^2(\Omega, \mathcal{F}, \mu_{P_r}; M)$ for all $\tau \in T$. So, the integrals

$$\langle \tilde{\omega} \rangle = \int_\Omega \tilde{\omega}_\tau(\omega) d\mu_{P_r}(\omega) = \int_M x_\tau dF_\tau(x) = \int_M x_\tau f_\tau(x) dx \tag{I.1}$$

define the mean value of the stochastic process $\tilde{\omega}_\tau(\omega)$ over the probability space of the "outside" $(\Omega, \mathcal{F}, \mu_{P_r})$. Here $f_\tau(x) = \partial_x F_\tau(x)$, $x \in M$ is the density function of stochastic probability distribution of the "outside". The fluctuations $\delta\tilde{\omega}_\tau(\omega)$ and the two time-scales covariance $\text{cov}\,(\tilde{\omega}_{\tau_1}(\omega), \tilde{\omega}_{\tau_2}(\omega))$ are defined by the expressions

$$\delta\tilde{\omega}_\tau(\omega) = \tilde{\omega}_\tau(\omega) - \langle \tilde{\omega}_\tau \rangle, \tag{I.2}$$

$$\text{cov}\,(\tilde{\omega}_{\tau_1}, \tilde{\omega}_{\tau_2}) = \int_\Omega \delta\tilde{\omega}_{\tau_1}(\omega) \otimes \delta\tilde{\omega}_{\tau_2}(\omega) d\mu_{P_r}(\omega), \tag{I.3}$$

for all $\tau \in T$ and $(\tau_1, \tau_2) \in T \times T$. In the expression of covariance (I.3) the two time-scales joint stochastic distribution function of the "outside" $F_{\tau_1,\tau_2}(x_1, x_2) = \mu_{P_r}(\tilde{\omega}_{\tau_1}^{-1}(x_1) \cap \cap \tilde{\omega}_{\tau_2}^{1}(x_2))$ is also supposed to be given. The coupling stochastic electromagnetic fields between the "outside" and the embedded plasma system are supposed to have the following form

$$\mathbf{E}^E(\mathbf{r}, t; \tilde{\omega}_\tau(\omega)) = \mathbf{E}_0^E(\mathbf{r}, t) + \mathbf{E}_1^E(\mathbf{r}, t; \tilde{\omega}_\tau(\omega)), \tag{I.4}$$

$$\mathbf{B}^E(\mathbf{r}, t; \tilde{\omega}_\tau(\omega)) = \mathbf{B}_0^E(\mathbf{r}, t) + \mathbf{B}_1^E(\mathbf{r}, t; \tilde{\omega}_\tau(\omega)), \tag{I.5}$$

or the electromagnetic potentials

$$\varphi^E(\mathbf{r}, t; \tilde{\omega}_\tau(\omega)) = \varphi_0^E(\mathbf{r}, t) + \varphi_1^E(\mathbf{r}, t; \tilde{\omega}_\tau(\omega)), \tag{I.6}$$

$$\mathbf{A}^E(\mathbf{r}, t; \tilde{\omega}_\tau(\omega)) = \mathbf{A}_0^E(\mathbf{r}, t) + \mathbf{A}_1^E(\mathbf{r}, t; \tilde{\omega}_\tau(\omega)), \tag{I.7}$$

for all $(\tau, \omega) \in T \times \Omega$. These imposed "external" fluctuations and electromagnetic coupling effects are required to remain in the frame of linear response theory for all $(\tau, \omega) \in T \times \Omega$. The "outside" of the plasma system is assumed to have memoryless dynamics and a very large (approximately infinite) number of independent identically distributed "elementary" random variables. So, the $\tilde{\omega}_\tau(\omega)$, $F_\tau(x)$, $F_{\tau_1,\tau_2}(x_1, x_2)$, and the other higher finite dimensional distributions $F_{\tau_1,\ldots,\tau_n}(x_1, \ldots, x_n)$ define a Gauss process with Markovian property. Consequently, the covariance of the "outside" $\mathrm{cov}\,(\tilde{\omega}_{\tau_F}, \omega_{\tau_P})$ for all $\tau_F \geq \tau_P$, τ_F, $\tau_P \in T$ has the following property

$$(\mathrm{cov}\,(\tilde{\omega}_{\tau_F}, \tilde{\omega}_{\tau_P});\quad \phi_k \otimes \phi_l)_{M^2} = \int_\Omega ((\delta\tilde{\omega}_{\tau_F}(\omega) \otimes \delta\tilde{\omega}_{\tau_P}(\omega));$$

$$\phi_k \otimes \phi_l)_{M^2} d\mu_{P_r}^{RG}(\omega) = (\langle\tilde{\omega}_{\tau_F} \otimes \tilde{\omega}_{\tau_P}\rangle;\quad \phi_k \otimes \phi_l)_{M^2} - (\langle\tilde{\omega}_{\tau_F}\rangle \otimes \langle\tilde{\omega}_{\tau_P}\rangle; \tag{I.8a}$$

$$\phi_k \otimes \phi_l)_{M^2} = \sum_{\alpha \in N} f_{k,\alpha}(\tau_F) g_{\alpha,l}(\tau_P) \qquad \text{for all} \quad k, l \in N,$$

where $f, g \in L^2(T, M^2)$, $(M^2 \equiv M \otimes M)$ are suitable $M \otimes M$ valued functions. Here $\otimes$ is a tensor product on the separable Hilbert space M with the O.N. basis $\{\phi_K\}$, $(k = 1, 2, \ldots)$, $\mu_{P_r}^{RG}(\omega)$ is a Radon–Gaussian probability measure on the probability event state space of the "outside" Ω. The $(\cdot;\cdot)_{M^2}$ denotes the inner product on the separable Hilbert space $M^2 \equiv M \otimes M$, and $\phi_k \otimes \phi_l$, $k, l \in N$ is an orthonormal basis for it [4].

The Gauss–Markov Liouville dynamics

The basic assumption for the approximation of time-scales is $\tau_{\mathrm{out}}^{CH} > > > > > \tau_{\mathrm{sys}}^{CH}$, and the "feed-back" of the dynamics of the plasma system to the stochastic (Gauss–Markov) dynamics of the "outside" is neglected. This treatment of the "outside" and "plasma system" makes it possible to separate and decouple the statistical time-scale of the plasma system t from the stochastic time-scale of the "outside" τ in the following sense

$$\begin{aligned}
&\{\hat{V}_\tau, \delta_{r_i}\}_- = 0, \qquad \{\hat{C}_\tau, \partial_{r_i}\}_- = 0, \\
&\{\hat{V}_\tau, \partial_{\mathbf{P}_i}\}_- = 0, \qquad \{\hat{C}_\tau, \partial_{\mathbf{P}_i}\}_- = 0, \qquad \hat{V}_\tau \cdot \equiv \int_M \cdot\, dF_\tau^{RG}(x), \\
&\{\hat{V}_\tau, \partial_t\}_- = 0, \qquad \{\hat{C}_\tau, \partial_t\}_- = 0, \qquad \hat{C}_\tau \cdot \equiv -\int_M \cdot\, dF_\tau^{RG}(x), \\
&\{\hat{V}_\tau, \int dt\}_- = 0, \qquad \{\hat{C}_\tau, \int dt\}_- = 0;
\end{aligned} \tag{I.9}$$

where the symbolic [5] stochastic "averaging" projector operator $\hat{V}_\tau$ and stochastic "fluctuating" projector operator $\hat{C}_\tau$ mean the aforedescribed procedures (I.1), (I.2) with respect to the Radon–Gaussian stochastic probability distribution of the "outside"

$F_\tau^{RG}(x)$. Without the restriction of generality of the treatment and using the formal properties of the symbolic stochastic projectors $\hat{V}_\tau + \hat{C}_\tau = \hat{I}$, $\hat{V}_\tau^2 = \hat{V}_\tau$, $\hat{V}_\tau \hat{C}_\tau = \hat{C}_\tau \hat{V}_\tau = 0$, $\hat{C}_\tau^2 = \hat{C}_\tau$ for all $\tau \in T$ one can suppose that

$$\begin{aligned} &\hat{V}_\tau\, \mathbf{E}^E(\mathbf{r}, t; \tilde{\omega}_\tau(\omega)) = \mathbf{E}_0^E(\mathbf{r}, t), \qquad &&\hat{V}_\tau\, \mathbf{E}_1^E(\mathbf{r}, t; \tilde{\omega}_\tau(\omega)) = 0, \\ &\hat{V}_\tau\, \mathbf{B}^E(\mathbf{r}, t; \tilde{\omega}_\tau(\omega)) = \mathbf{B}_0^E(\mathbf{r}, t), \qquad &&\hat{V}_\tau\, \mathbf{B}_1(\mathbf{r}, t; \tilde{\omega}_\tau(\omega)) = 0, \end{aligned} \tag{I.10}$$

or the electromagnetic potentials

$$\begin{aligned} &\hat{V}_\tau\, \phi^E(\mathbf{r}, t; \tilde{\omega}_\tau(\omega)) = \phi_0^E(\mathbf{r}, t), \qquad &&\hat{V}_\tau\, \varphi_1^E(\mathbf{r}, t; \tilde{\omega}_\tau(\omega)) = 0, \\ &\hat{V}_\tau\, \mathbf{A}^E(\mathbf{r}, t; \tilde{\omega}_\tau(\omega)) = \mathbf{A}_0^E(\mathbf{r}, t), \qquad &&\hat{V}_\tau\, A_1^E(\mathbf{r}, t; \tilde{\omega}_\tau(\omega)) = 0. \end{aligned} \tag{I.11}$$

By the choice of the separable Hilbert state space of the "outside" M one can define the different physical models of the "outside". Applying the formal properties of the symbolic Radon–Gaussian projectors and the assumptions (I.10), (I.11) the stochastic electromagnetic fields and potentials can be split uniquely into mutually independent two parts, i.e.

$$\begin{aligned} \mathbf{E}^E(\mathbf{r}, t; \tilde{\omega}_\tau(\omega)) &= \hat{V}_\tau\, \mathbf{E}^E(\mathbf{r}, t; \tilde{\omega}_\tau(\omega)) + \hat{C}_\tau \mathbf{E}^E(\mathbf{r}, t; \tilde{\omega}_\tau(\omega)), \\ \mathbf{B}^E(\mathbf{r}, t; \tilde{\omega}_\tau(\omega)) &= \hat{V}_\tau\, \mathbf{B}^E(\mathbf{r}, t; \tilde{\omega}_\tau(\omega)) + \hat{C}_\tau \mathbf{B}^E(\mathbf{r}, t; \tilde{\omega}_\tau(\omega)), \end{aligned} \tag{I.12}$$

$$\begin{aligned} \varphi^E(\mathbf{r}, t; \tilde{\omega}_\tau(\omega)) &= \hat{V}_\tau\, \varphi^E(\mathbf{r}, t; \tilde{\omega}_\tau(\omega)) + \hat{C}_\tau \varphi^E(\mathbf{r}, t; \tilde{\omega}_\tau(\omega)), \\ \mathbf{A}^E(\mathbf{r}, t; \tilde{\omega}_\tau(\omega)) &= \hat{V}_\tau\, \mathbf{A}^E(\mathbf{r}, t; \tilde{\omega}_\tau(\omega)) + \hat{C}_\tau \mathbf{A}^E(\mathbf{r}, t; \tilde{\omega}_\tau(\omega)). \end{aligned} \tag{I.13}$$

Thus, the dynamical equation of a single n_j-th particle of the aforedescribed plasma system will have the form

$$dt(m_j \mathbf{v}_{n_j}) = \mathbf{F}_0(\mathbf{E}_0^E, \mathbf{B}_0^E, \Phi) + \mathbf{F}_1(\mathbf{E}_1^E(\tilde{\omega}_\tau), \mathbf{B}_1^E(\tilde{\omega}_\tau)). \tag{I.14}$$

The "pure" deterministic force

$$\begin{aligned} \mathbf{F}_0(\mathbf{E}_0, \mathbf{B}_0, \Phi) = &+ e_j C^{-1} \mathbf{v}_{n_j} \Lambda (\partial_{\mathbf{r}_{n_j}} \Lambda \mathbf{A}_0^E(\mathbf{r}_{n_j}, t)) - e_j C^{-1} \partial_t \mathbf{A}_0^E(\mathbf{r}_{n_j}, t) - \\ &- e_j \partial_{\mathbf{r}_{n_j}} \varphi_0^E(\mathbf{r}_{n_j}, t) - \sum_{i=1}^{\mathcal{N}} \sum_{\substack{n_i = 1 \\ (n_i \neq n_j)}}^{N_i} \frac{1}{2} \partial_{\mathbf{r}_{n_j}} \Phi(|\mathbf{r}_{n_j} - \mathbf{r}_{n_i}|) \end{aligned} \tag{I.15}$$

and "pure" stochastic force

$$\begin{aligned} \mathbf{F}_1(\mathbf{E}_1^E(\tilde{\omega}_\tau), \mathbf{B}_1^E(\tilde{\omega})) = &+ e_j C^{-1} \mathbf{v}_{n_j} \Lambda (\partial_{\mathbf{r}_{n_j}} \Lambda \mathbf{A}_1^E(\mathbf{r}_{n_j}, t; \tilde{\omega}(\omega))) - \\ &- e_j C^{-1} \partial_t A^E(\mathbf{r}_{n_j}, t; \tilde{\omega}_\tau(\omega)) - e_j \partial_{\mathbf{r}_{n_j}} \phi_1^E(\mathbf{r}_{n_j}, \tilde{\omega}_\tau(\omega)) \end{aligned} \tag{I.16}$$

are for all $n_j\, j = 1, \ldots, \mathcal{N}$; $n_j = 1, \ldots, N_j$. The dynamical equations of type (I.14) can be considered as the set of Langevin equations coupled by the Coulomb fields $\Phi(|\mathbf{r}|)$. Taking the interactions and the couplings between the plasma system and the "outside" into account the Gauss–Markov Hamiltonian of the system is

$$H(t; \tilde{\omega}_\tau(\omega)) = H_0(t) + H_1(\tilde{\omega}_\tau(\omega)), \tag{I.17}$$

where

$$H_0(t)=\sum_{j=1}^{\mathcal{N}}\sum_{n_j=1}^{N_j}\frac{(\vec{\mathcal{P}}\,(\mathbf{r}_{n_j},t;\tilde{\omega}_\tau(\omega))-e_jC^{-1}\mathbf{A}^E(\mathbf{r}_{n_j},t;\tilde{\omega}(\omega)))^2}{2m_j}+$$

$$+\sum_{\substack{i=1\\(i=j,n_i\neq n_j)}}^{\mathcal{N}}\sum_{n_i=1}^{N_i}\frac{1}{2}\Phi(|\mathbf{r}_{n_j}-\mathbf{r}_{n_i}|)+e_j\varphi_0^E(\mathbf{r}_{n_j},t), \tag{I.18}$$

and

$$H_1(\tilde{\omega}_\tau(\omega))=\sum_{j=1}^{\mathcal{N}}\sum_{n_j=1}^{N_j}e_j\varphi_1^E(\mathbf{r}_{n_j},t;\tilde{\omega}_\tau(\omega))\qquad\text{for all}\quad(\tau,\omega)\in T\times\Omega. \tag{I.19}$$

Here, the $\vec{\mathcal{P}}\,(\mathbf{r}_{n_j},t;\tilde{\omega}_\tau(\omega))$ is the stochastic generalized momentum of the system:

$$\vec{\mathcal{P}}\,(\tilde{\omega}_\tau(\omega))\equiv\vec{\mathcal{P}}\,(\mathbf{r},\mathbf{v},t;\tilde{\omega}_\tau(\omega))=m\mathbf{v}+\frac{1}{C}\mathbf{A}^E(\mathbf{r},t;\tilde{\omega}_\tau(\omega)), \tag{I.20}$$

consequently, the stochastic Hamiltonian equations are

$$\frac{\partial H(t;\tilde{\omega}_\tau(\omega))}{\partial\vec{\mathcal{P}}_{n_j}(\tilde{\omega}_\tau(\omega))}=\mathbf{r}_{n_j}\qquad\text{and}\qquad\frac{\partial H(t;\tilde{\omega}_\tau(\omega))}{\partial\mathbf{r}_{n_j}}=\vec{\mathcal{P}}_{n_j}(\tilde{\omega}_\tau(\omega))$$

for all $(\tau,\omega)\in T\times\Omega$ and $j=1,\ldots,\mathcal{N}$, $n_j=1,\ldots,N_j$. From the statistical point of view the nonequilibrium dynamics of the embedded plasma system is described by the stochastic (Gauss–Markov) Liouville operator

$$\hat{L}_N(\omega_\tau(\omega))=\{\,,H(t;\tilde{\omega}_\tau(\omega))\}_P, \tag{I.21}$$

where $\{\,.\,,.\,\}_P$ means the Poisson bracket $|N=N_1+\ldots+N_{\mathcal{N}}|$. Performing the transformation $\vec{\mathcal{P}}\,(\tilde{\omega}_\tau(\omega))\to\mathbf{P}$ in (I.21) the $\hat{L}_N(\omega_\tau(\omega))$ split into two independent parts

$$\hat{L}_N(\mathbf{r},\mathbf{P},t;\tilde{\omega}_\tau(\omega))\equiv\hat{L}_{0_N}(\mathbf{r},\mathbf{P},t)+\hat{L}_{1_N}(\mathbf{r},\mathbf{P},t;\tilde{\omega}_\tau(\omega)) \tag{I.22}$$

with the following properties

$$\hat{V}_\tau\hat{L}_N(\mathbf{r},\mathbf{P},t;\tilde{\omega}_\tau(\omega))=\hat{L}_{0_N}(\mathbf{r},\mathbf{P},t),\qquad\hat{V}_\tau\hat{L}_{1_N}(\mathbf{r},\mathbf{P},t;\tilde{\omega}_\tau(\omega))=0,$$

$$\{\hat{V}_\tau;\hat{L}_{0_N}(\mathbf{r},\mathbf{P},t)\}_-=0,\qquad\{\hat{V}_\tau;\hat{L}_{1_N}(\mathbf{r},\mathbf{P},t;\omega_\tau(\omega))\}_-\neq0,$$

$$\{\hat{C}_\tau;\hat{L}_{0_N}(\mathbf{r},\mathbf{P},t)\}_-=0,\qquad\{\hat{C}_\tau;\hat{L}_{1_N}(\mathbf{r},\mathbf{P},t;\tilde{\omega}_\tau(\omega))\}_-\neq0. \tag{I.23}$$

The time evolution of the embedded plasma system is governed by the Gauss–Markov Liouville equation

$$(\partial_t+\hat{L}_{0_N}(\mathbf{r},\mathbf{P},t)+\hat{L}_{1_N}(\mathbf{r},\mathbf{P},t;\tilde{\omega}_\tau(\omega)))F_N(\mathbf{r},\mathbf{P},t;\omega_\tau(\omega))=0,$$

$$F_N(\mathbf{r},\mathbf{P},t_0;\tilde{\omega}_\tau(\omega))=F_N^0(\mathbf{r},\mathbf{P};\tilde{\omega}_\tau(\omega)), \tag{I.24}$$

where $F_N(\mathbf{r},\mathbf{P},t;\tilde{\omega}_\tau(\omega))$ is the N particle V normed Bogoliubov distribution function for all fixed $(\tau,\omega)\in T\times\Omega$. The stochastic Liouville equation defines a stochastic Cauchy problem for $t\geq t_0$ time instants. The "deterministic" Liouville operator $\hat{L}_{0_N}(\mathbf{r},\mathbf{P},t)$

and the "pure" stochastic Gauss–Markov Liouville operator $\hat{L}_{1_N}(\mathbf{r}, \mathbf{P}, t; \tilde{\omega}_\tau(\omega))$ have the following detailed form

$$\hat{L}_{0_N}(\mathbf{r}, \mathbf{P}, t) = \sum_{j=1}^{\mathcal{N}} \sum_{n_j=1}^{N_j} \frac{\mathbf{P}_{n_j}}{m_j} \partial_{\mathbf{r}_{n_j}} + \mathbf{F}_0(\mathbf{r}_{n_j}, \mathbf{P}_{n_j}, t) \partial_{\mathbf{P}_{n_j}} + \sum_{\substack{i=1 \\ (i=j, n_i \neq n_j)}}^{\mathcal{N}} \sum_{n_i=1}^{N_i} \frac{1}{2} \Theta_{n_i, n_j}, \tag{I.25}$$

$$\hat{L}_{1_N}(\mathbf{r}, \mathbf{P}, t; \tilde{\omega}_\tau(\omega)) = \sum_{j=1}^{\mathcal{N}} \sum_{n_j=1}^{N_j} \mathbf{F}_1(\mathbf{r}_{n_j}, \mathbf{P}_{n_j}, t; \tilde{\omega}_\tau(\omega)) \partial_{\mathbf{P}_{n_j}}, \tag{I.26}$$

where the "pure" deterministic force

$$\mathbf{F}_0(\mathbf{r}_{n_j}, \mathbf{P}_{n_j}, t) = e_j \left(\mathbf{E}_0^E(\mathbf{r}_{n_j}, t) + C^{-1} \frac{\mathbf{P}_{n_j}}{m_j} \Lambda \mathbf{B}_0^E(\mathbf{r}_{n_j}, t) \right), \tag{I.27}$$

and the "pure" stochastic (Gauss–Markov) force

$$\mathbf{F}_1(\mathbf{r}_{n_j}, \mathbf{P}_{n_j}, t; \tilde{\omega}_\tau(\omega)) = e_j \left(\mathbf{E}_1^E(\mathbf{r}_{n_j}, t; \tilde{\omega}_\tau(\omega)) + C^{-1} \frac{\mathbf{P}_{n_j}}{m_j} \Lambda \mathbf{B}_1^E(\mathbf{r}_{n_j}, t; \tilde{\omega}_\tau(\omega)) \right) \tag{I.28}$$

act on the n_j-th particle of the embedded plasma system. The Coulomb interaction is taken into account by the term

$$\Theta_{n_j, n_i} = \partial_{\mathbf{r}_{n_j}} \Phi(|\mathbf{r}_{n_j} - \mathbf{r}_{n_i}|) (\partial_{\mathbf{P}_{n_j}} - \partial_{\mathbf{P}_{n_i}}). \tag{I.29}$$

From the physical point of view, for each fixed $(\tau, \omega) \in T \times \Omega$, the nonequilibrium statistical behaviour of the system is described by a "pure" deterministic Liouville equation. Consequently, the Gauss–Markov stochasticity of the N particle Bogoliubov distribution function $F_N(\mathbf{r}, \mathbf{P}, t; \tilde{\omega}_\tau(\omega))$, $(\mathbf{r}, \mathbf{P}) \in \Gamma = \mathbb{R}^{6N}$ originates directly from the appearance of Gauss–Markov electromagnetic coupling between the embedded plasma system and the "outside". Furthermore, this phase space Γ distribution function has all the same stochastic properties (I.8), (I.9) as the "outside". Thus, the N particle phase space distribution can be split uniquely into two mutually independent parts in the following way

$$F_N(\mathbf{r}, \mathbf{P}, t; \tilde{\omega}_\tau(\omega)) = \hat{V}_\tau F_N(\mathbf{r}, \mathbf{P}, t; \tilde{\omega}_\tau(\omega)) + \hat{C}_\tau F(\mathbf{r}, \mathbf{P}, t; \tilde{\omega}_\tau(\omega)), \tag{I.30}$$

$$\begin{aligned} \hat{V}_\tau F_N(\mathbf{r}, \mathbf{P}, t; \tilde{\omega}_\tau(\omega)) &= F_{0_N}(\mathbf{r}, \mathbf{P}, t), \\ \hat{C}_\tau F_N(\mathbf{r}, \mathbf{P}, t; \tilde{\omega}_\tau(\omega)) &= F_{1_N}(\mathbf{r}, \mathbf{P}, t; \tilde{\omega}_\tau(\omega)). \end{aligned} \tag{I.31}$$

The physical meaning of this decomposition is that the N particle phase space distribution function consists of a "pure" deterministic phase space distribution density $F_{0_N}(\mathbf{r}, \mathbf{P}, t)$ and an independent Gauss–Markovian phase distribution density fluctuation $F_{1_N}(\mathbf{r}, \mathbf{P}, t; \tilde{\omega}_\tau(\omega))$. All the relevant information about the dynamics of the system are contained by the first order stochastic momentum equations of the Gauss–Markov Liouville equation (I.24). Using the formal properties of $\hat{V}_\tau$, $\hat{C}_\tau$ and commutation and decomposition properties the Gauss–Markov momentum equa-

tions for $F_{0_N}(\mathbf{r}, \mathbf{P}, t)$ and $F_{1_N}(\mathbf{r}, \mathbf{P}, t; \tilde{\omega}_\tau(\omega))$ will have the following form

$$\partial_t F_{0_N}(\mathbf{r}, \mathbf{P}, t) = -\hat{L}_{0_N}(\mathbf{r}, \mathbf{P}, t) F_{0_N}(\mathbf{r}, \mathbf{P}, t) - \hat{V}_\tau(\hat{L}_{1_N}(\mathbf{r}, \mathbf{P}, t; \tilde{\omega}_\tau(\omega))$$
$$F_{1_N}(\mathbf{r}, \mathbf{P}, t; t; \tilde{\omega}_\tau(\omega)))$$

and

$$\partial_t F_{1_N}(\mathbf{r}, \mathbf{P}, t; \tilde{\omega}_\tau(\omega)) = (\hat{I} - \hat{V}_\tau)(-\hat{L}_{0_N}(\mathbf{r}, \mathbf{P}, t; \tilde{\omega}_\tau(\omega)) F_{1_N}(\mathbf{r}, \mathbf{P}, t; \tilde{\omega}_\tau(\omega))) -$$
$$-\hat{L}_{1_N}(\mathbf{r}, \mathbf{P}, t; \tilde{\omega}_\tau(\omega)) F_{0_N}(\mathbf{r}, \mathbf{P}, t), \tag{I.32}$$

or

$$\partial_t F_{1_N}(\mathbf{r}, \mathbf{P}, t; \tilde{\omega}_\tau(\omega)) = -\hat{L}_{0_N}(\mathbf{r}, \mathbf{P}, t) F_{1_N}(\mathbf{r}, \mathbf{P}, t; \tilde{\omega}_\tau(\omega)) +$$
$$+(\hat{V}_\tau - \hat{I})(\hat{L}_{1_N}(\mathbf{r}, \mathbf{P}, t; \tilde{\omega}_\tau(\omega)) F_{1_N}(\mathbf{r}, \mathbf{P}, t; \tilde{\omega}_\tau(\omega))) - \hat{L}_{1_N}(\mathbf{r}, \mathbf{P}, t; \tilde{\omega}_\tau(\omega)) F_{0_N}(\mathbf{r}, \mathbf{P}, t).$$

These stochastic momentum equations express the fact that the dynamical equations of the "incompressible" deterministic phase fluid and the "compressible" Gauss–Markov fluctuating phase fluid are coupled. Evidently these Gauss–Markov momentum equations are entirely based on the aforedescribed separation and decoupling of the statistical and stochastic time-scales. To obtain the S_α particle V normed Bogoliubov reduced distribution function $F_{S_\alpha}(\mathbf{r}, \mathbf{P}, t; \tilde{\omega}_\tau(\omega))$ the following integral operator can be defined

$$\hat{A}_{S_\alpha} = \frac{1}{V^{(N_\alpha - S_\alpha)} V^{N_1} \dots V^{N_{\alpha-1}} V^{N_{\alpha+1}} \dots V^{N_{\mathcal{N}}}} \times$$
$$\times \int_{\mathbb{R}^{6(N-S_\alpha)}} \prod_{n_1=1}^{N_1} d^3\mathbf{r}_{n_1} d^3\mathbf{P}_{n_1} \dots \prod_{n_\alpha = S_\alpha + 1}^{N_\alpha} d^3\mathbf{r}_{n_\alpha} d^3\mathbf{P}_{n_\alpha} \dots \times \dots \prod_{n_{\mathcal{N}}=1}^{N_{\mathcal{N}}} d^3\mathbf{r}_{n_{\mathcal{N}}} d^3\mathbf{P}_{n_{\mathcal{N}}}, \tag{I.33}$$

where $S_\alpha = 1, \dots, N_\alpha, \alpha = 1, \dots, \mathcal{N}$. Using the commutability of the $\sum_\sigma$ (σ-summation) and LIM (limit) procedures with the operators $\hat{V}_\tau$ and $\hat{C}_\tau$, the integral operator $\hat{A}_{S_\alpha}$ has the commutative relations

$$\{\hat{A}_{S_\alpha}, \hat{V}_\tau\}_- = 0 \qquad \text{and} \qquad \{\hat{A}_{S_\alpha}, \hat{C}_\tau\}_- = 0 \tag{I.34}$$

for all $S_\alpha = 1; \dots, N_\alpha$. Acting the $\hat{A}_{S_\alpha}$ on the N particle distribution function $F_N(\mathbf{r}, \mathbf{P}, t; \tilde{\omega}_\tau(\omega))$ the following relation is obtained

$$F_{S_\alpha}(\mathbf{r}, \mathbf{P}, t; \tilde{\omega}_\tau(\omega)) = \hat{A}_{S_\alpha} F_N(\mathbf{r}, \mathbf{P}, t; \tilde{\omega}_\tau(\omega)) \tag{I.35}$$

for all $(\tau, \omega) \in T \times \Omega$. Retaining the Gauss–Markov properties of the "outside" in the S_α reduced distribution functions, the $F_{S_\alpha}(\mathbf{r}, \mathbf{P}, t; \tilde{\omega}_\tau(\omega))$ can also be split uniquely into two mutually independent parts

$$F_{S_\alpha}(\mathbf{r}, \mathbf{P}, t; \tilde{\omega}_\tau(\omega)) = \hat{V}_\tau F_{S_\alpha}(\mathbf{r}, \mathbf{P}, t; \tilde{\omega}_\tau(\omega)) + \hat{C}_\tau F_{S_\alpha}(\mathbf{r}, \mathbf{P}, t; \tilde{\omega}_\tau(\omega)), \tag{I.36}$$

$$\hat{V}_\tau F_{S_\alpha}(\mathbf{r}, \mathbf{P}, t; \tilde{\omega}_\tau(\omega)) = F_{0_{S_\alpha}}(\mathbf{r}, \mathbf{P}, t) \quad \text{and} \quad \hat{C}_\tau F_{S_\alpha}(\mathbf{r}, \mathbf{P}, t; \tilde{\omega}_\tau(\omega)) =$$
$$= F_{1_{S_\alpha}}(\mathbf{r}, \mathbf{P}, t; \tilde{\omega}_\tau(\omega)), \tag{I.37}$$

which includes all the S_α arbitrary kinetic levels. This arbitrary kinetic level decomposability of the Gauss–Markov reduced distribution functions means the dimensions of the phase space or subspace to be independent of the deterministic and stochastic dynamics of the plasma system. Carrying out the Mayer's expansion of the S_α reduced distribution functions and considering that the Coulomb interaction potential ϕ couples both the deterministic and Gauss–Markov dynamics of the plasma particles, the arbitrary many particle correlation functions $C_{S_\alpha}(\mathbf{r}_1, \mathbf{P}_1, \ldots, \mathbf{r}_{S_\alpha}, \mathbf{P}_{S_\alpha}, t; \tilde{\omega}(\omega))$ restrain the Gauss–Markov properties of the "outside" and have the following decomposed form

$$\begin{aligned} C_{S_\alpha}(\mathbf{r}_1, \mathbf{P}_1, \ldots, \mathbf{r}_{S_\alpha}, \mathbf{P}_{S_\alpha}, t; \tilde{\omega}_\tau(\omega)) &= \hat{V}_\tau C_{S_\alpha}(\mathbf{r}_1, \mathbf{P}_1, \ldots, \mathbf{r}_{S_\alpha}, \mathbf{P}_{S_\alpha}, t; \tilde{\omega}_\tau(\omega)) + \\ &+ \hat{C}_\tau C_{S_\alpha}(\mathbf{r}_1, \mathbf{P}_1, \ldots, \mathbf{r}_{S_\alpha}, \mathbf{P}_{S_\alpha}, t; \tilde{\omega}_\tau(\omega)), \\ &\vdots \\ C_{2_\alpha}(\mathbf{r}_1, \mathbf{P}_1, \mathbf{r}_2, \mathbf{P}_2, t; \tilde{\omega}_\tau(\omega)) &= \hat{V}_\tau C_{2_\alpha}(\mathbf{r}_1, \mathbf{P}_1, \mathbf{r}_2, \mathbf{P}_2, t; \tilde{\omega}_\tau(\omega)) + \\ &+ \hat{C}_\tau C_{2_\alpha}(\mathbf{r}_1, \mathbf{P}_1, \mathbf{r}_2, \mathbf{P}_2, t; \tilde{\omega}(\omega)) \end{aligned} \tag{I.38}$$

and

$$\begin{aligned} \hat{V}_\tau C_{S_\alpha}(\mathbf{r}_1, \mathbf{P}_1, \ldots, \mathbf{r}_{S_\alpha}, \mathbf{P}_{S_\alpha}, t; \tilde{\omega}_\tau(\omega)) &= C_{0S_\alpha}(\mathbf{r}_1, \mathbf{P}_1, \ldots, \mathbf{r}_{S_\alpha}, \mathbf{P}_{S_\alpha}, t), \\ \hat{C}_\tau C_{S_\alpha}(\mathbf{r}_1, \mathbf{P}_1, \ldots, \mathbf{r}_{S_\alpha}, \mathbf{P}_{S_\alpha}, t; \tilde{\omega}_\tau(\omega)) &= C_{1S_\alpha}(\mathbf{r}_1, \mathbf{P}_1, \ldots, \mathbf{r}_{S_\alpha}, \mathbf{P}_{S_\alpha}, t; \tilde{\omega}_\tau(\omega)), \\ &\vdots \\ \hat{V}_\tau C_{2_\alpha}(\mathbf{r}_1, \mathbf{P}_1, \mathbf{r}_2, \mathbf{P}_2, t; \tilde{\omega}_\tau(\omega)) &= C_{0_{2_\alpha}}(\mathbf{r}_1, \mathbf{P}_1, \mathbf{r}_2, \mathbf{P}_2, t), \\ \hat{C}_\tau C_{2_\alpha}(\mathbf{r}_1, \mathbf{P}_1, \mathbf{r}_2, \mathbf{P}_2, t; \tilde{\omega}_\tau(\omega)) &= C_{1_{1_\alpha}}(\mathbf{r}_1, \mathbf{P}_1, \mathbf{r}_2, \mathbf{P}_2, t; \tilde{\omega}_\tau(\omega)). \end{aligned} \tag{I.39}$$

This unique and mutually independent decomposability of the S_α ($S_\alpha = 1, \ldots, N_\alpha$, $\alpha = 1, \ldots, \mathcal{N}$) arbitrary kinetic level correlation functions shows that it is necessary for the arbitrary kinetic level "pure" deterministic and "pure" Gauss–Markov reduced phase space distribution function to contain both the "individual" and "collective" dynamical effects of the plasma system.

The basic approximation to this electromagnetic coupling between the "embedded" plasma system and the "outside" is the aforedescribed separation and decoupling of the statistical t and stochastic (Gauss–Markov) τ time-scales. This crucial assumption makes it possible to treat and study the arbitrary kinetic level Gauss–Markov dynamics of the "embedded" plasma system coherently. By the application of an "ergodic like" Gauss–Markov model to the fast turbulent time-scale t_F with respect to the slow regular time-scale t_{SL} the multi time-scales weak and moderately strong plasma turbulence can be coherently described in the frame of this stochastic treatment [7]. Finally, if this approximation fails the Gauss–Markov stochastic projectors $\hat{V}_\tau$, $\hat{C}_\tau$ do not satisfy the commutation relations (I.9). This failure will produce an enormous complexity of the description. The second part of this paper will contain the Gauss–Markov kinetic theory of the "embedded" plasma system.

References

1. I. Gyarmati, Non-equilibrium Thermodynamics, Springer-Verlag, Berlin, 1970.
2. K. Lelkes, Proc. of International Conference on Plasma Physics 1984, Lausanne, Switzerland.
3. P. Hanggi and H. Thomas, Phys. Rep., *88*, 209, 1982.
4. G. Dewitt–Morette and K. D. Elworthy, Phys. Rep., *77*, 123, 1981.
5. I. M. Besieris and W. Stasiak, J. Math. Phys., *17*, 1976, No 9.
6. Pao-Liu Chow, in Probabilistic Analysis and Related Topics, ed. by A. T. Bharucha-Reid, Vol. 1, Academic Press, New York, 1978, p. 1.
7. K. Lelkes, Proc. of International Conference on Plasma Physics 1982, Göteborg, Sweden.
8. G. Ecker, Theory of Fully Ionized Plasmas, Academic Press, New York, 1972.

Acta Physica Hungarica, 63 (3—4), pp. 321—329 (1988)

AMPLIFICATION OF B–G WAVES IN A PRE-STRESSED PIEZOELECTRIC HALF SPACE OF HEXAGONAL SYMMETRY

M. GANGULY and A. K. PAL

Department of Mathematics, Jadavpur University
Calcutta-700032, India

(Received in revised form 17 April 1986)

The present paper deals with the propagation of B–G waves in a pre-stressed hexagonal piezoelectric half space which is coupled with a semiconducting half space through an air gap. Analytical expressions for the amplification coefficient and velocity of such waves have been derived and compared with the corresponding expressions when the pre-stressed conditions are absent.

1. Introduction

In a series of papers Soluch [1, 2] for the first time studied the amplification of B–G waves in a structure which consists of a piezoelectric crystal of class 6 mm and a semiconductor separated by an air gap. In his papers he investigated the effects of the size of the air gap and diffusion in the semiconductor etc., in wave parameters like velocity and amplification.

In the present paper, a similar problem has been attempted when the piezoelectric half space is pre-stressed and ultimately it has been found that such pre-stressed conditions greatly influence the above mentioned parameters.

2. The differential equations and their solutions

Following Soluch [2] we consider a structure consisting of a pre-stressed piezoelectric half space $x_2 \geq 0$ and a semiconducting half space $x_2 \leq -h$ separated by an air gap of width h. The other two directions of the coordinate axes x_1 and x_3 are taken along the direction of wave propagation and tangential to the surface of the piezoelectric half space. The system to be analyzed is shown in Fig. 1. v_e and v_s are the velocities of the electrons and the B–G wave, respectively.

The basic equations of the different regions together with their solutions are presented in the following sections.

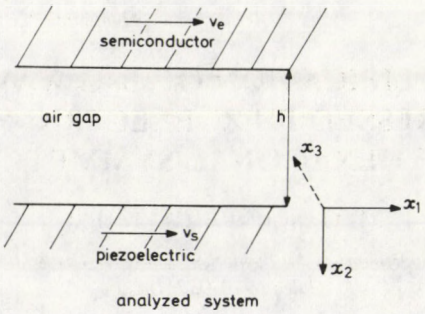

Fig. 1

Piezoelectric region

From the equations of state and from the electrostatic equations of a hexagonal piezoelectric crystal together with the pertinent equations of motion

$$\frac{\partial}{\partial x_i}\left(\sigma_{ik}\frac{\partial u_j}{\partial x_k}\right)+\frac{\partial T_{ij}}{\partial x_i}=\rho\ddot{u}_i \tag{2.1}$$

for a pre-stressed medium (Bolotin [3], Nalamwar and Epstein [4]) four coupled partial differential equation for the mechanical displacement components u_i ($i=1, 2, 3$) and the electric potential φ can be obtained. Since we are interested in the propagation of transverse B–G waves, the displacement components u_1 and u_2 can be taken to be zero and the remaining unknowns u_3 and the piezoelectric potential φ are independent of the x_3 coordinate resulting in the following two coupled partial differential equations (Ganguly [5])

$$[\sigma_{11}u_{3,11}+2\sigma_{12}u_{3,21}+\sigma_{22}u_{3,22}]+c_{44}\nabla^2u_3+e_{15}\nabla^2\varphi=\rho\ddot{u}_3, \tag{2.2}$$

$$e_{15}\nabla^2u_3-\varepsilon_{11}\nabla^2\varphi=0, \tag{2.3}$$

where ∇^2 is the two dimensional Laplace operator

$$\nabla^2=\frac{\partial^2}{\partial x_1^2}+\frac{\partial^2}{\partial x_2^2}.$$

Introducing a new potential function ψ defined by the relation

$$\psi=\varphi-\frac{e_{15}}{\varepsilon_{11}}u_3, \tag{2.4}$$

the above two equations further reduce to the following

$$\rho\ddot{u}_3=\bar{c}_{44}\nabla^2u_3+\sigma_{11}u_{3,11}+\sigma_{22}u_{3,22}+2\sigma_{12}u_{3,21}, \tag{2.5}$$

$$\nabla^2\psi=0, \tag{2.6}$$

where

$$\bar{c}_{44}=c_{44}+\frac{e_{15}^2}{\varepsilon_{11}}. \tag{2.7}$$

σ_{ik} are the initial stress components in the medium, ρ is the material density, u_3 the displacement component, e_{15} the piezoelectric constant, ε_{11} the dielectric constant and φ the piezoelectric potential of the medium. Dot denotes time derivative and an index preceeded by a comma signifies derivatives with respect to space variable.

We take the solutions of (2.5) and (2.6) in the form

$$u_3=A\exp(-\xi_2 x_2)\exp\{i(\xi_1 x_1-\omega t)\}, \tag{2.8}$$

$$\psi=B\exp(-\xi_1 x_2)\exp\{i(\xi_1 x_1-\omega t)\}, \tag{2.9}$$

where ξ_1 and ξ_2 are wave propagation and decay constants, respectively. A and B are constant amplitudes and ω is the angular frequency. Using the above two equations we get from (2.4)

$$\varphi=\left[A\frac{e_{15}}{\varepsilon_{11}}\exp(-\xi_2 x_2)+B\exp(-\xi_1 x_2)\right]\exp[i(\xi_1 x_1-\omega t)]. \tag{2.10}$$

Substituting the values of u_3 and ψ from (2.8) and (2.9) in (2.5) we find (Ganguly [5])

$$\xi_2^2(\bar{c}_{44}+\sigma_{22})-\xi_1^2(\bar{c}_{44}+\sigma_{11})-2i\xi_1\xi_2\sigma_{12}+\rho\omega^2=0. \tag{2.11}$$

The other equation (2.6) is automatically satisfied by the above choice.

The air gap region

In this region there will be no displacement component and the electric potential φ must satisfy Laplace's equation

$$\nabla^2\varphi=0, \tag{2.12}$$

the solution of which has the following form

$$\varphi=[c\exp(\xi_1 x_2)+D\exp(-\xi_1 x_2)]\cdot\exp[i(\xi_1 x_1-\omega t)]. \tag{2.13}$$

The semiconductor region

If the semiconductor is isotropic dielectrically then Poisson's equation has the following form

$$\nabla^2\varphi=\frac{en}{\varepsilon_s}, \tag{2.14}$$

where n is the *ac* component of the electron concentration.

The current continuity equation is given by (Seeger [6])

$$\nabla \cdot \bar{J} = e\dot{n}, \tag{2.15}$$

where $\bar{J}$ is the electron current density vector.

After neglecting the effect of generation, recombination and trapping, the linearized equation of state for the electric current density assumes the form

$$\bar{J} = -\sigma \nabla \varphi - e\bar{v}_e n + De\nabla n, \tag{2.16}$$

where

$$\sigma = e\mu n_0, \tag{2.17}$$

$$\bar{v}_e = -\mu E_0, \tag{2.18}$$

and $\bar{E}_0$ is the constant electric field intensity vector, μ the mobility constant and D the diffusion constant, respectively.

From (2.15) and (2.16) we find

$$\sigma \nabla^2 \varphi + e\nabla(\bar{v}_e n) - De\nabla^2 n + e\dot{n} = 0. \tag{2.19}$$

Let us seek the solutions of (2.14) and (2.19) in the following form

$$n = E \exp\{q\xi_1(x_2 + h)\} \cdot \exp\{i(\xi_1 x_1 - \omega t)\}, \tag{2.20}$$

$$\varphi = F \exp\{q\xi_1(x_2 + h)\} \cdot \exp\{i(\xi_1 x_1 - \omega t)\}. \tag{2.21}$$

Inserting the above expressions for n and φ in (2.14) and (2.19) we get the following two algebraic equations

$$\frac{eE}{\varepsilon_s} - F\xi_1^2(q^2 - 1) = 0, \tag{2.22}$$

$$E\{-ei\omega - De\xi_1^2(q^2 - 1) + e\bar{v}_e\xi_1(q + i)\} + F\{\xi_1^2(q^2 - 1)\sigma\} = 0. \tag{2.23}$$

Hence for non-trivial solution we must have

$$\begin{vmatrix} \frac{e}{\varepsilon_s} & -\xi_1^2(q^2 - 1) \\ \{-ei\omega - De\xi_1^2(q^2 - 1) + ev_e\xi_1(q + i)\} & \xi_1^2(q^2 - 1)\sigma \end{vmatrix} = 0. \tag{2.24}$$

Out of the four roots of this equation two can be eliminated by the conditions at infinity as in Kaliski [7] and only two roots are meaningful namely

$$q_1 = 1,$$

$$q_2 = \frac{1}{2D\xi_1^2}\left\{\bar{v}_e\xi_1 + \left[\bar{v}_e^2\xi_1^2 - 4D\xi_1^2\left\{i(\omega - \bar{v}_e\xi_1) - \frac{\sigma}{\varepsilon_s} - D\xi_1^2\right\}\right]^{\frac{1}{2}}\right\}. \tag{2.25}$$

Using (2.14), (2.20) and (2.21) we find the following relation between E and F

$$\frac{e}{\varepsilon_s} E = F\xi_1^2(q^2-1),$$

which shows E becomes zero when q assumes the value $q_1 = 1$.

We thus find the following expressions for n and φ from Eqs (2.20), (2.21) and (2.25)

$$n = E \exp[q_2\xi_1(x_2+h)] \exp[i(\xi_1 x_1 - \omega t)], \tag{2.26}$$

$$\varphi = \{F \exp[\xi_1(x_2+h)] + G \exp[q_2\xi_1(x_2+h)]\} \exp\{i(\xi_1 x_1 - \omega t)\}. \tag{2.27}$$

In addition, the constants E and G are related by the following expression

$$E = G(q_2^2-1)\varepsilon_s \frac{\xi_1^2}{e}. \tag{2.28}$$

3. Boundary conditions of the problem

Since in the present problem we wish to study the propagation of B–G waves in a structure consisting of an initially stressed piezoelectric half space $x_2 \geq 0$ and a semiconducting half space $x_2 \leq -h$ separated by an air gap of width h we find two bounding surfaces $x_2 = 0$ and $x_2 = -h$.

For the boundary $x_2 = 0$

i) $$\varphi_{,1}|_{x_2=0^+} = \varphi_{,1}|_{x_2=0^-}, \tag{3.1}$$

ii) $$D_2|_{x_2=0^+} = D_2|_{x_2=0^-}, \tag{3.2}$$

iii) $$T_{23} + \sigma_{2k} u_{3,k}|_{x_2=0^+} = 0. \tag{3.3}$$

For the boundary $x_2 = -h$

iv) $$\varphi_{,1}|_{x_2=-h^+} = \varphi_{,1}|_{x_2=-h^-}, \tag{3.4}$$

v) $$D_2|_{x_2=-h^+} = D_2|_{x_2=-h^-}, \tag{3.5}$$

vi) $$J_2|_{x_2=-h^-} = 0. \tag{3.6}$$

Inserting the values of (2.8), (2.10), (2.13), (2.16), (2.26), (2.27) in the above equations (3.1)–(3.6) we find the following set of equations

$$A\left(\frac{e_{15}}{\varepsilon_{11}}\right) + B - C - D = 0, \tag{3.7}$$

$$B\varepsilon_{11} + c\varepsilon_{11}^0 - D\varepsilon_{11}^0 = 0, \tag{3.8}$$

$$A\{\xi_2(\bar{c}_{44} + \sigma_{22}) - i\xi_1\sigma_{21}\} + Be_{15}\xi_1 = 0, \tag{3.9}$$

$$c\exp(-\xi_1 h)+D\exp(\xi_1 h)-F-G=0, \tag{3.10}$$

$$c\varepsilon_{11}^0\exp(-\xi_1 h)-D\varepsilon_{11}^0\exp(\xi_1 h)-F\varepsilon_s-Gq_2\varepsilon_s=0, \tag{3.11}$$

$$E\{-e\bar{v}_e+Deq_2\xi_1\}-F\sigma\xi_1-Gq_2\xi_1\sigma=0, \tag{3.12}$$

where ε_{11}^0 is the vacuum permittivity.

The above set of equations (3.7)–(3.12) together with the relation given by (2.28) contain a set of seven linear algebraic equations. For non-trivial solution of these equations we must have

$$\begin{vmatrix}
\frac{e_{15}}{\varepsilon_{11}} & 1 & -1 & -1 & 0 & 0 & 0 \\
0 & \varepsilon_{11} & \varepsilon_{11}^0 & -\varepsilon_{11}^0 & 0 & 0 & 0 \\
[(\bar{c}_{44}+\sigma_{22})\cdot\xi_2-i\sigma_{21}\xi_1] & e_{15}\xi_1 & 0 & 0 & 0 & 0 & 0 \\
0 & 0 & \exp(-\xi_1 h) & \exp(\xi_1 h) & 0 & -1 & -1 \\
0 & 0 & \varepsilon_{11}^0\exp(-\xi_1 h) & [-\varepsilon_{11}^0\cdot\exp(\xi_1 h)] & 0 & -\varepsilon_s & -q_2\varepsilon_s \\
0 & 0 & 0 & 0 & (-e\bar{v}_e+Deq_2\xi_1) & -\sigma\xi_1 & -q_2\xi_1\sigma \\
0 & 0 & 0 & 0 & 1 & 0 & \left[-(q_2^2-1)\frac{\varepsilon_s}{e}\xi_1^2\right]
\end{vmatrix} = 0. \tag{3.13}$$

Expanding the above determinantal equation we find

$$\frac{\xi_2}{\xi_1}=\frac{1}{(\bar{c}_{44}+\sigma_{22})}\left\{\left(\frac{M}{L}\right)e_{15}+i\sigma_{21}\right\}, \tag{3.14}$$

where

$$\frac{M}{L}=\frac{\left[\left(\frac{e_{15}\varepsilon_{11}^0}{\varepsilon_{11}}\cos h(\xi_1 h)\right)\{\varepsilon_s\xi_1^2(-\bar{v}_e+Dq_2\xi_1)(1+q_2)\}+\frac{e_{15}(\varepsilon_{11}^0)^2}{\varepsilon_{11}}\cdot\right.}{\left.\cdot\{(-\bar{v}_e+Dq_2\xi_1)(1+q_2)\varepsilon_s\xi_1^2-2\sigma\xi_1\}\cdot\sin h(\xi_1 h)\right]}$$

$$\frac{}{\{[(1+q_2)\varepsilon_s^2\xi_1^2(-\bar{v}_e+Dq_2\xi_1)]\cdot[(\varepsilon_{11}+\varepsilon_{11}^0)\cos h(\xi_1 h)-\varepsilon_{11}\exp(-\xi_1 h)]+}$$

$$+[\varepsilon_s\xi_1^2(1+q_2)(-\bar{v}_e+Dq_2\xi_1)-\sigma\xi_1]\cdot[\varepsilon_{11}^0(\varepsilon_{11}^0+\varepsilon_{11})\cdot$$

$$\cdot\sin h(\xi_1 h)+\varepsilon_{11}\varepsilon_{11}^0\exp(-\xi_1 h)]\}. \tag{3.15}$$

4. Determination of the phase velocity and amplification/attenuation co-efficient of the wave

Phase velocity

From Eq. (2.11) we have the following relation between ξ_1 and ξ_2

$$\left(\frac{\xi_2}{\xi_1}\right)^2(\bar{c}_{44}+\sigma_{22})-(\bar{c}_{44}+\sigma_{11})-2i\left(\frac{\xi_2}{\xi_1}\right)\sigma_{12}+\rho v_s^2=0, \tag{4.1}$$

where $v_s\left(=\frac{\omega}{\xi_1}\right)$ is the phase velocity of the surface wave.

Inserting the value of ξ_2/ξ_1, from (3.14) in (4.1) we find

$$v_s=\frac{1}{\sqrt{\rho}}\left\{(\bar{c}_{44}+\sigma_{11})-\frac{\left(\frac{M}{L}e_{15}+i\sigma_{21}\right)}{(\bar{c}_{44}+\sigma_{22})}\left[\left(\frac{M}{L}e_{15}+i\sigma_{21}\right)-2i\right]\right\}^{\frac{1}{2}}. \tag{4.2}$$

This gives the phase velocity of the B–G wave.

In the absence of pre-stressed conditions the expression for the phase velocity of the propagating wave is given by

$$v_s^*=\frac{1}{\sqrt{\rho}}\left\{\bar{c}_{44}-\frac{M}{L}\cdot\frac{e_{15}}{c_{44}}\left(\frac{M}{L}e_{15}-2i\right)\right\}^{\frac{1}{2}}. \tag{4.3}$$

Eliminating M/L between (4.2) and (4.3) we find the following relation between v_s and v_s^*

$$\rho^2[v_s^2(\bar{c}_{44}+\sigma_{22})-v_s^{*2}\bar{c}_{44}]^2+2\rho([\bar{c}_{44}(\sigma_{11}+\sigma_{22})+\sigma_{11}\sigma_{22}+\sigma_{21}^2])$$
$$\cdot\{v_s^{*2}\bar{c}_{44}-v_s^2(\bar{c}_{44}+\sigma_{22})\}=4\rho v_s^{*2}\bar{c}_{44}\sigma_{21}^2-[(\bar{c}_{44}\cdot(\sigma_{11}+\sigma_{22})+$$
$$+\sigma_{11}\sigma_{22}+\sigma_{21}^2-2\sigma_{21})+4\sigma_{21}(\bar{c}_{44}(\sigma_{11}+\sigma_{22})+\sigma_{11}\sigma_{22}+\sigma_{21}^2-2\sigma_{21})+4\sigma_{21}^2\bar{c}_{44}^2]. \tag{4.4}$$

Amplification co-efficient

To determine the amplification co-efficient of the surface wave we substitute

$$\xi_1=\alpha+i\beta, \qquad \beta<<\alpha$$

in the dispersion equation (2.11) and follow the technique of Kaliski [7]. We thus find the following equation.

$$\xi_2(\bar{c}_{44}+\sigma_{22})-(\alpha^2-\beta^2)(\bar{c}_{44}+\sigma_{11})+2\beta\xi_2\sigma_{12}-$$
$$-2i\alpha\beta(\bar{c}_{44}+\sigma_{11})-2i\alpha\sigma_{12}\xi_2=0. \tag{4.5}$$

Equating the imaginary part and real part of this equation to zero we find

$$\beta=-\frac{\xi_2\sigma_{12}}{(\bar{c}_{44}+\sigma_{11})} \tag{4.6}$$

and

$$\beta^2(\bar{c}_{44}+\sigma_{11})+2\beta\sigma_{12}\xi_2+\{\xi_2^2(\bar{c}_{44}+\sigma_{22})-\alpha^2(\bar{c}_{44}+\sigma_{11})+\rho\omega^2\}=0. \tag{4.7}$$

The negative value of β in (4.6) implies that it is a case of amplification.

From (4.7) we find the two roots as follows

$$\beta_{1,2}=\frac{1}{(\bar{c}_{44}+\sigma_{11})}\{-\sigma_{12}\xi_2\pm(\xi_2^2\sigma_{12}^2-(\bar{c}_{44}+\sigma_{11})[\xi_2^2(\bar{c}_{44}+\sigma_{22})-$$
$$-\alpha^2(\bar{c}_{44}+\sigma_{11})+\rho\omega^2])^{\frac{1}{2}}\}. \tag{4.8}$$

The above two values of β given by the Eq. (4.8) become identical to the one given by the Eq. (4.6) when the discriminant

$$\xi_2^2\sigma_{12}^2-(\bar{c}_{44}+\sigma_{11})[\xi_2^2(\bar{c}_{44}+\sigma_{22})-\alpha^2(\bar{c}_{44}+\sigma_{11})+\rho\omega^2]=0.$$

For positive values of the discriminant two distinctly different values for the amplification coefficient β can be obtained; one of which is negative and the other may have positive or negative value. This indicates both the possibilities of amplification and/or attenuation. Similarly it can be seen that for negative values of the discriminant, only amplification of the wave can be obtained.

In the absence of initial stress, the amplification or attenuation coefficient β^* of the wave can be determined from the equation

$$\beta^{*2}\bar{c}_{44}+(\xi_2^2-\alpha^2)\bar{c}_{44}+\rho\omega^2=0,$$

which is obtained by substituting the initial stress terms equal to zero in Eq. (4.7).

The roots of the above equation are

$$\beta_{1,2}^*=\pm\frac{1}{\bar{c}_{44}}\{\bar{c}_{44}[(\alpha^2-\xi_2^2)-\rho\omega^2]\}^{\frac{1}{2}}. \tag{4.9}$$

5. Discussion

To summarize the above analysis we find that the dispersion equation (2.11) relates angular frequency ω, wave number ξ_1 and the decay constant ξ_2. The determinantal equation (2.24) obtained for non-trivial solutions in the semi-conducting half space involves in addition to ξ_1 and ω the decay parameter q for the surface wave. Similarly the determinantal equation (3.13) obtained from the boundary condition of the problem contains in addition to the material constants ξ_1 and the decay parameter q_2, the decay constant ξ_2. In such wave propagation problems, numerical techniques are generally adopted (White and Tseng [8]). To proceed with such method we first eliminate q from the equation (3.13) using Eqs (2.24) or (2.25) so that we find a relation only in ξ_1, ξ_2 and ω. White's technique consists in finding a set of values for ξ_1, ξ_2 and ω which would satisfy equation (2.11) and the equation obtained after eliminating q, the decay parameter in the semi-conducting region. To do this, values for the wave number ξ_1 and the angular frequency ω are assigned and then Eq. (2.11) is solved for the decay constant ξ_2. The decay constant together with the preassigned values for the wave number and angular frequency are then

substituted in the equation obtained after eliminating q from the determinantal equation (2.24/2.25) and (3.13) to see whether it is satisfied. If not, new values for the wave number ξ_1 and the angular frequency ω are chosen and substituting them in the dispersion equation (2.11) the value for the decay constant is derived.

The process is continued until a set of values for the decay constant, angular frequency and wave number are obtained for which both the equations mentioned earlier are satisfied.

The values for the decay constant ξ_2, angular frequency ω and wave number ξ_1 thus obtained are substituted in Eqs (4.2), (4.3), (4.8) and (4.9) to obtain the exact values of the phase velocity and amplification co-efficient of the surface wave in the presence and absence of the initial stresses.

References

1. W. Soluch, J. Appl. Phys., *45*, 3714, 1974.
2. W. Soluch, IEEE Trans. Sonics Ultrason., SU-*24*, 43, 1977.
3. V. V. Bolotin, Nonconservative problems of the theory of elastic stability, Macmillan, New York, pp. 43–46, 1963.
4. A. L. Nalamwar and M. Epstein, J. Appl. Phys., *47*, 43, 1976.
5. M. Ganguly, Proc. Indian Natn. Sci. Acad., *50A*, 375, 1984.
6. K. Seegar, Semi-conductor physics, Springer Verlag, New York, 1973.
7. S. Kaliski et al. Proc. Vibr. Problems, *5*, 1, 1966.
8. R. M. White and C. C. Tseng, J. Acoust. Soc. Am., *38*, 4274, 1967.

Acta Physica Hungarica, 63 (3—4), pp. 331—340 (1988)

PHONON CONDUCTIVITY OF InSb IN THE TEMPERATURE RANGE 2–800 K

A. H. AWAD

Department of Physics, College of Education
University of Basrah, Basrah, Iraq

(Received in revised form 12 May 1986)

The lattice thermal conductivity of InSb has been calculated in the temperature range 2–800 K in the frame of Dubey's model, which makes use of Guthrie's classification of three-phonon scattering events. Excellent agreement has been found between the theoretical and experimental values of the phonon conductivity over a wide range of temperatures. The temperature dependence of three-phonon scattering relaxation rate has been calculated for both class I and class II events in the study of phonon conductivity of InSb. The percentage contributions of transverse and longitudinal phonons have been studied separately in the temperature range of investigation. The role of four-phonon processes is also included at high temperatures. The percentage contributions of the three-phonon normal and umklapp processes towards τ_{3ph}^{-1} have also been investigated.

1. Introduction

The lattice thermal conductivity of InSb has been studied by several workers [1–5] experimentally as well as theoretically at low and high temperatures, and it is now established that the Callaway [6] model could not get good agreement in the high temperature region. It should be noted that the Callaway model is an exception due to the fact that it does not make any distinction between transverse and longitudinal phonons. Holland [1] modified the Callaway model, making it applicable at all temperatures by considering the two mode conduction of phonons.

The three phonon scattering relaxation rates were further studied by Guthrie [7] by dividing the phonon–phonon scattering events into two classes: Class I events in which the carrier phonon is annihilated by combination, and class II events in which annihilation takes place by splitting. Recently, considering the rate of $\tau_{3ph,N}^{-1}$ and $\tau_{3ph,U}^{-1}$ and following Guthrie's classification of the phonon–phonon scattering events Dubey [8] studied the thermal conductivity of a sample by proposing a new expression for τ_{3ph}^{-1} as

$$\tau_{3ph}^{-1} = (B_{N,\mathrm{I}} + B_{U,\mathrm{I}} e^{-\theta/\alpha T}) g(w) T^{m_{\mathrm{I}}(T)} + \\ + (B_{N,\mathrm{II}} + B_{U,\mathrm{II}} e^{-\theta/\alpha T}) g(w) T^{m_{\mathrm{II}}(T)} . \quad (1)$$

Terms are explained in the following Section. The aim of the present work is to calculate the lattice thermal conductivity of InSb in the frame of the expression for the three-phonon scattering relaxation rate proposed by Dubey. The separate contribution of transverse and longitudinal phonons towards the total lattice thermal conductivity has also been studied by calculating their percentage contributions. The percentage contribution of the three N and U processes scattering relaxation rates toward τ_{3ph}^{-1} have been studied.

2. Theory

In the present model Dubey [8] used the same frequency dependence $g(w)$ for N and U-processes due to the fact that $g(w)$ depend only on polarisation branches. At the same time, the same value of $m(T)$ is used to both N and U-processes due to the fact that Guthrie [7] obtained the same value of $m(T)$ for both processes. The temperature exponent $m(T)$ has four values 1, 2, 3 and 4 for transverse phonons and three values 1, 2 and 3 for the longitudinal phonons corresponding to the different temperature ranges. Due to lack of an expression for the exact value of $m(T)$, Dubey [8] suggested the use of the average value of the upper and lower bounds of $m(T)$ reported by Guthrie [7]. Thus, the expression for $m(T)$ used in the present communication is given by

$$m_{\mathrm{I}}(T)=X_{\max}(e^{X_{\max}}-1)^{-1}+0.5X_{\max} \tag{2}$$

for class I events and

$$m_{\mathrm{II}}(T)=0.5+0.5X_{\max}e^{0.5X_{\max}}(e^{X_{\max}}-1)^{-1} \tag{3}$$

for class II events, where $X_{\max}=\hbar w_{\max}/K_B T$, $\hbar$ is the Planck constant divided by 2π, K_B is the Boltzmann constant and $w_{\max}$ is the phonon frequency at the boundary of the Brillouin zone.

The Guthrie [7] classification leads to the participation of transverse phonons in class I events only, while longitudinal phonons participate in class I as well as in class II. As a result, Dubey [8] proposed an expression for $\tau_{3ph,T}^{-1}$ for transverse phonons as

$$\tau_{3ph,T}^{-1}=(B_{TN,\mathrm{I}}+B_{TU,\mathrm{I}}e^{-\theta/\alpha T})wT^{m_{T,\mathrm{I}}(T)}. \tag{4}$$

Similarly, the expression for $\tau_{3ph,L}^{-1}$ for longitudinal phonons is given by

$$\begin{aligned}\tau_{3ph,L}^{-1}=&(B_{LN,\mathrm{I}}+B_{LU,\mathrm{I}}e^{-\theta/\alpha T})w^2T^{m_{L,\mathrm{I}}(T)};\\ &+(B_{LN,\mathrm{II}}+B_{LU,\mathrm{II}}e^{-\theta/\alpha T})w^2T^{m_{L,\mathrm{II}}(T)},\end{aligned} \tag{5}$$

where B_N and B_U are the scattering strength of three-phonon normal and umklapp processes, respectively, suffixes N and U are used to represent normal and umklapp

processes, θ is the Debye temperature of the sample and α is a constant, $g(w)$ is the function of phonon frequency w, $g(w)=w^2$ for longitudinal phonons and w for transverse phonons which are the same as obtained by Herring [9].

The phase and group velocities of phonons inside the conductivity integral have been corrected by using a modified dispersion relation [4, 10]

$$k=(w/v)(1+rw^2), \tag{6}$$

where k is the phonon wave vector, w is the phonon frequency, r is a constant which depends on the dispersion curve of the sample under study and can be calculated with the help of the experimental dispersion curve and v is the phonon velocity.

Assuming spherical symmetry of Brillouin zone for all three polarization branches, one longitudinal and two transverse, and that each phonon contributes separately towards the total lattice thermal conductivity, the contribution of each branch can be expressed as [6]

$$K_i=(1/6\pi^2)\int \tau_{ci}V_{gi}^2(\hbar^2w^2/K_BT^2)(e^{\hbar w/K_BT}-1)^{-2} e^{\hbar w/K_BT}k^2dk+\Delta K, \tag{7}$$

where the integral is performed over the first Brillouin zone, suffix i stands for polarization branches. Vg is the group velocity corresponding to the polarization branch, ΔK is the correction term [6] due to the three phonon N-processes and its contribution can be ignored [11–13] compared to the contribution due to the first term in Eq. (7) and τ_{ci}^{-1} is the combined scattering relaxation rate given by

$$\tau_c^{-1}=\tau_B^{-1}+\tau_{pt}^{-1}+\tau_{3ph}^{-1}+\tau_{4ph}^{-1}, \tag{8}$$

where τ_B^{-1} is the boundary scattering relaxation rate [14], τ_{pt}^{-1} is the point defect scattering relaxation rate [15], τ_{3ph}^{-1} is the three-phonon scattering relaxation rate [8] and τ_{4ph}^{-1} is the four-phonon scattering relaxation rate [16, 17]. The expressions used for the scattering relaxation rates are given in Table I. The expression for the lattice thermal conductivity in the frame of SDV [10] model can be expressed as

$$K=K_T+K_L, \tag{9}$$

where K_T and K_L are the contributions due to transverse and longitudinal phonons, respectively, and are given by

$$K_T=\left(\frac{c}{v_{T1}}\right)\int_0^{\theta_1/T}\tau_{c,T}x^4e^x(e^x-1)^{-2}(1+R_1x^2)^2(1+3R_1x^2)^{-1}dx+$$

$$+\left(\frac{c}{v_{T2}}\right)\int_{\theta_1/T}^{\theta_2/T}\tau_{c,T}x^4e^x(e^x-1)^{-2}(1+R_2x^2)^2(1+3R_2x^2)^{-1}dx, \tag{10}$$

$$K_L = \left(\frac{c}{2v_{L1}}\right) \int_0^{\theta_3/T} \tau_{c,L} x^4 e^x (e^x - 1)^{-2} (1 + R_3 x^2)^2 (1 + 3R_3 x^2)^{-1} dx +$$

$$+ \left(\frac{c}{2v_{L2}}\right) \int_{\theta_3/T}^{\theta_4/T} \tau_{c,L} x^4 e^x (e^x - 1)^{-2} (1 + R_4 x^2)^2 (1 + 3R_4 x^2)^{-1} dx, \qquad (11)$$

where

$$c = \frac{K_B}{3\pi^2}\left(\frac{K_B T}{\hbar}\right)^3, \quad R_i = r_i (K_B T/\hbar)^2, \quad \theta_i = \hbar w_i / K_B,$$

$i = 1, 2, 3$ and 4, r_1 and r_2 are dispersion constants for transverse phonons in the ranges $0 - 1/2k_{max}$ and $1/2k_{max} - k_{max}$, respectively, r_3 and r_4 are the same for longitudinal phonons, v_{T1} and v_{T2} are the transverse phonon velocities in the range

Table I

Scattering relaxation rates. In these expressions v is the average phonon velocity, L is the Casimir length of the crystal, A is the point defect scattering strength, V is the atomic volume, f_i is the atomic fraction of the i-th impurity whose mass is m_i, m is the mass of the host lattice, $\Delta m = m - m_i$, B's are constant and k_{max} is the zone boundary of the first Brillonin zone

Scattering processes	Relaxation rates
Crystal boundary [14]	$\tau_B^{-1} = v/L$
Impurities [15]	$\tau_{pt}^{-1} = Aw^4, \quad A = \frac{V}{4\pi v_{si}^3} f_i \left(\frac{\Delta m}{m}\right)^2$
Three-phonon processes	τ_{3ph}^{-1}
Normal processes [9] (N-processes)	$\tau_{3ph,N}^{-1}$
Transverse	$\tau_{TN}^{-1} = B_T w T^4$ at low temperatures
Longitudinal	$\tau_{LN}^{-1} = B_L w^2 T^3$
Transverse	$\tau_{TN}^{-1} = B'_T w T$ at high temperature
Longitudinal	$\tau_{LN}^{-1} = B'_L w^2 T$
Umklapp processes (U processes)	$\tau_{3ph,U}^{-1}$
Klemens [25]	$\tau_U^{-1} = B_U w^2 T^3 e^{-\vartheta/\alpha T}$ at low temperature
Klemens [26]	$\tau_U^{-1} = B'_U w T^3 e^{-\vartheta/\alpha T}$
Holland [1] (for transverse)	$\tau_U^{-1} = B_{TU} w^2 / \sinh(\hbar w / K_B T)$ $1/2k_{max} - k_{max}$
	$\tau_U^{-1} = 0, \qquad 0 - k_{max}$
Callaway [6]	$\tau_U^{-1} = B_U w^2 T^3$
Klemens [26]	$\tau_U^{-1} = B'_U w^2 T$ at high temperature
Four-phonon processes [16, 17]	$\tau_{4ph}^{-1} = B w^2 T^2$

$0-1/2k_{max}$ and $1/2k_{max}-k_{max}$. v_{L1} and v_{L2} are the same for longitudinal phonons, w_1 and w_3 are the frequencies of transverse and longitudinal phonons at $1/2k_{max}$, respectively, and w_2 and w_4 are the same at k_{max}.

3. Results and discussion

The boundary scattering relaxation rates $\tau_{B,T}^{-1}$, $\tau_{B,L}^{-1}$ and the point-defect scattering strength A have been adjusted at 2 K and 8 K, respectively. At low temperatures, $\tau_{3ph,N}^{-1} \gg \tau_{3ph,U}^{-1}$. Thus an approximate value of $B_{TN,I}$, $B_{LN,I}$ and $B_{LN,II}$ have been calculated at 15 K ignoring the contribution due to $\tau_{3ph,U}^{-1}$. The three-phonon U-processes dominate over N-processes at high temperatures. Therefore, one can neglect the role of three-phonon N-processes. $B_{TU,I}$, $B_{LU,I}$ and $B_{LU,II}$ at 200 K have been estimated. The four-phonon scattering strength B_{HT} and B_{HL} are calculated at 600 K. The experimental data are taken from the earlier report of Holland [18] and other constants related to the dispersion curve are taken from the earlier report of Dubey et al [4].

Using the constants and parameters reported in Table II, the lattice thermal conductivity of InSb has been calculated in the temperature range 2–800 K in the frame of the expression proposed by Dubey [8] by calculating the contribution of the transverse and longitudinal phonons separately. The results shown in Fig. 1 are in good agreement with the experimental data, also near conductivity maxima in which region Dubey and Verman [4] did not observe good agreement. The separate

Table II

Values of constants and parameters used in the calculation of phonon conductivity of InSb in the temperature range 2–800 K

v_{T1} (cm/s)	2.28×10^5	$B_{TN,I}$(deg^{-m})	1.0×10^{-12}
V_{T2} (cm/s)	0.82×10^5	$B_{TU,I}$ (deg^{-m})	4.25×10^{-6}
v_{L1} (cm/s)	3.77×10^5	$B_{LN,I}$ (s · deg^{-m})	1.0×10^{-23}
v_{L2} (cm/s)	3.77×10^5	$B_{LU,I}$ (s · deg^{-m})	1.0×10^{-20}
O_1 (K)	56	$B_{LN,II}$ (s · deg^{-m})	1.0×10^{-21}
O_2 (K)	62	$B_{LU,II}$ (s · deg^{-m})	2.0×10^{-17}
O_3 (K)	101.5	B_{HT} (s · deg^{-2})	1.0×10^{-24}
O_4 (K)	170	B_{HL} (s · deg^{-2})	1.0×10^{-23}
O_D (K)	172.5		
α	1.5		
r_1 (s^2)	9.665×10^{-27}		
r_2 (s^2)	2.618×10^{-27}		
r_3 (s^2)	0		
r_4 (s^2)	1.37×10^{-27}		
τ_{BT}^{-1} (s^{-1})	4×10^5		
τ_{BL}^{-1} s^{-1})	4.2×10^5		
A (s^3)	4.2×10^{-44}		

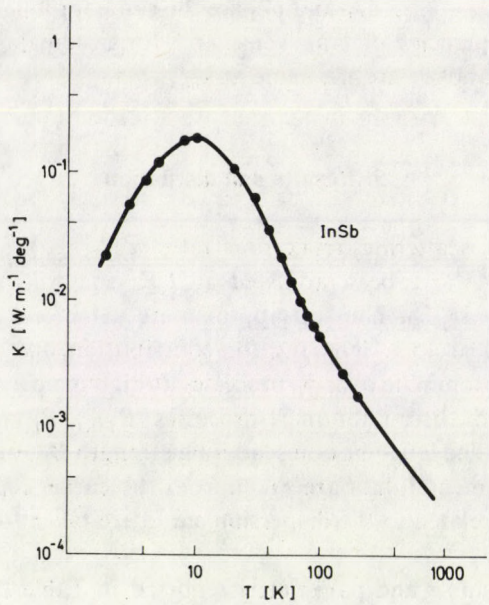

Fig. 1. Total lattice thermal conductivity of InSb in the temperature range 2–800 K. Solid line shows the calculated values and circles are the experimental points

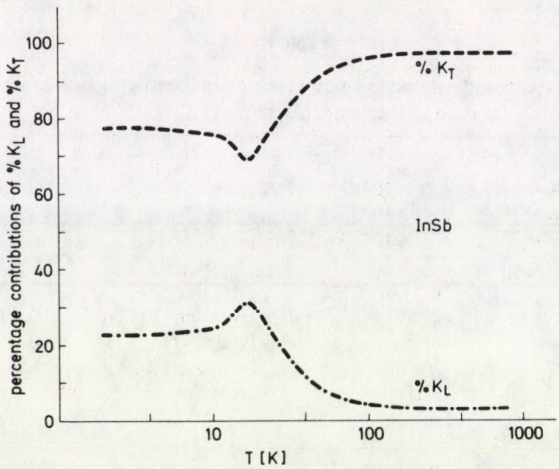

Fig. 2. The percentage contributions $\%\, K_T$ and $\%\, K_L$ towards the total lattice thermal conductivity of InSb due to transverse and longitudinal phonons, respectively. Dashed and dot–dash lines represent $\%\, K_T$ and $\%\, K_L$, respectively

percentage contributions of transverse and longitudinal phonons towards the total lattice thermal conductivity can be studied with the help of Fig. 2. From Fig. 2 it can be seen that at high temperatures the transverse phonons are mainly responsible for the transfer of heat, which is in agreement with the results reported by previous workers [1, 5, 19–23]. It is also clear that in the low temperature region the ratio $\% K_T/\% K_L$ depends upon the factor

$$2(v_L\tau_{B,L}^{-1}/v_T\tau_{B,T}^{-1}) = 2(v_L/v_T)^2$$

which indicates that at very low temperature $\% K_T$ is larger than $\% K_L$. At higher temperature towards the conductivity maxima, $\% K_T$ begins to decrease while the reverse is true for longitudinal phonons. At a certain temperature, the transverse contribution begins to increase again. This nature of such variation in the curve is due to the role of the point-defect scattering [10]. A similar nature is also obtained by Sharma et al. [10] for Ge, Dubey and Verma [24] for Si, Awad and Dubey [23] for Mg_2Ge and Mg_2Si and Al-Edani et al [5] for InSb and GaAs.

Table III

The value of the temperature exponent $m(T)$ used to calculate the lattice thermal conductivity of InSb. $m_{T,I}(T)$ is the temperature exponent of the three-phonon scattering relaxation rate due to transverse phonons for class I events, whereas $m_{L,M}(T)$ and $m_{L,N}(T)$ are the same due to longitudinal phonons for class I and class II events, respectively

T[K]	$m_{T,I}(T)$	$m_{L,I}(T)$	$m_{L,II}(T)$
2	4	3	0.5
4	4	3	0.5
6	4	3	0.5
8	3.8783	3	0.5002
10	3.1120	3	0.5017
20	1.6962	3	0.5606
30	1.3329	2.8530	0.6672
40	1.1926	2.1865	0.7579
50	1.1249	1.8173	0.8212
60	1.0874	1.5937	0.8650
70	1.0645	1.4490	0.8954
80	1.0495	1.3507	0.9169
90	1.0392	1.2810	0.9327
100	1.0318	1.2299	0.9445
200	1.0079	1.0594	0.9852
300	1.0035	1.0266	0.9933
400	1.0020	1.0150	0.9962
500	1.0012	1.0096	0.9975
600	1.0008	1.0066	0.9983
700	1.0006	1.0049	0.9987
800	1.0005	1.0037	0.9990

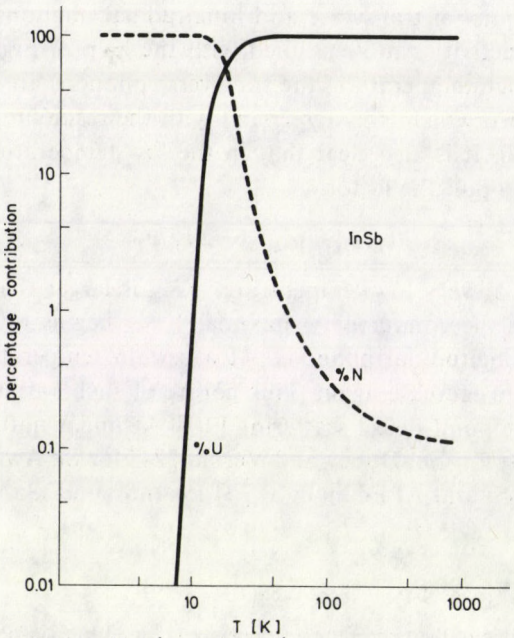

Fig. 3. The percentage contributions $\%\,\tau^{-1}_{3ph,N}$ and $\%\,\tau^{-1}_{3ph,U}$ processes towards the $\tau^{-1}_{3ph,T}$ for class I events for transverse phonons for InSb in the temperature range 2–800 K. Solid and dashed lines represent $\%\,\tau^{-1}_{3ph,U}$ and $\%\,\tau^{-1}_{3ph,N}$, respectively

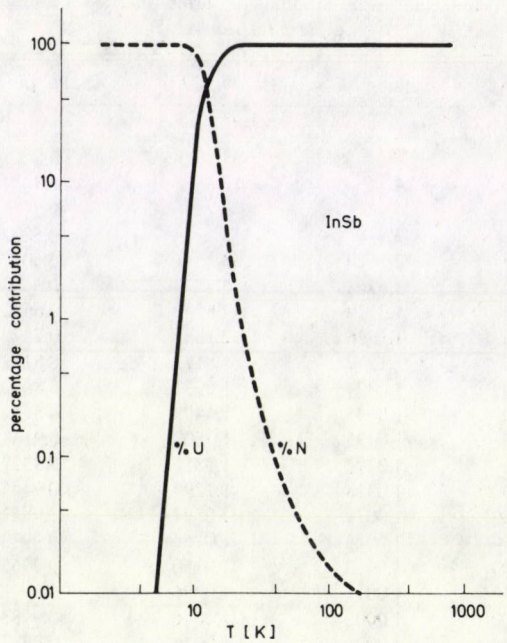

Fig. 4. The percentage contributions $\%\,\tau^{-1}_{3ph,N}$ and $\%\,\tau^{-1}_{3ph,U}$ processes towards $\tau^{-1}_{3ph,L}$ for class I events for longitudinal phonons for InSb in the temperatures range 2–800 K. Solid and dashed lines represent $\%\,\tau^{-1}_{3ph,U}$ and $\%\,\tau^{-1}_{3ph,N}$, respectively

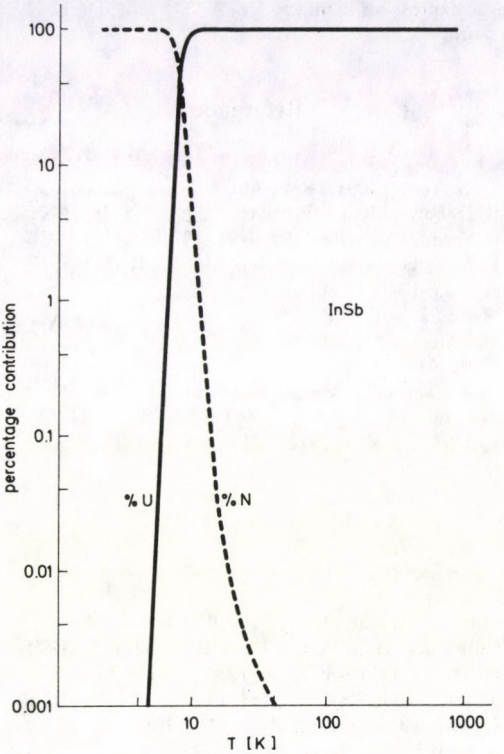

Fig. 5. The percentage contributions $\%\ \tau_{3ph,N}^{-1}$ and $\%\ \tau_{3ph,U}^{-1}$ towards $\tau_{3ph,L}^{-1}$ for class II events for InSb in the temperature range 2–800 K. Solid and dashed lines represent $\%\ \tau_{3ph,U}^{-1}$ and $\%\ \tau_{3ph,N}^{-1}$, respectively

The temperature exponents can be calculated for both transverse and longitudinal phonons in the temperature range of study with the help of Eqs (2) and (3) and the results obtained are reported in Table III. It can be seen that at low temperatures $m_{T,I}(T)$ and $m_{L,I}(T)$ tend to 4 and 3, respectively, which is similar to the results obtained by Herring [9]. It can be seen that at high temperatures $m_{T,I}(T)$, $m_{L,I}(T)$ and $m_{L,II}(T)$ tend to unity. Thus τ_{3ph}^{-1} reduces to $\tau_{3ph}^{-1} \propto T$ due to $e^{-\theta/\alpha T}$ which tends to unity at high temperatures, which is similar to the earlier finding of Herring [9].

The percentage contribution of three–phonon N and U processes can be analyzed via Figs 3–5. From these Figures, it can be seen that at low temperatures $\tau_{3ph,N}^{-1}$ dominates over $\tau_{3ph,U}^{-1}$ for both transverse and longitudinal phonons. As a result, the three-phonon N-processes play a dominating role in the lattice thermal conductivity. At high temperatures, $\tau_{3ph,U}^{-1}$ dominates over $\tau_{3ph,N}^{-1}$, which shows that the lattice thermal resistivity is mainly due to three-phonon U-processes. These results are similar to those obtained by previous workers [8, 20, 23].

* * *

The author wishes to express his thanks to Dr. W. S. Redda, Dr. R. H. Misho and Dr. K. S. Dubey for their help during the work.

References

1. M. G. Holland, Phys. Rev., *132*, 2461, 1963.
2. C. M. Bhandari and G. S. Verma, Phys. Rev., *140*, A 2101, 1965.
3. R. H. Misho and K. S. Dubey, Indian J. Pure Appl. Phys., *15*, 48, 1977.
4. K. S. Dubey and G. S. Verma, Phys. Rev., *B4*, 4491, 1971.
5. M. C. Al-Edani and K. S. Dubey, Phys. Stat. Sol., (b) *86*, 741, 1978.
6. J. Callaway, Phys. Rev., *113*, 1046, 1959.
7. G. L. Guthrie, Phys. Rev., *152* 801, 1966.
8. K. S. Dubey, J. Thermal Anal., *19*, 1980.
9. C. Herring, Phys. Rev., *95*, 954, 1964.
10. P. C. Sharma, K. S. Dubey and G. S. Verma, Phys. Rev., *B3*, 1985, 1971.
11. K. S. Dubey, Indian J. Pure Appl. Phys., *11*, 265, 1973.
12. K. S. Dubey, Phys. Stat. Sol., *81*, K83, 1977.
13. K. S. Dubey, J. Physique, *37*, 265, 1976.
14. H. B. Casimir, Physica, *5*, 595, 1938.
15. P. G. Klemens, Proc. Roy. Soc. London, *68*, 1113, 1955.
16. I. Pomeranchuk, Phys. Rev., *60*, 82, 1941.
17. I. Pomeranchuk, J. Phys. U.S.S.R., *4*, 259, 1941.
18. M. G. Holland, Phys. Rev., *134*, A471, 1964.
19. Y. P. Joshi and G. S. Verma, Phys. Rev., *B1*, 750, 1970.
20. P. C. Sharma, K. S. Dubey and G. S. Verma, Phys. Rev., *B4*, 1306, 1971.
21. K. S. Dubey and R. H. Misho, J. Therm. Anal., *12*, 223, 1978.
22. K. S. Dubey, Indian J., Pure Appl. Phys., *15*, 455, 1977.
23. A. H. Awad and K. S. Dubey, J. Therm. Anal., *24*, 233, 1982.
24. K. S. Dubey and G. S. Verma, Phys. Rev., *B7*, 2879, 1973.
25. P. G. Klemens, Solid State Physics, ed. by F. Seitz and Turnbull, Academic Press Inc. New York. 7. 1, 1958.
26. P. G. Klemens, Proc. Roy. Soc. London, *A208*, 108, 1951.

Acta Physica Hungarica, 63 (3—4), pp. 341—345 (1988)

VARIATION OF ELECTRONIC TRANSITION MOMENT FOR THE BAND SYSTEM ($B1 \rightarrow X^1\Sigma^+$) OF PbO

N. RAJAMANICKAM*

Department of Physics, University of Mysore, Mysore 570006 India

(Received in revised form 5 June 1986)

The Franck–Condon factors and r-centroids have been computed by the more reliable numerical integration procedure for the bands of the ($B1 \rightarrow X^1\Sigma^+$) system of the PbO molecule, using the suitable potential. The electronic transition moment variation with internuclear distance has been re-evaluated and this is represented by

$$R_e(r) = \text{const.}\,(0.525r - 1)$$

in the range of 2.022×10^{-10} m $\leq r \leq 2.144 \times 10^{-10}$ m. It is interesting that this representation is found to be similar to the form of $R_e(r)$ for the band systems ($AO^+ \rightarrow X^1\Sigma^+$) and ($D1 \rightarrow X^1\Sigma^+$) of PbO. Also the relative band strengths are derived. The form of $R_e(r)$ reported by Dube et al is found to be in error.

1. Introduction

While investigating the electronic transition moment (R_e) variation with internuclear distance (r) for the band system ($D1 \rightarrow X^1\Sigma^+$) of PbO [1], some discrepancies were noticed between the form of $R_e(r)$ for PbO($B1 \rightarrow X^1\Sigma^+$) band system reported by Dube et al [2]. Therefore the reliable values of Franck–Condon factors ($q_{v'v''}$) and r-centroids ($\bar{r}_{v'v''}$) for the bands of the ($B1 \rightarrow X^1\Sigma^+$) system of the PbO molecule have been computed by the more accurate numerical integration procedure using the suitable potential and the form of $R_e(r)$ has been re-evaluated in the present study. It is also noted that the form of $R_e(e)$ reported by Dube et al [2] is in error.

2. Theory

Mathematically one can write for the intensity $I_{v'v''}$ of a molecular band for a $v' \rightarrow v''$ transition in emission [3] as

$$I_{v'v''} = DN_{v'} E^4_{v'v''} p_{v'v''}, \tag{1}$$

* Present address: Department of Physics, VHNSN College Virudhunagar 626002, India

where D is a constant partly depending on the geometry of the apparatus, $N_{v'}$ is the population of the level v', $E_{v'v''}(=\lambda_{v'v''}^{-1})$, the energy quantum and $p_{v'v''}$ the band strength which in terms of electronic transition moment R_e is given by

$$p_{v'v''} = R_e^2(\bar{r}_{v'v''})q_{v'v''} . \tag{2}$$

The quantities $q_{v'v''}$ and $\bar{r}_{v'v''}$ defined as the Franck–Condon (FC) factors and $\bar{r}$-centroids respectively, can be expressed in terms of the vibrational wave functions ψ of the levels v' and v'' as

$$q_{v'v''} = [\int \psi_{v'}\psi_{v''}dr]^2 \tag{3}$$

and

$$\bar{r}_{v'v''} = \frac{\int \psi_{v'} r \psi_{v''} dr}{\int \psi_{v'}\psi_{v''}dr} . \tag{4}$$

The functional form of $R_e(\bar{r}_{v'v''})$ can be obtained from the plot of $(I/E^4q)_{v'v''}^{1/2}$ vs $\bar{r}_{v'v''}$ and the relative band strengths can be evaluated using the relation $S_{v'v''} = p_{v'v''}/p_{02}$.

3. Franck–Condon factors and r-centroids

For a proper understanding of the intensity distributions in the band systems of the molecules, it is necessary to choose a suitable potential. The potential energy curves for the electronic states of B- and X- of PbO have been constructed using the Morse [4] function and by Rydberg–Klein–Rees (RKR) procedure as modified by Vanderslice et al [5]. It is found that the Morse function represents the potential energy curves of the two states quite adequately since the RKR curve is nearly similar to the Morse curve.

The computation of the FC factors is made by Bates's method [6] of numerical integration according to the detailed procedure provided by Tawde and Sreedhara Murthy [7]. Morse [4] wave functions were calculated using TDC-316 computer at intervals of 0.005×10^{-10} m for the range of r from 1.65×10^{-10} m to 2.35×10^{-10} m for every observed vibrational level of each state. Once the appropriate wave functions are obtained, the FC factors can be evaluated by integrating the expression (3). In the case of Morse function, Fraser and Jarmain [8] gave a procedure for the analytical integration of the overlap integral. The results are generally, however, only indicative of trends [9]. The integration is therefore carried out numerically in the present study. The definition of r-centroid offers a method of computing r-centroids directly. Integrals in Eqs (3) and (4) for the FC factors ($q_{v'v''}$) and $\bar{r}$-centroids ($\bar{r}_{v'v''}$) were computed numerically and the results are entered in Table I. The r-centroids were computed by graphical and quadratic equation methods [10] and listed just for comparison. The molecular constants [11, 12] used in the present study are listed in Table II.

Dube et al [2] have reported Morse FC factors by the approximate analytical integration method [8] and the r-centroids by the quadratic equation method [10].

Table I

Franck–Condon factors ($q_{v'v''}$) and $\bar{r}$-centroids ($\bar{r}_{v'v''}$)

v',v''	$q_{v'v''}$		$\bar{r}_{v'v''}(\mathrm{m}) \times 10^{-10}$			
					Quadratic	
	Present study*	Dube et al [2]	Numerical integration*	Graphical	Present study	Dube et al [2]
0,1	0.166	0.157808	2.022	2.022	2.033	2.020
0.2	0.247	0.23807	2.053	2.052	2.068	2.052
0.3	0.237	0.23597	2.083	2.083	2.107	2.092
0.4	0.163	0.17418	2.113	2.113	2.152	2.116
0,5	0.085	0.1026639	2.144	2.146	2.204	2.148

* values used in the present investigation

Table II

Molecular constants

Molecular state	B		X	
	Present study	Dube et al [2]	Present study	Dube et al [2]
$\omega_e(\mathrm{m}^{-1}) \times 10^2$	498.0	489.0	721.8	721.26
$\omega_e X_e(\mathrm{m}^{-1}) \times 10^2$	2.20	2.20	3.70	3.70
$r_e(\mathrm{m}) \times 10^{-10}$	2.0709	2.071	1.9216	1.922

The molecular constants used by them and the reported $q_{v'v''}$ and $\bar{r}_{v'v''}$ values are also given in Tables I and II for comparison.

In the presented study, $q_{v'v''}$ and $\bar{r}_{v'v''}$ have been evaluated by the more accurate numerical integration method using the reliable values of molecular constants and therefore can be considered reliable.

4. Variation of electronic transition moment and band strengths

The intensities ($I_{v'v''}$) of (0, 1), (0, 2), (0, 3), (0, 4), (0, 5) bands reported by Dube et al [2] have been used here to re-evaluate the electronic transition moment variation with internuclear distance for the band system ($B-X$) of PbO. Graphical plot of $(IE^{-4}/q)^{1/2}_{v'v''}$ versus $\bar{r}_{v'v''}$ is shown in Fig. 1 and it is observed that the variation of R_e with $\bar{r}_{v'v''}$ is linear. A least squares fitting was followed to obtain

$$R_e(r) = \text{const.}\,(0.525r - 1) \tag{5}$$

in the range of $2.022 \times 10^{-10}\ \mathrm{m} \leq r \leq 2.144 \times {}^{-10}\ \mathrm{m}$. The form of $R_e(r)$ for the band system ($B-X$) of PbO is given in Fig. 1. The standard deviation is found to be 0.7 for the least-squares fitted straight line.

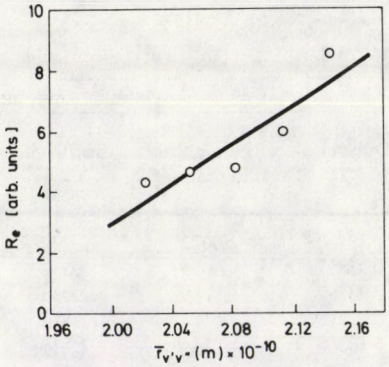

Fig. 1. Variation of R_e with r for PbO($B-X$) band system

The form of $R_e(r)$ represented by Eq. (5) is adopted in conjunction with Eq. (2) to calculate the band strengths using the computed $q_{v'v''}$ values. The band strengths have been relatively scaled with the value for the most intense band (0, 2) as unity. The relative band strengths ($S_{v'v''}$) for the PbO($B-X$) system are entered in Table III along with the intensities, $I_{v'v''}$. The required wavelengths ($\lambda_{v'v''}$) have been collected from the work of Bloomenthal [13] and listed.

5. Results and discussion

The $R_e(r)$ expression obtained by Dube et al [2] is $R_e(r) = \text{const.}\,(1-0.5408r)$ for the PbO($B-X$) band system. In the case of the PbO($A-X$ and $D-X$) band systems, Prahllad et al [14] and Rajamanickam [1] have measured the integrated intensities and interpreted with Morse $q_{v'v''}$ and $\bar{r}_{v'v''}$ values to arrive at the variation of electronic transition moments with internuclear distance, respectively, as $R_e(r) = = \text{const.}\,(0.521r-1)$ and $R_e(r) = \text{const.}\,(0.54r-1)$ which are similar to Eq. (5). One can expect such a similarity for the band systems ($A-X$), ($B-X$) and ($D-X$) of PbO. Therefore the present study results are significant.

Table III

Relative band strengths ($S_{v'v''}$)

v', v''	$\lambda_{v'v''}$(m) × 10^{-10}	$I_{v'v''}$	$S_{v'v''}$
0,1	4657.98	66.2	0.420
0.2	4816.90	100.0	1.000
0.3	4983.79	88.6	1.387
0.4	5162.31	81.6	1.302
0,5	5353.82	75.2	0.896

Acknowledgements

The author thanks the University Grants Commission, New Delhi, and the University of Mysore for the award of FIP fellowship.

References

1. N. Rajamanickam, JQSRT, *37*, 207, 1987.
2. P. S. Dube, K. N. Upadhya and D. K. Rai, JQSRT, *10*, 1191, 1970.
3. R. W. Nicholls, Extrait der Annales de Geophysique, *20*, 144, 1964.
4. P. M. Morse, Phys. Rev., *34*, 57, 1929.
5. J. T. Vanderslice, E. A. Mason, W. G. Maisch and E. R. Lippincott, J. Chem. Phys., *33*, 614, 1960.
6. D. R. Bates, Proc. Roy. Soc., A*196*, 217, 1949.
7. N. R. Tawde and N. Sreedhara Murthy, Physica, *25*, 610, 1959.
8. P. A. Fraser and W. R. Jarmain, Proc. Phys. Soc., A*66*, 1145, 1953.
9. W. R. Jarmain and P. A. Fraser, Proc. Phys. Soc., A*66*, 1153, 1953.
10. R. W. Nicholls and W. R. Jarmain, Proc. Phys. Soc., A*69*, 253, 1956.
11. H. G. Howell, Proc. Roy. Soc., A*153*, 683, 1936.
12. R. F. Barrow, J. L. Deutsch and D. N. Travis, Nature, *191*, 374, 1961.
13. S. Bloomenthal, Phys. Rev., *35*, 34, 1930.
14. U. D. Prahllad, B. N. Murthy and N. S. Murthy, JQSRT, *28*, 71, 1982.

Acta Physica Hungarica, 63 (3—4), pp. 347—352 (1988)

FLUX MEASUREMENT OF SPUTTERED ATOMS WITH LIF METHOD IN ONE LASER SHOT

J. S. BAKOS and P. LÁSZTITY

Department of Experimental Physics, Institute of Physics
Technical University, 1521 Budapest, Hungary

(Received in revised form 22 July 1986)

An experimental set-up is proposed for measuring impurity atom fluxes in fusion devices "in situ" with the aid of LIF method by using only one laser shot. It is shown that this method has the same sensitivity as that of earlier measuring arrangements.

1. Introduction

Laser induced fluorescence (LIF) [1], [2] based on tunable high power dye lasers is successfully applied to plasma diagnostics [3], [4]. It is used in impurity atom flux measurements in fusion devices [5], and in laboratory experiments investigating the phenomenon of sputtering. With the aid of LIF the origin of the impurities in tokamaks can be clarified. Their velocity distribution, local density and consequently their flux can be measured. But in all experiments performed till now absolute atom density measurements and velocity distribution measurements intended to obtain the impurity atom fluxes were performed separately. The velocity distribution of atoms i.e. the velocity profile has been obtained usually in laboratory experiments using many shots of narrow band tunable lasers and monoenergetic beam of single species bombarding the surface. Impurity density distribution measurement is performed "in situ" in tokamak using also many shots of a broad band laser. Atomic flux in the tokamak can be calculated using the result of laboratory velocity profile measurement and the density measurement in the tokamak. But uncertainty arises in the flux calculation because there are many species of atoms of different energy distribution in the tokamak contrary to that in the laboratory velocity profile measurement. Therefore the need arises to measure the velocity profile and local density of the impurity atoms "in situ" in the tokamak in one laser shot so as to determine the atomic flux.

In this paper we discuss the possibility of the simultaneous measurement of the velocity profile and the atom density to determine the impurity atom flux "in situ" in the tokamak in one laser shot using the measuring set-up proposed by us.

2. Atom density measurement

With the aid of LIF method one can determine the atom density in a vapour saturating the resonant transition of the atoms by an intense and long enough laser pulse [6]. The total local atom density (n) can be calculated from the detected number of resonance fluorescence photons (N) emitted in a solid angle Ω from an excitation volume V, as follows [6]:

$$n = \frac{2N}{\tau A_{21}} \frac{4\pi}{T\Omega V} \tag{1}$$

in the case of so-called two-level atoms (Fig. 1a) and

$$n = N \frac{\Sigma_i A_{2i} - A_{21}}{A_{23}} \frac{4\pi}{T\Omega V} \tag{2}$$

in the case of three-level atoms (Fig. 1b). T is the optical transmission of the detection optics, A_{2i} is the spontaneous transition rate from the 2nd level to the ith level. i can take other values than 1 and 3 in general case, when transitions to other levels are also possible and taken into account. τ is the duration of the laser pulse. In this way the local density of atoms having resonant transition wavelength within the laser bandwidth can be calculated using one laser shot.

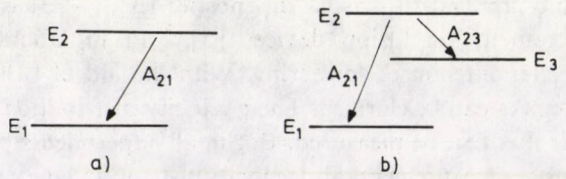

Fig. 1a. Level scheme of a two-level atom with spontaneous transition rate
Fig. 1b. Level scheme of a three-level atom with spontaneous transition rates

3. Flux measurement in one laser shot

If we are interested not only in the density of the impurities in the plasma or in that of sputtered atoms in the case of laboratory experiments, but also in their flux, then we have to measure their velocity distribution too, because the flux φ_i of the atoms in a given direction can be calculated as:

$$\varphi_i = n\bar{v}_i, \tag{3}$$

where

$$\bar{v}_i = \frac{\int v_i f(v_i) dv_i}{\int f(v_i) dv_i} \tag{4}$$

is the mean velocity. The velocity distribution $f(v_i)$ of the atoms is defined so that:

$$\int f(v_i)dv_i = n. \tag{5}$$

The velocity distribution can be obtained by measuring the spectral distribution of the emitted fluorescence radiation, or the lineshape of the absorption spectrum in the required direction if the linewidth of the transition is predominantly caused by the Doppler effect. Namely:

$$v_i = \frac{c}{\nu_0}(\nu - \nu_0) \tag{6}$$

and the spectral distribution:

$$g(\nu)d\nu = f\left(\frac{c}{\nu_0}(\nu - \nu_0)\right)\frac{c}{\nu_0}d\nu, \tag{7}$$

consequently:

$$\bar{v}_i = \frac{c}{\nu_0}\frac{\int \nu' g(\nu)d\nu}{\int g(\nu)d\nu} = \frac{c}{\nu_0}\bar{\nu}', \tag{8}$$

where $\nu_0 = \Delta E/h$ is the transition frequency, ν is the Doppler-shifted frequency, and $\nu' = \nu - \nu_0$. If the spectral distribution is measured in one laser shot the flux of the atoms is also determined:

$$\varphi_i = \frac{c}{\nu_0}\int \nu' g(\nu)d\nu, \tag{9}$$

together with the density:

$$n = \int g(\nu)d\nu, \tag{10}$$

according to (3), (4) and (5).

The Doppler-broadened spectrum of the atoms can be measured in one laser shot

- if a narrow laser line is scanned over the Doppler profile of the atoms during the laser shot [7], and the fluorescence light is detected simultaneously (the intensity of the fluorescence light is proportional to the absorption at the given wavelength of the excitation), or
- if all atoms are excited simultaneously with a broad band laser radiation and the emitted fluorescence spectrum is detected with a multichannel detector device.

The measuring set-up of the first method is really equivalent to a one-channel device with rapid frequency scanning where the scanning time is far shorter than the time scale of the processes to be investigated. The second experimental apparatus is that of really many channels.

The question arises whether the sensitivity is sufficient if the fluorescence light is detected spectrally resolved. But it can be recognised in a simple way that the same part of atoms is excited in measuring the absorption by detecting the whole emission intensity using narrow band excitation. Namely, this is equivalent to the first method, i.e. to the step by step measurement usually done till now using many shots. The only difference is in the sensitivity of the instruments detecting the spectrum of the fluorescence, which problem is discussed at the end of our paper.

4. The experimental set-up

One possible realization of the measurement of the Doppler-broadened emission spectrum is that which can be done by using Fabry–Pérot interferometer as a dispersion element and optical multichannel analyser in circular scanning mode [8] (see Fig. 2).

In many cases the main impurity in tokamak is the iron (Fe, $m=93.73\cdot 10^{-27}$ kg), which is of three-level atom with the emitted wavelength $\lambda=0.382$ μm. According to the sputtering experiments the mean velocity of iron atoms $\bar{v}_i=10^4$ m/s [9]. Provided that the velocity distribution can be approximated roughly by Maxwell–Boltzmann distribution, the spectral width of the fluorescence light $\tilde{\nu}'_D=1.18\ \text{cm}^{-1}$. If we want to resolve 10 points in the spectral distribution to obtain the Doppler profile, the required spectral resolution of our device $\delta\tilde{\nu}'_D=0.118\ \text{cm}^{-1}$. These two data give the free spectral range and the finess of the Fabry–Pérot interferometer (Fig. 3), which means that the spacing of the plates $L=4.2$ mm and the reflectivity of the mirrors $R=0.73$. The focal length f_2 of the lens L_2 used in the arrangement in Fig. 3 will be determined by the size of the pixels of the OMA. Namely, the radial dimension of the ring corresponding to the resolution $\delta\tilde{\nu}'_D$ of the interferometer has to coincide with or has to be larger than the dimension of the pixel. Furthermore, the illuminated area on the detector has to be smaller than the overall sensitive size of the detector. If the OMA which we intend to use is the one described in [8], then the detecting area is of 1 cm × 1 cm with 512 channels and the maximum space resolution is about 20μm. The radius of a ring and the radial width (δr) corresponding to the resolved frequency interval $\delta\tilde{\nu}'_D$ are given as [10], [11]

$$r_p^2=\frac{cf_2^2}{L\nu_0}p, \tag{11}$$

$$\delta r_p=\frac{\delta\tilde{\nu}'_D}{\tilde{\nu}_0}\frac{f_2^2}{r_p} \tag{12}$$

in the focal plane of the lens after the Fabry–Pérot interferometer. c is the velocity of the light, ν_0 is the frequency and $\tilde{\nu}_0$ is the wave number of the center of the line, and p is the interference order. If we choose for the focal length $f_2=5$ cm the radius

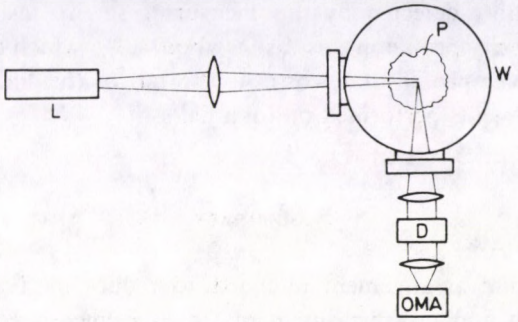

Fig. 2. Experimental arrangement for measuring velocity distribution of atoms by using only one laser shot. L is a broad band ($\Delta\nu_L > \nu'_D$) tunable laser for the excitation of atoms, D is the Fabry–Pérot interferometer, OMA is an optical multichannel analyser, and P is the plasma in the chamber W

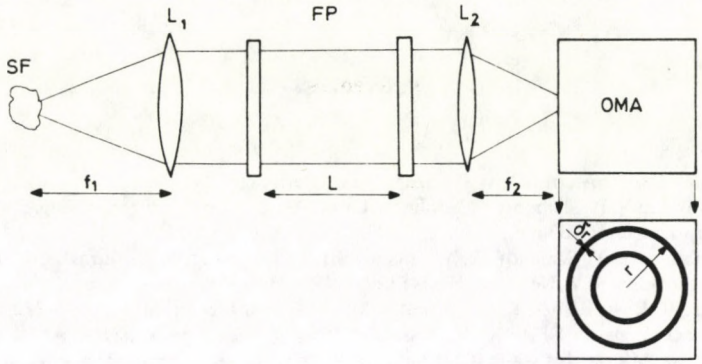

Fig. 3. A common Fabry–Pérot arrangement. SF is the source of the fluorescence, f_1 and f_2 are the focal lengths of the lenses L_1 and L_2, respectively, FP is the Fabry–Pérot interferometer, L is the distance between its plates

$r \sim 1$ mm (< 5 mm) and $\delta r \sim 0.02$ mm according to the requirements. With this choice we achieve the maximum intensity of the light on the target of the OMA which is limited by the spatial resolution.

Finally, let us discuss the sensitivity of our method. Typical excitation volume and observation solid angle in tokamak experiments are 1 cm^3 and 10^{-3} sr, respectively [5]. The smallest total atom density measured in tokamak experiments was $n \sim 10^{12}$ l/m^3 [5]. Taking in the expression (2) the factors other than n, V and Ω to be in the range of unity, we obtain for the number of photons achieving the detector $N \sim 10^2$ in $\delta\tilde{\nu}'_D = 0.118$ cm^{-1} bandwidth. The maximum sensitivity of the OMA described in [8] with cooled target is about 1–5 photons/s channel. As spatial resolution of 20 μm corresponds to 5 channels in circular scanning mode [8], the 10^2 photons are detected by 5 channels i.e. 20 photons/channel which is more than the limiting sensitivity of 1–5 photons/channel. That means that the 10^{12} l/m^3 impurity

density can be reliably detected by this measuring set up also. The accuracy of determining the velocity profile in this case is about 10%, which can be better at the centre of the Doppler profile and worse at the tail of the line. This accuracy is acceptable in experiments performed on tokamaks.

5. Summary

An experimental arrangement intended to reduce data acquisition time of velocity distribution and flux measurements in experiments performed on fusion devices is analysed. If the excitation of the impurity atoms is made by a broad band laser irradiation ($\Delta\nu_{\mathrm{LASER}} > \nu'_{\mathrm{DOPPLER}}$) and the detection of the fluorescence light is made by a Fabry–Pérot interferometer monitored by a modified vidicon type OMA, velocity distribution and flux of atoms can be measured by using only one laser shot.

References

1. W. Demtröder, Laser Spectroscopy, Springer Verlag, Berlin etc., 1981.
2. V. S. Letokhov and V. P. Chebotayev, Nonlinear Laser Spectroscopy, Springer Verlag, Berlin etc., 1977.
3. D. D. Burgess and C. H. Skinner, J. Phys. B, *B7*, L297, 1974.
4. G. T. Razdobarin, V. V. Semenov, L. V. Sokolova, I. P. Folomkin, V. S. Burakov, P. Ya. Misakov, P. A. Namenkov and S. V. Nechaev, Nucl. Fusion, *19*, 1439, 1979.
5. C. H. Muller III, D. R. Eames, K. H. Burrell and S. C. Bates, J. Nucl. Mater., *111–112*, 56, 1982.
6. P. Bogen, Proceedings of ICPIG XVI., Düsseldorf 1983., Invited Papers, p. 164.
7. K. Muraoka, M. Maeda, T. Okada, C. Honda, M. Hamamoto, K. Uchino, T. Kajiwara, Y. Matsuda, Y. Itsumi, M. Akazaki, T. Kawamoto, R. Kumazawa, S. Okamura, H. R. Garner and RFC-XX-M Group, J. Nucl. Mater., *128–129*, 977, 1984.
8. J. Fünfschilling, M. Brülhart, H. R. Hidber and I. Zschokke-Gränacher, Rev. Sci. Instrum., *55(2)*, 153, 1984.
9. E. Hintz, J. Nucl. Mater., *93–94*, 86, 1980.
10. M. Born and E. Wolf, Principles of Optics, Pergamon Press, Oxford etc., 1970.
11. G. Hird, Izmeren'ie Lazernih Parametrov, Mir, Moscow, 1970.

Acta Physica Hungarica, 63 (3—4), pp. 353—364 (1988)

SOME SOLUTIONS OF EINSTEIN–BORN–INFELD FIELD EQUATIONS

Z. K. VAD

Baja Observatory of the Hungarian Academy of Sciences
6501 Baja, Hungary

(Received in revised form 23 July 1986)

The equations of Born–Infeld electrodynamics are coupled with the Einstein equations. A three-parameter family of spherical static solutions of these equations is presented which describe the gravitational field of a charged source having mass and magnetic monopole moment. Among these solutions, considering the ratio of mass and charge a wide class proves to be different from the well-known Reissner–Nordström type.

1. Introduction

One of the purposes of the classical field theory is to make it possible to deduce the mechanical characteristics of particles from those of the field produced by a particle.

This program cannot be carried out within the domain of classical electrodynamics. There are two basic facts that prevent the identification of the corresponding physical quantities. The first of these is that the Maxwell theory assigns an infinite value to the mass-energy. The second is that the energy and momentum deduced from the stress-energy tensor of the field produced by a point-like particle do not transform as a four-vector. In order to remove these imperfections we might modify the classical electrodynamics to fulfil the requirements mentioned above (invariance properties, finite mass-energy and appropriate transformation law). A wide class of nonlinear electrodynamics can be constructed in this way. They are essentially based upon arbitrary assumptions. We investigate here the typical nonlinear effects in the theory constructed by Born and Infeld in 1930 [1]. Among the nonlinear electrodynamics the Born–Infeld theory is one of the simplest. In the following we will study how the nonlinearity manifests itself in the behaviour of well-known solutions of the coupled Einstein equations. The Born–Infeld theory is characterized by the following Lagrangian [1]:

$$L = \frac{b^2}{4\pi}(1 - \Phi^{\frac{1}{2}}). \tag{1.1}$$

Here the function Φ has the form:

$$\Phi = 1 + \frac{I_1}{2b^2} - \frac{I_2^2}{b^4},$$

where the quantities I_1 and I_2 are the scalar invariants of the field tensor $F_{\mu\nu}$, i.e.

$$I_1 = F_{\mu\nu}F^{\mu\nu}, \qquad I_2 = \frac{1}{4}F_{\mu\nu}F^{*\mu\nu}.$$

The symbol * denotes the duality operation in the usual way:

$$F^*_{\mu\nu} = \frac{1}{2}\sqrt{-g}\,\epsilon_{\mu\nu\alpha\beta}F^{\alpha\beta}.$$

Physically the parameter b corresponds to the largest possible value of the field strength [1]. The Maxwell theory can be retained from the Born–Infeld one as b tends to infinity. Calculating the mass of an electron's field we get the expression [1]:

$$m_{el} = 1.2361\ldots e^{\frac{3}{2}}b^{\frac{1}{2}}.$$

We will use a system of units such that the gravitational constant G and the speed of light be equal to one.

2. The metric and field equations

The purpose of the present investigation is to derive some exact spherically symmetric, static solutions for the nonlinear electromagnetic field described by the Born–Infeld theory. This means we have four Killing vectors [2] $\mathbf{K}_i$ $(i=0, 1, 2, 3)$. It is well known that there exists an asymptotically flat coordinate system $(t, r, \vartheta, \varphi)$ in which the Killing vectors of this symmetry have the following form [3]:

$$\begin{aligned} K_0^\mu &= (1, 0, \quad 0, \qquad 0 \quad), \\ K_1^\mu &= (0, 0, \sin\varphi, \operatorname{ctg}\vartheta\cos\varphi), \\ K_2^\mu &= (0, 0, \cos\varphi, -\operatorname{ctg}\vartheta\sin\varphi), \\ K_3^\mu &= (0, 0, \quad 0, \qquad 1 \quad). \end{aligned} \tag{2.1}$$

We number the coordinates as

$$x^0 = t, \quad x^1 = r, \quad x^2 = \vartheta, \quad x^3 = \varphi.$$

In this coordinate system the line element has the form [4]:

$$ds^2 = -e^\nu dt^2 + e^\lambda dr^2 + r^2 d\Omega^2, \tag{2.2}$$

where λ and ν depend on r only, i.e. $\lambda=\lambda(r)$, $\nu=\nu(r)$. Calculating the relevant components of Einstein's tensor for the metric (2.2) we obtain the following equations [4]

$$8\pi T_1^1=-e^{-\lambda}\left(\frac{\nu'}{r}+\frac{1}{r^2}\right)+\frac{1}{r^2}, \tag{2.3}$$

$$8\pi T_0^0=-e^{-\lambda}\left(\frac{1}{r^2}-\frac{\lambda'}{r}\right)+\frac{1}{r^2}, \tag{2.4}$$

where $T_{\mu\nu}$ is the stress-energy tensor of the field and a comma denotes the derivative with respect to the coordinate r. In order to get the stress-energy tensor $T_{\mu\nu}$ we perform the variation $\delta(L\sqrt{-g})$ of Lagrangian (1.1) in such a way that the potentials are not varied while the components of the metric tensor are. This variation is given by the equation

$$\delta(L\sqrt{-g})=-\frac{1}{16\pi}\sqrt{-g}\,\Phi^{-\frac{1}{2}}\delta I_1+$$

$$+\frac{1}{4\pi b^2}\Phi^{-\frac{1}{2}}I_2\sqrt{-g}\,\delta I_2+L\delta\sqrt{-g}. \tag{2.5}$$

Calculating the variations of I_1 and I_2 we get

$$\delta I_1=2F_{\mu\nu}F^{\nu}_{\alpha}\,\delta g^{\mu\alpha} \tag{2.6}$$

and

$$\delta I_2=-\frac{I_2}{2}g_{\mu\nu}\delta g^{\mu\nu}+F^{*}_{\mu\alpha}F^{\alpha}_{\nu}\delta g^{\mu\nu}. \tag{2.7}$$

By means of expressions (2.5), (2.6), (2.7) $T_{\mu\nu}$ can be written in the form

$$T_{\mu\nu}=\frac{1}{4\pi}\{-\Phi^{-\frac{1}{2}}F_{\mu\alpha}F^{\alpha}_{\nu}-b^2(1-\Phi^{\frac{1}{2}})g_{\mu\nu}\}+\frac{1}{4\pi b^2}\cdot\frac{I_2^2}{\Phi^{\frac{1}{2}}}g_{\mu\nu}, \tag{2.8}$$

where we have taken into account the identity $F^{*}_{\mu\alpha}F^{\alpha}_{\nu}\equiv I_2 g_{\mu\nu}$. A straightforward computation yields the field equations corresponding to the Lagrangian (1.1):

$$\nabla_{\mu}\left(\Phi^{-\frac{1}{2}}\left\{F^{\nu\mu}-\frac{I_2}{b^2}F^{*\nu\mu}\right\}\right)=0. \tag{2.9}$$

Here ∇_{μ} indicates covariant derivation. It goes without saying that the integrability conditions

$$F^{*\mu\nu}{}_{;\nu}=0 \tag{2.10}$$

originating from the relation $\mathbf{F}=\mathbf{dA}$ have to be satisfied. Both the stress-energy tensor (2.8) and the field equations (2.9) go over to those of the Maxwell theory in the limit $b\to+\infty$.

Now we assume that the field $F_{\mu\nu}$ has the same symmetry as the metric (2.2), i.e.

$$\mathbf{L}_{\mathbf{K}_i}\mathbf{F}=0, \qquad (i=0,1,2,3), \tag{2.11}$$

where $\mathbf{L}_{\mathbf{K}}$ stands for the Lie derivative with respect to Killing vector $\mathbf{K}$. As it is well-known, the most general solution of equations (2.11) has the following form [5]

$$F_{tr}=E(r), \qquad F_{t\vartheta}=F_{t\varphi}=F_{r\vartheta}=F_{r\varphi}=0,$$
$$F_{\vartheta\varphi}=P(r)\sin\vartheta, \tag{2.12}$$

where functions E and P are arbitrary and depend on r only.

Equations (2.10) imply that P is constant. The corresponding vector potential can be expressed as

$$A_\mu=(\Psi(r),0,0,P(1-\cos\vartheta)) \tag{2.13}$$

and

$$E=-\frac{d\Psi}{dr}.$$

Taking into account all these restrictions, the stress-energy tensor $T_{\mu\nu}$ can be reduced to the form

$$4\pi T_0^0=4\pi T_1^1=-\Phi^{-\frac{1}{2}}e^{-(\lambda+\nu)}E^2-b^2(1-\Phi^{\frac{1}{2}})+b^{-2}\Phi^{-\frac{1}{2}}I_2^2. \tag{2.14}$$

$T_0^0=T_1^1$ implies that the derivative of $\lambda+\nu$ with respect to r vanishes, so we can choose $\lambda+\nu=0$, i.e. $g^{00}g^{11}=-1$. In this case the invariants and the function Φ can be expressed as

$$I_1=-2\left(E^2-\frac{P^2}{r^4}\right), \tag{2.15}$$

$$I_2=-\frac{P\cdot E}{r^2}, \tag{2.16}$$

$$\Phi=\left(1-\frac{E^2}{b^2}\right)\left(1+\frac{P^2}{b^2r^4}\right). \tag{2.17}$$

Performing these reductions in Eqs (2.9) we get the following equation for the scalar potential

$$\frac{d}{dr}(r^2D)=0, \tag{2.18}$$

where

$$D=\left(\frac{1+\dfrac{P^2}{b^2r^4}}{1-\dfrac{E^2}{b^2}}\right)^{\frac{1}{2}}E. \tag{2.19}$$

The solution of Eq. (2.18) is $D=\frac{e}{r^2}$, where e is a constant of integration. After a short computation we obtain

$$E=\frac{e}{\sqrt{r_0^4+r^4}}, \tag{2.20}$$

where

$$r_0^4:=\frac{e^2+P^2}{b^2}.$$

Substituting this into the right hand side of the expression (2.17) we easily get

$$\Phi=\frac{r_1^4+r^4}{r^4(r_0^4+r^4)}, \tag{2.21}$$

where

$$r_1^4:=\frac{P^2}{b^2}.$$

It should be noted that the source of the field can be imagined as a finite sphere having radius r_0. To verify this assertion we recall that

$$F^{\mu\nu}{}_{;\mu;\nu}=0. \tag{2.22}$$

Here the semicolon indicates a covariant derivative. So if we define the four-current in the following way

$$4\pi J^\mu=-F^{\mu\nu}{}_{;\nu}, \tag{2.23}$$

we get a local conservation law for the quantity J^μ, i.e.

$$J^\mu{}_{;\mu}=0. \tag{2.24}$$

In the classical electrodynamics the expression (2.23) is one of the pairs of the Maxwell equations. In our case (2.23) is the definition of the four-current. $F^{\mu\nu}{}_{;\nu}$ and J^μ are determined by field equations (2.9). Substituting solution (2.20) into the right hand side of (2.23) we get the following equation for the charge density $\rho=J^t\sqrt{g_{tt}}$:

$$4\pi\rho=\sqrt{g_{tt}}r^{-2}\frac{d}{dr}(r^2E). \tag{2.25}$$

The metric of the hypersurface $t=$constant is given as [4]

$$dl^2=\gamma_{ik}\,dx^i\,dx^k=g_{tt}^{-1}dr^2+r^2d\Omega^2. \tag{2.26}$$

So the charge of the source Q can be calculated by the integral

$$Q=\frac{1}{4\pi}\int_0^{+\infty}\int_0^{2\pi}\int_0^{\pi}\rho g_{tt}^{-\frac{1}{2}}r^2\sin\vartheta\,d\vartheta\,d\varphi\,dr, \tag{2.27}$$

i.e. the total charge of the source equals e. Outside the sphere with radius r_0 the charge density rapidly tends to zero. For this reason r_0 can be regarded as the effective radius of the source. Having determined the function Φ we can express T_0^0 in terms of r. So, eventually T_0^0 can be written as

$$4\pi T_0^0 = \frac{e^2}{r^2\sqrt{r_0^4+r^4}} - b^2\left(1 - \frac{r_1^4+r^4}{r^2\sqrt{r_0^4+r^4}}\right). \tag{2.28}$$

Now we are able to solve Eq. (2.4). After substituting $Y=r^{-1}e^{\lambda}$ this equation becomes separable and we obtain

$$e^{-\lambda} = 1 - \frac{2m}{r} + \frac{1}{r}\int_r^{+\infty} t^2 G(t)dt \equiv h(r), \tag{2.29}$$

where

$$r^2 G(r) = 2b^2\{\sqrt{r_0^4+r^4} - r^2\}. \tag{2.30}$$

It has been taken into account that λ should satisfy the Newtonian limit $1-e^{-\lambda} \to \frac{2m}{r}$ as r tends to infinity (m is the mass of the source). Summarizing these results, we have a solution of the coupled Einstein–Born–Infeld equations which corresponds to the field of an electrically and magnetically charged source having mass. The charge of the source is mainly contained within a sphere with radius r_0. The geometry of the space-time is described by the line element

$$ds^2 = -h(r)dt^2 + h^{-1}(r)dr^2 + r^2 d\Omega^2, \tag{2.31}$$

where h is given by (2.29) and (2.30). The potentials of the electromagnetic field are given by

$$A_t = \frac{e}{r_0}\int_{\frac{r}{r_0}}^{+\infty} \frac{dx}{\sqrt{1+x^4}}, \qquad A_r = A_\vartheta = 0, \qquad A_\varphi = P(1-\cos\vartheta). \tag{2.32}$$

We stress that the potential A_0 and field strength $E = -\frac{dA_t}{dr}$ have finite values at the origin $r=0$.

3. The behaviour of the metric

First we investigate the asymptotic form of the metric (2.31). By means of expanding r^2G in powers of $\frac{r}{r_0}$ we get the following form (in the case when $r > r_0$)

$$r^2 G(r) = \frac{e^2+P^2}{r^2} + \frac{1}{r^2} O\left(\left[\frac{r_0}{r}\right]^4\right). \tag{3.1}$$

Performing the integration on the right hand side of the expression in (2.29) we obtain the formula

$$h(r)=1-\frac{2m}{r}+\frac{e^2+P^2}{r^2}+\frac{1}{r^2}O\left(\left[\frac{r_0}{r}\right]^4\right), \tag{3.2}$$

which is valid for $r>r_0$. As one would expect, the line element (2.31) becomes a Reissner–Nordström one in the first approximation, as it is clear from expression (3.2). In the limit $b\to+\infty$, the approximation (3.2) holds for the whole interval $0<r<+\infty$ as $r_0\to 0$, so we get precisely the Reissner–Nordström line element. From the asymptotic form of the metric we can find out that the parameter m is the mass of the source and the parameters e, P are the electric charge and magnetic monopole charge, respectively.

To obtain some analytical properties of the function h of r, let us write it in the form

$$h(x)=\frac{x-2\tilde{m}+2(\tilde{e}^2+\tilde{P}^2)H(x)}{x}\equiv\frac{\Delta(x)}{x}. \tag{3.3}$$

Here x stands for $\dfrac{r}{r_0}$ and $\tilde{m}=\dfrac{m}{r_0}$, $\tilde{e}=\dfrac{e}{r_0}$, $\tilde{P}=\dfrac{P}{r_0}$, where we have introduced

$$H(x)\equiv\int_x^{+\infty}(\sqrt{1+x^4}-x^2)dx. \tag{3.4}$$

The behaviour of $h(x)$ is determined by the analytical properties of H. First we calculate some derivatives of H with respect to x:

$$H'(x)=-(\sqrt{1+x^4}-x^2), \tag{3.5}$$

$$H''(x)=2x\left(1-\frac{x^2}{\sqrt{1+x^4}}\right), \tag{3.6}$$

$$H'''(x)=2\left(1-\frac{3x^2+x^6}{(1+x^4)^{\frac{3}{2}}}\right). \tag{3.7}$$

It is clear from (3.5) that H monotonously decreases as a function of x. From expression (3.6) we conclude that the curve $H=H(x)$ is convex from below for $x>0$ ($x=0$ is a point of inflection).

This curve of H is schematically represented in Fig. 1. From this diagram we see that there exist at most two zeros of $h(x)$, for the zeros of h are determined by the intersection points of the curve of H and the straight line $-x+2\tilde{m}$. In the case when $\tilde{m}>(\tilde{e}^2+\tilde{P}^2)H(0)$ there exists only one zero and the graph of h does not differ qualitatively from that of the Schwarzschild type. When $\tilde{m}<(\tilde{e}^2+\tilde{P}^2)H(0)$ there are two possibilities:

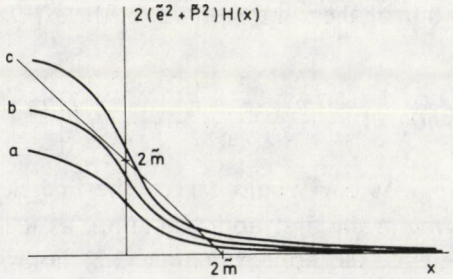

Fig. 1. The curves of $(\tilde{e}^2+\tilde{P}^2)H(x)$. The graphs *a*, *b*, *c* correspond to increasing values of $\tilde{e}^2+\tilde{P}^2$. The equation of the straight line appearing on the diagram is $-x+2\tilde{m}$. Its intersection points with the graph of $(\tilde{e}^2+\tilde{P}^2)H$ give the location of the horizons

When the derivative of $2(\tilde{e}^2+\tilde{P}^2)H$ at the origin is less than -1, i.e.

$$\sqrt{e^2+P^2} > \frac{1}{2b}, \tag{3.8}$$

(the special case $\tilde{m}=(\tilde{e}^2+\tilde{P}^2)H(0)$ will be discussed later), there exist two zeros, if $\tilde{m}$ is greater than a certain critical value $\tilde{m}_{\text{crit}}$, thus the graph of h is qualitatively similar to the Reissner–Nordström one. The existence of such a critical value of $\tilde{m}$ can be seen from Fig. 2. Zeros do not exist at values less than this critical value of $\tilde{m}$.

The second possibility is that

$$\sqrt{e^2+P^2} < \frac{1}{2b}, \qquad \text{i.e.} \quad 2(\tilde{e}^2+\tilde{P}^2)H'(0) > -1. \tag{3.9}$$

In this situation h has no zeros, as can easily be seen from Fig. 2. The solution being static, the zeros of h give the location of horizons, which are the singularities of the original coordinate system $(t, r, \vartheta, \varphi)$ (in fact they are pseudosingularities). We can get rid of these pseudosingularities by constructing a new, Kruskal-type coordinate

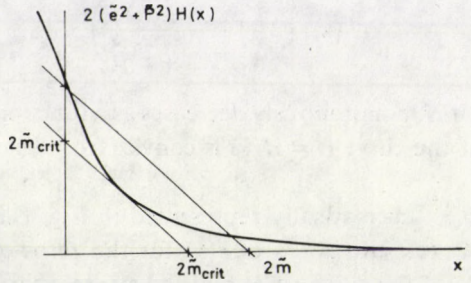

Fig. 2. The graph of $(\tilde{e}^2+\tilde{P}^2)H$ in the case when $\tilde{e}^2+\tilde{P}^2$ is so large that the function $(\tilde{e}^2+\tilde{P}^2)H$ has a tangential straight line with slope less than -1. The equation of the straight line with slope -1 determines the critical mass $\tilde{m}_{\text{crit}}$

system $(u, v, \vartheta, \varphi)$ in which the path of light becomes a straight line with slope ± 1. This means that we perform a coordinate transformation

$$u=u(t, r), \qquad v=v(t, r) \tag{3.10}$$

such that the line element acquires the form

$$ds^2=f^2(u, v)\,(du^2-dv^2)+r^2 d\Omega^2. \tag{3.11}$$

The function f^2 must be regular and positive at the pseudosingularities. Following the work of Graves and Brill [6] for the case of a single zero we find an appropriate transformation

$$u=2Ae^{\gamma r^*}\cdot\begin{Bmatrix}\cosh \gamma t\\ \sinh \gamma t\end{Bmatrix}, \tag{3.12}$$

$$v=2Ae^{\gamma r^*}\cdot\begin{Bmatrix}\sinh \gamma t\\ \cosh \gamma t\end{Bmatrix}, \tag{3.13}$$

where r^* is a "tortoise"-type coordinate for which $dr^*=h^{-1}dr$ holds; moreover, A and γ are constants. The choice of the function in the curly brackets depends on the intervals where $h \gtrless 0$, respectively. The function f^2 is given by the following formula:

$$f^2=h(r)\,e^{-2\gamma r^*}/4A^2\gamma\,. \tag{3.14}$$

The constant γ has to be chosen in such a way that f^2 be regular and positive at the zeros of $h\,r=r_i\,(i=1, 2)$. Expanding the function h in powers of $(r-r_i)$ around the pseudosingularities r_i one can see that such a choice is possible if and only if r_i is a simple zero of h. For the constant γ we obtain

$$\gamma_i=1+\frac{2(e^2+P^2)}{r_0^2}H'\left(\frac{r_i}{r_0}\right). \tag{3.15}$$

As a matter of fact, a single transformation like (3.12) and (3.13) cannot regularize more than one horizons, so the number of necessary transformations depends on the number of horizons.

Using exterior differential forms one can easily compute [3] the Riemann tensor in the following "static" orthonormal frame:

$$\begin{aligned} e_{\hat{t}}&=h^{-\frac{1}{2}}\frac{\partial}{\partial t},\\ e_{\hat{r}}&=h^{\frac{1}{2}}\frac{\partial}{\partial r},\\ e_{\hat{\vartheta}}&=r^{-1}\frac{\partial}{\partial \vartheta},\\ e_{\hat{\varphi}}&=(r\sin\vartheta)^{-1}\frac{\partial}{\partial \varphi}. \end{aligned} \tag{3.16}$$

For the nonvanishing components of the Riemann tensor we get

$$R_{\hat{t}\hat{r}\hat{t}\hat{r}} = \frac{h''}{2}, \tag{3.17}$$

$$R_{\hat{t}\hat{\vartheta}\hat{t}\hat{\vartheta}} = R_{\hat{t}\hat{\varphi}\hat{t}\hat{\varphi}} = \frac{h'}{2r}, \tag{3.18}$$

$$R_{\hat{r}\hat{\vartheta}\hat{r}\hat{\vartheta}} = R_{\hat{r}\hat{\varphi}\hat{r}\hat{\varphi}} = -\frac{h'}{2r}, \tag{3.19}$$

$$R_{\hat{\vartheta}\hat{\varphi}\hat{\vartheta}\hat{\varphi}} = \frac{1-h}{r^2}. \tag{3.20}$$

In each case the place $r=0$ is a real singularity of the space-time as it can be seen from the fact that the invariant $I = R_{\hat{\alpha}\hat{\beta}\hat{\gamma}\hat{\delta}} R^{\hat{\alpha}\hat{\beta}\hat{\gamma}\hat{\delta}}$ tends to infinity and the determinant of the metric tensor tends to zero as $r \to 0$. It is of interest to note that the geometry of the neighbourhood of the origin $r=0$ has particular features if the ratio $\frac{\tilde{m}}{\tilde{e}^2+\tilde{P}^2}$ is $H(0)$. In this situation there exists only a single horizon (see Fig. 3) and $-2\tilde{m}+(\tilde{P}^2+\tilde{e}^2)H(x)$ tends to zero as $r \to 0$, so

$$\lim_{r\to 0} h(r) = 1 - 2b\sqrt{e^2+P^2}. \tag{3.21}$$

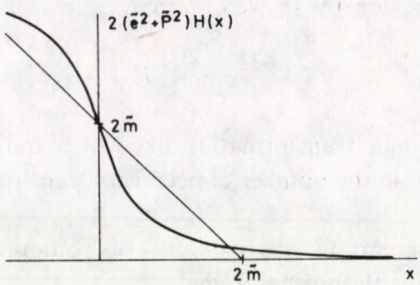

Fig. 3. The graph of $(\tilde{e}^2+\tilde{P}^2)H$ in the critical case when $\tilde{m}=(\tilde{e}^2+\tilde{P}^2)H(0)$

Moreover, by means of expression (3.6) we can see that h' vanishes at the origin. From (3.7) it follows that h'' is finite and positive there. So the components of the Riemann tensor appearing in expressions (3.17), (3.18) and (3.19) are finite (the) component (3.20) diverges as $r \to 0$). Now, let us consider an observer falling freely and radially into the origin $r=0$, carrying an orthonormal tetrad e_τ, e_ρ, e_ϑ, e_φ, along with him as he falls. The tidal forces felt by the observer are measured by the components of the Riemann tensor with respect to his orthonormal frame. This frame

can be connected with the "static" tetrad (3.16) by a boost with parameter Ψ in the r direction for e_τ is the four-velocity of the given geodesic, i.e.

$$e_\tau = \cosh \Psi e_{\hat{t}} + \sinh \Psi e_{\hat{r}} \,,$$

$$e_\rho = \sinh \Psi e_{\hat{t}} + \cosh \Psi e_{\hat{r}} \,,$$

$$e_{\vartheta'} = e_{\hat{\vartheta}}, \qquad e_{\varphi'} = e_{\hat{\varphi}}. \tag{3.22}$$

Like in the Schwarzschild case it can be shown that the "static frame" components (3.17)–(3.20) are invariant for the boost (3.22). For this reason the equation of the geodesic deviation evaluated in the local inertial frame of the observer is

$$\frac{D^2 \xi^j}{d\tau^2} = -R_{\tau j \tau k} \xi^k. \tag{3.23}$$

We have seen that all of the components $R_{\tau j \tau k}$ appearing in Eq. (3.23) are finite. Unlike the Schwarzschild case this equation says that two freely moving particles, momentarily at rest in the observer's local, inertial frame, and separated by the 3-vector $\xi = \xi^j e_j$ will accelerate apart with a finite relative acceleration. In this way an observer travelling along a radial geodesic feels finite tidal forces but he cannot be represented on the space-time after a finite lapse of his proper time.

4. Conclusions

The modification of the Maxwell equations that makes them nonlinear changes the character of the spherically symmetric, static solutions of the coupled field equations with the parameters m, e, P. These new solutions, unlike the Reissner–Nordström ones which have a single horizon only in the case $m^2 = e^2 + P^2$, have a single horizon only if $\tilde{m} > (\tilde{e}^2 + \tilde{P}^2) H(0)$. Moreover, in this situation the dependence of the metric on r agrees with that of the Schwarzschild metric. These solutions show features similar to the Reissner–Nordström metric only if $e^2 + P^2$ has a sufficiently large value and $\tilde{m}$ is in a certain narrow interval. The singular behaviour of the space-time geometry near the origin $r = 0$ decreases if m reaches the value $(\tilde{e}^2 + \tilde{P}^2) H(0)$. In this situation observers travelling towards the singularity feel finite tidal forces.

Acknowledgement

I would like to thank Dr. Á. Sebestyén for helpful discussion and encouragement.

References

1. M. Born and L. Infeld, Proc. Roy. Soc. A*144*, 425, 1934.
2. W. M. Boothby, An Introduction to Differentiable Manifolds and Riemannian Geometry, Academic Press, New York, 1976.
3. L. Landau and E. Lifschitz, The Classical Theory of Fields, Pergamon Press, London and New York, 1975.
5. D. D. Kramer and H. Stephani, Exact Solutions of Einsteins Field Equations, VEB Deutscher Verlag der Wiessenschaften, Berlin 1980.
6. J. C. Graves and D. R. Brill, Phys. Rev., *120*, 1507, 1960.

Acta Physica Hungarica, 63 (3—4), pp. 365—372 (1988)

HOLLOW CATHODE AND HIGH VOLTAGE PLANE CATHODE TYPE DISCHARGES FOR CHARGE TRANSFER REACTIONS

K. RÓZSA, P. MEZEI, P. APAI, M. JÁNOSSY

Central Research Institute for Physics
1525 Budapest, Hungary

S. CHINEN

Toyota Technical College, Department of Physics
471 Toyota, Japan

F. HOWORKA, I. KUEN and M. GRINDHAMMER

Institute for Experimental Physics, University of Innsbruck
A 6020 Innsbruck, Austria

(Received in revised form 31 July 1986)

Decreasing the pressure in the hollow cathode discharge, simultaneously ensuring room for the expanding negative glow, allows the discharge to transit from the hollow cathode type into a high voltage discharge where the cathode cavity is filled with the cathode glow. Such an arrangement seems to be very effective for endoergic charge transfer excitation as it was observed in a He–Cu system. Voltage–current characteristics of the transition region are also presented.

1. Introduction

Penning and Veenemans [1] described in 1930 the shiny part of the discharge called cathode glow at the cathode surface in cold cathode abnormal glow discharges. The phenomenon is due to the excitation of gas atoms and molecules by positive ions formed in the negative glow and in the cathode dark space, which are accelerated by the cathode fall.

This effect has recently been studied by Kuen and Howorka [2] in a cylindrical hollow cathode discharge. In a He–Xe mixture the intensity of the Xe II 104.8, 98.9 and 97.3 nm lines shows a maximum near the cathode surface. A similar effect was found on N II resonant lines (64.5 and 108.5 nm) in an He–N_2 mixture [3]. All of these lines are believed to be excited by fast ions via endoergic charge transfer.

Reprint requests to: K. Rózsa, Central Research Institute for Physics, H-1525 Budapest, P.O.B. 49. Hungary

To use fast ion excitation for laser purposes, however, it is necessary to concentrate the cathode glow in a similar way like the negative glow is concentrated in the hollow cathode discharge. As in the cathode region the length of the different shiny and dark spaces are increasing with decreasing pressure, to fill the cavity with the cathode glow we need lower pressure than in the conventional hollow cathode discharge having the same cavity diameter. On the other hand, a room has to be ensured for the expanding negative glow to avoid the phenomenon of the obstructed discharge. In such an arrangement using a Cu cathode and He as a filling gas we have observed endoergic charge transfer between He ions and the sputtered Cu atoms [4].

A schematic cross section of the discharge tube with the different parts of the discharge is illustrated in Fig. 1. Fig. 1a (relatively high pressure) shows the hollow cathode discharge. Fig. 1b shows the discharge at lower pressure. The room above the cathode is filled now with the expanded negative glow, while the cavity matches the size of the cathode glow. As the cavity diameter is much smaller than the length of the negative glow we may call this discharge a plane cathode type high voltage discharge.

In this paper we report detailed measurements on the current–voltage characteristics of these two discharges and the transition region. Intensities of different spectral lines measured in the cathode cavity are also compared.

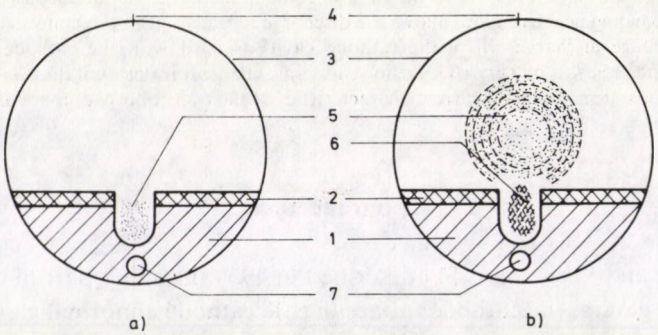

Fig. 1. Discharge arrangement to study fast ion excitation 1. cathode, 2. insulator, 3. glass envelope, 4. anode, 5. negative glow, 6. cathode glow, 7. water cooling. In Fig. 1a the pressure is high enough to form a hollow cathode discharge. In Fig. 1b the negative glow is much larger and the cavity is filled with the cathode glow, due to the decreased pressure

2. Experimental

Measurements were carried out using 50 Hz half wave rectified a.c. and direct current as well. In Fig. 2 the electrical arrangement of the a.c. measurements is shown. As a ballast resistor 8 electric light bulbs (220 V, 40 W) were connected in series to the discharge tube.

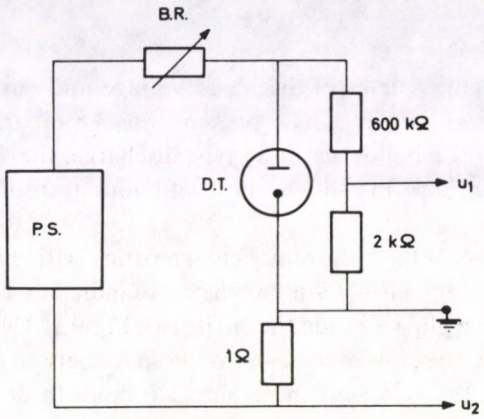

Fig. 2. Electrical arrangement. P.S.: power supply; B.R.: ballast resistor; D.T.: discharge tube. U_1 voltage is proportional to the discharge voltage, U_2 to the current

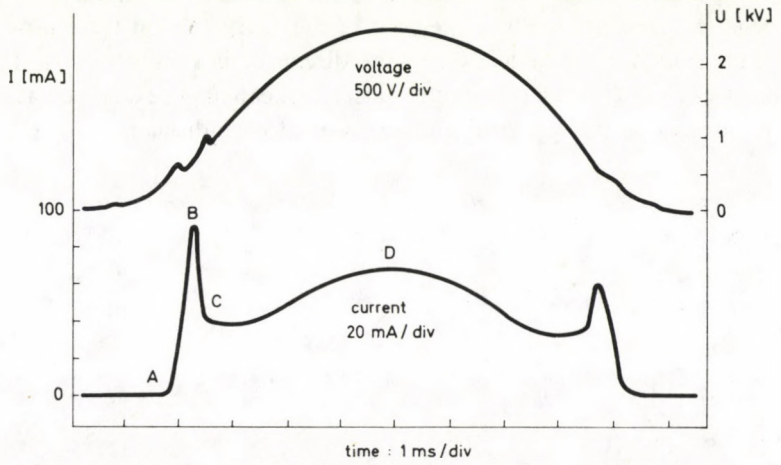

Fig. 3. Oscilloscope curves of discharge voltage and current as they were obtained in a.c. measurement at a pressure of 4.8 mbar. A–B: hollow cathode type discharge, B–C: transition region, C–D: plane cathode type discharge

In the case of the d.c. measurements high voltage power supply and high power ballast resistor were used. The discharge tube used for d.c. measurements has water-cooled cathode.

In all the experiments the diameter of the cathode cavity was 5 mm and He was used as the filling gas.

3. Results

Typical oscilloscope curves of discharge voltage and current obtained in a.c. measurements are shown in Fig. 3. The pressure was 4.8 mbar. The AB part of the curves corresponds to the hollow cathode type discharge, the CD part to the plane cathode type discharge and BC shows the continuous transition between the two stages.

Fig. 4 shows the voltage–current characteristics with halfwave rectified a.c. excitation. At the pressure value of 9 mbar the curve indicates a hollow cathode type behaviour. The negative glow is inside the cavity (see Fig. 1a). Decreasing the pressure below 4 mbar the negative glow expands into the space between the cathode and the anode (Fig. 1b), while the voltage is increasing 3–6 times to the value of that of the hollow cathode discharge. The negative slope part corresponds to the BC part of the curve shown in Fig. 3.

There is an intermediate pressure region (around 5 mbar) where the transition between these two types of discharges can be observed. In this case first the voltage is increasing with increasing current and still a hollow cathode discharge exists. Then the curve has a negative slope; the voltage increases further while the current decreases and the negative glow gradually comes out of the cavity. When the characteristics has a positive slope again the feature of the discharge is similar to Fig. 1b. These measurements indicate that the state of the discharge can also be changed at constant pressure by increasing the electrical input power into the discharge.

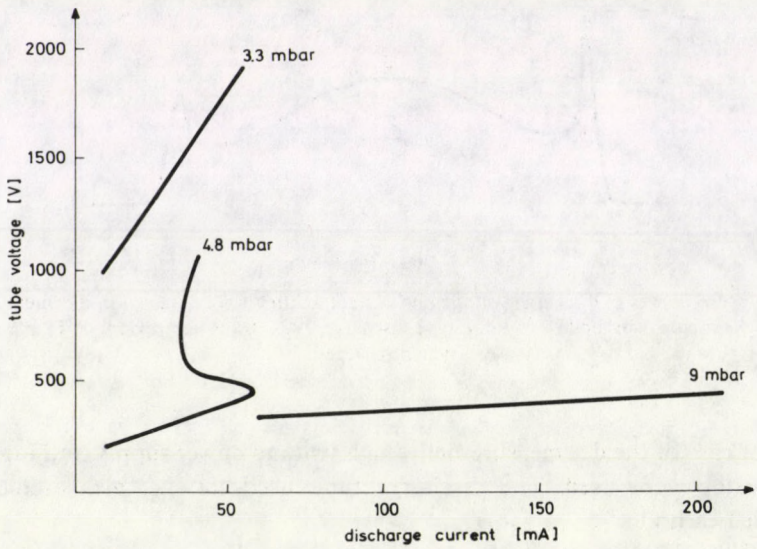

Fig. 4. Voltage–current characteristics of the discharge at different He pressures using pulsed excitation. At 9 mbar conventional hollow cathode discharge, at 3.3 mbar flat cathode discharge while at 4.8 mbar the transition region can be seen

Similar features were found in the direct current measurements. The voltage–current characteristics can be seen in Fig. 5. Here the transition was also observed around the same pressure region as in the a.c. measurements.

With decreasing pressure the transition region of the characteristics is gradually disappearing. Around 4 mbar a short beginning part of the curve still indicates the hollow cathode discharge but shortly after we can see the plane cathode like cathode glow behaviour. With further decreasing pressure the characteristics only has one inflexion point. Below 2 mbar the characteristics shows the typical cathode glow behaviour with no starting part and no inflexion point.

Comparing the d.c. measurements of Fig. 5 with the curves of pulsed excitation in Fig. 4 it can be seen that the turning point can be observed even at higher pressure using d.c. excitation. The reason of this may be due to temperature effects. The gas temperature in the cavity is higher in the d.c. discharge. Having large ballast volume the gas density in the cavity may be similar to that in lower pressure using pulsed excitation. This explanation is supported by the observed spontaneous transition from the hollow cathode type to the plane cathode type discharge. The transition usually occurred after one–two minutes of operating time depending on the actual current and pressure.

The negative slope of the curves depends on the characteristics of the electrical power supply as well. Exciting the discharge with an ideal current generator the negative slope should not exist. Increasing the value of the ballast resistors we found that the current region where the negative slope exists is decreasing.

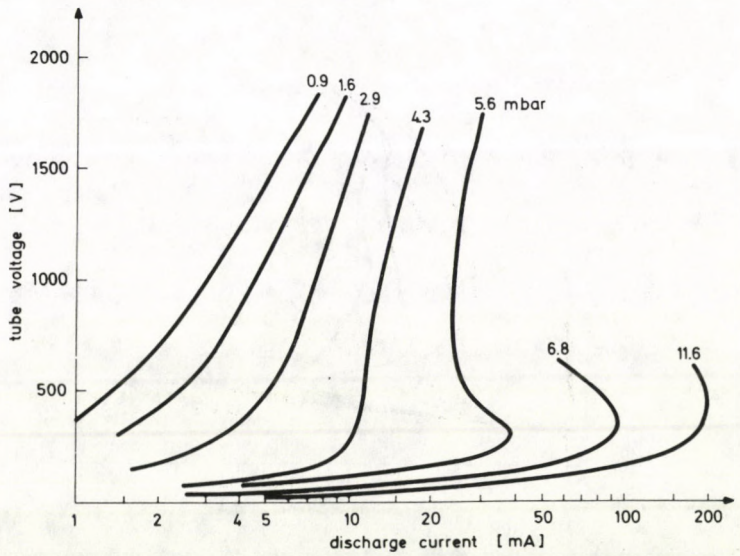

Fig. 5. Voltage–current characteristics of the discharge at different He pressures excited by direct current

This effect is shown in Fig. 6 where the voltage–current characteristics obtained in d.c. discharge are presented at pressures 4.6 and 5.3 mbar. At the higher pressure only hollow cathode discharge behaviour was found up to 120 mA. Two curves were measured at both pressures using 2.46 and 9.4 kohm ballast resistors. In the case of 2.46 kohm resistor the whole transition curve was stable. Using 9.4 kohm ballast resistor where the turning point was reached the discharge rapidly passed the negative slope of the discharge. At still higher resistors the transition became very fast but then due to the limited voltage of our power supply we could not measure the high voltage type discharge. The curves were directly plotted by an X–Y recorder. The continuous lines were plotted as the input electric power was increased and the dashed lines as it was decreased. The obtained hysteresis is probably due to the temperature effect. After the high electric input power the gas density of the cathode cavity may be smaller due to the higher local temperature of the gas.

The plane cathode type discharge concentrates the cathode glow into the cathode cavity. The high voltage of this discharge accelerates the ions into the cavity and makes favourable conditions for endoergic charge transfer excitations.

For studying charge transfer reactions we measured the intensities of the 493.1 and 436.5 nm Cu ion lines as a function of the pressure. The energies of the upper levels of these transitions from the atomic ground state are 24.58 and 25.69 eV, respectively. Compared to the ionization energy of the He (24.586 eV), the upper level of the 493.1 nm transition can be excited by thermal energy charge transfer, however, the 436.5 nm transition is probably excited by fast ions via endoergic charge transfer. The intensities were always measured in the centre of the cathode cavity.

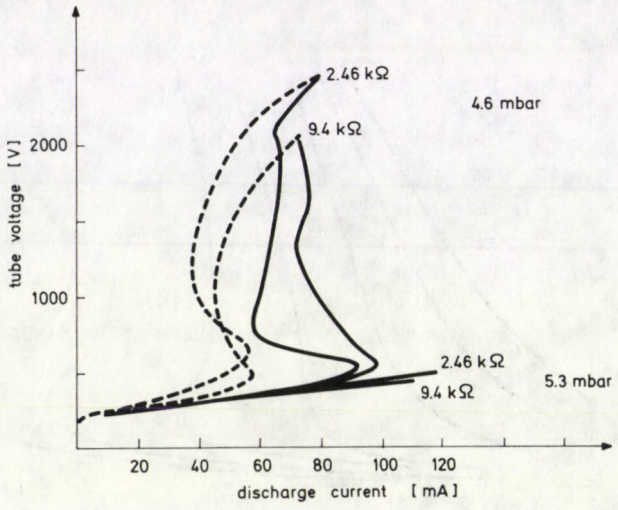

Fig. 6. Voltage–current characteristics of the discharge excited by direct current using different ballast resistors. At 4.6 mbar a hysteresis can be seen. The solid lines represent the increasing and the dashed lines the decreasing discharge current (5.3 mbar)

Thus, the higher pressure points correspond to the hollow cathode discharge, while the low pressure part of the curves shows the intensities in the cathode glow.

The results can be seen in Fig. 7 where the intensities of both spectral lines are plotted as a function of the pressure at 200 mA discharge current. Both lines have one maximum in the hollow cathode discharge range (7–15 mbar). In the high voltage type discharge the intensities increased again (probably due to the stronger sputtering).

However, the Cu II line excited by thermal energy charge transfer was about six times more intense in the negative glow than in the cathode glow region. On the other hand, the 436.5 nm line was twice as strong in the cathode glow as in the hollow cathode discharge due to the presence of fast ions in the cathode cavity using the high voltage type cathode glow discharge.

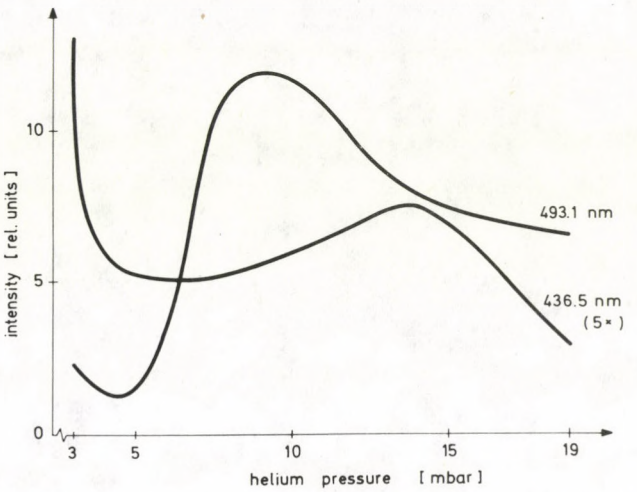

Fig. 7. Pressure dependence of two Cu II lines at 200 mA discharge current. Above 8 mbar we have a hollow cathode discharge, at lower pressure a flat cathode discharge. The 436.5 nm line is excited by endoergic and the 493.1 nm line by thermal energy charge transfer

Acknowledgements

Thanks are due to Prof. K. G. Müller (Univ. Essen), to Dr. G. Rubin, to Dr. L. Csillag (CRIP Budapest) and to Prof. K. Fujii (Ibaraki University) for helpful discussions and to Mr. J. Tóth for the mechanical construction of the discharge tube and for help in the measurements.

References

1. F. M. Penning and C. F. Veenemans, Z. Physik, *62*, 1930.
2. W. Federer, I. Kuen, W. Lindinger, W. Dobler and F. Howorka, Proc. 3rd Int. Swarm Seminar, Innsbruck, p. 174, 1983.
3. F. Howorka, I. Kuen, XVI Int. Conference on Phenomena in Ionized Gases (ICPIG), Book of Abstracts, p. 560, 1983.
4. K. Rózsa, F. Howorka, I. Kuen, S. Chinen, P. Apai, P. Mezei and M. Jánossy, Contr. 4th Symposium on Atomic and Surface Physics, Maria Alm, p. 66, 1984.

Acta Physica Hungarica, 63 (3—4), pp. 373—375 (1988)

SHORT COMMUNICATIONS

INFLUENCE OF QUASISTATIONARY STATES ON RESONANT SCATTERING OF ELECTRONS BY ALKALI ATOMS

I. I. CHERLENYAK, V. I. LENGYEL

Uzhgorod State University, Uzhgorod 294000, USSR

and

E. P. SABAD

Uzhgorod Department of Institute for Nuclear Research
Academy of Sciences of the Ukrainian SSR
Uzhgorod 294000, USSR

(Received 23 July 1985)

In analogy with the resonant scattering of nucleons on nuclei, which occurs via the intermediate phase, namely the formation of the short-lived compound state, the scattering of electrons on atoms also has resonance character, which is due to the formation of quasistationary autodetachment states (AS).

For the description of these processes the Feshbach method turned out to be very fruitful. This method was first developed for the description of nuclear scattering and later, with minor corrections, which take into account the special features of atomic systems, it was adopted to electron–atom scattering. But in full extent the Feshbach method seems to be quite complicated and cumbersome.

In this work we report the results of calculations of elastic electron–lithium and electron–sodium scattering as well as of the excitation of the 2p level of the Li atom. The calculations were carried by using the modified Feshbach method (MFM) suggested by Balashov et al [1] and applied by us to the description of the resonant scattering of electrons on ions and atoms [2]. We believe that the MFM can also be successfully applied to the description of nuclear scattering. However, in the case of electron–atom scattering where the exact form of interaction between the particles is known the approbation of this method can be carried out with greater confidence.

According to MFM the wave function (WF) of the system "incident particle + + target" can be represented in a form

$$\Psi\, LS\pi(\mathbf{r}_1, \ldots, \mathbf{r}_N, \mathbf{r}) = \sum_\alpha \hat{A}\,[\psi_\alpha(\mathbf{r}_1, \ldots, \mathbf{r}_N) F_\alpha(\mathbf{r})] + \\ + \sum_\mu \Lambda_\mu \Phi_\mu(\mathbf{r}_1, {}_N; \mathbf{r}_N, \mathbf{r}). \qquad (1)$$

Here $\hat{A}$ is the antisymmetrization operator, ψ_α are duly symmetrized atom WF, L, S, π are orbital momentum, spin and parity of the system, respectively. According to MFM the sum over α had to contain only those channels which are open at a given energy. Functions Φ_μ describe the AS of the negative ion Li^- or Na^- and are found by diagonalizing the Hamiltonian of the system on the closed channels subspace. Namely, functions Φ_μ are constructed in the following way

$$\Phi_\mu = \sum_{n_1 l_1 n_2 l_2} \beta_\mu(n_1 l_1, n_2 l_2; \mathrm{LMS}) \Theta^{\mathrm{LMS}}_{n_1 l_1 n_2 l_2}, \tag{2}$$

$$\Theta^{\mathrm{LMS}}_{n_1 l_1 n_2 l_2} = \sum_{m_1 m_2 \mu_1 \mu_2} C^{\mathrm{LM}}_{l_1 m_2 l_2 m_2} C^{\mathrm{SMs}}_{\frac{1}{2}\mu_1 \frac{1}{2}\mu_2} \hat{A}[\Psi_{\mathrm{core}} \varphi_{n_1 l_1 m_2 \mu_1} \varphi_{n_2 l_2 m_2 \mu_2}], \tag{3}$$

where $C^{\mathrm{LM}}_{l_1 m_1 l_2 m_2}$ are vector addition coefficients, ψ_{core} are WF of the core (singly ionized positive ion), $\varphi_{nlm\mu}$ are WF of electrons which move in the field of the core. Substitution of WF (1) into the Schrödinger equation which is taken in a projected form

$$\langle \delta\Psi | H - E | \Psi \rangle = 0 \tag{4}$$

brings us to a system of equations for the functions $F_\alpha(\mathbf{r})$ and coefficients A_μ [2]. Using the solution of the system of open channels equations which are found via direct numerical solution as well as using WF (2) obtained beforehand we obtain under certain conditions [2] the expression for the transition matrix in a closed form which contains resonance terms of a Breit–Wigner type.

In Fig. 1 the calculated cross-sections both of elastic scattering and the excitation of the $2p$ level of the Li atom for a scattering angle of 90° are shown. The calculations exhibit the presence of three resonances below $3s$ threshold Li, namely $^1S^e$ ($E = 3.09$ eV, $\Gamma = 0.08$ eV), $^3P^0$ ($E = 3.28$ eV, $\Gamma = 0.12$ eV), $^3S^e$ ($E = 3.36$ eV, $\Gamma = 0.07$ eV) which

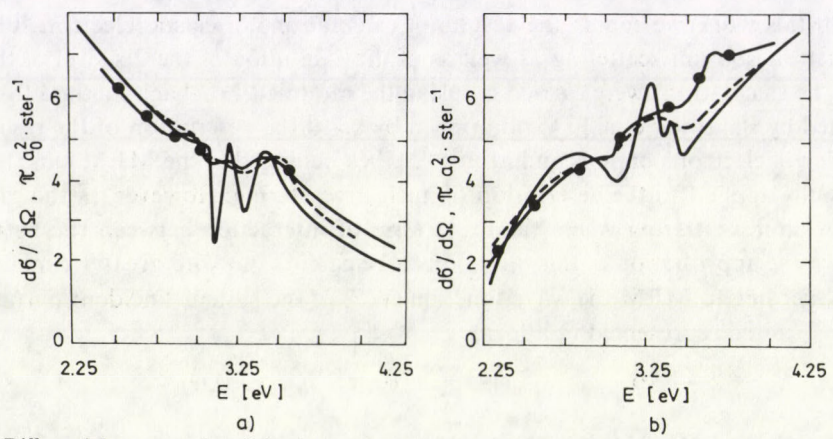

Fig. 1. Differential cross-section of elastic e + Li scattering (a) and $2p$ level excitation at 90° (b) as a function of energy: ———present calculation; — — —averaged calculation; ●—●—● experiment [3]

are due to the formation of AS. In this Figure the results of experimental measurements are also shown [3]. As is seen from the Figure, the theoretical cross-section which is averaged over electron energy distribution in the beam ($\Delta = 0.3$ eV) coincides quite well with the experiment [3].

In Fig. 2 the partial cross-sections of scattering of ultracold electrons on Na are shown. At the energy ~ 0.01 eV the phase-shifts and corresponding cross-sections have resonance behaviour, which is due to the quasistationary state of elastic type, namely tunnelling along translational degree of freedom (shape-resonance).

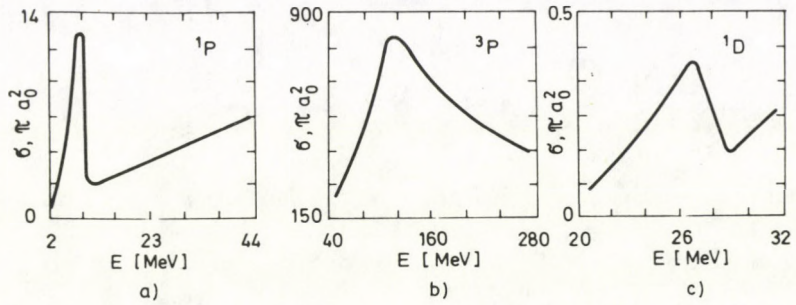

Fig. 2. Partial cross-sections of elastic e+Na scattering: a — ^1P wave; b — ^3P wave; c — ^1D wave

References

1. V. V. Balashov, S. I. Grishanova, I. M. Kruglova and V. S. Senashenko, Opt. and Spectr. (USSR), *28*, 859, 1970.
2. M. I. Haysak, V. I. Lengyel, V. T. Navrotsky and E. P. Sabad, Ukr. Phys. J. (USSR), *27*, 1617, 1982.
3. S. M. Kazakov, V. I. Lengyel, E. A. Masalowich, E. P. Sabad, K. V. Khristoforov and I. I. Cherlenyak, Ukr. Phys. J. (USSR), *30*, 537, 1985.

Acta Physica Hungarica, 63 (3—4), pp. 377—380 (1988)

MODIFIED FESHBACH METHOD FOR THE DESCRIPTION OF ELECTRON–ATOM SCATTERING

V. I. LENGYEL, V. T. NAVROTSKY

Uzhgorod State University, Uzhgorod 294000, USSR

and

E. P. SABAD

Uzhgorod Department of Institute for Nuclear Research
Academy of Sciences of the Ukrainian SSR
Uzhgorod 294000, USSR

(Received in revised form 15 May 1986)

The study of resonances in nuclear–nucleon scattering is a very rich source of knowledge about the structure of nuclei which allows one to carry out a careful selection of theoretical models, on the one hand, and is important for applications on the other. The foundations of the general theory of resonance phenomena in a nuclear scattering were laid by Feshbach (see, e.g. [1], and literature cited there). Feshbach's approach is grounded on N. Bohr's idea about the short-lived compound state which is formed as a result of capturing the incident nucleon by the target. It turned out that in collision processes of electrons with atoms and ions the quasistationary short-lived states of the "incident electron + target" system also play an important role. Since the main mode of decay of these states is a radiation-free transition of electron into a continuum, these states were called autoionizing states (AIS). Their decay is manifested in a resonance structure of scattering cross-sections.

The main features of Feshbach approach turned out to be very fruitful in a theory of electron–atom collisions and allowed to obtain a dynamical description of resonances in atomic scattering. However, the realization of Feshbach's method in its full length turned out to be very cumbersome. The successful modification of the Feshbach method was suggested by V. Balashov et al [2], and it was applied by us for the description of resonances in electron–atom scattering. In spite of essential simplifications this method offers excellent results.

Let us consider the application of this modification to the description of resonances in electron–atom collisions. The problem of the nonrelativistic scattering of electrons on atoms is reduced to the problem of solving the Schrödinger equation

$$(H-E)\Psi=0, \tag{1}$$

where H is the Hamiltonian of the "incident electron + target" system. Ψ is the wave function.

The starting point of the approximation in question is the following construction for wave function

$$\Psi = \sum_{\gamma} A[\varphi_\gamma F_\gamma] + \sum_{\mu} \Lambda_\mu \Phi_\mu , \tag{2}$$

where φ_γ is the wave function of atom in γ state, A is an operator of antisymmetrization, the function F_γ describes the motion of a scattered electrons in γ-channel, Φ_μ are the wave functions of AIS. These wave functions Φ_μ are built on a limited basis of atomic wave functions Θ_μ. Though basis wave functions Θ_μ are taken in a one-electron approximation, the interelectron correlations are taken into account in Φ_μ. This expansion is quite similar to that used in the resonating group method for the description of resonance nuclear scattering as it was proposed by Wildermuth and Tang [1].

From the Schrödinger equation in a projected form

$$\langle \delta\Psi | H - E | \Psi \rangle = 0 \tag{3}$$

the system of equations follows, which in a compact matrix notation can be written in a form

$$LF = -X\Lambda, \tag{4}$$

$$\langle X | F \rangle + (\varepsilon - E)\Lambda = 0, \tag{5}$$

where L is an integro-differential operator, X is matrix element $X = \langle \varphi | H | \Phi \rangle$.

Let us write the solution of (4) in a form

$$F(r) = F^{\circ}(r) + \int dr' G(r, r') X(r') \Lambda, \tag{6}$$

where $F^{\circ}(r)$ is regular at the origin ($r=0$) solution of (4) without right side and $G(r, r')$ is the corresponding Green matrix.

For finding Λ it would be necessary to solve the system of linear nonhomogeneous equations (5). At this stage the main, so-called diagonalization assumption is introduced. According to this assumption one can neglect the nondiagonal terms $\langle X_\mu | G | X_\nu \rangle, \mu \neq \nu$ or, in other words, one neglects the coupling between different AIS through open channels. This assumption immediately allows one to obtain the expression for Λ and the transition matrix T in Breit–Wigner form [3]. Diagonalizational assumption means deviation from the original Feshbach method or resonating group method for that matter. But it has a certain advantage because of the considerable simplification of numerical calculations.

This method has been already successfully applied for the description of resonance photoionization [2] and resonance scattering of electrons on atoms and ions [3].

As an illustration of the application of this method we show in Figs 1 and 2 the results of total cross-section calculations of the excitation of the $2p$ level of He^+ and the $3p\ ^2P^0$ level of Mg^+. In the energy behaviour of the curves one can clearly observe the clear-cut manifestation of resonances, which are due to AIS converging to the thresholds $n=3$ of He^+ and $4s\ ^2S$ of Mg^+.

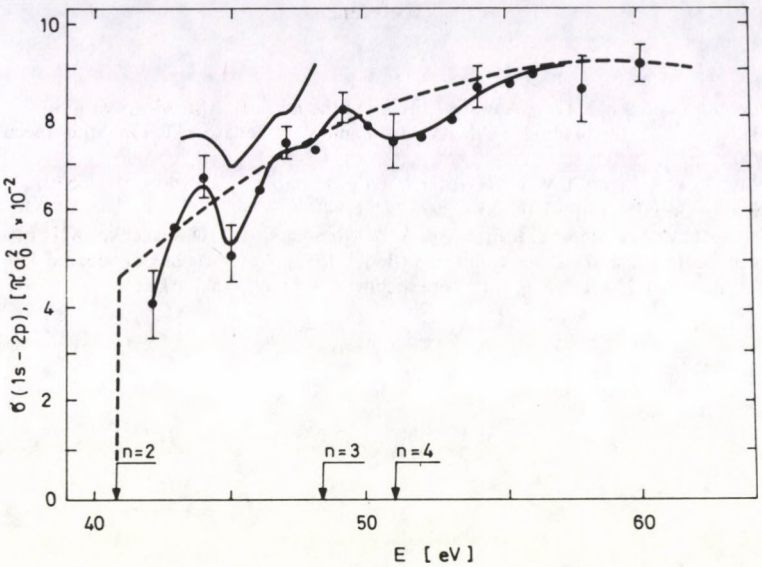

Fig. 1. Total cross-section of excitation of $2p$ level of He^+ by electron impact: ♦ — experiment [4]; ——— — averaged experiment [4]; – – – – — present calculation

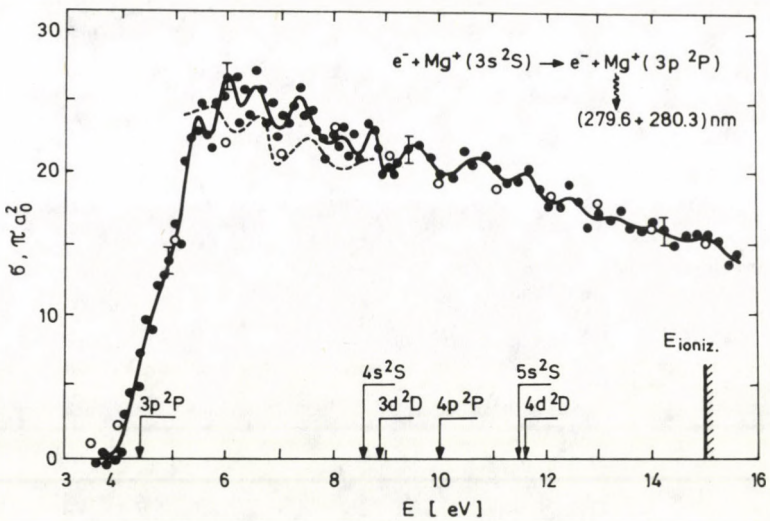

Fig. 2. Total cross-section of excitation of $3p\ ^2P^0$ level of Mg^+ by electron impact: – – – – — present calculation; ● — experiment [5]; ——— — averaged experiment [5]; ○ — experiment [6]

References

1. K. Wildermuth and Y. C. Tang, A unified theory of the nucleus, Mir, Moscow, 1980.
2. V. V. Balashov, S. I. Grishanova, I. M. Kruglova and V. S. Senashenko. Opt. and Spectr. (USSR), *28*, 859, 1970.
3. M. I. Haysak, V. I. Lengyel, V. T. Navrotsky and E. P. Sabad, Ukr. Phys. J. (USSR), *27*, 1617, 1982.
4. Y. N. Semenyuk, Ukr. Phys. J. (USSR), *29*, 1252, 1984.
5. I. P. Zapesochny, A. I. Imre, V. I. Frontov, A. N. Gomonay, A. I. Dashchenko, XIII Int. Conf. on the Physics of Electronic and Atomic Collisions (Berlin, 1983): Abstracts of Contributed Papers, p. 743.
6. V. A. Kel'man, A. I. Dashchenko, I. P. Zapesochny, A. I. Imre, Dokl. Akad. Nauk. SSSR (USSR)., *220*, 65, 1975.

Acta Physica Hungarica, 63 (3—4), pp. 381—383 (1988)

BOOK REVIEWS

High-Energy Physics, Edited by Stephan L. Mintz and Arnold Perlmutter, Plenum Press, New York and London, 1985

This volume contains the papers submitted to the High Energy Physics portion of the 1983 Orbis Scientiae (Miami) dedicated to the eightieth year of Professor P.A.M. Dirac.

The study of high-energy physics continues on many fronts. In this volume, experts report on the latest exciting and productive advances in their areas of specialization, including magnetic monopoles, proton decay, very-high-energy colliders, glueballs, supersymmetric couplings, supergravity grand unification, Kaluza–Klein theories, the $N = 4$ model, gravitational waves, gravitational gauge fields.

High-Energy Physics will be valuable to those working in the field, as well as those working in theoretical and mathematical physics, statistical mechanics, astronomy, cosmology, and space physics.

I. Lovas

Density Functional Methods in Physics, Edited by Reiner M. Dreizler and Joao da Providencia, NATO ASI Series B, Physics; Vol. 123, Plenum Press, New York and London, 1985, pp. 533.

The idea of trying to represent the ground state (and perhaps some of the excited states as well) of atomic, molecular, and solid state systems in terms of the diagonal part of the one-body reduced density matrix is an old one.

At the NATO Summer School (Alcabideche, Portugal, 1983) on "Density Functional Methods in Physics" substantial progress was reported in the development of the general principles and the basic formalism as well as an impressive number of applications, including the fields of nuclear physics in addition to the traditional domains.

The proceedings volume contains all the main lectures presented at the School as well as two of the four short contributions offered.

The first three lectures address mainly the mathematical foundations. This is continued in the fourth, where an existence theorem for time dependent density functional methods is presented. In the fourth lecture we also find the transition to the discussion of atomic and molecular system, which is continued in the subsequent three lectures. Solid state applications as well as further insight into the structure of the theory are found in the following three lectures. After an interlude on hadronic systems, the concluding lectures deal with a variety of aspects from the world of nuclear physics and the corresponding development of the general formalism. Each lecture cites detailed references.

This book is recommended to physicists and quantum chemists.

I. Nagy

GEORGE L. TRIGG: *Experimente der modernen Physik.* Übersetzung aus dem Englischen: K. H. Heinig und H. R. Kissener, Akademie-Verlag, Berlin, 1984, 128 Seiten

Der Titel ist irreführend, denn wie die Einleitung besagt, handelt es sich nicht um Experimente der letzten Jahren, sondern um solche, die die moderne Physik unterstützen. In diesem Taschenbuch sind die grundlegenden Experimente in neun Kapiteln zusammengefasst.

Der Ursprung der Quantenkonzeption. In diesem Kapitel wird die erste experimentelle Arbeit behandelt, die die Formel des Emissionsvermögens der schwarzen Körper überprüft. Durch die Ergebnisse von Lummer und Pringsheim angeregt, modifizierte Planck seine eigene, theoretische Arbeit und begründete seine Gleichung im Dezember 1900. Bei der Einfügung der Vorstellungen von Boltzmann in seine Theorie fand er, dass die Energie eines Oszillators ein ganzzahliges Vielfaches einer Grundeinheit sein muss, die proportional zur Frequenz ist. Das resultierende Strahlungsgesetz beschreibt die experimentellen Ergebnisse sehr gut.

Die Elementenumwandlung. Mit der Radioaktivität, entdeckt durch Becquerel i. J. 1896 liess sich später nachweisen, dass das Atom eine Struktur besitzt. Dieses Kapitel behandelt die, von Rutherford und Soddy entdeckte Änderung der Natur eines Atoms. Die Untersuchung begann mit der seltsamen Veränderlichkeit der Intensität der Thoriumstrahlung mit Hilfe der hervorgerufenen elektrischen Entladung. Die Apparatur von Rutherford und Soddy zur Untersuchung der Thoriumemanation wird ausführlich beschrieben. Auf diesem, von beiden Forschern gefundenen Weg leitete Soddy 10 Jahre später die Gesetze der radioaktiven Umwandlung in der heutigen Form ab.

Die Existenz der Atome. Ende des 19. Jahrhunderts gab es keine zwingende Notwendigkeit, an die Existenz von Atomen zu glauben. Die Zweifel der Skeptiker wurden durch eine einzige Forschungsarbeit von Perrin beseitigt, für die Perrin im Jahre 1926 den Nobelpreis für Physik erhielt. Im Jahre 1827 entdeckte der Botaniker Brown die nach ihm benannte Erscheinung. Diejenigen, die diese Erscheinung untersuchten, gelangten zu der Schlussfolgerung, sie müsse molekularen Ursprungs sein. Nach Perrin lässt sich durch die Brownsche Bewegung auf die Existenz von Molekülen schliessen. Ohne quantitative Beweise, wie sie auch Perrin liefert, wären die Argumente wertlos. Die Experimente waren einfach: In zwei verschiedenen Höhen einer Emulsion aus Teilchen bekannter Grösse und Dichte waren bei konstanter Temperatur die Konzentrationen zu bestimmen. Die nun noch zu bestimmende Grösse war der Teilchenradius. Auch hierfür fand Perrin mehrere Messmethoden um eine Kontrolle zu haben. Im letzten Teil seiner Arbeit gibt er andere Methoden zur Bestimmung der Avogadroschen Zahl bekannt. Alle Methoden liefern Ergebnisse, die mit seinen eigenen vergleichbar sind.

Der Atomkern. Das Atom galt seit den Experimenten von Rutherford und Soddy nicht mehr als unveränderlich, aber keine Untersuchung sagte etwas über die Atomstruktur aus. Entscheidende Entwicklung war die Untersuchung der Streuung von α Teilchen, die Geiger und Marsden unter der Leitung von Rutherford durchführten. Der Apparat von Geiger und Marsden, sowie die wichtigsten Ergebnisse werden bekannt gegeben. Rutherfords Theorie besagt, dass die Streuung unterschiedlich schneller α Teilchen umgekehrt proportional zur vierten Potenz der Geschwindigkeit ist. Geiger und Marsden bestätigen diese Theorie. Das Atom mit einem Kern hatte sich als Realität erwiesen.

Stösse von Elektronen mit Atomen. Zu Beginn dieses Jahrhunderts wurden zahlreiche Messungen der Ionisationspotentiale für verschiedene Gase durchgeführt, so auch von Franck und Hertz. Für verschiedene Elemente bestimmten sie Grössen, die sie für Ionisationspotentiale hielten. Ursprünglich beabsichtigten die beiden Wissenschaftler eine vermutete Korrelation der Ionisationspotentiale mit den Atomradien nachzuweisen. Die Zunahme des Kollektorstroms hatte folgende Ursache: Die Atome oder Moleküle wurden durch die einfallenden Elektronen in einen höheren Energiezustand angeregt und emittierten Strahlung. Diese Strahlung wiederum löste aus der Kollektorplatte Fotoelektronen aus. Es gilt offenbar für ein atomares System, dass dieses nur in bestimmten Zustanden mit bestimmten diskreten Energiewerten existieren kann. Noch während dieser Experimente übernahm Bohr diese Idee als eines der Grundpostulate seiner Atomtheorie.

Der Fotoeffekt. Anfangs galt der Begriff des Quants als ein Aspekt des Verhaltens strahlender Oszillatoren und nicht als Merkmal der Strahlung selbst. Der Quantenbegriff existierte gerade fünf Jahre, als Einstein diese Möglichkeit aufgriff um die eigentümlichen Effekte beim Fotoeffekt zu erklären. Sein Vorschlag zur Erklärung der Erscheinung beruhte auf einer radikalen Erweiterung der ursprünglichen Planckschen Quantenhypothese. Einsteins Vorstellung veranlasste Millikan zu umfassenden Experimenten, deren Ergebnisse 1916 veröffentlicht wurden.

Räumliche Orientierung atomarer Magnete. Eines der Grundpostulate der Bohrschen Atomtheorie war, dass bestimmte dynamische Grössen periodischer Bewegungen nur diskrete Werte annehmen können. Ein merkwürdiges Ergebnis, das die Anwendung dieser Regel brachte, ist die Erscheinung, die als „Räumliche Quantisierung" bekannt wurde. Der Drehimpulsvektor des Atoms, das sich in einem magnetischen Feld befindet, kann nur bestimmte, diskrete Orientierungswinkel bezüglich der Feldrichtung bilden. In einem inhomogenen Magnetfeld erfährt ein magnetischer Dipol nicht nur ein Drehmoment, sondern auch eine Kraft, deren Betrag vom Winkel zwischen dem Dipol und dem Gradienten des Magnetfeldes abhängt. Wenn die Atommagnete nur in bestimmten Richtungen orientiert sein können, dann sind die Ablenkungen auf einige Werte beschränkt und der Strahl wird in mehrere Teile aufgespalten. Diesen Effekt beobachtete Stern, der seine Analyse zur Veröffentlichung einreichte und mit seinem Mitarbeiter Gerlach Experimente durchführte. Die Diskussion zeigte, dass das Ergebnis klar zugunsten der Quantenhypothese entscheidet, die im Gegensatz zum klassischen Verhalten steht.

Teilcheneigenschaften des Lichtes. In der Maxwellschen Theorie war ein Mechanismus für die

Streuung elektromagnetischer Wellen gut vorstellbar. Das zeitabhängige elektrische Feld der Welle regte die Elektronen im streuenden Medium zu erzwungenen Schwingungen an und die Elektronen emittierten ihrerseits Strahlung. Diese Theorie stiess auf zunehmende Schwierigkeiten, z. B. dass die Strahlung eine andere Frequenz als die Einfallende besass. Compton schlug vor, die Konzeption des Quants zur Beschreibung der Streuung anzuwenden und baute auf dieser Grundlage eine Theorie auf. Der wichtigste Schritt war die Ableitung der Beziehung zwischen den Wellenlängen der einfallenden und der gestreuten Welle und dem Streuwinkel.

Welleneigenschaften der Materie. Ende 1924 war die Vorstellung, dass das Verhalten elektromagnetischer Strahlung sowohl wellenartige als auch teilchenartige Aspekte zeigt, allgemein akzeptiert. Damals hatte Louis de Broglie den genialen Einfall: Warum sollte dasselbe nicht auch für die Materie gelten? Davisson und sein Mitarbeiter Germer führten einige Routinemessungen über die Streuung von Elektronen an einigen grossen Nickelkristallen durch. Sie entdeckten etwas Signifikantes, das sie nicht gesucht hatten und waren bereit, Ergebnisse zu akzeptieren, die den Erwartungen nicht entsprachen. Sie wendeten die Beugungsgitterformel auf die Elektronenstrahlen an und erhielten dabei Wellenlängen, die im allgemeinen gut mit den Werten nach de Broglie's Beziehung übereinstimmten. Eine Frage blieb jedoch offen. Es war noch denkbar, dass das in diesen Experimenten gefundene wellenartige Verhalten für Elektronen spezifisch sei. Zeigte vielleicht eine andere Materie die gleichen Eigenschaften? Die Antwort darauf wurde 1930 gefunden, als Stern und seine Mitarbeiter nachwiesen, dass Atome und Moleküle ebenfalls wellenartige Eigenschaften besassen, wobei die Wellenlänge durch de Broglie's Beziehung gegeben war.

In den beiden Anhängen wird die Beschreibung eines Quadrantenelektrometers und eine Bemerkung über die numerische Bezeichnung für Kristalle gegeben.

T. Mátrai

Manuscript received by Akadémiai Kiadó:
22 August 1986
Manuscript received by the Printers:
1 September 1986
Date of publication 30 November 1988

PRINTED IN HUNGARY

Akadémiai Kiadó és Nyomda Vállalat, Budapest

NOTES TO CONTRIBUTORS

I. PAPERS will be considered for publication in Acta Physica Hungarica only if they have not previously been published or submitted for publication elsewhere. They may be written in English, French, German or Russian.

Papers should be submitted to

Prof. I. Kovács, Editor
Department of Atomic Physics, Technical University
1521 Budapest, Budafoki út 8, Hungary

Papers may be either articles with abstracts or short communications. Both should be as concise as possible, articles in general not exceeding 25 typed pages, short communications 8 typed pages.

II. MANUSCRIPTS

1. Papers should be submitted in three copies.
2. The text of papers must be of high stylistic standard, requiring minor corrections only.
3. Manuscripts should be typed in double spacing on good quality paper, with generous margins.
4. The name of the author(s) and of the institutes where the work was carried out should appear on the first page of the manuscript.
5. Particular care should be taken with mathematical expressions. The following should be clearly distinguished, e.g. by underlining in different colours: special founts (italics, script, bold type, Greek, Gothic, etc.); capital and small letters; subscripts and superscripts, e.g. x^2, x_3; small *l* and l; zero and capital O; in expressions written by hand: *e* and *l*, *n* and *u*, *v* and v, etc.

A List of Symbols on a separate sheet should be attached to each paper.

6. References should be numbered serially and listed at the end of the paper in the following form: J. Ise and W. D. Fretter, Phys. Rev., *76*, 933, 1949.

For books, please give the initials and family name of the author(s), title, name of publisher, place and year of publication, e.g.: J. C. Slater, Quantum Theory of Atomic Structures, I. McGraw-Hill Book Company, Inc., New York, 1960.

References should be given in the text in the following forms: Heisenberg [5] or [5].

7. Captions to illustrations should be listed on a separate sheet, not inserted in the text.
8. In papers submitted to Acta Physica all measures should be expressed in SI units.

III. ILLUSTRATIONS AND TABLES

1. Each paper should be accompanied by three sets of illustrations, one of which must be ready for the blockmaker. The other sets attached to the copies of the manuscript may be rough drawings in pencil or photocopies.
2. Illustrations must not be inserted in the text.
3. All illustrations should be identified in blue pencil by the author's name, abbreviated title of the paper and figure number.
4. Tables should be typed on separate pages and have captions describing their content. Clear wording of column heads is advisable. Tables should be numbered in Roman numerals (I, II, III, etc.).

IV. RETURN OF MATERIAL

Owing to high postage costs, the Editorial Office cannot undertake to return *all* material not accepted for any reason for publication. Of papers to be revised (for not being in conformity with the above Notes or other reasons) only *one* copy will be returned. Material rejected for lack of space or on account of the Referees' opinion will not be returned to authors outside Europe.

Periodicals of the Hungarian Academy of Sciences are obtainable at the following addresses:

AUSTRALIA
C.B.D. LIBRARY AND SUBSCRIPTION SERVICE
Box 4886, G.P.O., *Sydney N.S.W. 2001*
COSMOS BOOKSHOP, 145 Ackland Street
St. Kilda (Melbourne), Victoria 3182

AUSTRIA
GLOBUS, Höchstädtplatz 3, *1206 Wien XX*

BELGIUM
OFFICE INTERNATIONAL DES PERIODIQUES
Avenue Louise, 485, *1050 Bruxelles*
E. STORY-SCIENTIA P.V.B.A.
P. van Duyseplein 8, *9000 Gent*

BULGARIA
HEMUS, Bulvar Ruszki 6, *Sofia*

CANADA
PANNONIA BOOKS, P.O. Box 1017
Postal Station "B", *Toronto, Ont. M5T 2T8*

CHINA
CNPICOR, Periodical Department, P.O. Box 50
Peking

CZECHOSLOVAKIA
MAD'ARSKA KULTURA, Národni třida 22
115 66 Praha
PNS DOVOZ TISKU, Vinohradská 46, *Praha 2*
PNS DOVOZ TLAČE, *Bratislava 2*

DENMARK
EJNAR MUNKSGAARD, 35, Nørre Søgade
1370 Copenhagen K

FEDERAL REPUBLIC OF GERMANY
KUNST UND WISSEN ERICH BIEBER
Postfach 46, *7000 Stuttgart 1*

FINLAND
AKATEEMINEN KIRJAKAUPPA, P.O. Box 128
00101 Helsinki 10

FRANCE
DAWSON-FRANCE S.A., B.P. 40, *91121 Palaiseau*
OFFICE INTERNATIONAL DE DOCUMENTATION ET LIBRAIRIE, 48 rue Gay-Lussac
75240 Paris, Cedex 05

GERMAN DEMOCRATIC REPUBLIC
HAUS DER UNGARISCHEN KULTUR
Karl Liebknecht-Straße 9, *DDR-102 Berlin*

GREAT BRITAIN
BLACKWELL'S PERIODICALS DIVISION
Hythe Bridge Street, *Oxford OX1 2ET*
BUMPUS, HALDANE AND MAXWELL LTD.
Cowper Works, *Olney, Bucks MK46 4BN*
COLLET'S HOLDINGS LTD., Denington Estate,
Wellingborough, Northants NN8 2QT
WM DAWSON AND SONS LTD., Cannon House
Folkstone, Kent CT19 5EE
H. K. LEWIS AND CO., 136 Gower Street
London WC1E 6BS

GREECE
KOSTARAKIS BROTHERS INTERNATIONAL BOOKSELLERS, 2 Hippokratous Street, *Athens-143*

HOLLAND
FAXON EUROPE, P.O. Box 167
1000 AD Amsterdam
MARTINUS NIJHOFF B. V.
Lange Voorhout 9–11, *Den Haag*
SWETS SUBSCRIPTION SERVICE
P.O. Box 830, 2160 Sz Lisse

INDIA
ALLIED PUBLISHING PVT. LTD.
750 Mount Road, *Madras 600002*
CENTRAL NEWS AGENCY PVT. LTD.
Connaught Circus, *New Delhi 110001*
INTERNATIONAL BOOK HOUSE PVT. LTD.
Madame Cama Road, *Bombay 400039*

ITALY
D. E. A., Via Lima 28, *00198 Roma*
INTERSCIENTIA, Via Mazzé 28, *10149 Torino*
LIBRERIA COMMISSIONARIA SANSONI
Via Lamarmora 45, *50121 Firenze*
SANTO VANASIA, Via M. Macchi 58
20124 Milano

JAPAN
KINOKUNIYA COMPANY LTD.
Journal Department, P.O. Box 55
Chitose, *Tokyo 156*
MARUZEN COMPANY LTD., Book Department
P.O. Box 5050 Tokyo International, *Tokyo 100-31*
NAUKA LTD., Import Department
2-30-19 Minami Ikebukuro, Toshima-ku, *Tokyo 171*

KOREA
CHULPANMUL, *Phenjan*

NORWAY
TANUM-TIDSKRIFT-SENTRALEN A.S.
Karl Johansgata 43, *1000 Oslo*

POLAND
WĘGIERSKI INSTYTUT KULTURY
Marszalkowska 80, *00-517 Warszawa*
CKP I W, ul. Towarowa 28, *00-958 Warszawa*

ROUMANIA
D. E. P., *Bucuresti*
ILEXIM, Calea Grivitei 64–66, *Bucuresti*

SOVIET UNION
SOYUZPECHAT — IMPORT, *Moscow*
and the post offices in each town
MEZHDUNARODNAYA KNIGA, *Moscow G-200*

SPAIN
DIAZ DE SANTOS Lagasca 95, *Madrid 6*

SWEDEN
ESSELTE TIDSKRIFTSCENTRALEN
Box 62, *101 20 Stockholm*

SWITZERLAND
KARGER LIBRI AG, Petersgraben 31, *4011 Basel*

USA
EBSCO SUBSCRIPTION SERVICES
P.O. Box 1943, *Birmingham, Alabama 35201*
F. W. FAXON COMPANY, INC.
15 Southwest Park, *Westwood Mass. 02090*
MAJOR SCIENTIFIC SUBSCRIPTIONS
1851 Diplomat, P.O. Box 819074,
Pallas, Tx. 75381-9074
READ-MORE PUBLICATIONS, INC.
140 Cedar Street, *New York, N. Y. 10006*

YUGOSLAVIA
JUGOSLOVENSKA KNJIGA, Terazije 27, *Beograd*
FORUM, Vojvode Mišića 1, *21000 Novi Sad*

Index: 26.022